FRONTIERS IN SEAFLOOR GEODESY

EDITED BY: Ryota Hino, Keiichi Tadokoro and Laura Wallace
PUBLISHED IN: Frontiers in Earth Science

frontiers Research Topics

ISSN 1664-8714
ISBN 978-2-88971-423-0
DOI 10.3389/978-2-88971-423-0

About Frontiers

Frontiers is more than just an open-access publisher of scholarly articles: it is a pioneering approach to the world of academia, radically improving the way scholarly research is managed. The grand vision of Frontiers is a world where all people have an equal opportunity to seek, share and generate knowledge. Frontiers provides immediate and permanent online open access to all its publications, but this alone is not enough to realize our grand goals.

Frontiers Journal Series

The Frontiers Journal Series is a multi-tier and interdisciplinary set of open-access, online journals, promising a paradigm shift from the current review, selection and dissemination processes in academic publishing. All Frontiers journals are driven by researchers for researchers; therefore, they constitute a service to the scholarly community. At the same time, the Frontiers Journal Series operates on a revolutionary invention, the tiered publishing system, initially addressing specific communities of scholars, and gradually climbing up to broader public understanding, thus serving the interests of the lay society, too.

Dedication to Quality

Each Frontiers article is a landmark of the highest quality, thanks to genuinely collaborative interactions between authors and review editors, who include some of the world's best academicians. Research must be certified by peers before entering a stream of knowledge that may eventually reach the public - and shape society; therefore, Frontiers only applies the most rigorous and unbiased reviews.
Frontiers revolutionizes research publishing by freely delivering the most outstanding research, evaluated with no bias from both the academic and social point of view. By applying the most advanced information technologies, Frontiers is catapulting scholarly publishing into a new generation.

What are Frontiers Research Topics?

Frontiers Research Topics are very popular trademarks of the Frontiers Journals Series: they are collections of at least ten articles, all centered on a particular subject. With their unique mix of varied contributions from Original Research to Review Articles, Frontiers Research Topics unify the most influential researchers, the latest key findings and historical advances in a hot research area! Find out more on how to host your own Frontiers Research Topic or contribute to one as an author by contacting the Frontiers Editorial Office: frontiersin.org/about/contact

FRONTIERS IN SEAFLOOR GEODESY

Topic Editors:
Ryota Hino, Tohoku University, Japan
Keiichi Tadokoro, Nagoya University, Japan
Laura Wallace, University of Texas at Austin, United States

Citation: Hino, R., Tadokoro, K., Wallace, L., eds. (2021). Frontiers in Seafloor Geodesy. Lausanne: Frontiers Media SA. doi: 10.3389/978-2-88971-423-0

Table of Contents

frontiers in Earth Science

EDITORIAL
published: 09 August 2021
doi: 10.3389/feart.2021.744217

Editorial: Frontiers in Seafloor Geodesy

Ryota Hino[1]*, *Keiichi Tadokoro*[2] *and Laura Wallace*[3,4]

[1]Graduate School of Science, Tohoku University, Sendai, Japan, [2]Earthquake and Volcano Research Center, Graduate School of Environmental Studies, Nagoya University, Nagoya, Japan, [3]Institute of Geophysics, University of Texas at Austin, Austin, TX, United States, [4]GNS Science, Lower Hutt, New Zealand

Keywords: GNSS-acoustic, seafloor pressure, ocean models, differential bathymetry, tilt and strain observations

Editorial on Research Topic

Frontiers in Seafloor Geodesy

Seafloor geodetic methods, including techniques such as GNSS-Acoustic surveys (and other forms of acoustic ranging), and monitoring of changes in seafloor pressure, and downhole pressure allow for measuring crustal deformation over Earth's vast areas that are covered by water and therefore inaccessible to traditional geodetic techniques developed for onshore use. Since the 1980s when the concept of seafloor displacement monitoring with precise acoustic ranging was proposed, significant efforts have been made to implement and improve seafloor geodetic measurements to reveal the motion and deformation of oceanic tectonic plates, earthquake processes at subduction zones and other plate boundaries, and the deformation of submarine volcanoes and spreading centers (Bürgmann and Chadwell, 2014). Although remarkable technological progress has been made to increase the precision and scales of observations with improving the reliability and cost-effectiveness of the instrumentation, there still remain a number of difficulties to overcome in seafloor geodetic observations. This Research Topic gathers field experiments and/or new techniques and perspectives obtained through a range of data acquisition efforts in order to leverage them to advance in seafloor geodetic research.

The GNSS-Acoustic technique obtains a precise location of seafloor transponder arrays (often deployed on benchmarks) by combining locations of an observation platform on the sea surface determined by GNSS observations and acoustic ranging between the transponders and the platform. Repeated measurements of the benchmark positions over years allow centimeter-level resolution of horizontal tectonic motions of the seafloor. Measurements of coseismic and postseismic deformation near the hypocenters of offshore earthquakes (e.g., Tadokoro et al., 2006), including those of the 2011 Tohoku Earthquake (Kido et al., 2011; Sato et al., 2011; Tomita et al., 2017), and ~cm/yr resolution of interseismic deformation field at the Peru-Chile Trench (Gagnon et al., 2005) and the offshore Nankai Trough (Yokota et al., 2016) are pronounced achievements of the seafloor observations of this kind. Chen et al. (this issue) reported crustal deformation related to rifting at the Okinawa trough, which is in the early stage of backarc opening. They utilize GNSS-A measurements acquired over 10 years, to reveal rifting rates at ~43 mm/yr.

In the development of the GNSS-Acoustic technique, much effort has been made to increase the accuracies of underwater acoustic ranging. Watanabe et al. (this issue) describe a technique of jointly estimating benchmark locations and sound speed structure in the ocean. This technique is routinely used by the Japan Coast Guard in their GNSS-A surveys. In a similar vein, Honsho et al. (this issue) applied a novel cross correlation method to acoustic ranging to reduce uncertainties in two-way travel time measurements.

As measurement uncertainties decrease, displacement time series of GNSS-Acoustic surveys are expected to provide not only a long-term average rate of deformation, but also to reveal temporal fluctuations in deformation rate associated with episodic tectonic motions (Yokota and Ishikawa, 2020), such as Slow Slip Events (SSEs). However, reliability of transient deformation event detections is

OPEN ACCESS

Edited and reviewed by:
Carolina Lithgow-Bertelloni, UCLA Department of Earth, Planetary, and Space Sciences, United States

***Correspondence:**
Ryota Hino
hino@tohoku.ac.jp

Specialty section:
This article was submitted to Solid Earth Geophysics, a section of the journal Frontiers in Earth Science

Received: *20 July 2021*
Accepted: *27 July 2021*
Published: *09 August 2021*

Citation:
Hino R, Tadokoro K and Wallace L (2021) Editorial: Frontiers in Seafloor Geodesy. Front. Earth Sci. 9:744217. doi: 10.3389/feart.2021.744217

not solely dependent on the measurement accuracies, but also relies in an increased temporal frequency of repeated measurements, demanding technological developments to increase the efficiency of field measurements. Ishikawa et al. (this issue) review how onboard instrumentation and survey strategies have been improved by the Japanese Coast Guard and Nakamura et al. (this issue) evaluate optimum survey geometries, to improve of observational efficiencies. Utilizing unmanned craft equipped with navigation and acoustic ranging systems of equivalent quality to those on research ships, as reported by Sakic et al., Iinuma et al. and Tadokoro et al. (this issue) helps to decrease costs of each survey and thus increase the number of GNSS-Acoustic surveys that can be undertaken, potentially even moving towards continuous, real-time measurements (Tadokoro et al., this issue).

Recent success in monitoring spatio-temporal variation of interplate slip rates along subduction zones is a societally important motivation for geoscientists to build offshore geodetic monitoring networks at largely un-instrumented offshore subduction zones. Murakami et al. (this issue) demonstrate the need for GNSS-Acoustic observations to evaluate interplate coupling strength off the Hokkaido, Japan, where an interplate earthquakes with destructive tsunami is considered to be impending based on the paleotsunami geological research (Ioki and Tanioka, 2016).

Vertical displacement on the seafloor can be detected as a change in water pressure. As precise, low-power, and robust pressure sensors are now widely available, small Ocean Bottom Pressure Recorders (OBPRs) have been developed which can free-fall from a ship (to settle on the seafloor) and recovered with acoustic release systems, following the designs of Ocean Bottom Seismographs (OBSs). Seafloor deformation associated with various tectonic phonemena have been recorded by 1–2 years deployment of OBPRs, such as the pre- co- and post-seismic deformations associated with the 2011 Tohoku Earthquake (e.g., Iinuma et al., 2012; Iinuma et al., 2016), Slow Slip Events (SSEs) on the subduction interfaces (Wallace et al., 2016; Sato et al., 2017), as well as inflation and deflation associated with submarine volcanic eruptions (e.g., Chadwick et al., 2012). Because pressure sensors also detect sea level changes due to tsunami, real-time seafloor pressure monitoring by submarine cabled systems has now been realized in several subduction zones to improve reliability of early tsunami warning immediately after large earthquakes (e.g., Aoi et al., 2020). The pressure records obtained by such seafloor networks are also expected to shed light on vertical tectonic motions on these offshore plate boundaries.

There are two major challenges for seafloor pressure measurements to enhance their ability to detect centimeter-level tectonic motions: removal of long-term instrumental drift intrinsic to pressure sensors, and shorter-term pressure fluctuation caused by oceanographical phenomena. Drift rate of the pressure sensors commonly used for seafloor geodetic applications is order of $1/10^4$ per year of the pressure sensor full range (e.g., Polster et al., 2009), which is equivalent to several cm to tens of cm per year for pressure sensors intended for thousands of meters water depth. The drift rate is much larger than expected rates of vertical motions associated with secular tectonic motions, which are mm to cm/yr. Recent careful laboratory experiments clarify that the drift characteristics is complex, and the rate is dependent on the time history of applied pressure, making it difficult to estimate the drift rate through laboratory tests prior to deployment (Kajikawa and Kobata, 2019). Matsumoto and Araki (this issue) compare drift rates of pressure sensors deployed along the DONET cabled network at the offshore Nankai Trough, with those obtained by pressurization of the same sensors in the laboratory prior to the deployment, to exemplify the difficulty of this approach and to emphasize importance of *in-situ* sensor calibration. Wilcock et al. (this issue) show the viability of a new method of *in situ* calibration (the "A-0-A" method) during a 30 months deployment of this system on the MARS cable beneath Monterey Bay. Their results demonstrate the accuracy of seafloor pressure records corrected by the method is better than $1/10^5$ per year, providing a promising approach to measure secular vertical deformation at plate boundaries with OBPRs.

Short-term oceanographical fluctuations present another major challenge for resolving tectonic deformation with OBPRs. Removal of common mode fluctuations in ocean bottom pressure records from nearby stations (e.g., Ito et al., 2013; Hino et al., 2014) is a common way to address this issue, assuming that the oceanographical pressure variations have spatial similarities over a broader scale than tectonic deformation events. Another approach is to calculate the pressure variations based on ocean circulation models (e.g., Inazu et al., 2012). Dobashi and Inazu (this issue) assess the performance of different global ocean models to predict seafloor pressure at several subduction zones. Their work also demonstrates the importance of incorporating atmospheric pressure changes into the ocean models—they obtain a better agreement between the seafloor pressure data and model predictions. It is clear from this and other studies that integration of physical oceanography is key to improving use of seafloor pressure measurements to reveal tectonic deformation.

This research topic includes three papers providing interpretations of seafloor geodetic records in terms of physical oceanographic processes. Nagao et al. (this issue) discuss how meandering of Kuroshio current influences seafloor pressure recorded along the Nankai Trough based on DONET observations. Hasegawa et al. (this issue) analyzed seafloor pressure and sea surface records using a high-resolution ocean assimilation model and discuss how sea water density anomalies may have significant effects on the seafloor pressure variability. Using the same ocean assimilation model, Yokota et al. (this issue) interpret underwater sound speed structure, estimated during GNSS-A data analyses, and conclude that the sound structure represents local scale heterogeneity which cannot be reproduced by the ocean model.

Measurements of pressure change in the formation beneath the seafloor via subseafloor observatories is promising approach to detect transient crustal deformation with a higher signal-to-noise ratio than other seafloor geodetic methods, including smaller-scale, possibly more frequent, tectonic events than those that can be detected by observations on the seafloor. This technique relies on formation pressure changes as a

proxy for volumetric strain and have provided valuable data set regarding slow slip event (SSE) activity (e.g., Davis et al., 2015; Araki et al., 2017) at offshore subduction zones. Ariyoshi et al. (this issue) report an episodic changes in pore pressure observed at a borehole observatory connected to DONET, as a result of migrating SSEs occurring on the offshore Nankai Trough.

Tilt measurements have a long history as a tool for continuous monitoring of crustal deformation. Owing to the high sensitivity of tiltmeters in the frequency band specific to SSEs, a number of important characteristics of SSEs have been clarified by the tilt observation network covering onshore of SW Japan (e.g., Hirose et al., 2010). To fully realize offshore tilt measurements, extensive efforts have been made. Shiobara et al. (this issue) report the present status of development of a new ocean-bottom tiltmeter, using mass-position of a three-component broadband seismometer with observed data obtained by field trials.

Repeated multibeam bathymetric surveys can provide spatial variations in seafloor deformation over broad area, in contrast to other geodetic measurements that detect a motion at an observing point. Although large uncertainties in measured displacement place limits on the applications of this method, the results of differentiating bathymetric maps before and after the 2011 Tohoku Earthquake constrained the coseismic slip distribution near the Japan Trench owing to the extremely large displacement (tens of meters) by the earthquake (Fujiwara et al., 2011). Fujiwara (this issue) overviews the factors influencing uncertainties of shipboard bathymetry measurements, and suggest ways to enhance resolution as much as possible, and to assess the data quality.

Seafloor geodetic measurements aim to measure crustal deformation in response to tectonic processes, but long-term monitoring of other geophysical parameters is needed to understand the physical processes behind the observed crustal deformation. For example, several studies have shown that fluid migration and hydrological changes within the solid Earth may play significant roles in fault slip processes (Bhattacharya and Viesca, 2019; Warren-Smith et al., 2019). Electromagnetic field measurements are sensitive to the distribution of fluids, and long term-monitoring of this will help to constrain models for the role of fluid migration in the occurrence of tectonic deformation processes. Kasaya et al. (this issue) present a system to measure changes in resistivity and self-potential at the seafloor, applied in this case to a hydrothermal system.

Seafloor geodetic techniques are also being developed for shallow water environments. De Martino et al. (this issue) report on horizontal and vertical crustal deformation associated with volcanic activity at Campi Flegrei Caldera, Italy. They successfully detected deformation using 4 years of GNSS measurements on buoys attached to the seafloor in a shallow (<100 m) water environment. The team also employs a range of other measurements at each buoy (seafloor pressure, ocean bottom seismology) to enhance monitoring ability of this dangerous volcanic system.

Seafloor geodesy is a rapidly emerging field, and is continually revealing new insights into a range of offshore tectonic processes in plate boundary zones. As presented in this research topic, major efforts to improve observational technologies are underway to enhance our detection ability of subsea tectonic motions. In addition to hardware development, it is equally important to distinguish between tectonic seafloor motions and physical oceanographical and/or meteorological variations in seafloor geodetic observations. Acquisition of additional seafloor geodetic and oceanographic observations are necessary to improve our ability to detect offshore tectonic deformation, and collaborations between physical oceanographers and solid Earth scientists will lead to breakthroughs in developing novel methods enhance signal-to-noise ratios of the offshore geodetic observations. We expect that such efforts will also benefit ocean environmental monitoring.

AUTHOR CONTRIBUTIONS

RH wrote this article, while KT and LW provided comments for improvement on this brief overview.

FUNDING

This work was supported partly by JSPS KAKENHI JP19H05596.

ACKNOWLEDGMENTS

We thank Valerio Acocella and Ursula Rabar for having encouraged us submit this Research Topic and for all their support throughout.

REFERENCES

Aoi, S., Asano, Y., Kunugi, T., Kimura, T., Uehira, K., Takahashi, N., et al. (2020). MOWLAS: NIED Observation Network for Earthquake, Tsunami and Volcano. *Earth Planets Space* 72 (1), 126. doi:10.1186/s40623-020-01250-x

Araki, E., Saffer, D. M., Kopf, A. J., Wallace, L. M., Kimura, T., Machida, Y., et al. (2017). Recurring and Triggered Slow-Slip Events Near the Trench at the Nankai Trough Subduction Megathrust. *Science* 356, 1157–1160. doi:10.1126/science.aan3120

Bhattacharya, P., and Viesca, R. C. (2019). Fluid-induced Aseismic Fault Slip Outpaces Pore-Fluid Migration. *Science* 364, 464–468. doi:10.1126/science.aaw7354

Bürgmann, R., and Chadwell, D. (2014). Seafloor Geodesy. *Annu. Rev. Earth Planet. Sci.* 42, 509–534. doi:10.1146/annurev-earth-060313-054953

Chadwick, W. W., Nooner, S. L., Butterfield, D. A., and Lilley, M. D. (2012). Seafloor Deformation and Forecasts of the April 2011 Eruption at Axial Seamount. *Nat. Geosci* 5, 474–477. doi:10.1038/ngeo1464

Davis, E. E., Villinger, H., and Sun, T. (2015). Slow and Delayed Deformation and Uplift of the Outermost Subduction Prism Following ETS and Seismogenic Slip Events beneath Nicoya Peninsula, Costa Rica. *Earth Planet. Sci. Lett.* 410, 117–127. doi:10.1016/j.epsl.2014.11.015

Fujiwara, T., Kodaira, S., No, T., Kaiho, Y., Takahashi, N., and Kaneda, Y. (2011). The 2011 Tohoku-Oki Earthquake: Displacement Reaching the Trench axis. *Science* 334 (6060), 1240. doi:10.1126/science.1211554

Gagnon, K., Chadwell, C. D., and Norabuena, E. (2005). Measuring the Onset of Locking in the Peru-Chile Trench with GPS and Acoustic Measurements. *Nature* 434, 205–208. doi:10.1038/nature03412

Hino, R., Inazu, D., Ohta, Y., Ito, Y., Suzuki, S., Iinuma, T., et al. (2014). Was the 2011 Tohoku-Oki Earthquake Preceded by Aseismic Preslip? Examination of Seafloor Vertical Deformation Data Near the Epicenter. *Mar. Geophys. Res.* 35, 181–190. doi:10.1007/s11001-013-9208-2

Hirose, H., Asano, Y., Obara, K., Kimura, T., Matsuzawa, T., Tanaka, S., et al. (2010). Slow Earthquakes Linked along Dip in the Nankai Subduction Zone: Fig. 1. *Science* 330, 1502. doi:10.1126/science.1197102pmid:2114838410.1126/science.1197102

Iinuma, T., Hino, R., Kido, M., Inazu, D., Osada, Y., Ito, Y., et al. (2012). Coseismic Slip Distribution of the 2011 off the Pacific Coast of Tohoku Earthquake (M9.0) Refined by Means of Seafloor Geodetic Data. *J. Geophys. Res.* 117, a–n. doi:10.1029/2012JB009186

Iinuma, T., Hino, R., Uchida, N., Nakamura, W., Kido, M., Osada, Y., et al. (2016). Seafloor Observations Indicate Spatial Separation of Coseismic and Postseismic Slips in the 2011 Tohoku Earthquake. *Nat. Commun.* 7, 13506. doi:10.1038/ncomms13506

Inazu, D., Hino, R., and Fujimoto, H. (2012). A Global Barotropic Ocean Model Driven by Synoptic Atmospheric Disturbances for Detecting Seafloor Vertical Displacements from *In Situ* Ocean Bottom Pressure Measurements. *Mar. Geophys. Res.* 33, 127–148. doi:10.1007/s11001-012-9151-7

Ioki, K., and Tanioka, Y. (2016). Re-estimated Fault Model of the 17th century Great Earthquake off Hokkaido Using Tsunami deposit Data. *Earth Planet. Sci. Lett.* 433, 133–138. doi:10.1016/j.epsl.2015.10.009

Ito, Y., Hino, R., Kido, M., Fujimoto, H., Osada, Y., Inazu, D., et al. (2013). Episodic Slow Slip Events in the Japan Subduction Zone before the 2011 Tohoku-Oki Earthquake. *Tectonophysics* 600, 14–26. doi:10.1016/j.tecto.2012.08.022

Kajikawa, H., and Kobata, T. (2019). Evaluation and Correction for Long-Term Drift of Hydraulic Pressure Gauges Monitoring Stable and Constant Pressures. *Measurement* 134, 33–39. doi:10.1016/j.measurement.2018.10.051

Kido, M., Osada, Y., Fujimoto, H., Hino, R., and Ito, Y. (2011). Trench-normal Variation in Observed Seafloor Displacements Associated with the 2011 Tohoku-Oki Earthquake. *Geophys. Res. Lett.* 38, a–n. doi:10.1029/2011GL050057

Polster, A., Fabian, M., and Villinger, H. (2009). Effective Resolution and Drift of Paroscientific Pressure Sensors Derived from Long-Term Seafloor Measurements. *Geochem. Geophys. Geosyst.* 10, a–n. doi:10.1029/2009GC002532

Sato, M., Ishikawa, T., Ujihara, N., Yoshida, S., Fujita, M., Mochizuki, M., et al. (2011). Displacement above the Hypocenter of the 2011 Tohoku-Oki Earthquake. *Science* 332, 1395. doi:10.1126/science.1207401

Sato, T., Hasegawa, S., Kono, A., Shiobara, H., Yagi, T., Yamada, T., et al. (2017). Detection of Vertical Motion during a Slow-Slip Event off the Boso Peninsula, Japan, by Ocean Bottom Pressure Gauges. *Geophys. Res. Lett.* 44, 2710–2715. doi:10.1002/2017GL072838

Tadokoro, K., Ando, M., Ikuta, R., Okuda, T., Besana, G. M., Sugimoto, S., et al. (2006). Observation of Coseismic Seafloor Crustal Deformation Due toM7 Class Offshore Earthquakes. *Geophys. Res. Lett.* 33, L23306. doi:10.1029/2006GL026742

Tomita, F., Kido, M., Ohta, Y., Iinuma, T., and Hino, R. (2017). Along-trench Variation in Seafloor Displacements after the 2011 Tohoku Earthquake. *Sci. Adv.* 3, e1700113. doi:10.1126/sciadv.1700113

Wallace, L. M., Webb, S. C., Ito, Y., Mochizuki, K., Hino, R., Henrys, S., et al. (2016). Slow Slip Near the Trench at the Hikurangi Subduction Zone, New Zealand. *Science* 352, 701–704. doi:10.1126/science.aaf2349

Warren-Smith, E., Fry, B., Wallace, L., Chon, E., Henrys, S., Sheehan, A., et al. (2019). Episodic Stress and Fluid Pressure Cycling in Subducting Oceanic Crust during Slow Slip. *Nat. Geosci.* 12, 475–481. doi:10.1038/s41561-019-0367-x

Yokota, Y., and Ishikawa, T. (2020). Shallow Slow Slip Events along the Nankai Trough Detected by GNSS-A. *Sci. Adv.* 6, eaay5786. doi:10.1126/sciadv.aay5786

Conflict of Interest: The authors declare that the research was conducted in the absence of any commercial or financial relationships that could be construed as a potential conflict of interest.

Publisher's Note: All claims expressed in this article are solely those of the authors and do not necessarily represent those of their affiliated organizations, or those of the publisher, the editors and the reviewers. Any product that may be evaluated in this article, or claim that may be made by its manufacturer, is not guaranteed or endorsed by the publisher.

frontiers in Earth Science

TECHNOLOGY AND CODE
published: 30 April 2020
doi: 10.3389/feart.2020.00123

A Marine-Buoy-Mounted System for Continuous and Real-Time Measurment of Seafloor Crustal Deformation

Keiichi Tadokoro[1], Natsuki Kinugasa[1], Teruyuki Kato[2], Yukihiro Terada[3] and Kenjiro Matsuhiro[4]*

[1] Earthquake and Volcano Research Center, Graduate School of Environmental Studies, Nagoya University, Nagoya, Japan, [2] Hot Springs Research Institute of Kanagawa Prefecture, Odawara, Japan, [3] National Institute of Technology, Kochi College, Nankoku, Japan, [4] Technical Center, Nagoya University, Nagoya, Japan

In this paper, we describe the development of a continuous real-time system capable of measuring seafloor crustal deformation using the global satellite navigation system (GNSS)/Acoustic technique and a moored buoy. A program developed was implemented on the buoy to automatically distinguish the onset of a direct acoustic wave even if that wave had been contaminated with reflected waves and to detect the true travel-times by onboard processing rather transferring raw waveforms to the ground base station. This onboard procedure contributed to reduce the data size over a satellite communication. We conducted an operations test for a total of 106 days and found that the acoustic ranging and data transmissions were frequently interrupted by an unstable power supply, resulting in only 21% of the transmitted data being received at the ground base station. Nevertheless, we did not find any problem with continuous acoustic ranging measurement except for the above-mentioned power supply failure.

Keywords: GNSS buoy, GNSS/Acoustic, seafloor crustal deformation, acoustic ranging, technical development

OPEN ACCESS

Edited by:
Takashi Nakagawa, The University of Hong Kong, Hong Kong

Reviewed by:
Motoyuki Kido, Tohoku University, Japan
Pierre Sakic, GFZ German Research Centre for Geosciences, Germany

****Correspondence:***
Keiichi Tadokoro
tad@seis.nagoya-u.ac.jp

Specialty section:
This article was submitted to Solid Earth Geophysics, a section of the journal Frontiers in Earth Science

Received: *12 February 2020*
Accepted: *31 March 2020*
Published: *30 April 2020*

Citation:
Tadokoro K, Kinugasa N, Kato T, Terada Y and Matsuhiro K (2020) A Marine-Buoy-Mounted System for Continuous and Real-Time Measurment of Seafloor Crustal Deformation. Front. Earth Sci. 8:123. doi: 10.3389/feart.2020.00123

INTRODUCTION

A system for seafloor crustal deformation measurement using the global satellite navigation system (GNSS) and acoustic techniques has been developed over the last 20 years (e.g., Spiess et al., 1998; Fujimoto, 2006; Fujita et al., 2006; Tadokoro et al., 2006; Ikuta et al., 2008). The system measures seafloor crustal deformations by making repeated measurements of the positions of several acoustic transponders placed on the seafloor. The system has contributed much to the understanding of various geophysical and seismological phenomena, such as the motions of plates or blocks (Spiess et al., 1998; Chadwell and Spiess, 2008; Yasuda et al., 2017; Chen et al., 2018), plate convergence and interplate coupling (Gagnon et al., 2005; Fujita et al., 2006; Matsumoto et al., 2008; Tadokoro et al., 2012, 2018; Watanabe et al., 2014, 2018; Yasuda et al., 2014; Yokota et al., 2015, 2016; Nishimura et al., 2018; Kimura et al., 2019), co-seismic displacements (Kido et al., 2006, 2011; Tadokoro et al., 2006; Sato et al., 2011a; Iinuma et al., 2012), and post-seismic deformations (Matsumoto et al., 2006; Sato et al., 2011b; Tomita et al., 2015, 2017; Iinuma et al., 2016).

The next objective is to add continuous real-time measurement capability to the system to detect transient events, such as slow slips, and to provide quick response for geodetical events. As

currently implemented, the GNSS/Acoustic measurements are performed using research vessels, which restricts observations during a campaign to long time intervals of more than several months. Recently, the Japan Coast Guard made a significant effort to obtain high frequency measurements with vessels, and successfully detected an off-shore slow slip event with seafloor displacements of about 5–10 cm (Yokota and Ishikawa, 2020). Nevertheless, the observation frequency was still limited to 6–8 times a year. Thus, to achieve the above stated objective, it is essential to develop techniques using alternative sea-surface platforms instead of vessels. Kido et al. (2015, 2018) and Imano et al. (2019) reported the development and operational tests of a GNSS/Acoustic measurement system using a small moored buoy and an autonomous surface vehicle. Other researchers have evaluated the use of the Wave Glider (Liquid Robotics, Inc.) as a novel platform for GNSS/Acoustic measurements (Chadwell, 2013; Sathiakumar et al., 2016).

Our research group was tasked with developing a system capable of continuous real-time measurement of seafloor crustal deformations using the GNSS/Acoustic technique. In this development, a moored buoy was employed as a sea-surface platform as the plan is to eventually integrate the developed system into existing GNSS buoys to enhance their function (Kato et al., 2018). The GNSS buoy system was developed in around 1997 for tsunami early warning purposes, and the particular GNSS buoys under successfully recorded tsunamis generated by the 2001 Peru earthquake, the 2003 Tokachi-Oki earthquake in Japan (Kato et al., 2001), and an earthquake that occurred off the southern coast of Japan in 2004 (Kato et al., 2005). The developed GNSS buoy system has been employed in the nationwide ocean wave information network for ports and harbors (NOWPHAS) wave monitoring system installed along the Japanese coast from approximately 2008. The NOWPHAS provided real-time records of the tsunamis after the *Mw* 9.0 Tohoku-oki earthquake, which were used to significantly upgrade the tsunami warning level after the earthquake (Ozaki, 2011).

In this paper, we describe the developed observation system that was installed on a moored buoy and report the results of acoustic ranging tests.

BUOY-MOUNTED ACOUSTIC RANGING SYSTEM

The buoy-mounted system for the GNSS/Acoustic measurement is composed of the following five components (**Figure 1**): (1) an acoustic ranging controller (developed by Kaiyo Denshi Co., Ltd.) and an acoustic transducer; (2) a signal processing computer (PC Engines alix3d3) running a Linux OS; (3) a GNSS receiver (Hitachi Zosen) equipped with a network solution module (RTNet, GPS Solutions Inc.; Rocken et al., 2004) that employs the precise point positioning with ambiguity resolution (PPP-AR) algorithm (Mervart et al., 2008); (4) a gyroscope (SBG Systems Ellipse-N); and 5) a satellite communications modem. The signal processing computer, GNSS receiver, gyroscope data storage, and satellite modem are all connected in a single Ethernet network via a switching hub and all the data are transmitted in real-time to a ground base station via a satellite link.

The acoustic ranging controller transmits an ultrasonic wave with a signal length of 14.322 ms in the form of a fifth-order *M*-sequence wave with six-cycle carrier waves per unit digit on carrier wave frequency of 12.987 kHz (Tadokoro et al., 2006). The signal timing is synchronized to the 1 PPS (Pulse Per Second) signal and the National Marine Electronics Association (NMEA) recommended minimum (RMC) sentence from a GPS time server (Garmin GPS 19x HVS). The acoustic ranging controller works by receiving commands from the signal processing computer. Once the acoustic ranging controller has received a wake-up command, it starts and automatically continues signal transmission with a fixed interval written in a configuration file in the signal processing computer. It is possible in principle to remotely manage the acoustic ranging controller, including the pinging interval, by modifying the configuration file via satellite communication. The signal processing computer can automatically restart the acoustic ranging controller in the event the power has been temporarily interrupted. The transmitted acoustic signal is received at a pre-installed seafloor transponder. The transponder once records the acoustic signal and returns it to the buoy-mounted acoustic ranging controller after a turn-around-time of 1.024 s to avoid reverberations in the sea. The acoustic ranging controller samples the received signal at 16-bits at a frequency of 500 kHz, then stores the waveform for 64.512 ms before sending the associated data to the USB 2.0 connected signal processing computer at 230,400 bps. After the computer receives the signal, it automatically detects the onset of the returned acoustic signal within about 20 ms using our original programming code described later. The position of the buoy is computed as per the PPP-AR algorithm once per second in real-time by the network module in the GNSS receiver. Note that the PPP-AR positioning in the system relies on precise orbits and clock correction parameters obtained from the regional data of the GNSS Earth Observation Network System (GEONET) operated by the Geospatial Information Authority of Japan (Kato et al., 2017). When tested, the accuracy of our PPP-AR positioning is within a few centimeters for all dimensions including the vertical component in the presence of fixed carrier phase ambiguity (Terada et al., 2015; Kato et al., 2018). As we are more interested in the position of the acoustic transducer rather than that of the GNSS antenna itself, the attitude of buoy is measured using the gyroscope (SBG Systems Ellipse-N) once per second.

The buoy-mounted system was installed on a moored buoy which is anchored 32 km off Cape Ashizuri, Japan (**Figure 2**), on March 28, 2018 for an operational test. The water depth is about 800 m. The buoy, named Kuroshio-Bokujyo No. 18 (**Figure 3**), is operated by the Kochi Prefecture as a floating fish aggregation device and had a diameter of 8 m and a height of more than 8 m above sea level. The system components were installed in waterproof boxes and affixed to the deck of the buoy. The necessary power was generated using five 135-Watt 18-Volt solar panels connected in a series and is stored in 24 V (12 × 2 V) valve-regulated stationary lead-acid batteries with a capacity of 300 Ah (10-h rate). The acoustic ranging controller and GPS time

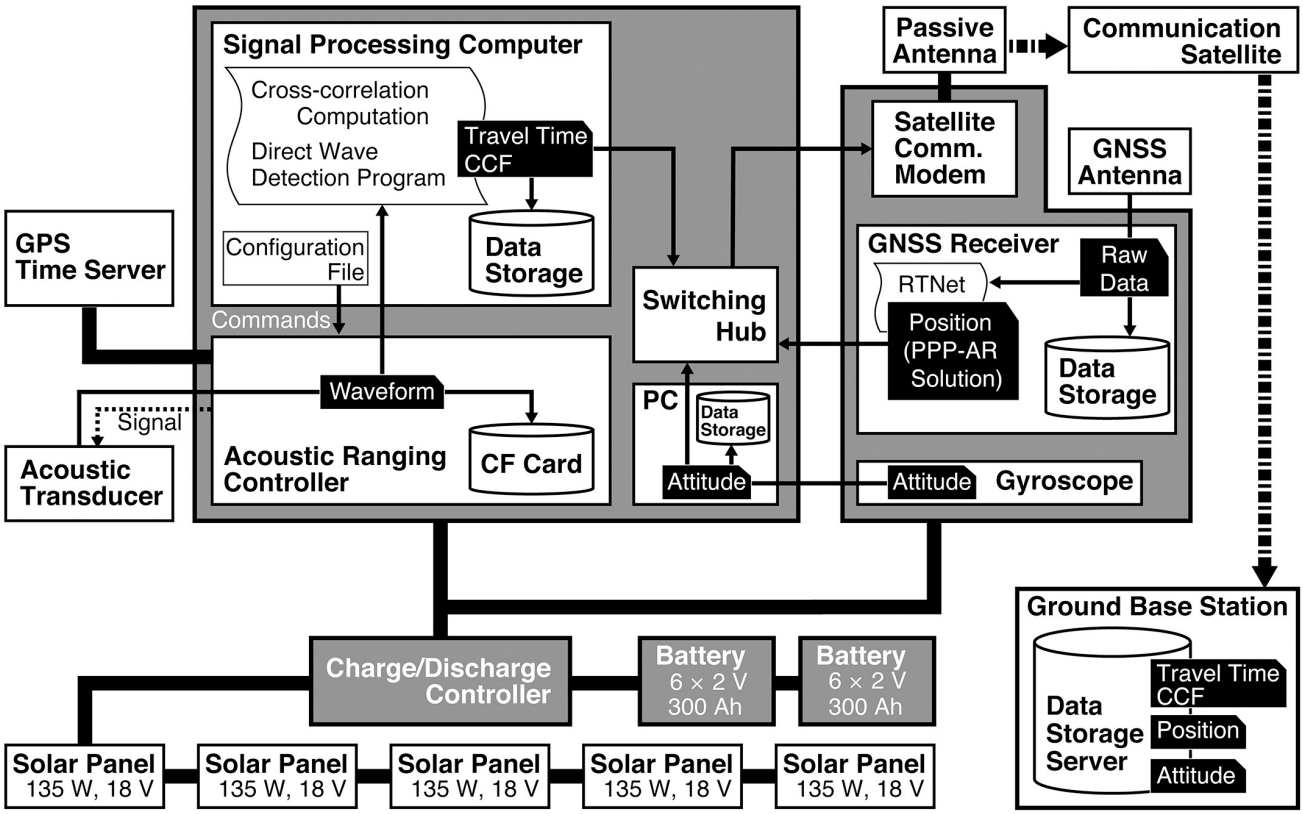

FIGURE 1 | Diagram showing system configuration of buoy-mounted components and data flow. Frames painted gray indicate the waterproof boxes.

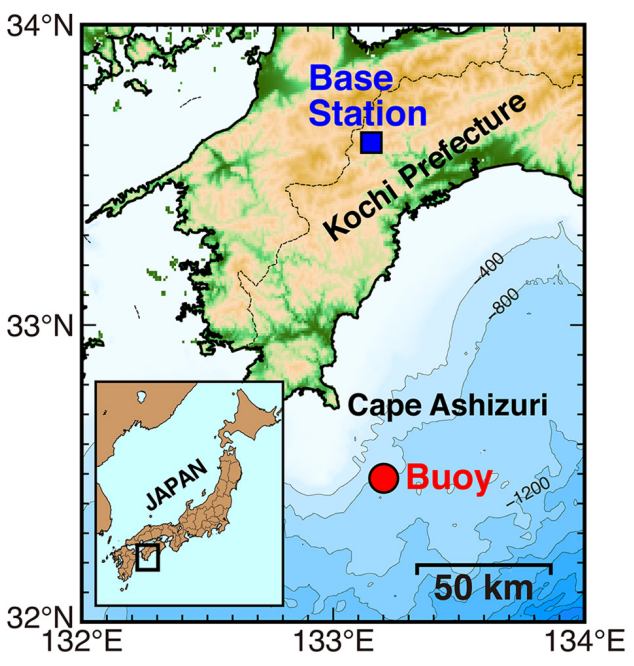

FIGURE 2 | Locations of test site, Kuroshio-Bokujyo No. 18 buoy (red solid circle) and ground base station (blue solid square). Topography and bathymetry data are provided from SRTM30_PLUS (Becker et al., 2009).

server operated at 24 VDC while the other instruments operated at 12 VDC, converted from 24 V using a DC/DC converter. Antennas for the GNSS, Trimble Zephyr 2 Geodetic, and satellite communications were mounted on the top of the buoy. The precise relative position between the acoustic transducer and GNSS antenna was 9.98 m vertically and 4.18 m horizontally in the coordinate system fixed on the buoy.

The acoustic transducer was mounted at about 1.7 m below sea level with a stainless pole rigidly attached to the buoy (**Figure 3B**). To eliminate interference from acoustic waves reflected from the surface of the sea, the acoustic transducer was initially installed in a conical antireflection cover with soundproofing rubber. However, even with these precautions, multiple reflections inside of the cover were frequently detected because the soundproofing rubber became detached probably due to wave vibrations, and this made it difficult to distinguish the onset of the direct wave. To overcome this, the antireflective cover was removed as it was found to significantly reduce the confusion effects of the multiple reflections. The travel-time differences between the direct and sea-surface reflected waves were estimated to be almost 1.3–1.8 ms, which was sufficient to ensure that the direct wave could be easily distinguished even if the acoustic wave was contaminated by sea-surface reflections.

The data recorded on the buoy were transmitted to a ground base station through a commercial communications satellite operated by Thuraya Telecommunications Company where it

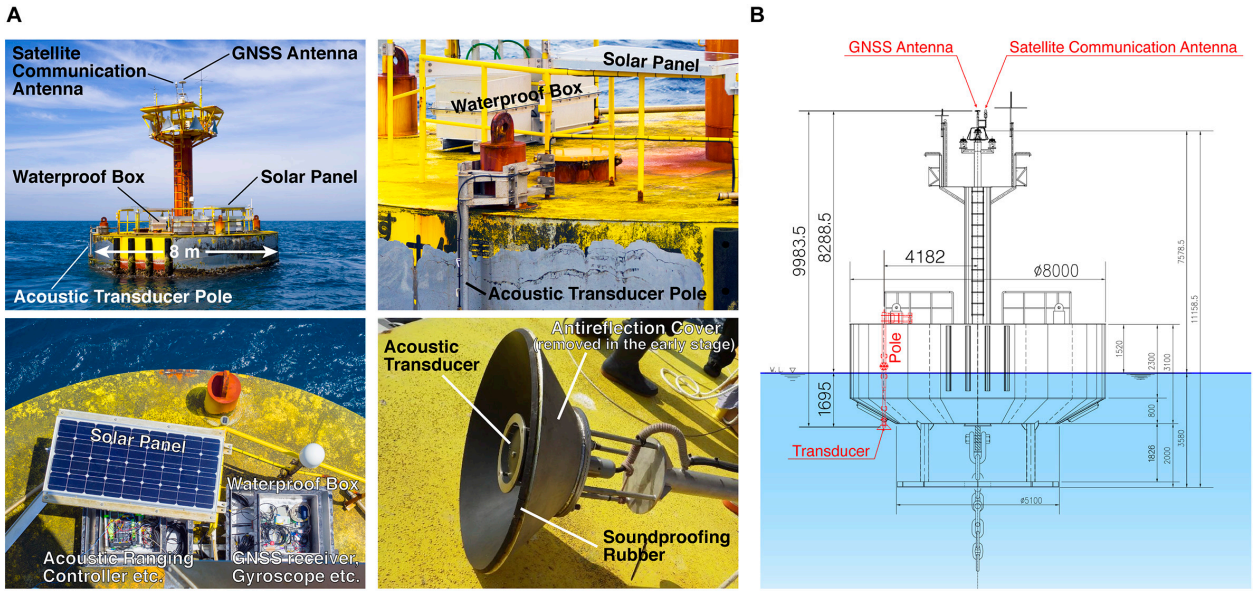

FIGURE 3 | (A) Kuroshio-Bokujyo No. 18 buoy equipped with our system. The antireflection cover around the acoustic transducer has been removed. **(B)** Side view of the design drawing of the buoy.

FIGURE 4 | Photo of an ocean bottom acoustic transponder installed in the test site. The black device fixed on the top is the acoustic transducer.

was stored in a data storage server. The ground base station was in the inland town of Niyodogawa, Kochi Prefecture (**Figure 2**), which is 30 km from the southern coast of Japan and is therefore unlikely to be affected in the event of a tsunami due to a major subduction earthquake. The original acoustic waveform, raw GNSS, and gyroscope measurement data were also stored on-board for quality check and postprocess.

The ocean bottom acoustic transponders (**Figure 4**) were equipped with batteries with a planned life span of 5 years and electronic circuit boards mounted in a 17-inch diameter glass sphere along with an acoustic transducer. The seafloor benchmark, which consisted of three ocean bottom acoustic transponders, was installed on June 5, 2017 by the vessel Yuge Maru of the National Institute of Technology, Yuge College. The triangular configuration of the three transponders covered the area under the drifting sea surface buoy (**Figure 5A**). The locations of the transponders were selected based on the anchoring point of the buoy, the mooring chain length, and the dominant direction of the ocean current.

CONTINUOUS ACOUSTIC RANGING TESTS

Continuous acoustic ranging tests were performed for a total of 106 days during the following four periods: March 28–31, June 2–July 12, and November 16–December 17 in 2018; and March 24–April 25, 2019. The buoy position (i.e., the positions of the buoy-mounted GNSS antenna) every 10 min is shown in **Figure 5**. Note that the positions from March to July, 2018 were obtained via a post-processed PPP analysis conducted using commercial software (GrafNav of NovAtel, Inc.) as PPP-AR solutions from the system on the buoy were intermittently unavailable during this period. The positions after November, 2018 were computed by the PPP-AR algorithm on the buoy. The

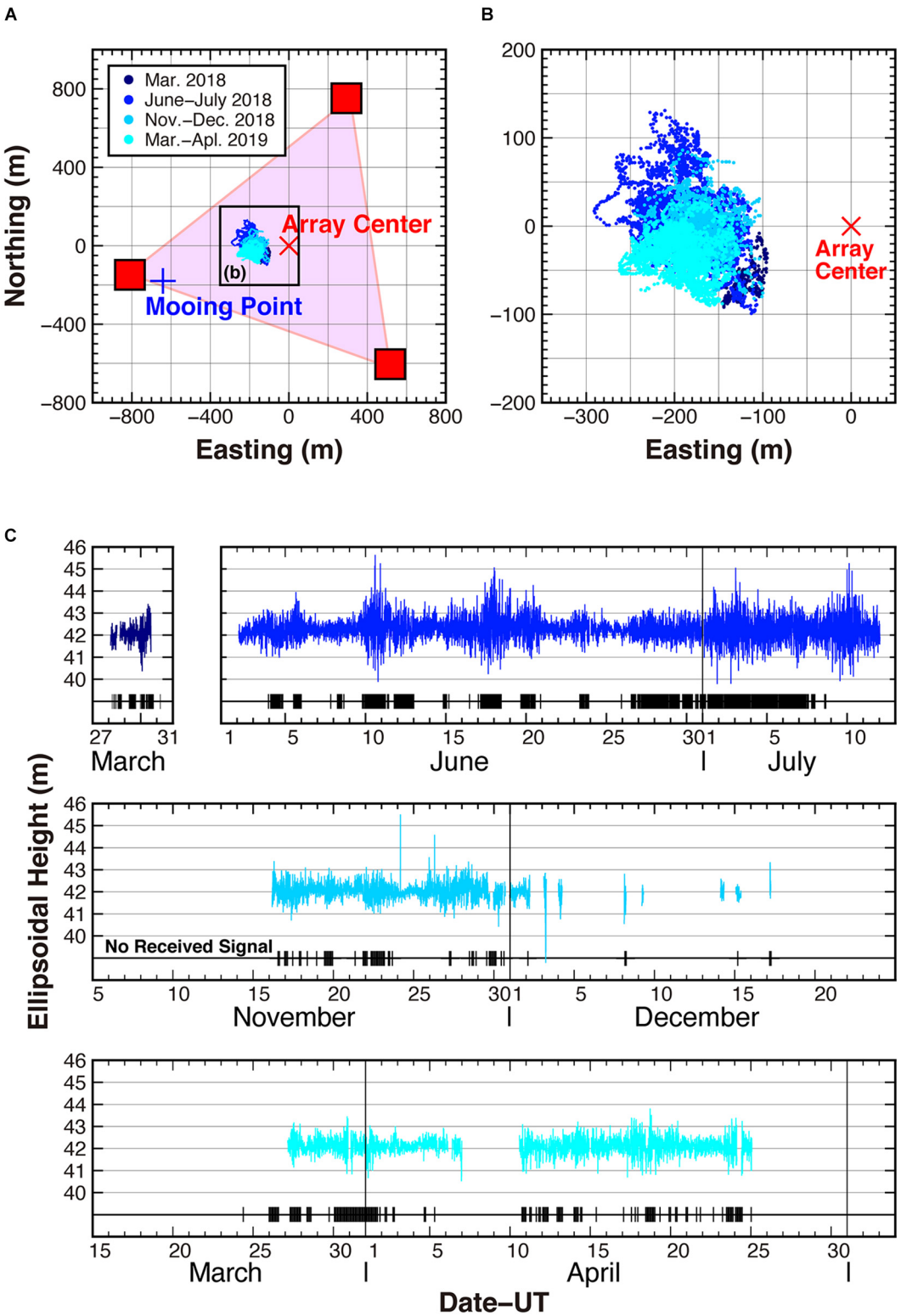

FIGURE 5 | Positions of the buoy-mounted GNSS antenna during the operational test period determined by post-processed PPP (until July) and PPP-AR (after November). **(A)** and **(B)** Horizontal positions (small dots). Different colors indicate differences in period shown by the legend in **(A)**. Red squares, red cross, and blue plus indicate the positions of ocean bottom acoustic transponders, center of the triangular transponder array, and anchored point of the buoy, respectively. **(C)** Ellipsoidal height after the tidal correction on the basis of NAO.99b model (Matsumoto et al., 2000). Black ticks indicate timings of no acoustic signal is recorded at the buoy-mounted acoustic ranging controller.

fluctuations in the ellipsoidal height due to the ocean tide were corrected using the NAO.99b model (Matsumoto et al., 2000). The test site was in an area of the strong east-northeastward Kuroshio ocean current, and the buoy drifted in the east-northeast direction from the anchored point and remained there for the entire period. The buoy drifted almost 100–250 m to the west of the array center, that is, the center of the triangle formed by the three ocean bottom acoustic transponders, which was the desired buoy position relative to the transponder formation (Kido et al., 2018; Imano et al., 2019). As the buoy well followed the movement of the sea-surface, the effects of heavy waves and/or swells due to cold and stagnant fronts (March 30 and July 5–7, 2018), low pressures (June 6, 18–21, and 24, 2018), and severe tropical storms or typhoons (June 11, July 2–4, and July 9–11, 2018) can all be seen in the time series of the ellipsoidal height.

It is known that temporal variations in the speed of sound in the ocean directly affect the accuracy of acoustic ranging, and short-period internal waves are one of the phenomena contributing to temporal variations in the speed of sound. In addition, the time scale of internal waves is known to be tens of minutes at a minimum (e.g., Ali, 1993). Matsui et al. (2019) reported that short-period, less than 1 h, internal waves arises fluctuations of sound-speed in the shallow layer causing large uncertainty of seafloor position. With this in mind, acoustic signals were transmitted sequentially to the three ocean bottom transponders at 3-min intervals; thus, each transponder received a signal every 9 min. This interval was chosen to balance the power consumption and keeping up the temporal variation in the sound speed associated with the internal wave.

A number of problems were encountered during the time the test was underway. The test unexpectedly terminated on March 28, 2018 when the circuit breaker in the battery charge controller forced to cut the power. The data transfer to the ground base station stopped on June 10, 2018 when the satellite modem disconnected. To prevent future occurrences of these situations, we implemented disconnection monitoring and a self-rebooting algorithm to the satellite modem. The data storage on the buoy terminated on June 13, 2018, probably due to high CPU load in the buoy-mounted server along with a communication port error. After this time, the devices handling the acoustic ranging data were no longer connected to the satellite communication modem, and no acoustic data were sent to the ground base station from November to December, 2018. Also, after November 29 or so, the acoustic ranging was frequently interrupted by unstable power, which was thought to be due to the lack of sunshine in the winter season.

In the original configuration installed on the buoy in 2018, the signal processing computer was connected to the GNSS receiver as a temporary data server via an RS-232C communication interface. However, in an attempt to resolve the above issues and improve system reliability before restarting the test on March 24, 2019, the data flow and connections between components were reconfigured to use Ethernet. Although the test was restarted on March 24, 2019, the power supply continued to be a problem that affected the data transfer to the ground base station until it finally terminated on April 11. The acoustic ranging was interrupted from April 6 to April 10, 2019.

The results from the continuous acoustic ranging test are shown in **Figure 6**. The acoustic ranging itself successfully continued throughout the test period as long as power was supplied to the system, as indicated by the red bars in **Figure 6**, although data transfer to the ground base station was intermittent. A total of 41,083 acoustic signals were transmitted from the buoy while the buoy-mounted acoustic ranging controller successfully received a total of 35,316 waveforms (86%) from the ocean bottom transponders. Nothing was recorded in the remaining 5767 files (14%), as indicated by the black bars in **Figure 6**, due to failures in automatic header detection by the acoustic ranging controller (**Figure 5C**). The ocean bottom transponders transmit a header signal prior to the main signal for the acoustic ranging to notify the buoy-mounted acoustic ranging controller the signal transmission. The acoustic ranging controller start the waveform recording after detecting the header signal. If the acoustic ranging controller fails to detect the header signal, nothing is recorded in the file. After the waveform data was manually reviewed, no clear returned signal was recognized in 1073 additional waveforms. A total of only 7553 signals (21% of the total number of successfully recorded signals) were transmitted to the ground base station through the satellite link, as indicated by the blue bars in **Figure 6**. Examples of acoustic ranging data received at the ground base station over the period of an hour are shown in **Figure 7**. The transmission time stamps of the acoustic signal transmissions are shown in the second column in **Figure 7**. In this example, the acoustic ranging data was successively transferred to the ground base station at 3-min intervals.

Examples of the acoustic waveform recorded in the buoy-mounted acoustic ranging controller are shown in **Figure 8**, where it can be seen that the buoy-based acoustic ranging system provided high quality waveforms based on the high maximum value of the absolute cross-correlation function (CCF) between the received and transmitted (reference) signals (**Figure 9**). This situation is different from those of conventional observations made using moving vessels with acoustic transducers mounted on a rod.

REDUCTION OF ACOUSTIC RANGING DATA SIZE

The raw acoustic ranging waveform data from the developed system was 64 KB (=64.512 ms $\times$ 500 kHz $\times$ 2 byte + 1024 byte of header information and spare areas) in size. If this were to be transmitted without modification over a satellite link, it would cost more than $200,000 USD per year. Thus, we reduced the data down to a final size of 60 bytes, which is less than 1/1000 the size of the raw data. The data transferred to the ground base station only contained information related to the travel time of the direct wave as shown in **Figure 7**.

It is necessary to use the travel time of direct wave for the accurate acoustic ranging. The recorded waveforms were

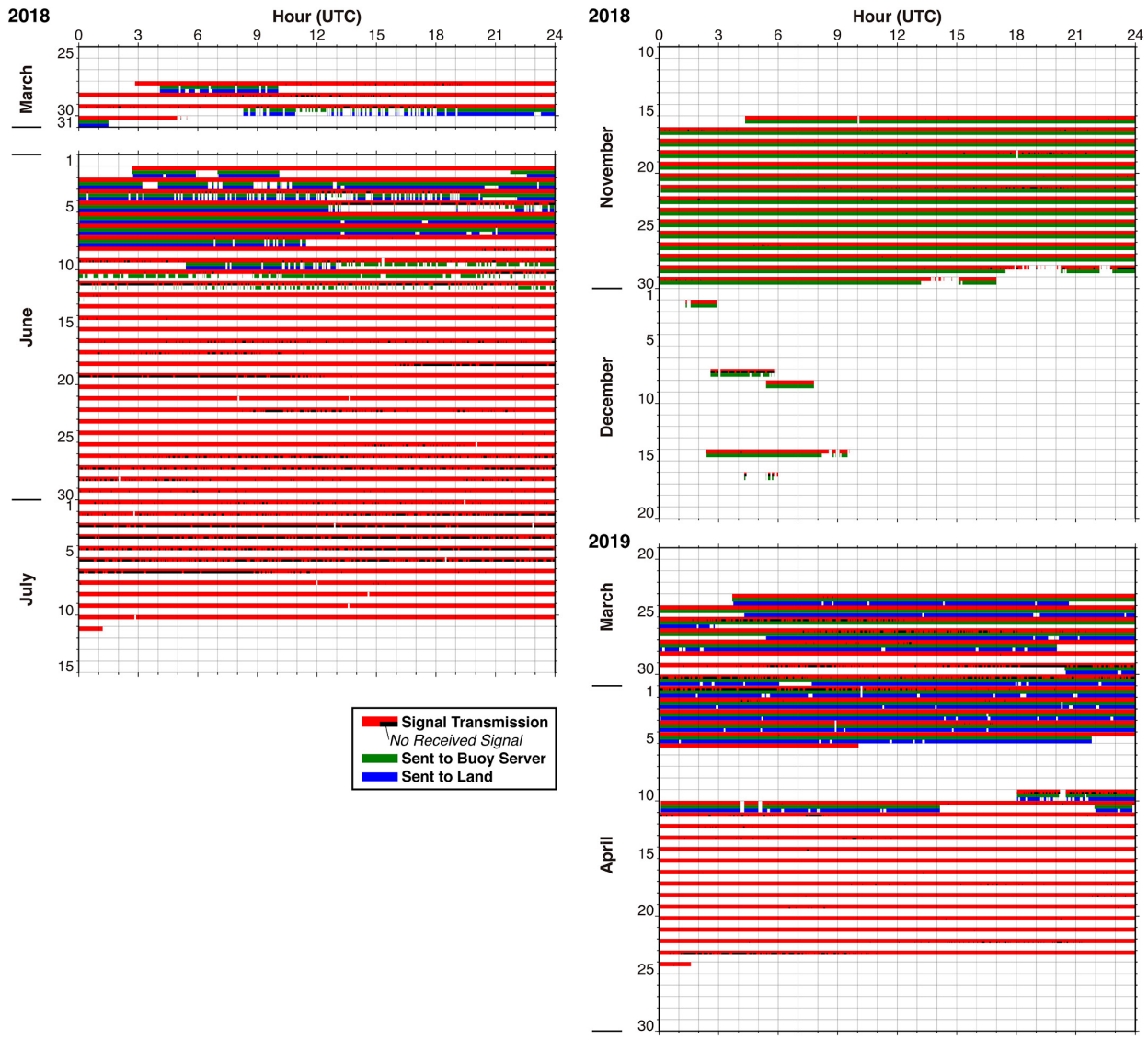

FIGURE 6 | Diagram showing the status of acoustic ranging test. Red: buoy-mounted acoustic ranging controller transmitted the acoustic signal to the ocean bottom transponder, black: nothing was recorded at the acoustic ranging controller (the signal receiving was failed), green: the acoustic waveform was sent to the signal processing computer, blue: the acoustic waveform was sent to the data storage server at the ground base station via the satellite communication.

frequently contaminated by waves reflected from the sea-surface, buoy body, and seafloor (**Figure 8B**), which was also reported by Imano et al. (2015). The onset of a direct wave is determined based on the timing of the maximum CCF value. However, it has been empirically known that reflected waves exhibit multiple CCF peaks, and that the maximum CCF value is sometimes attained during the onset of the subsequent reflected wave (**Figure 8B**), resulting in the direct wave onset being misrecognized (Tadokoro et al., 2012). In this study, it was found that the maximum CCF value was attained at the time of the reflected wave onset for 1250 of the total 35,316 waveforms over the course of the entire test period.

To address this, the energy ratio (ER) was introduced to aid in identifying the correct direct wave onset. The ER is defined as the average wave energy within the time window just after a target time relative to that just before the same target time as follows (e.g., Han et al., 2008):

$$\gamma_i = \frac{1}{W_a}\sum_{j=i}^{i+W_a}(s_j)^2 \Bigg/ \frac{1}{W_b}\sum_{j=i-d-W_b}^{i-d}(s_j)^2 \qquad (1)$$

where γ_i is the energy ratio at the i-th sample, s_j is the amplitude of the acoustic wave at the j-th sample ($j \geq 1$), d (≥ 1) is the time shift, and W_a (≥ 1) and W_b (≥ 1) are the lengths of the following and preceding windows at the target sample, respectively. Originally, the two windows W_a and W_b were defined as having the same length. Here, the windows had a length of 195 samples (0.390 ms), which corresponded to 5 cycles

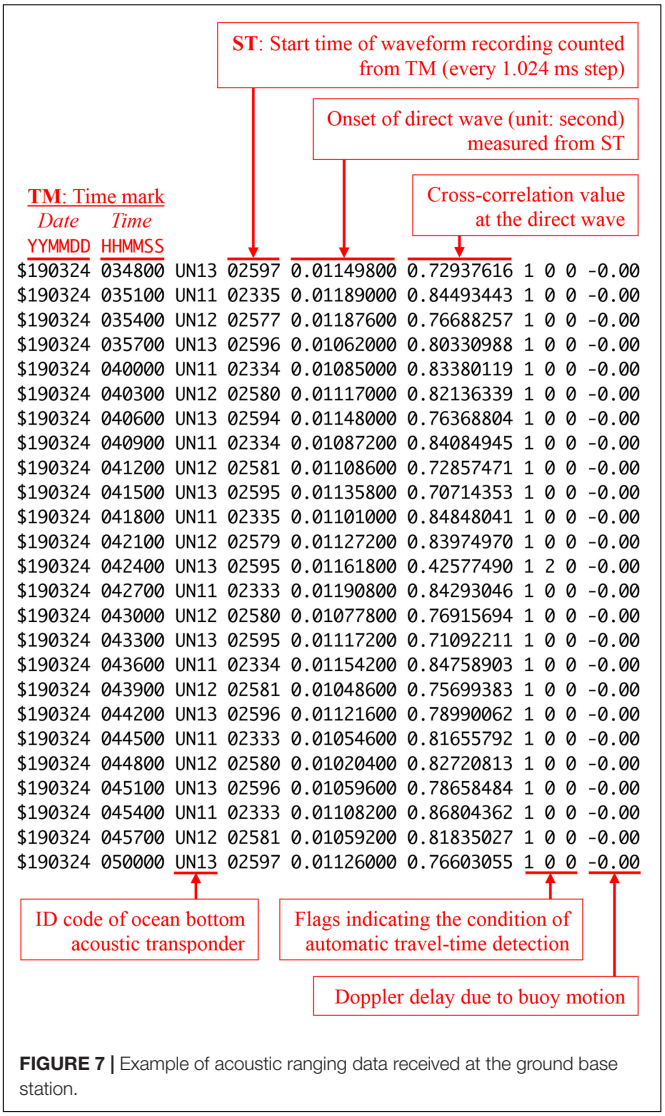

FIGURE 7 | Example of acoustic ranging data received at the ground base station.

of the acoustic signal. Because the wave sample started at $j = 1$, W_b was reset at $i - d - 1$ for the case of $i - d - W_b < 1$. The time shift d was set at 117 (0.234 ms), which corresponded to three cycles, to avoid the transitional vibration of the element inside the acoustic transducer. The direct wave onset could then be detected from a relatively high CCF peak accompanied by a high ER value.

An algorithm was developed to automatically recognize the correct direct wave onset in the buoy-mounted signal processing computer. First, the CCF peak with the maximum value throughout the waveform was identified as Peak-3. Next, Peak-2, the highest peak in the second largest envelope of CCF prior to Peak-3 and Peak-1, the highest peak in the third largest envelope of CCF prior to Peak-2 were identified as each are candidates for the direct wave onset. Finally, the algorithm evaluates whether or not each peak corresponds to the direct wave in order of the peak number on the basis of thresholds set using the CCF and ER values. In essence, relatively high CCF peaks are unconditionally identified as indicators of the direct wave onset. In contrast, low CCF peaks indicate no direct wave is present. If none of the

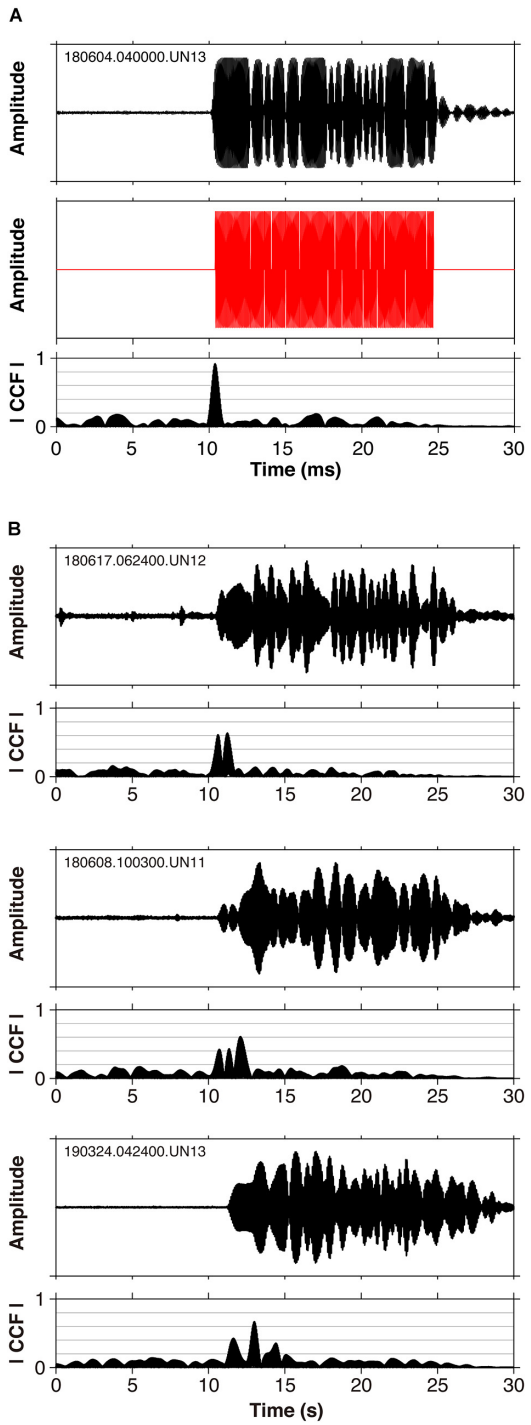

FIGURE 8 | Examples of received acoustic waveform on the buoy-mounted acoustic ranging controller. **(A)** Waveform with high signal-to-noise ratio. Top: received waveform middle: theoretical transmitted signal from the buoy mounted acoustic transducer, bottom: absolute cross-correlation function (CCF) between the received and transmitted (reference) signals. The maximum value of the cross-correlation function is 0.92. **(B)** Waveforms with obvious reflected waves. Each noticeable peak of CCF corresponds to the onset of the direct or the reflected waves. Top and middle: reflected waves from the buoy body or the sea bottom are included, bottom: reflected waves from the sea surface are included.

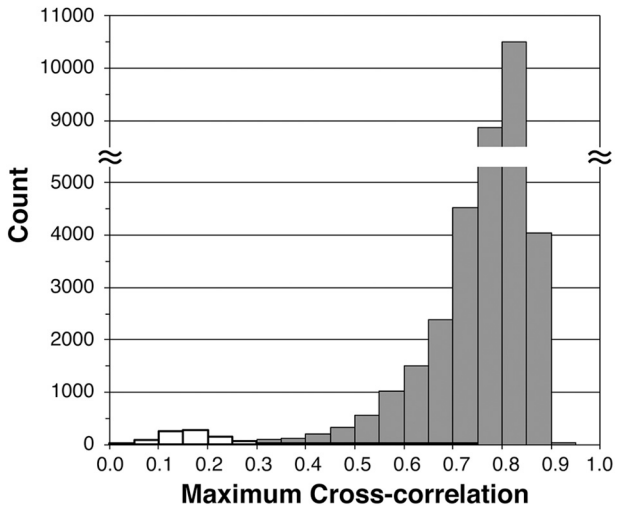

FIGURE 9 | Histogram of the maximum value of CCF. The white bars show the frequency distribution for the waveforms without significant acoustic ranging signal.

three identified CCF peaks exceed the thresholds, the waveform is rejected as containing no clear return. However, if a CCF value is somewhat below the maximum, the CCF peak can still be recognized as indicating a direct wave onset if the ER value is large enough at the peak (**Figure 10**). Note that the CCF values are rounded to two decimal places in our programming code, and the plots in **Figure 10** are discretely distributed. The algorithm was successful and only misrecognized direct wave onsets in 136 waveforms or 0.39% of the data (**Table 1**), which was equivalent to less than twice a day. Most of these cases (112 data) were misrecognized as direct wave onsets due to the extremely small path difference between the direct and reflected waves, which caused an overlap of the CCF peak corresponding to the reflected wave on the direct wave peak. This was identified as a limitation of the present algorithm.

DISCUSSION

In general, our primary purpose was achieved as the acoustic ranging every 3 min continued successfully throughout the test periods. However, the acoustic ranging controller frequently experienced power failures, especially during the winter season. The power delivery for satellite communications did not fully recover even in April, and completely stopped on April 11 (**Figure 6**). The total electric power consumption amounted to 624 Wh (=26 W × 24 h) per day for all components on the buoy, and theoretically, the buoy-mounted system continued to work for an assumed non-sunshine period of about 11.5 days

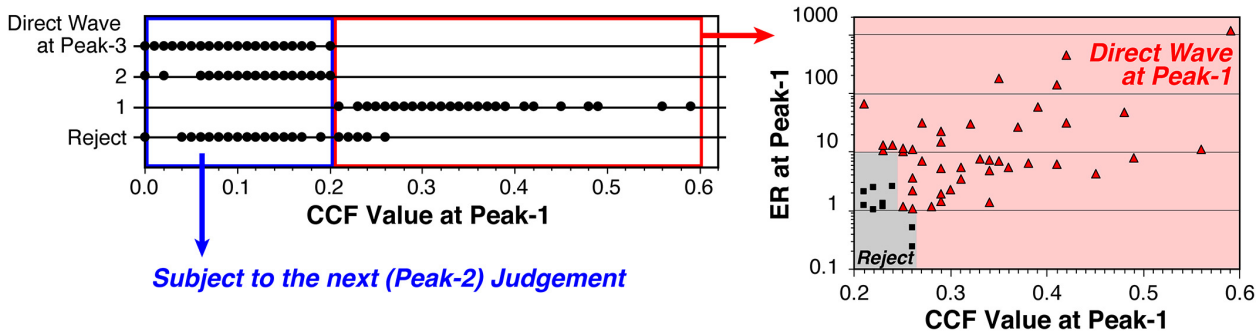

FIGURE 10 | Example of thresholds to recognize the direct wave onset on the basis of the CCF and ER values. Graphs displayed here are for the judgment at Peak-1 among the waveform data recorded on the buoy from March 28 to July 12, 2018. For this case, the peaks with CCF values >0.20 (red square frame in the left panel) are judged whether they correspond to the direct wave onset (red shadow in the right panel) or Reject (gray shadow in the right panel). The peaks with CCF values ≥0.27 unconditionally correspond to the direct wave onset. The peaks with CCF values >0.20 and <0.27 are judged to be the direct wave onset or Reject depending on both their CCF and ER values. The remaining data (blue square frame in the left panel) are subjected to the judgment at Peak-2.

TABLE 1 | Result of the automatic recognition of the direct wave onset.

		Actual (manually checked) Direct wave onset at:				Total
		Peak-1	Peak-2	Peak-3	Reject	
Judged (automatically picked) Direct wave onset at:	Peak-1	**83**	0	1	1	85
	Peak-2	1	**1044**	1	3	1,049
	Peak-3	0	3	**32,987**	3	32,993
	Reject	1	6	4	**1066**	1077
Inseparable peak*		5	107			112
Total		90	1160	32,993	1073	**35,316**

**The CCF peaks overlapped due to extremely short path difference between the direct and the reflected waves. The colored values indicate the number of data.*

(=300 Ah × 24 V/624 Wh). The power supply system on the buoy was conservatively designed to operate for 5 days without any sunshine. Approximately 5–6 days were required to recover the power. Thus, it is assumed that chronic power delivery shortages caused excess electric power consumption relative to the charging power even when there was enough sunshine until the batteries were fully depleted.

This is thought to have occurred for the following reasons. A center pillar with a diameter of 8 m and a height of more than 4 m was constructed on the deck of the buoy (**Figure 3**), and a structure with an area of 2.4 m × 2.4 m was positioned on the top of the center pillar. As the solar panels were mounted 1 m above the deck and connected in series (**Figure 1**), it is likely that some portion of the solar panel modules fell into the shadow of the above-mentioned objects. When this happened, the designed power-generation voltage may have not been acquired even under daylight conditions because of the series connection. The power problems are a critical issue that must be resolved for continuous operation. In the future, we plan to redesign the system so that the solar panels are connected in parallel to ensure adequate power delivery. In addition, the power supply lines for the 12 VDC and 24 VDC systems will be separated.

All electronic components and batteries were stored in five waterproof boxes mounted on the deck of the buoy. The boxes were 102 cm (W) × 74 cm (D) × 50 cm (H) size and weighted 85 kg in aggregate. The present buoy has enough space (8 m in diameter) and buoyancy force (1.45×10^6 N) to support the installation of this equipment. However, when this system is applied in practical applications, it is not realistic to deploy many huge platforms similar to the current setup. Thus, it will be necessary to reduce the size and weight of the equipment to allow installation on platforms with limited payload capacity. To accomplish this, it will be necessary to reduce the power consumption of each electronic component in order to reduce the size of the batteries and solar charge/discharge controller, which occupy three waterproof boxes in total (**Figure 1**). In other words, more than half of the boxes are used to store electric power supply components. Reducing the power consumption will also contribute to solving the insufficient power delivery problem. In the present system, three independent processors were used to process the acoustic ranging data, gyroscope measurement data, and PPP-AR positioning of GNSS data. In the future, this could be reduced by using a single compact PC with multiple functions, which would also simplify the signal transmission lines and wiring.

The purpose of our system is seafloor positioning. Our system is still in the testing phase, and we are developing a positioning algorithm for point survey specific to the present buoy measurement. It is desirable to measure the sound speed profile continuously because temporal and spatial variations in sound speed also directly affects the accuracy of seafloor positioning. Nevertheless, the continuous measurement of sound speed has not been realized in our system. Instead, we plan to estimate variations in sound speed, that appear in the time series of acoustic travel time (e.g., Kido et al., 2008), together with the seafloor positions as demonstrated in previous studies (Fujita et al., 2006; Ikuta et al., 2008; Honsho and Kido, 2017). Average sound speed profiles should be measured with research vessel at some time interval, once a year for our case. Imano et al. (2019) reported accuracy of seafloor positioning from a smaller buoy than ours in the ocean with a depth of about 3000 m. Their buoy was slackly moored, and it drifted within a circle of 4000 m radius due to the strong Kuroshio ocean current. The extreme drifting effect caused decrease in positioning accuracy down to about 1 m. In contrast, the large and heavy buoy we used was moored more tightly. The buoy, therefore, drifted within the area of about only 150–200 m even under the strong Kuroshio current (**Figure 5**). We should demonstrate an advantage of our tightly-moored buoy on the basis of the seafloor positioning accuracy with the positioning algorithm that we are developing now.

CONCLUSION

In this study, we developed a system capable of continuous and real-time measurement to measure seafloor crustal deformation using the GNSS/Acoustic technique. The following summarizes our findings after conducting operational tests using a moored buoy for 106 days:

1. If sufficient electrical power is supplied, the developed system can continuously transmit acoustic ranging to the on-land station via the satellite link;
2. The system on the buoy was able to acquire high-quality acoustic waveforms;
3. More than 99% of the direct acoustic wave onsets at the buoy were correctly distinguished based on the energy ratio factor as well as the cross-correlation value even if those waveforms had been corrupted with reflected waves; and
4. The system on the buoy successfully contributed to reduce the data size over a satellite communication.

In terms of future work, we plan to resolve the identified problems in the electrical system so that the project can advance to the operational stage.

DATA AVAILABILITY STATEMENT

The datasets generated for this study are available on request to the corresponding author. We are preparing a website distributing the archived data at http://www.tsunamigps.com.

AUTHOR CONTRIBUTIONS

KT designed the entire system, coded the programs that implemented the cross-correlation computation and automatic detection of the onset of direct the acoustic wave, analyzed the acoustic ranging data, and conducted GNSS positioning. NK contributed by revising the system and programs, testing the system prior to installation, retrieving the data, and organizing the database. TK and YT conceived and promoted this study.

KM provided technical support and advice on the configuration of the system, and fabricated the metal parts.

FUNDING

KT, NK, TK, and YT acknowledge financial support from JSPS KAKENHI Grant Number JP16H06310: "A challenge to develop GNSS buoy system for high-functional tsunami monitoring and continuous observation of ocean-bottom crustal movements."

ACKNOWLEDGMENTS

The authors would like to thank reviewers for their constructive comments. We thank Kochi Prefecture, Japan, for allowing us to use one of their fishery buoys for this study. We are grateful to the captain and crew of the vessel Yuge Maru of the National Institute of Technology, Yuge College, for their support during the installation of the ocean bottom acoustic transponders.

REFERENCES

Ali, H. B. (1993). Oceanic variability in shallow-water acoustics and the dual role of the sea bottom. *IEEE J. Ocean Eng.* 18, 31–41. doi: 10.1109/48.211498

Becker, J. J., Sandwell, D. T., Smith, W. H. F., Braud, J., Binder, B., Depner, J., et al. (2009). Global bathymetry and elevation data at 30 arc seconds resolution: SRTM30_PLUS. *Mar. Geodesy* 32, 355–371. doi: 10.1080/01490410903297766

Chadwell, C. D. (2013). "GPS-acoustic seafloor geodesy using a wave glider," in *Proceedings of the Abstract G14A-01 presented at 2013 Fall Meeting*, (San Francisco, CA: AGU).

Chadwell, C. D., and Spiess, F. N. (2008). Plate motion at the ridge-transform boundary of the south Cleft segment of the Juan de Fuca Ridge from GPS-Acoustic data. *J. Geophys. Res.* 113:B04415. doi: 10.1029/2007JB004936

Chen, H.-Y., Ikuta, R., Lin, C.-H., Hsu, Y.-J., Kohmi, T., Wang, C.-C., et al. (2018). Back-arc opening in the western end of the Okinawa Trough revealed from GNSS/Acoustic Measurements. *Geophys. Res. Lett.* 45, 137–145. doi: 10.1002/2017GL075724

Fujimoto, H. (2006). Ocean bottom crustal movement observation using GPS/Acoustic system by universities in Japan. *J. Geod. Soc. Jpn.* 52, 265–272. doi: 10.11366/sokuchi1954.52.265

Fujita, M., Ishikawa, T., Mochizuki, M., Sato, M., Toyama, S., Katayama, M., et al., (2006). GPS/Acoustic seafloor geodetic observation: method of data analysis and its application. *Earth Planet. Space* 58, 265–275. doi: 10.1186/BF03351923

Gagnon, K., Chadwell, C. D., and Norabuena, E. (2005). Measuring the onset of locking in the Peru-Chile trench with GPS and acoustic measurements. *Nature* 434, 205–208. doi: 10.1038/nature03412

Han, L., Wong, J., Bancroft, J. C., and Stewart, R. R. (2008). Automatic time picking and velocity determination on full waveform sonic well logs. *CREWES Res. Rep.* 20:5.1–5.13.

Honsho, C., and Kido, M. (2017). Comprehensive analysis of traveltime data collected through GPS-acoustic observation of seafloor crustal movements. *J. Geophys. Res.* 122, 8583–8599. doi: 10.1002/2017JB014733

Iinuma, T., Hino, R., Kido, M., Inazu, D., Osada, Y., Ito, Y., et al. (2012). Coseismic slip distribution of the 2011 off the Pacific Coast of Tohoku Earthquake (M9.0) refined by means of seafloor geodetic data. *J. Geophys. Res.* 117:B07409. doi: 10.1029/2012JB009186

Iinuma, T., Hino, R., Uchida, N., Nakamura, W., Kido, M., Osada, Y., et al. (2016). Seafloor observations indicate spatial separation of coseismic and postseismic slips in the 2011 Tohoku earthquake. *Nat. Commun.* 7:13506. doi: 10.1038/ncomms13506

Ikuta, R., Tadokoro, K., Ando, M., Okuda, T., Sugimoto, S., Takatani, K., et al. (2008). A new GPS-Acoustic method for measuring ocean floor crustal deformation: application to the Nankai Trough. *J. Geophys. Res.* 113:B02401. doi: 10.1029/2006JB004875

Imano, M., Kido, M., Honsho, C., Ohta, Y., Takahashi, N., Fukuda, T., et al. (2019). Assessment of directional accuracy of GNSS-Acoustic measurement using a slackly moored buoy. *Prog. Earth Planet. Sci.* 6:56. doi: 10.1186/s40645-019-0302-1

Imano, M., Kido, M., Ohta, Y., Fukuda, T., Ochi, H., Takahashi, N., et al. (2015). "Improvement in the accuracy of real-time GPS/Acoustic measurements using a multi-purpose moored buoy system by removal of acoustic multipath," in *Proceedings of the International Symposium on Geodesy for Earthquake and Natural Hazards (GENAH), IAG Symposia 145*, ed. M. Hashimoto (Berlin: Springer), 105–114. doi: 10.1007/1345_2015_192

Kato, T., Terada, Y., Ito, K., Hattori, R., Abe, T., Miyake, T., et al. (2005). Tsunami due to the 2004 September 5th off the Kii peninsula earthquake. Japan, recorded by a new GPS buoy. *Earth Planet. Space* 57, 297–301. doi: 10.1186/BF03352566

Kato, T., Terada, Y., Kinoshita, M., Kakimoto, H., Issiki, H., Moriguchi, T., et al. (2001). "A new tsunami monitoring system using RTK-GPS," in *Proceedings of International Tsunami Symposium 2001 (ITS 2001)*, Seattle, WA, 645–651.

Kato, T., Terada, Y., Tadokoro, K., Futamura, A., Toyoshima, M., Yamamoto, S., et al. (2017). "GNSS buoy array in the ocean for a synthetic geohazards monitoring system," in *Proceedings of The 27th International Ocean and Polar Engineering Conference*, San Francisco, CA.

Kato, T., Terada, Y., Tadokoro, K., Kinugasa, N., Futamura, A., Toyoshima, M., et al. (2018). Development of GNSS buoy for a synthetic geohazard monitoring system. *J. Disaster Res.* 13, 460–471. doi: 10.20965/jdr.2018.p0460

Kido, M., Fujimoto, H., Hino, R., Ohta, Y., Osada, Y., Iinuma, T., et al. (2015). "Progress in the project for development of GPS/Acoustic technique over the Last 4 years," in *Prceeding of the International Symposium on Geodesy for Earthquake and Natural Hazards (GENAH), International Association of Geodesy Symposia*, Vol. 145, ed. M. Hashimoto (Cham: Springer), 3–10. doi: 10.1007/1345_2015_127

Kido, M., Fujimoto, H., Miura, S., Osada, Y., Tsuka, K., and Tabei, T. (2006). Seafloor displacement at Kumano-nada caused by the 2004 off Kii Peninsula earthquakes, detected through repeated GPS/Acoustic surveys. *Earth Planet. Space* 58, 911–915. doi: 10.1186/BF03351996

Kido, M., Imano, M., Ohta, Y., Fukuda, T., Takahashi, N., Tsubone, S., et al. (2018). Onboard realtime processing of GPS-acoustic data for moored buoy-based observation. *J. Disaster Res.* 13, 472–488. doi: 10.20965/jdr.2018.p0472

Kido, M., Osada, Y., and Fujimoto, H. (2008). Temporal variation of sound speed in ocean: a comparison between GPS/acoustic and in situ measurements. *Earth Planet. Space* 60, 229–234. doi: 10.1186/BF03352785

Kido, M., Osada, Y., Fujimoto, H., Hino, R., and Ito, Y. (2011). Trench-normal variation in observed seafloor displacements associated with the 2011 Tohoku-Oki earthquake. *Geophys. Res. Lett.* 38:L24303. doi: 10.1029/2011GL050057

Kimura, H., Tadokoro, K., and Ito, T. (2019). Interplate coupling distribution along the Nankai Trough in southwest Japan estimated from the block motion model based on onshore GNSS and seafloor GNSS/A observations. *J. Geophys. Res.* 124, 6140–6164. doi: 10.1029/2018JB016159

Matsui, R., Kido, M., Niwa, Y., and Honsho, C. (2019). Effects of disturbance of seawater excited by internal wave on GNSS-acoustic positioning. *Mar. Geophys. Res.* 40, 541–555. doi: 10.1007/s11001-019-09394-6

Matsumoto, K., Takanezawa, T., and Ooe, M. (2000). Ocean tide models developed by assimilating TOPEX/POSEIDON altimeter data into hydrodynamical model: a global model and a regional model around Japan. *J. Oceanogr.* 56, 567–581. doi: 10.1023/A:1011157212596

Matsumoto, Y., Fujita, M., Ishikawa, T., Mochizuki, M., Yabuki, T., and Asada, A. (2006). Undersea co-seismic crustal movements associated with the 2005 Off Miyagi Prefecture Earthquake detected by GPS/acoustic seafloor geodetic observation. *Earth Planet. Space* 58, 1573–1576. doi: 10.1186/BF03352663

Matsumoto, Y., Ishikawa, T., Fujita, M., Sato, M., Saito, H., Mochizuki, M., et al. (2008). Weak interplate coupling beneath the subduction zone off Fukushima, NE Japan, inferred from GPS/acoustic seafloor geodetic observation. *Earth Planet. Space* 60:e9–e12. doi: 10.1186/BF03353114

Mervart, L., Lukes, Z., Rocken, C., and Iwabuchi, T. (2008). "Precise point positioning with ambiguity resolution in real-time," in *Proceedings of 21st International Technical Meeting of the Satellite Division of The Institute of Navigation (ION GNSS 2008)*, Savannah, GA, 397–405.

Nishimura, T., Yokota, Y., Tadokoro, K., and Ochi, T. (2018). Strain partitioning and interplate coupling along the northern margin of the Philippine Sea plate, estimated from Global Navigation Satellite System and Global Positioning System-Acoustic data. *Geosphere* 14, 535–551. doi: 10.1130/GES01529.1

Ozaki, T. (2011). Outline of the 2011 off the Pacific coast of Tohoku Earthquake (Mw 9.0): Tsunami warnings/advisories and observations. *Earth Planet. Space* 63, 827–830. doi: 10.5047/eps.2011.06.029

Rocken, C., Mervart, L., Lukes, Z., Johnson, J., Kanzaki, H., Kakimoto, M., et al. (2004). "Testing a new network RTK software system," in *Proceedings of 17th International Technical Meeting of the Satellite Division of The Institute of Navigation (ION GNSS 2004)*, Long Beach, CA, 2831–2839.

Sathiakumar, S., Barbot, S., Hill, E., Peng, D., Zerucha, J., Suhaimee, S., et al. (2016). "Seafloor geodesy using wave gliders to study earthquake and tsunami hazards at subduction zones," in *Proceedings of the Abstract G31A-1046 presented at 2016 Fall Meeting*, (San Francisco, CA: AGU).

Sato, M., Ishikawa, T., Ujihara, N., Yoshida, S., Fujita, M., Mochizuki, M., et al. (2011a). Displacement above the hypocenter of the 2011 Tohoku-oki earthquake. *Science* 332:1395. doi: 10.1126/science.1207401

Sato, M., Saito, H., Ishikawa, T., Matsumoto, Y., Fujita, M., Mochizuki, M., et al. (2011b). Restoration of interplate locking after the 2005 Off-Miyagi Prefecture earthquake, detected by GPS/acoustic seafloor geodetic observation. *Geophys. Res. Lett.* 38:L01312. doi: 10.1029/2010GL045689

Spiess, F. N., Chadwell, C. D., Hildebrand, J. A., Young, L. E., Purcell, G. H. Jr., and Dragert, H. (1998). Precise GPS/Acoustic positioning of seafloor reference points for tectonic studies. *Phys. Earth Planet. Inter.* 108, 101–112. doi: 10.1016/S0031-9201(98)00089-2

Tadokoro, K., Ando, M., Ikuta, R., Okuda, T., Besana, G. M., Sugimoto, S., et al. (2006). Observation of coseismic seafloor crustal deformation due to M7 class offshore earthquakes. *Geophys. Res. Lett.* 33:L23306. doi: 10.1029/2006GL026742

Tadokoro, K., Ikuta, R., Watanabe, T., Ando, M., Okuda, T., Nagai, S., et al. (2012). Interseismic seafloor crustal deformation immediately above the source region of anticipated megathrust earthquake along the Nankai Trough. *Japan. Geophys. Res. Lett.* 39:L10306. doi: 10.1029/2012GL051696

Tadokoro, K., Nakamura, M., Ando, M., Kimura, H., Watanabe, T., and Matsuhiro, K. (2018). Interplate coupling state at the Nansei-Shoto (Ryukyu) Trench, Japan, deduced from seafloor crustal deformation measurements. *Geophys. Res. Lett.* 45, 6869–6877. doi: 10.1029/2018GL078655

Terada, Y., Kato, T., Nagai, T., Koshimura, S., Imada, N., Sakaue, H., et al. (2015). "Recent developments of GPS tsunami meter for a far offshore observations," in *Proceedings of the International Symposium on Geodesy for Earthquake and Natural Hazards (GENAH), International Association of Geodesy Symposia*, Vol. 145, ed. M. Hashimoto (Cham: Springer), 145–153. doi: 10.1007/1345_2015_151

Tomita, F., Kido, M., Ohta, Y., Iinuma, T., and Hino, R. (2017). Along-trench variation in seafloor displacements after the 2011 Tohoku earthquake. *Sci. Adv.* 3:e1700113. doi: 10.1126/sciadv.1700113

Tomita, F., Kido, M., Osada, Y., Hino, R., Ohta, Y., and Iinuma, T. (2015). First measurement of the displacement rate of the Pacific Plate near the Japan Trench after the 2011 Tohoku-Oki earthquake using GPS/acoustic technique. *Geophys. Res. Lett.* 42, 8391–8397. doi: 10.1002/2015GL065746

Watanabe, S., Bock, Y., Melgar, D., and Tadokoro, K. (2018). Tsunami scenarios based on interseismic models along the Nankai trough, Japan, from seafloor and onshore geodesy. *J. Geophys. Res.* 123, 2448–2461. doi: 10.1002/2017JB014799

Watanabe, S., Sato, M., Fujita, M., Ishikawa, T., Yokota, Y., Ujihara, N., et al. (2014). Evidence of viscoelastic deformation following the 2011 Tohoku-Oki earthquake revealed from seafloor geodetic observation. *Geophys. Res. Lett.* 41, 5789–5796. doi: 10.1002/2014GL061134

Yasuda, K., Tadokoro, K., Ikuta, R., Watanabe, T., Nagai, S., Okuda, T., et al. (2014). Interplate locking condition derived from seafloor geodetic data at the northernmost part of the Suruga Trough. *Japan. Geophys. Res. Lett.* 41, 5806–5812. doi: 10.1002/2014GL060945

Yasuda, K., Tadokoro, K., Taniguchi, S., Kimura, H., and Matsuhiro, K. (2017). Interplate locking condition derived from seafloor geodetic observation in the shallowest subduction segment at the Central Nankai Trough. *Japan. Geophys. Res. Lett.* 44, 3572–3579. doi: 10.1002/2017GL072918

Yokota, Y., and Ishikawa, T. (2020). Shallow slow slip events along the Nankai Trough detected by GNSS-A. *Sci. Adv.* 6:aay5786. doi: 10.1126/sciadv.aay5786

Yokota, Y., Ishikawa, T., Sato, M., Watanabe, S., Saito, H., Ujihara, N., et al. (2015). Heterogeneous interplate coupling along the Nankai Trough. Japan, detected by GPS-acoustic seafloor geodetic observation. *Prog. Earth Planet. Sci.* 2:10. doi: 10.1186/s40645-015-0040-y

Yokota, Y., Ishikawa, T., Watanabe, S., Tashiro, T., and Asada, A. (2016). Seafloor geodetic constraints on interplate coupling of the Nankai Trough megathrust zone. *Nature* 534, 374–377. doi: 10.1038/nature17632

Conflict of Interest: The authors declare that the research was conducted in the absence of any commercial or financial relationships that could be construed as a potential conflict of interest.

frontiers in Earth Science

MINI REVIEW
published: 15 May 2020
doi: 10.3389/feart.2020.00150

History of On-Board Equipment Improvement for GNSS-A Observation With Focus on Observation Frequency

Tadashi Ishikawa[1], Yusuke Yokota[2]*, Shun-ichi Watanabe[1] and Yuto Nakamura[1]*

[1] Hydrographic and Oceanographic Department, Japan Coast Guard, Tokyo, Japan, [2] Institute of Industrial Science, University of Tokyo, Tokyo, Japan

The Global Navigation Satellite System-Acoustic ranging combination technique (GNSS-A) is a seafloor geodetic technique that enables precise global seafloor positioning to detect subseafloor geophysical phenomena. The technique requires a sea surface observation platform that combines GNSS positioning and acoustic ranging. Currently, a survey vessel is used as the platform, which entails substantial financial and human resources costs, which makes increasing observation frequency difficult. It is possible to detect long-term average seafloor movement at the centimeter level, but it is difficult to detect short-term variation due to the insufficiency of observation frequency. The terrestrial GNSS observation network has detected temporal changes in crustal deformation fields. These precise observations provide useful information on the megathrust seismogenic zone. To detect such phenomena on the seafloor, the temporal resolution of the GNSS-A observation needs to be improved. Advances in vessel equipment technology are crucial for increasing observation frequency. In this paper, we review the historical development of the Japan Coast Guard's GNSS-A observation system, focusing on technological developments of on-board equipment installed on a sea surface platform, and explain how such improvements have increased observation frequency over time. In the present, ranging frequency has improved from 40–60 s to 15–20 s by the introduction of the multiple ranging system, resulting in more frequent observations up to five times per year for an individual site.

Keywords: GNSS-A, underwater acoustics, seafloor geodesy, subduction zone, megathrust earthquake

OPEN ACCESS

Edited by:
Keiichi Tadokoro, Nagoya University, Japan

Reviewed by:
Motoyuki Kido, Tohoku University, Japan
Takeshi Iinuma, Japan Agency for Marine-Earth Science and Technology, Japan

****Correspondence:***
Tadashi Ishikawa
ishikawa@jodc.go.jp
Yusuke Yokota
yyokota@iis.u-tokyo.ac.jp

Specialty section:
This article was submitted to Solid Earth Geophysics, a section of the journal Frontiers in Earth Science

Received: *07 February 2020*
Accepted: *21 April 2020*
Published: *15 May 2020*

Citation:
Ishikawa T, Yokota Y, Watanabe S and Nakamura Y (2020) History of On-Board Equipment Improvement for GNSS-A Observation With Focus on Observation Frequency. Front. Earth Sci. 8:150. doi: 10.3389/feart.2020.00150

INTRODUCTION

Space geodetic techniques have been used to monitor crustal deformation. In particular, Global Navigation Satellite System (GNSS) observation networks have been used to reveal detailed information from terrestrial crustal deformation fields and discover various geophysical phenomena. However, to elucidate the physical processes of huge earthquakes that occur around tectonic subduction zones, it is important to observe crustal deformation on the seafloor just above the focal region. The GNSS-Acoustic ranging combination technique (GNSS-A) was proposed and developed to extend the GNSS to the seafloor (Spiess, 1985; Asada and Yabuki, 2001; Fujita et al., 2006). This seafloor geodetic technique has been used to detect various subseafloor geophysical

phenomena that cannot be detected using terrestrial observation and has been providing fruitful knowledge for geophysics, especially for seismology.

The GNSS-A technique has a shortcoming in terms of temporal resolution. Although on-line continuous observation has been achieved using the GNSS, the GNSS-A can observe only several times a year in general. Increasing the observation frequency of the GNSS-A is difficult because a sea surface platform that combines GNSS positioning and acoustic ranging is required. At present, a vessel is used as the platform, which encompasses substantial operating expenses and human resources. One of the most important findings from the study of GNSS-A is the detection of huge co-seismic seafloor displacements due to the 2011 Tohoku-Oki earthquake in Japan (Sato et al., 2011; Kido et al., 2011). However, because that observation was conducted several weeks after the earthquake, it is difficult to separate the co- and post-seismic contribution from the observed displacements. Another important finding from a more recent study is the estimation of the coupling condition of the plate boundary along the Nankai Trough from GNSS-A-derived inter-seismic seafloor movement (Yokota et al., 2016). Because the observation is conducted several times a year, it takes several years to accumulate the data necessary to achieve sufficient accuracy. Therefore, the plate coupling condition estimated from GNSS-A data is currently only a long-term average value. Although the terrestrial GNSS network reveals temporal changes in plate coupling (e.g., Ochi, 2015), it is difficult to detect such phenomena using the GNSS-A. To monitor various geophysical phenomena more accurately, it is essential to improve the temporal resolution of the GNSS-A.

In the last two decades, various slow earthquakes that have the potential to cause huge megathrust earthquakes have been detected around subduction zones. The relationship between slow earthquakes and huge earthquakes is an important research topic in the present seismology (e.g., Obara and Kato, 2016). The terrestrial GNSS network has detected long-term slow earthquakes lasting months or years called slow slip events (SSEs). Recently, GNSS-A has been used to detect SSEs in offshore regions (Yokota and Ishikawa, 2020). However, GNSS-A lacks the capability to accurately determine the duration of such events, due to the insufficiency of observation frequency.

The ideal solution to improve the temporal resolution of the GNSS-A is continuous observation using an unmanned sea surface platform instead of a vessel. An unmanned sea surface platform has been developed by some research groups (Takahashi et al., 2014; Chadwell, 2016; Kato et al., 2018; Tadokoro et al., 2020), but it has not yet been put into use for stable observation. It is therefore now important to develop a technology that increases the frequency of vessel-based observation, which is limited by the high costs associated with using a ship, including vessel operation time.

Advancements in vessel equipment and acoustic ranging technology are indispensable to increase the observation frequency of the GNSS-A. Since the mid-1990s, we, the Japan Coast Guard research group, have been developing observation technology to increase the observation frequency and positioning accuracy. This paper briefly reviews the historical development of the Japan Coast Guard's observation system.

GNSS-A OBSERVATION SYSTEM

Basic Concept

Figure 1A shows a schematic of the GNSS-A observation system. It consists of a sea surface unit and a seafloor unit. The on-board equipment consists of a GNSS positioning system, an acoustic transducer, and a dynamic motion sensor set on a surface vehicle. At each site that is surveyed, the seafloor unit usually consists of four acoustic mirror transponders that are arranged on a rough circle with its radius equal to the depth of the transponders' placement.

The observation system measures the global position of the seafloor transponders according to the International Terrestrial Reference Frame (ITRF). The position of the GNSS antenna is determined by baseline kinematic GNSS analysis. In addition to the GNSS positioning, the dynamic motion sensor records the vessel's attitude. By combining the information on the position of the GNSS antenna and the vessel's attitude, we can determine the global position of the on-board acoustic transducer according to the ITRF. The distance between the on-board transducer and the seafloor transponders are measured by acoustic ranging. Each transponder receives the acoustic signal and then sends it back to the on-board transducer. The positions of the seafloor transponders are determined by combining the information on the position of the on-board transducer and the acoustic signal travel time. In this process, each travel time is converted to distance using an underwater sound speed profile that is acquired every few hours using temperature and salinity profilers.

Acoustic Ranging

Acoustic ranging is performed to precisely determine the relative position between the on-board transducer and the seafloor acoustic mirror transponders. As mentioned above, the transponders act as signal re-transmitters that receive and then return acoustic signals that were sent from the on-board transducer. In the positioning analysis, correction of underwater sound speed is a key to achieve centimeter accuracy (Fujita et al., 2006; Yokota et al., 2018). Thus, the installation of multiple transponders is necessary to accurately estimate perturbations of underwater sound speed (Kido, 2007).

The on-board transducer transmits two bi-phase modulation acoustic signals at a carrier wave frequency of 10 kHz. The first signal is used to identify each transponder and the second is used for ranging. The sequence code of the modulation used in the system is the maximum length sequence (M-sequence) code. The 8th and 9th order M-sequence codes are used for the identification and ranging signals, respectively. One bit of the code consists of four cycles of the carrier wave. Four phases are repeated 255 times for the identification signal and 511 times for the ranging signal, with each signal lasting 102.0 and 204.4 ms, respectively, with 102.0 ms separation (**Figure 2A**). The total time for one signal including the interval is about 400 ms.

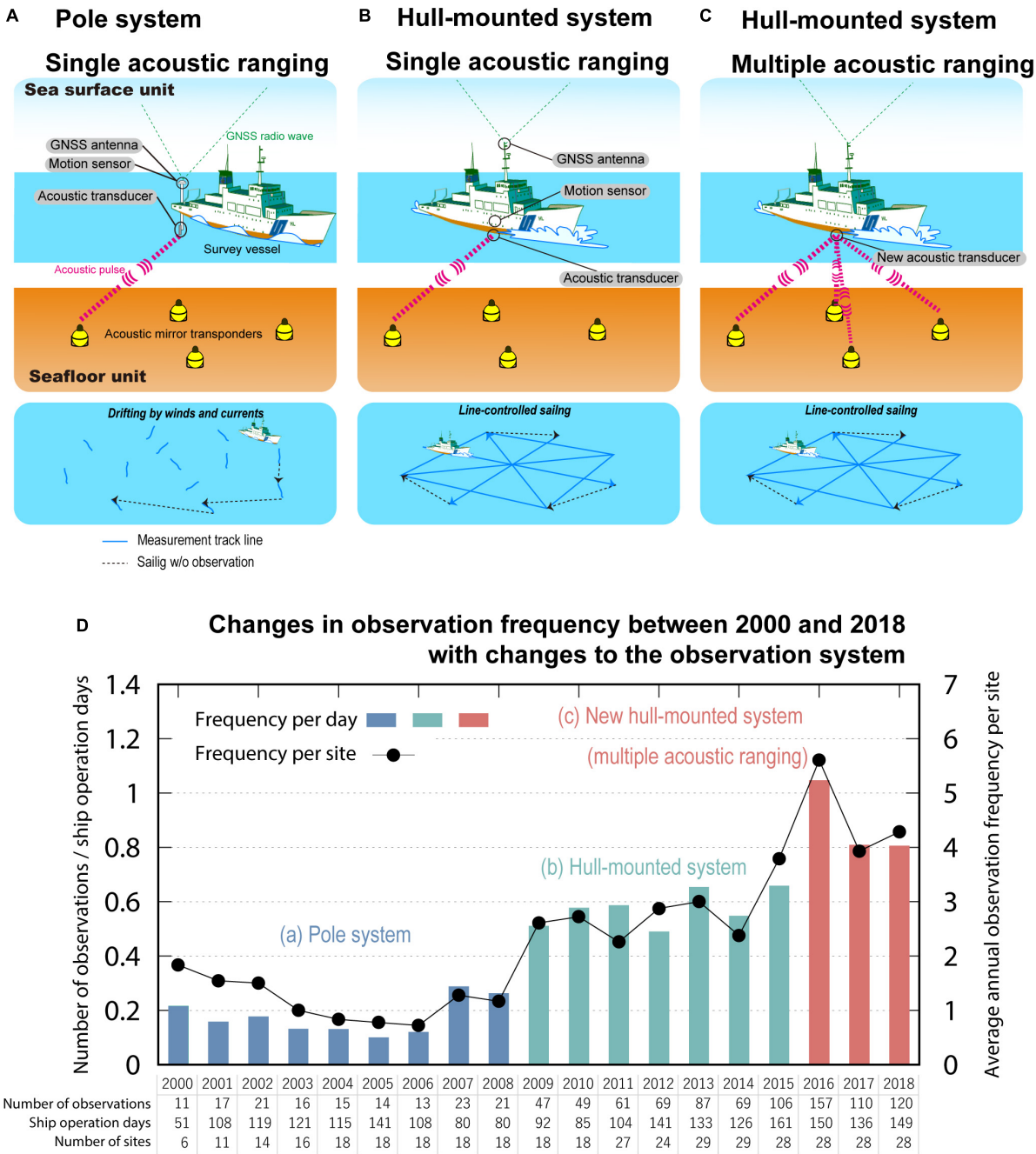

FIGURE 1 | History of the Japan Coast Guard's Global Navigation Satellite System-Acoustic ranging combination technique (GNSS-A) observation system. **(A)** Schematic of the GNSS-A pole system. **(B)** Schematic of the GNSS-A hull-mounted system. **(C)** Schematic of the GNSS-A hull-mounted system with a new transducer for multiple acoustic ranging. **(D)** Changes in observation frequency between 2000 and 2018 with changes to the observation system.

As explained above, the seafloor transponder receives the acoustic signals. If the identification signal code matches that of the transponder, the transponder records the succeeding ranging signal. After a prescribed interval time set for each transponder, the transponder returns the recoded ranging signal together with a new identification signal to the sea surface.

During the acoustic ranging, the sea surface transducer digitally records both the signals that were transmitted and received at a sampling frequency of 200 kHz. The precise round-trip travel time is calculated by cross-correlation between the syntheticsignal and the received ranging signal (Asada and Yabuki, 2001). The onset of the received signal can be identified as the maximum peak in the correlogram, taking advantage of the

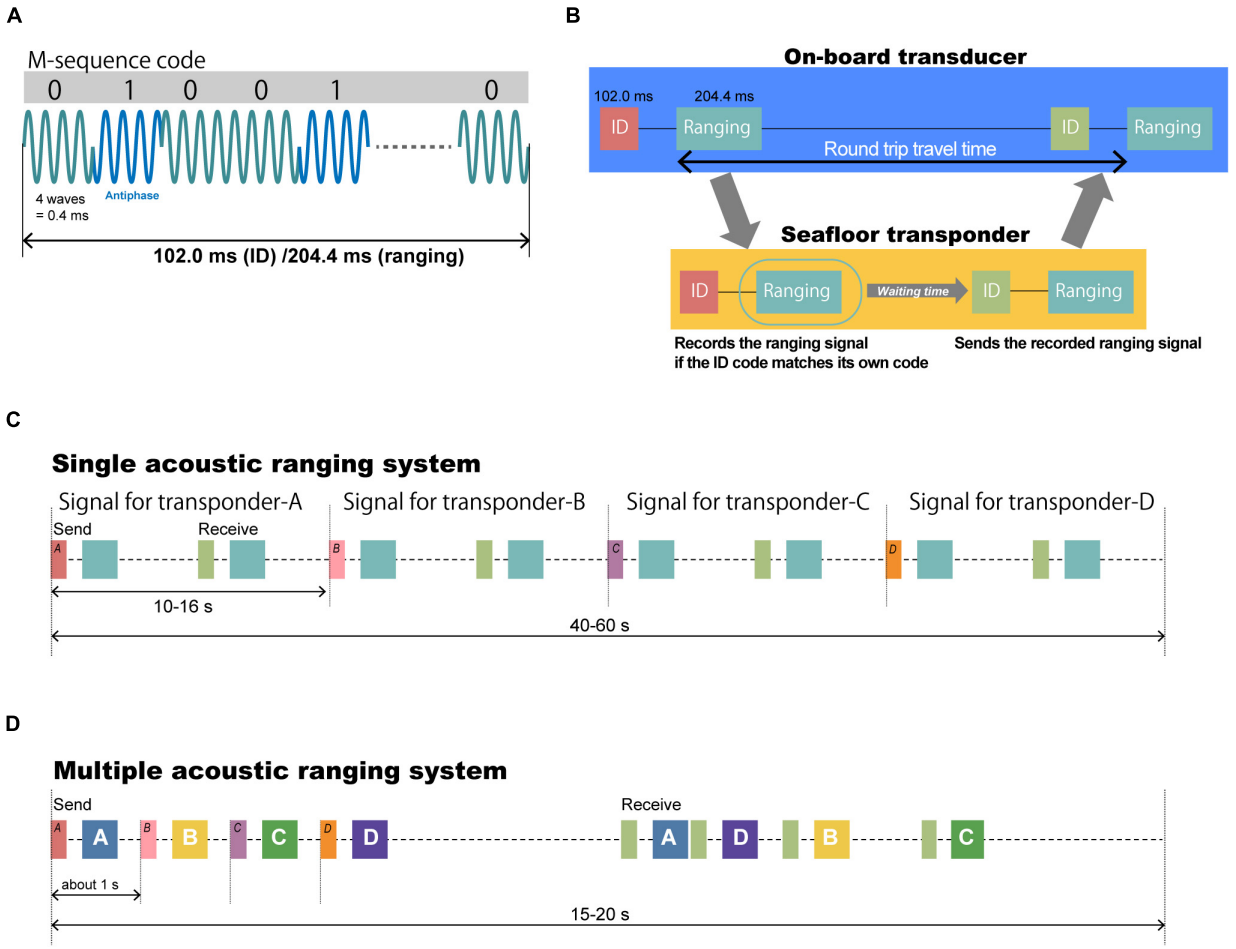

FIGURE 2 | Outline of the acoustic ranging system. **(A)** Acoustic waves coded by four-wave M-sequence signals. **(B)** Flowchart of transmission and reception of acoustic signals. Comparison of transmission and reception sequences in **(C)** the single acoustic ranging system (pole system and hull-mounted system) and **(D)** the multiple acoustic ranging system (new hull-mounted system). ID, identification signal.

characteristics of the M-sequence code. The flow of the acoustic ranging process is shown in **Figure 2B**.

HISTORY OF CHANGES TO THE SEA SURFACE UNIT

Pole System

A schematic of the GNSS-A pole system is shown in **Figure 1A**. This early system was used from 2000 (the first year of our observations) to 2008. The on-board equipment was mounted on a rigid 8-m-long pole attached to the stern of the vessel. A GNSS antenna and a motion sensor was attached to the top of the pole, and an acoustic transducer was attached to the bottom of the pole. The pole was not a permanent fixture and therefore had to be installed for each observation campaign. During acoustic measurement, it was necessary to have the bottom of the pole to which the transducer was attached extend into the sea. To avoid noise caused by propellers and deformation of the pole due to excessive load in the water, acoustic measurement was only possible when the vessel was drifting. We initially used an aluminum alloy pole, but in July 2002 we changed to a stiffer stainless steel pole to decrease the effects of pole deformation.

There were substantial problems with the pole system. The first problem was the difficulty of moving the vessel along an ideally balanced line over the transponders. The GNSS-A positioning technique is an underwater analog of GNSS positioning, and the vessel plays the role of the satellite in the GNSS. As with the dilution of precision (DOP) of the GNSS positioning due to bad satellite geometry, the vessel's track line has a large effect on the accuracy of seafloor positioning. An example of the survey line is shown in **Figure 1A**. If the entire region above the transponders can be covered in a well-balanced manner, then accuracy is maintained, but the data density varies by location because the vessel's position during the survey is not well-controlled.

Another problem was that observation was inefficient. The time required to transfer the vessel between the track lines was almost equal to that required for acoustic measurements (**Figure 1A**). In addition, human operations on the deck were

necessary to move the acoustic transducer up and down for vessel transfers. To ensure that deck operations were carried out safely, measurements were restricted during the night, and even during the day, measurements were often canceled because of bad weather. Thus, observation took up a lot of ship time in addition to the time required to conduct acoustic measurements.

Errors in the GNSS-A are mainly caused by variation in the atmosphere/ionosphere along the path of the GNSS radio wave and by underwater temperature/salinity along the path of the acoustic wave. Because the underwater perturbation has larger spatial and temporal scale than the GNSS-A observation time, i.e., several kilometers and hours, it tends to cause systematic bias error for positioning. Therefore, developing an analysis method for estimating the underwater conditions in detail is an important research target for GNSS-A observation. The method for decreasing systematic bias error by estimating the sound speed structure analytically has been developed (e.g., Fujita et al., 2006; Ikuta et al., 2008; Yokota et al., 2019). In these models, sufficiently distributed acoustic travel time data are needed for sound speed estimation. Specifically, adding the data to decrease random noise errors, several hundreds of acoustic travel time data for each transponder are required. As such, the number of acoustic signals that the four transponders were to receive using the pole system was empirically set at around 5,000. To obtain a sufficient amount of data, 2–4 days were spent at one site. Because a single observation took several days, weather pose problems. Therefore, it was not always possible to obtain a sufficient amount of data.

Hull-Mounted System

From 2009, the on-board equipment was permanently mounted on the vessel. In this hull-mounted system, the acoustic transducer is attached to the hull and the GNSS antenna is attached to the top of the main mast (**Figure 1B**). When the vessel is dry-docked, the relative position between the GNSS antenna and the transducer is determined by total stations and GNSS used in terrestrial survey. The attitude of the vessel is measured by a dynamic motion sensor and used to determine the coordinates of the transducer relative to those of the GNSS antenna.

Measurements are conducted while the vessel moves along an ideal well-balanced track line. In addition, measurement is possible during both day and night because human operations on the deck are no longer necessary and there are less interruptions to measurements due to vessel transfer between track lines compared with the pole system. Thus, measurement accuracy is improved over that of the pole system (Sato et al., 2013b) and the observation time for a single site is decreased from 2–4 days to 16–24 h.

The required number of acoustic signals was set to about 5,000, as was empirically determined in the pole system era. However, the hull-mounted system requires less signals because of high efficiency in obtaining well-balanced data. In 2015, we investigated data collected using the hull-mounted system and concluded that about 3,500 acoustic signals are enough to take measurements. Thus, the observation time is decreased to about three quarters.

Hull-Mounted System With Multiple Acoustic Ranging

As mentioned above, the on-board transducer transmits two acoustic signals: an identification signal and a ranging signal. Each transponder has an identification code to distinguish each other and operates only when receiving the same identification code. Acoustic ranging is conducted by sequentially transmitting the two signals to four seafloor transponders, with the identification signal changed to match that of each transponder with each successive attempt (i.e., each cycle). **Figure 2C** shows one cycle of acoustic ranging for four transponders. The signal transmission interval, which depends on the depth of the transponders, is 10–16 s. Therefore, it takes 40–60 s to complete one cycle measurement for the transponder array.

To increase the observation frequency, it is necessary to decrease the observation time. Thus, a new transducer called multiple acoustic ranging has been developed that enables multiple transmissions and receptions in one sequence (**Figure 1C**; Yokota and Okumura, 2015; Yokota et al., 2017). This new transducer transmits acoustic signals successively without waiting to receive each reply signal from the seafloor transponders but instead receives all the reply signals at one time (**Figure 2D**). In the conventional system, the ranging signals are all coded using the same M-sequence code. In the new multiple acoustic ranging system, the ranging signal is coded using different M-sequence codes for each transponder to avoid crosstalk between receiving signals. Because the ranging signals that are received have different codes, overlapping signals can be separated by cross-correlation processing.

The signal transmission length for one transponder is about 0.4 s and transmission intervals are set to 1 s to protect the internal electric circuit. The length of the transmission sequence takes roughly the number of transponders multiplied by 1 s. Because the first returned signal arrives before the transmission of the last signal in the case of shallow transponder depth, the possible number of transmitted signals depends on the transponder depth. Because the receiving sequence requires a time length that is enough to receive signals from the farthest transponder, it is set to about 10–16 s depending on the transponder depth. The entire process takes 15–20 s, which is much shorter than that of the conventional system, which takes 40–60 s. By measuring the signals from the four transponders simultaneously in one sequence, the observation is completed in about 3–4 h, which is a quarter of that of the conventional system.

SUMMARY OF OBSERVATION FREQUENCY IMPROVEMENT

Figure 1D shows the time series of the ratio of number of observations to ship operation days and the average annual observation frequency for each observation system per site. Although there is variability due to the effects of weather and equipment failure, the graph roughly shows the evolution of system ability to increase observation frequency.

In 2008 and earlier, the pole system era, the ratio was 0.1–0.3 and the observation frequency was about one time annually per site. This is insufficient to measure crustal deformations at the centimeter level. In this era, we increased the observation frequency for seismologically important sites, but decreased the observation frequency for other sites. In this manner, we succeeded in obtaining the first seafloor movement velocity at a site off Miyagi where an M7-class earthquake has repeatedly occurred. Fujita et al. (2006) revealed a high degree of interplate locking offshore Miyagi from the data of 7 GNSS-A measurements taken during a 3-year period (2002–2005). Matsumoto et al. (2008) suggested low interplate locking offshore Fukushima.

From 2009, the hull-mounted system era, the ratio was improved to 0.5–0.6 and the annual observation frequency was increased to 2–3 times. By optimizing the number of acoustic signals from 5,000 to 3,500 in 2015, the observation frequency exceeded three times as much as that of the pole system annually per site. Because this frequency is sufficient to measure long-term (4–5 years) movement rate (i.e., mean velocity) at the centimeter level, it is possible to make observations at the same frequency for almost all sites. Thus, the spatial heterogeneity of seafloor crustal deformation has been revealed from wide-area measurement data along the Japan Trench (Sato et al., 2013a) and along the Nankai Trough (Yokota et al., 2015, 2016).

After the installation of the new hull-mounted multi-acoustic ranging system in 2016, the ratio exceeds 1.0 and the observation frequency is now over five times annually per site. In 2017, the frequency decreased due to electrical failure of the transducer. In the present day, considering the importance of disaster prevention in the Nankai Trough, we have set the observation frequency for each site along the Japan Trench and the Nankai Trough to 3 times per year and 4–8 times per year, respectively. High-frequency observation along the Nankai Trough might disclose temporal changes of inter-seismic coupling on a yearly basis.

In response to seismological demand, short-term geodetic phenomena such as SSEs need to be detected with certainty. Therefore, increasing the observation frequency of affected sites is essential, and the development of a new sea surface platform rather than a vessel is required. There are already studies on a GNSS buoy (Takahashi et al., 2014; Kato et al., 2018; Tadokoro et al., 2020) and an automated vehicle (Chadwell, 2016), but the feasibility of such a system needs to be examined, considering both operation safety and costs. Also, examination of various possibilities in sea surface platform engineering will continue to be essential.

AUTHOR CONTRIBUTIONS

TI designed the study. YY, TI, and SW led the development of the observation system to increase observation frequency. TI and YY wrote this manuscript. YY, TI, SW, and YN participated in discussion about the observation system and made comments to improve the manuscript.

FUNDING

The submission of the manuscript was funded by the Japan Coast Guard.

ACKNOWLEDGMENTS

We thank the reviewers for their helpful comments and suggestions. We thank the many staff members from the Hydrographic and Oceanographic Department, Japan Coast Guard, including the crew of the survey vessels Takuyo, Shoyo, Meiyo, and Kaiyo for their support in our observations and technological developments. We especially thank the active senior staff members from the Geodesy and Geophysics Office, Hydrographic and Oceanographic Department, Japan Coast Guard, for their devoted maintenance and management of the equipment.

REFERENCES

Asada, A., and Yabuki, T. (2001). Centimeter-level positioning on the seafloor. *Proc. Jpn. Acad. Ser. B* 77, 7–12. doi: 10.2183/pjab.77.7

Chadwell, C. D. (2016). "Campaign-style GPS-Acoustic with wave gliders and permanent seafloor benchmarks," in *Proceedings of the Subduction Zone Observatory Workshop, Boise Center, Boise, ID, Sep. 29 – Oct. 1 2016*, Boise, ID.

Fujita, M., Ishikawa, T., Mochizuki, M., Sato, M., Toyama, S.-I., Katayama, M., et al. (2006). GPS/acoustic seafloor geodetic observation: method of data analysis and its application. *Earth Planets Space* 58, 265–275. doi: 10.1007/s00190-013-0649-9

Ikuta, R., Tadokoro, K., Ando, M., Okuda, T., Sugimoto, S., Takatani, K., et al. (2008). A new GPS-acoustic method for measuring ocean floor crustal deformation: application to the Nankai Trough. *J. Geophys. Res.* 113:B02401. doi: 10.1029/2006JB004875

Kato, T., Terada, Y., Tadokoro, K., Kinugasa, N., Futamura, A., Toyoshima, M., et al. (2018). Development of GNSS buoy for a synthetic geohazard monitoring system. *J. Disaster Res.* 13, 460–471. doi: 10.20965/jdr.2018.p0460

Kido, M. (2007). Detecting horizontal gradient of sound speed in ocean. *Earth Planets Space* 59, e33–e36. doi: 10.1186/BF03352027

Kido, M., Osada, Y., Fujimoto, H., Hino, R., and Ito, Y. (2011). Trench-normal variation in observed seafloor displacements associated with the 2011 Tohoku-oki earthquake. *Geophys. Res. Lett.* 38:L24303. doi: 10.1029/2011GL050057

Matsumoto, Y., Ishikawa, T., Fujita, M., Sato, M., Saito, H., Mochizuki, M., et al. (2008). Weak interplate coupling beneath the subduction zone off Fukushima, NE Japan, inferred from GPS/acoustic seafloor geodetic observation. *Earth Planets Space* 60, e9–e12. doi: 10.1186/BF03353114

Obara, K., and Kato, A. (2016). Connecting slow earthquakes to huge earthquakes. *Science* 353, 253–257. doi: 10.1126/science.aaf1512

Ochi, T. (2015). Temporal change in plate coupling and long-term slow slip events in southwestern Japan. *Earth. Planet. Sci. Lett.* 431, 8–14. doi: 10.1016/j.epsl.2015.09.012

Sato, M., Fujita, M., Matsumoto, Y., Ishikawa, T., Saito, H., Mochizuki, M., et al. (2013a). Interplate coupling off northeastern Japan before the 2011 Tohoku-oki earthquake, inferred from seafloor geodetic data. *J. Geophys. Res. Solid Earth* 118, 3860–3869. doi: 10.1002/jgrb.50275

Sato, M., Fujita, M., Matsumoto, Y., Saito, H., Ishikawa, T., and Asakura, T. (2013b). Improvement of GPS/acoustic seafloor positioning precision through controlling the ship's track line. *J. Geod.* 118, 1–10. doi: 10.1007/s00190-013-0649-9

Sato, M., Ishikawa, T., Ujihara, N., Yoshida, S., Fujita, M., Mochizuki, M., et al. (2011). Displacement above the hypocenter of the 2011 Tohoku-oki earthquake. *Science* 332:1395. doi: 10.1126/science.1207401

Spiess, F. N. (1985). Suboceanic geodetic measurements. *IEEE Trans. Geosci. Remote Sens.* 23, 502–510.

Tadokoro, K., Kinugasa, N., Kato, T., Terada, Y., and Matsuhiro, K. (2020). A Marine-buoy-mounted system for continuous and real-time measurment of seafloor crustal deformation. *Front. Earth Sci.* 8:123. doi: 10.3389/feart.2020.00123

Takahashi, N., Ishihara, Y., Ochi, H., Fukuda, T., Tahara, J., Maeda, Y., et al. (2014). New buoy observation system for tsunami and crustal deformation. *Mar. Geophys. Res.* 35, 243–253. doi: 10.1007/s11001-014-9235-7

Yokota, Y., and Ishikawa, T. (2020). Shallow slow slip events along the Nankai Trough detected by GNSS-A. *Sci. Adv.* 6:eaay5786. doi: 10.1126/sciadv.aay5786

Yokota, Y., Ishikawa, T., Sato, M., Watanabe, S.-I., Saito, H., Ujihara, N., et al. (2015). Heterogeneous interplate coupling along the Nankai Trough, Japan, detected by GPS-acoustic seafloor geodetic observation. *Progr. Earth Planet. Sci.* 2:10. doi: 10.1186/s40645-015-0040-y

Yokota, Y., Ishikawa, T., and Watanabe, S. (2018). Seafloor crustal deformation data along the subduction zones around Japan obtained by GNSS-A observations. *Sci. Data* 5:180182. doi: 10.1038/sdata.2018.182

Yokota, Y., Ishikawa, T., and Watanabe, S. (2019). Gradient field of undersea sound speed structure extracted from the GNSS-A oceanography. *Mar. Geophys. Res.* 40, 493–504. doi: 10.1007/s11001-018-9362-7

Yokota, Y., Ishikawa, T., Watanabe, S., Tashiro, T., and Asada, A. (2016). Seafloor geodetic constraints on interplate coupling of the Nankai Trough megathrust zone. *Nature* 534, 374–377. doi: 10.1038/nature17632

Yokota, Y., and Okumura, M. (2015). Study for improving efficiency in seafloor geodetic observation by means of multi-acoustic ranging. *Rep. Hydro. Ocean Res.* 52, 79–87.

Yokota, Y., Tashiro, T., and Shimomura, H. (2017). Implementation of multi-acoustic ranging system. *Rep. Hydro. Ocean Res.* 54, 32–37.

Conflict of Interest: The authors declare that the research was conducted in the absence of any commercial or financial relationships that could be construed as a potential conflict of interest.

frontiers in Earth Science

BRIEF RESEARCH REPORT
published: 04 August 2020
doi: 10.3389/feart.2020.00331

Kilometer-Scale Sound Speed Structure That Affects GNSS-A Observation: Case Study off the Kii Channel

Yusuke Yokota[1], Tadashi Ishikawa[2], Shun-ichi Watanabe[2] and Yuto Nakamura[2]*

[1] *Institute of Industrial Science, University of Tokyo, Tokyo, Japan,* [2] *Hydrographic and Oceanographic Department, Japan Coast Guard, Tokyo, Japan*

The Global Navigation Satellite System-Acoustic ranging combination technique (GNSS-A) is a recently developed technology to precisely detect seafloor crustal deformation. This method can also estimate km-scale underwater sound speed structure (SSS) as a by-product of monitoring seafloor crustal deformation. This paper evaluates the validity of the spatial gradient and its temporal variation of the SSS estimated by GNSS-A observations off the Kii channel before and after Kuroshio meandering. According to the comparison of the JCOPE2M reanalysis data and the *in situ* observation data, the GNSS-A estimated SSS has local structures that are not reproduced in this reanalysis but were detected by *in situ* data. In addition, we investigate the effect of observation time on the stability of SSS estimation. The results suggest that the sufficient time required for stable estimation depends on the spatial coverage of observation data, which depends on the depth of the site. As a result, the time resolution was derived to be about one hour at a site whose depth is 1500 m.

Keywords: GNSS-A, GNSS-A oceanography, sound speed structure, Kuroshio, Kii channel

OPEN ACCESS

Edited by:
Keiichi Tadokoro, Nagoya University, Japan

Reviewed by:
Shohei Minato, Delft University of Technology, Netherlands
How-Wei Chen, National Central University, Taiwan

****Correspondence:***
Yusuke Yokota
yyokota@iis.u-tokyo.ac.jp

Specialty section:
This article was submitted to Environmental Informatics and Remote Sensing, a section of the journal Frontiers in Earth Science

Received: *03 April 2020*
Accepted: *16 July 2020*
Published: *04 August 2020*

Citation:
Yokota Y, Ishikawa T, Watanabe S and Nakamura Y (2020) Kilometer-Scale Sound Speed Structure That Affects GNSS-A Observation: Case Study off the Kii Channel. Front. Earth Sci. 8:331. doi: 10.3389/feart.2020.00331

INTRODUCTION

The Global Navigation Satellite System-Acoustic ranging combination technique (GNSS-A) was proposed and developed to extend the geodetic network to the seafloor by combining GNSS positioning with acoustic ranging technology (Spiess, 1985; Asada and Yabuki, 2001; Fujita et al., 2006). This observation technique makes it possible to accurately measure the seafloor movement and to detect various subseafloor geophysical phenomena due to co-, post-, and inter-seismic phases following a huge earthquake cycle (e.g., Sato et al., 2011; Watanabe et al., 2014; Yokota et al., 2016). Recently, Yokota and Ishikawa (2020) reported detection of tiny transient signals due to slow slip events. To monitor this kind of transient signals continuously, it is indispensable to upgrade the GNSS-A accuracy, which requires a better understanding of the underwater sound speed structure (SSS).

The uncertainty of the SSS is a major error source of GNSS-A observation. Our group has been developing analysis methods to estimate the SSS from GNSS-A observation (Fujita et al., 2006; Yokota et al., 2019). For example, Yokota and Ishikawa (2019) confirmed that the GNSS-A estimated SSS off the Bungo channel is almost consistent with the temperature gradient structure caused by the Kuroshio.

Detailed SSS was discussed using, e.g., seismic survey (Ruddick et al., 2009; Papenberg et al., 2010). Seismic oceanography was also conducted in the Kuroshio region (Tsuji et al., 2005; Nakamura et al., 2006). However, it is not possible to obtain this kind of data at various points at low cost and with high frequency. While seismic oceanography is suitable for understanding the details of complexity and ocean physical characteristics of fine scale ocean, GNSS-A oceanography might be useful for understanding location characteristics and long-term characteristics (seasonal changes and relationships with seafloor topographies). Understanding SSS effect in each technique may also lead to upgrading the accuracy of each technique.

This paper conducts surveys on the spatial gradient of SSS that affects the GNSS-A, by comparison between its analysis results and the ocean structure off the Kii channel before and after Kuroshio meandering. The estimated parameters are compared with ocean reanalysis data and *in situ* expendable bathythermographs (XBTs) and expendable conductivity temperature depth (XCTD) profilers data. The results depend on whether the Kuroshio is meandering or not. Especially in the case when the Kuroshio meandered, GNSS-A estimated SSS has a gradient that was not reproduced in the reanalysis used for the comparison. Additionally, we examine the temporal variation of the gradient parameters.

METHODS

Gradient Parameters Extraction

In the GNSS-A, to measure the movement of the seafloor accurately, the absolute position of a relay point located on the sea surface is determined by the GNSS, and the relative position between the relay point and the seafloor station is determined by acoustic ranging. As a result, the absolute seafloor position can be determined. The observation system is shown in **Figure 1A**. Please see Yokota et al. (2018) for details.

In the present day, the horizontal positioning accuracy of the GNSS-A is about 2 cm (1σ). Because the spatiotemporal variations of the SSS are more complex and larger than those of the ionosphere/troposphere which affect the GNSS positioning, the uncertainty of SSS is the largest error source of GNSS-A. Data obtained from *in situ* observations such as XBT/XCTD measurements can constrain the SSS, but cannot cover all of these variations in detail. Therefore, developing an analysis method for estimating the SSS in detail is an important research target for GNSS-A observation.

After the early work of Fujita et al. (2006) which estimates the temporal variation of the SSS by quadratic polynomial approximation, various techniques to process underwater SSS have been studied. Yokota et al. (2019) reinterpreted Fujita's method and developed a technique that determines the shallow horizontal gradient of the SSS by performing pseudo-tomographic analysis within the triangle V_1 (**Figure 1B**) connecting the moving ship and the seafloor station. Additionally, estimation of the SSS when fluctuations occur in deeper regions has been improved by using another triangle V_2 (**Figure 1B**). Their detailed methodologies are described in Yokota (2019), Yokota and Ishikawa (2019), and Yokota et al. (2019).

Here, only the SSS estimation procedure (Figure 2 in Yokota et al., 2019) is described. First, we generate a horizontal layered SSS from XBT/XCTD observations as an initial parameter. After that, in the inversion analysis, an effect for each acoustic shot due to temporal and spatial changes is corrected. Here, the removal operations of the long-period component and the short-period V_1 and V_2 are performed step by step, and the routine is repeatedly performed until convergence. The parameters obtained here include high-rate GNSS errors as well as complex disturbances in the ocean. At present, it is difficult to properly evaluate this amount of error, and the evaluation method is a future research topic.

As discussed in Yokota (2019), the tendency of SSS depends on V_1/V_2. When V_1/V_2 is higher than the survey line range for the diameter of the array, which is about 2 in this study, the effect of shallower gradient becomes stronger, and when V_1/V_2 is lower than 2, the effect of deeper gradient becomes stronger. The depth tendencies of SSS cannot be determined quantitatively.

Generally, to understand the ocean structure, satellite observations are used to capture the global ocean surface property and *in situ* observations, such as XBT/XCTD, Argo float, are used to capture the vertical profile at a local point. In the GNSS-A, the overview of the horizontal gradient of the SSS is obtained. Because the spatial range of the obtained gradient depends on the size of the transponder deployment region, which is typically in the range of 2–6 km, the GNSS-A estimated SSS can have a slightly different perspective than those of other ocean observations. The GNSS-A may reveal structures that cannot be detected by other observations. Although there is no other way to precisely measure SSS in km-scale than costly XBT/XCTD dense observations, we examine the appropriateness of the GNSS-A estimation results by comparing with other data having different spatial scales such as *in situ* and reanalysis data.

Data

Here, we use the data obtained at two sites off the Kii channel, namely, MRT1 and MRT2 (**Figure 1C**) in June 2013 (1306), April 2018 (1804), July 2018 (1807), and November 2018 (1811). The gradient parameters estimated from GNSS-A data for each observation campaign are represented as vectors V_1 and V_2 as shown in **Figure 2**. Although the vectors can be obtained for each acoustic shot data continuously, in section "RESULTS," we discuss using the time average value from all acoustic shot data. Temporal variation of gradient vectors will be discussed in section "DISCUSSION."

Supplementary Figure S1 shows residuals of travel time before and after corrections of V_1 and V_2 (colored cross for each station) (A and B), average sound speeds estimated before (gray line) and after corrections of V_1 and V_2 (colored line for each station) (C), and the position of the vessel relative to the center of the station array (D) for each shot in the final solution. For example, in the case of MRT2-1804 (**Supplementary Figure S1bC**), estimated average sound speeds for station-N (north) are always faster than station-S (south). As a

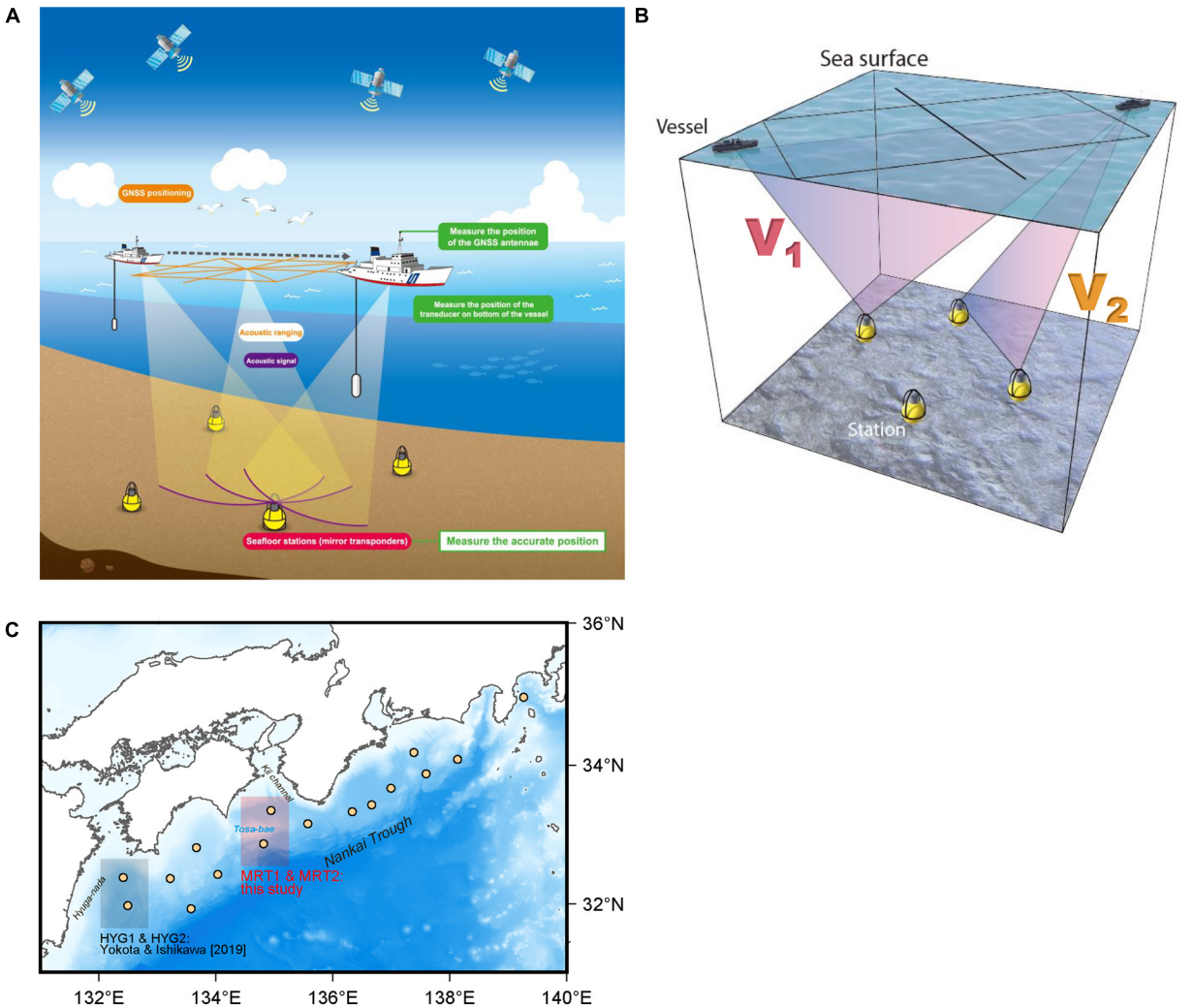

FIGURE 1 | (A) A schematic image of the GNSS-A system. **(B)** A schematic image of scanning SSS. These figures are modified after Yokota et al. (2018, 2019). **(C)** GNSS-A sites (orange circles) along the Nankai Trough as of November 2018.

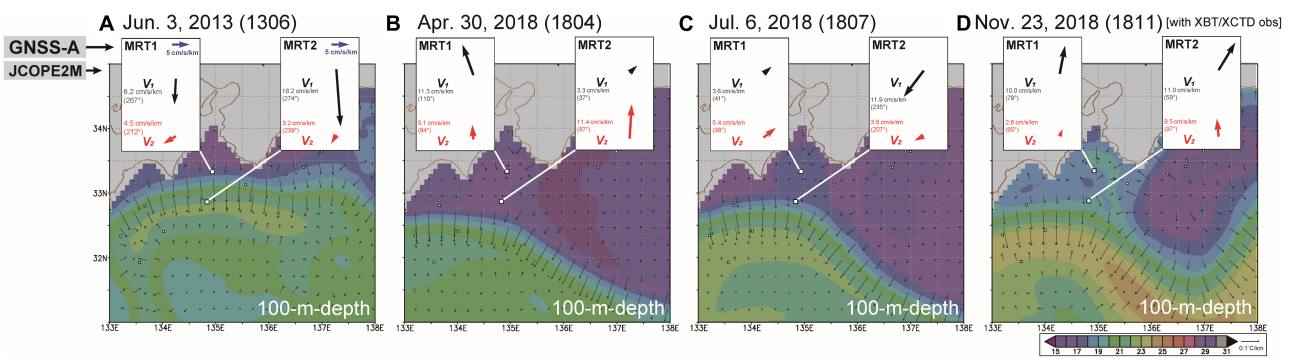

FIGURE 2 | Gradient parameters extracted in GNSS-A [black (V_1) and red (V_2) vectors] and 100 m-depth temperature fields of the JCOPE2M reanalysis on observation dates, **(A)** June 3, 2013, **(B)** April 30, 2018, **(C)** July 6, 2018, and **(D)** November 23, 2018 for MRT1 and MRT2. The value of each vector (absolute value and counterclockwise angle from east) is written beside the vector. Scales of the water temperature and the temperature gradient vector of the JCOPE2M reanalysis are shown on the bottom right.

result, a large northward V_2 was obtained, suggesting the effect of deeper northward gradient. In the cases of 1811 (**Supplementary Figure S1dC**), although estimation results at both stations show temporal changes, it can be inferred from the small average V_2 that the effects of the shallower gradients were larger.

Each vector in **Figure 2** is pointing in the direction of higher sound speed. In 1306 and 1811, V_1 is sufficiently larger than V_2. This suggests that the SSS has a gradient only in the relatively shallow layers. However, the thickness of the gradient layer cannot be uniquely estimated. In contrast, the result obtained at site MRT2 in 1804 shows that V_2 is larger than V_1. This suggests that a gradient has emerged in a relatively deeper region. Small vectors at site MRT1 in 1807 suggest a weak gradient SSS.

RESULTS

Comparison With JCOPE2M Reanalysis

JCOPE2M is a new ocean reanalysis data that is an advanced version of JCOPE2 used in our previous studies (Yokota and Ishikawa, 2019; Yokota et al., 2019). JCOPE2M is a data targeting the northwestern Pacific Ocean, produced by assimilating satellite and *in situ* observation data to an ocean model using a multi-scale three-dimensional variational scheme (Miyazawa et al., 2017, 2019). The model is based on the Princeton Ocean Model, with a horizontal resolution of 1/12 degrees. The model can express 10–100 km scale oceanographic phenomena, but detailed structure on the km-scale has not been completely represented. Here, we compare the GNSS-A estimated gradient vector of SSS with the JCOPE2M reanalysis.

Figure 2 shows the temperature and its gradient at 100 m depth, derived from the reanalysis during each observation campaign. In 1306, the northern edge of the Kuroshio lies around the vicinity of MRT1 and MRT2. The large southward gradient field V_1 is consistent with the reanalysis (**Figure 2A**). This result is similar as ones off the Bungo channel (Yokota and Ishikawa, 2019), when the Kuroshio flows near the GNSS-A site.

After August 2017, when the Kuroshio began to meander, the southward gradient vectors around the two sites in the JCOPE2M reanalysis changed because warm seawater advected to the south (**Figures 2B–D**). In 1807 (**Figure 2C**), site MRT1 was located far from Kuroshio, and site MRT2 was located at the edge region of Kuroshio. Small extracted vectors at site MRT1 and southward vectors at site MRT2 are consistent with the reanalysis.

In 1804 (**Figure 2B**), the reanalysis indicates very weak gradients around the sites, because the Kuroshio was far away from the sites. In contrast, GNSS-A estimates a northward gradient vector which is inconsistent with reanalysis. In 1811 (**Figure 2D**), northward vectors at MRT2 were also inconsistent with a slight southward gradient in the reanalysis.

Comparison With *in situ* Sound Speed Observation

To fill the gap between the GNSS-A estimation and the reanalysis, *in situ* observation was carried out along a line crossing the Kuroshio in 1811. XBT/XCTD were dropped sequentially at evenly spaced points as shown in **Figure 3A**. **Figure 3B** shows the cross section of the underwater SSS, generated from the XBT and XCTD data. A shallow seafloor hill topography called the Tosa-bae bump is located between MRT1 and MRT2. It is possible that this structure affects the fine scale ocean structure in this region. The area of this topography is masked in **Figure 3B**.

This result shows that there is a northward gradient around 33.2–33.5N and a southward gradient around 32.7–32.8N which are consistent with the reanalysis. The northward GNSS-A result at site MRT1 is thought to reflect the 33.2–33.5N gradient. In addition, different from the comparison at the Hyuga-nada sites in Yokota and Ishikawa (2019), there is partially complicated structure that does not appear in the reanalysis around 32.8–32.9N (200–300 m depth).

The northward GNSS-A result at site MRT2, which is inconsistent with the reanalysis, may reflect the km-scale structure around 32.8–32.9N shown in this *in situ* observation. The qualitative depth of a gradient structure can be inferred from the discussions in Yokota (2019) and Yokota and Ishikawa (2019). In the case of this GNSS-A estimation result ($V_1/V_2 \geq 2$), we can indicate a possibility that there was a shallower side simple structure as shown in the *in situ* observation, though the quantitative depth cannot be determined. The comparison results suggest that GNSS-A was also affected not only by 100 km scale SSS as estimated by reanalysis but also by km-scale SSS as detected by detailed direct observation.

However, without costly dense (spatial and temporal) *in situ* observation, it is difficult to verify the GNSS-A extraction results in such a complicated case. To apply the GNSS-A estimated SSS oceanographically and to enhance the GNSS-A observation accuracy, more oceanographic *in situ* observations and validations will be necessary.

The km-scale structure may reflect the complexity of the underwater structure, such as internal gravity waves. In the vicinity of our study area, the Tosa-bae bump may have triggered such a complicated SSS. Matsui et al. (2019) showed that internal gravity waves driven by such topographic peaks affect GNSS-A positioning accuracy, using numerical simulation.

DISCUSSION

Temporal Resolution

Up to the above section, we discussed using gradient values that have been time averaged over the entire observation time in each observation campaign. In principle, the gradient vector is estimated for each acoustic shot, which makes it possible to detect the time variation of the gradient vector. Yokota and Ishikawa (2019) and Yokota et al. (2019) visualized the time variation of the gradient vectors using one round of the survey line as shown in **Figure 4A**. However, the estimation of the gradient vector is stable only when the survey lines cover the whole observation area. **Figures 4B–D** show the effect of data coverage on the estimation of gradient vector in the cases using half, one third, and a quarter of all survey lines.

Figure 4 shows that the gradient vectors become unstable as the coverage of the observation area becomes narrower. As shown in the layout of the survey lines, the estimation sensitivity is

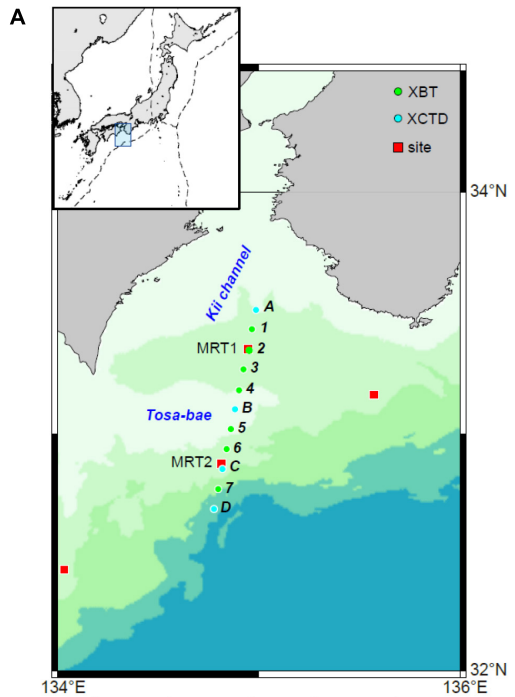

A	33.5131N	134.9858E	Nov. 23	ETC12:51	XCTD
1	33.4332N	134.9653E	Nov. 23	ETC13:19	XBT
2	33.3450N	134.9517E	Nov. 23	ETC11:34	XBT
3	33.2662N	134.9233E	Nov. 23	ETC14:18	XBT
4	33.1789N	134.9013E	Nov. 23	ETC14:51	XBT
B	33.0996N	134.8812E	Nov. 23	ETC15:22	XCTD
5	33.0168N	134.8604E	Nov. 23	ETC15:48	XBT
6	32.9334N	134.8393E	Nov. 23	ETC16:16	XBT
C	32.8500N	134.8185E	Nov. 23	ETC16:44	XCTD
7	32.7656N	134.7973E	Nov. 23	ETC17:22	XBT
D	32.6824N	134.7766E	Nov. 23	ETC17:43	XCTD

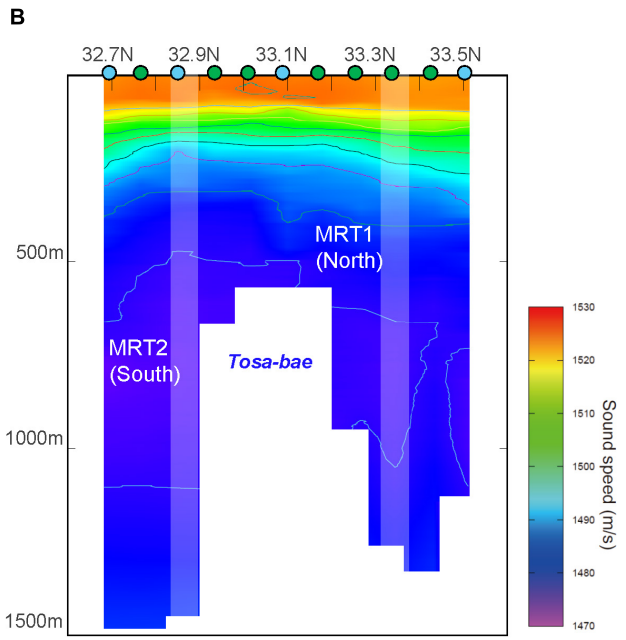

FIGURE 3 | (A) Locations of the seafloor sites and direct sound speed observation points in November 2018. Red squares indicate seafloor sites MRT1 and MRT2. Green and light-blue circles indicate XBT and XCTD observation points, respectively. Details of XBT and XCTD casts are listed in the bottom table. **(B)** Resultant SSS cross section of direct observations. White bars indicate regions around sites MRT1 and MRT2. Green and blue circles at the surface indicate positions of the XBT and XCTD casts, respectively.

weak when the survey lines are perpendicular to the gradient, because the data coverage area in the direction of the gradient becomes narrower. In most cases, the SSS around site MRT2 has a meridional gradient since the flow of Kuroshio off the Kii channel is mainly eastward. Therefore, when the survey line covers only in the zonal direction (for example, in **Figure 4D**, second vector), a correct gradient cannot be detected.

From the above discussion, the time resolution of the GNSS-A estimated gradient vector for site MRT2 is about one hour at best, which is enough time to evenly cover the observation area. However, as with the case of spatial resolution, there is almost no model or *in situ* observation that can explain the hourly order fluctuations, making it difficult to verify whether the temporal variation of the estimated gradient vector reflects the actual underwater structure.

As shown in **Figure 1B**, the survey line length is set to be broadened depending on the depth so that the triangle size is large enough for stable estimation. Practically, the diagonal length of the survey lines is set to be approximately twice the depth of the site. Therefore, the observation time required to evenly cover all directions depends on the depth of the site. In the case of MRT2, whose depth is 1500 m, the time resolution is about one hour. Thus, the time resolution T at a site with an arbitrary depth is estimated as follows:

$$T \sim 1 * depth(m)/1500(m)[hour] \quad (1)$$

The time resolution derived from this relationship is about 2 h for a 3000 m depth site, and about 40 min for a 1000 m depth site. However, this is just a provisional result that needs to be confirmed by further research.

Future Works

It is considered that the gradient SSSs off the Kii channel shown here reflects not only the large structures due to the

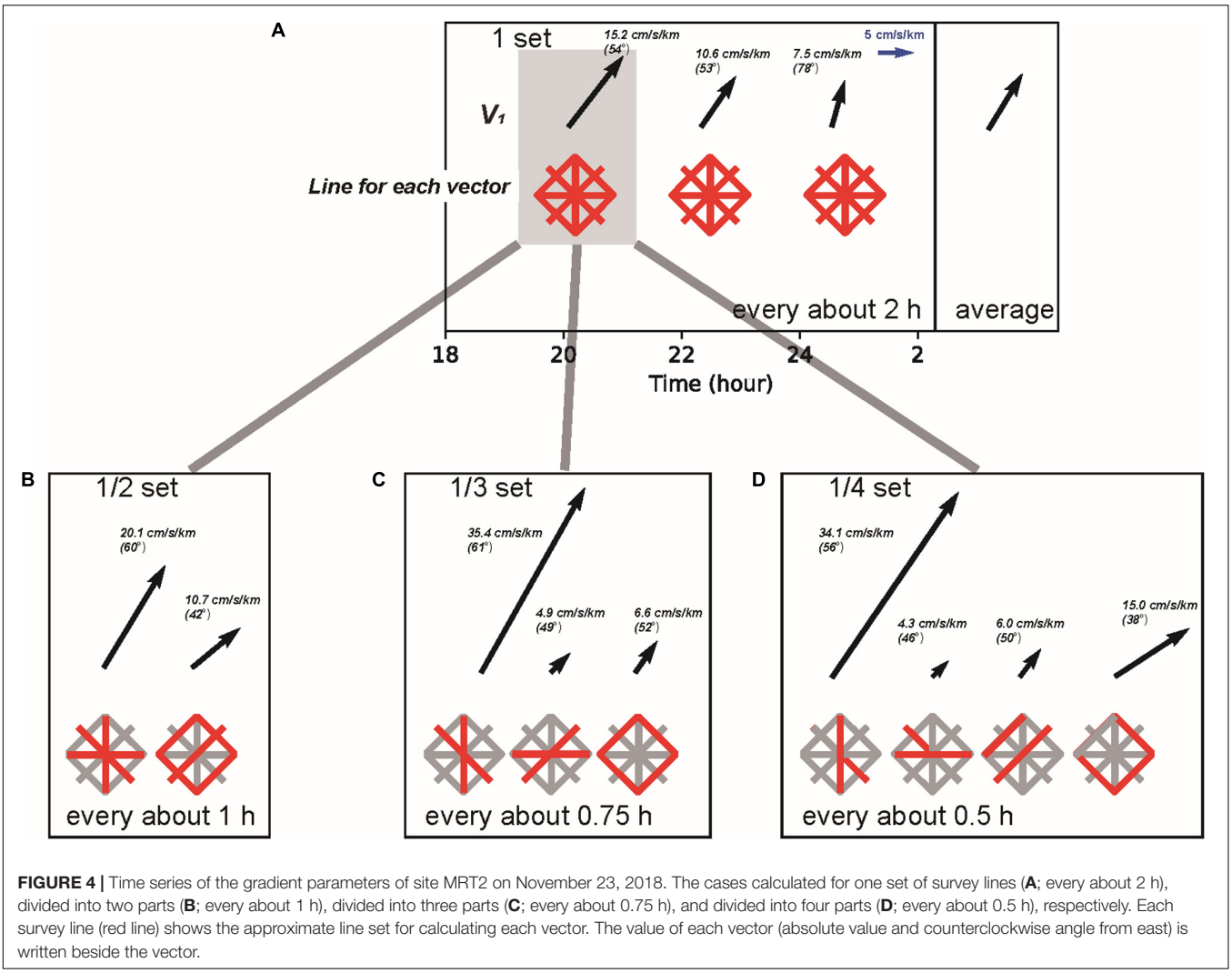

FIGURE 4 | Time series of the gradient parameters of site MRT2 on November 23, 2018. The cases calculated for one set of survey lines (**A**; every about 2 h), divided into two parts (**B**; every about 1 h), divided into three parts (**C**; every about 0.75 h), and divided into four parts (**D**; every about 0.5 h), respectively. Each survey line (red line) shows the approximate line set for calculating each vector. The value of each vector (absolute value and counterclockwise angle from east) is written beside the vector.

Kuroshio but also fine scale fluctuations that are not easy to obtain appropriate data for comparison. In the future, further confirmation of the estimated gradient parameters will contribute not only to improve the accuracy of GNSS-A observations but also to assist the exploration of km-scale ocean fields that cannot be easily observed with the existing oceanographic methods. Since the GNSS-A observation network is deployed around Japan, we will proceed with discussions on regional differences and seasonal changes in features of km-scale structures that can be estimated by GNSS-A oceanography.

DATA AVAILABILITY STATEMENT

The datasets presented in this study can be found in online repositories. The names of the repository/repositories and accession number(s) can be found below: All data needed to evaluate the conclusions are present in the article. The XBT/XCTD underwater sound speed data is available in the PANGAEA website (Seafloor Geodesy Group et al., 2020; https://doi.pangaea.de/10.1594/PANGAEA.915138). Additional data related to this paper are available on request to the corresponding author. The JCOPE2M data is available in the JCOPE2M website (http://www.jamstec.go.jp/jcope/htdocs/e/home.html).

AUTHOR CONTRIBUTIONS

YY designed the study and wrote this manuscript. YY and TI led the direct observation of SSS. YY, TI, SW, and YN discussed about the analysis method and commented to improving the manuscript. All authors contributed to the article and approved the submitted version.

FUNDING

The submission of this manuscript was funded by the University of Tokyo.

ACKNOWLEDGMENTS

We would like to thank the Geospatial Information Authority of Japan (GSI) for providing high-rate GNSS data for the kinematic GNSS analysis and daily coordinates of the GEONET sites (Sagiya et al., 2000; Nakagawa et al., 2009) on the GSI website. Many members of the staff of the Hydrographic and Oceanographic Department, Japan Coast Guard, including the crew of the survey vessels Takuyo, Shoyo, Meiyo, and Kaiyo, supported our observations and technological developments. We also thank for devoted maintenance and management by active and senior staffs in the Geodesy and Geophysics Office, Hydrographic and Oceanographic Department of Japan Coast Guard.

SUPPLEMENTARY MATERIAL

The Supplementary Material for this article can be found online at: https://www.frontiersin.org/articles/10.3389/feart.2020.00331/full#supplementary-material

FIGURE S1 | Residual time series of the travel time data for acoustic shots on observation dates, **(a)** June 3, 2013, **(b)** April 30, 2018, **(c)** July 6, 2018, and **(d)** November 23, 2018 for MRT1 and MRT2. Colored crosses and lines indicate residuals and average sound speeds for each station, respectively. After 1306, seafloor stations were replaced at MRT2. **(A)** Residual time series before corrections of V_1 and V_2. **(B)** Residual time series after corrections of V_1 and V_2. **(C)** Average sound speeds estimated before (gray) and after corrections of V_1 and V_2 (colored). **(D)** Time series of the vessel positions from the center (blue: eastward, red: northward).

REFERENCES

Asada, A., and Yabuki, T. (2001). Centimeter-level positioning on the seafloor. *Proc. Jpn Acad. Ser. B* 77, 7–12. doi: 10.2183/pjab.77.7

Fujita, M., Ishikawa, T., Mochizuki, M., Sato, M., Toyama, S., Katayama, M., et al. (2006). GPS/acoustic seafloor geodetic observation: method of data analysis and its application. *Earth Planet. Space* 58, 265–275. doi: 10.1007/s00190-013-0649-9

Matsui, T., Kido, M., Niwa, Y., and Honsho, C. (2019). Effects of disturbance of seawater excited by internal wave on GNSS-acoustic positioning. *Mar. Geophys. Res.* 40, 541–555. doi: 10.1007/s11001-019-09394-6

Miyazawa, Y., Kuwano-Yoshida, A., Doi, T., Nishikawa, T., Narazaki, T., Fukuoka, T., et al. (2019). Temperature profiling measurements by sea turtles improve ocean state estimation in the Kuroshio-Oyashio Confluence region. *Ocean Dyn.* 69, 267–282. doi: 10.1007/s10236-018-1238-5

Miyazawa, Y., Varlamov, S. M., Miyama, T., Guo, X. T., Hihara, T., Kiyomatsu, K., et al. (2017). Assimilation of high-resolution sea surface temperature data into an operational nowcast/forecast system around Japan using a multi-scale three dimensional variational scheme. *Ocean Dyn.* 67, 713–728. doi: 10.1007/s10236-017-1056-1

Nakagawa, H., Toyofuku, T., Kotani, K., Miyahara, B., Iwashita, C., Kawamoto, S., et al. (2009). Development and validation of GEONET new analysis strategy (Version 4). *J. Geograph. Surv. Inst.* 118, 1–8.

Nakamura, Y., Noguchi, T., Tsuji, T., Itoh, S., Niino, H., and Matsuoka, T. (2006). Simultaneous seismic reflection and physical oceanographic observations of oceanic fine structure in the Kuroshio extension front. *Geophys. Res. Lett.* 33:L23605. doi: 10.1029/2006GL027437

Papenberg, C., Klaeschen, D., Krahmann, G., and Hobbs, R. W. (2010). Ocean temperature and salinity inverted from combined hydrographic and seismic data. *Geophys. Res. Lett.* 37:L04601. doi: 10.1029/2009GL042115

Ruddick, B., Song, H., Dong, C., and Pinheiro, L. (2009). Water column seismic images as maps of temperature gradient. *Oceanography* 22, 192–205. doi: 10.5670/oceanog.2009.19

Sagiya, T., Miyazaki, S., and Tada, T. (2000). Continuous GPS array and present-day crustal deformation of Japan. *Pure Appl. Geophys.* 157, 2303–2322. doi: 10.1007/PL00022507

Sato, M., Ishikawa, T., Ujihara, N., Yoshida, S., Fujita, M., Mochizuki, M., et al. (2011). Displacement above the hypocenter of the 2011 Tohoku-oki earthquake. *Science* 332:1395. doi: 10.1126/science.1207401

Seafloor Geodesy Group, Yokota, Y., and Ishikawa, T. (2020). *Cross-section underwater sound speed observation data off the Kii Channel on November 23, 2018*. *PANGAEA* doi: 10.1594/PANGAEA.915138

Spiess, F. N. (1985). Suboceanic geodetic measurements. *IEEE Trans. Geosci. Remote Sensing GE* 23, 502–510. doi: 10.1109/tgrs.1985.289441

Tsuji, T., Noguchi, T., Niino, H., Matsuoka, T., Nakamura, Y., Tokuyama, H., et al. (2005). Two-dimensional mapping of fine structures in the Kuroshio Current using seismic reflection data. *Geophys. Res. Lett.* 32:L14609. doi: 10.1029/2005GL023095

Watanabe, S., Sato, M., Fujita, M., Ishikawa, T., Yokota, Y., Ujihara, N., et al. (2014). Evidence of viscoelastic deformation following the 2011 Tohoku-oki earthquake revealed from seafloor geodetic observation. *Geophys. Res. Lett.* 41, 5789–5796. doi: 10.1002/2014GL061134

Yokota, Y. (2019). Quantitative interpretation of the ability of the GNSS-A to monitor underwater structure. *J. Mar. Acoust. Soc. Jpn.* 46, 116–129.

Yokota, Y., and Ishikawa, T. (2019). Gradient field of undersea sound speed structure extracted from the GNSS-A oceanography: GNSS-A as a sensor for detecting sound speed gradient. *SN Appl. Sci.* 1:693. doi: 10.1007/s42452-019-0699-6

Yokota, Y., and Ishikawa, T. (2020). Shallow slow slip events along the Nankai Trough detected by GNSS-A. *Sci. Adv.* 6:eaay5786. doi: 10.1126/sciadv.aay5786

Yokota, Y., Ishikawa, T., and Watanabe, S. (2018). Seafloor crustal deformation data along the subduction zones around Japan obtained by GNSS-A observations. *Sci. Data* 5:180182. doi: 10.1038/sdata.2018.182

Yokota, Y., Ishikawa, T., and Watanabe, S. (2019). Gradient field of undersea sound speed structure extracted from the GNSS-A oceanography. *Mar. Geophys. Res.* 40, 493–504. doi: 10.1007/s11001-018-9362-7

Yokota, Y., Ishikawa, T., Watanabe, S., Tashiro, T., and Asada, A. (2016). Seafloor geodetic constraints on interplate coupling of the Nankai Trough megathrust zone. *Nature* 534, 374–377. doi: 10.1038/nature17632

Conflict of Interest: The authors declare that the research was conducted in the absence of any commercial or financial relationships that could be construed as a potential conflict of interest.

frontiers in Earth Science

TECHNOLOGY AND CODE
published: 20 November 2020
doi: 10.3389/feart.2020.597532

GARPOS: Analysis Software for the GNSS-A Seafloor Positioning With Simultaneous Estimation of Sound Speed Structure

Shun-ichi Watanabe[1]*, *Tadashi Ishikawa*[1], *Yusuke Yokota*[2] and *Yuto Nakamura*[1]

[1]Hydrographic and Oceanographic Department, Japan Coast Guard, Tokyo, Japan, [2]Institute of Industrial Science, University of Tokyo, Tokyo, Japan

Global Navigation Satellite System–Acoustic ranging combined seafloor geodetic technique (GNSS-A) has extended the geodetic observation network into the ocean. The key issue for analyzing the GNSS-A data is how to correct the effect of sound speed variation in the seawater. We constructed a generalized observation equation and developed a method to directly extract the gradient sound speed structure by introducing appropriate statistical properties in the observation equation, especially the data correlation term. In the proposed scheme, we calculate the posterior probability based on the empirical Bayes approach using the Akaike's Bayesian Information Criterion for model selection. This approach enabled us to suppress the overfitting of sound speed variables and thus to extract simpler sound speed field and stable seafloor positions from the GNSS-A dataset. The proposed procedure is implemented in the Python-based software "GARPOS" (GNSS-Acoustic Ranging combined POsitioning Solver).

Keywords: GNSS-A, seafloor geodesy, sound speed structure, GNSS-A methodology, GNSS-A oceanography

OPEN ACCESS

Edited by:
Keiichi Tadokoro,
Nagoya University, Japan

Reviewed by:
Chie Honsho,
Tohoku University, Japan
Ryoya Ikuta,
Shizuoka University, Japan

***Correspondence:**
Shun-ichi Watanabe
s-watanabe@jodc.go.jp

Specialty section:
This article was submitted to Solid Earth Geophysics, a section of the journal Frontiers in Earth Science

Received: *21 August 2020*
Accepted: *07 October 2020*
Published: *20 November 2020*

Citation:
Watanabe S, Ishikawa T, Yokota Y and Nakamura Y (2020) GARPOS: Analysis Software for the GNSS-A Seafloor Positioning With Simultaneous Estimation of Sound Speed Structure. Front. Earth Sci. 8:597532. doi: 10.3389/feart.2020.597532

INTRODUCTION

Basic Configurations of the GNSS-A Observation

Precise measurements of seafloor position in the global reference frame opens the door to the "global" geodesy in the true sense of the word. It extended the observation network for crustal deformation into the ocean and has revealed the tectonic processes in the subduction zone including megathrust earthquakes (e.g., Bürgmann and Chadwell, 2014; Fujimoto, 2014, for review). Many findings have been reported especially in the northwestern Pacific along the Nankai Trough (e.g., Yokota et al., 2016; Yasuda et al., 2017; Yokota and Ishikawa, 2020), and the Japan Trench (e.g., Kido et al., 2011; Sato et al., 2011; Watanabe et al., 2014; Tomita et al., 2015; Tomita et al., 2017). These achievements owe to the development of GNSS-A (Global Navigation Satellite System–Acoustic ranging combined) seafloor positioning technique, proposed by Spiess (1980).

Abbreviations: ABIC, Akaike Bayesian Information Criterion; ATD offset, Antenna–Transducer offset; GNSS, Global Navigation Satellite System; GNSS-A, Global Navigation Satellite System–Acoustic Ranging combined technique; pdf, probability density function.

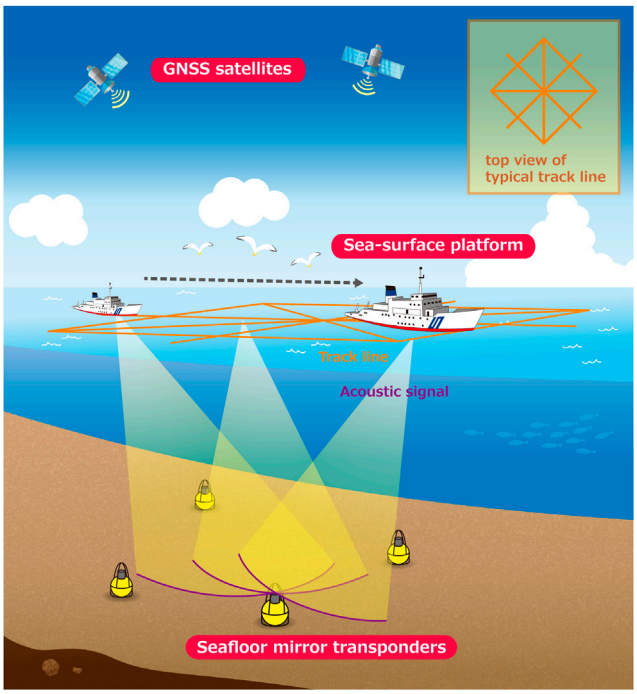

FIGURE 1 | Schematic image of the GNSS-A system in the move-around configuration.

Observers can take various ways to design the GNSS-A observation for the positioning of the seafloor benchmark. They have to solve the difficulties not only in the technical realizations of GNSS-A subcomponents such as the acoustic ranging and the kinematic GNSS positioning, but also in designing the observation configurations and analytical models to resolve the strongly correlated parameters. For example, because the acoustic ranging observations are performed only on the sea surface, the sound speed perturbations and the depth of the benchmark are strongly correlated.

In the very first attempt for the realization, Spiess et al. (1998) derived horizontal displacement using a stationary sea-surface unit which was approximately placed on the horizontal center of the array of multiple seafloor mirror transponders. They determined the relative positions and depths of the transponders in advance. The relative horizontal positions of the sea-surface unit to the transponder array can be determined by acoustic ranging data, to be compared with its global positions determined by space geodetic technique. In this "stationary" GNSS-A configuration, the temporal variation of sound speed is less likely to affect the apparent horizontal position under the assumption that the sound speed structure is horizontally stratified. Inversely, comparing the residuals of acoustic travel time from multiple transponders, Osada et al. (2003) succeeded in estimating the temporal variation of sound speed from the acoustic data. Kido et al. (2008) modified the expression to validate the stationary configuration for a loosely tied buoy even in the case where the sound speed has spatial variations. The stationary GNSS-A configuration is applied mainly by the groups in the Scripps Institution of Oceanography (e.g., Gagnon et al., 2005; Chadwell and Spiess, 2008) and in the Tohoku University (e.g., Fujimoto, 2014; Tomita et al., 2015; Tomita et al., 2017).

On the other hand, Obana et al. (2000) and Asada and Yabuki (2001) took a "move-around" approach where the 3-dimensional position of single transponder can be estimated by collecting the acoustic data from various relay points on the sea surface. **Figure 1** shows the schematic image of move-around configuration. The move-around GNSS-A configuration is developed and practicalized mainly by the collaborative group of the Japan Coast Guard and the University of Tokyo, and the Nagoya University. Unlike the stationary configuration, the horizontal positions of transponders are vulnerable to bias errors of sound speed field. Fujita et al. (2006) and Ikuta et al. (2008) then developed the methods estimating both the positions and the temporal variations of sound speed.

Similar to the effects of distribution of the GNSS satellites on the positioning, well-distributed acoustic data is expected to decrease the bias errors of the estimated transponders' positions in the move-around configuration. By implementing the sailing observations where the sea-surface unit sails over the transponder array to collect geometrically symmetric data, positioning accuracy and observation efficiency have improved (Sato et al., 2013; Ishikawa et al., 2020).

In order to enhance the stability of positioning, an assumption that the geometry of transponder array is constant over whole observation period is usually adopted (e.g., Matsumoto et al., 2008; Watanabe et al., 2014; Chen et al., 2018; Yokota et al., 2018). Misestimates of sound speed cause the positional biases parallel to the averaged acoustic-ray direction, which results in the distortion of the estimated array geometry. Constraining the array geometry contributes to reducing the bias error in the sound speed estimates and the transponders' centroid position.

It should be noted that these two configurations are compatible under the adequate assumptions and constraints. Recently, the group in the Tohoku University uses not only the stationary but also the move-around observation data collected for determining the array geometry (Honsho and Kido, 2017).

Recent Improvements on GNSS-A Analytical Procedures

In the late 2010s, analytical procedures with the estimation of the spatial sound speed gradient for the move-around configuration have been developed. In the earlier stage of the move-around GNSS-A development, the spatial variations of sound speed were approximated as the temporal variations, because most of the sound speed change are confined in the shallowest portion along the acoustic ray paths (e.g., Watanabe and Uchida, 2016). Actually, Yokota et al. (2019) extracted the spatial gradient of the sound speed in the shallow layer from the estimated temporal sound speed variation. However, the smoothly modeled temporal variations cannot represent the transponder-dependent variation which is caused by the sound speed gradient in the relatively deeper portion. Therefore, Yokota et al. (2019) extracted the transponder-dependent correction term from the residuals of the results derived by the conventional method of Fujita et al. (2006).

Yasuda et al. (2017) took a different approach where the sound speed structure shallower than 1,000 m is assumed to be inclined in one direction due to the Kuroshio current flowing near their sites in the offshore region south of Kii Peninsula, Japan. Because their model reflects the specific oceanographic feature, the estimated parameters are easier to be interpreted than that of Yokota et al. (2019) which has higher degree of freedom to extract the oceanographic features.

Meanwhile, Honsho et al. (2019) showed a more general expression for one-directional sound speed gradient. As they mentioned, the gradient terms in their formulation correspond to the extracted features in Yokota et al. (2019). The work by Honsho et al. (2019) showed the possibility to connect all the GNSS-A configurations into a unified GNSS-A solver. However, due to the limitation in resolving the general gradient structure, an additional constraint was taken for the practical application, which is essentially the same formulation as Yasuda et al. (2017).

In this study, to overcome the limitation above, we propose a method to directly extract the gradient sound speed structure by introducing appropriate statistical properties in the observation equation. This paper first shows the reconstructed general observation equation for GNSS-A, in which the continuity of the sound speed field in time and space is assumed. The generalized formulation approximately includes the practical solutions in the previous studies by Yasuda et al. (2017), Yokota et al. (2019), and Honsho et al. (2019) as special cases. We then describe the analytical procedure to derive the posterior probability based on the empirical Bayes approach using the Akaike's Bayesian Information Criterion (ABIC; Akaike, 1980) for model selection. We obtain the solution which maximizes the posterior probability under the empirically selected prior distribution. This is implemented in the Python-based software "GARPOS" (GNSS-Acoustic Ranging combined POsitioning Solver; Watanabe et al., 2020a, available at https://doi.org/10.5281/zenodo.3992688).

METHODOLOGY

Positioning of Sea-Surface Transducer

The key subcomponent of the GNSS-A is the global positioning of the transducer, generally realized by GNSS observation. Whereas acoustic measurement determines the relative position of the seafloor transponder and the sea-surface transducer, GNSS plays a role to align them to the earth-centered, earth-fixed (ECEF) coordinates such as the International Terrestrial Reference Frame (ITRF). When the transducer's position, $\boldsymbol{P}(t)$, is determined in the GNSS's reference frame, a realization of the ITRF, the global positions of transponders can be estimated.

It should be noted that the transponders' positions are generally a function of time, including the solid earth tide as well as global and local crustal deformation (e.g., IERS Conventions, 2010). For the purpose of detecting crustal deformation, it is better to determine the seafloor positions in the solid-earth-tide-free coordinates. Because the observation area is limited to several-kilometers-width, solid-earth-tide-free solutions can be obtained when the trajectory of the transducer is determined in the solid-earth-tide-free coordinates. Hereafter, the positions are expressed in solid-earth-tide-free coordinates in this paper.

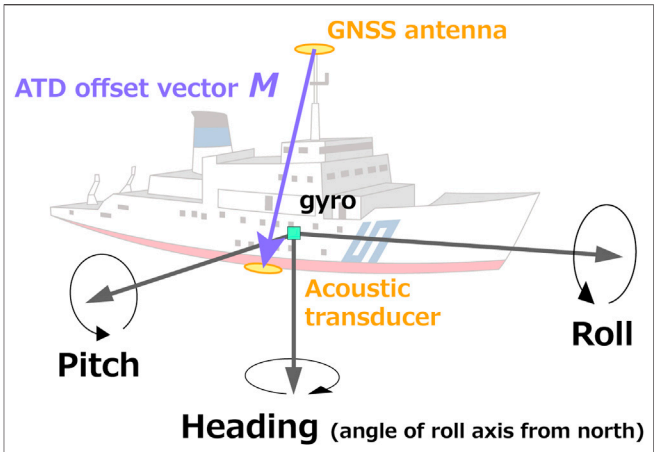

FIGURE 2 | Definitions of the attitude parameters and the ATD offset vector for the sea-surface platform. Heading is zero when the roll axis directs to the north. The roll and pitch axes direct forward and rightward (portside) of the vessel, respectively.

In order to determine $\boldsymbol{P}(t)$ in the ECEF coordinates, a set of GNSS antenna/receiver and a gyro sensor should be mounted on the sea-surface unit. The positions of GNSS antenna, $\boldsymbol{Q}(t)$, can be determined using any of appropriate kinematic GNSS solvers. The gyro sensor provides the attitude of the sea-surface platform, $\boldsymbol{\Theta}(t) = [\,\theta_r \quad \theta_p \quad \theta_h\,]^T$, i.e., roll, pitch, and heading (**Figure 2**). Because the attitude values are aligned to the local ENU coordinates, it is convenient to transform $\boldsymbol{Q}(t)$ from ECEF to local ENU coordinates, i.e., $\boldsymbol{Q}(t) = [\,Q_e \quad Q_n \quad Q_u\,]^T$. Using the relative position of the transducer to the GNSS antenna in the gyro's rectangular coordinate (called "ATD offset" hereafter; **Figure 2**), $\boldsymbol{M} = [\,M_r \quad M_p \quad M_h\,]^T$, we obtain the transducer's position in the local ENU coordinates as,

$$\boldsymbol{P}(t) = \boldsymbol{Q}(t) + \boldsymbol{R}(\boldsymbol{\Theta}(t))\boldsymbol{M}, \tag{1.1}$$

with,

$$R(\boldsymbol{\Theta}) = \begin{bmatrix} 0 & 1 & 0 \\ 1 & 0 & 0 \\ 0 & 0 & -1 \end{bmatrix} \begin{bmatrix} \cos\theta_h & -\sin\theta_h & 0 \\ \sin\theta_h & \cos\theta_h & 0 \\ 0 & 0 & 1 \end{bmatrix} \begin{bmatrix} \cos\theta_p & 0 & \sin\theta_p \\ 0 & 1 & 0 \\ -\sin\theta_p & 0 & \cos\theta_p \end{bmatrix} \begin{bmatrix} 1 & 0 & 0 \\ 0 & \cos\theta_r & -\sin\theta_r \\ 0 & \sin\theta_r & \cos\theta_r \end{bmatrix}. \tag{1.2}$$

The ATD offset values should be measured before the GNSS-A observation.

Underwater Acoustic Ranging

Another key subcomponent is the technique to measure the acoustic travel time between the sea-surface transducer and the seafloor transponders. The techniques for the precise ranging using acoustic mirror-type transponders had been developed and practicalized in early studies (e.g., Spiess, 1980; Nagaya, 1995). Measuring round-trip travel time reduces the effect of advection of the media between the instruments.

The round-trip travel time for the ith acoustic signal to the jth transponder, T_i, is calculated as a function of the relative position of the transponder to the transducer and the 4-dimensional sound speed field, $V(e, n, u, t)$, i.e.,

$$T_i = T_i^c\Big(\boldsymbol{P}(t_{i_+}), \boldsymbol{P}(t_{i_-}), \boldsymbol{X}_j, V(e, n, u, t)\Big), \tag{2}$$

where t_{i_+}, t_{i_-}, and $\boldsymbol{X}_j$ are the transmitted and received time for the ith acoustic signal, and the position of seafloor transponder numbered j, respectively. Note that j is a function of i.

Although the concrete expression is provided as the eikonal equation (e.g., Jensen et al., 2011; Sakic et al., 2018), it requires much computational resources to numerically solve. When the sound speed structure is assumed to be horizontally stratified, we can apply a heuristic approach based on the Snell's law (e.g., Hovem, 2013), which has an advantage in computation time (e.g., Chadwell and Sweeney, 2010; Sakic et al., 2018).

Therefore, we decomposed the 4-dimensional sound speed field into a horizontally stratified stational sound speed profile and a perturbation to obtain the following travel time expression:

$$\begin{aligned} &T_i^c\Big(\boldsymbol{P}(t_{i_+}),\ \boldsymbol{P}(t_{i_-}), \boldsymbol{X}_j, V(e, n, u, t)\Big) \\ &= \exp(-\gamma_i) \cdot \tau_i\Big(\boldsymbol{P}(t_{i_+}),\ \boldsymbol{P}(t_{i_-}), \boldsymbol{X}_j, V_0(u)\Big), \end{aligned} \tag{3}$$

where τ_i and $V_0(u)$ denote the reference travel time and the reference sound speed profile, respectively. $V_0(u)$ is given as a piecewise linear function of height, so that the propagation length along the radial component and the propagation time can be calculated for the given incidence angle according to the Snell's law (e.g., Hovem, 2013; Sakic et al., 2018). The expression of the correction coefficient, $\exp(-\gamma_i)$, is selected for the simplification in the following expansion. It represents the discrepancy ratio of the actual travel time to the reference, which caused by the spatial and temporal perturbations of the sound speed field.

In the right-hand side of **Eq. 3**, γ_i and $\boldsymbol{X}_j$ are assigned as the estimator. **Eq. 1** gives the transducer's position $\boldsymbol{P}(t)$ as a function of the GNSS antenna's position $\boldsymbol{Q}(t)$, the attitude vector $\boldsymbol{\Theta}(t)$, and the ATD offset $\boldsymbol{M}$. The time-independent parameter $\boldsymbol{M}$ can be also assigned as the estimator when the variation of the attitude value is large enough to resolve the parameter. Hence, the reference travel time can be rewritten as $\tau_i = \tau_i(\boldsymbol{X}_j, \boldsymbol{M} | \boldsymbol{Q}(t), \boldsymbol{\Theta}(t), V_0(u))$, where the variables on the left and right sides of the vertical bar indicate the estimators and the observables, respectively.

Sound Speed Perturbation Model

In seawater, sound speed is empirically determined as a function of temperature, salinity, and pressure (e.g., Del Grosso, 1974). Because these variables strongly depend on the water depth, the vertical variation of the sound speed is much larger than the horizontal variation in the observation scale. Thus, $|\gamma_i| \ll 1$ will be satisfied in most cases where the reference sound speed appropriately represents the sound speed field. In such cases, the average sound speed along the actual ray path is expressed as $\overline{V_0} + \delta V_i \sim \overline{V_0} + \gamma_i \overline{V_0}$, where $\overline{V_0}$ denotes the average sound speed of the reference profile.

Recalling that the sound speed field is continuous and usually smooth in time and space within the observation scale, we can introduce a scalar field which is continuous with time and acoustic instruments' positions, i.e., $\Gamma(t, \boldsymbol{P}, \boldsymbol{X})$, from which the correction coefficient is extracted. Because the temporal variation of the sound speed structure is small during the travel of the acoustic signal and is usually concentrated in the shallower portion of the sea, γ_i is approximated by the average of the transmission and the reception times, i.e., $\gamma_i \equiv \frac{1}{2} \sum_{l=i_+, i_-} \Gamma(t_l, \boldsymbol{P}(t_l), \boldsymbol{X}_j)$. The function $\Gamma(t, \boldsymbol{P}, \boldsymbol{X})$ can be called the sound speed perturbation model.

For simplification, we put the sound speed perturbation model as time-varying linear spatial function in space as follows:

$$\Gamma(t,\ \boldsymbol{P},\ \boldsymbol{X}) \equiv \alpha_0(t) + \boldsymbol{\alpha}_1(t) \cdot \frac{\boldsymbol{P}}{L^*} + \boldsymbol{\alpha}_2(t) \cdot \frac{\boldsymbol{X}}{L^*}, \tag{4}$$

where L^* indicates the characteristic length of the observation site (typically in several kilometers). $\alpha_0(t)$, $\boldsymbol{\alpha}_1(t)$ and $\boldsymbol{\alpha}_2(t)$ are the time-dependent coefficients for each term. Because the vertical variation of $\boldsymbol{P}$ and $\boldsymbol{X}$ are much smaller than the horizontal variation, we can practically ignore the vertical component of $\boldsymbol{\alpha}_1(t)$ and $\boldsymbol{\alpha}_2(t)$. Thus, $\boldsymbol{\alpha}_1(t)$ and $\boldsymbol{\alpha}_2(t)$ are reduced to a 2-dimensional vector to denote the horizontal gradient.

Each coefficient can be represented by a linear combination of basis functions $\Phi_k(t)$:

$$\begin{cases} \alpha_0(t) = \sum_{k=0}^{K_a} a_k^0 \Phi_k^0(t) \\ \boldsymbol{\alpha}_1(t) = \sum_{k=0}^{K_b} \left(a_k^{1E} \Phi_k^{1E}(t),\ a_k^{1N} \Phi_k^{1N}(t),\ 0\right), \\ \boldsymbol{\alpha}_2(t) = \sum_{k=0}^{K_c} \left(a_k^{2E} \Phi_k^{2E}(t),\ a_k^{2N} \Phi_k^{2N}(t),\ 0\right) \end{cases} \tag{5}$$

where $a_k^{\langle\cdot\rangle}$ are the coefficients of the kth basis function, $\Phi_k^{\langle\cdot\rangle}(t)$, for each term named $\langle\cdot\rangle$. E and N in $\langle\cdot\rangle$ denote the eastward and northward components of the vector, respectively. For simplification, we compile these coefficients into vector $\boldsymbol{a}$, hereafter.

Because the initial values for $\boldsymbol{M}$ and $\boldsymbol{X}_j$ are usually obtained in the precision of less than meters prior to the GNSS-A analysis, we approximate $\boldsymbol{P}$ and $\boldsymbol{X}_j$ in Γ substituting the initial values, i.e., $\boldsymbol{M}^0$ and $\boldsymbol{X}_j^0$, and not updating them with the iteration. This reduces the number of estimation parameters in the correction term, i.e., $\gamma_i = \gamma_i(\boldsymbol{a} | \boldsymbol{X}_j^0, \boldsymbol{M}^0, \boldsymbol{Q}(t), \boldsymbol{\Theta}(t))$.

Rigid Array Constraints

Usually, the local deformation within the transponders' array is assumed to be sufficiently small, so that the same array geometry parameters can be used throughout all visits. Because the relative positions of the transponders in the array are strongly coupled

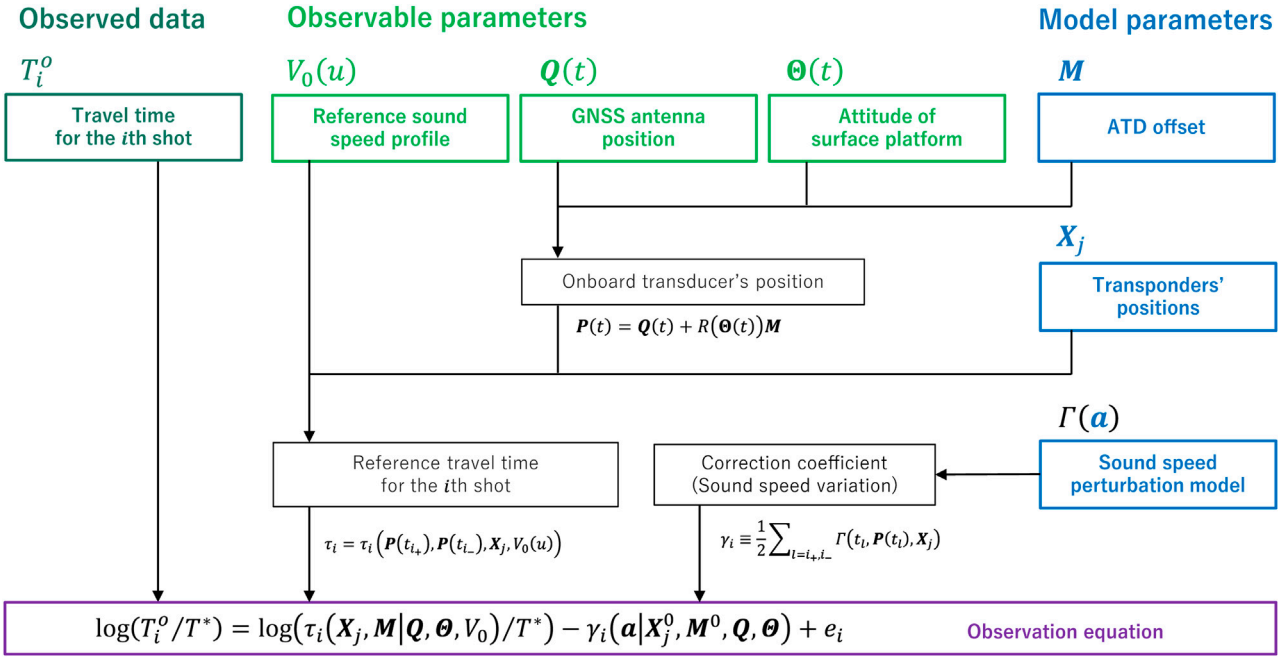

FIGURE 3 | Flow chart to construct the observation equation.

with the sound speed estimates and the position of array centroid, constraining the array geometry is expected to stabilize the GNSS-A solutions. Matsumoto et al. (2008) developed the rigid-array constraint method, which has been adopted in the subsequent studies (e.g., Watanabe et al., 2014; Yokota et al., 2016) except in the cases where the rigid-array assumption is inadequate (e.g., Sato et al., 2011).

To implement the rigid-array constraint, slight change in the observation equation is needed. We divide the transponders' positions as $\boldsymbol{X}_j = \overline{\boldsymbol{X}_j} + \boldsymbol{\Delta X}$, where $\overline{\boldsymbol{X}_j}$ and $\boldsymbol{\Delta X}$ denote the relative positions of each transponder and the parallel translation of the transponder array, respectively. The array geometry, $\overline{\boldsymbol{X}_j}$, should be determined prior to the analytical procedure, using the data of multiple observation visits.

Meanwhile, $\overline{\boldsymbol{X}_j}$ can also be determined simultaneously with the positioning procedure by combining the data vectors, model parameter vectors, and observation equation for all series of the observation visits, as the original formulation of Matsumoto et al. (2008). However, it requires huge computational resources to solve all the parameters, as the number of observations increases. Therefore, we are not concerned with the simultaneous determination of the array geometry in the present paper.

ANALYTICAL PROCEDURES

Observation Equation

In the GNSS-A analysis, observed travel time, T_i^o, are compared with the model, T_i^c. For the interpretability of variables and the simplification in the expansion, we took the logarithms of travel time. Summarizing the above expansion, we put the following observation equation for ith acoustic round-trip travel time:

$$\log(T_i^o/T^*) = \log\left(\tau_i\left(\boldsymbol{X}_j, \boldsymbol{M}|\boldsymbol{Q}, \boldsymbol{\Theta}, V_0\right)/T^*\right) - \gamma_i\left(\boldsymbol{a}|\boldsymbol{X}_j^0, \boldsymbol{M}^0, \boldsymbol{Q}, \boldsymbol{\Theta}\right) + e_i, \tag{6.1}$$

or in the form with the rigid-array constraint,

$$\log(T_i^o/T^*) = \log\left(\tau_i\left(\boldsymbol{\Delta X}, \boldsymbol{M}|\overline{\boldsymbol{X}_j}, \boldsymbol{Q}, \boldsymbol{\Theta}, V_0\right)/T^*\right) - \gamma_i\left(\boldsymbol{a}|\boldsymbol{X}_j^0, \boldsymbol{M}^0, \boldsymbol{Q}, \boldsymbol{\Theta}\right) + e_i, \tag{6.2}$$

where T^* is the characteristic travel time and e_i is the observation error vector. **Figure 3** indicates the summary for constructing the observation equation. It should be noted that, in this formulation, the continuity of sound speed field is assumed.

This section shows the algorithm to estimate the model parameters from the nonlinear observation equation (**Eq. 6**). We took a Bayesian approach because of its simple expression when incorporating prior information. Furthermore, it provides a well-defined index for the model selection, i.e., the Akaike's Bayesian Information Criterion (ABIC; Akaike, 1980). The expansion shown in this section is based on Tarantola and Valette (1982) and Matsu'ura et al. (2007).

Prior Information

The observation equation can be rewritten as,

$$\boldsymbol{y} = \boldsymbol{f}(\boldsymbol{x}) + \boldsymbol{e}, \tag{7}$$

where $\boldsymbol{x} = \begin{bmatrix} \boldsymbol{X}_j^T & \boldsymbol{M}^T & \boldsymbol{a}^T \end{bmatrix}^T$, $y_i = \log(T_i^o/T^*)$, and $f_i = \log(\tau_i/T^*) - \gamma_i$. Let us consider the direct prior information for the model parameters $\boldsymbol{X}_j$ and $\boldsymbol{M}$ written as,

$$\begin{bmatrix} \boldsymbol{X}_j^0 \\ \boldsymbol{M}^0 \end{bmatrix} = \begin{bmatrix} \boldsymbol{X}_j \\ \boldsymbol{M} \end{bmatrix} + \begin{bmatrix} \boldsymbol{d}_X \\ \boldsymbol{d}_M \end{bmatrix}, \tag{8}$$

where $\boldsymbol{X}_j^0$, $\boldsymbol{M}^0$, and $\boldsymbol{d} = \begin{bmatrix} \boldsymbol{d}_X^T & \boldsymbol{d}_M^T \end{bmatrix}^T$ denote the predicted model parameter vectors and the error vector, respectively. Let us assume that $\boldsymbol{d}_X$ and $\boldsymbol{d}_M$ follow a normal distribution with a variance-covariance of $D_X(\rho^2)$ and $D_M(\rho^2)$, whose scale can be adjusted by a hyperparameter ρ^2, i.e., $D_X = \rho^2\widetilde{D_X}$ and $D_M = \rho^2\widetilde{D_M}$, respectively. The prior probability density function (pdf) for the constraints can be written as,

$$p\left(\boldsymbol{X}_j, \boldsymbol{M}; \rho^2\right) = c \cdot \exp\left[-\frac{1}{2}\left(\begin{bmatrix} \boldsymbol{X}_j^0 \\ \boldsymbol{M}^0 \end{bmatrix} - \begin{bmatrix} \boldsymbol{X}_j \\ \boldsymbol{M} \end{bmatrix} \right)^T \begin{bmatrix} D_X(\rho^2) & 0 \\ 0 & D_M(\rho^2) \end{bmatrix}^{-1} \left(\begin{bmatrix} \boldsymbol{X}_j^0 \\ \boldsymbol{M}^0 \end{bmatrix} - \begin{bmatrix} \boldsymbol{X}_j \\ \boldsymbol{M} \end{bmatrix} \right) \right], \tag{9}$$

where c denotes the normalization constant.

For the model parameter $\boldsymbol{a}$, an indirect prior information can be applied that the temporal change of sound speed perturbation model Γ is small. Specifically, the roughness which can be defined by the derivatives of each term in **Eq. 4** should be small. In this study, we use the square of second derivative as roughness ϕ, whereas Ikuta et al. (2008) used the first derivative. When using the B-spline functions $\Phi_k^{\langle\cdot\rangle}(t)$ (e.g., de Boor, 1978) as the basis of temporal sound speed variation, the roughness can be written in a vector form, i.e.,

$$\phi = \int_t \left(\frac{\partial^2 \alpha_{\langle\cdot\rangle}(t)}{\partial t^2} \right)^2 dt = \boldsymbol{a}^{\langle\cdot\rangle T} H_{\langle\cdot\rangle} \boldsymbol{a}^{\langle\cdot\rangle}, \tag{10.1}$$

where,

$$H_{\langle\cdot\rangle_{ij}} = \int \frac{\partial^2 \Phi_i^{\langle\cdot\rangle}(t)}{\partial t^2} \frac{\partial^2 \Phi_j^{\langle\cdot\rangle}(t)}{\partial t^2} dt. \tag{10.2}$$

Then, the prior pdf can be written using the hyperparameter $\lambda_{\langle\cdot\rangle}$ as,

$$p\left(\boldsymbol{a}^{\langle\cdot\rangle}; \lambda_{\langle\cdot\rangle}^2\right) = c \cdot \exp\left[-\frac{1}{2\lambda_{\langle\cdot\rangle}^2} \boldsymbol{a}^{\langle\cdot\rangle T} H_{\langle\cdot\rangle} \boldsymbol{a}^{\langle\cdot\rangle} \right], \tag{11}$$

where c denotes the normalization constant.

Combining these prior informations, we obtain the following prior pdf:

$$p(\boldsymbol{x}; \rho^2, \boldsymbol{\lambda}^2) = (2\pi)^{-\frac{g}{2}} \left\| \Lambda_G \right\|^{\frac{1}{2}} \exp\left[-\frac{1}{2}(\boldsymbol{x}^0 - \boldsymbol{x})^T G(\rho^2, \boldsymbol{\lambda}^2)(\boldsymbol{x}^0 - \boldsymbol{x}) \right], \tag{12.1}$$

with $\lambda^2 = \begin{bmatrix} \lambda_0^2 & \lambda_{1E}^2 & \lambda_{1N}^2 & \lambda_{2E}^2 & \lambda_{2N}^2 \end{bmatrix}$, $\boldsymbol{x}^0 = \begin{bmatrix} \boldsymbol{X}_j^{0T} & \boldsymbol{M}^{0T} & \boldsymbol{0}^T \end{bmatrix}^T$, and,

$$G(\rho^2, \boldsymbol{\lambda}^2) = \begin{bmatrix} D_X(\rho^2)^{-1} & & & & & & & \\ & D_M(\rho^2)^{-1} & & & & & & \\ & & H_0/\lambda_0^2 & & & & & \\ & & & H_{1E}/\lambda_{1E}^2 & & & & \\ & & & & H_{1N}/\lambda_{1N}^2 & & & \\ & & & & & H_{2E}/\lambda_{2E}^2 & & \\ & & & & & & H_{2N}/\lambda_{2N}^2 & \end{bmatrix}, \tag{12.2}$$

where g and $||\Lambda_G||$ represent the rank of G and the absolute value of the product of non-zero eigenvalues of G, respectively.

Variance-Covariance of Data Error

Now for the observed data, we take the assumption that $\boldsymbol{e}$ also follows a normal distribution with a variance-covariance of $\sigma^2 E$, i.e.,

$$p(\boldsymbol{y}|\boldsymbol{x}; \sigma^2) = (2\pi\sigma^2)^{-\frac{n}{2}} |E|^{-\frac{1}{2}} \exp\left[-\frac{1}{2\sigma^2}(\boldsymbol{y} - \boldsymbol{f}(\boldsymbol{x}))^T E^{-1}(\boldsymbol{y} - \boldsymbol{f}(\boldsymbol{x})) \right], \tag{13}$$

where n is the number of data and $|\cdot|$ denotes the determinant of the matrix.

The major error sources for the measurement and calculation of travel time are 1) measurement error when reading the return signal, 2) transducer's positioning error, and 3) modeling error of the sound speed field. Non-diagonal components of E are caused not by measurement error, but by transducer's positioning error and sound speed modeling error. The transducer's positioning error may have temporal correlation which comes from the kinematic GNSS noise. The modeling error has spatio-temporal correlation because the sound speed variation is modeled by a smooth function of space and time. Thus, we assumed the following covariance terms using two hyperparameters, i.e., μ_t and μ_{MT}, to adjust the non-diagonal component of E:

$$E_{ij}(\mu_t, \mu_{MT}) = \begin{cases} \sqrt{E_{ii}E_{jj}} \exp\left(-\frac{|t_i - t_j|}{\mu_t} \right) & \text{if the transponders for } i \text{ and } j \text{ are the same} \\ \mu_{MT}\sqrt{E_{ii}E_{jj}} \exp\left(-\frac{|t_i - t_j|}{\mu_t} \right) & \text{for others} \end{cases}, \tag{14}$$

whose formulation refers to Fukahata and Wright (2008). **Eq. 14** means that the densely sampled data would have smaller weights in the model than the isolated data. A factor $\mu_{MT} \in [0, 1]$ was introduced to surpress the error correlation between the different transponders because the acoustic rays for different transponders take separate paths as the depths increases. Consideration of the non-diagonal components of the data variance-covariance contributes to reduce the complexity of the model against the excessively high-rate data sampling.

Subsequently, we consider the diagonal component of E which controls the weight of individual data. Because the measurement errors of acoustic travel time are caused by mis-reading of the return signal, it is independent on the travel time value. Therefore, it is reasonable to put the assumption that the error of $T_i^o - T_i^c$ follows a normal distribution. Nonetheless, because the GNSS-A typically gives the precision of $T_i^o/T_i^c \sim 1 \pm 10^{-4}$, we can suppose that T_i^o/T_i^c approximately follows a log-normal distribution as assumed in **Eq. 13**. In order to put the same weight for all measured travel time in the real scale, we applied $E_{ii} = (T^*/T_i^o)^2$ for scaling the diagonal component.

Posterior Probability

The posterior pdf after the data acquisition, which can be defined to be equal to the likelihood of the model parameter with the given data, can be written as,

$$p(\boldsymbol{x};\sigma^2,\mu_t,\mu_{MT},\rho^2,\boldsymbol{\lambda}^2|\boldsymbol{y}) = c\cdot(2\pi\sigma^2)^{-\frac{(n+g)}{2}}|E|^{-\frac{1}{2}}\left\|\widetilde{\Lambda_G}\right\|^{\frac{1}{2}}\exp\left[-\frac{1}{2\sigma^2}s(\boldsymbol{x})\right], \tag{15.1}$$

with,

$$s(\boldsymbol{x}) = (\boldsymbol{y}-\boldsymbol{f}(\boldsymbol{x}))^T E^{-1}(\boldsymbol{y}-\boldsymbol{f}(\boldsymbol{x})) + (\boldsymbol{x}^0-\boldsymbol{x})^T\tilde{G}(\boldsymbol{x}^0-\boldsymbol{x}), \tag{15.2}$$

where $\tilde{G} = \sigma^2 G(\rho^2, \boldsymbol{\lambda}^2)$ and $\left\|\widetilde{\Lambda_G}\right\|$ represents the absolute value of the product of non-zero eigenvalues of $\tilde{G}$.

Defining $\hat{\boldsymbol{x}}(\sigma^2,\mu_t,\mu_{MT},\rho^2,\boldsymbol{\lambda}^2)$ as $\boldsymbol{x}$ that maximizes the posterior probability (**Eq. 15**) under the given hyperparameters, the partial derivative of $p(\boldsymbol{x}|\boldsymbol{y})$ with respect to $\boldsymbol{x}$ should be zero for $\boldsymbol{x} = \hat{\boldsymbol{x}}$. Hence, $\hat{\boldsymbol{x}}$ should satisfy the following equation:

$$A(\hat{\boldsymbol{x}})^T E^{-1}(\boldsymbol{y}-\boldsymbol{f}(\hat{\boldsymbol{x}})) + \tilde{G}(\boldsymbol{x}^0-\hat{\boldsymbol{x}}) = 0, \tag{16.1}$$

where $A(\boldsymbol{x})$ is the Jacobian matrix at point $\boldsymbol{x}$ defined as,

$$A(\boldsymbol{x}) = \begin{bmatrix} \frac{\partial f_1}{\partial x_{k1}}(\boldsymbol{x}) & \cdots & \frac{\partial f_1}{\partial x_{km}}(\boldsymbol{x}) \\ \vdots & \ddots & \vdots \\ \frac{\partial f_n}{\partial x_{k1}}(\boldsymbol{x}) & \cdots & \frac{\partial f_n}{\partial x_{km}}(\boldsymbol{x}) \end{bmatrix}. \tag{16.2}$$

We can solve the nonlinear equation (**Eq. 16**) numerically by performing an iterative method, where $\boldsymbol{x}_k$ is corrected in each step with the following algorithm:

$$\boldsymbol{x}_{k+1} = \boldsymbol{x}_k + \left(A(\boldsymbol{x}_k)^T E^{-1} A(\boldsymbol{x}_k) + \tilde{G}\right)^{-1}\left(A(\boldsymbol{x}_k)^T E^{-1}(\boldsymbol{y}-\boldsymbol{f}(\boldsymbol{x}_k)) + \tilde{G}(\boldsymbol{x}^0-\boldsymbol{x}_k)\right), \tag{17}$$

to satisfy the following convergence criteria:

$$A(\boldsymbol{x}_k)^T E^{-1}(\boldsymbol{y}-\boldsymbol{f}(\boldsymbol{x}_k)) + \tilde{G}(\boldsymbol{x}^0-\boldsymbol{x}_k) \ll 1. \tag{18}$$

Ignoring the term $O((\boldsymbol{x}-\hat{\boldsymbol{x}})^2)$ in $\boldsymbol{f}(\boldsymbol{x})$ around $\hat{\boldsymbol{x}}$, $s(\boldsymbol{x})$ can be rewritten as,

$$s(\boldsymbol{x}) \sim s(\hat{\boldsymbol{x}}) + (\boldsymbol{x}-\hat{\boldsymbol{x}})^T\left(A(\hat{\boldsymbol{x}})^T E^{-1} A(\hat{\boldsymbol{x}}) + \tilde{G}\right)(\boldsymbol{x}-\hat{\boldsymbol{x}}). \tag{19}$$

Therefore, the linearized variance-covariance matrix around $\hat{\boldsymbol{x}}$ can be obtained as,

$$\hat{C} = \sigma^2\left(A(\hat{\boldsymbol{x}})^T E^{-1} A(\hat{\boldsymbol{x}}) + \tilde{G}\right)^{-1}. \tag{20}$$

Hyperparameter Tuning

The appropriate values of the hyperparameters can be determined by minimizing Akaike's Bayesian Information Criteria (ABIC; Akaike, 1980),

$$ABIC = -2\log\int p(\boldsymbol{y}|\boldsymbol{x};\sigma^2,\mu_t,\mu_{MT})p(\boldsymbol{x};\rho^2,\boldsymbol{\lambda}^2)d\boldsymbol{x} + 2N_{\mathrm{HP}}, \tag{21}$$

where N_{HP} denotes the number of hyperparameters. Although it is difficult to analytically calculate the integral for the marginal likelihood because of the nonlinearity in $\boldsymbol{f}(\boldsymbol{x})$, the Laplace's method can be applied in this case where the degree of freedom is sufficiently large and $s(\boldsymbol{x})$ can be almost unimodal. Thus, an approximated form for ABIC is obtained as follows:

$$ABIC \cong (n+g-m)\log s(\hat{\boldsymbol{x}}) - \log\left|E^{-1}\right| - \log\left\|\Lambda_G\right\| + \log\left|A(\hat{\boldsymbol{x}})^T E^{-1} A(\hat{\boldsymbol{x}}) + \tilde{G}\right| + const. \tag{22}$$

where m is the number of model parameters. For the derivation, we used the following relationship:

$$\sigma^2 = \frac{s(\hat{\boldsymbol{x}})}{n+g-m}, \tag{23}$$

which is derived from the condition that the partial derivative of ABIC with respect to σ^2 should be zero. We can tune the hyperparameters to minimize the approximated ABIC value defined in **Eq. 22**, to obtain the solution $\boldsymbol{x}^* = \hat{\boldsymbol{x}}(\sigma^{2^*},\mu_t^*,\mu_{MT}^*,\rho^{2^*},\boldsymbol{\lambda}^{2^*})$, where $*$ denotes the selected hyperparameters.

Features of "GARPOS"

GARPOS (Watanabe et al., 2020a; available at https://doi.org/10.5281/zenodo.3992688) has been developed to implement the GNSS-A analysis procedure. GARPOS is compatible with Python 3, with other packages NumPy, SciPy, pandas, and matplotlib. These packages are pre-installed in most of the Python distributions such as Anaconda. Sample scripts and data for testing GARPOS are also stored in the repository.

GARPOS is distributed as a series of files, which requires a driver script to run. The toolset consists of multiple Python files and a Fortran 90 library for ray tracing. GARPOS requires the following input files:

(I-1) Initial site parameter file (in Python's configuration format),
(I-2) Acoustic observation data file (in csv format),
(I-3) Reference sound speed data file (in csv format),
(I-4) Setting file (in Python's configuration format).

Initial site parameter file (I-1) contains the initial values of the transponders' positions, the ATD offset and the relevant prior covariance information, as well as the metadata for the observation site and conditions. Acoustic observation data file (I-2) contains the list of the observation data associated with each acoustic ranging, such as travel time, positions, attitude and other metadata. Reference sound speed data file (I-3) contains the reference sound speed profile approximated into a polygonal curve. Setting file (I-4) contains the parameters to control the analysis procedures including the hyper parameters. Users can

TABLE 1 | List of observable and estimation parameters used in GARPOS.

Parameter	Description	Name in I/O file	I/O file	Type	Unit
t_{i_+}	Transmit time	*ST*	I-2	Obs	s
t_{i_-}	Reception time	*RT*	I-2	Obs	s
$\boldsymbol{Q}(t_{i_+})$	Position of GNSS antenna at t_{i_+} in ENU coordinates	*ant_e0* *ant_n0* *ant_u0*	I-2	Obs	m
$\boldsymbol{Q}(t_{i_-})$	Position of GNSS antenna at t_{i_-} in ENU coordinates	*ant_e1* *ant_n1* *ant_u1*	I-2	Obs	m
$\boldsymbol{\Theta}(t_{i_+})$	Attitude of platform at t_{i_+}	*roll0* *pitch0* *head0*	I-2	Obs	deg.
$\boldsymbol{\Theta}(t_{i_-})$	Attitude of platform at t_{i_-}	*roll1* *pitch1* *head1*	I-2	Obs	deg.
γ_i	Correction coefficient	*Gamma*	O-2	Est	—
$\boldsymbol{M}^0$	Prior ATD offset	*ATDoffset*	I-1	Obs	m
$\boldsymbol{X}_j^0$	Prior position of transponder	*M{j}_dPos*	I-1	Obs	m
$\Delta\boldsymbol{X}^0$	Prior offset of transponder array	*DCentPos*	I-1	Obs	m
$\hat{\boldsymbol{M}}$	Posterior ATD offset	*ATDoffset*	O-1	Est	m
$\hat{\boldsymbol{X}}_j$	Posterior position of transponder	*M{j}_dPos*	O-1	Est	m
$\hat{\Delta\boldsymbol{X}}$	Posterior offset of transponder array	*dCentPos*	O-1	Est	m
$V_0(u)$	Reference sound speed profile	CSV table	I-3	Obs	m/s
K_a	Number of internal knots for $\boldsymbol{\alpha}_0$	*nmp0*	I-4	Setting	—
K_b	Number of internal knots for $\boldsymbol{\alpha}_1$	*nmp1*	I-4	Setting	—
K_c	Number of internal knots for $\boldsymbol{\alpha}_2$	*nmp2*	I-4	Setting	—

*Note that $K\begin{Bmatrix} a \\ b \\ c \end{Bmatrix} = nmp\begin{Bmatrix} 0 \\ 1 \\ 2 \end{Bmatrix} \times$ (*number of subset*) *in GARPOS.*

TABLE 2 | List of hyperparameter in GARPOS.

Hyper-parameter	Description	Formulation set in (I-4)	Name in Setting file	Unit
μ_t	Correlation length of data	μ_t	*mu_t*	min.
μ_{MT}	Data correlation coefficient b/w the different transponders	μ_{MT}	*mu_mt*	—
λ_0^2	Smoothness parameter for $\boldsymbol{\alpha}_0$	$\log_{10}\lambda_0^2$	*Log_Lambda0*	—
λ_{1E}^2	Smoothness parameter for $\boldsymbol{\alpha}_{1E}$	$\log_{10}\left(\frac{\lambda_{\langle\rangle}^2}{\lambda_0^2}\right)$	*Log_gradLambda*	—
λ_{1N}^2	Smoothness parameter for $\boldsymbol{\alpha}_{1N}$			—
λ_{2E}^2	Smoothness parameter for $\boldsymbol{\alpha}_{2E}$			—
λ_{2N}^2	Smoothness parameter for $\boldsymbol{\alpha}_{2N}$			—
σ^2	Scale of measurement error	N/A	N/A	—
ρ^2	Scale of a priori positioning error	N/A	N/A	m^2

Note that σ^2 is calculated analytically, and that ρ^2 is set in (I-2).

put the lists of candidates of hyperparameters in which the best combination may be within. The parameters *nmp*0, *nmp*1, and *nmp*2 in the setting file control the number of basis functions, K_a, K_b, and K_c in **Eq. 5**.

The results are written in the following output files:

(O-1) Estimated site parameter files (in Python's configuration format),
(O-2) Modified acoustic observation data file (in csv format),
(O-3) Model parameter list file (in csv format),
(O-4) Posterior variance-covariance matrix file (in csv format).

Estimated site parameter files (O-1) is written in the same format as the file (I-1). Modified acoustic observation data file (O-2) contains the calculated travel time data and the coefficients of sound speed perturbation model, as well as the original data/metadata set in (I-2). Model parameter list file (O-3) and posterior variance-covariance matrix file (O-4) contain the whole estimated model parameter vector and its variance-covariance, respectively.

Major input/output parmeters and hyperparameters for GARPOS are listed in **Tables 1** and **2**, respectively.

We developed GARPOS to be compatible with both observation configurations. When handling the GNSS-A data collected in the stationary configurations, we should process data with some constraints on model parameters. Specifically, 1) upward components of transponders' positions should be fixed to zero, and 2) spatial gradient components of the sound speed perturbation model should not be solved, i.e., *nmp*1 = *nmp*2 = 0, because these

TABLE 3 | Locations and observation periods of the GNSS-A observation sites used in this study.

Site	Latitude	Longitude	Height	Number of epochs	Observation period
TOS2	32.43 °N	134.03 °E	−1,740 m	31	2011.904–2019.863
MYGI	38.03 °N	142.92 °E	−1,640 m	33	2011.238–2019.803

parameters cannot be well resolved in the stationary configuration. Although further parameter tuning may be required for optimization, users can solve the seafloor position by GARPOS with the stationary data in addition to the move-around data.

APPLICATIONS TO THE ACTUAL DATA

Data and Settings

In order to verify the proposed analytical procedure, we reanalyzed the GNSS-A data at the sites named "TOS2" and "MYGI" (**Table 3**; **Figure 4**) in 2011–2019. The test sites were selected for several reasons: 1) whereas TOS2 is expected to move at almost constant rate, MYGI will show the transient displacement due to the postseismic crustal deformation of the 2011 Tohoku-oki earthquake; 2) the oceanographic environments are different, i.e., the effect of the Kuroshio current is dominant at TOS2; but 3) the depths of both sites are almost the same. The observation epochs used in this study is listed in **Supplementary Tables S1 and S2**. The datasets used in this study are available at https://doi.org/10.5281/zenodo.3993912 (Watanabe et al., 2020b).

Acoustic round-trip travel times were measured on the survey vessel using the hull-mounted acoustic transducer (e.g., Ishikawa et al., 2020). Processing delays in the acoustic devices were subtracted from the acoustic data beforehand.

Solid-earth-tide-free positions of GNSS antenna $\boldsymbol{Q}(t)$ were determined at 2 Hz by the open source software RTKLIB version 2.4.2 (Takasu, 2013) in post-processing kinematic Precise Point Positioning (PPP) mode, using the precise satellite orbit and the 30-s satellite clock solutions (final products) provided by the International GNSS Service (International GNSS Service, a; International GNSS Service, b), in the same procedures as Watanabe et al. (2020c). The ATD offset values for each vessel, $\boldsymbol{M}$, were measured by leveling, distance, and angle surveys before the first GNSS-A observation cruise, to be used as $\boldsymbol{M}^0$.

Along with the acoustic observations, the profiles of temperature and/or conductivity were measured by CTD, XCTD or XBT probes several times. The reference sound speed profile, $V_0(u)$, was calculated from the observed temperature and salinity profiles using the empirical relationship proposed by Del Grosso (1974). To save the computational cost for ray tracing, the profile was approximated into a polygonal curve with several tens of nodes (**Figure 5**).

During a GNSS-A survey, the vessel sails on a pre-determined track over the seafloor transponder array to collect geometrically balanced acoustic data (e.g., **Figure 1**). The along-track observation (called "subset", hereafter) is repeated several times by reversing the sailing direction in order to reduce the bias due to the errors in the ATD offset.

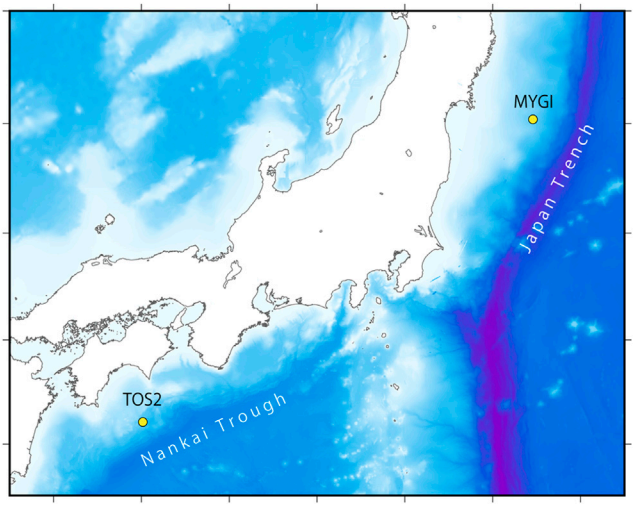

FIGURE 4 | Locations of the tested GNSS-A sites TOS2 and MYGI.

During an observation cruise, it occasionally took more than a few weeks to collect sufficient acoustic data at a single site due to weather conditions or other operational restrictions. Even so, we compiled a single dataset per site per cruise for the static seafloor positioning in practice, because the positional changes should be too small to detect. We call the collection of a single GNSS-A dataset "observation epoch" or "epoch", hereafter.

We set the parameters for the numbers of basis functions, K_a, K_b, and K_c, in **Eq. 5**, as $nmp0 = nmp1 = nmp2 = 15$ for both preprocess and main process. Knot intervals of B-spline basis functions were approximately 10–20 min. for most epochs.

Array Geometry Determination

In order to calculate the proper array geometry $\overline{\boldsymbol{X}_j}$ for the rigid-array constraint, we first determined the positions of each transponder for all observations. Note that not all transponders are used in each observation, for example, because of additional installation of transponders for replacing transponders which were decommissioned due to battery outage. $\overline{\boldsymbol{X}_j}$ and the positional difference of the array center for nth observation, $\boldsymbol{c}^{(n)}$ were calculated by solving the following simultaneous equations:

$$\begin{cases} \boldsymbol{X}_j^{(n)} = \delta_j^{(n)}\overline{\boldsymbol{X}_j} + \delta_j^{(n)}\boldsymbol{c}^{(n)} \quad (\text{for } j = 1 \ldots J \text{ and } n = 1 \ldots N) \\ 0 = \sum_{n=1}^{N} \boldsymbol{c}^{(n)} \end{cases}, \tag{24.1}$$

with,

$$\delta_j^{(n)} = \begin{cases} 1 & \text{if the transponder } j \text{ is used in } n \text{ th observation} \\ 0 & \text{others} \end{cases}, \tag{24.2}$$

where J and N are the number of transponders and observations, respectively, and $\boldsymbol{X}_j^{(n)}$ denotes the predetermined transponders' positions for the nth observation.

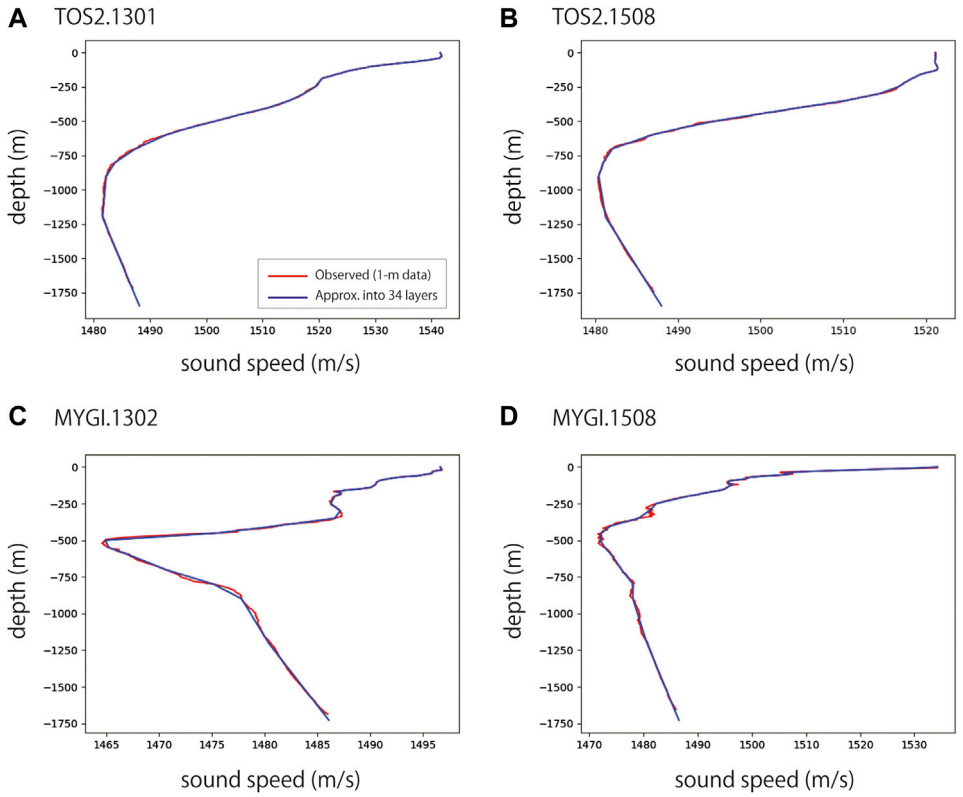

FIGURE 5 | Reference sound speed profiles (blue lines) for epochs **(A)** TOS2.1301 (January 2013), **(B)** TOS2.1508 (August 2015), **(C)** MYGI.1302 (February 2013), and **(D)** MYGI.1508 (August 2015). Red lines indicate 1-m sound speed profiles obtained from the 1-m layered XBT/XCTD data.

The preliminary array-free positioning was also used for the verification of the collected data. We eliminated the outliers whose discrepancies from the preliminary solution were larger than the arbitrary threshold. We set the threshold to be 5 times as large as the root mean square value (RMS) of the travel time residuals.

Hyperparameter Search

In order to get the solution $\boldsymbol{x}^*$, we should determine the appropriate values for the various hyperparameters, i.e., σ^2, μ_t, μ_{MT}, ρ^2, λ_0^2, λ_{1E}^2, λ_{1N}^2, λ_{2E}^2, and λ_{2N}^2. In the scheme of the ABIC minimization, σ^2 can be determined analytically by **Eq. 23**. It is reasonable to assume $\lambda_{1E}^2 = \lambda_{1N}^2 = \lambda_{2E}^2 = \lambda_{2N}^2$ because these hyperparameters control the smoothness of the spatial sound speed structure. We hereafter use a variable λ_g^2 to represent the value of these hyperparameters. For the purpose of single positioning, ρ should be a large number, for example in meter-order. The large ρ hardly changes the ABIC value and thus the solution.

In order to save the computational resources, we should further reduce the number of hyperparameters. We tentatively put $\mu_{MT} = 0.5$. For the sound speed variations, we had to assume the strong constancy of spatial sound speed structure to resolve them with the single transducer GNSS-A. For this reason, we selected the ratio of λ_0^2 and λ_g^2, as $\lambda_g^2 = 0.1\,\lambda_0^2$. The last two hyperparameters, μ_t and λ_0^2, were determined with the grid search method. The tested values for μ_t and λ_0^2 are μ_t = (0 min., 0.5 min., 1 min., 2 min., 3 min.) and $\lambda_0^2 = (10^{-3}, 10^{-2}, 10^{-1}, 10^{0}, 10^{1}, 10^{2})$, respectively.

RESULTS

Figure 6 shows the time series of the estimated positions at sites TOS2 and MYGI. The positions are aligned to the ITRF2014 (Altamimi et al., 2016) and transformed into local ENU coordinates. Comparing the time series derived by the existing scheme (SGOBS version 4.0.2; used in Yokota et al., 2019), GARPOS reproduced almost the same trends for both sites. GARPOS might have succeeded in slightly suppressing the dispersion around the averaged velocity extracted from the neighboring epochs. Whereas the previous method corrected the sound speed gradient structure with step-by-step procedure, the proposed method has an advantage in directly extracting the structure by simultaneous estimation of all parameters.

TOS2 is located offshore in the south of Shikoku Island, southwestern Japan, above the source region of the 1946 Nankaido earthquake (e.g., Sagiya and Thatcher, 1999) along the Nankai Trough. According to Yokota and Ishikawa (2020), who investigated the transient deformations at the GNSS-A sites along the Nankai Trough, no significant signal was detected at

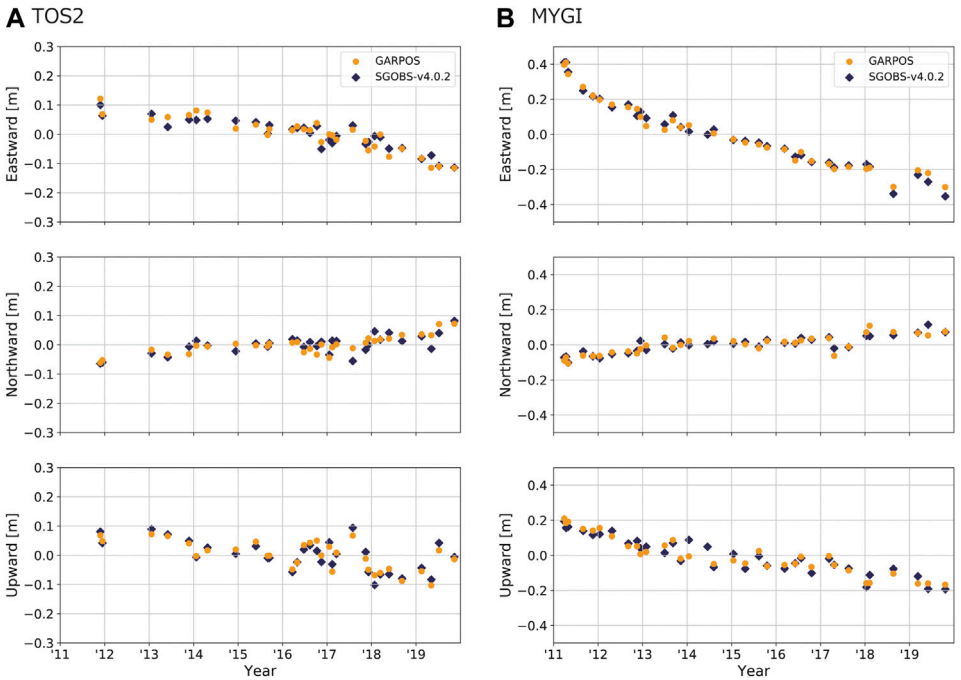

FIGURE 6 | Time series of displacement at **(A)** TOS2 and **(B)** MYGI solved by GARPOS (orange circles) and SGOBS version 4.0.2 (blue squares). The positions are aligned to the ITRF 2014.

TOS2. The results by the proposed method show the same trends as the conventional results. Although the trend of horizontal displacement seems to be changed in 2018 or 2019, careful inspection is needed because the transponders had been replaced during this period.

MYGI is located in the offshore east of Miyagi Prefecture, northeastern Japan, which experienced the 2011 Tohoku-oki earthquake (Sato et al., 2011). After the earthquake, significant westward postseismic movement and subsidence due to the viscoelastic relaxation has been observed at MYGI (Watanabe et al., 2014). The postseismic movements continue but appear to decay. It is true that the changes in the displacement rate at these sites are crucial in seismic and geodetic researches, but discussing these matters is beyond the scope of the present paper. The point is that the seafloor positioning results were well reproduced by the proposed method.

DISCUSSIONS

Interpretations for the Correction Coefficient

As mentioned in *Sound Speed Perturbation Model*, it is convenient to relate the correction coefficient to the sound speed perturbation by assuming the case for $|\gamma_i| \ll 1$ for better understanding, though observation equation (**Eq. 6**) is valid for arbitrary value of γ_i. For the relationship $\delta V_i \sim \gamma_i \overline{V_0}$, we can convert each term of Γ into the dimension of speed and speed gradient as, $\delta V_0(t) \equiv \overline{V_0}\alpha_0(t)$, $\boldsymbol{g}_1(t) \equiv \overline{V_0}\boldsymbol{\alpha}_1(t)$, and $\boldsymbol{g}_2(t) \equiv \overline{V_0}\boldsymbol{\alpha}_2(t)$.

The early models by Fujita et al. (2006) and Ikuta et al. (2008) took only the term $\delta V_0(t)$ into account. Whereas Ikuta et al. (2008) used the cubic B-spline functions as basis functions, Fujita et al. (2006) applied the multiple second degree polynomial functions with 10–20-min. time windows. Although these models do not include any transponder dependent term $\boldsymbol{g}_2(t)$, the transponder independent spatial gradient $\boldsymbol{g}_1(t)$ can be indirectly extracted as shown by Yokota et al. (2019).

In addition to estimating the term identical to δV_0, Yokota et al. (2019) implemented the additional process to estimate $\boldsymbol{g}_2$ from the residuals of the solution by the method of Fujita et al. (2006). Strictly, the derived parameters in their scheme, i.e., ΔV_1 and ΔV_2 in Yokota et al. (2019), are the same as $\boldsymbol{g}_1 + \boldsymbol{g}_2$ and $\boldsymbol{g}_2$ in this study, respectively. For these parameters, our team have already made a qualitative interpretation in Yokota and Ishikawa (2019).

In order to show the relationship with other conventional models, we expand the proposed formulation to those by Yasuda et al. (2017), Honsho et al. (2019), and Kinugasa et al. (2020). Because Honsho et al. (2019) practically assumed 1-directional sound speed gradient, they constructed the model basically in the 2-dimensional plane spanned by the gradient direction and vertical direction.

For simplification, we assume that the ray path is a straight line connecting both ends. Putting L^* equal to the depth of the observation site, the emission angle θ defined in Figure 3 of Honsho et al. (2019) can be expressed as,

$$\frac{X_j}{L^*} - \frac{P(t)}{L^*} = \tan\theta. \tag{25}$$

Furthermore, assuming that the transmit/reception positions are the same and that the difference between transmit/reception time is so small that $\alpha_0(t)$, $\alpha_1(t)$, and $\alpha_2(t)$ hardly change, γ_i can be written as,

$$\gamma_i = \alpha_0(t) + (\alpha_1(t) + \alpha_2(t))\frac{P(t)}{L^*} + \alpha_2(t)\tan\theta. \quad (26)$$

Because δT defined in Eqs 2 and 5 of Honsho et al. (2019) is equivalent to $T_i^c - \tau_i$ in our formulation, we have,

$$\left(\exp(-\gamma_i) - 1\right)\tau_i = \frac{1}{\cos\theta}\left(c_0(t) + g(t)x_0 + w(t)\tan\theta\right), \quad (27)$$

where $c_0(t)$, $g(t)$, $w(t)$, and $x_0 = P$ are defined in Eqs. 6–8 of Honsho et al. (2019) and the transducer's position in their formulation, respectively. Recalling that the slant range of acoustic ray path is $2L^*/\cos\theta$, the reference round-trip travel time can be written as,

$$\tau_i = \frac{2L^*}{\overline{V_0(u)}\cos\theta}. \quad (28)$$

Considering the case where $|\gamma_i| \ll 1$, **Eq. 27** is approximated to,

$$-\frac{2L^*}{\overline{V_0}}\gamma_i = c_0(t) + g(t)x_0 + w(t)\tan\theta. \quad (29)$$

From Eqs 26 and 29, the following relationships are derived:

$$c_0(t) = -\frac{2L^*}{\overline{V_0}}\alpha_0(t), \quad (30.1)$$

$$g(t) = -\frac{2}{\overline{V_0}}(\alpha_1(t) + \alpha_2(t)), \quad (30.2)$$

$$w(t) = -\frac{2L^*}{\overline{V_0}}\alpha_2(t). \quad (30.3)$$

In Honsho et al. (2019), $w(t)$ is extended to a 2-dimensional vector, i.e.,

$$\boldsymbol{w}(t) = -\frac{2L^*}{\overline{V_0}}\boldsymbol{\alpha}_2(t). \quad (31.1)$$

Similarly, when extending $g(t)$ to the 2-dimensional vector, we can use the following vector form:

$$\boldsymbol{g}(t) = -\frac{2}{\overline{V_0}}(\boldsymbol{\alpha}_1(t) + \boldsymbol{\alpha}_2(t)), \quad (31.2)$$

though they consequently use the assumption that $\boldsymbol{g}(t)$ is parallel to $\boldsymbol{w}(t)$. It is equivalent to the case that $\boldsymbol{\alpha}_1$ is parallel to $\boldsymbol{\alpha}_2$ in the proposed formulation.

Honsho et al. (2019) supposed the physical model where a spatially homogeneous 1-directional gradient of slowness lies in the certain layer, from sea-surface to the depth D, in the water. In such cases, $\boldsymbol{w}(t)$ is proportional to $\boldsymbol{g}(t)$, as $\boldsymbol{w} = (D/2)\boldsymbol{g}$. This is exactly the same assumption as the model by Yasuda et al. (2017). The model of Kinugasa et al. (2020) is the special case of those models where D equals to the water depth.

In the proposed method, the sound speed field is approximately interpreted by their models when the unit vector of $\boldsymbol{\alpha}_1$ is supposed to be same as that of $\boldsymbol{\alpha}_2$ and $|\boldsymbol{\alpha}_1| \geq |\boldsymbol{\alpha}_2|$. The depth of the gradient layer is calculated as,

$$D = \frac{2L^*}{1 + \boldsymbol{\alpha}_1/\boldsymbol{\alpha}_2}. \quad (32)$$

When $\boldsymbol{\alpha}_1 = \boldsymbol{\alpha}_2$, it concludes to the model of Kinugasa et al. (2020). Conversely, when $|\boldsymbol{\alpha}_2| \ll |\boldsymbol{\alpha}_1|$, sound speed gradient lies in the thin layer near the surface.

In addition to the simple model above, the proposed method can extract more complicated sound speed field, which partly described by Yokota and Ishikawa (2019). Extracted parameters for the sound speed perturbation indicate the complicity of oceanographic structure, as shown in the next section.

Validity of Extracted Sound Speed Perturbation Model

Typical examples for the estimation results for each observation, i.e., the time series of travel time residuals, and sound speed perturbation interpreted from the correction coefficient, are shown in **Figure 7**. Results for all the datasets are available in **Supplementary Figure S1**.

In the most cases for site TOS2, both terms of the estimated sound speed gradient vector stably direct south to southeast. Because the sound speed increases with the water temperature, it means that the water temperature is higher in the southern region. The results that $\boldsymbol{g}_2$ is comparable with $\boldsymbol{g}_1$ in many cases indicate that the gradient of water temperature continues to the deeper portion, as discussed in the previous section. This is consistent with the fact that the Kuroshio current continuously flows on the south of TOS2.

In contrast, the directions of gradient terms at MYGI have less constancy than TOS2. Unlike the area around TOS2 where the Kuroshio current dominantly affects the seawater structure, MYGI is located in an area with a complicated ocean current system (e.g., Yasuda, 2003; Miyazawa et al., 2009). Watanabe and Uchida (2016) have also shown that the temperature profiles at MYGI vary widely with observation epochs. These features cannot be resolved by the simpler model with single sound speed gradient parameter.

The complexity in the sound speed variation at MYGI tends to lead to large variations in the residual travel time. Nevertheless, the proposed method successfully extracted the smooth sound speed structure for many observation epochs, except a few epochs such as June 2013 (MYGI.1306.kaiyo_k4) and June 2019 (MYGI.1906.meiyo_m5) shown in **Supplementary Figure S1**. In these epochs, relatively larger values for the hyperparameter λ_0^2 were adopted and caused larger variations in each term of Γ. Possible causes of this include the systematic errors in other observation subcomponents such as the random walk noise in GNSS positioning, the drifts of gyro sensor, or the time synchronization error between the devices.

Preferred models for all the tested epochs had positive values for data correlation length, μ_t. It is considered that the plausible estimation of sound speed is realized by introducing the statistic information criteria and the information of data covariances.

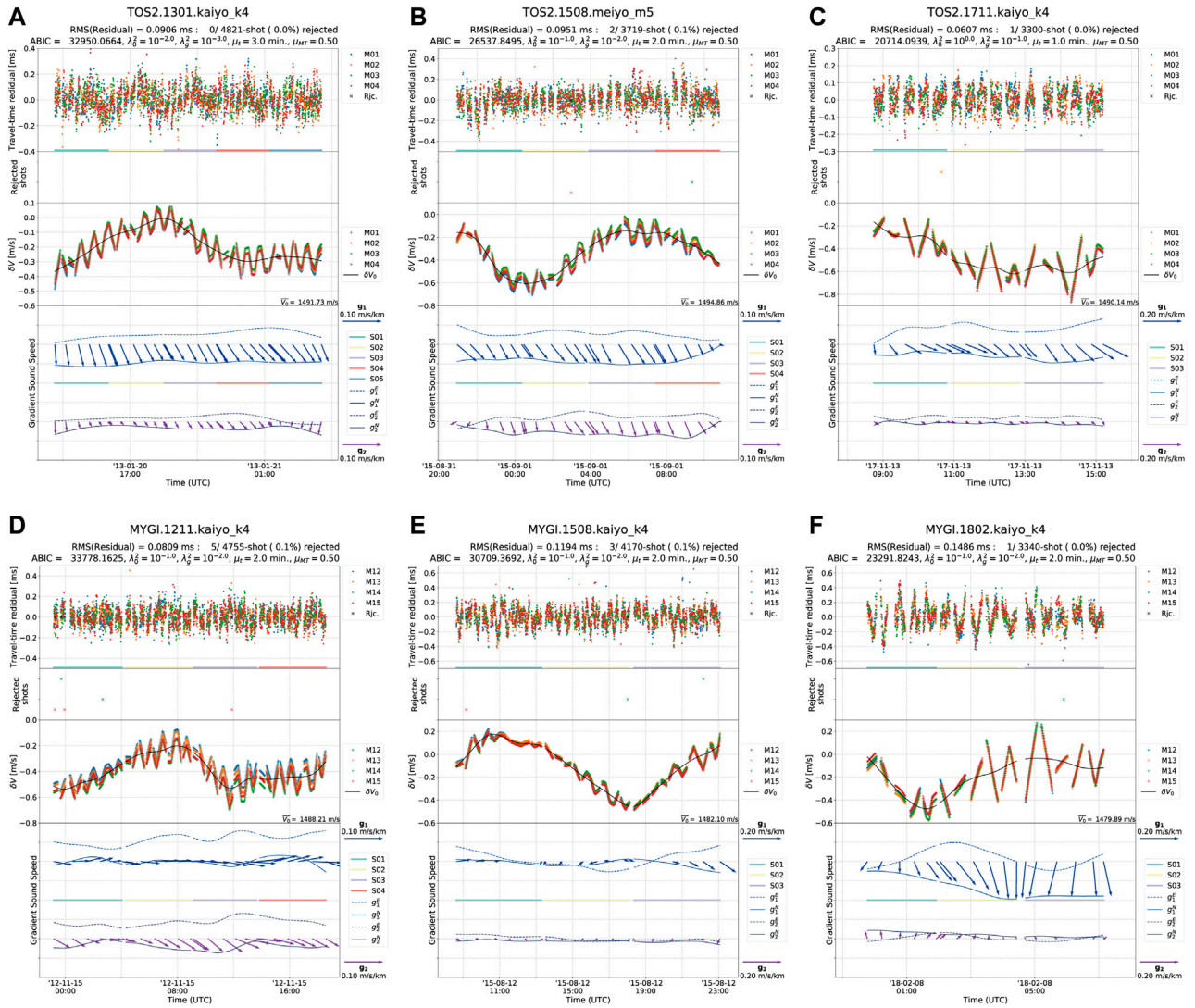

FIGURE 7 | Estimated results of the most preferred model for epochs **(A)** TOS2.1301.kaiyo_k4, **(B)** TOS2.1508.meiyo_m5, and **(C)** TOS2.1711.kaiyo_k4, **(D)** MYGI.1211.kaiyo_k4, **(E)** MYGI.1508. kaiyo_k4, and **(F)** MYGI.1802. kaiyo_k4. The top panels show the model residuals of the round-trip travel time. The second panels show the rejected acoustic data in the preprocessing step for determining the array geometry. The third panels indicate the sound speed perturbations, i.e., $\boldsymbol{\gamma}_i \overline{V_0}$ (the crosses), and $\delta V_0(t) \equiv \overline{V_0}\boldsymbol{\alpha}_0(t)$ (black line). The colors of the symbols in these panels identify the target transponders. The blue and purple arrows on the bottom panels indicate the spatial gradient of the sound speed perturbations in north-up expression, i.e., $\boldsymbol{g}_1(t) \equiv \overline{V_0}\boldsymbol{\alpha}_1(t)$, and $\boldsymbol{g}_2(t) \equiv \overline{V_0}\boldsymbol{\alpha}_2(t)$, respectively. Dotted lines and solid lines show the temporal variations of eastward and northward components, respectively. The colored horizontal lines denote the ranges of the observation subsets.

In order to discuss the effects of the data covariance, we tested the cases for the models without assuming the data correlation, i.e., $\mu_t = 0$. **Figure 8** shows the preferred models selected from $\lambda_0^2 = (10^{-3}, 10^{-2}, 10^{-1}, 10^{0}, 10^{1}, 10^{2}, 10^{3}, 10^{4})$ and $\mu_t = 0$. It is clear that the preferred models without assuming the data correlation have larger λ_0^2. Although the residuals of travel time were reduced in these models, overfittings occurred for each term of Γ. Comparing the preferred and less-preferred results, the existence of data covariance components contributes to suppressing the overfitting and to selecting a model with less perturbation by decreasing the impact of individual data on model parameters.

To confirm the stability of the seafloor positioning results, the differences of seafloor position for the tested models from the most preferred models are summarized in **Figure 9**. The differences in estimated positions for most of the tested models converged in several centimeters. For both sites, variations in the vertical component tend to be larger for larger values of λ_0^2. It indicates that finer hyperparameter tuning is not required when considering the application to seafloor positioning.

As another application of GNSS-A to oceanography, temporal changes of the oceanographic structure within the observation epoch can be extracted using the proposed method. For example, the estimated sound speed gradient $\boldsymbol{g}_1$ in the epoch of MYGI.1802.kaiyo_k4 (**Figure 7F**) suggests that the dominant

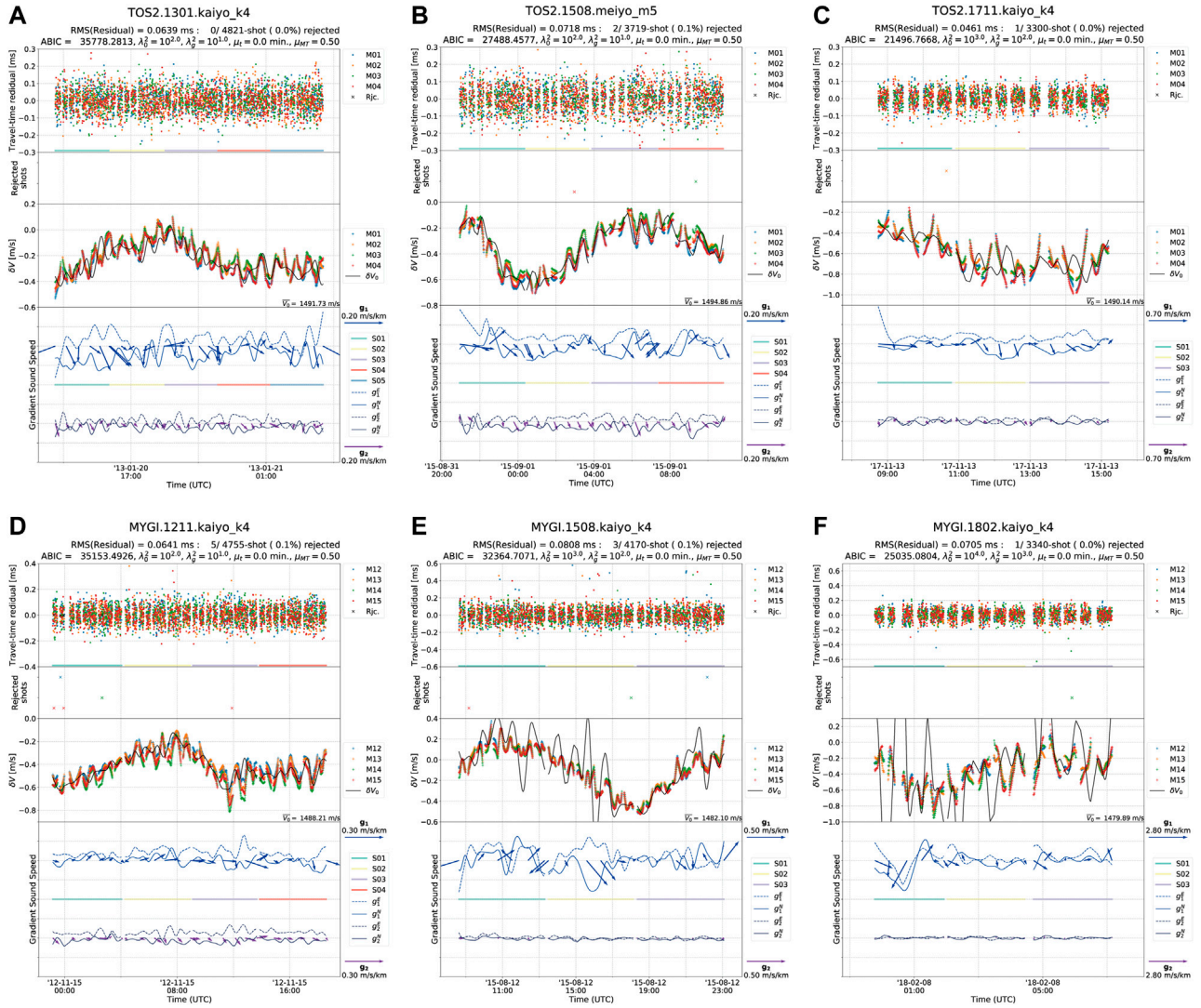

FIGURE 8 | Same as **Figure 7**, but for the most preferred model in the models with $\mu_t = 0$.

oceanographic structure had changed at 01:00–03:00 UTC. On the other hand, a temporal variation with a relatively short period of several tens of minutes remains in the travel time residuals, which might be caused by the internal gravity wave. To improve the detectability of relatively short-period perturbations, further adjustments and verifications of the proposed model will be required.

CONCLUSION

We reconstructed the GNSS-A observation equation and developed the Python-based software GARPOS to solve the seafloor position as well as the sound speed perturbations using the empirical Bayes approach. It provides a stable solution for a generally ill-posed problem caused by the correlation among the model parameters, by introducing the hyperparameter tuning based on the ABIC minimization and data covariance to rationalize the normalization constant of the posterior pdf.

The most important point is that the proposed method succeeded in directly extracting the time-dependent sound speed field with two end members of spatial gradient terms, which are roughly characterized by depths, even when the observers used only one sea-surface unit. Statistical approach allowed us to suppress the overfitting and thus to obtain simpler sound speed field from densely collected dataset. It successfully reproduced the stationary southward sound speed gradient at TOS2, which is consistent with the Kuroshio current.

On the other hand, model overfits were shown in several epochs. These overfits can be caused not only by the actually complicated sound speed field but also by other error sources which were not well included in the model. It means that the hyperparameter tuning also plays a role in the verification of

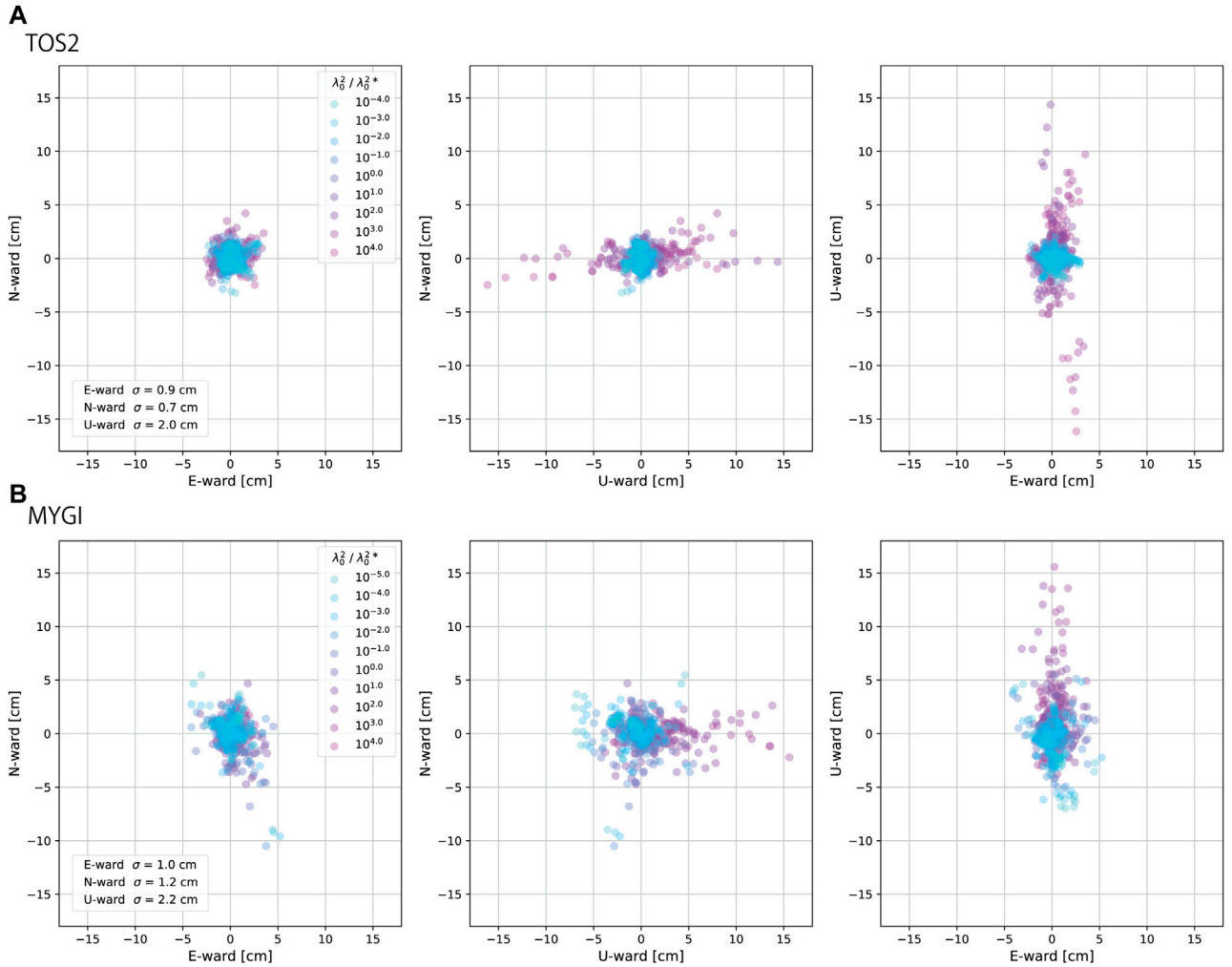

FIGURE 9 | Distributions of differences of positions of the tested models from the preferred ones at **(A)** TOS2 and **(B)** MYGI for northward-eastward **(left)**, northward-upward **(center)**, and upward-eastward **(right)** components. The colors of circles indicate the value of $\lambda_0^2/\lambda_0^{2*}$.

dataset and model. Error analyses in such cases might rather help improving the GNSS-A accuracy and methodology.

We suggested a simplified formatting for the GARPOS input files. Researchers can enter into the field of seafloor geodesy by collecting the listed data with adequate precision. Since each subcomponent of GNSS-A technique, i.e., GNSS positioning, acoustic ranging, and so on, has been well established, observers can combine them on their platform. Especially, GNSS-A is expected to be practicalized in the near future with an unmanned surface vehicle (Chadwell, 2016) or a buoy (e.g., Kinugasa et al., 2020; Tadokoro et al., 2020). Even in the case of the stationary observation due to small cruising speed, GARPOS may provide the solutions by making a slight modification in the prior variance-covariance matrix.

There is a room for improvement in setting the prior information for transponders' positions, $\boldsymbol{X}_j^0$. For instance, the displacement of transponder array from the previous epoch is predicted as small as several centimeters when the interval of observation visits is short. Such assumption leads to the application of the inter-epoch filtering. Furthermore, it has a possibility to progress to the kinematic seafloor positioning, as shown by Tomita et al. (2019). We expect that the publication of GARPOS on the open-access repository will enhance the researchers' engagement and the future development on the GNSS-A technique.

DATA AVAILABILITY STATEMENT

The datasets presented in this study can be found in online repositories. The names of the repository/repositories and accession number(s) can be found below: GARPOS v0.1.0 (https://zenodo.org/record/3992688); GNSS-A data obtained at the sites "TOS2" and "MYGI" in 2011-2019 (https://doi.org/10.5281/zenodo.3993912).

AUTHOR CONTRIBUTIONS

SW designed the study and wrote the manuscript. SW developed "GARPOS" and processed the data. SW, TI, YY, and YN discussed about the methodology and commented to improving the manuscript.

FUNDING

The submission of the manuscript was funded by the Japan Coast Guard.

ACKNOWLEDGMENTS

We thank many staff members from the Hydrographic and Oceanographic Department, Japan Coast Guard, including the crew of the survey vessels Takuyo, Shoyo, Meiyo, and Kaiyo for their support in our observations and technological developments. We especially thank the active senior staff members from the Geodesy and Geophysics Office, Hydrographic and Oceanographic Department, Japan Coast Guard, for their devoted maintenance and management of the equipment. We also thank the reviewers for their comments and suggestions for improving the manuscript.

SUPPLEMENTARY MATERIALS

The Supplementary Material for this article can be found online at: https://www.frontiersin.org/articles/10.3389/feart.2020.597532/full#supplementary-material

REFERENCES

Akaike, H. (1980). "Likelihood and the Bayes procedure", In *Bayesian statistics*. Editors J. M. Bernardo, et al., (Valencia, Spain: University Press), 143–166.

Altamimi, Z., Rebischung, P., Métivier, L., and Collilieux, X. (2016). ITRF2014: a new release of the International Terrestrial Reference Frame modeling nonlinear station motions. *J. Geophys. Res. Solid Earth* 121, 6109. doi:10.1002/2016JB013098.

Asada, A., and Yabuki, T. (2001). Centimeter-level positioning on the seafloor. *Proc. Jpn. Acad. Ser. B Phys. Biol. Sci.* 77, 7–12. doi:10.2183/pjab.77.7.

Bürgmann, R., and Chadwell, D. (2014). Seafloor geodesy. *Annu. Rev. Earth Planet Sci.* 42(1), 509–534. doi:10.1146/annurev-earth-060313-054953.

Chadwell, C. D. (2016). "Campaign-style GPS-Acoustic with wave gliders and permanent seafloor benchmarks", in *Proceedings of the subduction zone observatory workshop.* (Boise, ID:Boise Center), Sep. 29 – Oct. 1 2016.

Chadwell, C. D., and Spiess, F. N. (2008). Plate motion at the ridge-transform boundary of the south Cleft segment of the Juan de Fuca Ridge from GPS-Acoustic data. *J. Geophys. Res.* 113, B04415. doi:10.1029/2007JB004936.

Chadwell, C. D., and Sweeney, A. D. (2010). Acoustic ray-trace equations for seafloor geodesy. *Mar. Geodes.* 33(2–3), 164–186. doi:10.1080/01490419.2010.492283.

Chen, H.-Y., Ikuta, R., Lin, C.-H., Hsu, Y.-J., Kohmi, T., Wang, C.-C., et al. (2018). Back-arc opening in the western end of the Okinawa Trough revealed from GNSS/Acoustic Measurements. *Geophys. Res. Lett.* 45, 137–145, doi:10.1002/2017GL075724.

de Boor, C. (1978). *A practical guide to splines*. New York:Springer-Verlag, Vol. 27.

Del Grosso, V. A. (1974). New equation for the speed of sound in natural waters (with comparisons to other equations). *J. Acoust. Soc. Am.* 56, 1084–1091. doi:10.1121/1.1903388.

Fujimoto, H. (2014). Seafloor geodetic approaches to subduction thrust earthquakes, *Monogr. Environ. Earth Planets* 2, 23–63. doi:10.5047/meep.2014.00202.0023.

Fujita, M., Ishikawa, T., Mochizuki, M., Sato, M., Toyama, S., Katayama, M., et al. (2006). GPS/acoustic seafloor geodetic observation: method of data analysis and its application. *Earth Planets Space* 58, 265–275. doi:10.1186/BF03351923.

Fukahata, Y., and Wright, T. J. (2008). A non-linear geodetic data inversion using ABIC for slip distribution on a fault with an unknown dip angle. *Geophys. J. Int.* 173, 353–364. doi:10.1111/j.1365-246X.2007.03713.x.

Gagnon, K., Chadwell, C. D., and Norabuena, E. (2005). Measuring the onset of locking in the Peru-Chile trench with GPS and acoustic measurements. *Nature* 434(7030), 205–208. doi:10.1038/nature03412.

Honsho, C., and Kido, M. (2017). Comprehensive analysis of traveltime data collected through GPS-acoustic observation of seafloor crustal movements. *J. Geophys. Res. Solid Earth* 122, 8583–8599. doi:10.1002/2017JB014733.

Honsho, C., Kido, M., Tomita, F., and Uchida, N. (2019). Offshore postseismic deformation of the 2011 Tohoku earthquake revisited: application of an improved GPS-acoustic positioning method considering horizontal gradient of sound speed structure. *J. Geophys. Res. Solid Earth* 124, 5990. doi:10.1029/2018JB017135.

Hovem, J. M. (2013). "Ray trace modeling of underwater sound propagation", in *Modeling and measurement methods for acoustic waves and for acoustic microdevices*. Editor M. G. Beghi. (Rijeka, Croatia: IntechOpen). doi:10.5772/55935.

IERS Conventions (2010). Editors. G. Petit and B. Luzum. (IERS technical note; 36) frankfurt am main: Verlag des Bundesamts für Kartographie und Geodäsie, 179, ISBN 3-89888-989-6

Ikuta, R., Tadokoro, K., Ando, M., Okuda, T., Sugimoto, S., Takatani, K., et al. (2008). A new GPS-acoustic method for measuring ocean floor crustal deformation: application to the Nankai Trough. *J. Geophys. Res.* 113, B02401. doi:10.1029/2006JB004875.

International GNSS Service (a). *GNSS final combined orbit solution product*, Greenbelt, MD, USA: NASA Crustal Dynamics Data Information System (CDDIS). doi:10.5067/gnss/gnss_igsorb_001.

International GNSS Service (b). *GNSS final combined satellite and receiver clock solution (30 second) product*, Greenbelt, MD, USA: NASA Crustal Dynamics Data Information System (CDDIS). doi:10.5067/GNSS/gnss_igsclk30_001.

Ishikawa, T., Yokota, Y., Watanabe, S., and Nakamura, Y. (2020). History of on-board equipment improvement for GNSS-A observation with focus on observation frequency, *Front. Earth Sci.* 8, 150. doi:10.3389/feart.2020.00150.

Jensen, F. B., Kuperman, W. A., Porter, M. B., and Schmidt, H. (2011). *Computational ocean acoustics*, Vol. 97. New York, NY: Springer New York, ISBN:978-1-4419-8677-1.

Kido, M., Osada, Y., Fujimoto, H., Hino, R., and Ito, Y. (2011). Trench-normal variation in observed seafloor displacements associated with the 2011 Tohoku-Oki earthquake. *Geophys. Res. Lett.* 38, L24303. doi:10.1029/2011GL050057.

Kido, M., Osada, Y., and Fujimoto, H. (2008). Temporal variation of sound speed in ocean: a comparison between GPS/acoustic and *in situ* measurements. *Earth Planets Space* 60(3), 229–234, doi:10.1186/BF03352785.

Kinugasa, N., Tadokoro, K., Kato, T., and Terada, Y. (2020). Estimation of temporal and spatial variation of sound speed in ocean from GNSS-A measurements for observation using moored buoy. *Prog. Earth Planet. Sci.* 7, 21. https://doi.org/10.1186/s40645-020-00331-5.

Matsu'ura, M., Noda, A., and Fukahata, Y. (2007). Geodetic data inversion based on Bayesian formulation with direct and indirect prior information *Geophys. J. Int.* 171(3), 1342–1351. doi:10.1111/j.1365-246X.2007.03578.x.

Matsumoto, Y., Fujita, M., and Ishikawa, T. (2008). Development of multi-epoch method for determining seafloor station position [in Japanese], *Rep. Hydrogr. Oceanogr. Res.* 26, 16–22.

Miyazawa, Y., Zhang, R., Guo, X., Tamura, H., Ambe, D., Lee, J.-S., et al. (2009). Water mass variability in the western North Pacific detected in a 15-year eddy resolving ocean reanalysis. *J. Oceanogr.* 65, 737–756. doi:10.1007/s10872-009-0063-3.

Nagaya, Y. (1995). Basic study on a sea floor strain measurement using acoustic techniques [in Japanese with English abstracts]. *Rep. Hydrogr. Res.* 31, 67–76.

Obana, K., Katao, H., and Ando, M. (2000). Seafloor positioning system with GPS-acoustic link for crustal dynamics observation-a preliminary result from experiments in the sea-. *Earth Planets Space*. 52, 415–423. doi:10.1186/BF03352253.

Osada, Y., Fujimoto, H., Miura, S., Sweeney, A., Kanazawa, T., Nakao, S., et al. (2003). Estimation and correction for the effect of sound velocity variation on GPS/Acoustic seafloor positioning: an experiment off Hawaii Island. *Earth Planets Space* 55, e17–e20. doi:10.1186/BF03352464.

Sagiya, T., and Thatcher, W. (1999). Coseismic slip resolution along a plate boundary megathrust: the Nankai Trough, southwest Japan. *J. Geophys. Res.* 104(B1), 1111–1129. doi:10.1029/98JB02644.

Sakic, P., Ballu, V., Crawford, W. C., and Wöppelmann, G. (2018). Acoustic ray tracing comparisons in the context of geodetic precise off-shore positioning experiments. *Mar. Geodes.* 41(4), 315–330. doi:10.1080/01490419.2018.1438322.

Sato, M., Fujita, M., Matsumoto, Y., Saito, H., Ishikawa, T., and Asakura, T. (2013). Improvement of GPS/acoustic seafloor positioning precision through controlling the ship's track line. *J. Geodyn.* 87, 825–842. doi:10.1007/s00190-013-0649-9.

Sato, M., Ishikawa, T., Ujihara, N., Yoshida, S., Fujita, M., Mochizuki, M., et al. (2011). Displacement above the hypocenter of the 2011 Tohoku-oki earthquake. *Science* 332, 1395. doi:10.1126/science.1207401.

Spiess, F. N. (1980). Acoustic techniques for marine geodesy, *Mar. Geodes.* 4(1), 13–27. doi:10.1080/15210608009379369.

Spiess, F. N., Chadwell, C. D., Hildebrand, J. A., Young, L. E., Purcell, G. H., and Dragert, H. (1998). Precise GPS/Acoustic positioning of seafloor reference points for tectonic studies. *Phys. Earth Planet. In.* 108(2), 101–112. doi:10.1016/s0031-9201(98)00089-2.

Tadokoro, K., Kinugasa, N., Kato, T., Terada, Y., and Matsuhiro, K. (2020). A marine-buoy-mounted system for continuous and real-time measurment of seafloor crustal deformation. *Front. Earth Sci.* 8, 123. doi:10.3389/feart.2020.00123.

Takasu, T. (2013). *RTKLIB ver. 2.4.2: an open source program package for GNSS positioning*, http://www.rtklib.com/

Tarantola, A., and Valette, B. (1982). Generalized nonlinear inverse problems solved using the least squares criterion. *Rev. Geophys.* 20(2), 219–232. doi:10.1029/RG020i002p00219.

Tomita, F., Kido, M., Honsho, C., and Matsui, R. (2019). Development of a kinematic GNSS-Acoustic positioning method based on a state-space model. *Earth Planets Space* 71, 102. doi:10.1186/s40623-019-1082-y.

Tomita, F., Kido, M., Ohta, Y., Iinuma, T., and Hino, R. (2017). Along-trench variation in seafloor displacements after the 2011 Tohoku earthquake. *Sci. Adv.* 3(7), e1700113. doi:10.1126/sciadv.1700113.

Tomita, F., Kido, M., Osada, Y., Hino, R., Ohta, Y., and Iinuma, T. (2015). First measurement of the displacement rate of the Pacific Plate near the Japan Trench after the 2011 Tohoku-Oki earthquake using GPS/acoustic technique. *Geophys. Res. Lett.* 42, 8391–8397, doi:10.1002/2015GL065746.

Watanabe, S., Sato, M., Fujita, M., Ishikawa, T., Yokota, Y., Ujihara, N., et al. (2014). Evidence of viscoelastic deformation following the 2011 Tohoku-oki earthquake revealed from seafloor geodetic observation. *Geophys. Res. Lett.* 41, 5789–5796. doi:10.1002/2014GL061134.

Watanabe, S., Ishikawa, T., Yokota, Y., and Nakamura, Y. (2020a). GARPOS v0.1.0: analysis tool for GNSS-Acoustic seafloor positioning. *Zenodo*. Version 0.1.0. doi:10.5281/zenodo.3992688.

Watanabe, S., Ishikawa, T., Yokota, Y., and Nakamura, Y. (2020b). GNSS-A data obtained at the sites "TOS2" and "MYGI" in 2011-2019. *Zenodo*. doi:10.5281/zenodo.3993912.

Watanabe, S., and Uchida, T. (2016). Stable structures of temperature and salinity validated by the repeated measurements in the few-miles square regions off Japan coast in the western Pacific [in Japanese with English abstract]. *Rep. Hydro. Ocean. Res.* 53, 57–81.

Watanabe, S., Yokota, Y., and Ishikawa, T. (2020c). Stability test to validate the GNSS-A seafloor positioning with kinematic precise point positioning [in Japanese with English abstract and captions]. *J. Geod. Soc. Japan* 66, 1–7. doi:10.11366/sokuchi.66.1.

Yasuda, I. (2003). Hydrographic structure and variability in the kuroshio-oyashio transition area. *J. Oceanogr.* 59, 389–402. doi:10.1023/A:1025580313836.

Yasuda, K., Tadokoro, K., Taniguchi, S., Kimura, H., and Matsuhiro, K. (2017). Interplate locking condition derived from seafloor geodetic observation in the shallowest subduction segment at the Central Nankai Trough, Japan. *Geophys. Res. Lett.* 44, 3572–35790. doi:10.1002/2017GL072918.

Yokota, Y., and Ishikawa, T. (2019). Gradient field of undersea sound speed structure extracted from the GNSS-A oceanography: GNSS-A as a sensor for detecting sound speed gradient. *SN Appl. Sci.* 1, 693. doi:10.1007/s42452-019-0699-6.

Yokota, Y., and Ishikawa, T. (2020). Shallow slow slip events along the Nankai Trough detected by GNSS-A, *Sci. Adv.* 6(3), eaay5786. doi:10.1126/sciadv.aay5786.

Yokota, Y., Ishikawa, T., and Watanabe, S. (2019). Gradient field of undersea sound speed structure extracted from the GNSS-A oceanography. *Mar. Geophys. Res.* 40(4), 493–504. doi:10.1007/s11001-018-9362-7.

Yokota, Y., Ishikawa, T., and Watanabe, S. (2018). Seafloor crustal deformation data along the subduction zones around Japan obtained by GNSS-A observations. *Sci. Data* 5, 180182. doi:10.1038/sdata.2018.182.

Yokota, Y., Ishikawa, T., Watanabe, S., Tashiro, T., and Asada, A. (2016). Seafloor geodetic constraints on interplate coupling of the Nankai Trough megathrust zone. *Nature* 534, 374–377. doi:10.1038/nature17632.

Conflict of Interest: The authors declare that the research was conducted in the absence of any commercial or financial relationships that could be construed as a potential conflict of interest.

frontiers in Earth Science

ORIGINAL RESEARCH
published: 08 December 2020
doi: 10.3389/feart.2020.615178

Four Years of Continuous Seafloor Displacement Measurements in the Campi Flegrei Caldera

*Prospero De Martino[1,2], Sergio Guardato[1], Gian Paolo Donnarumma[1], Mario Dolce[1], Tiziana Trombetti[3], Francesco Chierici[4], Giovanni Macedonio[1], Laura Beranzoli[5] and Giovanni Iannaccone[1]**

[1]Istituto Nazionale di Geofisica e Vulcanologia, Sezione di Napoli Osservatorio Vesuviano, Napoli, Italy, [2]Istituto per il Rilevamento Elettromagnetico dell'Ambiente, Consiglio Nazionale delle Ricerche (IREA-CNR), Napoli, Italy, [3]Istituto di Scienze Marine, Consiglio Nazionale delle Ricerche (ISMAR-CNR), Bologna, Italy, [4]Istituto Nazionale di Astrofisica - Istituto di Radioastronomia, Bologna, Italy, [5]Istituto Nazionale di Geofisica e Vulcanologia, Sezione Roma2, Roma, Italy

We present 4 years of continuous seafloor deformation measurements carried out in the Campi Flegrei caldera (Southern Italy), one of the most hazardous and populated volcanic areas in the world. The seafloor sector of the caldera has been monitored since early 2016 by the MEDUSA marine research infrastructure, consisting of four instrumented buoys installed where sea depth is less than 100 m. Each MEDUSA buoy is equipped with a cabled, seafloor module with geophysical and oceanographic sensors and a subaerial GPS station providing seafloor deformation and other environmental measures. Since April 2016, the GPS vertical displacements at the four buoys show a continuous uplift of the seafloor with cumulative measured uplift ranging between 8 and 20 cm. Despite the data being affected by environmental noise associated with sea and meteorological conditions, the horizontal GPS displacements on the buoys show a trend coherent with a radial deformation pattern. We use jointly the GPS horizontal and vertical velocities of seafloor and on-land deformations for modeling the volcanic source, finding that a spherical source fits best the GPS data. The geodetic data produced by MEDUSA has now been integrated with the data flow of other monitoring networks deployed on land at Campi Flegrei.

Keywords: seafloor geodesy, volcano monitoring, Campi Flegrei caldera, Global Positioning System, time series, buoy

OPEN ACCESS

Edited by:
Keiichi Tadokoro, Nagoya University, Japan

Reviewed by:
Emily K. Montgomery-Brown, United States Geological Survey, United States
Maurizio Battaglia, United States Geological Survey (USGS), United States

****Correspondence:***
Giovanni Iannaccone
giovanni.iannaccone@ingv.it

Specialty section:
This article was submitted to Solid Earth Geophysics, a section of the journal Frontiers in Earth Science

Received: *08 October 2020*
Accepted: *20 November 2020*
Published: *08 December 2020*

Citation:
De Martino P, Guardato S, Donnarumma GP, Dolce M, Trombetti T, Chierici F, Macedonio G, Beranzoli L and Iannaccone G (2020) Four Years of Continuous Seafloor Displacement Measurements in the Campi Flegrei Caldera. Front. Earth Sci. 8:615178. doi: 10.3389/feart.2020.615178

INTRODUCTION

Seafloor geodesy is now an established branch of geodesy for precise underwater measurements of position and displacements and is used for monitoring submerged volcanic areas, tectonic deformation and subsidence related to offshore oil extraction. The main analysis methodologies used are based on acoustic waves propagation and pressure measurements.

Acoustic methods use travel time measurements of acoustic wave packets between two reference locations together with estimation of the seawater sound speed. Two main acoustic techniques have been developed: 1) a GPS-Acoustic combination technique (GPS/A) where a kinematic GPS on a platform at the sea surface is combined with acoustic wave ranging to determine the position of a network of transponder on the seafloor (Bürgman and Chadwell, 2014) This technique has been used extensively to investigate crustal deformation at oceanic spreading centers and subduction thrust faults; usually the measurements are performed in campaign-style with research vessels or light

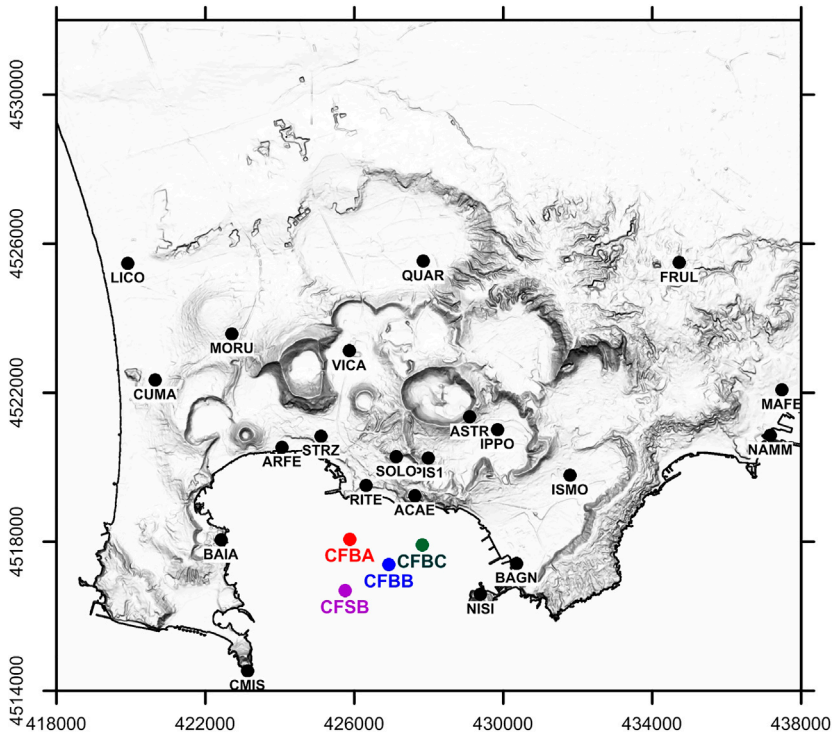

FIGURE 1 | Map of cGPS stations operating in the Campi Flegrei area. Black dots indicate the on land stations of the NeVoCGPS network; colored dots represent the cGPS stations installed on MEDUSA infrastructure.

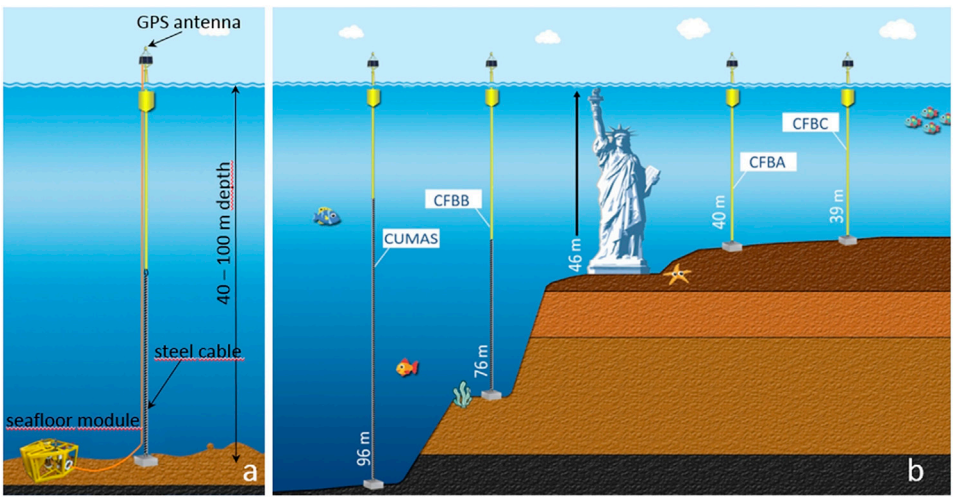

FIGURE 2 | Layout of the buoys. **(A)** schema of a buoy; **(B)** comparison of the length of each buoy installation with the Statue of Liberty in New York, United States. The rigid pole is shown in yellow and the flexible steel cable in black.

inexpensive floating GPS stations using a glider. 2) horizontal distance measurements between two or more transponders; this is applied to relative deformation measurements across geological features (Petersen et al., 2019).

The main limitation of the acoustic techniques arises from the variation over time of properties of the marine environment, with the consequent difficulty estimating the path length starting from the measurement of the propagation time.

Another common technique in marine geodesy that is suitable for monitoring vertical ground displacement is based on the variation of hydrostatic pressure at the sea bottom measured by a bottom pressure recorder (BPR). However, BPR measurement

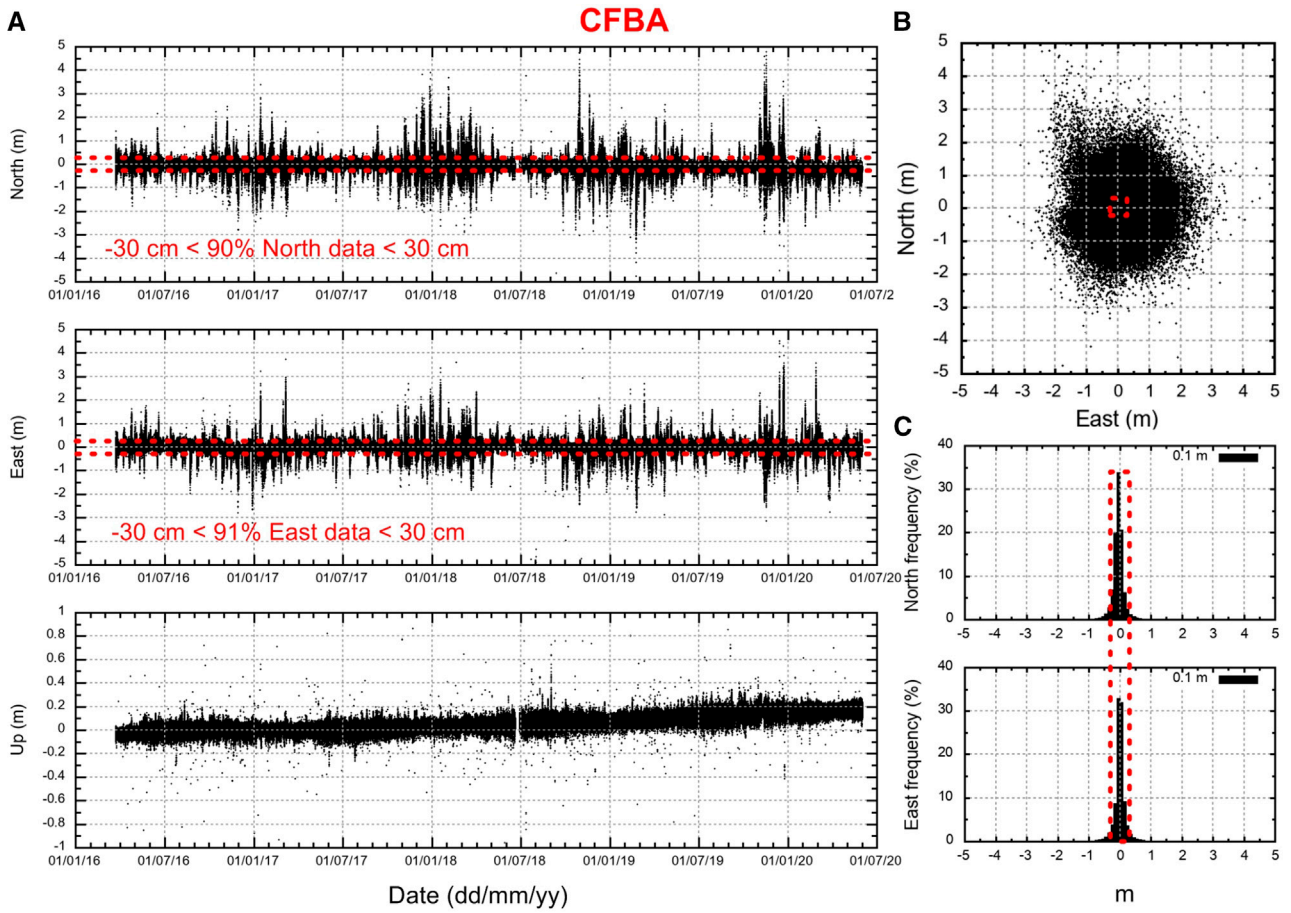

FIGURE 3 | GPS kinematic time series (30 sec sampling) of the CFBA station. **(A)** North (top row), East (middle row) and Up (bottom row) components; **(B)** GPS kinematic positions shown in the horizontal plane; **(C)** Frequency histogram of the horizontal components. Over 90% of the horizontal positions of the buoy are within 30 cm of the origin, taken as the mean horizontal position in the considered period.

suffers from greater uncertainties than GPS. To achieve the centimeter accuracy in the Up component need for seafloor deformation monitoring, BPR time series must be integrated with other complementary measurements such as sea level observations at local tide gauges, atmospheric pressure measurements and measures related to seawater column density (i.e. salinity and temperature). Moreover, an erratic instrumental drift of BPRs must be taken into account (Chierici et al., 2016).

Geodetic measurements on the seafloor are more frequently performed at large depths, typically greater than 1,000 m, than in shallow water. This is because the large variability over time of the sound speed strongly degrades the quality of acoustic measures. The sound speed in sea water depends on the temperature and salinity, which, in turn, are strongly affected by solar radiation, by seasonal cycles, and by water mixing due to sea currents. This variability is particularly pronounced in the shallow layers of coastal areas, where additionally, the presence of rivers or waste waters introduce further variability in water properties. Similarly, the variability of temperature and salinity over the time produces sea density changes detected as pressure variation by the BPR sensors. Consequently, long term pressure measurements are contaminated by a high level of noise that can be removed only with precise knowledge of the sea water density profile over the time (Chierici et al., 2016).

A new methodology for seafloor geodesy measurements suitable for shallow water environments, less than 100 m depth, was recently introduced in Southern Italy. A buoy, named CUMAS (Cabled Underwater Multidisciplinary Acquisition System, Iannaccone et al., 2009; Iannaccone et al., 2010) was deployed in November 2006, at a sea depth of 97 m in the Gulf of Pozzuoli, the marine sector of the Campi Flegrei volcanic area, for an experiment of acoustic data transmission. In 2012, the CUMAS buoy was equipped with a GPS station.

The CUMAS buoy consists of an underwater floating body attached to a concrete anchor ballast on the seafloor. The ballast holds the floating body fixed a few meters below the sea level so it is not affected by sea level variations (Iannaccone et al., 2009). A pole supporting a subaerial, top turret is inserted into the body, allowing a GPS station installed on top of the pole to be rigidly coupled to the seafloor and allowing direct recording of seafloor

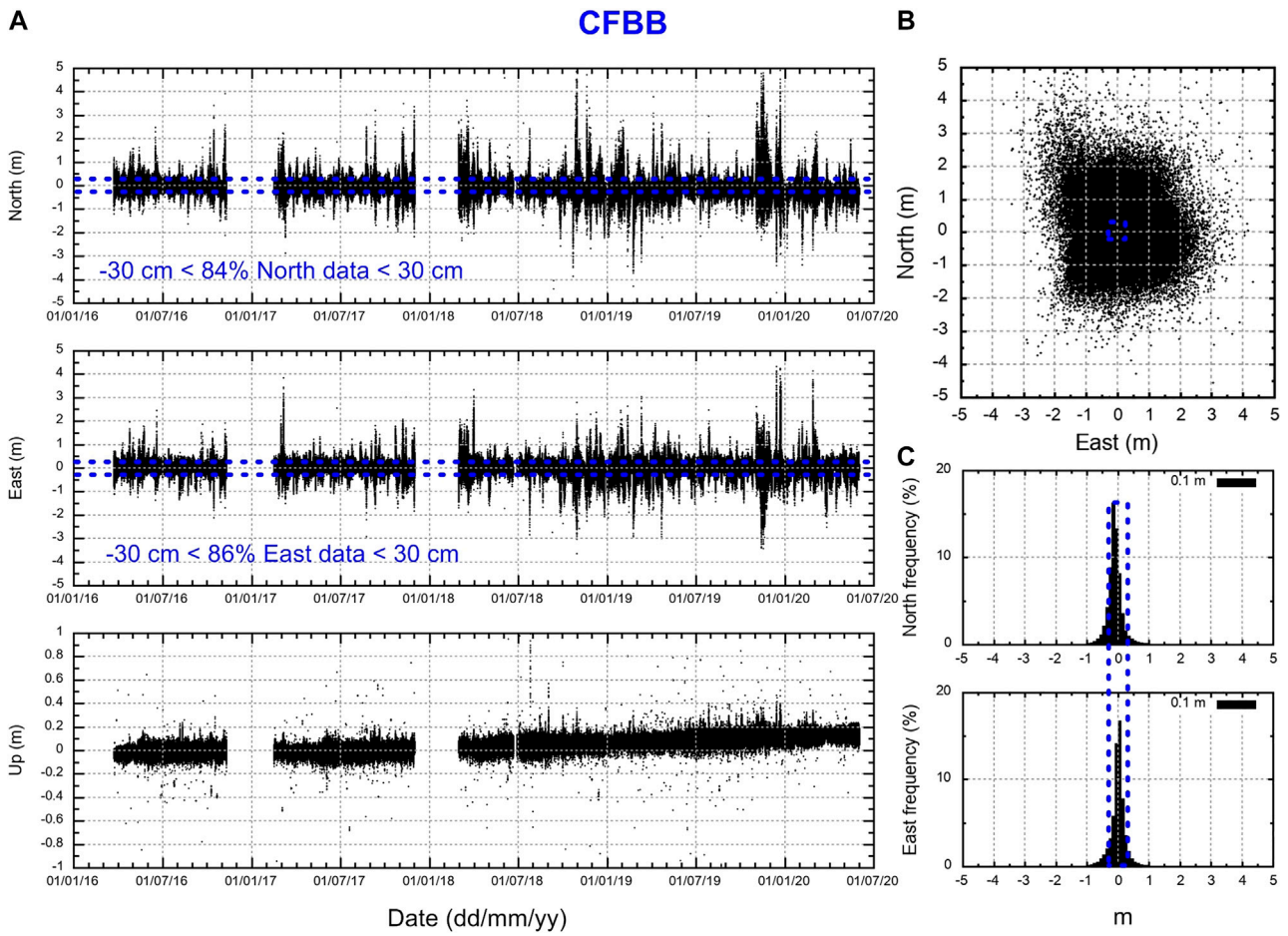

FIGURE 4 | GPS kinematic time series (30 s sampling) of the CFBB station. **(A)** North (top row), East (middle row) and Up (bottom row) components; **(B)** GPS kinematic positions shown in the horizontal plane; **(C)** Frequency histogram of the horizontal components. Over 85% of the horizontal positions of the buoy are within 30 cm of the origin, taken as the mean horizontal position in the considered period.

displacement. De Martino et al. (2014a) showed that the CUMAS GPS station measured a seafloor uplift of about 3–4 cm over 17 months from January 2012 to May 2013, demonstrating the validity of this conceptually simple system for geodetic measurements in shallow waters. Given the success of the CUMAS experiment, three new buoys with GPS stations were deployed in early 2016 in the Gulf of Pozzuoli, forming the MEDUSA (Multiparametric Elastic-beacon Devices and Underwater Sensor Acquisition system) infrastructure.

Here we present the data acquired in continuous mode by the GPS stations of the MEDUSA infrastructure for 4 years after April 2016 and examine their contribution to the interpretation of the ground deformation pattern of the Campi Flegrei caldera.

MATERIALS AND METHODS

MEDUSA Infrastructure Outline

The MEDUSA infrastructure consists of four spar buoys installed in the Gulf of Pozzuoli at 1.1 to 2.4 km from the coast and water depths less than 100 m (colored dots in **Figure 1**).

Two buoys (CFBA and CFBC), deployed where seafloor depth is about 40 m, have a long pole connecting the float and subaerial part to the ballast on the sea bottom. For these two buoys the distance between the GPS antenna and the ballast is about 47.5 m. The other two buoys (CUMAS prototype and CFBB), operating where seafloor depth is about 96 and 76 m respectively, use a steel cable to fasten the pole to the ballast (**Figure 2A**). CFBB has a pole the same length as for CFBA and CFBC joined to a steel cable of 33 m length, while the CUMAS buoy has a pole of 26 m long and a steel cable of 83 m. The floats of CUMAS and CFBB provide a buoyancy force acting on the ballast and keeping the steel cable under tension. Functionally, each buoy behaves as a system rigidly anchored to the seabed so the top of the buoy where the GPS antenna is installed follows directly vertical movement of the seabed. **Figure 2B**, shows in a simplified view the length of the buoys compared to a reference monument and also the proportion of the pole length for each buoy type.

Each buoy is connected by a power supply and data transmission cable to a seafloor module equipped with geophysical and oceanographic sensors placed a few meters

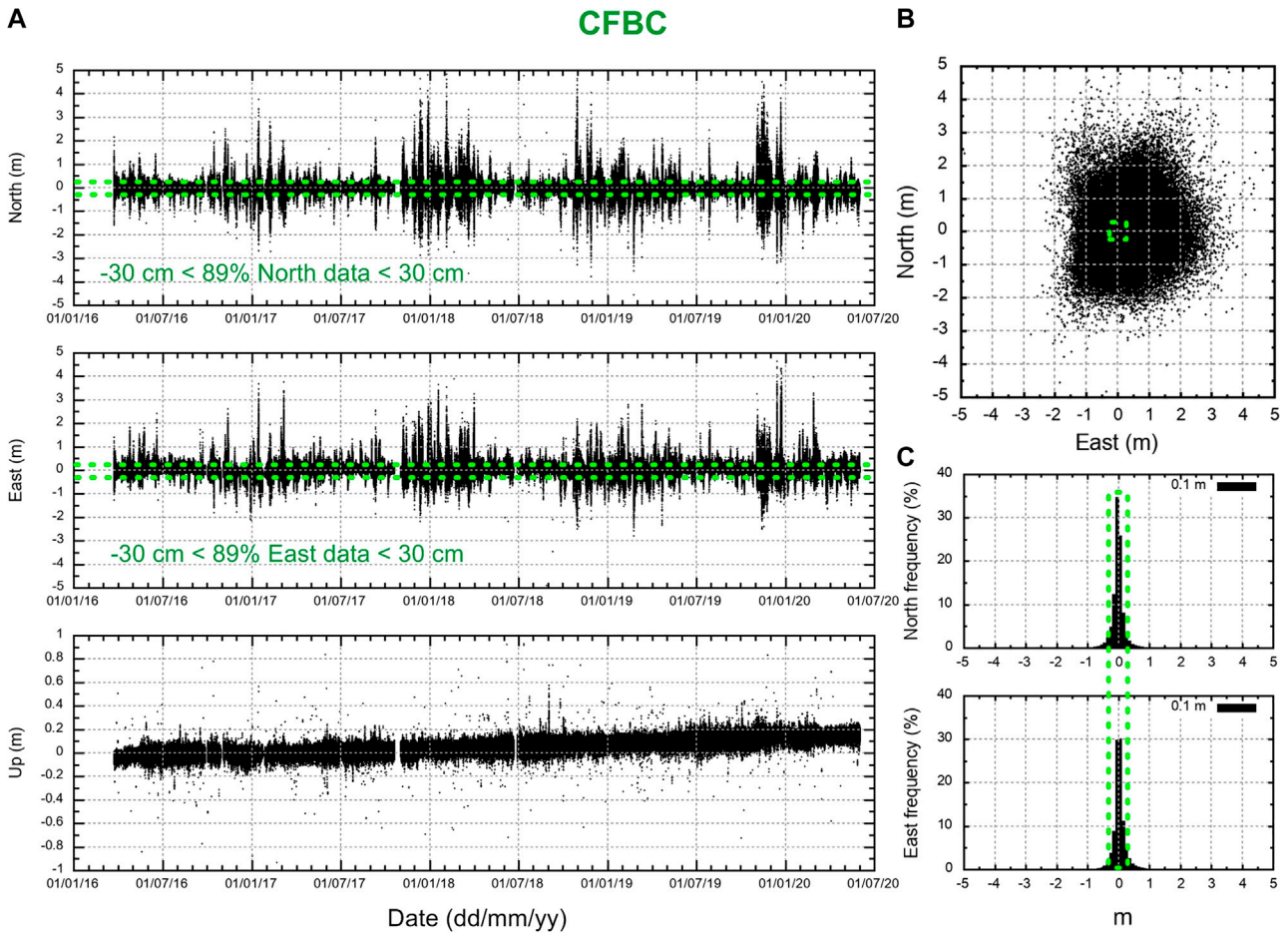

FIGURE 5 | GPS kinematic time series (30 s sampling) of the CFBC station. **(A)** North (top row), East (middle row) and Up (bottom row) components; **(B)** GPS kinematic positions shown in the horizontal plane; **(C)** Frequency histogram of the horizontal components. Over 90% of the horizontal positions of the buoy are within 30 cm of the origin, taken as the mean horizontal position in the considered period.

from the buoy ballast (**Figure 2A**). Each module includes: a three-component broadband seismic sensor, two low-frequency omnidirectional hydrophones, a three-component MEMS accelerometer and an absolute pressure recorder. A titanium vessel contains acquisition systems, status and control sensors, and electronics. Power supply, data transmission and clock signals to the module equipment are provided through an armored, electro-mechanical cable, which also serves for module handling and installation/recovery. On the top of the buoy, a subaerial turret hosts the power supply system (solar panels and buffer batteries), and data transmission and control electronics. Real-time data transmission to a land acquisition center is provided by 5 GHz Wi-Fi. Each buoy is equipped with a Leica GR10 GPS receiver and AR20 antenna. GPS data are acquired with a sampling interval of 30 s and downloaded daily by the INGV-Monitoring Center in Naples for storage and processing. A digital compass measuring the attitude of the buoy is mounted on the turret. One buoy is also equipped with a meteorological station (temperature, humidity, atmospheric pressure, wind direction and speed).

MEDUSA has allowed extension into the Gulf of Pozzuoli of the Campi Flegrei geophysical monitoring system, which was exclusively land-based before 2016, improving the observation and assessment of seafloor deformation in the area and observation and location of earthquakes. MEDUSA is fully integrated in the Campi Flegrei surveillance system: all the data acquired are transmitted to a unique, land acquisition center where they are analyzed and stored together with the data provided by the other land monitoring networks.

cGPS Data Processing and Time Series Analysis

Continuous Global Positioning System (cGPS) data are available since April 2016 for the CFBA, CFBB and CFBC stations and since July 2016 for the CFSB station. The cGPS data has been processed in kinematic mode with the open source program package RTKLIB ver. 2.4.2 (http://www.rtklib.com) to obtain positions of the buoys every 30 s. The reference station for cGPS data processing is LICO (**Figure 1**), located at

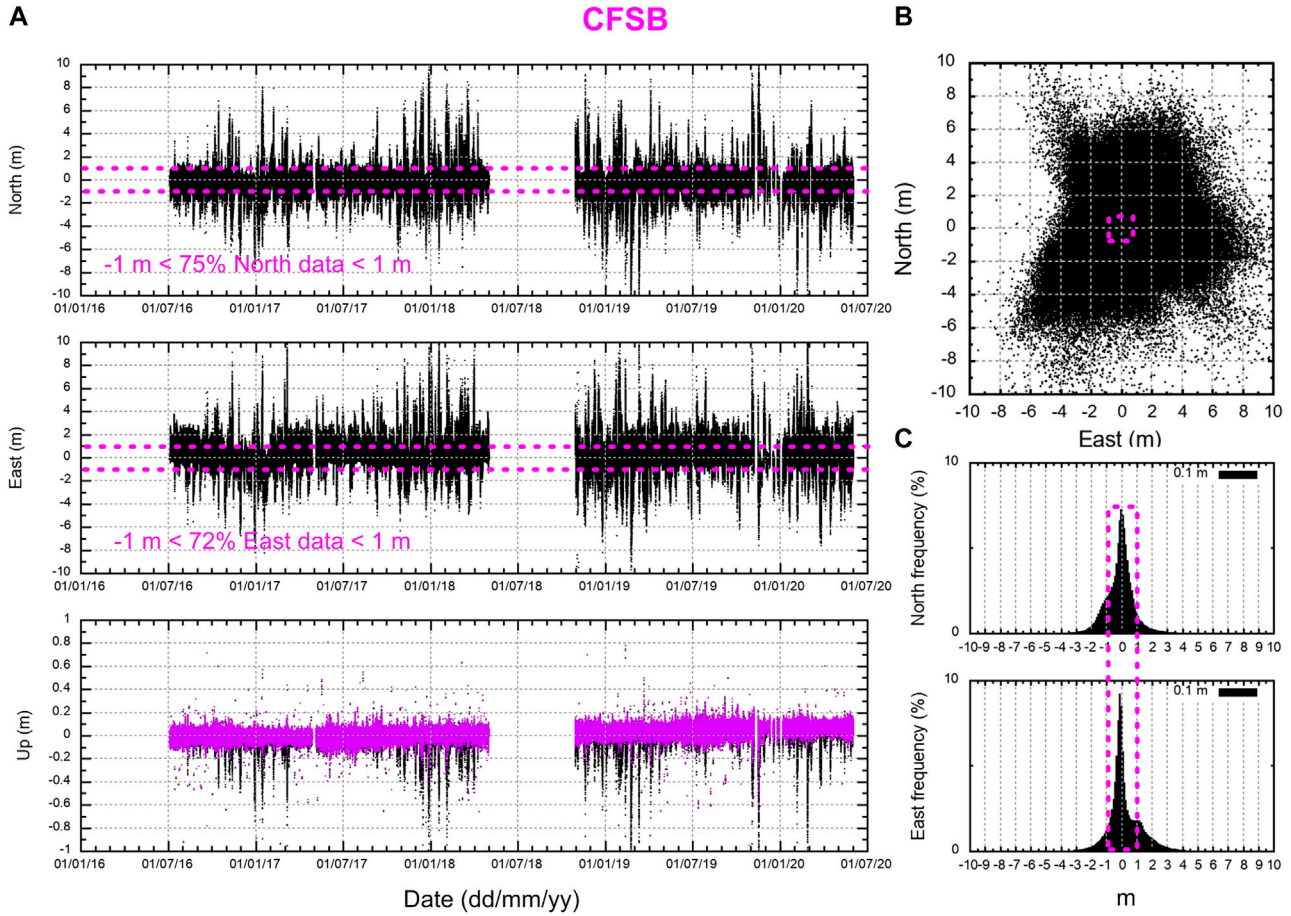

FIGURE 6 | GPS kinematic time series (30 s sampling) of the CFSB station. **(A)** North (top row), East (middle row) and Up (bottom row) components. In the Up plot are reported the raw data (black dots) superimposed to corrected data (magenta dots); **(B)** GPS kinematic positions shown in the horizontal plane; **(C)** Frequency histogram of the horizontal components. Only 70% of the horizontal positions of the buoy are within 1 m of the origin, taken as the mean horizontal position in the considered period.

TABLE 1 | Main physical characteristics of the buoys.

Buoy	Sea depth (m)	Pole length (m)	Cable length (m)	Distance of GPS antenna from the seafloor (m)
CFBA	40	43	0	47.5
CFBB	76	43	33	81
CFBC	39	43	0	47.5
CUMAS	96	20	83	108

a distance of about 10 km from the caldera center (a full description of the kinematic cGPS processing is reported in De Martino et al., 2014a).

The kinematic time series of the MEDUSA cGPS stations showing the position changes every 30 s for the North, East and Vertical (Up) components (m) are shown in **Figures 3A–6A**.

Note the different scale for the signal on the horizontal components (North and East) with respect to the vertical component (Up). This difference shows the influence of weather and sea conditions and marine water circulation on the horizontal components (**Figures 3B–6B**) which produces large fluctuations of the GPS signal, about 10% of which are above about 30 cm. Consequently, we consider that under bad weather conditions the measurements of the position of the buoys is unreliable and we remove all data with fluctuations above ±30 cm in the North and East components. As shown in **Figures 3C–5C**, about 10–15% of horizontal positions at CFBA, CFBB and CFBC are outside ±30 cm of the corresponding origin (mean position in the considered period) and were discarded to reduce the noise in the North and East components for these stations. Moreover, **Figures 3–6**, shows that the amplitudes of the GPS horizontal displacements for the three newer buoys (CFBA, CFBB and CFBC stations) are about one third of those of the older CUMAS buoy (CFSB station). This difference is due to the improved design of the new buoys compared to CUMAS and also to the greater length of the CUMAS steel cable (see **Table 1**).

The CFSB station is characterized by a very high noise level (**Figure 6**) and so is not been included in the horizontal component analysis. Its vertical component has been corrected

for vertical displacement induced by the horizontal movement of the buoy allowed by the long steel cable, as reported in De Martino et al. (2014a). This vertical correction is negligible for CFBA, CFBB and CFBC stations, due to the mechanical system adopted in the deployment of the three new buoys (Iannaccone et al., 2018).

In the Campi Flegrei caldera the deformation rates are relatively low (a few millimeters per month) and the trend of the displacement time-series can be best visualized with averaging to produce less frequent but more accurate positions (Larson et al., 2010). A weekly average is routinely applied (De Martino et al., 2014b) to data produced by the permanent Neapolitan Volcanic Continuous GPS (NeVoCGPS) network deployed on land (black circles in **Figure 1**. Here, for the MEDUSA data, we generate the weekly median time series of the cleaned kinematic solutions to which we applied an additional cleaning algorithm based on the interquartile range (IQR) statistic for outlier detection in the GPS position time series (Bock et al., 2000). An outlier is defined as having a residual with respect to the weekly median greater than 2 times the IQR. With this criterion, the algorithm removed about 5% of the kinematic data.

The weekly filtered GPS time series are shown in **Figure 7**. The uncertainties of the weekly positions (error bars) shown in **Figure 7** represent the interquartile range (IQR) of each weekly median solution.

In the considered period, the weekly time series show that the four buoys are subject to uplift and to radial horizontal movements with respect to the center of the caldera, as previously found by Iannaccone et al., 2018. **Table 2** reports the correlation between the cGPS horizontal components of the couples of the buoys CFBA, CFBB and CFBC, in the period between 1 March 2018 and 31 May 2020.

We interpret the high correlation between the horizontal components as due to the effect of the wind and marine currents acting coherently on the three buoys CFBA, CFBB and CFBC. The buoy CFSB is located at greater depth and is subject to larger horizontal fluctuations. For this reason we have not performed the correlation analysis for CFSB.

Figure 8 shows the vertical displacement observed at the RITE cGPS station located in the town of Pozzuoli, the area of maximum vertical deformation of the caldera, and at the four MEDUSA cGPS stations on the buoys.

The consistency of the vertical displacement patterns between the stations is remarkable with a maximum uplift of the seafloor of about 20 centimeters at the CFBA station in the last four years and a decay of amplitude moving from the center to the border of the caldera.

RESULTS

Recently, Iannaccone et al. (2018) demonstrated that a single Mogi model point source can explain both the onshore and seafloor deformation from cGPS data. They compared the expected vertical displacement in the marine sector to that predicted by a Mogi model computed using only horizontal and vertical, on-land, cGPS measurements in the period between April 2016 and July 2017. This period, however, was characterized by small vertical movements.

From July 2017 to May 2020, the Campi Flegrei caldera has been characterized by larger vertical motion with a constant, quasi-linear trend over time (http://www.ov.ingv.it/ov/it/bollettini/275.html). We use jointly the cGPS horizontal and vertical velocities of seafloor and onshore deformation for the modeling of the volcanic source.

The horizontal and vertical velocities, uncertainties, and noise properties were estimated from the weekly position time series of the 3 cGPS stations on the buoys (CFBA, CFBB and CFBC in **Figure 7**) and of the 21 cGPS stations deployed on land (De Martino et al., 2014b; Iannaccone et al., 2018), using the software package HECTOR (Bos et al., 2013). This software, based on the maximum likelihood estimation algorithm (MLE), estimates the linear trend in time series with temporally correlated noise. A flicker noise plus white noise model is assumed to take into account the existing noise signals in the time series and to compute more realistic uncertainties for the velocities (Mao et al., 1999; Williams 2008). An annual seasonal signal, partially caused by atmospheric loading, thermal expansion or multipath (Klos et al., 2018 and references therein), is estimated and removed.

The results of the velocity estimations are presented in **Table 3** and **Figure 9** (black arrows).

Next, we jointly inverted the horizontal and vertical deformation velocities measured at all the 24 cGPS stations (**Figure 1**) since July 2017 to investigate the caldera deformation. We used the dMODELS software package (Battaglia et al., 2013a; Battaglia et al., 2013b), which provides MATLAB functions and scripts to invert GPS data for the typical source shapes used in the volcanic environment (see eg: Gottsmann et al., 2006), such as spherical (McTigue, 1987), spheroidal (Yang et al., 1988) and sill (Fialko et al., 2001), embedded in a homogenous, isotropic, elastic half-space.

The results for different volcanic sources obtained by cGPS data inversion are listed in **Table 4**.

The statistics shows that a spherical source (McTigue, 1987) fits best the GPS deformation velocities. The sill-like source has larger values of Np (number of source parameters) and ${\chi_\nu}^2$ (chi-squared per degrees of freedom) and the spheroid has a smaller value of ${\chi_\nu}^2$ than the spherical source but also has 3 additional geometrical parameters (Battaglia et al., 2013b).

Figure 9 shows the observed and calculated horizontal and vertical cGPS velocity field for the spherical source. The position of the best fit source to the cGPS data from July 2017 to May 2020 (red cross in **Figure 9**) is very similar to source position inferred by Iannaccone et al., 2018 in the time span April 2016 to July 2017.

DISCUSSION AND CONCLUSION

After a test period and four years of operation and improvement of the quality control and analysis

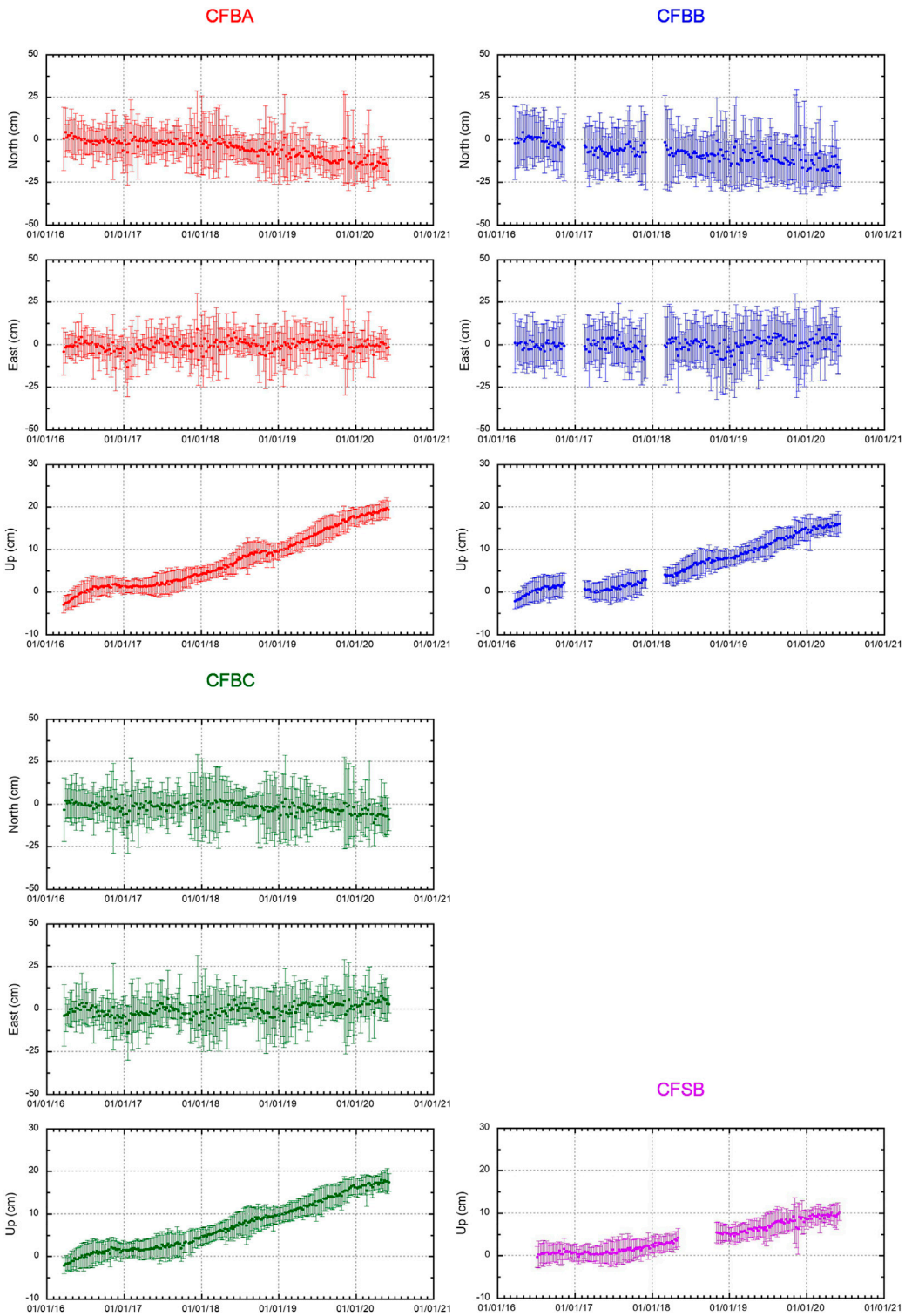

FIGURE 7 | Weekly filtered GPS time series of stations CFBA, CFBB and CFBC (three components) and CFSB (Up component only). The error bars represent the interquartile range (IQR) of each weekly median solution.

procedures, the MEDUSA infrastructure now contributes continuous geodetic data to volcanological monitoring and studies of the marine sector of the Campi Flegrei caldera. A first set of long-term, geodetic time-series from July 2017 to May 2020 highlights the coherence of the deformation pattern across the marine and land areas.

TABLE 2 | Correlation between the cGPS horizontal components of the buoys CFBA, CFBB and CFBC in the period between 1 March 2018 and 31 March 2020.

Buoys	Component	Correlation
CFBA-CFBB	North	0.87
CFBA-CFBC	North	0.81
CFBB-CFBC	North	0.86
CFBA-CFBB	East	0.87
CFBA-CFBC	East	0.86
CFBB-CFBC	East	0.77

The deformation field observed in the Campi Flegrei area is generally axi-symmetric with the maximum of vertical displacement measured at the RITE GPS station (**Figure 1**), at the center of the caldera (De Martino et al., 2014b). The vertical deformation decreases radially from the center and vanishes on the caldera's border, about 6 km away. In this work we confirm a similar pattern is obtained with the joint use of marine and land GPS data. We demonstrated that a spherical source (McTigue, 1987) is in good agreement with both the vertical and the horizontal cGPS measurements.

This simple symmetric pattern would be perturbed if there were a lateral intrusion, such as a dyke, in the marine sector in the future. In this case, MEDUSA measurements would be essential for an early detection of an eventual magma rise in the marine sector of the caldera.

Despite the high noise level of the horizontal GPS components of MEDUSA, our results showing coherence with the corresponding onshore data indicate that useful signal can be obtained. However, the methodology we used for the recovery of the horizontal deformation components can be applied only after an observed monotonic trend of at least 1-year. This limitation implies that this method is not practical for real-time application, unless it is possible to achieve a higher accuracy and further reduce noise due to marine weather effects on the horizontal data.

Given the overall length of the buoys, from 47.5 to 108 m (see **Table 1**), it would be very difficult to decrease their movement in the sea. However, noise reduction through data position correction can be performed using heading, pitch and roll measurements produced by a digital compass on the top of each buoy. The MEDUSA infrastructure inspired the University of Southern Florida to build and deploy a similar buoy (SUBGEO-Shallow Underwater Buoy for Geodesy) in Tampa bay, Florida, at a water depth of about 23 m (Xie et al., 2019). Using a digital compass installed on the buoy, Xie et al. (2019) demonstrate the possibility to recover both horizontal and vertical components of the seafloor motion at the base of the buoy with an uncertainty of 1–2 centimeters.

Application of a similar procedure is under study for the MEDUSA buoys which also are equipped with digital compass to measure pitch, roll and heading data.

We have shown that MEDUSA provides continuous GPS measurements in shallow water (less than 100 meter depth) with a comparable precision to the land GPS vertical displacement and competitive with other systems such those using seafloor pressure gauges or GPS-acoustic positioning.

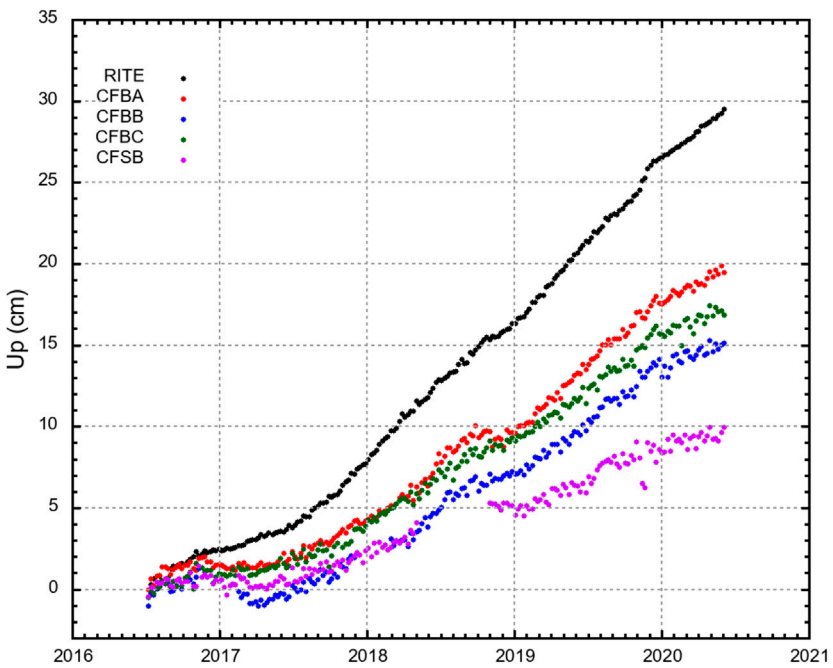

FIGURE 8 | Weekly UP time series recorded by MEDUSA cGPS stations on the buoys compared to data observed in the maximum deformation area at the RITE cGPS station.

TABLE 3 | cGPS station coordinates and component velocity and uncertainty from July 2017 to May 2020.

Station	Lat N (°)	Lon E (°)	North vel (mm/year)	North err (mm/year)	East vel (mm/year)	East err (mm/year)	Up vel (mm/year)	Up err (mm/year)
ACAE	40.820	14.141	17.1	0.2	36.9	1.5	70.0	0.8
ARFE	40.832	14.099	21.8	0.4	−34.0	1.1	40.0	0.4
ASTR	40.840	14.159	19.5	0.5	22.9	0.4	22.4	0.3
BAGN	40.804	14.174	−9.4	0.2	21.8	0.2	12.0	0.3
BAIA	40.809	14.080	−7.6	0.2	−25.2	0.6	15.2	0.6
CFBA	40.809	14.120	−51.9	2.7	−1.2	0.8	61.7	1.3
CFBB	40.803	14.132	−33.8	3.3	16.7	5.4	53.8	0.5
CFBC	40.808	14.143	−17.5	2.2	22.1	2.9	54.7	0.7
CMIS	40.778	14.089	−12.6	0.2	−9.9	0.3	7.0	0.4
CUMA	40.848	14.058	0.3	1.1	−9.3	0.5	3.5	0.4
FRUL	40.877	14.225	2.3	0.3	2.1	0.1	1.7	0.4
IPPO	40.837	14.167	14.1	0.3	21.9	0.3	15.2	0.4
ISMO	40.826	14.191	2.5	0.1	15.7	0.3	6.0	0.3
LICO	40.876	14.049	3.4	0.1	−5.3	0.3	0.5	0.5
MAFE	40.847	14.258	0.8	0.2	2.6	0.2	1.2	0.4
MORU	40.859	14.082	10.6	0.3	−11.4	0.7	6.7	0.6
NAMM	40.836	14.254	0.9	0.0	3.4	0.2	0.6	0.3
NISI	40.797	14.163	−17.7	0.2	19.8	0.2	14.5	0.3
PIS1	40.830	14.145	25.7	0.6	29.3	0.5	51.0	1.3
QUAR	40.877	14.143	11.7	0.8	1.4	0.3	4.9	0.5
RITE	40.823	14.126	24.8	0.6	3.8	0.2	90.7	1.3
SOLO	40.830	14.135	35.7	0.8	22.6	0.2	62.7	1.0
STRZ	40.835	14.111	40.0	0.9	−18.0	0.6	52.5	0.9
VICA	40.855	14.120	26.5	0.9	−4.6	0.3	17.0	0.6

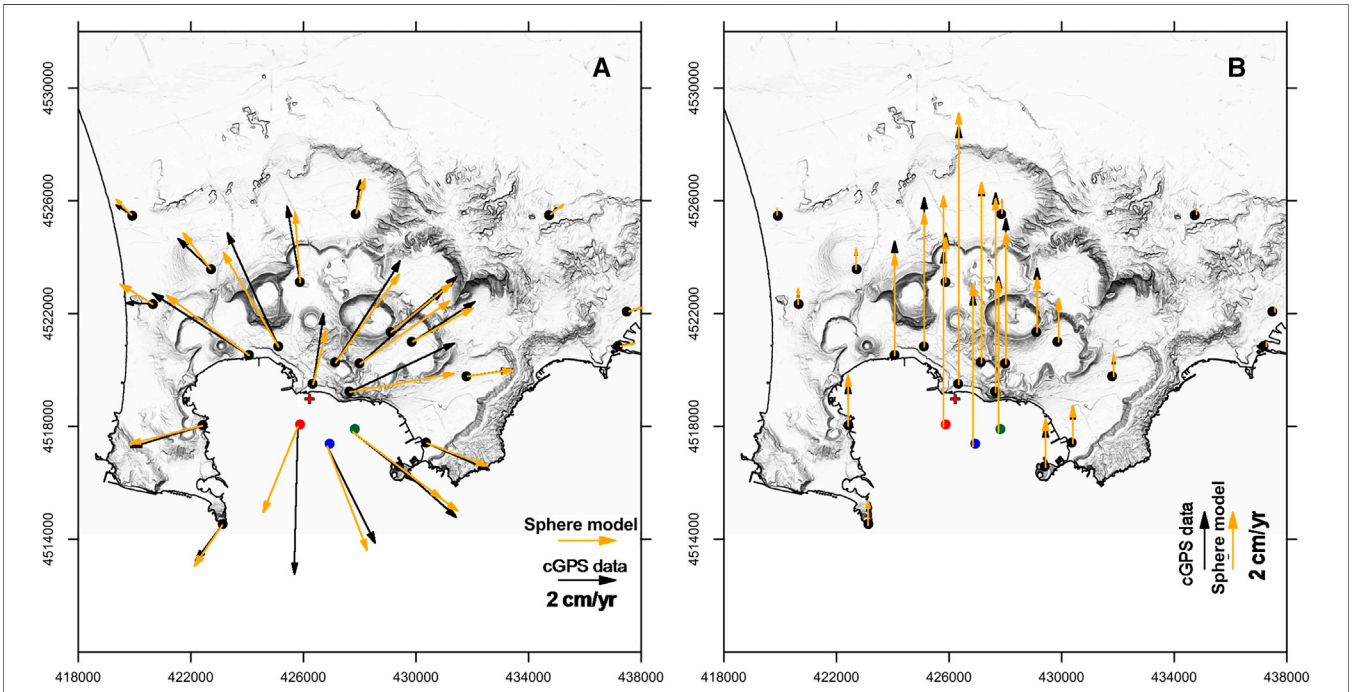

FIGURE 9 | (A) Horizontal and **(B)** vertical cGPS velocity fields at Campi Flegrei caldera from July 2017 to May 2020. Black and orange arrows indicate observed (**Table 3**) and calculated displacements assuming a spherical source (**Table 4**), respectively. The location of the source is indicated by a red cross.

The MEDUSA monitoring infrastructure is now permanently integrated into the multidisciplinary local monitoring network of Campi Flegrei and its data are routinely published within the periodical bulletins produced for the Italian Civil Protection Department and in the warning protocols in one of the highest risky area of the world.

TABLE 4 | Best fit parameters to cGPS data from Campi Flegrei caldera in **Table 3**.

Source	Statistics			Parameters			
	χ_v^2	*Np*	*v*	X (m)	Y (m)	Depth (m)	ΔV (m^3)
Sphere	12.9	4	14	426,193	4,518,980	2,630	2.93×10^6
Spheroid	9.1	7	11	426,171	4,518,825	2,617	2.96×10^6
Sill-like	38	5	13	426,125	4,518,970	4,026	3.47×10^6

DATA AVAILABILITY STATEMENT

The datasets presented in this study can be found in online repository: **http://portale.ov.ingv.it/medusa/download/four-years-of-continuous-seafloor-displacement-measurements**.

AUTHOR CONTRIBUTIONS

GI conceived the initial idea of the study, with all of the coauthors defining the methodology and strategy. SG, MD, and GD acquired cGPS data. PM provided the cGPS data processing, time series analysis (with contribution from GD, FC, and TT) and data modelling. GI, PM, and GM wrote the manuscript with input from all of the co-authors.

FUNDING

MEDUSA infrastructure was developed thanks to the financial support of the PAC01_00044-EMSO-MedIT project for the Enhancement of multidisciplinary marine research infrastructures in Southern Italy funded by MIUR (Ministry of Education, University and Research). We would like to acknowledge the support of the Contract INGV-DPC 2019-2021, Annex B2, Task 2: "Development of a real-time monitoring system for the ground deformation in the Neapolitan volcanic region using HR-GNSS measurements, and development of statistical and numerical models for the short-term vent opening probability in the Campi Flegrei caldera."

ACKNOWLEDGMENTS

We thank all the INGV-OV staff involved in the management and maintenance of the MEDUSA infrastructure and cGPS network. This work was performed under the Agreement between Istituto Nazionale di Geofisica e Vulcanologia and the Italian Presidenza del Consiglio dei Ministri, Dipartimento della Protezione Civile (DPC). This paper does not necessarily represent DPC official opinion and Policies.

REFERENCES

Battaglia, M., Cervelli, P. F., and Murray, J. R. (2013a). Modeling crustal deformation near activefaults and volcanic centers—a catalog of deformation models. *U.S. Geological Sur-vey Techniques and Methods*, 13 (B1), 75. Available at: pubs.usgs.gov/tm/tm13b1/

Battaglia, M., Cervelli, P. F., and Murray, J. R. (2013b). dMODELS: a MATLAB software package for modelling crustal deformation near active faults and volcanic centers. *J. Volcanol. Geoth. Res.* 254, 1–4. doi:10.1016/j.jvolgeores.2012.12.018

Bock, Y., Nikolaidis, R. M., de Jonge, P. J., and Bevis, M. (2000). Instantaneous geodetic positioning at medium distances with the Global Positioning System. *J. Geophys. Res.* 105 (B12), 28223–28253. doi:10.1029/2000JB900268

Bos, M. S., Fernandes, R. M. S., Williams, S. D. P., and Bastos, L. (2013). Fast error analysis of continuous GNSS observations with missing data. *J. Geod.* 87 (4), 351–360. doi:10.1007/s00190-012-0605-0

Bürgmann, R., and Chadwell, D. (2014). Sea floor geodesy. *Annu. Rev. Earth Planet Sci.* 42, 509–534. doi:10.1146/annurev-earth-060313-054953

Chierici, F., Iannaccone, G., Pignagnoli, L., Guardato, S., Locritani, M., Embriaco, D., et al. (2016). A new method to assess long-term sea-bottom vertical displacement in shallow water using a bottom pressure sensor: application to Campi Flegrei, southern Italy. *J. Geophys. Res.: Solid Earth* 121, 7775–7789. doi:10.1002/2016JB013459

De Martino, P., Guardato, S., Tammaro, U., Vassallo, M., and Iannaccone, G. (2014a). A first GPS measurement of vertical seafloor displacement in the Campi Flegrei caldera (Italy). *J. Volcanol. Geoth. Res.* 276, 145–151. doi:10.1016/j.jvolgeores.2014.03.003

De Martino, P., Tammaro, U., and Obrizzo, F. (2014b). GPS time series at Campi Flegrei caldera (2000–2013). *Ann. Geophys.* 57 (2), S0213. doi:10.4401/ag-6431

Fialko, Y., Khazan, Y., and Simons, M. (2001). Deformation due to a pressurized horizontal circular crack in an elastic half-space, with applications to volcano geodesy. *Geophys. J. Int.* 146, 181–190. doi:10.1046/j.1365-246x.2001.00452.x

Gottsmann, J., Rymer, H., and Berrino, G. (2006). Unrest at the Campi Flegrei caldera (Italy): a critical evaluation of source parameters from geodetic data inversion. *J. Volcanol. Geoth. Res.* 50, 132–145. doi:10.1016/j.jvolgeores.2005.07.002

Iannaccone, G., Guardato, S., Donnarumma, G. P., De Martino, P., Dolce, M., Macedonio, G., et al. (2018). Measurement of seafloor deformation in the marine sector of the Campi Flegrei caldera (Italy). *J. Geophys. Res. Solid Earth* 123, 66–83. doi:10.1002/2017JB014852

Iannaccone, G., Guardato, S., Vassallo, M., Elia, L., and Beranzoli, L. (2009). A new multidisciplinary marine monitoring system for the surveillance of volcanic and seismic areas. *Seismol Res. Lett.* 80 (2), 203–213. doi:10.1785/gssrl.80.2.203

Iannaccone, G., Vassallo, M., Elia, L., Guardato, S., Stabile, T. A., Satriano, C., et al. (2010). Long-term seafloor experiment with the CUMAS module: performance, noise analysis of geophysical signals, and suggestions about the design of a permanent network. *Seismol Res. Lett.* 81, 916–927. doi:10.1785/gssrl.81.6.916

Klos, A., Bos, M. S., and Bogusz, J. (2018). Detecting time-varying seasonal signal in GPS position time series with different noise levels. *GPS Solut.* 22, 21. doi:10.1007/s10291-017-0686-6

Larson, K. M., Poland, M., and Miklius, A. (2010). Volcano monitoring using gps: developing data analysis strategies based on the June 2007 Kilauea volcano intrusion and eruption. *J. Geophys. Res. Solid Earth* 115 (B7), B07406. doi:10.1029/2009JB007022

Mao, A., Harrison, C. G. A., and Dixon, T. H. (1999). Noise in GPS coordinate time series. *J. Geophys. Res.: Solid Earth* 104, 2797–2816. doi:10.1029/1998JB900033

McTigue, D. F. (1987). Elastic stress and deformation near a finite spherical magma body resolution of the point source paradox. *J. Geophys. Res.* 92 (B12), 12931–12940. doi:10.1029/jb092ib12p12931

Petersen, F., Kopp, H., Lange, D., Hannemann, K., and Urlaub, M. (2019). Measuring tectonic seafloor deformation and strain-build up with acoustic direct-path ranging. *J. Geodyn.* 124, 14–24. doi:10.1016/j.jog.2019.01.002

Williams, S. D. P. (2008). Cats: gps coordinate time series analysis software. *GPS Solut.* 12, 147–153. doi:10.1007/s10291-007-0086-4

Xie, S., Law, J., Russell, R., Dixon, T. H., Lembke, C., Malservisi, R., et al. (2019). Seafloor geodesy in shallow water with GPS on an anchored spar buoy. *J. Geophys. Res. Solid Earth* 124 (11), 12116–12140. doi:10.1029/2019JB018242

Yang, X.-M., Davis, P. M., and Dieterich, J. H. (1988). Deformation from inflation of a dippingfinite prolate spheroid in an elastic half-space as a model for volcanic stressing. *J. Geophys. Res.* 93 (B5), 4249–4257. doi:10.1029/jb093ib05p04249

Conflict of Interest: The authors declare that the research was conducted in the absence of any commercial or financial relationships that could be construed as a potential conflict of interest.

frontiers in Earth Science

ORIGINAL RESEARCH
published: 12 January 2021
doi: 10.3389/feart.2020.598270

Improving Detectability of Seafloor Deformation From Bottom Pressure Observations Using Numerical Ocean Models

Yoichiro Dobashi[1†] *and Daisuke Inazu*[2*]

[1]*Graduate School of Marine Science and Technology, Tokyo University of Marine Science and Technology, Tokyo, Japan,* [2]*Department of Marine Resources and Energy, Tokyo University of Marine Science and Technology, Tokyo, Japan*

OPEN ACCESS

Edited by:
Laura Wallace,
University of Texas at Austin,
United States

Reviewed by:
Meng Wei,
University of Rhode Island,
United States
Masanori Kameyama,
Ehime University, Japan

***Correspondence:**
Daisuke Inazu
inazud@m.kaiyodai.ac.jp

†Present Address:
Department of Port and Harbor, Pacific Consultants Co., Ltd., 3-22 Kanda-Nishikicho, Chiyoda, Tokyo 101-8462, Japan

Specialty section:
This article was submitted to Solid Earth Geophysics, a section of the journal Frontiers in Earth Science

Received: *24 August 2020*
Accepted: *17 November 2020*
Published: *12 January 2021*

Citation:
Dobashi Y and Inazu D (2021) Improving Detectability of Seafloor Deformation From Bottom Pressure Observations Using Numerical Ocean Models. Front. Earth Sci. 8:598270. doi: 10.3389/feart.2020.598270

We investigated ocean bottom pressure (OBP) observation data at six plate subduction zones around the Pacific Ocean. The six regions included the Hikurangi Trough, the Nankai Trough, the Japan Trench, the Aleutian Trench, the Cascadia Subduction Zone, and the Chile Trench. For the sake of improving the detectability of seafloor deformation using OBP observations, we used numerical ocean models to represent realistic oceanic variations, and subtracted them from the observed OBP data. The numerical ocean models included four ocean general circulation models (OGCMs) of HYCOM, GLORYS, ECCO2, and JCOPE2M, and a single-layer ocean model (SOM). The OGCMs are mainly driven by the wind forcing. The SOM is driven by wind and/or atmospheric pressure loading. The modeled OBP was subtracted from the observed OBP data, and root-mean-square (RMS) amplitudes of the residual OBP variations at a period of 3–90 days were evaluated by the respective regions and by the respective numerical ocean models. The OGCMs and SOM driven by wind alone (SOM_w) contributed to 5–27% RMS reduction in the residual OBP. When SOM driven by atmospheric pressure alone (SOM_p) was added to the modeled OBP, residual RMS amplitudes were additionally reduced by 2–15%. This indicates that the atmospheric pressure is necessary to explain substantial amounts of observed OBP variations at the period. The residual RMS amplitudes were 1.0–1.7 hPa when SOM_p was added. The RMS reduction was relatively effective as 16–42% at the Hikurangi Trough, the Nankai Trough, and the Japan Trench. The residual RMS amplitudes were relatively small as 1.0–1.1 hPa at the Nankai Trough and the Chile Trench. These results were discussed with previous studies that had identified slow slips using OBP observations. We discussed on further accurate OBP modeling, and on improving detectability of seafloor deformation using OBP observation arrays.

Keywords: ocean bottom pressure, seafloor deformation, detectability, subduction zone, numerical ocean model, atmospheric pressure loading

INTRODUCTION

A quartz-crystal resonator was developed to measure absolute pressure changes with nano resolutions (Irish and Snodgrass, 1972; Wearn and Larson, 1982; Yilmaz et al., 2004). The technique has been applied to measure the absolute pressure changes at deep-sea (~103 m) bottom (Munk and Zetler, 1967; Nowroozi et al., 1969; Filloux, 1971). The ocean bottom pressure (OBP) observations have been increasingly carried out for various applications in geophysics (Inazu and Hino, 2011; Webb and Nooner, 2016; Paros, 2017): tsunamis (Filloux et al., 1983; Rabinovich and Eblé, 2015; Kubota et al., 2019), seismic/elastic vibrations of sea bottom and of ocean water (Nosov and Kolesov, 2007; Kubota et al., 2017; Nosov et al., 2018), tides (Munk et al., 1970; Eble and Gonzalez, 1991; Mofjeld et al., 1995), offshore storm surges (Beardsley et al., 1977; Mofjeld et al., 1996; Bailey et al., 2014), ocean currents (Chereskin et al., 2009; Park et al., 2010; Nagano et al., 2018), gravity variations (Park et al., 2008; Siegismund et al., 2011; Peralta-Ferriz et al., 2016), and seafloor vertical deformation due to submarine volcanos (Fox, 1999; Chadwick et al., 2012; Sasagawa et al., 2016) and earthquakes (Baba et al., 2006; Ito et al., 2011; Kubota et al., 2018; Itoh et al., 2019).

When elastic oscillations are not considered, the OBP is regarded as static pressure, and its recording ($P_B(t)$) at a location is represented as follows (Inazu et al., 2012):

$$P_B(t) = P_{\mathrm{ref}} + \Delta P_B(t), \tag{1}$$

$$\Delta P_B(t) = \Delta P_C(t) + \Delta P_T(t) + \Delta P_O(t) + \Delta P_A(t) + \Delta P_D(t) + \varepsilon(t). \tag{2}$$

$\Delta P_B(t)$ is pressure deviations around a reference pressure level according to the sea depth (P_{ref}), and is decomposed into geophysical and non-geophysical components. $\Delta P_C(t)$ indicates the seafloor vertical crustal deformation. $\Delta P_T(t)$ indicates the tides. $\Delta P_O(t)$ indicates the oceanic variations. $\Delta P_A(t)$ indicates the atmospheric pressure loading on sea surface. $\Delta P_D(t)$ indicates the non-geophysical, instrumental drifts (Watts and Kontonyanis, 1990; Polster et al., 2009; Kajikawa and Kobata, 2019). $\varepsilon(t)$ indicates residuals. The increase of 1 hPa in OBP is equivalent to the elevation of 1 cm in sea level or the subsidence of 1 cm in seafloor below OBP observation point.

When one investigates a particular phenomenon using OBP records, other components need to be estimated and removed. When dominant frequency of the target phenomenon is far from that of other noisy components, the target phenomenon is easily isolated using a Fourier analysis. However, time scales of slow seafloor deformation are comparable to those of oceanic variations. In particular, slow earthquakes with fault slips involve time scales of days to months and/or longer scales (Hirose and Obara, 2005). Vertical seafloor displacements associated with such slow slips are expected to be less than a few centimeters (Ohta et al., 2012) while oceanic variations are up to tens of centimeters in these time scales (Niiler et al., 1993; Donohue et al., 2010). Isolating slow seafloor deformation signals from OBP records is difficult.

Possible relationships between huge earthquakes and aseismic, slow earthquakes/slips at plate boundaries have been investigated and suggested (Ruiz et al., 2014; Tanaka et al., 2019; Baba et al., 2020). Seismological and geodetic efforts have been made to conduct campaign and continuous observations including OBP at the deep-sea bottom near the plate boundaries (Hirata et al., 2002; Hino et al., 2009; Kaneda et al., 2015; Wallace et al., 2016). It is necessary to develop suitable methods of separating slow seafloor deformation and oceanic variation in OBP observations.

We may suppose that spatial scales of earthquake slips ($<10^2$ km) (Ohta et al., 2012; Sato et al., 2017) are mostly shorter than those of oceanic variations ($>10^2$ km) in time scales of days to months (Niiler et al., 1993; Donohue et al., 2010). When spatially dense OBP observations are carried out, based on this assumption, one can take approaches to cancel (unknown) oceanic variations by simply differentiating nearby OBP stations from a reference OBP station (Ito et al., 2013; Ariyoshi et al., 2014; Wallace et al., 2016; Sato et al., 2017), or by estimating spatially-common components using statistical and/or machine learning methods (Emery and Thomson, 2001; Hino et al., 2014; He et al., 2020).

On the other hand, removing oceanic and other components from single OBP record is a straightforward approach. Tidal signals have been precisely estimated by observed records or numerical predictions (Tamura et al., 1991; Egbert and Erofeeva, 2002). Lower-frequency, non-tidal oceanic variations can be estimated by numerical ocean models, but their accuracy is not typically sufficient for detection of slow slips of less than a few centimeters in OBP observations (Fredrickson et al., 2019; Gomberg et al., 2019; Muramoto et al., 2019). Nevertheless, this approach of reducing ambient oceanic noises is fundamental, and is suitably applied for both multiple-station and single-station observations.

During this decade, there have been extensive OBP observations installed for seismic/geodetic monitoring of shallow plate subduction zones around the Pacific Ocean (**Figure 1**). Seafloor deformation due to slow slip has been found at a few specific regions and events (Ohta et al., 2012; Ito et al., 2013; Davis et al., 2015; Suzuki et al., 2016; Wallace et al., 2016). However, there was no report on general evaluations of detectability of slow seafloor deformation using OBP observations. Regional dependence of the detectability is not known. Accuracy of used numerical ocean models is not known in terms of OBP variations. In the present study, we investigate the current status of improving detectability of slow seafloor deformation using OBP observations. We utilize OBP data at several subduction zones around the Pacific Ocean, and available numerical ocean prediction models. The detectability is evaluated by root-mean-square (RMS) amplitude (i.e., standard deviation) of residual OBP time series at respective stations.

OCEAN BOTTOM PRESSURE OBSERVATIONS

We use OBP data listed in **Table 1**. Most of the OBP data are available at the Ocean Bottom Seismograph Instrument Pool (OBSIP) (http://www.obsip.org/). Data obtained at the Japan Trench were provided by Tohoku University (Hino et al.,

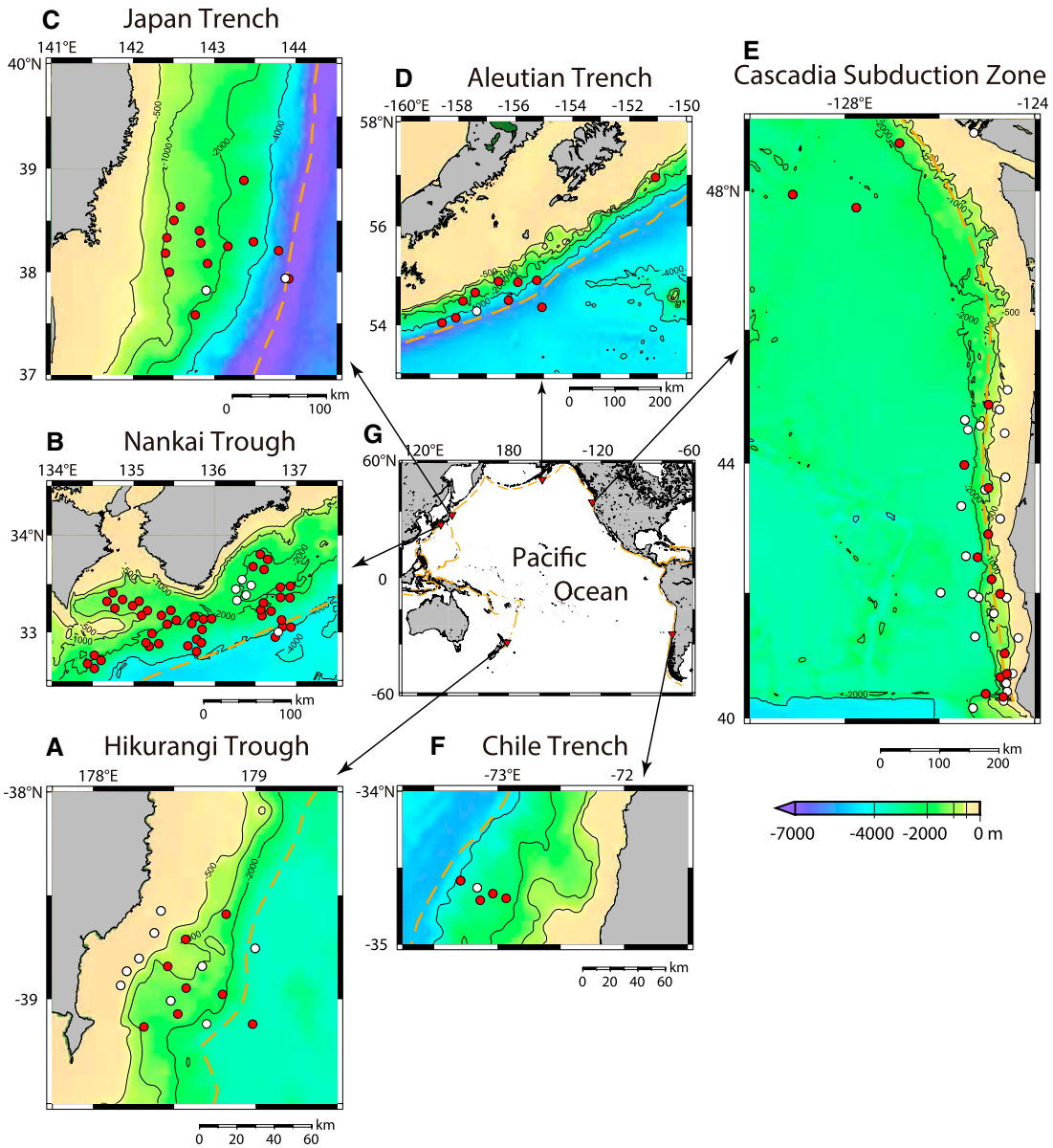

FIGURE 1 | Ocean bottom pressure observations at six subduction zones around the Pacific Ocean. The six subduction zones are **(A)** the Hikurangi Trough, **(B)** the Nankai Trough, **(C)** the Japan Trench, **(D)** the Aleutian Trench, **(E)** the Cascadia Subduction Zone, and **(F)** the Chile Trench. **(G)** shows the map of the Pacific Ocean with specific trench/trough axes (orange dashed lines) derived from Bird (2003). Red and white circles denote used and unused stations, respectively. See **Table 1** for detail. Isobaths of 500, 1,000, 2,000, and 4,000 m are shown.

2009; Hino et al., 2014). These were composed of campaign observations using pop-up-type autonomous gauges. DONET1/2 in Japan (Kaneda et al., 2015) and NEPTUNE-Canada (Barnes et al., 2015) are operated as seafloor cabled systems for long-term (>5 years) continuous observations. These observations are located at six subduction zones around the Pacific Ocean (**Figure 1**; **Table 1**). The S-net cabled observatory was installed along the Japan Trench and the Kuril Trench, and the observed data have recently become available (Aoi et al., 2020). However, the S-net OBP data are currently undergoing quality control (Kubota et al., 2020), and are not used in the present study.

Far offshore OBP observations are more sensitive to offshore fault motions than onshore Global Navigation Satellite System observations. We investigate the OBP data obtained at sea depths greater than 500 m (**Figure 1**). In addition, the utilized OBP data consist of approximately year-long continuous records, and we avoid using data with complicated drift or spike noise. *In-situ* OBP observations include various components as shown by **Eq. 2**. In the present study, oceanic variations at a period of 3–90 days

TABLE 1 | OBP observations and data.

Region	Project[a]	Observation type	Data used	Observation period	References
Hikurangi Trough	HOBITSS (OBSIP)	Pop up	8	Jul 2014–Jun 2015	Wallace et al. (2016)
Nankai Trough	DONET1/2	Cable	45	Jan 2018–Dec 2018	Kaneda et al. (2015)
Japan Trench	Tohoku Univ.	Pop up	14	May 2012–Nov 2013	Hino et al. (2014)
Aleutian Trench	AACSE (OBSIP)	Pop up	10	Jun 2018–Mar 2019	Barcheck et al. (2020)
Cascadia Subduction Zone	CI (OBSIP)	Pop up	12	Oct 2012–Jun 2013, Oct 2014–Sep 2015	Toomey et al. (2014)
	NEPTUNE Canada	Cable	3	Oct 2014–Sep 2015	Barnes et al. (2015)
Chile Trench	Chile PEPPER (OBSIP)	Pop up	4	May 2012–Mar 2013	Tréhu et al. (2020)

[a]*HOBITSS: Hikurangi Ocean Bottom Investigation of Tremor and Slow Slip, DONET: Dense Oceanfloor Network system for Earthquakes and Tsunamis, AACSE: Alaska Amphibious Community Seismic Experiment, CI: Cascadia Initiative, NEPTUNE: North-East Pacific Time-series Undersea Networked Experiments, PEPPER: Project Evaluating Prism Post-Earthquake Response.*

TABLE 2 | Numerical ocean models.

Model[a]	Institution	Horizontal resolution	Vertical layers	Coverage	External forcing	Reanalysis of external forcing	References
SOM	Tohoku Univ.	1/12°	1	Global	Wind, air pressure	JRA-55	Inazu et al. (2012)
HYCOM	NRL	1/12°	41	Global	Wind, heat/ freshwater	NAVGEM	Cummings and Smedstad (2013)
GLORYS	Mercator Ocean	1/12°	50	Global	Wind, heat/ freshwater	ERA-interim	Lellouche et al. (2018)
ECCO2	NASA/JPL	~18 km	50	Global	Wind, heat/ freshwater	NCEP	Menemenlis et al. (2008)
JCOPE2M	JAMSTEC	1/12°	46	Northwest Pacific	Wind, heat/ freshwater	NCEP	Miyazawa et al. (2017)

[a]*SOM: Single-layer Ocean Model, HYCOM: Hybrid Coordinate Ocean Model, GLORYS: GLobal Ocean ReanalYsis and Simulation, ECCO: Estimating the Circulation and Climate of the Ocean, JCOPE: Japan Coastal Ocean Predictability Experiment.*

are extracted using a band-pass filter to remove short-tide components and long-term instrumental drifts. The extracted oceanic variations are compared with numerical ocean models.

NUMERICAL OCEAN MODELS

Numerical ocean models with data assimilation have been developed to realistically predict and estimate oceanic states. Some of them have been available to end users. We use a single-layer ocean model and four multi-layer ocean models (**Table 2**). The single-layer global ocean model (SOM) was developed by one of the authors (Inazu et al., 2012; Inazu and Saito, 2016). Multi-layer models are referred to as the ocean general circulation models (OGCMs). We use three global models (HYCOM, GLORYS, and ECCO2), and one regional model around Japan (JCOPE2M). Horizontal resolutions are 1/12° for SOM, HYCOM, GLORYS, and JCOPE2M, and ~18 km for ECCO2. In terms of vertical resolution, these OGCMs contain 40–50 layers. Modeled oceans are driven by external forcing. The SOM is driven by wind and/or atmospheric pressure loading on the sea surface given by the JRA-55 reanalysis (Kobayashi et al., 2015). OGCMs are driven by wind forcing and heat/freshwater flux given by respective reanalysis datasets (**Table 2**).

Wind stress is the dominant driving force of ocean circulations with disturbances. The wind-driven ocean involves ~10^2 cm in sea level variations (i.e., ~10^2 hPa in OBP). Only the SOM takes into account the atmospheric pressure loading to drive the ocean. The sea level mostly shows an isostatic response via gravity waves to atmospheric pressure loading (i.e., 1 cm elevation in sea level to 1 hPa depression in atmospheric pressure). This is known as the inverted barometer response (Wunsch and Stammer, 1997). When the inverted barometer response is established, the seafloor hardly feels the atmospheric pressure loading. The inverted barometer response is conventionally assumed especially in deep-sea regions. Heat and freshwater effects on the sea level changes are expected to be relatively small (<1 mm in sea level) in deep-sea regions (Ponte, 2006).

OBSERVED AND MODELED OCEAN BOTTOM PRESSURE

The OBP is shown as an integrated water pressure from sea bottom to sea surface, including atmospheric pressure loading above sea surface. The calculations of OBP are described below for SOM and OGCMs.

According to Inazu et al. (2012), SOM provides sea surface height (η) at each horizontal grid. OBP at a location (P_{SOM}) is simply given by the pressure due to sea surface height anomaly (η) plus atmospheric pressure loading on sea surface (P_{atm}):

$$P_{\mathrm{SOM}}(t) = \rho_0 g\left(\eta(t) + H\right) + P_{\mathrm{atm}}(t), \tag{3}$$

where ρ_0, g, and H are constants of seawater density (1,035 kg/m^3), gravitational acceleration (9.81 m/s^2), and sea depth given at

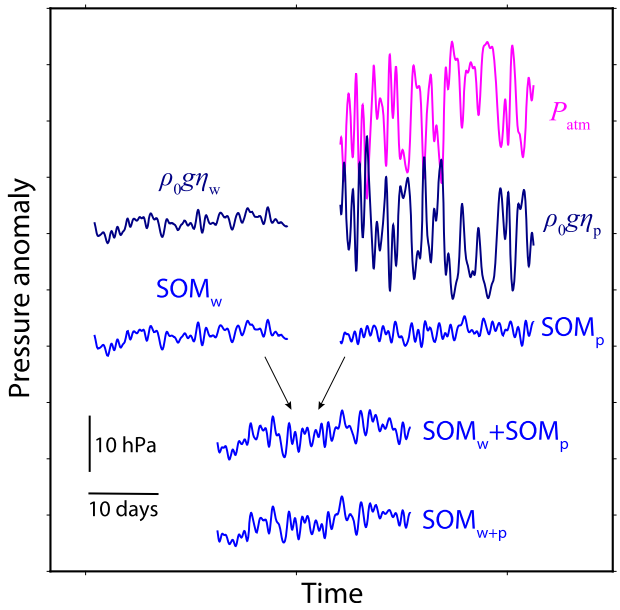

FIGURE 2 | Images of pressure variations at sea surface and sea bottom forced by wind and air pressure in SOM. $\rho_0 g\eta_w$ and $\rho_0 g\eta_p$ are sea level variations respectively forced by wind and atmospheric pressure (P_{atm}) in SOM. SOM_w, SOM_p, and SOM_{w+p} are resultant ocean bottom pressure variations forced by wind, atmospheric pressure, and both simultaneously.

each location, respectively. In the SOM, the wind and the air pressure at sea surface respectively drive the sea surface height and OBP. **Figure 2** shows a scheme of sea surface height and OBP driven by wind and air pressure. The sea surface height driven by wind alone (η_w), which is directly projected to OBP ($SOM_w = \rho_0 g\eta_w$). The sea surface height (η_p) driven by air pressure (P_{atm}) shows mostly an inverted barometer response. However, there are certain amounts of departures from the inverted barometer in OBP ($SOM_p = \rho_0 g\eta_p + P_{atm}$). Note that amplitude of SOM_p is smaller than those of $\rho_0 g\eta_p$ and P_{atm}, as indicated by **Figure 2**. The summation of OBP driven by respectively wind and air pressure ($SOM_w + SOM_p$) is almost the same as the OBP simultaneously driven by wind and pressure (SOM_{w+p}), indicating that non-linear effects are negligible. **Figure 3** shows spatial distributions of RMS amplitudes of OBP driven by wind alone (SOM_w), by air pressure alone (SOM_p), and by both simultaneously (SOM_{w+p}). SOM_{w+p} is mostly comparable to SOM_w. However, SOM_p is also evident especially at the Southern Ocean and at marginal seas (Inazu et al., 2006; Ponte and Vinogradov, 2007).

The OGCMs provide sea surface height (η) and temperature/salinity (T/S) at each vertical layer (depth: z), but currently do not include atmospheric pressure loading (i.e., P_{atm}). We calculate seawater density and pressure using these essential parameters. The EOS-80's equation of state for seawater (Fofonoff and Millard, 1983) is used to calculate the seawater density (ρ) from T, S, and hydrostatic pressure according to z. Vertical integration from sea bottom to sea surface is carried out to calculate OBP variations with a long-wave, hydrostatic approximation:

$$P_{OGCM}(t) = g\int_{-H}^{\eta(t)} \rho(t,z,T,S)\mathrm{d}z$$
$$= g\eta(t)\rho(t,0,T,S) + g\int_{-H}^{0} \rho(t,z,T,S)\mathrm{d}z. \quad (4)$$

Figure 4 shows an example of the calculation derived from HYCOM. It is evident that sea-surface height pressure (first term of **Eq. 4**) and sub-surface pressure (second term of **Eq. 4**) are inversely correlated. This compensation relationship between the sea-surface and the sub-surface pressure is typically predicted in a simplified two-layer ocean model (Gill, 1982; Unoki, 1993). The OBP is shown as an anomaly from the compensation.

As mentioned above, the calculated OBP from each ocean model is compared with observed OBP data at the period of 3–90 days. **Figure 5** shows an example at the Hikurangi Trough. Good agreement is found between the observation and SOM driven by both wind and air pressure (SOM_{w+p}), as was reported by Muramoto et al. (2019). The agreement is considerably good at periods $<10^1$ days. A multi-layer model (GLORYS) shows a worse fit to the observation. GLORYS as well as other multi-layer models are driven mainly by the wind forcing, but not by air pressure. Here, we add an OBP component driven by the air pressure alone using SOM (SOM_p) to the GLORYS's prediction. The agreement between the observed and modeled OBP is notably improved especially at periods <~10 days. This example indicates that the departure from an inverted barometer (SOM_p) is evident and should be incorporated to more accurately model the OBP at the period of 3–90 days even in the deep sea.

OBSERVED AND RESIDUAL OCEAN BOTTOM PRESSURE AT SIX SUBDUCTION ZONES

Comparisons between observed OBP and numerical ocean models are extended to the observation data around the Pacific Ocean (**Figure 1**; **Table 1**). Results at representative stations at the six subduction zones are shown in **Figures 6–11**. Overall results in the respective regions are listed in **Table 3**. Detailed statistics are found in **Supplementary Table S1**.

The SOM and three multi-layer models (HYCOM, GLORYS, ECCO2) are evaluated for all the observations at the six subduction zones (Hikurangi Trough, Nankai Trough, Japan Trench, Aleutian Trench, Cascadia Subduction Zone, and Chile Trench). In addition to these four global models, JCOPE2M which covers the northwest Pacific Ocean is also tested for the observations around Japan (Nankai Trough and Japan Trench). The OBP data are first compared to that derived from the SOM driven by wind alone (SOM_w), and those derived from the multi-layer models (HYCOM, GLORYS, ECCO2, and JCOPE2M). Subsequently, OBP derived from SOM driven by air pressure alone (SOM_p) is added to the OBP derived from SOM_w, HYCOM, GLORYS, ECCO2, and JCOPE2M, and those are subtracted from the observed OBP data. In this evaluation, we

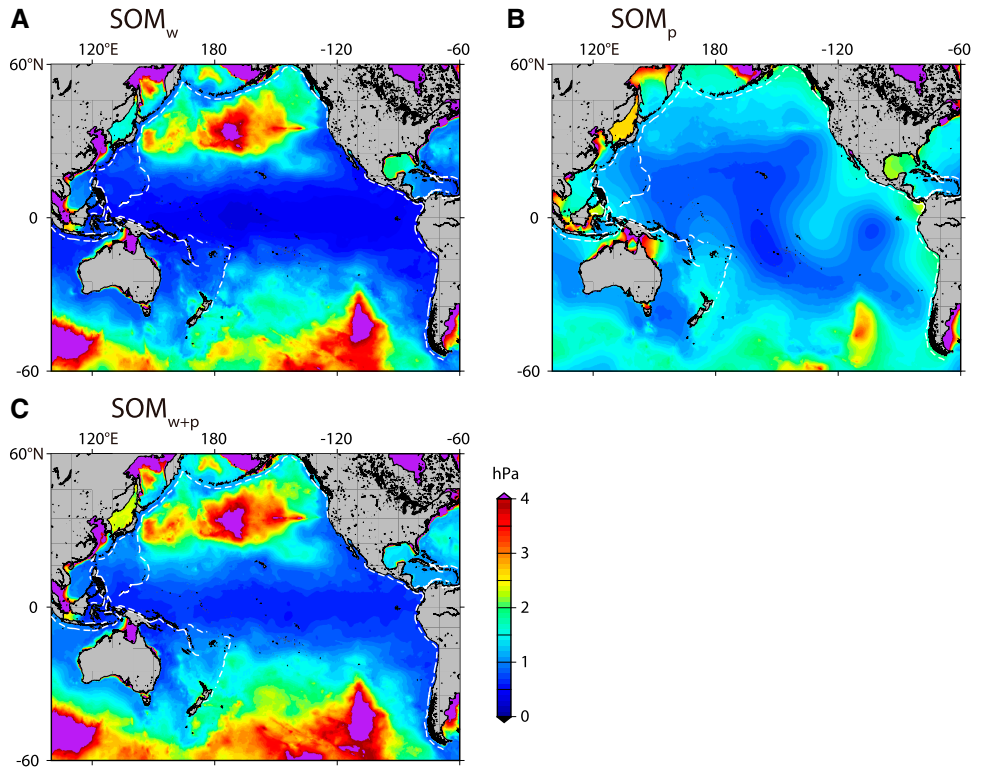

FIGURE 3 | Root-mean-square amplitudes of calculated ocean bottom pressure in SOM driven by **(A)** wind alone, **(B)** air pressure alone, and **(C)** both wind and air pressure.

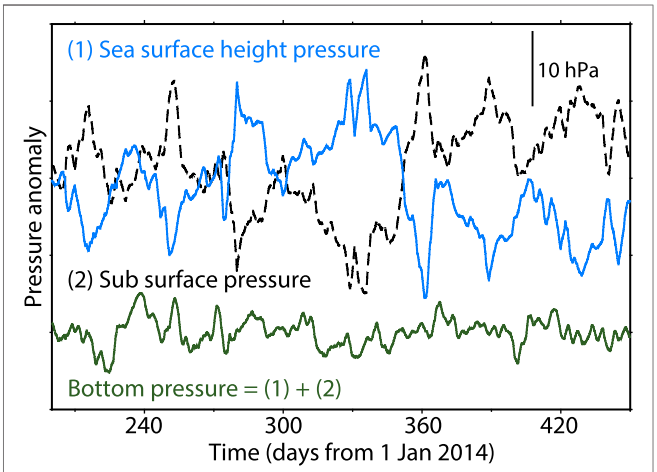

FIGURE 4 | Pressure variations derived from sea surface height (light blue), integration below static sea level (black dashed), and both combined (dark green). This is an example of LOBS4 (–39.1201°N, 178.9815°E) at the Hikurangi Trough, which is calculated from HYCOM.

use the RMS reduction rate which is defined at the period of 3–90 days by:

$$\text{RMS reduction rate} = 1 - \frac{\text{RMS}(\text{Observation} - \text{Model})}{\text{RMS}(\text{Observation})}. \quad (5)$$

Figure 6 shows the result at the Hikurangi Trough in which the HOBITSS project (Wallace et al., 2016) was carried out. Time series of eight stations from July 2014 to June 2015 were used in the present study. Mean RMS of these time series at the period of 3–90 days was 2.08 hPa. When SOM$_w$, HYCOM, GLORYS, and ECCO2 were applied, the residual RMS amplitudes were 1.51, 1.66, 1.63, and 1.59 hPa, showing 20–27% RMS reduction rates by the respective models. When SOM$_p$ was added to these models (SOM$_w$ + SOM$_p$, HYCOM + SOM$_p$, GLORYS + SOM$_p$, and ECCO2 + SOM$_p$), the residual RMS amplitudes were 1.21, 1.51, 1.30, and 1.46 hPa, indicating 27–42% reduction rates from 2.08 hPa. The contribution from SOM$_p$ was shown to be evident with 7–16% reduction rates. SOM$_w$ + SOM$_p$ provided the best RMS reduction of totally 42%, corresponding to a mean correlation coefficient of 0.82 between the observed and modeled OBP (**Table 3**).

Figure 7 shows the result at the Nankai Trough in which DONET1/2 (Kaneda et al., 2015) is operated. Time series of 45 stations from January 2018 to December 2018 were evaluated. Mean RMS of these time series was 1.19 hPa. When SOM$_w$, HYCOM, GLORYS, ECCO2, and JCOPE2M were applied, the residual RMS amplitudes were 1.13, 1.63, 1.66, 1.29, and 1.42 hPa. This indicates that SOM$_w$ provided 5% RMS reduction, but other OGCMs hardly contributed to the RMS reduction. When SOM$_p$ was added to these models (SOM$_w$ + SOM$_p$, HYCOM + SOM$_p$, GLORYS + SOM$_p$, ECCO2 + SOM$_p$, and JCOPE2M + SOM$_p$), the

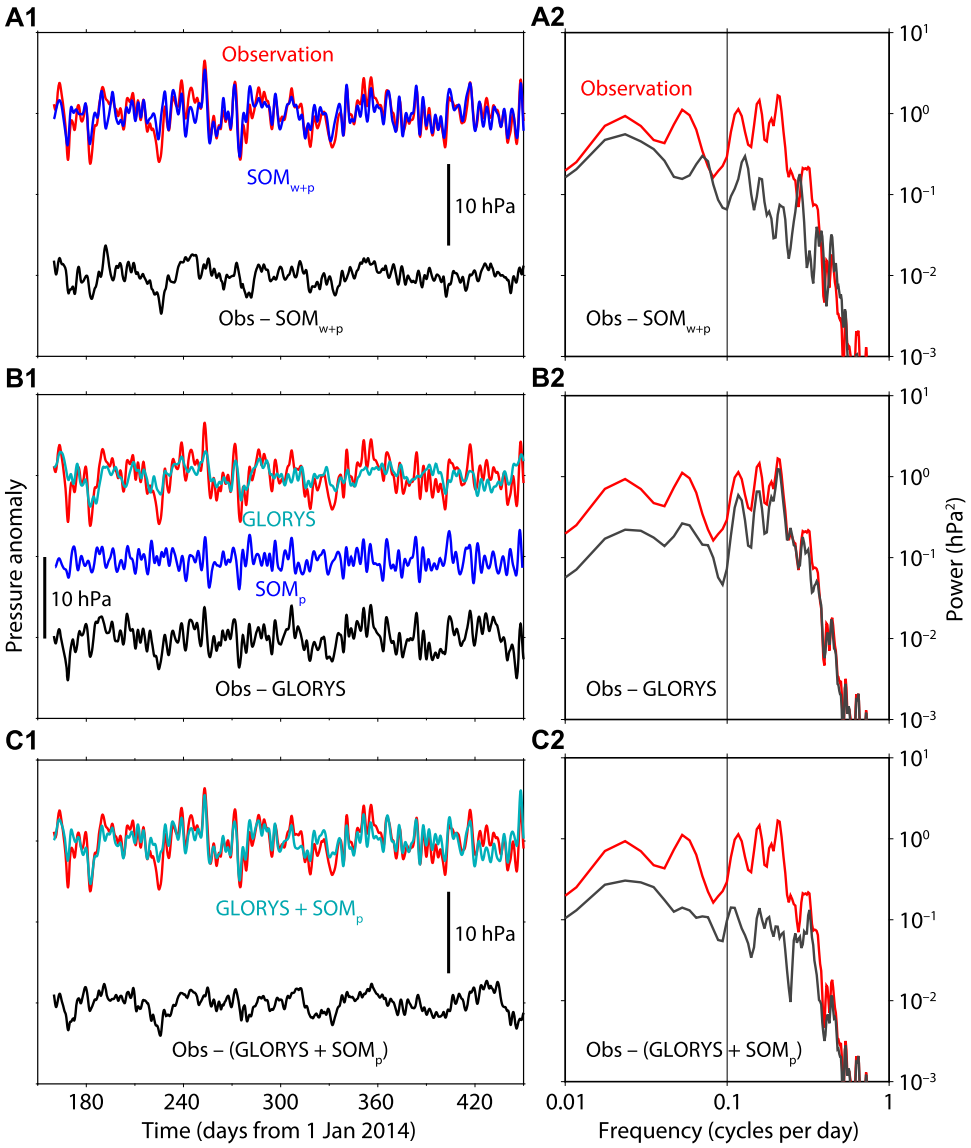

FIGURE 5 | Comparison of observed and modeled ocean bottom pressure in time **(left)** and frequency **(right)** domains. Red and black indicate observation and residual (observation minus model), respectively. Blue and cyan indicate SOM and GLORYS, respectively. This is an example of LOBS10 (–39.1333°N 178.3132°E) at the Hikurangi Trough.

residual RMS amplitudes were 0.98, 1.59, 1.66, 1.21, and 1.38 hPa. Only SOM_w + SOM_p provided the best RMS reduction of 17%, corresponding to a mean correlation coefficient of 0.58. SOM_p contributed more to the RMS reduction than SOM_w.

Figure 8 shows the result at the Japan Trench in which Tohoku University carried out campaign OBP observations (Hino et al., 2014). Time series of 14 stations from May 2012 to November 2013 were evaluated. Mean RMS of these time series was 1.60 hPa. When SOM_w, HYCOM, GLORYS, ECCO2, and JCOPE2M were applied, the residual RMS amplitudes were 1.49, 1.73, 1.57, 1.50, and 1.83 hPa. SOM_w and ECCO2 provided 6–7% RMS reduction. Other OGCMs hardly contributed to the RMS reduction. When SOM_p was added to these models (SOM_w + SOM_p, HYCOM + SOM_p, GLORYS + SOM_p, ECCO2 + SOM_p, and JCOPE2M + SOM_p), the residual RMS were 1.35, 1.70, 1.43, 1.39, and 1.71 hPa. This shows that SOM_w + SOM_p and ECCO2 + SOM_p provided RMS reduction of 13–16% (correlation coefficient of 0.54), indicating 7–9% contributions from SOM_p. Matsumoto et al. (2006) reported that atmospheric pressure loading was useful to explain OBP variations at offshore northern Japan. A comparable result was confirmed using SOM with substantial number of data.

Figure 9 shows the result at the Aleutian Trench in which the AASCE project (Barcheck et al., 2020) was carried out. Time series of 10 stations from June 2018 to March 2019 were used. Mean RMS of these time series was 2.02 hPa. When SOM_w, HYCOM, GLORYS, and ECCO2 were applied, the residual RMS amplitudes were 1.84, 1.74, 1.81, and

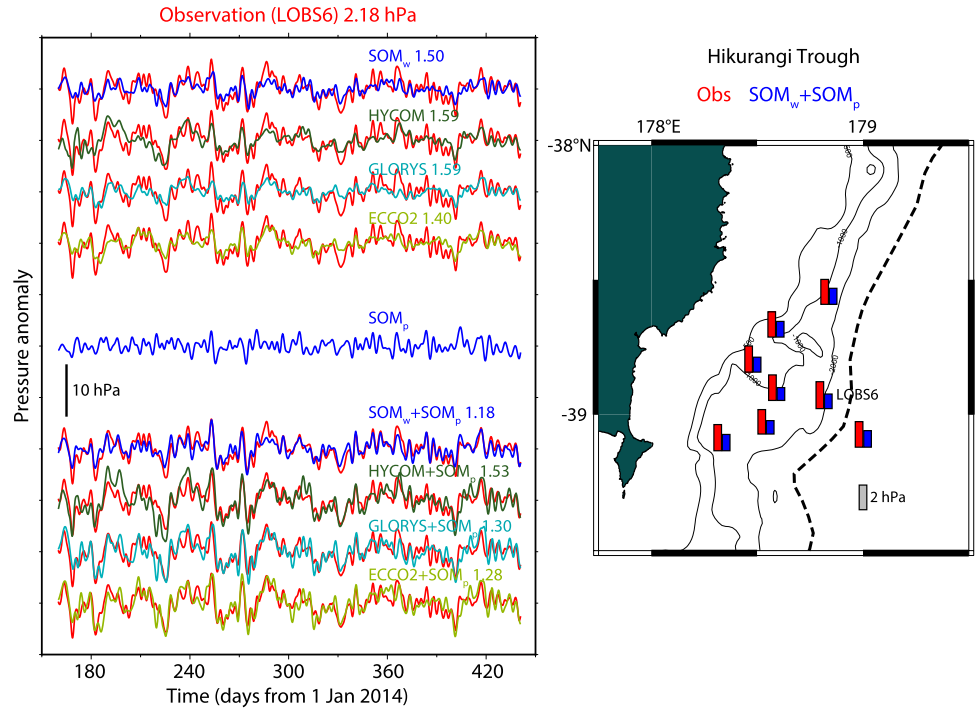

FIGURE 6 | Comparisons between observed and modeled ocean bottom pressure at LOBS6 at the Hikurangi Trough. Red indicates the observation at the period of 3–90 days. Blue, dark green, cyan, and light green indicate SOM, HYCOM, GLORYS, and ECCO2, respectively. Upper parts in left panel show comparisons to SOM forced by wind alone (SOM_w), HYCOM, GLORYS, and ECCO2. SOM forced by air pressure alone (SOM_p) (blue) is shown at the center. SOM_p respectively added to SOM_w, HYCOM, GLORYS, and ECCO2 are shown in the lower parts. Root-mean-square amplitude (in hPa) of the observed ocean bottom pressure is shown above the left panel. Root-mean-square amplitudes of residual (observed minus modeled) ocean bottom pressure are attached in the left panel for respective ocean models. Right panel shows the root-mean-square amplitudes of the observed and residual ocean bottom pressure with bar lengths. SOM_w + SOM_p is taken as the representative since this model contributed the best root-mean-square reduction between the models.

1.78 hPa, indicating 9–14% RMS reduction by the respective models. When SOM_p was added to these models (SOM_w + SOM_p, HYCOM + SOM_p, GLORYS + SOM_p, and ECCO2 + SOM_p), the residual RMS amplitudes were 1.78, 1.68, 1.76, and 1.75 hPa, indicating RMS reduction of 12–17% by the respective models. HYCOM + SOM_p provided the best RMS reduction of 17% (correlation coefficient of 0.55). SOM_p contributed to only 1–3% RMS reduction.

Figure 10 shows the result at the Cascadia Subduction Zone in which the CI project (Toomey et al., 2014) was carried out, and NEPTUNE-Canada (Barnes et al., 2015) is operated. We used time series of 15 stations from October 2012 to June 2013 and from October 2014 to September 2015. Mean RMS of these time series was 1.93 hPa. When SOM_w, HYCOM, GLORYS, and ECCO2, were applied, the residual RMS amplitudes were 1.80, 1.82, 1.72, and 1.77 hPa, indicating 6–11% RMS reduction by the respective models. When SOM_p was added, the residual RMS amplitudes were 1.82, 1.86, 1.68, and 1.80 hPa, indicating that SOM_p contributed to only less than 2% RMS reduction. GLORYS + SOM_p provided the best RMS reduction of 13% (correlation coefficient of 0.51).

Figure 11 shows the result at the Chile Trench in which the Chile PEPPER project (Tréhu et al., 2020) was carried out. Only four time series from May 2012 to March 2013 could be used. Mean RMS was 1.19 hPa. When SOM_w, HYCOM, GLORYS, and ECCO2, were applied, the residual RMS amplitudes were 1.15, 1.35, 1.19, and 1.21 hPa. This indicates <6% RMS reduction by the respective models. When SOM_p was added, the residual RMS amplitudes were 1.13, 1.38, 1.14, and 1.23 hPa. The contribution by SOM_p to the RMS reduction was small (<3%). SOM_w + SOM_p and GLORYS + SOM_p provided RMS reduction of 6–9% (correlation coefficient of 0.51).

The reduction of the residual RMS amplitudes provided by each ocean model with SOM_p is summarized in **Figure 12** and **Table 3** (see also **Supplementary Table S1**). The RMS reduction rate of the time series is regarded as a proxy of model accuracy. As shown in **Table 3**, SOM_w and/or OGCMs performed to represent observations at all the regions with RMS reduction of 5–27%. When SOM_p was added to SOM_w and OGCMs, the RMS reduction rates were up to 8–42% from the original oceanic variations at the period of 3–90 days. At the Hikurangi Trough, the Nankai Trough, and the Japan Trench, SOM_w was relatively accurate (5–27% reduction) compared to other OGCMs, and SOM_p was more effective (additional 9–15% reduction) than other regions. At the Aleutian Trench, HYCOM provided the best RMS reduction of 14%, and SOM_p contributed to additional 3% reduction, with a total reduction of 17%. Other models provided 12–13% RMS reduction. At the Cascadia Subduction Zone, GLORYS provided the best RMS reduction of 11%, and SOM_p contributed to additional 2% reduction, with a total reduction of 13%. At the Chile Trench,

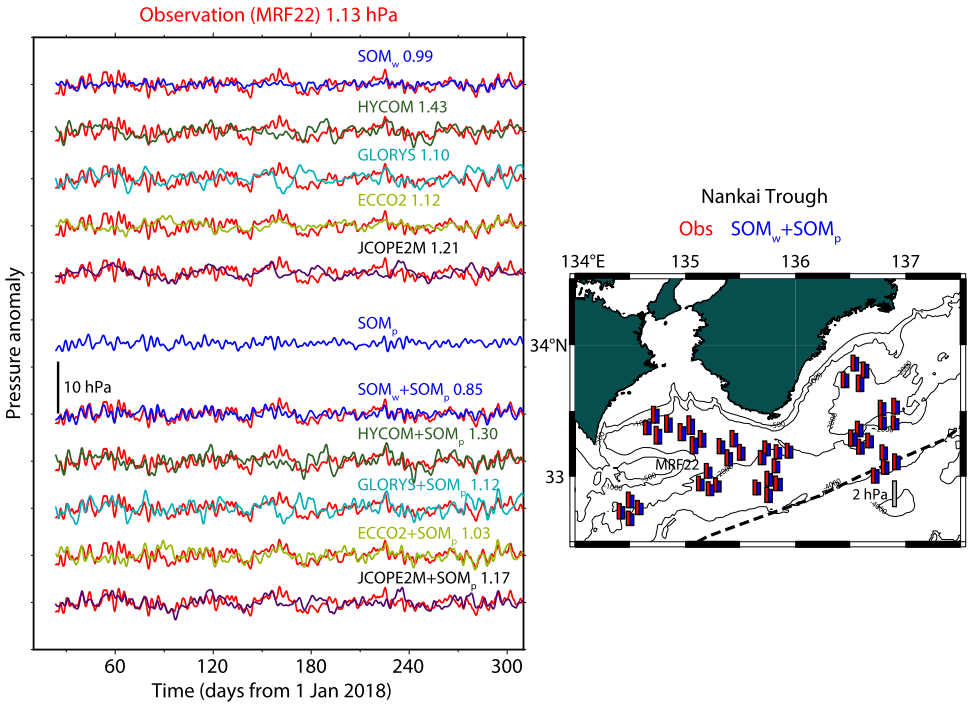

FIGURE 7 | Same as **Figure 6**, but for result at MRF22 at the Nankai Trough. Comparisons with JCOPE2M is added.

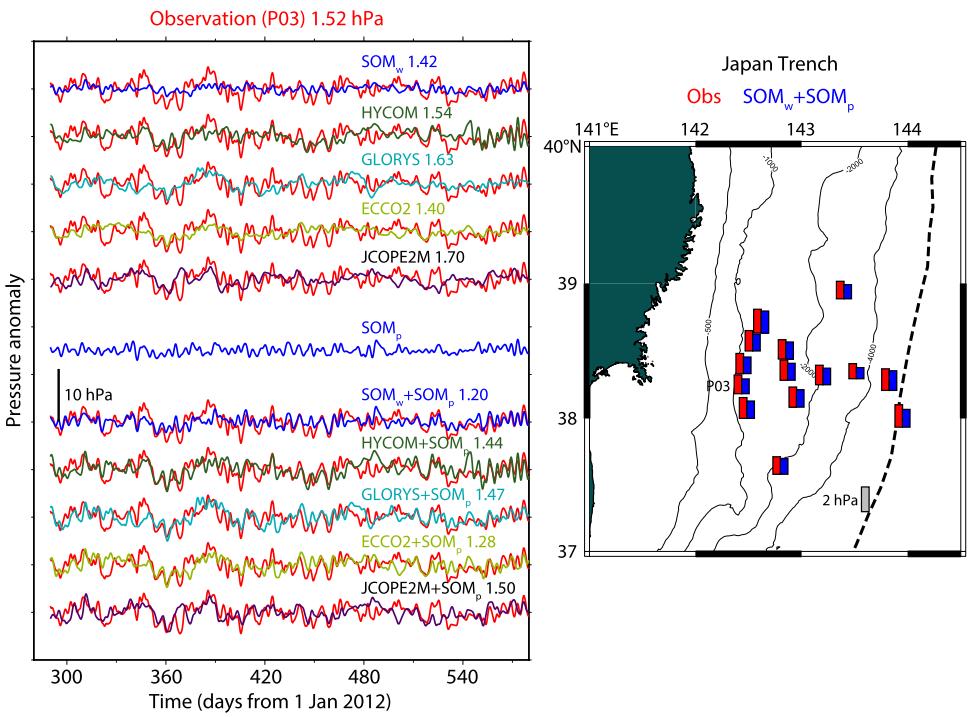

FIGURE 8 | Same as **Figure 6**, but for result at P03 at the Japan Trench. Comparisons with JCOPE2M is added.

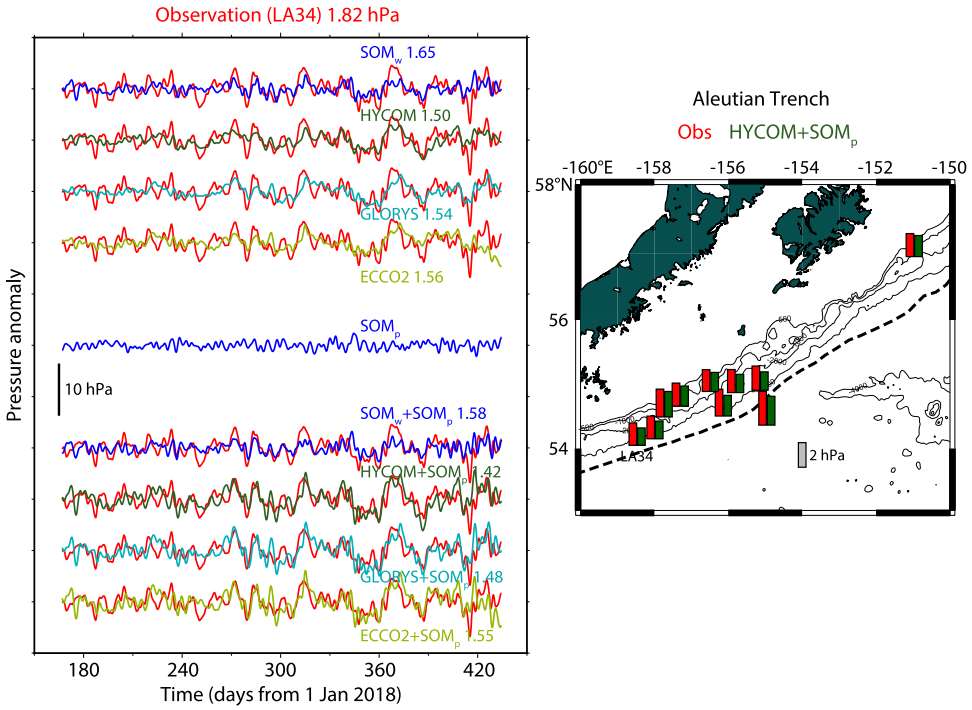

FIGURE 9 | Same as **Figure 6**, but for result at LA34 at the Aleutian Trench.

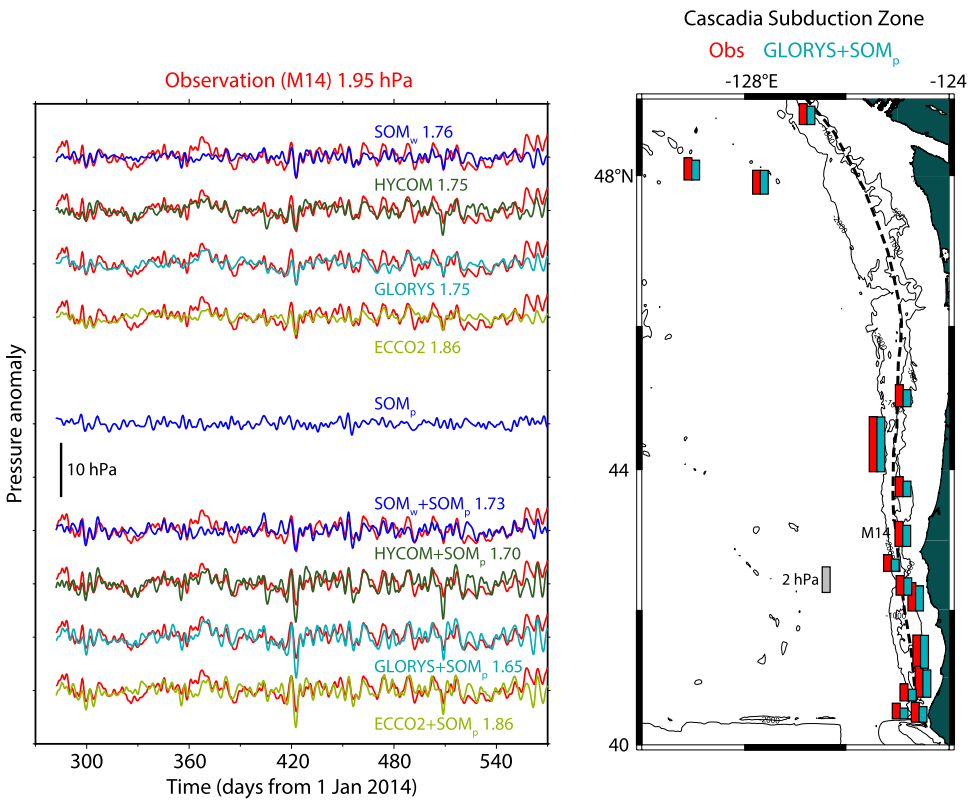

FIGURE 10 | Same as **Figure 6**, but for result at M14 at the Cascadia Subduction Zone.

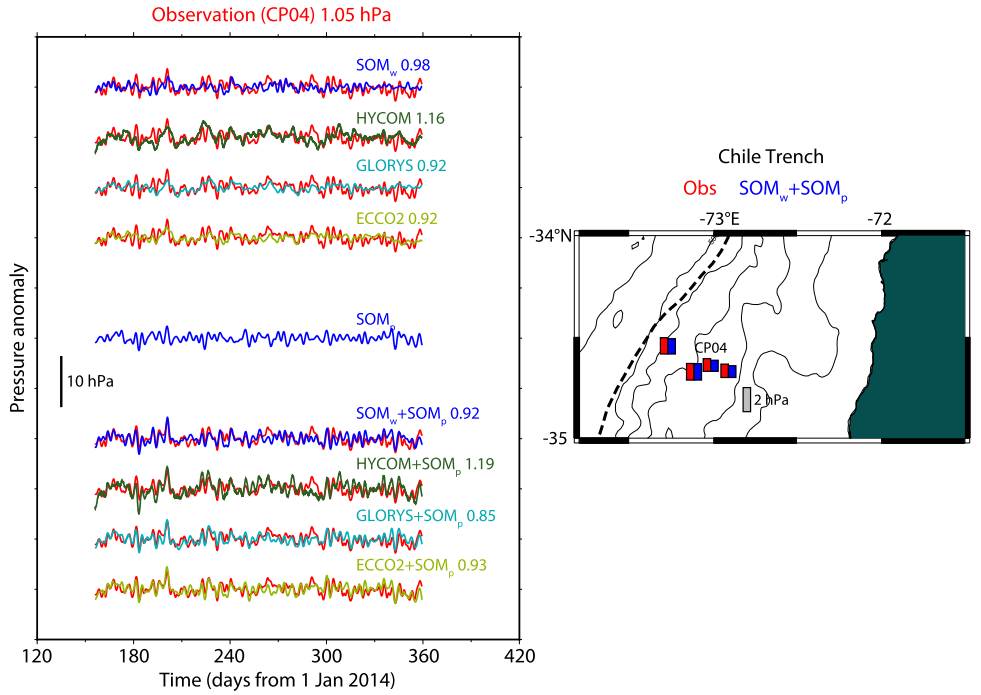

FIGURE 11 | Same as **Figure 6**, but for result at CP04 at the Chile Trench.

TABLE 3 | RMS amplitudes of observations and residual OBP with RMS reduction rate (**Eq. 5**) using respective ocean models.

Region	Observation	SOM_w ($+SOM_p$)[a]		HYCOM ($+SOM_p$)		GLORYS ($+SOM_p$)		ECCO2 ($+SOM_p$)		JCOPE2 ($+SOM_p$)	
	(hPa)	(hPa)	Rrr[b]	(hPa)	Rrr	(hPa)	Rrr	(hPa)	Rrr	(hPa)	Rrr
Hikurangi Trough	2.08	1.51 (1.21)	0.27 (0.42)	1.66 (1.51)	0.20 (0.27)	1.63 (1.30)	0.21 (0.37)	1.59 (1.46)	0.23 (0.30)		
Nankai Trough	1.19	1.13 (0.98)	0.05 (0.17)	1.63 (1.59)	–0.38 (–0.34)	1.66 (1.66)	–0.40 (–0.40)	1.29 (1.21)	–0.09 (–0.02)	1.42 (1.38)	–0.19 (–0.17)
Japan Trench	1.60	1.49 (1.35)	0.07 (0.16)	1.73 (1.70)	–0.08 (–0.06)	1.57 (1.43)	0.02 (0.11)	1.50 (1.39)	0.06 (0.13)	1.83 (1.71)	–0.14 (–0.07)
Aleutian Trench	2.02	1.84 (1.78)	0.09 (0.12)	1.74 (1.68)	0.14 (0.17)	1.81 (1.76)	0.10 (0.13)	1.78 (1.75)	0.12 (0.13)		
Cascadia Subduction Zone	1.93	1.80 (1.82)	0.07 (0.05)	1.82 (1.86)	0.06 (0.03)	1.72 (1.68)	0.11 (0.13)	1.77 (1.80)	0.08 (0.07)		
Chile Trench	1.22	1.15 (1.13)	0.06 (0.08)	1.35 (1.38)	–0.10 (–0.13)	1.19 (1.14)	0.03 (0.06)	1.21 (1.23)	0.01 (0.00)		

[a]*In each cell, values with and without brackets indicate the ocean models include SOM_p or not, respectively. These values are picked up from* ***Supplementary Table S1****.*
[b]*RMS reduction rate.*

SOM_w and GLORYS provided 3–6% RMS reduction, and SOM_p contributed to additional 2–3% reduction.

At the Hikurangi Trough, model representations were relatively good, and RMS reduction rates >20% were found by all the models (**Figure 6**). SOM was notably accurate as totally 42% RMS reduction including 15% contributions from SOM_p. In the western Pacific regions (Hikurangi Trough, Nankai Trough, and Japan Trench), SOM performed better than other OGCMs to represent OBP. SOM employed the Japanese reanalysis data (JRA-55) as external forcing to drive the ocean, while other ocean models employed US or EU data (**Table 2**). We speculate the accuracy of JRA-55 may be better than US/EU meteorological data in the western Pacific regions. In the eastern Pacific regions (Aleutian Trench, Cascadia Subduction Zone, and Chile Trench), HYCOM, GLORYS, and ECCO2 were slightly better than SOM or comparable to SOM. Differences of external forcing and/or incorporating vertical layers in OGCMs might contribute to these relative improvements.

As shown in **Table 3**; and **Figure 7**, OGCMs unexpectedly performed to increase the residual RMS amplitudes especially at the Nankai Trough. There is a strong western boundary current known as the Kuroshio current that frequently meanders in the vicinity of the Nankai Trough (Qiu and Miao, 2000; Ebuchi and Hanawa, 2003). Due to its meandering and associated mesoscale eddies, OBP also changes with several hPa changes in seasonal or longer time scales (Nagano et al., 2018). When ocean models wrongly represent Kuroshio variations, the residual RMS amplitudes possibly increase. In addition, if residual OBP time

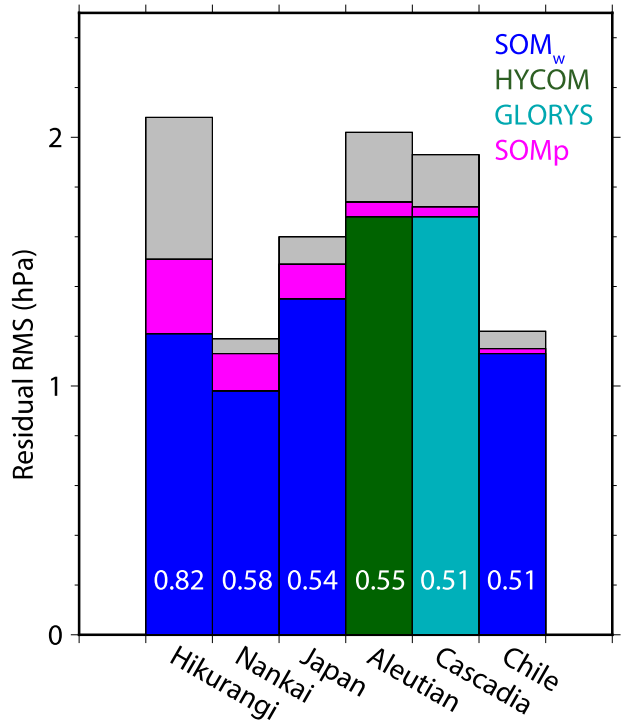

FIGURE 12 | Root-mean-square amplitudes of observed and residual ocean bottom pressure at the six subduction zones. Values are calculated as averages over the respective regions, taken from **Table 3**. White numbers are correlation coefficients corresponding to the root-mean-square reduction rates. Gray and magenta indicate model's contribution without and with SOM_p, respectively. At the Hikurangi Trough, the Nankai Trough, the Japan Trench, and the Chile Trench, $SOM_w + SOM_p$ is shown as the representative. At the Aleutian Trench, and the Cascadia Subduction Zone, HYCOM + SOM_p, and GLORYS + SOM_p are respectively the representatives.

series do not correlate well with SOM_p, the subtraction of SOM_p may also increase the residual RMS amplitude, which was found in some cases for the Nankai Trough (**Supplementary Table S1**). The SOM does not realistically capture the Kuroshio variations, but may weakly represent their features, potentially helping to reduce non-Kuroshio noises in OBP (**Figure 12**).

DETECTABILITY OF SEAFLOOR DEFORMATION AND FURTHER ROOT-MEAN-SQUARE REDUCTION

The RMS amplitude of residual OBP time series is crucial in terms of detectability of the seafloor deformation. Based on the result of **Figure 12**, the evaluations are carried out for the residual RMS amplitude derived from numerical ocean models with and without SOM_p.

At the Nankai Trough and the Chile Trench, the residual RMS was smallest. When SOM_p was added, the residual RMS amplitudes were 1.0–1.1 hPa. As shown in **Figures 7** and **11**, original RMS amplitudes were also small (1.1–1.2 hPa). The RMS reduction was 16% at the Nankai Trough, and 8% at the Chile Trench. The model accuracy was not so good at the Chile Trench, but the ambient oceanic noise was small there. At the Nankai Trough, possible slow slips were reported using the dense observatories of DONET (Suzuki et al., 2016). When one investigates slow seafloor deformation using OBP observations there, effects of the Kuroshio current should be carefully considered (Nagano et al., 2018). At the Chile Trench, there have only been a few relatively short observations (Tréhu et al., 2020). Future OBP observations at the Chile Trench may enable more detection of small fault slips compared to other regions.

At the Hikurangi Trough and the Japan Trench, the residual RMS amplitudes were both ~1.5 hPa when SOM_p was not considered. The residual RMS substantially decreased to 1.2–1.3 hPa when SOM_p was added. Original RMS amplitudes were 1.6 hPa at the Japan Trench, and 2.1 hPa at the Hikurangi Trough. The model accuracy of SOM was best at the Hikurangi Trough, although the ambient oceanic components were larger than other regions. The expected detectability is perhaps equivalent between the Hikurangi Trough and the Japan Trench. Previous studies have used OBP observations to identify specific slow slips (Ohta et al., 2012; Ito et al., 2013; Wallace et al., 2016). Recent efforts to improve sensitivities to find transient/ramp steps in OBP records have been increasingly made using ocean models, statistical methods, and/or machine learning in these regions (Hino et al., 2014; Gomberg et al., 2019; Muramoto et al., 2019; He et al., 2020).

At the Aleutian Trench and the Cascadia Subduction Zone, original RMS amplitudes were also large (1.9–2.0 hPa) compared to other regions. Contributions from SOM_p to RMS reduction were small (<0.1 hPa). The residual RMS amplitudes in both the regions were ~1.7 hPa, being still large when SOM_p was added. Detection of small seafloor deformation may be difficult in these regions compared to other regions, due to larger ambient oceanic noises and lack of model accuracy. By using a local ocean state estimation based on HYCOM boundary condition, Fredrickson et al. (2019) carried out an effort to reduce RMS of OBP observations at the Cascadia Subduction Zone partially same as those used in our study, and they also had obtained results quantitatively similar to our study.

The inverted barometer response of sea level has often been assumed to be robust for periods greater than a few days, indicating SOM_p has been often negligible. However, the results shown above suggested that SOM_p was mostly non-negligible and provided 2–15% RMS reduction in OBP in time scales of days to months (3–90 days) at the six subduction zones. Note that mean air pressure at the sea level over the global ocean has seasonal amplitudes of less than a few hPa (Ponte, 1993; Wunsch and Stammer, 1997). Seasonal changes of the total freshwater volume in the ocean may contribute to <1 hPa changes in OBP over the global ocean (Ponte et al., 2007). Sea level response to atmospheric Rossby-Haurwitz waves at a period of 5 days significantly deviates from the inverted barometer (Hirose et al., 2001; Mathers and Woodworth, 2004). Other mechanisms of departure from inverted barometer have been investigated as well (Stepanov and Hughes, 2006). The deviations from the inverted barometer (i.e., SOM_p) should be taken into account even in deep-sea regions when OBP observations are used to find small signals (<a few centimeters) of slow seafloor deformation.

We utilized a single-layer ocean model of Inazu et al. (2012) to provide SOM_p. Better representations of the oceanic variations induced by air pressure may be obtained by using OGCMs that represent realistic ocean interior. According to Ponte and Vinogradov (2007), air-pressure-induced OBP involves up to a 20% difference between stratified and non-stratified oceans. Comprehensive modeling including self-attraction and loading effects on seafloor (Stepanov and Hughes, 2004; Vinogradova et al., 2015) may help to improve representations of OBP variations. In addition to these reasonable ocean dynamics, boundary conditions of bathymetry and meteorological data should be also accurate to represent more realistic oceanic variations. Digital elevation models with global bathymetry are still going to be updated (Tozer et al., 2019). SOM employed the Japanese meteorological reanalysis data (JRA-55) which might be relatively accurate at Asia and western Pacific, compared to other regions. According to the result of **Figure 12**, substantial improvements at the Aleutian Trench, the Cascadia Subduction Zone, and the Chile Trench are expected if the accuracy of the meteorological data can be improved there.

Gomberg et al. (2019) and Fredrikson et al. (2019) respectively utilized local OGCMs with HYCOM-based boundary conditions to reduce RMS amplitudes of OBP observations for slow slip detections. The RMS reduction might be more efficient if air pressure to drive the ocean is incorporated into their ocean models. Recently, Androsov et al. (2020) showed that atmospheric pressure loading has a role to improve correlation between observed and modeled OBP of both daily and monthly time scales at the Southern Ocean. When air-pressure induced components (eg, SOM_p) become widely available in addition to wind-driven OGCMs, such ocean models will become more useful for marine geophysics applications.

In the present study, we used a band-pass filter to compare extracted oceanic signals as well as to systematically remove long-term drift in OBP data at several subduction zones. However, band-pass filtering has potential to obscure a ramp change which may correspond to a slow seafloor deformation. When one tries to isolate slow seafloor deformation, band-pass filtering is not appropriate in most cases, and long-term drift should be carefully estimated and removed using other approaches. In this paper, we have focused on accurate estimation of oceanic variations. Note that if oceanic variations are better estimated especially at long periods, this will also help to better estimate long-term drift component. Drift estimation has been conventionally done by fitting a function (typically exponential + linear) to de-tided OBP time series (Eble et al., 1989; Polster et al., 2009). However, better drift estimation is expected by fitting the function to the OBP residual after removing both tides and longer-period non-tidal oceanic variations. Improved drift estimation will contribute to better detectability of seafloor deformation.

SUMMARY

OBP observation data at six subduction zones around the Pacific Ocean were investigated to improve detectability of slow seafloor deformation signals. Numerical ocean models were used to reduce RMS of oceanic components in OBP records at a period of 3–90 days. The ocean models included HYCOM, GLORYS, ECCO2, JCOPE2M, and SOM. The RMS reduction rate using **Eq. 5** was used to measure accuracy of these models. The RMS reduction of 5–27% were provided using these models at the six regions. Departure from an inverted barometer response was calculated using SOM with atmospheric pressure loading, which was not considered in the currently available OGCMs. This component was effective with additional RMS reduction of 9–15% at the Hikurangi Trough, the Nankai Trough, and the Japan Trench. But the component was not so effective with only <3% RMS reduction in other regions (**Table 3**; **Figure 12**).

The RMS amplitudes of the residual OBP time series can be a proxy for detectability of slow seafloor deformation. The residual RMS amplitude depends on regions and accuracy of ocean models. As a result, the residual RMS amplitudes were 1.0–1.1 hPa at the Nankai Trough and the Chile Trench, 1.2–1.4 hPa at the Hikurangi Trough and the Japan Trench, and 1.7–1.8 hPa at the Aleutian Trench and the Cascadia Subduction Zone (**Table 3**; **Figure 12**). Detectability of slow seafloor deformation is expected to be better in regions with smaller residual RMS amplitudes.

These were the results for the data at specific observation periods. However, we expect that comparable features of the RMS reduction will be obtained for other data periods at the respective regions. Although there will be room to improve model accuracy, the present study evaluated the utility of currently available ocean models to reduce oceanic noise in OBP observations for detections of slow seafloor deformation in subduction zones. It is still not so easy to detect slow seafloor deformation of less than a few centimeters from single OBP station time series (Inazu et al., 2012; Muramoto et al., 2019). Further efforts will be suitably combined by differentiating time series and/or statistical method using a number of stations (Ito et al., 2013; Ariyoshi et al., 2014; Hino et al., 2014; Wallace et al., 2016).

Improving accuracy of numerical ocean models with data assimilation is essentially useful to accurately estimate and remove oceanic noises at each station. This study showed that OGCMs did not always perform better than SOM, and OBP changes induced by atmospheric pressure loading should be incorporated to enhance the representations of OBP variations at the period of 3–90 days. Improvements of accuracy of boundary conditions including external force (e.g, meteorological data) are also required as well as reasonable ocean dynamics for more precise estimation of OBP. Integrated approaches from oceanography and solid earth science are indispensable for improving future seafloor geodesy.

DATA AVAILABILITY STATEMENT

Most of the OBP observation data used were provided by the Ocean Bottom Seismograph Instrument Pool (http://www.obsip.org) which is funded by the National Science Foundation. The OBP observation data of the DONET1/2 observatory are available via the database of the National Research Institute for Earth

Science and Disaster Resilience (https://doi.org/10.17598/nied.0008). The OBP observation data of NEPTUNE Canada are available via the database of the Ocean Networks Canada (http://doi.org/10.17616/R3SK62). Ocean reanalysis datasets are available via respective data centers/servers of HYCOM (https://www.hycom.org/dataserver), GLORYS (https://resources.marine.copernicus.eu/?option=com_csw&task=results), ECCO2 (https://ecco-group.org/products.htm), and JCOPE2M (http://www.jamstec.go.jp/jcope/htdocs/e/distribution/index.html).

AUTHOR CONTRIBUTIONS

Both authors designed this research, carried out analyses, discussed the results, and wrote the paper.

FUNDING

This study was supported by JSPS KAKENHI Grant number 18K04654.

ACKNOWLEDGMENTS

We appreciate Prof. Ryota Hino, and Associate Prof. Yusaku Ohta of Tohoku University for kindly providing OBP data at the Japan Trench. Dr. Narumi Takahashi, Dr. Takeshi Nakamura, and Dr. Tatsuya Kubota of the National Research Institute for Earth Science and Disaster Resilience, Japan, kindly helped us to obtain OBP data of the DONET1/2 observatory. We thank Dr. Ruochao Zhang of the Japan Agency for Marine-Earth Science and Technology for providing comprehensive dataset of JCOPE2M. Discussion with Mr. Tomoya Muramoto of the National Institute of Advanced Industrial Science and Technology, Japan, was useful for analyzing OBP at the Hikurangi Trough. Comments from two reviewers and those from Dr. Laura Wallace, Guest Editor for the special issue, greatly improved the manuscript.

SUPPLEMENTARY MATERIAL

The Supplementary Material for this article can be found online at: https://www.frontiersin.org/articles/10.3389/feart.2020.598270/full#supplementary-material.

REFERENCES

Androsov, A., Boebel, O., Schröter, J., Danilov, S., Macrander, A., and Ivanciu, I. (2020). Ocean bottom pressure variability: Can it be reliably modeled? *J. Geophys. Res. Oceans* 125, e2019JC015469. doi:10.1029/2019JC015469

Aoi, S., Asano, Y., Kunugi, T., Kimura, T., Uehira, K., Takahashi, N., et al. (2020). MOWLAS: NIED observation network for earthquake, tsunami and volcano. *Earth Planets Space* 72, 126. doi:10.1186/s40623-020-01250-x

Ariyoshi, K., Nakata, R., Matsuzawa, T., Hino, R., Hori, T., Hasegawa, A., et al. (2014). The detectability of shallow slow earthquakes by the Dense Oceanfloor Network system for Earthquakes and Tsunamis (DONET) in Tonankai district, Japan. *Mar. Geophys. Res.* 35, 295–310. doi:10.1007/s11001-013-9192-6

Baba, S., Takeo, A., Obara, K., Matsuzawa, T., and Maeda, T. (2020). Comprehensive detection of very low frequency earthquakes off the Hokkaido and Tohoku Pacic coasts, Northeastern Japan. *J. Geophys. Res. Solid Earth.* 125, e2019JB017988. doi:10.1029/2019JB017988

Baba, T., Hirata, K., Hori, T., and Sakaguchi, H. (2006). Offshore geodetic data conducive to the estimation of the afterslip distribution following the 2003 Tokachi-oki earthquake. *Earth Planet Sci. Lett.* 241, 281–292. doi:10.1016/j.epsl.2005.10.019

Bailey, K., DiVeglio, C., and Welty, A. (2014). "An examination of the June 2013 East Coast meteotsunami captured by NOAA observing systems." in NOAA Technical Report, NOS CO-OPS 079, 42.

Barcheck, G., Abers, G. A., Adams, A. N., Bécel, A., Collins, J., Gaherty, J. B., et al. (2020). The Alaska amphibious community seismic experiment. *Seismol. Res. Lett.* 91, 3054–3063. doi:10.1785/0220200189

Barnes, C. R., Best, M. M. R., Johnson, F. R., and Pirenne, B. (2015). "NEPTUNE Canada: installation and initial operation of the world's first regional cabled ocean observatory." in *Seafloor observatories*. (Berlin, Germany: Springer Praxis Books. Springer), 415–438. doi:10.1007/978-3-642-11374-1_16

Beardsley, R. C., Mofjeld, H., Wimbush, M., Flagg, C. N., and Vermersch, J. A., Jr. (1977). Ocean tides and weather-induced bottom pressure fluctuations in the middle-Atlantic bight. *J. Geophys. Res. Oceans and Atmospheres* 82, 3175–3182. doi:10.1029/JC082i021p03175

Bird, P. (2003). An updated digital model of plate boundaries. *Geochem. Geophys. Geosyst.* 4, 1027. doi:10.1029/2001GC000252

Chadwick, W. W., Jr., Nooner, S. L., Butterfield, D. A., and Lilley, M. D. (2012). Seafloor deformation and forecasts of the April 2011 eruption at axial seamount. *Nat. Geosci.* 5, 474–477. doi:10.1038/ngeo1464

Chereskin, T. K., Donohue, K. A., Watts, D. R., Tracey, K. L., Firing, Y. L., and Cutting, A. L. (2009). Strong bottom currents and cyclogenesis in Drake Passage. *Geophys. Res. Lett.* 36, L23602. doi:10.1029/2009GL040940

Cummings, J. A., and Smedstad, O. M. (2013). "Variational data analysis for the global ocean." in *Data assimilation for atmospheric, oceanic and hydrologic applications*. (Berlin, Germany: Springer-Verlag), 303–343. doi:10.1007/978-3-642-35088-7_13

Davis, E. E., Villinger, H., and Sun, T. (2015). Slow and delayed deformation and uplift of the outermost subduction prism following ETS and seismogenic slip events beneath Nicoya Peninsula, Costa Rica. *Earth Planet Sci. Lett.* 410, 117–127. doi:10.1016/j.epsl.2014.11.015

Donohue, K. A., Watts, D. R., Tracey, K. L., Greene, A. D., and Kennelly, M. (2010). Mapping circulation in the Kuroshio Extension with an array of current and pressure recording inverted echo sounders. *J. Atmos. Ocean. Technol.* 27, 507–527. doi:10.1175/2009JTECHO686.1

Eble, M. C., Gonzalez, F. I., Mattens, D. M., and Milburn, H. B. (1989). "Instrumentation, field operations, and data processing for PMEL deep ocean bottom pressure measurements." in *NOAA technical memorandum ERL PMEL*. (Washington, DC: US Government Printing Office), 89, 71.

Eble, M. C., and Gonzalez, F. I. (1991). Deep-ocean bottom pressure measurements in the northeast Pacific. *J. Atmos. Oceanic Technol.* 8, 221–233. doi:10.1175/1520-0426(1991)008<0221:DOBPMI>2.0.CO;2

Ebuchi, N., and Hanawa, K. (2003). Influence of mesoscale eddies on variations of the Kuroshio path south of Japan. *J. Oceanogr.* 59, 25–36. doi:10.1023/A:1022856122033

Egbert, G. D., and Erofeeva, S. Y. (2002). Efficient inverse modeling of barotropic ocean tides. *J. Atmos. Oceanic Technol.* 19, 183–204. doi:10.1175/1520-0426(2002)019<0183:EIMOBO>2.0.CO;2

Emery, W. J., and Thomson, R. E. (2001). *Data analysis methods in physical oceanography*. Second and Revised Edn. Amsterdam, Netherlands: Elsevier Science, 638. doi:10.1016/B978-0-444-50756-3.X5000-X

Filloux, J. H. (1971). Deep-sea tide observations from the northeastern Pacific. *Deep-Sea Res.* 18, 275–284. doi:10.1016/0011-7471(71)90118-5

Filloux, J. H. (1983). Pressure fluctuations on the open-ocean floor off the Gulf of California: Tides, earthquakes, tsunamis. *J. Phys. Oceanogr.* 13, 783–796. doi:10.1175/1520-0485(1983)013<0783:PFOTOO>2.0.CO;2

Fofonoff, N. P., and Millard, R. C., Jr. (1983). "Algorithms for the computation of fundamental properties of seawater," *UNESCO Technical Papers in Marine Sciences; 44*. (Paris, France: UNESCO), 53.

Fox, C. G. (1999). In situ ground deformation measurements from the summit of Axial Volcano during the 1998 volcanic episode. *Geophys. Res. Lett.* 26, 3437–3440. doi:10.1029/1999GL900491

Fredrickson, E. K., Wilcock, W. S. D., Schmidt, D. A., MacCready, P., Roland, E., Kurapov, A. L., et al. (2019). Optimizing sensor configurations for the detection of slow-slip earthquakes in seafloor pressure records, using the Cascadia Subduction Zone as a case study. *J. Geophys. Res. Solid Earth* 124, 13504–13531. doi:10.1029/2019JB018053

Gill, A. E. (1982). "Adjustment under gravity of a density-stratified fluid," in *Atmosphere-ocean dynamics*. (San Diego, CA: Academic Press), 117–188. doi:10.1016/S0074-6142(08)60031-5

Gomberg, J., Hautala, S., Johnson, P., and Chiswell, S. (2019). Separating sea and slow slip signals on the seafloor. *J. Geophys. Res. Solid Earth* 124, 13486–13503. doi:10.1029/2019JB018285

He, B., Wei, M., Watts, D. R., and Shen, Y. (2020). Detecting slow slip events from seafloor pressure data using machine learning. *Geophys. Res. Lett.* 47, e2020GL087579. doi:10.1029/2020GL087579

Hino, R., Ii, S., Iinuma, T., and Fujimoto, H. (2009). Continuous long-term seafloor pressure observation for detecting slow-slip interplate events in Miyagi-Oki on the landward Japan Trench slope. *J. Disaster Res.* 4, 72–82. doi:10.20965/jdr.2009.p0072

Hino, R., Inazu, D., Ohta, Y., Ito, Y., Suzuki, S., Iinuma, T., et al. (2014). Was the 2011 Tohoku-Oki earthquake preceded by aseismic preslip? Examination of seafloor vertical deformation data near the epicenter. *Mar. Geophys. Res.* 35, 181–190. doi:10.1007/s11001-013-9208-2

Hirata, K., Aoyagi, M., Mikada, H., Kawaguchi, K., Kaiho, Y., Iwase, R., et al. (2002). Real-time geophysical measurements on the deep seafloor using submarine cable in the southern Kurile subduction zone. *IEEE J. Ocean. Eng.* 27, 170–181. doi:10.1109/joe.2002.1002471

Hirose, H., and Obara, K. (2005). Repeating short- and long-term slow slip events with deep tremor activity around the Bungo channel region, southwest Japan. *Earth Planets Space* 57, 961–972. doi:10.1186/BF03351875

Hirose, N., Fukumori, I., and Ponte, R. M. (2001). A non-isostatic global sea level response to barometric pressure near 5 days. *Geophys. Res. Lett.* 28, 2441–2444. doi:10.1029/2001GL012907

Inazu, D., Hino, R., and Fujimoto, H. (2012). A global barotropic ocean model driven by synoptic atmospheric disturbances for detecting seafloor vertical displacements from in situ ocean bottom pressure measurements. *Mar. Geophys. Res.* 33, 127–148. doi:10.1007/s11001-012-9151-7

Inazu, D., and Hino, R. (2011). Temperature correction and usefulness of ocean bottom pressure data from cabled seafloor observatories around Japan for analyses of tsunamis, ocean tides, and low-frequency geophysical phenomena. *Earth Planets Space* 63, 1133–1149. doi:10.5047/eps.2011.07.014

Inazu, D., Hirose, N., Kizu, S., and Hanawa, K. (2006). Zonally asymmetric response of the Japan Sea to synoptic pressure forcing. *J. Oceanogr.* 62, 909–916. doi:10.1007/s10872-006-0108-9

Inazu, D., and Saito, T. (2016). Global tsunami simulation using a grid rotation transformation in a latitude–longitude coordinate system. *Nat. Hazards* 80, 759–773. doi:10.1007/s11069-015-1995-0

Irish, J. D., and Snodgrass, F. E. (1972). Quartz crystals as multipurpose oceanographic sensors—I. Pressure. *Deep-Sea Res.* 19, 165–169. doi:10.1016/0011-7471(72)90049-6

Ito, Y., Hino, R., Kido, M., Fujimoto, H., Osada, Y., Inazu, D., et al. (2013). Episodic slow slip events in the Japan subduction zone before the 2011 Tohoku-Oki earthquake. *Tectonophysics* 600, 14–26. doi:10.1016/j.tecto.2012.08.022

Ito, Y., Tsuji, T., Osada, Y., Kido, M., Inazu, D., Hayashi, Y., et al. (2011). Frontal wedge deformation near the source region of the 2011 Tohoku-Oki earthquake. *Geophys. Res. Lett.* 38, L00G05. doi:10.1029/2011GL048355

Itoh, Y., Nishimura, T., Ariyoshi, K., and Matsumoto, H. (2019). Interplate slip following the 2003 Tokachi-oki earthquake from ocean bottom pressure gauge and land GNSS data. *J. Geophys. Res. Solid Earth* 124, 4205–4230. doi:10.1029/2018JB016328

Kajikawa, H., and Kobata, T. (2019). Different long-term characteristics of hydraulic pressure gauges under constant pressure applications. *Acta IMEKO* 8, 19–24. doi:10.21014/acta_imeko.v8i3.665

Kaneda, Y., Kawaguchi, K., Araki, E., Matsumoto, H., Nakamura, T., Kamiya, S., et al. (2015). "Development and application of an advanced ocean floor network system for megathrust earthquakes and tsunamis," in *Seafloor observatories*. (Berlin, Germany: Springer Praxis Books. Springer), 643–662. doi:10.1007/978-3-642-11374-1_25

Kobayashi, S., Ota, Y., Harada, Y., Ebita, A., Moriya, M., Onoda, H., et al. (2015). The JRA-55 Reanalysis: general specifications and basic characteristics. *J. Meteorol. Soc. Jpn.* 93, 5–48. doi:10.2151/jmsj.2015-001

Kubota, T., Chikasada, N. Y., Hino, R., Ohta, Y., and Otsuka, H. (2020). "Preliminary assessment of quality of the S-net long-term ocean bottom pressure observation in the northern part of the Japan Trench for detecting crustal deformation," in JpGU-AGU Joint Meeting, Virtual Meeting, SCG66.

Kubota, T., Hino, R., Inazu, D., and Suzuki, S. (2019). Fault model of the 2012 doublet earthquake, near the up-dip end of the 2011 Tohoku-Oki earthquake, based on a near-field tsunami: implications for intraplate stress state. *Prog. Earth Planet. Sci.* 6, 67. doi:10.1186/s40645-019-0313-y

Kubota, T., Saito, T., Suzuki, W., and Hino, R. (2017). Estimation of seismic centroid moment tensor using ocean bottom pressure gauges as seismometers. *Geophys. Res. Lett.* 44, 10907–10915. doi:10.1002/2017GL075386

Kubota, T., Suzuki, W., Nakamura, T., Chikasada, N. Y., Aoi, S., Takahashi, N., et al. (2018). Tsunami source inversion using time-derivative waveform of offshore pressure records to reduce effects of non-tsunami components. *Geophys. J. Int.* 215, 1200–1214. doi:10.1093/gji/ggy345

Lellouche, J.-M., Greiner, E., Le Galloudec, O., Garric, G., Regnier, C., Drevillon, M., et al. (2018). Recent updates to the Copernicus Marine Service global ocean monitoring and forecasting real-time 1/12 high-resolution system. *Ocean Sci.* 14, 1093–1126. doi:10.5194/os-14-1093-2018

Mathers, E. L., and Woodworth, P. L. (2004). A study of departures from the inverse-barometer response of sea level to air-pressure forcing at a period of 5 days. *Q. J. R. Meteorol. Soc.* 130, 725–738. doi:10.1256/qj.03.46

Matsumoto, K., Sato, T., Fujimoto, H., Tamura, Y., Nishino, M., Hino, R., et al. (2006). Ocean bottom pressure observation off Sanriku and comparison with ocean tide models, altimetry, and barotropic signals from ocean models. *Geophys. Res. Lett.* 33, L16602. doi:10.1029/2006GL026706

Menemenlis, D., Campin, J.-M., Heimbach, P., Hill, C., Lee, T., Nguyen, A., et al. (2008). ECCO2: high resolution global ocean and sea ice data synthesis. *Mercator Ocean Quarterly Newsletter* 31, 13–21.

Miyazawa, Y., Varlamov, S. M., Miyama, T., Guo, X., Hihara, T., Kiyomatsu, K., et al. (2017). Assimilation of high-resolution sea surface temperature data into an operational nowcast/forecast system around Japan using a multi-scale three-dimensional variational scheme. *Ocean Dynam.* 67, 713–728. doi:10.1007/s10236-017-1056-1

Mofjeld, H. O., González, F. I., Eble, M. C., and Newman, J. C. (1995). Ocean tides in the continental margin off the pacific northwest shelf. *J. Geophys. Res. Oceans* 100, 10789–10800. doi:10.1029/95JC00687

Mofjeld, H. O., González, F. I., and Eble, M. C. (1996). Subtidal bottom pressure observed at Axial Seamount in the northeastern continental margin of the Pacific Ocean. *J. Geophys. Res. Oceans* 101, 16381–16390. doi:10.1029/96JC01451

Munk, W. H., and Zetler, B. D. (1967). Deep-sea tides: a problem. *Science* 158, 884–886. doi:10.1126/science.158.3803.884

Munk, W., Snodgrass, F., and Wimbush, M. (1970). Tides off-shore: transition from California coastal to deep-sea waters. *Geophys. Astrophys. Fluid Dynam.* 1, 161–235. doi:10.1080/03091927009365772

Muramoto, T., Ito, Y., Inazu, D., Wallace, L. M., Hino, R., Suzuki, S., et al. (2019). Seaoor crustal deformation on ocean bottom pressure records with nontidal variability corrections: application to Hikurangi margin, New Zealand. *Geophys. Res. Lett.* 46, 303–310. doi:10.1029/2018GL080830

Nagano, A., Hasegawa, T., Matsumoto, H., and Ariyoshi, K. (2018). Bottom pressure change associated with the 2004–2005 large meander of the Kuroshio south of Japan. *Ocean Dynam.* 68, 847–865. doi:10.1007/s10236-018-1169-1

Niiler, P. P., Filloux, J., Liu, W. T., Samelson, R. M., Paduan, J. D., and Paulson, C. A. (1993). Wind-forced variability of the deep eastern North Pacific: observations of seafloor pressure and abyssal currents. *J. Geophys. Res. Oceans* 98, 22589–22602. doi:10.1029/93JC01288

Nosov, M. A., and Kolesov, S. V. (2007). Elastic oscillations of water column in the 2003 Tokachi-oki tsunami source: in-situ measurements and 3-D numerical

modelling. *Nat. Hazards Earth Syst. Sci.* 7, 243–249. doi:10.5194/nhess-7-243-2007

Nosov, M., Karpov, V., Kolesov, S., Sementsov, K., Matsumoto, H., and Kaneda, Y. (2018). Relationship between pressure variations at the ocean bottom and the acceleration of its motion during a submarine earthquake. *Earth Planets Space* 70, 100. doi:10.1186/s40623-018-0874-9

Nowroozi, A. A., Kuo, J., and Ewing, M. (1969). Solid earth and oceanic tides recorded on the ocean floor off the coast of northern California. *J. Geophys. Res. Solid Earth* 74, 605–614. doi:10.1029/JB074i002p00605

Ohta, Y., Hino, R., Inazu, D., Ohzono, M., Ito, Y., Mishina, M., et al. (2012). Geodetic constraints on afterslip characteristics following the March 9, 2011, Sanriku-Oki earthquake, Japan. *Geophys. Res. Lett.* 39, L16304. doi:10.1029/2012GL052430

Park, J.-H., Donohue, K. A., Watts, D. R., and Rainville, L. (2010). Distribution of deep near-inertial waves observed in the Kuroshio Extension. *J. Oceanogr.* 66, 709–717. doi:10.1007/s10872-010-0058-0

Park, J.-H., Watts, D. R., Donohue, K. A., and Jayne, S. R. (2008). A comparison of in situ bottom pressure array measurements with GRACE estimates in the Kuroshio Extension. *Geophys. Res. Lett.* 35, L17601. doi:10.1029/2008GL034778

Paros, J. M. (2017). *Seismic + oceanic sensors (SOS) for ocean disasters and geodesy*. Redmond, WA: Paroscientific, Inc.

Peralta-Ferriz, C., Morison, J. H., and Wallace, J. M. (2016). Proxy representation of Arctic ocean bottom pressure variability: bridging gaps in GRACE observations. *Geophys. Res. Lett.* 43, 9183–9191. doi:10.1002/2016GL070137

Polster, A., Fabian, M., and Villinger, H. (2009). Effective resolution and drift of Paroscientific pressure sensors derived from long-term seafloor measurements. *Geochem. Geophys. Geosyst.* 10, Q08008. doi:10.1029/2009GC002532

Ponte, R. M. (2006). Oceanic response to surface loading effects neglected in volume-conserving models. *J. Phys. Oceanogr.* 36, 426–434. doi:10.1175/JPO2843.1

Ponte, R. M., Quinn, K. J., Wunsch, C., and Heimbach, P. (2007). A comparison of model and GRACE estimates of the large-scale seasonal cycle in ocean bottom pressure. *Geophys. Res. Lett.* 34, L09603. doi:10.1029/2007GL029599

Ponte, R. M. (1993). Variability in a homogeneous global ocean forced by barometric pressure. *Dynam. Atmos. Oceans* 18, 209–234. doi:10.1016/0377-0265(93)90010-5

Ponte, R. M., and Vinogradov, S. V. (2007). Effects of stratification on the large-scale ocean response to barometric pressure. *J. Phys. Oceanogr.* 37, 245–258. doi:10.1175/JPO3010.1

Qiu, B., and Miao, W. (2000). Kuroshio path variations south of Japan: Bimodality as a self-sustained internal oscillation. *J. Phys. Oceanogr.* 30, 2124–2137. doi:10.1175/1520-0485(2000)030<2124:KPVSOJ>2.0.CO;2

Rabinovich, A. B., and Eblé, M. C. (2015). Deep-ocean measurements of tsunami waves. *Pure Appl. Geophys.* 172, 3281–3312. doi:10.1007/s00024-015-1058-1

Ruiz, S., Metois, M., Fuenzalida, A., Ruiz, J., Leyton, F., Grandin, R., et al. (2014). Intense foreshocks and a slow slip event preceded the 2014 Iquique Mw 8.1 earthquake. *Science* 345, 1165–1169. doi:10.1126/science.1256074

Sasagawa, G., Cook, M. J., and Zumberge, M. A. (2016). Drift-corrected seaoor pressure observations of vertical deformation at Axial Seamount 2013-2014. *Earth Space Sci.* 3, 381–385 doi:10.1002/2016EA000190

Sato, T., Hasegawa, S., Kono, A., Shiobara, H., Yagi, T., Yamada, T., et al. (2017). Detection of vertical motion during a slow-slip event off the Boso Peninsula, Japan, by ocean bottom pressure gauges. *Geophys. Res. Lett.* 44, 2710–2715. doi:10.1002/2017GL072838

Siegismund, F., Romanova, V., Köhl, A., and Stammer, D. (2011). Ocean bottom pressure variations estimated from gravity, nonsteric sea surface height and hydrodynamic model simulations. *J. Geophys. Res. Oceans* 116, C07021. doi:10.1029/2010JC006727

Stepanov, V. N., and Hughes, C. W. (2004). Parameterization of ocean self-attraction and loading in numerical models of the ocean circulation. *J. Geophys. Res. Oceans* 109, C03037. doi:10.1029/2003JC002034

Stepanov, V. N., and Hughes, C. W. (2006). Propagation of signals in basin-scale ocean bottom pressure from a barotropic model. *J. Geophys. Res. Oceans* 111, C12002. doi:10.1029/2005JC003450

Suzuki, K., Nakano, M., Takahashi, N., Hori, T., Kamiya, S., Araki, E., et al. (2016). Synchronous changes in the seismicity rate and ocean-bottom hydrostatic pressures along the Nankai trough: a possible slow slip event detected by the Dense Oceanfloor Network system for Earthquakes and Tsunamis (DONET). *Tectonophysics* 680, 90–98. doi:10.1016/j.tecto.2016.05.012

Tamura, Y., Sato, T., Ooe, M., and Ishiguro, M. (1991). A procedure for tidal analysis with a Bayesian information criterion. *Geophys. J. Int.* 104, 507–516. doi:10.1111/j.1365-246X.1991.tb05697.x

Tanaka, S., Matsuzawa, T., and Asano, Y. (2019). Shallow low-frequency tremor in the northern Japan Trench subduction zone. *Geophys. Res. Lett.* 46, 5217–5224. doi:10.1029/2019GL082817

Toomey, D. R., Allen, R. M., Barclay, A. H., Bell, S. W., Bromirski, P. D., Carlson, R. L., et al. (2014). The Cascadia Initiative: a sea change in seismological studies of subduction zones. *Oceanography* 27, 138–150. doi:10.5670/oceanog.2014.49

Tozer, B., Sandwell, D. T., Smith, W. H. F., Olson, C., Beale, J. R., and Wessel, P. (2019). Global bathymetry and topography at 15 arc sec: SRTM15+. *Earth Space Sci.* 6, 1847–1864. doi:10.1029/2019EA000658

Tréhu, A. M., de Moor, A., Madrid, J. M., Sáez, M., Chadwell, C. D., Ortega-Culaciati, F., et al. (2020). Post-seismic response of the outer accretionary prism after the 2010 Maule earthquake, Chile. *Geosphere* 16, 13–32. doi:10.1130/GES02102.1

Unoki, S. (1993). "Waves and tides in a density-stratified ocean," in *Physical oceanography in coastal seas*. (Tokyo, Japan: Tokai University Press), 329–397. [in Japanese].

Vinogradova, N. T., Ponte, R. M., Quinn, K. J., Tamisiea, M. E., Campin, J.-M., and Davis, J. L. (2015). Dynamic adjustment of the ocean circulation to self-attraction and loading effects. *J. Phys. Oceanogr.* 45, 678–689. doi:10.1175/JPO-D-14-0150.1

Wallace, L. M., Webb, S. C., Ito, Y., Mochizuki, K., Hino, R., Henrys, S., et al. (2016). Slow slip near the trench at the Hikurangi subduction zone, New Zealand. *Science* 352, 701–704. doi:10.1126/science.aaf2349

Watts, D. R., and Kontoyiannis, H. (1990). Deep-ocean bottom pressure measurement: Drift removal and performance. *J. Atmos. Oceanic Technol.* 7, 296–306. doi:10.1175/1520-0426(1990)007<0296:DOBPMD>2.0.CO;2

Wearn, R. B., Jr., and Larson, N. G. (1982). Measurements of sensitivities and drift of Digiquartz pressure sensors. *Deep-Sea Res.* 29, 111–134. doi:10.1016/0198-0149(82)90064-4

Webb, S. C., and Nooner, S. L. (2016). High-resolution seafloor absolute pressure gauge measurements using a better counting method. *J. Atmos. Ocean. Technol.* 33, 1859–1874. doi:10.1175/JTECH-D-15-0114.1

Wunsch, C., and Stammer, D. (1997). Atmospheric loading and the oceanic "inverted barometer" effect. *Rev. Geophys.* 35, 79–107. doi:10.1029/96RG03037

Yilmaz, M., Migliacio, P., and Bernard, E. (2004). "Broadband vibrating quartz pressure sensors for tsunameter and other oceanographic applications." in Proceedings of the MTS/IEEE Techno-Ocean '04, Kobe, Japan, November 2004, 3, 1381–1387. doi:10.1109/OCEANS.2004.1405783

Conflict of Interest: The authors declare that the research was conducted in the absence of any commercial or financial relationships that could be construed as a potential conflict of interest.

The handling editor declared a past co-authorship with one of the authors (DI).

frontiers in Earth Science

ORIGINAL RESEARCH
published: 12 January 2021
doi: 10.3389/feart.2020.600966

Drift Characteristics of DONET Pressure Sensors Determined From *In-Situ* and Experimental Measurements

Hiroyuki Matsumoto and Eiichiro Araki*

Research Institute for Marine Geodynamics, Japan Agency for Marine-Earth Science and Technology, Yokosuka, Japan

DONET, the dense ocean-floor network system for earthquakes and tsunamis, began operations in the Nankai Trough, SW Japan, in 2010. The present study focuses on pressure sensors that are being used as tsunami meters to measure changes in hydraulic pressure. Pressure sensors typically show a drift in their readings over their operational lifespan. DONET pressure sensors can act as geodetic sensors measuring vertical crustal deformation change over time if the sensor drift can be accurately corrected. Monitoring crustal deformation before the occurrence of megathrust earthquakes is performed by discriminating between the vertical crustal deformation and the sensor drift of the pressure sensors. Therefore, in this study, we evaluated the sensor drift shown by the DONET pressure sensors since their deployment into the deep-sea, by removing the tidal component and confirming the occurrence of sensor drift. We evaluated the initial behavior of pressure sensors before deep-sea deployment using our own high-accuracy pressure standard. Our experiment involved 20-MPa pressurization for the pressure sensors under an ambient temperature of 2°C for a duration of 1 month. Some sensor drifts in our experiment correspond in rate and direction to those from the *in-situ* measurements determined to be in the initial stage. Our experiment suggests that the pre-deployment pressurization of pressure sensors can be an effective procedure to determine the sensor drift after sensor deployment into the deep-sea.

Keywords: DONET, pressure sensor, sensor drift, *in-situ* measurement, experiment, pressure standard

OPEN ACCESS

Edited by:
Laura Wallace,
University of Texas at Austin,
United States

Reviewed by:
Katherine Woods,
Victoria University of Wellington,
New Zealand
Glenn Sasagawa,
University of California, San Diego,
United States

****Correspondence:***
Hiroyuki Matsumoto
hmatsumoto@jamstec.go.jp

Specialty section:
This article was submitted to Solid Earth Geophysics, a section of the journal Frontiers in Earth Science

Received: *31 August 2020*
Accepted: *16 November 2020*
Published: *12 January 2021*

Citation:
Matsumoto H and Araki E (2021) Drift Characteristics of DONET Pressure Sensors Determined From In-Situ *and Experimental Measurements. Front. Earth Sci. 8:600966. doi: 10.3389/feart.2020.600966*

1 INTRODUCTION

The Japan Agency for Marine-Earth Science and Technology (JAMSTEC) began developing a new dense seafloor observation network linked by submarine cables in 2006, located off the Kii Peninsula, SW Japan, where the last megathrust earthquake, that is, the Tonankai earthquake, occurred in 1944 (Kaneda et al., 2015; Kawaguchi et al., 2015). This observation network is named the "Dense Ocean-floor Network System for Earthquakes and Tsunamis" (DONET). It was first launched in 2011 with 20 observation stations, each with a three-component broadband seismometer, a three-component accelerometer, a tsunami meter, and other geophysical sensors. The same observation network was deployed in the western region of the first DONET where the last Nankai earthquake occurred in 1946. The first and second DONETs are referred to as DONET1 and DONET2, respectively. These stations cover the anticipated Tonankai and Nankai earthquake source regions and aim to monitor both long-term seismic activity and the geophysical characteristics of megathrust earthquakes and

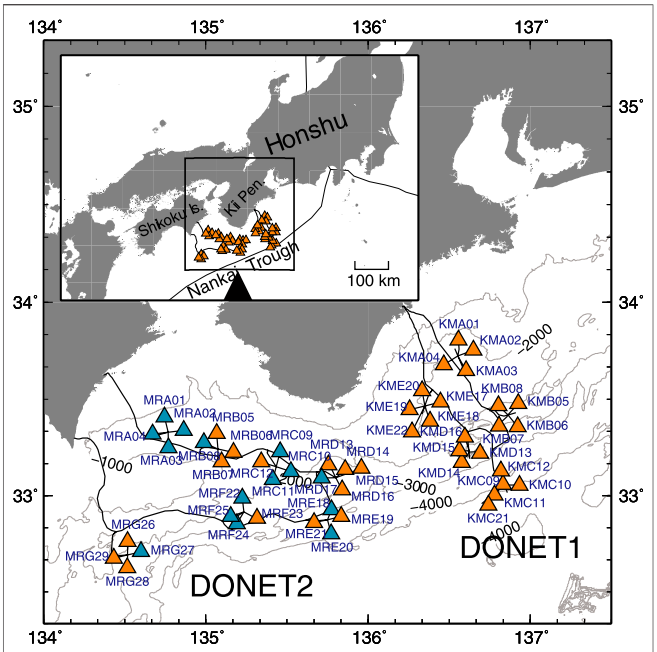

FIGURE 1 | Observatories and submarine cable layout of DONET denoted by triangles and solid lines, respectively. The blue triangles represent the specific stations in which pressure sensors were installed after the present experiments.

tsunamis. The data from DONET are intended to be used for high-precision earthquake prediction modeling, to detect precursory movements before a megathrust earthquake, and contribute to mitigating disasters caused by earthquakes and tsunamis by providing critical alert information (Takahashi et al., 2017).

The DONET1 observatories were installed and became operational between 2010 and 2011, while the DONET2 observatories were installed and became operational between 2014 and 2016. The DONET observatory operation was transferred to the National Research Institute for Earth Science and Disaster Resilience (NIED) following its installation. The 51 observatories are now fully operational, and real-time measurements are being sent to the landing stations. **Figure 1** shows the locations of the DONET observatories. The observatories were deployed in an area approaching the Nankai Trough at water depths between 1,300 and 4,500 m. A backbone cable approximately 300 km long connects five science nodes for DONET1, a 400 km backbone cable connects seven science nodes for DONET2, and an extension cable connects each science node to four or five observatories. In combination, these are capable of real-time transmission of collected data from the seafloor to the landing station. DONET has an advantage over other systems in that the dense observatory network can be operated in the same way as inland networks.

The present study focuses on pressure sensors that are employed as tsunami meters to detect hydraulic pressure changes. Pressure sensors specify their standard performance in terms of both hysteresis and repeatability; however, no details of the sensors' long-term stability have yet been explicitly defined. It was long assumed that drift in a pressure sensor's readings cannot be avoided during long-term measurements. This sensor drift has been studied through *in-situ* measurements since the 1980s (Chiswell and Lukas, 1989; Watts and Kontoyiannis, 1990; Eble and González, 1991; Fujimoto et al., 2003; Polster et al., 2009), although corresponding laboratory experiments have been scarce (Wearn and Larson, 1982; Kobata, 2005; Kajikawa and Kobata, 2019). For example, Watts and Kontoyiannis (1990) used *in-situ* measurements to compare the sensor drift between bellows-type and Bourdon-type pressure sensors and used the data to identify an exponential decay over time. Polster et al. (2009) evaluated sensor drift variations from the *in-situ* pressure data derived from the Deep Ocean Assessment and Reporting of Tsunamis (DART), Leibniz Institute of Marine Sciences (IFM-GEOMAR), Logatchev Long-term Environmental Monitoring (LOLEM), and Circulation Obviation Retrofit Kits (CORK) stations, using datasets spanning between 2 months and 9 years. Their results suggest that sensor drift increases with increasing deployment depth. In contrast to these *in-situ* studies, researchers have encountered difficulties in accurately controlling continuous pressure loading in laboratory experiments. Wearn and Larson (1982) conducted an experiment in which 0.6 MPa of continuous pressure was applied to pressure sensors for a duration of approximately 160 days with one release lasting 1.5 days in the middle of the experimental period. Their results indicated that even if pressure was released once and then applied again, the sensor drift continued to follow the predicted drift curve. Through the works described here, it can be seen that sensor drift has been closely examined since the first use of pressure data in geophysical research. Sensor drift is not considered a major issue for tsunami detection because tsunamis are a short-term phenomenon. However, fully understanding the rate and extent of sensor drift is critical when pressure sensors are used as geodetic instruments. One of the objectives of DONET is to detect crustal deformation before the occurrence of megathrust earthquakes (Ariyoshi et al., 2014). Hence, we should aim to understand the characteristics of sensor drift in this situation before we can quantitatively estimate crustal deformation using these pressure sensors.

In the present study, we examined the data from DONET pressure sensors for a period when JAMSTEC was responsible for the DONET dataset (i.e., before the end of March 2016), and carried out a specialized laboratory experiment to answer the following questions: 1) Can we predict the initial behavior of a pressure sensor in the deep-sea before its deployment? 2) Can the sensor drift be mitigated by pressure loading preconditioning before its deployment? An associated study was published in which the sensor drift was estimated by differentiation between the initial and the last obtained data within the experimental period (Matsumoto et al., 2018), suggesting that the sensor drift rate from the experiment was overestimated. Therefore, we process the experimental data by extrapolating the drift model to estimate the long-term drift rate of the DONET pressure sensors. We analyze the DONET data of the pressure sensors

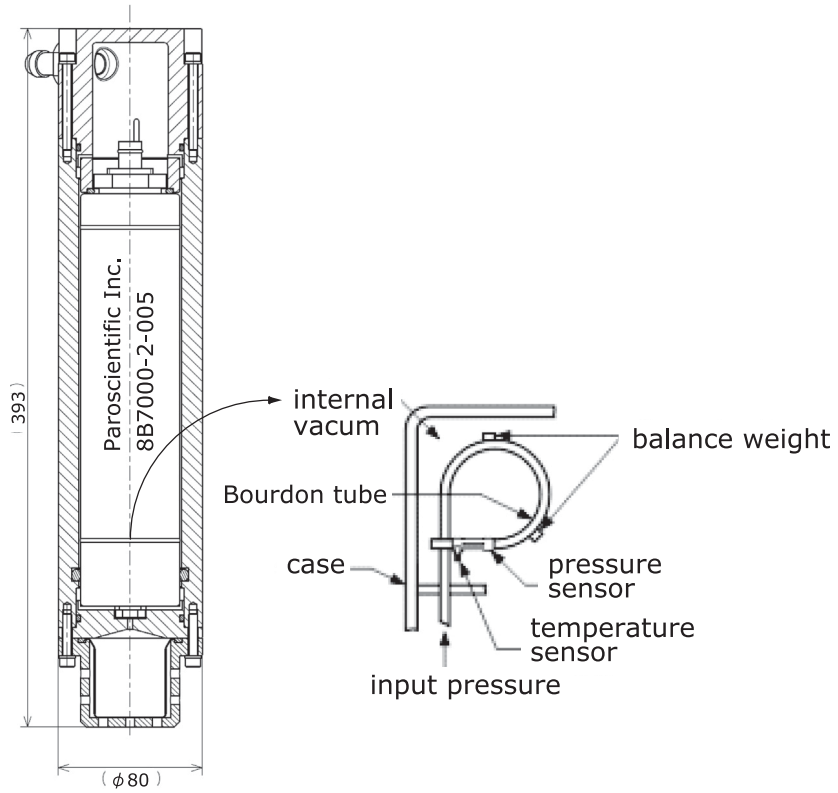

FIGURE 2 | Schematics of the oil filled pressure sensor **(left)** designed for DONET and internal mechanism **(right)**, courtesy of Paroscientific, Inc.

after deployment and compare them with the experimental results obtained from sensors pressurized prior to deployment into the deep-sea.

2 *IN-SITU* MEASUREMENT

2.1 DONET Pressure Sensors

Absolute quartz oscillation pressure sensors (Paroscientific Inc., Digiquartz® Depth Sensor, model: 8B7000-2-005, pressure range: 0–68.95 MPa) are used as tsunami meters in DONET. Generally, pressure sensor mechanisms employ either bellows or Bourdon tubes as high pressure-to-load generators. In DONET, the pressure sensors are of the Bourdon tube-type. Two sets of frequency output signals are sent from each pressure sensor. The pressure applied to the Bourdon tube generates an uncoiling force, which applies tension to the quartz crystal to increase its resonant frequency. A temperature-sensitive crystal was used for thermal correction (**Figure 2**). Thus, the pressure sensor measures quartz oscillations that are representative of both pressure and temperature. It has been reported that pressure sensors with a Bourdon tube have a smaller mechanical drift than those with a bellows tube (Watts and Kontoyiannis, 1990). In general, sensor drift is a very slow phenomenon driven by the release of internal stress, which may be attributed to the assembly of the sensor or the aging of mechanical or electronic components (Polster et al., 2009; Paros and Kobayashi, 2016).

The first DONET observatory was deployed at the KMA03 location in the center of the Kumano Trough in March 2010, followed by the other observatories (**Figure 1**). The construction of DONET observatories requires a two-step operation by a remotely-operated vehicle (ROV); step 1 is to install a sensor unit and step 2 is to connect it with a science node located approximately 10 km away. This two-step operation creates a time gap between the installation and boot-up of a pressure sensor. Additionally, an initial quality control operation was sometimes required for some observatories. Therefore, it should be noted that data availability does not always correspond to the deployment date of a pressure sensor.

The final output of the DONET is 10 Hz pressure data derived from the processing of two sets of pressure and temperature frequencies. As these pressure sensors are intended to provide information about vertical crustal deformation, the tidal component, which makes up the majority of the observed pressure change, must be removed to detect such small-scale geodetic phenomena and sensor drift. For this reason, we examine the acquired data to produce de-tided pressure data using tide coefficient analysis in terms of harmonics. In this way, the recorded data can be used to evaluate long-term sensor drift in DONET pressure sensors.

2.2 Data Analysis

Short-term pressure data were used as a trial for our data processing procedure before full-scale analysis. After validation

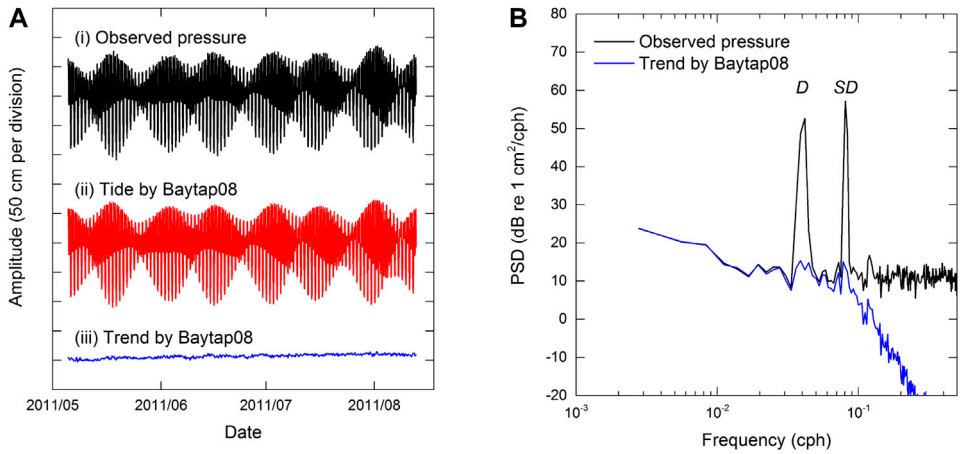

FIGURE 3 | (A) Example of pressure waveforms recorded at KMA01: i) original observed waveform, ii) tide component analyzed by Baytap08, and iii) trend component. **(B)** Spectrum of the observed pressure and trend component analyzed by Baytap08. D and SD represent the diurnal and semi-diurnal tide components, respectively.

of our data processing, the technique can be applied to all other observatories in the network. For the harmonic analysis in this study, the Baytap08 program based on the Baytap-G program (Tamura et al., 1991) was applied to the acquired pressure data and the results were divided into periodic tide and trend components; the latter reflects the sensor drift. Before applying Baytap08 to the data for the entire period, we processed the pressure data obtained at KMA01 for a duration of 100 days, spanning from May 5 to August 12, 2010, using the following procedure:

(1) Pressure data are converted to water depth using the hydrostatic formulation recommended by UNESCO (UNESCO, 1983).
(2) The water depth measured by the conductivity-temperature-depth (CTD) sensor installed on the ROV used during the observatory construction was subtracted.
(3) The original pressure data are resampled from 10 Hz to 1-hourly data so that Baytap08 can be applied.

The processed observational data, as well as the periodic tide and aperiodic components derived by Baytap08, are shown in **Figure 3A**, in which each tick on the vertical axis represents 50 cm water depth, equivalent to 50 hPa in pressure change. It is clear that the measurements from the *in-situ* pressure sensors are dominated by the periodic tide; however, other aperiodic pressure changes are identifiable, as shown in the trend plot in **Figure 3A**. These aperiodic pressure changes include sensor drift, sensor noise, local environmental pressure, and vertical deformation of the seafloor; these vary in amplitude up to ±3.2 cm standard deviation (SD) over the approximately 100-days analytical period.

To validate the tide removal analyzed by Baytap08, we compared the observed data with the trend component solved by Baytap08 in the frequency domain. The observed pressure (water depth) change and trend components from Baytap08 are compared in **Figure 3B** in terms of frequency. In this figure, the four major tidal signals with relatively large amplitudes represent the semi-diurnal tide components, M_2 and S_2, and the diurnal tide components, O_1 and K_1, respectively. The trend component from Baytap08 shows that these major tidal components are significantly reduced compared to the observed pressure. In the high-frequency domain ($> 10^{-1}$ h^{-1}), a considerable gap exists between the pressure from the observations and the trend produced by Baytap08. This is because fluctuations of a frequency higher than that of the semi-diurnal tide are analyzed as irregular components in Baytap08, which is separated from the observation. The amplitudes between the observed and the processed waveforms are coincident in the lower frequency range, smaller than that of the diurnal tide, because the contribution of non-tidal components, including surface currents such as the *Kuroshio* current, remain in the trend component (Nagano et al., 2018). Additionally, barometric and seasonal signals may contribute to water pressure changes in this low-frequency band. According to **Figure 3B**, the trend from Baytap08 still shows small peaks at frequencies corresponding to the diurnal and semi-diurnal tide components. However, as the observations closely correspond to the trend from Baytap08 in the low-frequency band, we consider this as confirmation of successful data processing to extract non-tidal components from the observations with respect to very low-frequency phenomena such as crustal deformation or sensor drift.

2.3 DONET Pressure Sensor Drift

Here, we examine the pressure sensor drift occurring at the DONET observatories, assuming that the non-tidal component determined by the above-described process corresponds to sensor drift. The tidal component of the *in-situ* pressure measurements was removed by the analysis of Baytap08. **Figure 4** represents the de-tided pressures of the DONET1 observation by order of the science node (i.e., KMA thorough KME) for the entire period up to April 2016. The DONET1 observatories were deployed in 2010

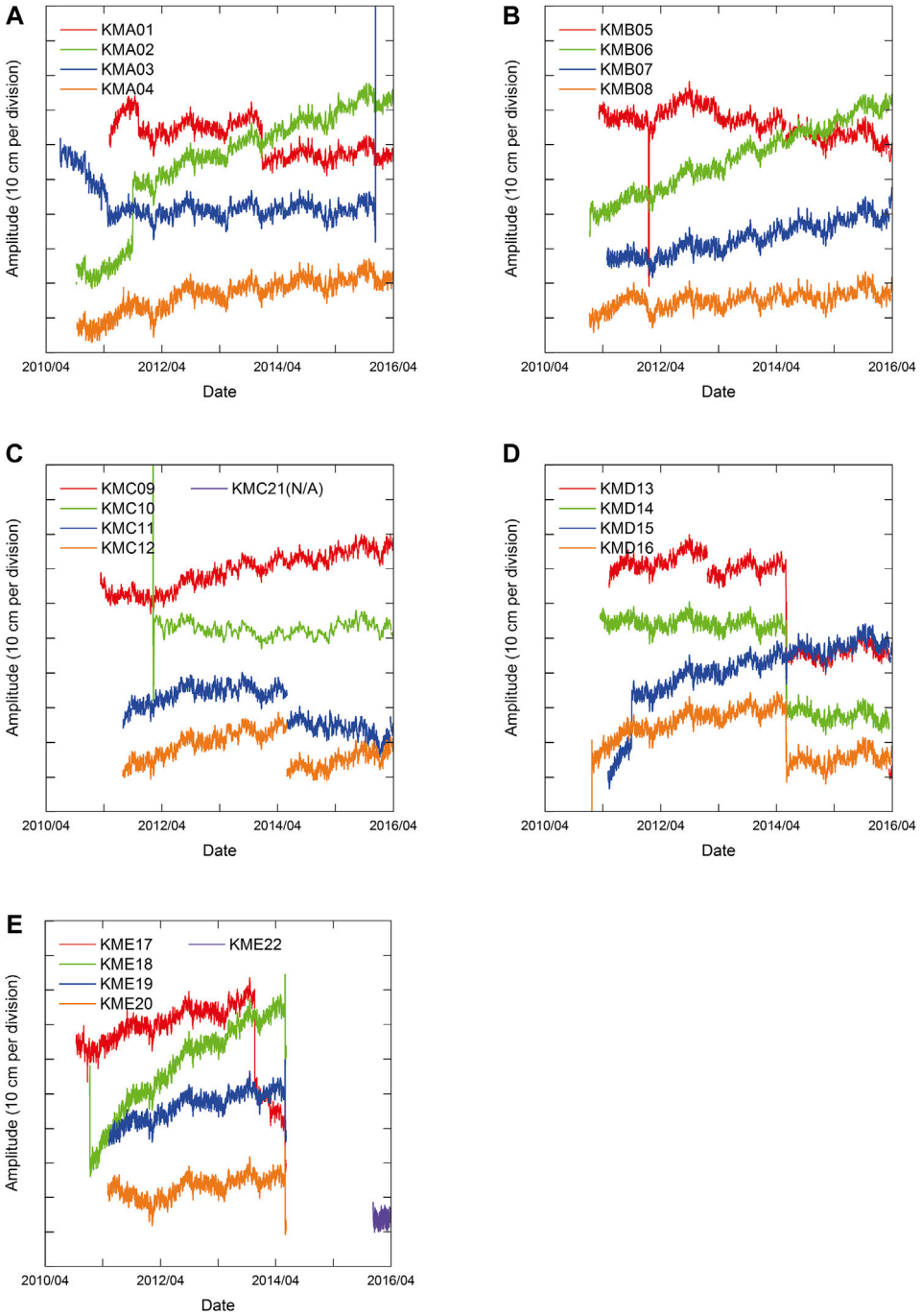

FIGURE 4 | (A) Trend component of pressure sensors analyzed by Baytap08 of KMA observatories. Each tick on the vertical axis represents 10 cm water depth change. **(B)** KMB, **(C)** KMC, **(D)** KMD, and **(E)** KME observatories are presented in the same form as **(A)**.

and 2011, except for two observatories, KMC21 and KME22, which were deployed in 2016. **Figure 5** shows the de-tided pressures of the DONET2 observation with the same form as **Figure 4**. The DONET2 observatories were deployed for a period between 2014 and 2016; therefore, the plots begin in 2014. For all pressure sensors, seasonal sea surface fluctuations are commonly recorded, as they cannot be predicted by Baytap08. Although further processing can be applied to remove such low-frequency aperiodic components, we consider sensor drift to be a more long-term phenomenon. It should be noted that unexpected or unexplained small pressure steps (less than a few tens of cm) were observed in a small number of pressure sensors.

As for the DONET1 observations shown in **Figure 4**, more than 5-years pressurization was achieved for many pressure

sensors up to April 2016. Large data gaps were observed in some pressure sensors in June 2014 due to the maintenance (replacement) of the science node. Pressure sensors of KME17 through KME20 have been available since March 2015 after the replacement of the science node; however, the baselines of pressure drift have been shifted out of the panel. The other large pressure step (offset) observed at KMA03 in December 2015 is attributed to the replacement of the sensor unit itself. In general, sensor drift is characterized by a monotonic increase, except in an initial response (Polster et al., 2009). Some pressure sensors indicate that the trend changes are identified between the initial and the latter stages. For example, KMA03, which was the first DONET observatory deployed, shows a relatively large negative drift, amounting to a reduction of 20 cm over the 11 months before the first major pressure step. Additional pressure steps were identified in the records of KMA01, KMA02, KMA03, KMD15, and KME17; in each case, the drift rate or the direction changes after the steps. Following their corresponding steps, the trends of KMA01, KMA03, and KMD15 became gentler, whereas the trend of KME17 became negative. The drift of KMC09 and KME20 showed initially negative trends for the first ten months before becoming positive. For all pressure sensors, weak exponential behavior followed by a strong linear trend can be identified. The largest drift is seen at KME18, with a change of approximately 45 cm water depth, over 3.5 years, resulting in an average drift rate of 13 cm of water depth per year. In contrast, a relatively small drift of less than 10 cm of water depth was observed at KMB05, KMB08, and KMD14 over the entire period of *in-situ* measurement.

As for the DONET2 observations shown in **Figure 5**, the data acquisition period is relatively short compared to DONET1. The second half of the installation of the main submarine cable of DONET2 was conducted between September and October 2015; all the *in-situ* data of DONET2 were not available during this period. The first observatory of DONET2 is MRA03, which was installed in March 2014, and the *in-situ* data are available from April 2014. As such, some interruptions were present at the beginning of the processed data. The overall long-term trend of the DONET2 pressure sensors tended to be in a positive direction. MRA02, MRA03, and MRA04 showed a larger sensor drift rate (approximately 20 cm/year) in the positive direction than the others. MRD16 and MRD17, which were deployed in February 2016, show a negative trend, which is a typical initial response of the Paroscientific Bourdon-tube type pressure sensor. More long-term trends based on the *in-situ* measurements of DONET2 pressure sensors have been discussed elsewhere (Matsumoto et al., 2018). The long-term trend of DONET pressure sensors varies with time and is comparable to that of other *in-situ* observations performed with the same type of mechanical pressure sensors (Polster et al., 2009).

3 LABORATORY EXPERIMENT

3.1 Pressure Standard

The pressure sensors used in DONET specify their hysteresis and repeatability as less than ±0.005% of the full-scale pressure range, corresponding to ±34.5 hPa, which is equivalent to a water depth of ±34.5 cm. However, as there are currently no estimations of their long-term stability, we conducted a long-term pressurization test by designing and implementing a laboratory experiment. Our main objective for this experiment was to determine whether the pressure sensor drift rate can be predicted before deployment, thus quantifying the reproducibility of a sensor's after-deployment characteristics and understanding how sensor drift can be released by pre-deployment pressurization.

A pressure standard (i.e., a dead weight pressure calibrator) and a temperature-controlled oil chamber were used as the primary laboratory equipment (**Figure 6A**). This equipment consists of a high-accuracy pressure standard comprising a dead weight and piston gauge (DH Instruments Inc., PG7302), pressure calibrator/controller (DH Instruments Inc., PPCH), and pressure monitor (DH Instruments Inc., RPM4), as well as an additional temperature-controlled oil chamber, where the pressure sensors would be set. A schematic block diagram of the experimental setup is shown in **Figure 6B**. Static hydraulic pressure can be continuously applied to pressure sensors under a constant temperature that is similar to the environment of the deep-sea. A manifold upon which a maximum of 13 pressure sensors can be mounted is also prepared, allowing the same pressure to be simultaneously applied to all pressure sensors. The output frequencies for both temperature and pressure were measured every 5 s using two frequency counters for each pressure sensor, linked sequentially by a multiplexer. Hence, the sample rate for each pressure sensor was approximately 1 min. This style of continuous pressurization was first examined in 2009, although some operational difficulties were encountered at an early stage (Matsumoto et al., 2018). Hence, we discuss the results examined for 15 pressure sensors to be deployed into the DONET2 observatories in this paper.

In the long-term pressurization test, we selected a common configuration of 20 MPa and 2°C for the applied pressure and the oil chamber, respectively, which replicates the deep-sea environment at a water depth of 2,000 m; this is consistent with the typical conditions of the DONET observatories. The duration of static pressure loading was approximately one month (**Figure 7**). As the sensitivity for barometric pressure is 1 Pa/Pa in all devices, the barometric pressure change is not negligible for long-term measurements. The barometric pressure was measured by the barometer installed on the PG7302 and compensated as the piston gauge's contribution to the pressure sensor drift.

Ambient temperature change is one of the most significant factors affecting long-term constant pressurization. The pressurization test was performed under thermal conditions where the variation in the ambient temperature of the pressure sensors, referred to as the temperature-controlled oil chamber, was less than 0.1°C. Although the temperature of the laboratory room is automatically controlled by air conditioners, any change in ambient temperature directly affects the piston-cylinder effective area and the 1/4-inch high-pressure pipe connecting the pressure standard and oil chamber. Ambient temperature fluctuations, measured on the

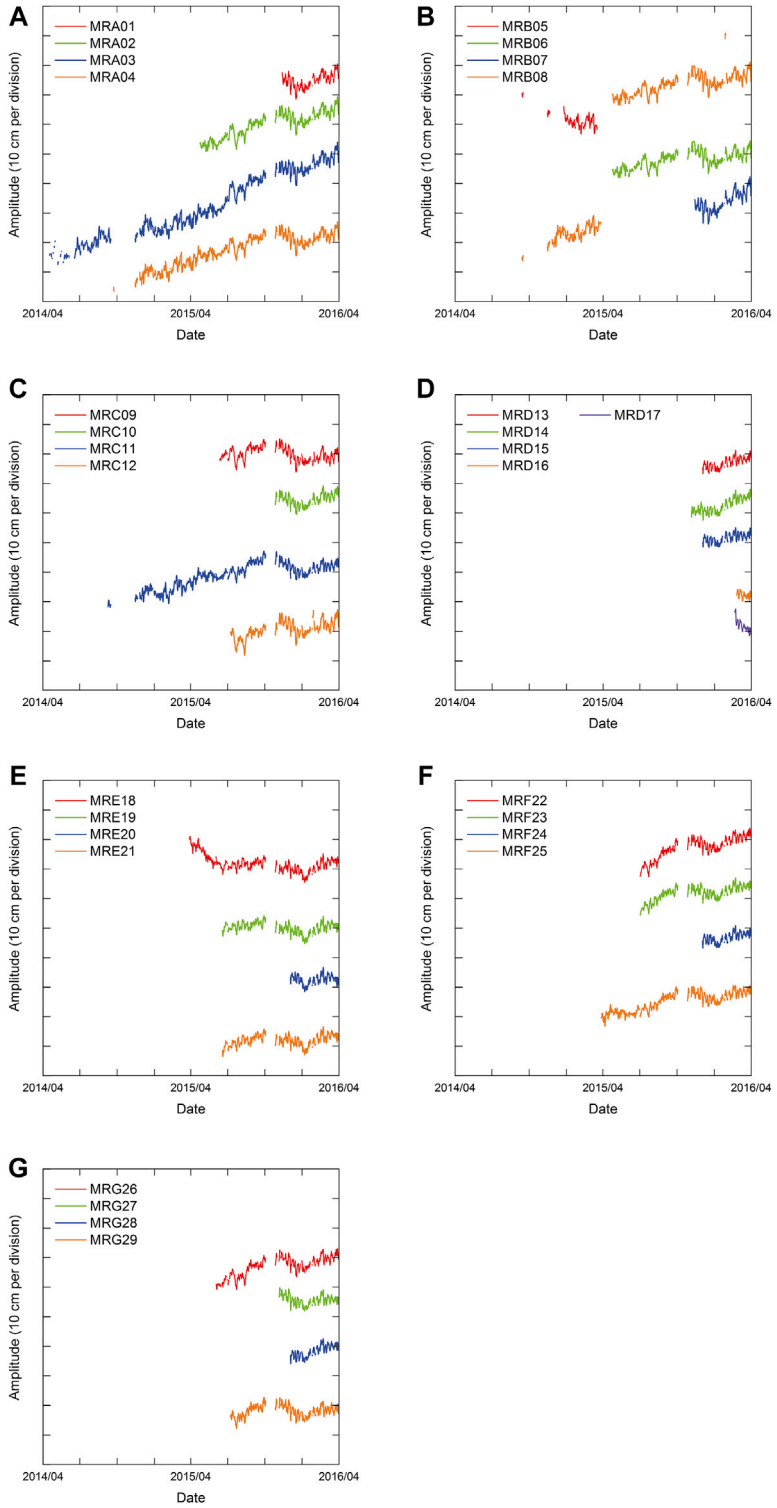

FIGURE 5 | (A) Trend component of pressure sensors analyzed by Baytap08 of MRA observatories. Each tick on the vertical axis represents 10 cm water depth change. **(B)** MRB, **(C)** MRC, **(D)** MRD, **(E)** MRE, **(F)** MRF, and **(G)** MRG observatories are presented in the same form as **(A)**.

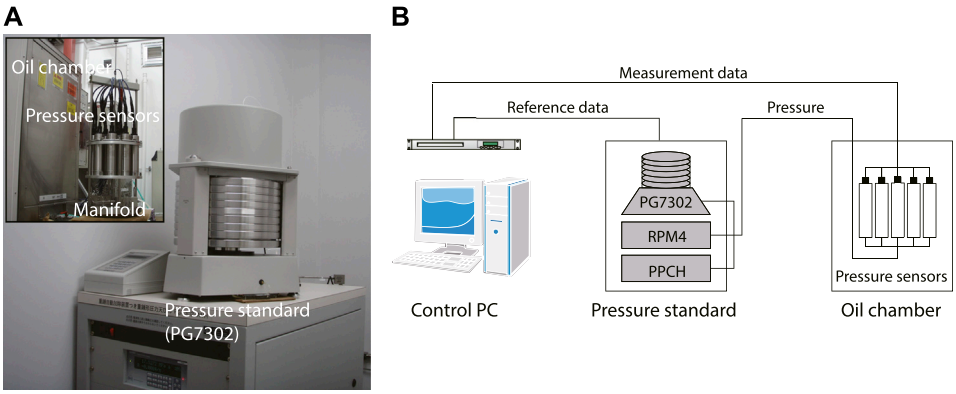

FIGURE 6 | (A) Pressure standard and the temperature-controlled oil chamber (inset) used in the present study. **(B)** Schematic block diagram of the experimental setup.

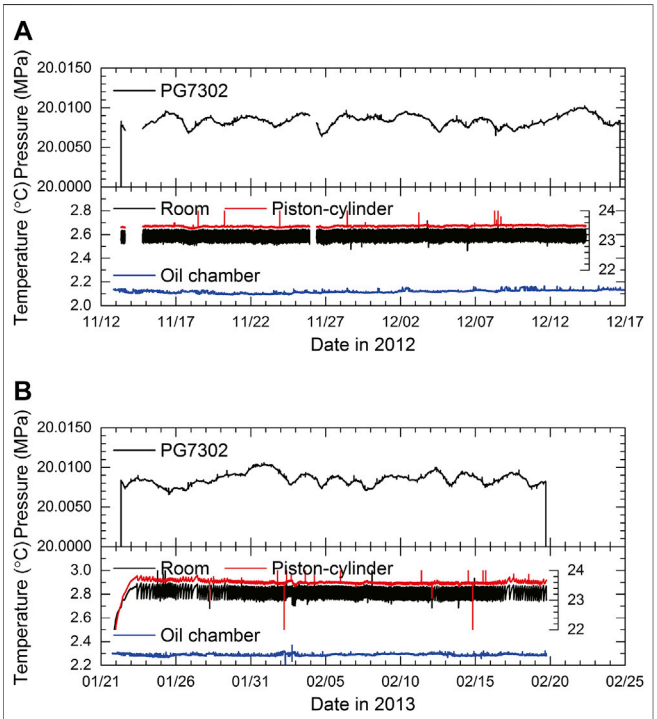

FIGURE 7 | (A) Applied pressure and ambient temperatures (a different scale is used for room and piston-cylinder) during the experiment conducted in 2012. **(B)** The experiment in 2013 is presented in the same form as **(A)**.

PG7302, were less than 0.5°C during the experimental period (**Figure 7**). The temperature change of the piston-cylinder inside the PG7302, however, was measured to be less than 0.05°C. The PG7302's piston-cylinder temperature coefficient is 10 ppm/°C, so an error of 0.1 ppm can be expected. The PG7302 calculates the calibrated pressure value (i.e., the reference pressure) taking into account ambient temperature and humidity, which, respectively, contribute to the effective area of the piston-cylinder and buoyancy of the dead weight.

3.2 Experimental Results

Two experiments were conducted for 15 pressure sensors in total; the first and second pressurization tests were started in November 2012 and January 2013, respectively. The pressurization durations for the first and second tests were 34 and 29 days, respectively. Five pressure sensors were examined repeatedly to ensure the reproducibility of the sensor drift behavior.

The pressure deviation of each pressure sensor from PG7302 (i.e., the reference pressure) is plotted in **Figure 8** for the two pressurization tests. Black dots and red lines respectively represent the measurements and the fitted curves by an equation combining exponential and linear components (Polster et al., 2009).

$$P(t) = A_1 \exp(A_2 t) + A_3 t + A_4 \quad (1)$$

Here, P is an approximated function regarding the pressure deviation and t is the elapsed time from the pressurization. Coefficient A_1 is related to the amplitude of the exponential trend; A_2 and A_3 are coefficients representing the acceleration of the exponential and linear trends, respectively; and A_4 is the pressure offset. The coefficients A_1 through A_4 are determined by the least-squares method using the MATLAB® fminsearch function.

In the first test conducted in November 2012, the reference pressure was not available for one day at the early stage of pressurization; however, exponential decay was identified for all pressure sensors. An exponential trend was diminished in a few days, except for one pressure sensor (SN123980), which lasted for more than 10 days. Then, a linear trend follows but the direction of the sensor drift varies. An unexpected pressure step in a few hecto-Pascal with a duration of a few hours was observed in one pressure sensor (SN123974) during pressurization; thus, the fitted function, that is, **Eq. 1**, begins after disappearance of this effect.

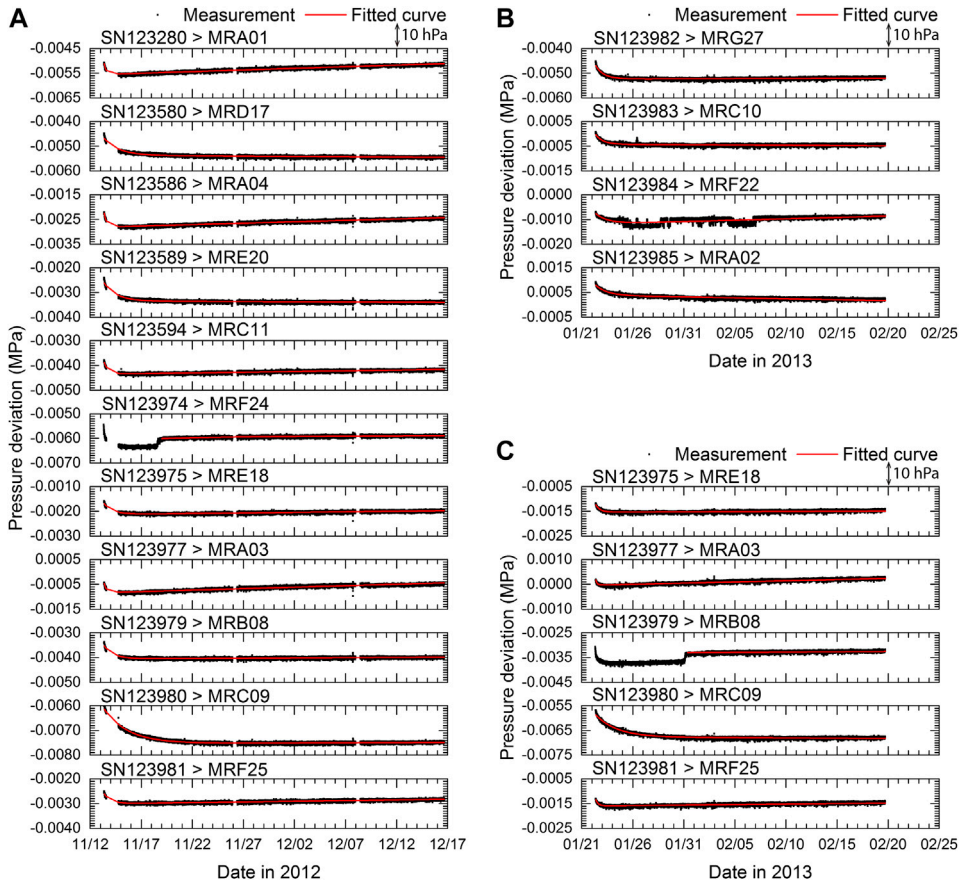

FIGURE 8 | Deviation from the pressure standard (i.e., the reference pressure) during the experiment. The serial numbers of a pressure sensor and the observatory names to be deployed into the DONET observatories are shown in each panel. The vertical axis represents the absolute pressure deviation in mega-Pascal. The fitted curves derived from **Eq. 1** are also plotted as red lines. Experiments were conducted in **(A)** November 2012 and **(B, C)** January 2013. **(C)** Five pressure sensors were repeatedly pressurized.

In the second test conducted in January 2013, five pressure sensors, SN123975, SN123977, SN123979, SN123980, and SN123981 were pressurized again for one month. The time gap between the first and the second tests was more than one month, suggesting that the hysteresis effect induced by the first test did not appear in the second test (Kajikawa and Kobata, 2019). Comparing the two pressurization tests, +5 to +10 hPa offsets of pressure deviation from the reference were identified, which might be attributed to the difference in the ambient temperature of the pressure sensors (**Figure 7**). A pressure step was observed on SN123979; however, this phenomenon was not observed in the first test. The starting time for the evaluation of sensor drift for SN123979 was set after the pressure step. The pressure sensor SN123980 showed a slow exponential decrease in pressure, as was observed in the first test. Although the pressure sensor SN123984 showed some pressure steps in the first half of pressurization, it appeared that this unstable behavior was not observed in the second half of pressurization.

4 DISCUSSION

4.1 Estimation of Sensor Drift

One of the objectives of the present study is to determine whether the sensor drift can be characterized before deployment. The information of some DONET2 observatories and corresponding pressure sensors examined in the present experiments are summarized in **Table 1**. The *in-situ* observation of MRA03 is discussed first because MRA03 is not only the first DONET2 observatory but also a repeatedly pressurized sensor in the experiment. The de-tided trend of MRA03 analyzed by Baytap08 is shown in **Figure 9**, in which the fitted curve derived by **Eq. 1** is also plotted. The starting time of the fitted curve is set to as March 16, 2014 (**Table 1**), although *in-situ* data are available after April 2014 because of the initial quality control. The pressure deviation increases with time, but the initial exponential trend cannot be recognized. Coefficient A_3 associated with the linear trend provides the drift rate of a pressure sensor. Our analysis suggests that the drift rate of the

TABLE 1 | Information of DONET pressure sensors and installed/connected date to the observatories.

Observatory	Water depth (m)	Experiment in 2012	Experiment in 2013	Installation date	Connection date
MRA01	1,375	SN123280		2014/09/20	2014/09/22
MRA02	1,360		SN123985	2014/09/14	2015/04/18
MRA03	1,352	SN123977	SN123977	2014/03/16	2014/03/16
MRA04	1,372	SN123586		2014/09/14	2014/09/21
MRB08	1.262	SN123979	SN123979	2014/09/06	2014/09/12
MRC09	1,555	SN123980	SN123980	2014/09/15	2015/06/10
MRC10	1,720		SN123983	2015/07/04	2015/07/06
MRC11	2,001	SN123594		2014/09/05	2014/09 07
MRD17	2,700	SN123580		2016/02/08	2016/02/18
MRE18	3,548	SN123975	SN123975	2015/03/15	2015/03/27
MRE20	3,603	SN123589		2015/06/24	2015/11/16
MRF22	2,104		SN123984	2015/04/16	2015/05/28
MRF24	2,393	SN123974		2015/07/04	2015/11/28
MRF25	2,278	SN123981	SN123981	2014/11/27	2015/03/17
MRG27	2,494		SN123982	2015/06/25	2015/10/29

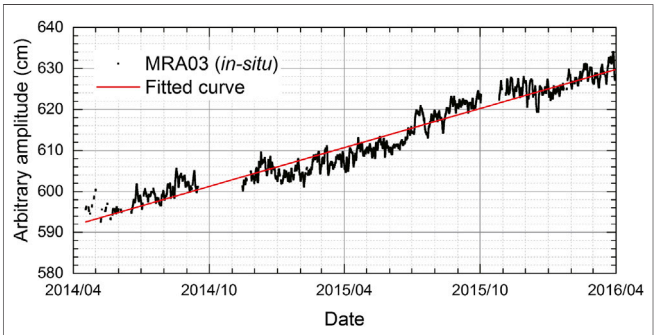

FIGURE 9 | *In-situ* measurement after tidal correction of MRA03. The fitted curve derived from **Eq. 1** is plotted as a red line.

pressure sensor of MRA03 is +0.052 cm/day (i.e., approximately +19 cm/year) based on 2 years of observations.

Our experiment is relatively short compared to the *in-situ* measurements. According to previous studies regarding the *in-situ* measurements of pressure sensors, it is suggested that sensor drift is dominated by a linear trend (Watts and Kontoyiannis, 1990; Polster et al., 2009). Therefore, we focus on the variation of coefficient A_3 in **Eq. 1** associated with the linear trend in the experiment. **Figure 10** shows the time series of the pressure deviation of the pressure sensor (SN123977) deployed at MRA03 by two pressurizations and the final fitted curves derived by **Eq. 1**. The bottom box of each panel represents the variation of coefficient A_3 when the analytical period is extended day-by-day. Coefficient A_3 varies in the initial three days and is then reduced with time, suggesting that the limitation of coefficient A_3 can correspond to the drift rate of the pressure sensor. Assuming that the variation of coefficient A_3 is approximated by an exponential function, we can obtain the expected drift rate of a pressure sensor. The coefficient A_3 yields +2.95 Pa/day (i.e., +10.76 cm/year) and +0.99 Pa/day (i.e., +3.61 cm/year) for the first and second pressurization tests, respectively, as indicated by the dashed line in the panels.

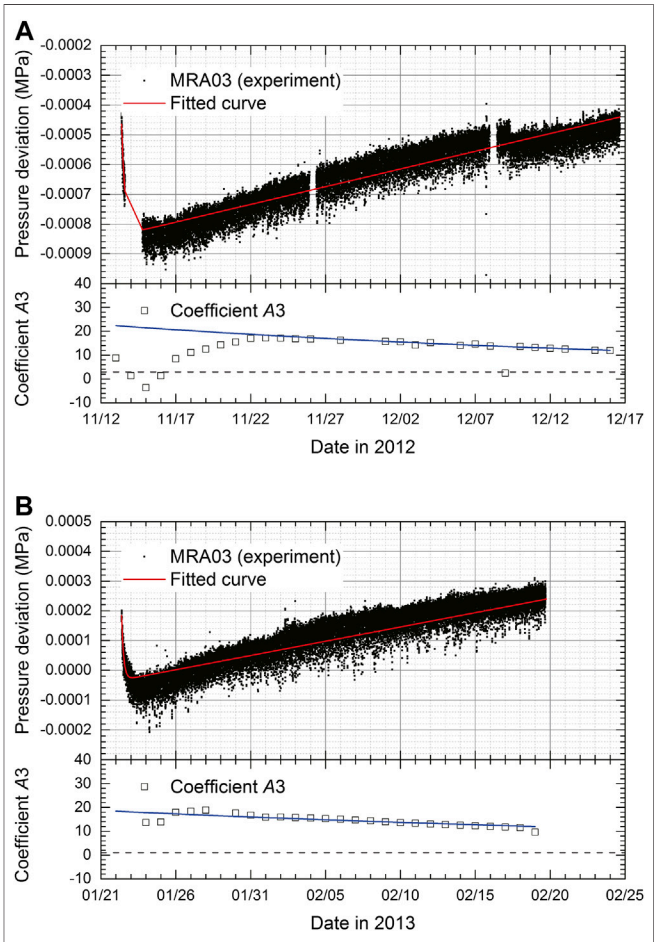

FIGURE 10 | (A) Deviation from the pressure standard (reference pressure) of the MRA03 pressure sensor **(top)** and variation of coefficient A_3 during the experiment **(bottom)**. The unit is Pa/day. The blue and dashed lines represent the exponential approximation of coefficient A_3 and its limit value, respectively. **(B)** The experiment in 2013 is presented in the same form as **(A)**.

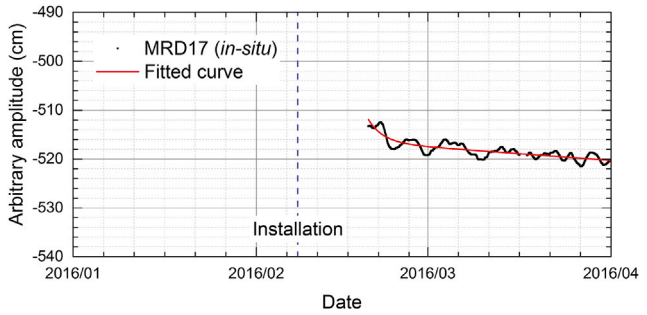

FIGURE 11 | *In-situ* measurement after tidal correction of MRD17. The fitted curve derived from **Eq. 1** is plotted as a red line. The installation date of the pressure sensor is indicated by the purple dashed line.

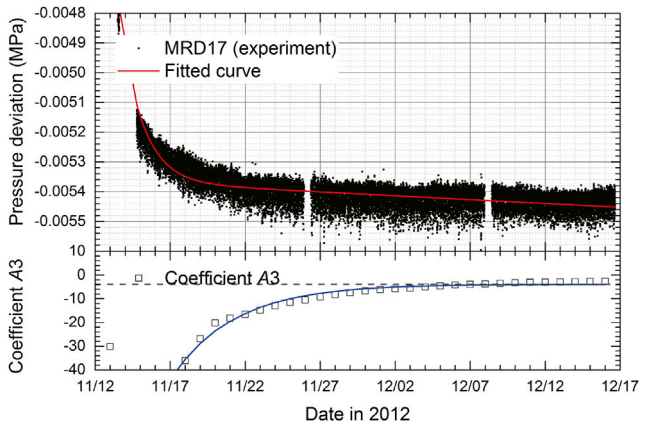

FIGURE 12 | Deviation from the pressure standard (reference pressure) of the MRD17 pressure sensor and variation of coefficient A_3 during the experiment. The unit is Pa/day.

Another instance in which the duration of pressurization is close to that in the experiment is presented. The pressure sensor of MRD17 was installed on February 8, 2016 and connected to the DONET on February 18, 2016 (**Table 1**), suggesting that the initial behavior can be investigated more than that of MRA03. The variation in the pressure deviation of MRD17 (SN123580) is shown in **Figure 11**, in the same form as **Figure 9**. The drift rate (coefficient A_3) of the MRD17 pressure sensor based on the *in-situ* measurement is −0.088 cm/day (i.e., −32.12 cm/year). An exponential trend was observed more than 10 days after installation. Applying the same procedure to predict the drift rate for the MRD17 pressure sensor, the coefficient A_3 yields −3.87 Pa/day (i.e., −14.12 cm/year) (**Figure 12**).

4.2 Comparison With *In-Situ* Measurements

The distribution of drift rate of 15 pressure sensors from the *in-situ* measurements and the experiments are plotted in **Figure 13**, in which some significant pressure sensors and repeatedly pressurized sensors are indicated by DONET observatory names. Each plot is classified by different colors according to

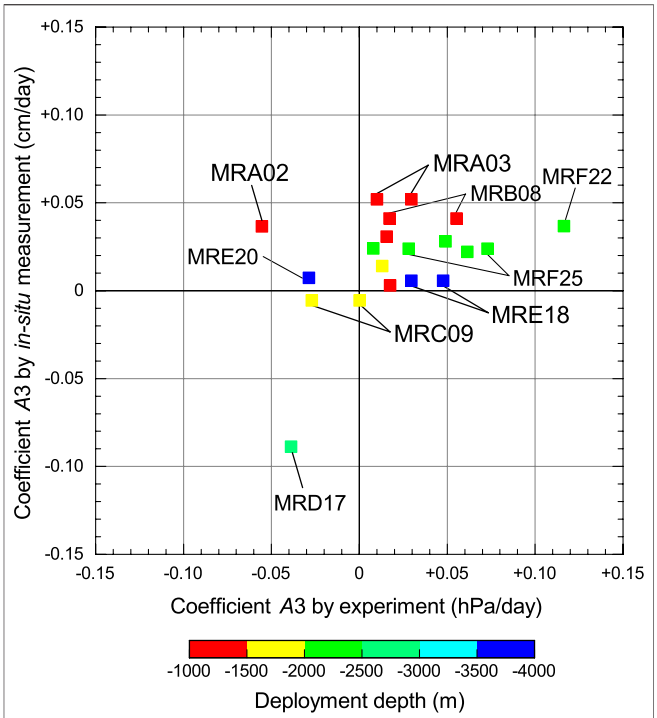

FIGURE 13 | Sensor drift rate from the *in-situ* measurements plotted against values from the experiments. Observatory names are indicated for some significant results and repeatedly examined sensors. Colors represent the deployment depth of each sensor.

the deployment depth. Five pressure sensors were examined (pressurized) repeatedly; therefore, in total, 20 datasets were available. Overall, the drift rate of the *in-situ* measurement can be predicted by the experiment for many pressure sensors. However, the averaged error for all pressure sensors is +0.0036 hPa/day (i.e., +1.32 cm/year) with a ±0.039 hPa/day (i.e., ±14.33 cm/year) standard deviation (SD). Three pressure sensors deployed at MRA02 (SN123985), MRC09 (SN123980), and MRE20 (SN123589) showed different directions of sensor drift between the *in-situ* measurements and the experiments. The pressure sensors of MRA02 and MRE20 showed a positive drift rate in the *in-situ* measurement, while the experiment suggested a negative direction. These two pressure sensors did not show a positive linear component drift during the experiment (**Figure 8**), suggesting that the initial decreasing drift was dominated by the exponential component. On the other hand, the *in-situ* pressure data examined were for five to seven months after deployment (**Table 1**); therefore, we might evaluate the sensor drift using the linear component in the *in-situ* measurement. This is one possible reason why the directions of sensor drift were opposite, and much longer pressurization than one month might result in the positive sensor drift in the experiment, as observed in the *in-situ* measurement. The pressure sensor of MRC09 may be unique. The *in-situ* measurement of MRC09 suggests that the drift rate based on the fitted curve is negative, but the drift rate is very small (**Figure 5**). Two experiments regarding the pressure sensor of MRC09 resulted in different directions of the sensor drift,

suggesting that one-month pressurization may not be sufficient for this pressure sensor because the pressure sensor indicated a very long initial exponential trend (**Figure 8**). This result suggests that pressure sensors may require a longer duration of continuous pressurization to better characterize and explain any differences in the direction of sensor drift between the lab pressurizations and the *in-situ* measurements to evaluate the true sensor drift rate. This also highlights that the behavior of sensor drift is unique to individual sensors.

The experiments of two pressure sensors are over- and under-estimated; MRF22 (SN123984) shows a large drift rate compared to the *in-situ* measurement. On the other hand, MRD17 (SN123580) shows a small drift rate compared to the *in-situ* measurement, although the directions of the sensor drift correspond to the *in-situ* and the experimental measurements. Both pressure sensors yielded a linear trend virtually in the experiment. As such, we cannot explain the reason for observation of large discrepancies in drift rates, although the difference in the pressurization period may be a primary cause.

The pressure sensors showing relatively large drift rates were deployed at depths shallower than 1,500 m, although the period of data analyzed was different for each station and the number of pressure sensors analyzed was only 15, making statistical interpretations difficult. All plots of five pressure sensors deployed between 2,000 and 2,500 m are distributed in the middle drift rate range, particularly after deployment; however, these sensor drift rates that are pressurized by the equivalent pressure of deployment depth do not always correlate with the experimental drift rates. Our laboratory experiment can predict the sensor drift rate within a certain range but the quantitative prediction of drift rate has not yet been achieved; perhaps, this is due to the short pressurization period.

4.3 Future Perspectives for Crustal Deformation Monitoring

The present study provides insights into the interpretation of observations from DONET pressure sensors, from the point of view of crustal deformation monitoring. The contribution of the inter-plate coupling to the vertical crustal deformation superposing the *in-situ* pressure measurements is expected to be less than 1 cm/year (i.e., approximately 0.003 cm/day) around the Nankai Trough based on on-land GNSS measurements (Sagiya et al., 2000). Thus, the pressure sensors employed in the DONET are capable of detecting such small pressure changes sufficiently with respect to the sensor resolution. On the other hand, the *in-situ* measurement indicates that the sensor drift is dominant over these timescales, ranging from a few to a few tens of centimeters per year. Our laboratory experiment also supports that sensor drift cannot be negligible if pressure sensors are used for the long-term monitoring of crustal deformation. According to **Figure 13**, the errors in the drift rate derived from the experiments of the repeatedly pressurized sensors vary from 0.018 (MRE18) to 0.045 hPa/day (MRF25), suggesting that uncertainties of our drift rate estimation based on the experiments are 6–16 hPa/year. These uncertainties exceed the expected vertical crustal deformation in the Nankai Trough.

One of the difficulties in sensor drift correction is that the drift varies from sensor to sensor. For example, the sensor drift behavior is dominated by an exponential trend followed by a linear trend commonly; however, its transition timeline is not identical between the pressure sensors. We conducted the pressurization test repeatedly for some pressure sensors, noting that the pressure sensors readings are repeatable for the sensor's specifications (**Figure 8**). This suggests that the present experiment may help to predict the duration of the exponential trend after deployment in the deep-sea. If the observation period is limited by pressure sensors, for example, a pop-up (campaign)-type pressure observation system, this procedure is useful for selecting pressure sensors in which an exponential trend diminishes early following deployment and pressurization.

Some of the DONET pressure sensors recorded unexpected pressure steps with offsets of more than a few tens of centimeters in their long-term operation (**Figure 4**). Changes in the direction and rate of sensor drift were identified at the pressure steps. We did not observe apparent pressure steps (offsets >10 cm) causing significant drift rate and direction changes in the experiments, as observed in the DONET1 pressure sensors after the deployment. On the other hand, small pressure steps (offsets <1 hPa) were identified, which did not appear to affect sensor drift behavior. The mechanism of pressure steps may be different between the experimental and *in-situ* measurements. We could not constrain the origin of the pressure steps because it is difficult to predict when this unexpected phenomenon occurs even in laboratory experiments. We do not anticipate such pressure steps (offsets) in the evaluation of sensor drift rate; in other words, our approach can be applied to pressure sensors showing a monotonic drift only to a certain degree.

As for the direction of sensor drift, our study shows that 18 of 20 dataset sensors correspond to each other. As the total number of examined pressure sensors is limited (15 sensors), a statistical investigation may be difficult; further, the direction of sensor drift can be predicted by the pre-pressurization. As mentioned earlier, the outliers (i.e., pressure sensors of MRA02 and MRE20) from the predictions are interpreted by the difference between the analytical time windows after pressurization, suggesting that an appropriate pressurization period should be sought. However, it is acknowledged that the comparison of the drift rate between the experimental and *in-situ* measurements do not always show adequate correlations with each other. One possible reason for this is attributed to the difference in the pressurization period. The duration of pressurization in the experiment is 1 month, suggesting that it is too short to evaluate long-term sensor drift over a year. As errors in the drift rate between the experimental and the *in-situ* measurements are larger than the expected crustal deformation, the experimental results cannot be applied to correct the sensor drift directly. Further investigation is needed to calibrate the DONET pressure sensor using the current experimental results. Alternatively, our team has developed a mobile pressure calibrator (i.e., a campaign-type pressure calibration system) carrying the pre-calibrated pressure to the seafloor by an ROV and using this to calibrate the *in-situ* pressure sensors, which may improve our ability to evaluate smaller crustal deformation signals (Machida et al., 2020).

Accurate measurement of crustal deformation is crucial for monitoring active submarine volcanoes because it allows us to

detect eruption-related magma movement. Sensor drift correction of the *in-situ* pressure measurements contributed to predicting an episodic series of submarine volcanic eruptions of the axial seamount over time (Nooner and Chadwick, 2016). During the eruption series of the Axial Seamount, continuous 60-cm uplift was detected by self-calibrated pressure recorders for a period of 17 months in 2013 through 2015 (Sasagawa et al., 2016). Our approach to estimating the drift rate before deployment may be applicable to such large deformations (>a few tens of centimeters per year) effectively. ROV operation is usually required for the campaign-style *in-situ* calibration; however, active submarine volcanoes sometimes prevent ROV from accessing spots of interest; consequently, *in-situ* calibration operation cannot be performed. We have assessed some pressure sensors using the present procedure before assembling the campaign-type pressure observation system to be deployed near Izu-Oshima Island, an active volcanic island of Japan, to detect seafloor deformation induced by the magma movement. The results of this experiment and related surveys will be reported in the future.

5 CONCLUSION

In the 2010s, 51 pressure sensors were deployed into the deep-sea, at depths between 1,300 and 4,500 m, to form part of the DONET observatories. The present study focuses on the sensor drift of the DONET pressure sensors during the initial period operated by JAMSTEC.

We obtained the *in-situ* measurement dataset from DONET for a period of up to 6 years. The *in-situ* data were processed to remove the tidal component. Although the seasonal sea surface changes, local current effects and other unpredictable aperiodic fluctuations are represented in the tidally-corrected data, and the sensor drift of pressure sensors is determined. Considering the long-term characteristics, sensor drift continued after deployment, even after similar pressurization for 1 month before deployment. Assuming that the initial behavior of sensor drift is dominated by an exponential trend, we fitted the sensor drift to a combination of exponential and linear functions over time.

We conducted a laboratory experiment, wherein continuous pressurization of 20 MPa was applied for 1 month at an ambient temperature of 2°C, to the pressure sensors to be deployed into the deep-sea. Comparing the sensor drift from the experiment with the *in-situ* measurements, it was found that they correlate with each other in terms of the rate and direction of drift. For some pressure sensors, however, the experimental sensor drift was found to be in the opposite direction to that derived from the *in-situ* measurements. This may be attributed to the comparatively short pressurization time of the pressure sensor considering a longer than normal exponential decay for some sensors. It is suggested that according to the drift rate, the present experiment overestimated +1.32 ± 14.33 cm/year standard deviation (SD). We conclude that continuous pressurization should be applied until the first appearance of the transition between an exponential and a linear trend to evaluate the drift rate of pressure sensors in the laboratory because a linear trend is typically used to determine the long-term sensor drift.

Our experiment indicates that there remain uncertainties in our approach toward prediction by pre-pressurization for correction of sensor drift of *in-situ* measurements. Recently, a new procedure for estimating sensor drift by means of an *in-situ* calibration has been proposed (Sasagawa and Zumberge, 2013; Machida et al., 2019). These methods recommend that calibrated pressure obtained at the seafloor be used to correct sensor drift. In any situation, some calibration of the *in-situ* pressure sensors, such as the self-calibration technique or an *in-situ* reference pressure sensor, is required to correct sensor drift, which may be difficult to distinguish from crustal deformation.

DATA AVAILABILITY STATEMENT

The original contributions presented in the study are included in the article/Supplementary Material, further inquiries can be directed to the corresponding author.

AUTHOR CONTRIBUTIONS

HM is the main author of the manuscript. HM and EA are the main contributors to the data processing and analysis.

FUNDING

This work was partially supported by the Japan Society for the Promotion of Science (JSPS), Grant-in-Aid for Scientific Research (KAKENHI), JP19H02411.

ACKNOWLEDGMENTS

DONET has been developed and constructed as a project supported by the Ministry of Education, Culture, Sports, Science and Technology (MEXT) in Japan. We are grateful to LW and two reviewers, whose comments allowed us to improve the quality of the manuscript. Technical support and discussions with Tetsuya Ishizuka and Masaki Kobayashi were helpful for the development of the laboratory experiment.

REFERENCES

Ariyoshi, K., Nakata, R., Matsuzawa, T., Hino, R., Hori, T., Hasegawa, A., et al. (2014). The detectability of shallow slow earthquakes by the Dense Oceanfloor Network system for Earthquakes and Tsunamis (DONET) in Tonankai district, Japan. *Mar. Geophys. Res.* 35, 295–310. doi:10.1007/s11001-013-9192-6

Chiswell, S. M., and Lukas, R. (1989). The low-frequency drift of Paroscientific pressure transducers. *J. Atmos. Ocean. Technol.* 6, 389–395. doi:10.1175/1520-0426(1989)006<0389:TLFDOP>2.0.CO;2

Eble, M. C., and González, F. I. (1991). Deep-ocean bottom pressure measurements in the northern Pacific. *J. Atmos. Ocean. Technol.* 8, 221–233. doi:10.1175/1520-0426(1991)008<0221:DOBPMI>2

Fujimoto, H., Mochizuki, M., Mitsuzawa, K., Tamaki, T., and Sato, T. (2003). Ocean bottom pressure variations in the southeastern Pacific following the 1997-98 El Nino event. *Geophys. Res. Lett.* 30, 1456. doi:10.1029/2002GL016677

Kajikawa, H., and Kobata, T. (2019). Evaluation and correction for long-term drift of hydraulic pressure gauges monitoring stable and constant pressures. *Measurement* 134, 33–39. doi:10.1016/j.measurement.2018.10.051

Kaneda, Y., Kawaguchi, K., Araki, E., Matsumoto, H., Nakamura, T., Kamiya, S., et al. (2015). "Development and application of an advanced ocean floor network system for megathrust earthquakes and tsunamis," in *Seafloor observatories.* (Berlin, Heidelberg, Germany: Springer), 643–662. doi:10.1007/978-3-642-11374-1_25

Kawaguchi, K., Kaneko, S., Nishida, T., and Komine, T. (2015). "Construction of the DONET real-time seafloor observatory for earthquakes and tsunami monitoring," in *Seafloor observatories.* (Berlin, Heidelberg, Germany: Springer), 221–228. doi:10.1007/978-3-642-11374-1_10

Kobata, T. (2005). Characterization of quartz Bourdon-type high-pressure transducers. *Metrologia* 42, S235–S238. doi:10.1088/0026-1394/42/6/S20

Machida, Y., Araki, E., Nishida, S., Kimura, T., and Matsumoto, H. (2019). On the accuracy of quartz pressure sensor in the seafloor affected by transport condition. *IEEE J. Ocean. Eng.* 44, 1049–1057. doi:10.1109/JOE.2018.2855478

Machida, Y., Nishida, S., Kimura, T., and Araki, E. (2020). Mobile pressure calibrator for the development of submarine geodetic monitoring systems. *J. Geophys. Res. Solid Earth* 125, e2020JB020284. doi:10.1029/2020JB020284

Matsumoto, H., Araki, E., and Kawaguchi, K. (2018). Experimental evaluation of initial characteristics of DONET pressure sensors. *Mar. Technol. Soc. J.* 52 (3), 109–119. doi:10.4031/MTSJ.52.3.3

Nagano, A., Hasegawa, T., Matsumoto, H., and Ariyoshi, K. (2018). Bottom pressure change associated with the 2004-2005 large meander of the Kuroshio south of Japan. *Ocean Dynam.* 68, 847–865. doi:10.1007/s10236-018-1169-1

Nooner, S. L., and Chadwick, W. W., Jr. (2016). Inflation-predictable behavior and co-eruption deformation at axial seamount. *Science* 354, 1399–1403. doi:10.1126/science.aah4666

Paros, J. M., and Kobayashi, T. (2016). Root causes of quartz sensor drift. Proscientific, Inc., Technical Note Doc. No. G8101, Rev. A.

Polster, A., Fabian, M., and Villinger, H. (2009). Effective resolution and drift of paroscientific pressure sensors derived from long-term seafloor measurements. *Geochem. Geophys. Geosyst.* 10, Q08008. doi:10.1029/2009GC002532

Sagiya, T., Miyazaki, S., and Tada, T. (2000). Continuous GPS array and present-day crustal deformation of Japan. *Pure Appl. Geophys.* 157, 2302–2322. doi:10.1007/PL00022507

Sasagawa, G., Cook, M. J., and Zumberge, M. A. (2016). Drift-corrected seafloor pressure observations of vertical deformation at Axial seamount 2013-2014. *Earth Space Sci.* 3, 381–385. doi:10.1002/2016EA000190

Sasagawa, G., and Zumberge, M. A. (2013). A self-calibrating pressure recorder for detecting seafloor hight change. *IEEE J. Ocean. Eng.* 38, 447–454. doi:10.1109/JOE.2012.2233312

Takahashi, N., Imai, K., Ishibashi, M., Sueki, K., Obayashi, R., Tanabe, T., et al. (2017). Real-time tsunami prediction system using DONET. *J. Disaster Res.* 12, 766–774. doi:10.20965/jdr.2017.p0766

Tamura, Y., Sato, T., Ooe, M., and Ishiguro, M. (1991). A procedure for tidal analysis with a Bayesian information criterion. *Geophys. J. Int.* 104, 507–516. doi:10.1111/j.1365-246X.1991.tb05697.x

UNESCO (1983). Algorithms for computation of fundamental properties of seawater. UNESCO, UNESCO Technical Papers in Marine Sciences 44, 54.

Watts, D. R., and Kontoyiannis, H. (1990). Deep-ocean bottom pressure measurement: drift removal and performance. *J. Atmos. Ocean. Technol.* 7, 296–306. doi:10.1175/1520-0426(1990)007<0296:DOBPMD>2.0.CO;2

Wearn, R., and Larson, N. (1982). Measurements of the sensitivities and drift of Digiquartz pressure sensors. *Deep-Sea Res.* 29, 111–134. doi:10.1016/0198-0149(82)90064-4

Conflict of Interest: The authors declare that the research was conducted in the absence of any commercial or financial relationships that could be construed as a potential conflict of interest.

The handling editor declared a past co-authorship with one of the authors EA.

frontiers in Earth Science

ORIGINAL RESEARCH
published: 14 January 2021
doi: 10.3389/feart.2020.583481

Seafloor Pressure Change Excited at the Northwest Corner of the Shikoku Basin by the Formation of the Kuroshio Large-Meander in September 2017

Akira Nagano[1], Yusuke Yamashita[2], Keisuke Ariyoshi[3], Takuya Hasegawa[4,5], Hiroyuki Matsumoto[3] and Masanao Shinohara[6]*

[1]Global Ocean Observation Research Center, Japan Agency for Marine-Earth Science and Technology (JAMSTEC), Yokosuka, Japan, [2]Disaster Prevention Research Institute, Kyoto University, Kyoto, Japan, [3]Research and Development Center for Earthquake and Tsunami Forecasting, JAMSTEC, Yokohama, Japan, [4]Faculty of Environmental Earth Science, Hokkaido University, Sapporo, Japan, [5]Graduate School of Science, Tohoku University, Sendai, Japan, [6]Earthquake Research Institute, The University of Tokyo, Tokyo, Japan

OPEN ACCESS

Edited by:
Ryota Hino,
Tohoku University, Japan

Reviewed by:
Daisuke Inazu,
Tokyo University of Marine Science and Technology, Japan
Shusaku Sugimoto,
Tohoku University, Japan
William Wilcock,
University of Washington, United States
Erik Fredrickson,
University of Washington, United States, in collaboration with reviewer [WW].

***Correspondence:**
Akira Nagano
nagano@jamstec.go.jp

Specialty section:
This article was submitted to Solid Earth Geophysics, a section of the journal Frontiers in Earth Science

Received: *15 July 2020*
Accepted: *30 November 2020*
Published: *14 January 2021*

Citation:
Nagano A, Yamashita Y, Ariyoshi K, Hasegawa T, Matsumoto H and Shinohara M (2021) Seafloor Pressure Change Excited at the Northwest Corner of the Shikoku Basin by the Formation of the Kuroshio Large-Meander in September 2017. Front. Earth Sci. 8:583481. doi: 10.3389/feart.2020.583481

The Kuroshio takes a greatly southward displaced path called a large-meander (LM) path off the southern coast of Japan on interannual to decadal time scales. The transition of the current path from a non-large-meander path to an LM path is the most salient ocean current variation south of Japan. The change in pressure on the seafloor due to the formation of the LM path in September 2017 is of critical importance to understand the dynamics of the LM path and to distinguish the change due to the Kuroshio path variation from changes due to crustal deformation. Hence, we examined the seafloor pressure across the continental slope off the eastern coast of Kyushu for the period March 2014 to April 2019. The pressure and its cross-slope gradient over the continental slope shallower than 3,000 m beneath near the Kuroshio are invariable. As a mesoscale current path disturbance, called a small meander, passed over the observation stations, the pressure decreased by approximately 0.1 dbar on the continental slope deeper than 3000 m and was kept low until the end of the observation period (April 2019). The pressure decrease is consistent with the changes in sea surface height and subsurface water density and is caused by the baroclinic enhancement of the Shikoku Basin local recirculation. This seafloor pressure change implies a strengthening of the deep southwestward current, possibly as a part of a deep cyclonic circulation in the Shikoku Basin. The present study demonstrated that, in addition to altimetric sea surface height data, hydrographic data are useful to distinguish the ocean variation in seafloor pressure from the variation due to crustal deformation, and vice versa.

Keywords: Kuroshio, recirculation, sea surface height, ocean bottom pressure, large meander, Shikoku basin

1 INTRODUCTION

Winds blowing over the whole subtropical North Pacific drive a basin-scale anticyclonic circulation, which is referred as the North Pacific subtropical gyre. Because of the combined effect of the Earth's rotation and curvature, so-called the β-effect, the subtropical gyre current is concentrated on the western boundary of the basin, forming the western boundary current, i.e., the Kuroshio (e.g., Stommel, 1948; Munk, 1950; Pedlosky, 1996). The Kuroshio originates in the region to the east of the

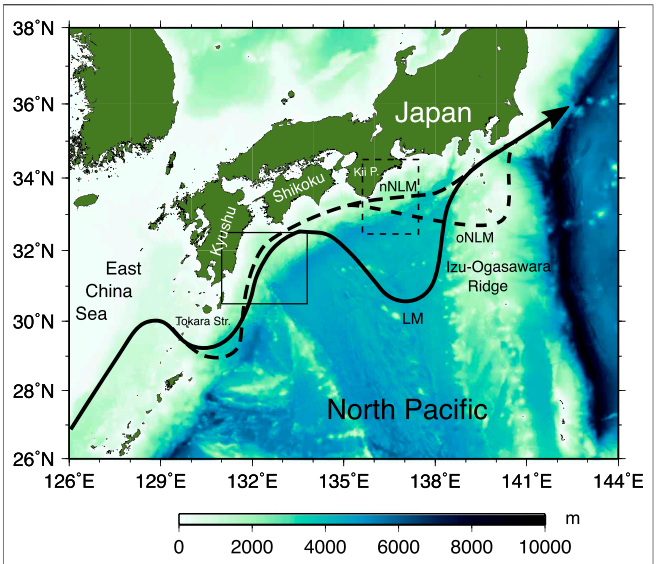

FIGURE 1 | Schematic diagram of the Kuroshio south of Japan with bottom topography. Solid and dashed lines show large-meander (LM) and offshore non-large-meander (oNLM) and nearshore non-large-meander (oNLM) paths, respectively. Ocean bottom pressure gauges (OBPs) were deployed in the regions east of Kyushu (solid square) and southeast of the Kii Peninsula (dashed square).

Philippines. It then flows northeastward in the East China Sea, and after passing the Tokara Strait, proceeds eastward in the region south of Japan (e.g., Nitani, 1972). Since the Kuroshio transports a huge amount of heat and materials northward, the variations in the Kuroshio have great influence on the global climate (e.g., Latif and Barnett, 1994; Kuwano-Yoshida and Minobe, 2017), fisheries (e.g., Tian et al., 2014; Kobari et al., 2020), and so on.

Furthermore, the variations of the Kuroshio flowing over the Nankai Trough, where the Philippine Sea Plate subducts beneath the Eurasia Plate and the seismic activity is particularly high (e.g., Ando, 1975; Ishibashi, 2004), are of great concern for seismologists to monitor the change in pressure on the seafloor due to crustal deformation caused by slow slip events (e.g., Schwartz and Rokosky, 2007) by using data collected by ocean bottom pressure gauges (OBPs) (e.g., Ariyoshi et al., 2014; Suzuki et al., 2016). The durations of slow slip events are days to years (e.g., Schwartz and Rokosky, 2007), which are similar to the timescales of the variations of the Kuroshio (Kawabe, 1987). To distinguish the seafloor pressure change due to crustal deformation from that related to the Kuroshio variation, it should be essential to reveal the characteristics of the seafloor pressure variations related to the Kuroshio.

It is well-known that to the south of Japan, the Kuroshio follows either of two types of paths: large-meander (LM) and non-large-meander (NLM) paths (**Figure 1**) (Yoshida, 1964; Taft, 1972; Kawabe, 1985; Kawabe, 1995). The LM path is located relatively offshore and is associated with a cyclonic eddy south of Japan (Taft, 1972; Kawabe, 1985), whereas the NLM path is located near the coast to the west of the Kii Peninsula and takes nearshore NLM (nNLM) or offshore NLM (oNLM) paths from the south of the Kii Peninsula to the Izu-Ogasawara Ridge (Kawabe, 1985; Kawabe, 1995). The transitions from the NLM path to the LM path are preceded by the occurrences of mesoscale current path disturbances, called small meanders, southeast of Kyushu and their developments (e.g., Shoji, 1972; Nagano and Kawabe, 2004).

Nagano et al. (2019) reported that the LM paths from 1981 to 1984 and from 2017 to the present have characteristics different from other past LM paths. The peculiarity of the 1981–1984 LM path had been reported by Kawabe (2005). Nagano et al. (2019) called the LM paths except for the 1981–1984 and 2017–present LM paths the stable type. The stable-type LM path is formed from the nNLM path through the development of a small meander (e.g., Kawabe, 1986; Kawabe, 1995; Nagano et al., 2013; Nagano et al., 2018). The development of the small meander is caused by the baroclinic instability of the small meander eddy in association with the forward-shifted (eastward-shifted) deep cyclonic eddy (Nagano et al., 2018). While the Kuroshio takes the LM path of this type, the current path is quite stable to the west of the Izu-Ogasawara Ridge as in the case of the 2004–2005 LM path.

Meanwhile, the 1981–1984 and 2017–present LM paths are called the unstable type by Nagano et al. (2019). The unstable-type LM path is formed from the oNLM path after the coalescence of the small meander eddy with a cyclonic eddy east of the Kii Peninsula (Kawabe, 2005; Nagano et al., 2019). The formation of the unstable-type LM path is not attributed to the baroclinic instability of the deep eddy (Nagano et al., 2019). The large meander of the unstable type has a greater zonal scale than that of the stable type and protrudes from the eastern boundary of the Shikoku Basin (Nagano et al., 2019). The LM path of this type is accompanied by fluctuations on the timescale of months, so that the sea levels at Miyake-jima and Hachijo-jima Islands are greatly variable.

The characteristics of the stable- and unstable-type LM paths are attributed to differences in the deep current structure, but these differences are unidentifiable from sea surface observations by tide gauges and satellites. Temporal changes in deep current velocity have been conventionally observed by current meters installed to mooring lines; such observations were made by Taft (1978); Taira and Teramoto (1985); Fukasawa and Teramoto (1986), and others. However, because of the present active fishing operations around Japan, there are concerns that subsurface mooring systems be damaged or destroyed by vandalism, and hence, such long-term mooring observations are now impracticable. On the other hand, deployment of platform equipped with instruments on the seabed is feasible even in the Kuroshio region around Japan. Around the Nankai Trough, megathrust earthquakes have repeatedly occurred at intervals of approximately 100–150 years (Ando, 1975; Ishibashi, 2004). Because the latest megathrust earthquake occurred approximately 70 years ago, the next devastating earthquake is anticipated to occur in the near future (Nakano et al., 2018). Therefore, in addition to seismometers, many OBPs have been deployed on the seabed to monitor earthquakes and tsunamis around the trough slope off the southern coast of Japan.

Besides current velocity, hydrostatic pressure is a fundamental parameter for understanding the physical mechanisms of ocean

current variations (e.g., Gill, 1982). Seafloor pressure, in particular, is a quantity that is integrated from the sea surface to the bottom, and therefore, retains useful information on variations in sea surface height (SSH) and water density from the sea surface to the bottom. Because ocean circulation currents are mostly in geostrophic balance, the variations of the deep currents are linked to the variations in seafloor pressure. In addition, the Kuroshio is considered strongly affected by the steep continental-side slopes of the Nankai Trough; Nagano et al. (2013) reported that the offshore border of the Kuroshio and the bathymetric contour of 4000 m are coincident. The effects of the bottom topography on the Kuroshio will be revealed from an examination of the seafloor pressure variations.

Nagano et al. (2018) examined the seafloor pressure change in the region south of Shikoku associated with the 2004–2005 LM path of the Kuroshio, a stable-type LM path. They demonstrated that after the eastward propagation of a deep cyclonic eddy leading to the small meander propagation, the deep Kuroshio current was enhanced in the LM period. The enhancement of the deep Kuroshio current indicates the strengthening of the vertically uniform flow component of the Kuroshio, which has a tendency to follow the isobaths of the continental slope because of potential vorticity conservation (e.g., Cushman-Roisin and Beckers, 2011). Hence, the stability of the stable-type LM path is attributed to the enhancement of the topographic steering of the current due to the strengthened deep Kuroshio current.

A small meander of the Kuroshio occurred to the southeast of Kyushu in February 2017, propagated to the south of the Kii Peninsula, and was coalesced with a cyclonic eddy east of the Kii Peninsula in August 2017. The meander trough of the Kuroshio began to stay just to the east of the Izu-Ogasawara Ridge in early September (i.e., the onset of the LM path) and, then, the sea level difference between Kushimoto and Uragami, the index of the LM path, became stable and small (Nagano et al., 2019). The LM path is active at present as of November 2020 although the cyclonic LM eddy has been separated from the Kuroshio. It is unknown whether or not the unstable-type LM path of the Kuroshio is associated with the substantial deep current following the isobaths of the continental slope and is influenced by the topographic steering. The OBP observation during the unstable-type LM period will reveal how seafloor pressure changes by the LM formation. In addition, the mechanism may be inferred using the OBP data along with hydrographic data as revealed from acoustic data (Nagano et al., 2018) and *in situ* hydrographic data (Hasegawa et al., 2019). Further, knowledge on the seafloor pressure changes due to variations in the Kuroshio will help distinguish these changes from the seafloor pressure variation due to crustal deformation.

In this study, we analyzed the variations in seafloor pressure across the Kuroshio from March 2014 to April 2019 to reveal the characteristics of seafloor pressure changes off the eastern coast of Kyushu in association with the formation of the 2017–present LM path of the Kuroshio. During the whole observation period, no significant crustal deformation was observed; hence, this observation is favorable for obtaining information on the influence of the Kuroshio current variations on seafloor pressure in advance to distinguish them from the variations due to crustal deformation. Consequently, we found a seafloor pressure change related to the formation of the LM path. In addition, by using altimetric SSH and hydrographic data collected during the period 2017–2019, we revealed that the seafloor pressure change is attributable to the change of the vertical water density distribution associated with the formation of the LM path and demonstrated that hydrographic data in combination with SSH data are useful to identify the seafloor pressure variation due to the Kuroshio variation and to distinguish it from the variation due to crustal deformation.

2 OBSERVATIONS AND DATA

2.1 OBP Data

As described by Nagano et al. (2019), the OBP observation off the eastern coast of Kyushu was initiated on March 12, 2014. Until now, the OBPs have been replaced five times (**Table 1**). **Figures 2A**, **3** show the locations and periods of the OBP observations east of Kyushu of which we analyzed the data in this study, respectively. We used the OBP data in the first to fourth observation periods collected at the sites indicated by an open circle in **Figure 2A** (the first three observation periods) and a triangle (the fourth observation period). In the fifth observation period, the OBP data were obtained at stations crossing the slope from P1 to P4 indicated by crosses. Each OBP was equipped with a digiquartz pressure transducer (Models 8B4000-2 and 8B7000-2) manufactured by Paroscientific, Inc., Redmond, USA. The accuracy and

TABLE 1 | Locations and water depths (m) of the OBP stations, and regression coefficients *A* (dbar), *B* (10^{-3} d^{-1}), *C* (10^{-3} dbar d^{-1}), and *D* (dbar) in **Eq. (1)** at stations P1 to P4 for OBP observation periods.

Station	Location	Depth	Period					*A*	*B*	*C*	*D*
P1	31.05°N, 132.70°E	4863	Jan 14	2016	–	Feb 8	2017	0.74	–0.61	0.25	4684.74
	31.07°N, 132.70°E	4858	Mar 24	2017	–	Jan 8	2019	0.54	–0.07	–0.07	4742.57
P2	31.21°N, 132.59°E	3160	Mar 23	2017	–	Apr 17	2019	0.91	–0.13	–0.13	3053.91
P3	31.40°N, 132.58°E	2835	Mar 17	2014	–	Jan 3	2015	1.00	–0.03	–0.15	2764.00
	31.40°N, 132.59°E	2811	Jan 15	2015	–	Jan 2	2016	0.59	0.00	0.00	2727.59
	31.40°N, 132.58°E	2521	Jan 13	2016	–	Feb 8	2017	0.76	0.35	0.59	2770.76
	31.37°N, 132.48°E	2337	Feb 18	2017	–	Mar 22	2017	0.78	0.11	0.12	2244.78
	31.33°N, 132.50°E	2384	Mar 23	2017	–	Apr 17	2019	0.75	0.44	–0.11	2297.76
P4	31.46°N, 132.41°E	2617	Mar 24	2017	–	Feb 24	2019	0.94	–0.09	–0.09	2520.94

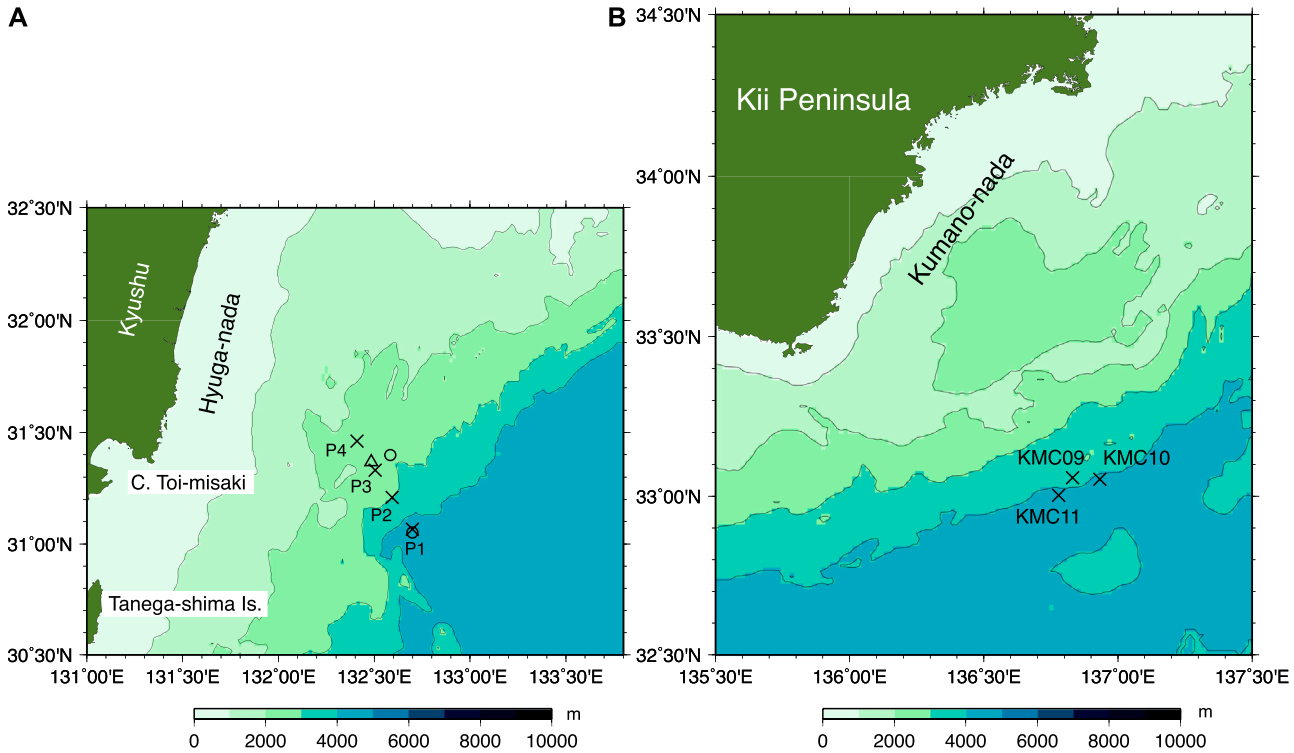

FIGURE 2 | (A) Locations of ocean bottom pressure gauges (OBPs) deployed in the solid square shown in **Fig. 1**. Open circles, a triangle, and crosses show the OBP sites in the first three observation periods, fourth observation period, and fifth observation period, respectively (**Table 1**). **(B)** Locations of OBP stations KMC09, KMC10, and KMC11 (crosses) of the Dense Oceanfloor Network system for Earthquakes and Tsunamis (DONET) off the southeastern coast of the Kii Peninsula in the dashed square shown in **Figure 1**. Contour intervals of the bottom topography are 1000 m.

resolution of the sensors were 0.01% of the full-scale range and 10 ppb, respectively (Houston and Paros, 1998). After taking into account the maximum pressure in the observations, the absolute accuracies for the fourth observation period and other observation periods were 0.04 and 0.07 dbar, respectively.

The OBP data are known to include substantial sensor drifts in some cases. In the present data, substantial sensor drifts are included, as shown for the data in the fifth observation period by solid thin lines in **Supplementary Figure S1**. Accordingly, following to Watts and Kontoyiannis (1990); Polster et al. (2009); Nagano et al. (2018); Hasegawa et al. (2019); Nagano et al. (2019) we estimated the sensor drift p_d by the nonlinear least square fitting as

$$p_d = A \exp(Bt) + C\,t + D, \quad (1)$$

where t is time (days). Thus, we obtained the coefficients A, B, C, and D (**Table 1**). The coefficients for the data in the fifth observation period are comparable to those in the first four observation periods estimated by Nagano et al. (2019). Then, the sensor drifts (as shown for the fifth observation period by solid thick lines in **Supplementary Figure S1**) were removed from the OBP data. Further, we suppressed tidal variations by

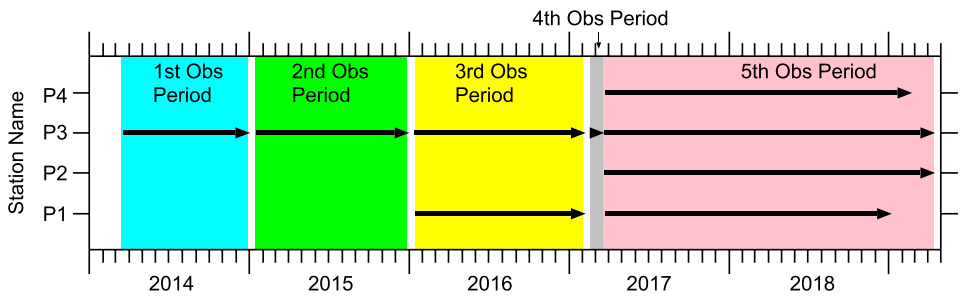

FIGURE 3 | First to fifth observation periods at OBP stations P1, P2, P3, and P4 listed in **Table 1**.

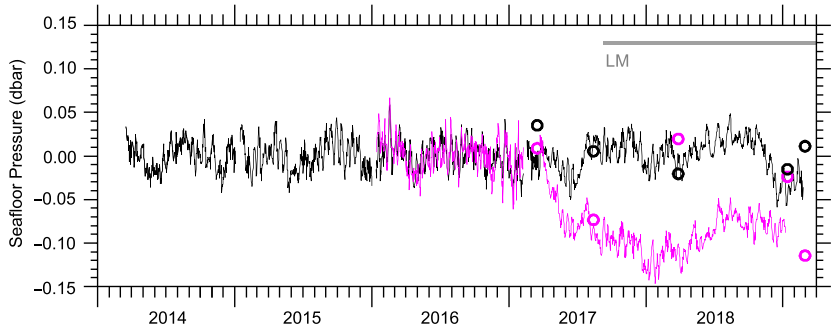

FIGURE 4 | Variations in OBP-measured seafloor pressure at stations P1 (magenta lines) and P3 (black lines) and estimated seafloor pressure based on CTD/XCTD and altimetric SSH data at P1 (magenta open circles) and P3 (black open circles). The fifth time series (March 2017–January 2019) at P1 is shown after subtracting 0.086 dbar to connect with the time series until February 2017. For comparison with the OBP-measured time series, 1.05 dbar was added to the estimated pressure values. Gray horizontal line denotes the LM period.

using the tide-eliminating filter of Thompson (1983) and calculated the daily mean values in dbar. Assuming a Gaussian error distribution, the errors of the daily mean values are less than approximately 0.002 dbar. These values are smaller than the natural range of variation (>0.05 dbar) (**Figure 4**).

The OBP stations in the first three (open circle) and fourth (triangle) observation periods were located within an approximate spatial scale of mesoscale disturbances of the Kuroshio current path, i.e., small meanders, from station P3 in the fifth observation period. Therefore, we combined the data of these stations into a single time series at P3 from March 2014 to March 2019 (black lines in **Figure 4**). Note that the time series until March 2017 at P3 is the same as that examined by Nagano et al. (2019). There seems to be no remarkable discontinuity of the seafloor pressure variation between the observation periods at P3.

The seafloor pressure time series data at station P1 were obtained in the third (an open circle in **Figure 2**) and fifth observation periods. seafloor pressure at P1 steeply decreased by ~0.1 dbar within approximately 3 months after the deployment of the OBP in March 2017. A remarkable discontinuity of the seafloor pressure variation is present at P1 between the third and fifth observation periods. We subtracted the discrepancy between the ends of these time series (0.086 dbar) from the time series in the fifth observation period to connect them. Thus, we obtained the time series at P1 from January 2016 to January 2019 (magenta lines in **Figure 4**). As explained in **Section 3.2**, we estimated the seafloor pressure change at P1 from altimetric SSH and hydrographic data (described below in this section), and examined the validity of the OBP-measured pressure change by comparing them with each other. The estimated pressure decrease from March 17 to August 12, 2017 (0.08 dbar) (magenta open circles in **Figure 4** and **Table 2**) is found to be coincident with the measured pressure decrease (magenta line in **Figure 4**). Also, a similar steep pressure decrease was observed at P2 after the deployment in March 2017. Therefore, the steep pressure decreases measured by the OBPs at P1 and P2 are considered to be caused not by sensor drifts but by the ocean variation.

In addition, we used the OBP data from July to October 2017 at stations KMC09 (33°03.503′N, 136°49.879′E), KMC10 (33°03.200′N, 136°56.009′E), and KMC11 (33°00.195′N, 136°46.739′E) of the Dense Oceanfloor Network system for Earthquakes and Tsunamis (DONET). Except for KMC09, they were installed on the lower continental slope deeper than 4000 m off the southeastern coast of the Kii Peninsula (**Figure 2B**). The deployment depths of the OBPs at KMC09, KMC10, and KMC11 are 3511, 4247, and 4378 m, respectively. The pressure sensors installed to the OBPs are Paroscientific, Inc. digiquartz pressure transducers Model 8B7000-2. The DONET OBP observations have been performed since August 2011, so that the initial large sensor drifts ceased and no remarkable trends are found during the short study period of the 4 months. Therefore, in this study, we calculated the daily mean values after the suppression of the tidal variations by the tide-eliminating filter of Thompson (1983) without removal of the sensor drifts. Same as for the OBP observations east of Kyushu, the errors of the daily mean values of the DONET OBP data are less than 0.002 dbar.

TABLE 2 | Altimetric SSH η, geopotential distance D_{1500}, and seafloor pressure p_b in **Eq. 3** estimated from the hydrographic data at offshore station P1 and onshore station P3.

Observation day		P1			P3		
		η	D_{1500}	p_b	η	D_{1500}	p_b
Mar 17	2017	1.156	2.197	−1.041	1.170	2.185	−1.015
Aug 14	2017	1.386	2.509	−1.123	1.340	2.385	−1.045
Mar 28	2018	1.387	2.418	−1.031	1.382	2.453	−1.071
Jan 13	2019	1.466	2.540	−1.074	1.409	2.474	−1.065
Mar 1	2019	1.415	2.579	−1.165	1.340	2.379	−1.039

The values of η *and* D_{1500} *are scaled by* $g\overline{\rho_b}$ *and are expressed in units of dbar as in the case of* p_b *(dbar).*

2.2 Hydrographic Data

From 2017 to 2019, five sets of hydrographic observations were obtained at stations P1 to P4 (**Figure 2**) by using conductivity-temperature-depth (CTD) and expendable CTD (XCTD) profilers. In the March 2017, March 2018, January 2019, and March 2019 cruises, we obtained the vertical profiles of temperature and salinity down to depths greater than 1500 m by using XCTD-4 probes (Tsurumi-Seiki Co., Ltd., Yokohama, Japan). In the August 2017 cruise, temperature and salinity profiles were collected down to depths of approximately 2000 dbar by using a CTD SBE 911plus (Sea-Bird Electronics, Inc., Bellevue).

The nominal accuracies for CTD temperature and conductivity are 0.001°C and 0.0003 Sm^{-1}, respectively, which is equivalent to 0.003 in practical salinity unit (psu). The differences between CTD and XCTD values are 0.05°C for temperature and 0.05 (psu) for salinity (Mizuno and Watanabe, 1998). It should be noted that, because XCTD probes have no pressure sensors, sensor depths are inferred from the fall rate and the inferred values can be biased. For CTD-4 probes, the depth bias is approximately 5 m (Tsurumi-Seiki Co., Ltd.).

2.3 Altimetric SSH Data

We used daily absolute SSH values from February 1, 2014 to March 31, 2019, which were obtained by adding the mean dynamic height topographic values (MDT_CNES-CLS13, Rio et al., 2011) to the Archiving, Validation and Interpretation of Satellite Oceanographic (AVISO) delayed-time updated mapped SSH anomaly data (AVISO, 2008). The SSH data are publicly available through the Copernicus Marine and Environment Monitoring Service (CMEMS).

3 RESULTS AND DISCUSSION

3.1 Seafloor Pressure Change due to the Formation of the Kuroshio LM Path

Throughout the whole observation periods from 2014 to 2019, the most remarkable seafloor pressure change was observed at station P1 prior to the formation of the 2017–present LM path (**Figure 4**). Therefore, we focused on the seafloor pressure changes in the fifth observation period from March 2017 to April 2019. **Figure 5** shows the daily mean anomaly in seafloor pressure across the continental slope to the east of Kyushu in this period. As shown in the SSH map for February 17, 2017 (**Figure 6A**), the Kuroshio current, indicated by a sharp SSH gradient between 80 and 120 cm, was located to the west of station P4 prior to the transition to the LM path. There exists a discontinuity of the pressure variations between stations P2 (**Figure 5C**) and P3 (**Figure 5B**). In particular, the steep pressure decrease of approximately 0.1 dbar from March to May 2017 was commonly observed at offshore stations P1 (**Figure 5D**) and P2 (**Figure 5C**) over the lower continental slope between depths of approximately 3000 and 4000 m.

During the period of the pressure decrease over the lower slope, SSH also varies in association with the northeastward propagation of a small meander, which brought about the LM path after coalesced with a cyclonic eddy off the eastern coast of the Kii Peninsula as reported by Nagano et al. (2019). Just before the decrease in pressure over the lower continental slope (March 2017), a negative SSH disturbance due to the small meander reached the south of the OBP stations (**Figure 6B**). Subsequently, as the small meander propagated northward in April, the SSH at the OBP sites decreased greatly (**Figure 6C**). SSH continued to be low until June (**Figures 6D,E**) and returned to higher values in August (**Figure 7A**). Meanwhile, the pressure over the lower slope was maintained low until the end of the OBP observation at least (**Figures 5C,D**).

At onshore stations P3 and P4 over the mid-continental slope, there was no remarkable pressure change though SSH greatly decreased by ~50 cm from February 2017 over these stations in June (**Figure 6E**) and July (**Figure 6F**) 2017. This no remarkable seafloor pressure change in the formation of the unstable-type LM path is different from the fact that in association with a large seafloor pressure depression, the small meander developed to the stable-type 2004–2005 LM path through the baroclinic instability (Nagano et al., 2018). In fact, the SSH depression related to the formation of the 2017–present LM path has a peculiar horizontal structure in the June SSH map (**Figure 6E**); the area of the SSH depression i.e., the perturbation streamline, is "leaned" against the Kuroshio current so as to attenuate the onshore cyclonic shear, as illustrated for the case of anticyclonic shear current in **Figure 7** of Pedlosky (1987). Judging from this horizontal structure of the SSH depression, the kinetic energy of the disturbance is likely derived from the kinetic energy of the Kuroshio current. In other words, the barotropic instability is effective for the moderate development of the disturbance. Numerical examinations by Nagano and Kawabe (2005) support the theory that the barotropic instability is effective in the initial stage of development of small meanders in the region southeast of Kyushu.

The cross-slope variation in seafloor pressure is indicative of the geostrophic deep current velocity variation in the direction parallel to the isobaths of the slope. Note that the temperature and salinity, and therefore, water density below the main pycnocline are quite uniform and do not change greatly during the study period. To evaluate the geostrophic current velocity based on seafloor pressure gradient between two neighboring OBP stations with different depths, we assumed that the pressure variation above the deeper station at a depth of the shallower station will be approximate to the variation at the seafloor pressure variation at the deeper station. Thus, the geostrophic current velocity variation can be expressed as, $v_b' = (1/f\overline{\rho})\partial p_b'/\partial x$ where p_b' is the pressure variation on the seafloor, f is the Coriolis parameter, $\overline{\rho}$ is the mean potential density, and x is the horizontal coordinate directed offshoreward along the OBP observation line. The horizontal gradient in the seafloor pressure variation, i.e., $\partial p_b'/\partial x$, was calculated by the difference in seafloor pressure variation at the neighboring two stations divided by the distance.

The seafloor pressure decrease over the lower slope caused a rapid decrease in pressure difference between P2 and P3, i.e., the northeastward bottom velocity anomaly on the slope between 2300 and 3000 m depths (red line in **Figure 8**). The velocity

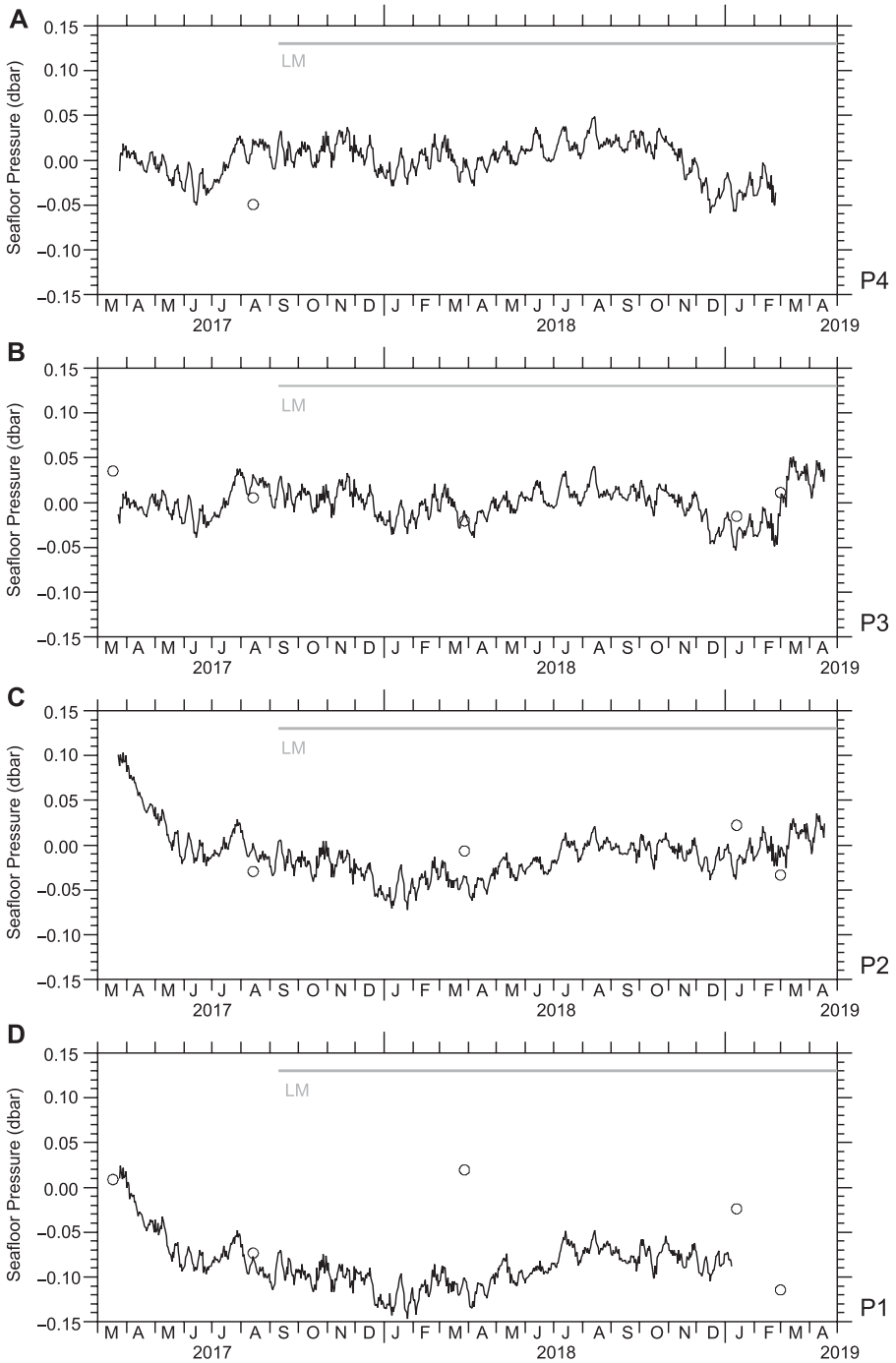

FIGURE 5 | OBP-measured seafloor pressure variations from March 2017 to April 2019 (fifth observation period) at the OBP stations: **(A)** P4, **(B)** P3, **(C)** P2, and **(D)** P1 (solid thin lines); and seafloor pressure estimated from CTD/XCTD and altimetric SSH data (open circles). For comparison between the OBP-measured time series and estimated values, the estimated values are shown after adding 1.05 dbar, and OBP-measured pressure at P1 and P2 are shown after subtraction of 0.086 and 0.010 dbar, respectively. The Kuroshio LM period is denoted by the horizontal gray line.

anomaly decreased by more than 80 cms^{-1} over approximately 3 months from March to May 2017. Fukasawa and Teramoto (1986) observed an abrupt reversal of a deep current of approximately 40 cms^{-1} from the west to the east during the formation of the 1981–1984 LM path by current meters installed at levels deeper than approximately 2,000 m over the lower slope deeper than 3,000 m off Cape Shiono-misaki, which is the southern tip of the Kii Peninsula. The maximal variation range of deep current velocity along the slope observed by Fukasawa and Teramoto (1986) was ~80 cms^{-1}. The

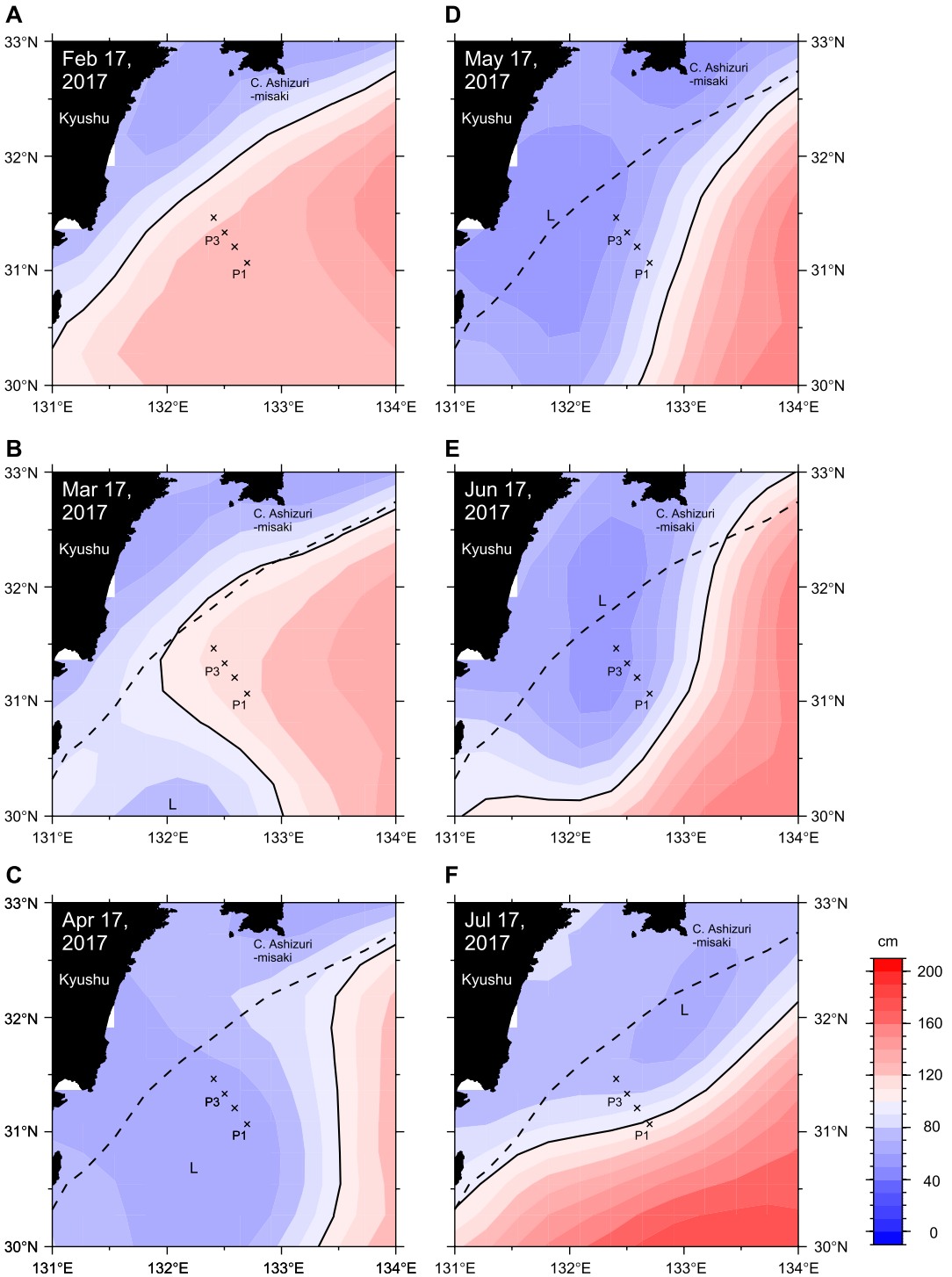

FIGURE 6 | Maps of absolute SSH (cm) off the eastern coast of Kyushu from **(A)** February 17 to **(E)** July 17, 2017 every one month. Paths of the Kuroshio current, defined as 100 cm contours of daily SSH, are delineated by the black solid curves. The current path on February 17, 2017 is shown in panels **(B)** to **(F)** by the black dashed curve as a representative NLM path prior to the transition to the LM path. Crosses indicate the locations of the OBP sites. The SSH depression associated with the small meander is denoted by letter L.

magnitudes and the depth ranges of the deep current changes are coincident in both unstable-type LM paths during the periods 1981–1984 and 2017–present, although the observation areas are approximately 400 km apart. We confirmed that, approximately 5 months after the seafloor pressure drop southeast of Kyushu, seafloor pressure was

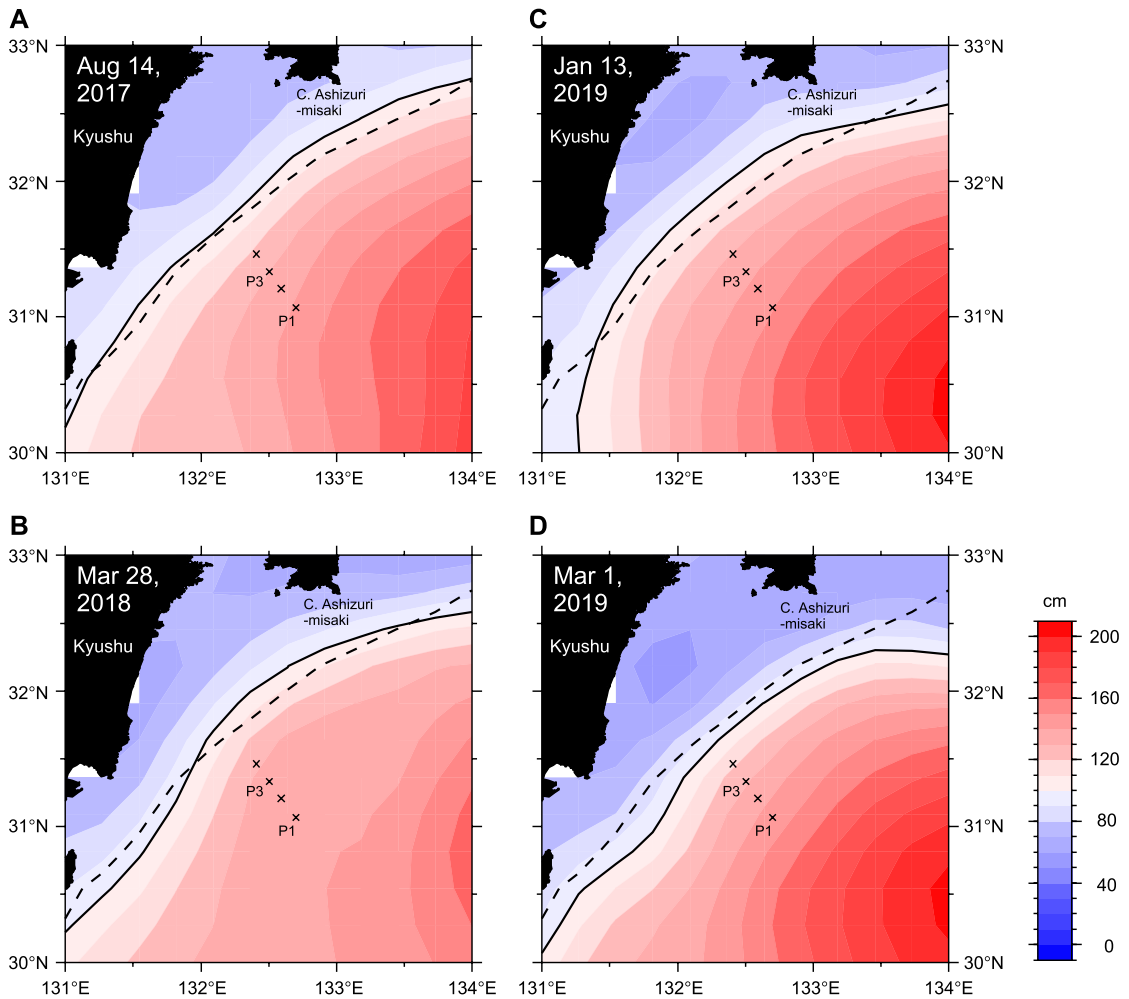

FIGURE 7 | Same as in **Fig. 6**, but for **(A)** August 14, 2017, **(B)** March 28, 2018, **(C)** January 13, 2019, and **(D)** March 1, 2019.

depressed over the lower continental slope deeper than 4000 m to the southeast of the Kii Peninsula, as discussed in **Section 3.3**. Therefore, the formation of the unstable-type LM path is anticipated to intensify the cyclonic deep circulation along the northern periphery of the Shikoku Basin as suggested its existence by Fukasawa et al. (1987).

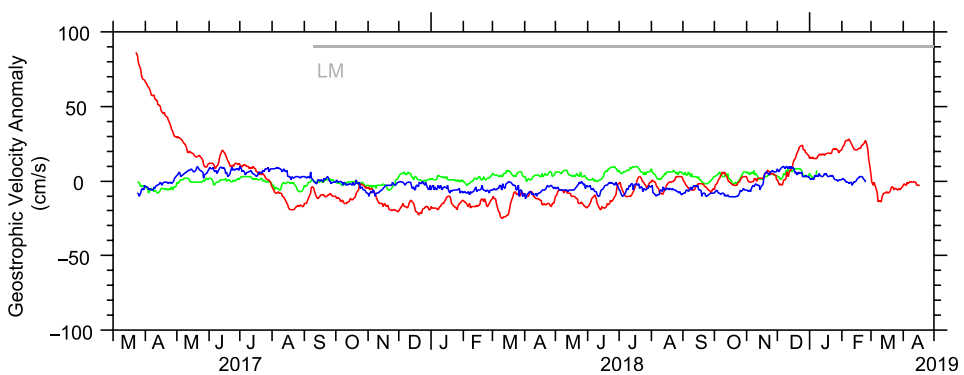

FIGURE 8 | Geostrophic velocity anomalies in the fifth observation period (March 2017–April 2019) estimated from the seafloor pressure difference between P1 and P2 (blue line), P2 and P3 (red line), and P3 and P4 (green line). Positive anomalies show northeastward current anomalies. The LM period is indicated by the horizontal gray line.

Nagano et al. (2018) also found a decrease in the upslope seafloor pressure gradient over the 2000–4000 m depth slope off Shikoku during the formation of the 2004–2005 stable-type LM path, but the magnitude (equivalent to ~10 cm s^{-1} velocity anomaly change) is quite smaller than the velocity changes due to the formations of the 1981–1984 LM path (Fukasawa and Teramoto, 1986) and the 2017–present LM path in this study. As described below, the greater pressure drop over the lower continental slope due to the unstable-type LM path can be attributed to the strong baroclinic change in the local recirculation south of Shikoku, which was studied by (Nishiyama et al. 1980; Nishiyama et al. 1981) and was called the Shikoku Basin local recirculation by Nagano et al. (2013).

If the LM path of the Kuroshio is controlled by the bottom slope, the enhancement in seafloor pressure gradient, or geostrophic deep current velocity, over the mid-continental slope, i.e., P3 and P4, should be observed in association with the formation of the LM path, as explained in **Section 1** and demonstrated by Nagano et al. (2018) for the case of the stable-type LM during the period 2004–2005. However, during the LM period from 2017 to the present, no salient deep Kuroshio current intensification, i.e., increase in seafloor pressure gradient, was observed beneath the Kuroshio between P3 and P4 (green line in **Figure 8**). The topographic steering is likely to be less effective for the 2017–present LM path than for the stable-type LM for 2004–2005. The weak topographic steering may be responsible for the unstable character of the 2017–present LM path.

3.2 Hydrographic Changes Related to Changes in Seafloor Pressure

The potential density at the OBP observation line changed corresponding to the seafloor pressure change in the transition to the LM path (**Figure 9**). On March 17, 2017, the head of a small meander approached the observation line (black contour in **Figure 6B**), and the main pycnocline denoted by a layer between isopycnal surfaces of approximately 25–27σ_θ did not vary across the observation line (**Figure 9A**). This nearly flat structure of isopycnal surfaces is typical of the offshore border of the Kuroshio in the NLM period. Meanwhile, after the pressure drop over the lower slope in August 2017 (**Figure 9B**) and during the subsequent LM period as in March 2018 (**Figure 9C**), January 2019 (**Figure 9D**), and March 2019 (**Figure 9E**), the main pycnocline further deepens offshore-ward, i.e., southeastward, owing to the strengthening of the Shikoku Basin local recirculation despite the existence of seasonal variations in the upper layer (shallower than approximately 300 m). After August 2017, the isopycnal surfaces below a level of approximately 26σ_θ at the offshore stations were deeper than those in March (white contours). Further, associated with the intensification of the recirculation, the offshore SSH in the LM period (**Figure 7**) is higher than that in February 2017 before the LM formation, i.e., a representative SSH state in the NLM period (**Figure 6A**).

In **Figures 10A–C**, we show the vertical profiles of potential temperature, salinity, and potential density collected at the offshore-most station P1, respectively. The main pycnocline

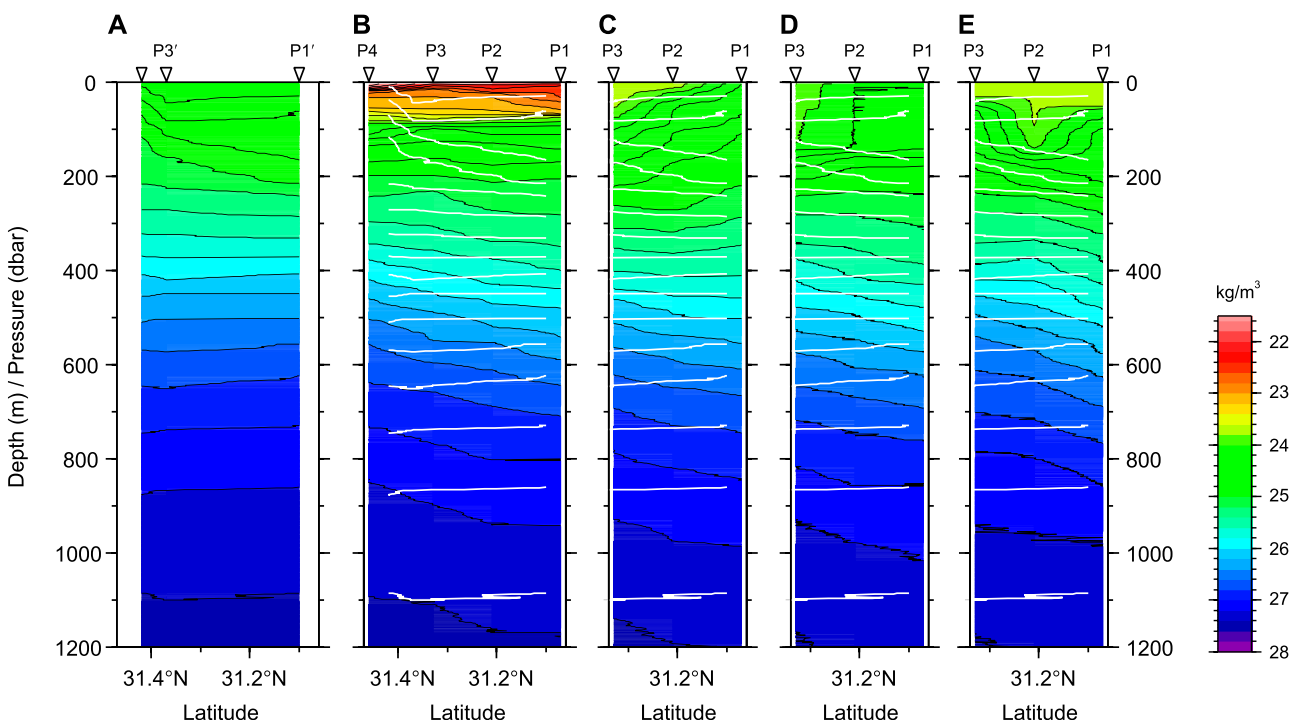

FIGURE 9 | Snapshot sections of potential density σ_θ (kg m^{-3}, color shading and black contours) east of Kyushu in **(A)** March 2017, **(B)** August 2017, **(C)** March 2018, **(D)** January 2019, and **(E)** March 2019. The contour interval is 0.2 kg m^{-3}. For comparison, isopycnals in **(A)** March 2017 are shown by white contours in panels **(B)**, **(C)**, **(D)**, and **(E)**. The inverted triangles indicate the hydrographic stations.

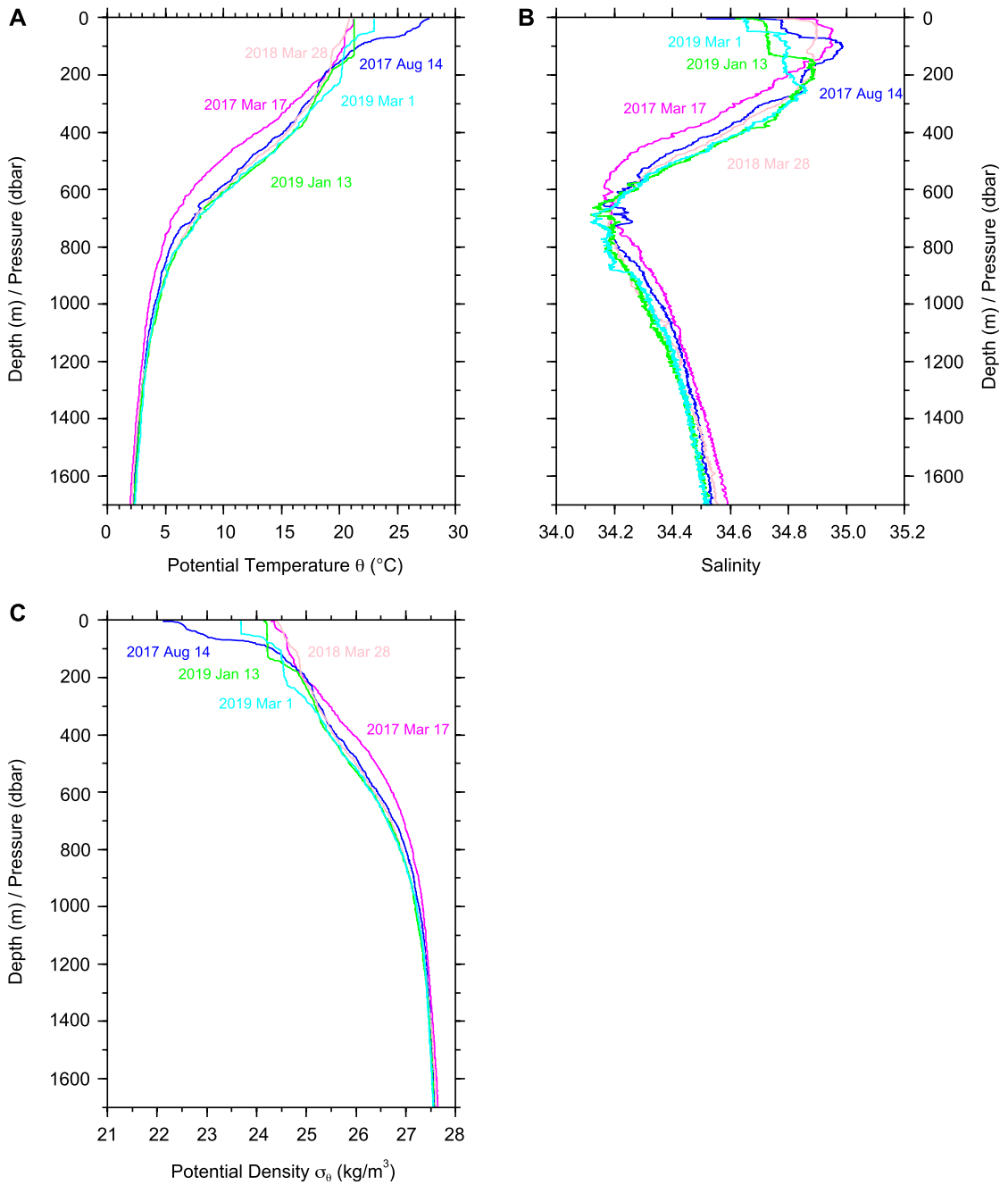

FIGURE 10 | Vertical distributions of **(A)** potential temperature θ (°C), **(B)** salinity in psu, and **(C)** potential density σ_θ (kg m^{-3}) at P1 in March 17, 2017 (magenta line), August 14, 2017 (blue line), March 28, 2018 (pink line), January 13, 2019 (green line), and March 1, 2019 (cyan line). Their observation times and seafloor pressure based on hydrographic and SSH data are indicated by magenta open circles in **Figure 4** and black open circles in **Figure 5D**.

was approximately 100 m shallower in March 2017 than in other periods (**Figures 10C**); it was also ~3°C colder (**Figures 10A**) and ~0.1 (psu) fresher (**Figures 10B**) around a depth of approximately 600 m, as derived from the North Pacific intermediate water characterized by the salinity minimum (approximately 700 m depth) in the LM period.

Using the hydrographic data, we computed the geopotential distance (m) at a depth of 1500 m or dbar relative to the sea surface as follows:

$$D_{1500} = \frac{1}{g}\int_{0\,\mathrm{m}}^{1500\,\mathrm{m}} \delta\, \mathrm{d}z, \qquad (2)$$

where z is the upward vertical coordinate; g = 9.81 m s^{-2}, the gravitational acceleration; and δ is the specific volume anomaly derived from the potential temperature and salinity data. For calculation, we discretized the vertical integration into summation of the 1-m value of δ from the sea surface (z = 0 m) to 1500 m or dbar. D_{1500} is a measure of the extent to which the density stratification mitigates the pressure loading due to an SSH change. Assuming the hydrostatic equilibrium and invariable deep-water density, the variation in seafloor pressure (p_b') can be approximated as

$$p_b' \approx g\overline{\rho_b}(\eta' - D_{1500}'), \quad (3)$$

where $\overline{\rho_b}$ is the mean water density below the depth of 1500 m; η', the SSH variation; and D_{1500}', geopotential distance variation (Nagano et al., 2018). By using **Eq. (3)**, we estimated seafloor pressure at the OBP stations based on altimetric SSH and hydrographic data (open circles in **Figures 4**,**5**) for comparison with the pressure measured by OBPs.

Just before the pressure drop over the lower slope (March 17, 2017), the values of seafloor pressure at P1 and P3 estimated from the altimetric SSH and hydrographic data are −1.041 and −1.015 dbar, respectively (**Table 2**). Taking into account the error of altimetric SSH observation (~3 cm) and lack of calculations below a depth of 1,500 m, their difference (0.026) may be insignificant. After the passage of the small meander off the eastern coast of Kyushu (August 14, 2017), the estimated seafloor pressure at P1 was decreased to −1.123 dbar. The decrease in seafloor pressure is similar to that in the pressure measured by the OBP (**Figure 5D**) and is principally due to the increase in D_{1500} (**Table 2**), i.e., the decrease is attributed to the baroclinic intensification of the Shikoku Basin local recirculation. As the local recirculation weakens in association with the decay of the LM path, the pressure over the lower slope will gradually increase.

However, possibly because the resolution of altimetric SSH data is too low in space and time to resolve the small-scale and high-frequency SSH fluctuations, the estimated seafloor pressure was sometimes not in agreement with the measured seafloor pressure as in the case of March 28, 2018. For example, in March 2018, the isopycnal surfaces in the top 200 m shoals southeastward (**Figure 9C**). An SSH fluctuation associated with this submesoscale (<25 km) density fluctuation cannot be fully detected by the satellite altimetry. The amplitudes of such small-scale SSH fluctuations are considered to be of the order of 10 cm, which is nearly equivalent to the discrepancy of the seafloor pressure values in March 2018, as expected from the root-mean-square differences between altimetric SSH and dynamic height based on hydrographic data in the subtropical gyre interior region calculated by Nagano et al. (2016). Meanwhile, at P3, the estimated seafloor pressure varied within a smaller range of ~0.06 dbar. Small-scale and high-frequency fluctuations may be more frequently present at P1 than P3.

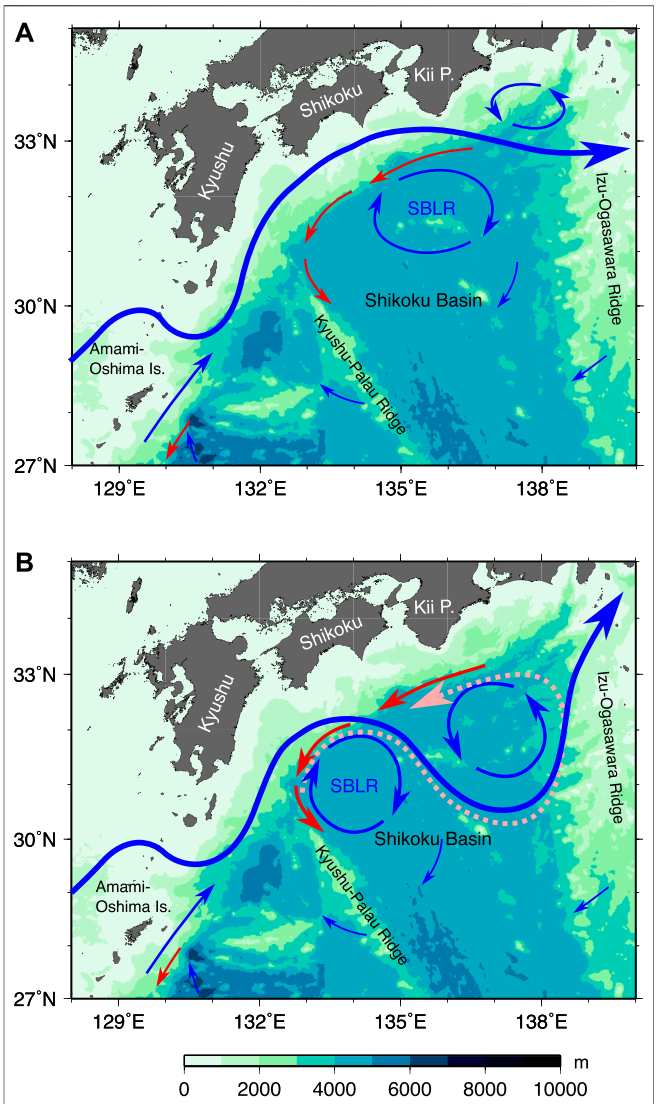

FIGURE 11 | Schematic diagrams of the sea surface (blue curve) and deep (red curve) currents for the **(A)** NLM and **(B)** LM paths. The expected propagation path of the fluctuation of the seafloor pressure decrease originated in the western limb of the Shikoku Basin local recirculation (SBLR) associated with the formation of the LM path is indicated by pink dotted curve.

3.3 Relation to the Seafloor Pressure Change South of the Kii Peninsula

In **Figure 11A**, the red curves show the deep currents that flow to the south of Shikoku (Worthington and Kawai, 1972; Taft, 1978; Fukasawa et al., 1987) and to the east of the Kyushu-Palau Ridge (Fukasawa et al., 1995) seeing the center of the Shikoku Basin to the left. It is reasonable that the offshore deepening of the main pycnocline and low seafloor pressure due to the strengthening of the Shikoku Basin local recirculation during the LM period should intensify the deep currents south of Shikoku and east of Kyushu as in **Figure 11B**. However, because the deep current south of the Kii Peninsula observed by Fukasawa and Teramoto (1986) is close to the cyclonic eddy south of the Kii Peninsula

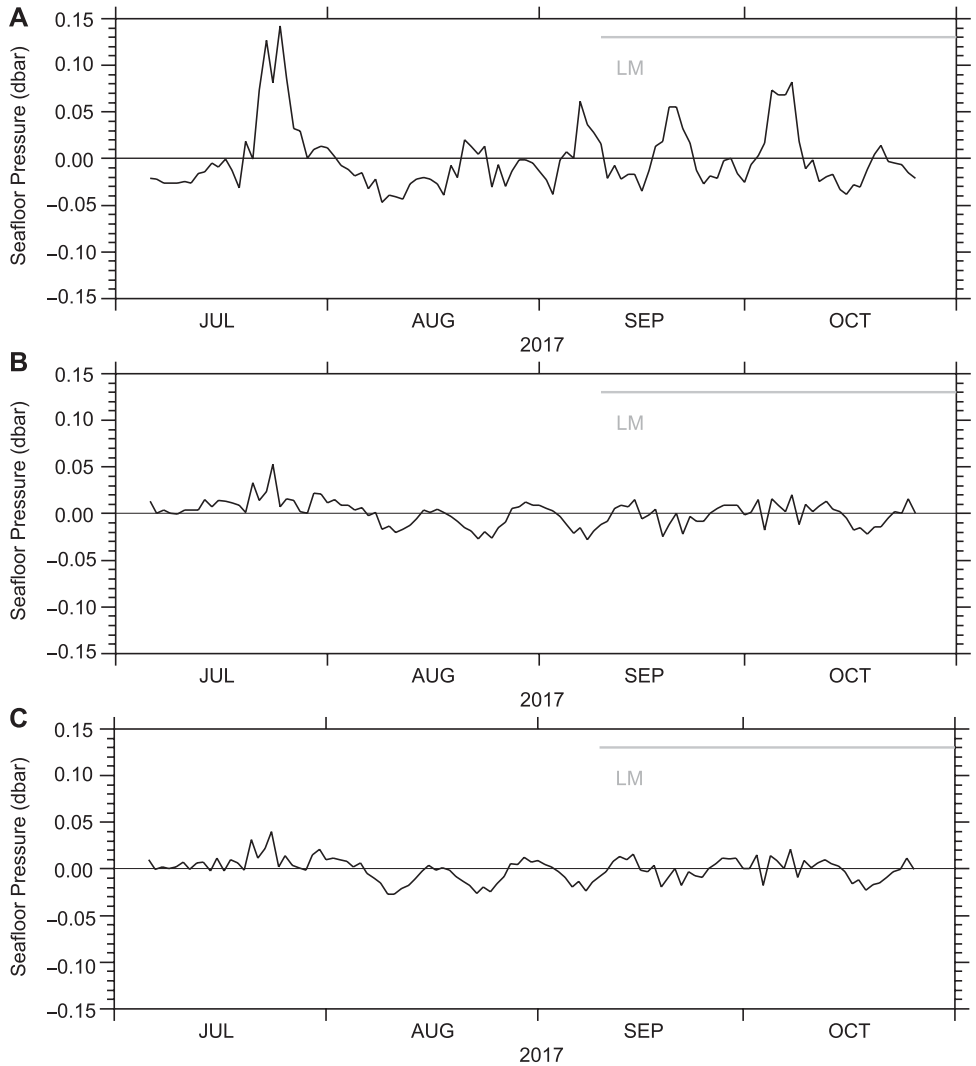

FIGURE 12 | OBP-measured daily mean seafloor pressure variations from July to October 2017 at **(A)** KMC09, **(B)** KMC10, and **(C)** KMC11. The Kuroshio LM period is shown by the horizontal gray line. Thin horizontal line indicates zero.

rather than the Shikoku Basin local recirculation, the deep current change off the Kii Peninsula is not under the direct influence of the local recirculation (**Figure 11B**). Considering that the main pycnocline shoals toward the center of the cyclonic eddy south of the Kii Peninsula (Nagano et al., 2010), the pressure disturbance originating from the recirculation may be advected by the deep Kuroshio current and also propagate along the cyclonic eddy south of the Kii Peninsula (pink dotted curve in **Figure 11B**). The transmitted pressure change may generate the westward deep current to the south of the Kii Peninsula.

To the southeast of the Kii Peninsula, seafloor pressure was depressed by ~0.05 dbar from late July to early August 2017 and continued to be low fluctuating on time scales of ~10–20 days, which is similar to the current velocity oscillation at the period of ~25 days observed by Fukasawa and Teramoto (1986), thereafter based on the data collected at stations KMC10 and KMC11 of DONET over the lower continental slope deeper than 4,000 m (**Figures 12B,C**). Meanwhile, no corresponding step-like decrease in pressure was identified at the shallower KMC09 station despite that a large peak (>0.15 dbar) was observed in late July (**Figure 12A**). The time lag between the decrease in seafloor pressure to the east of Kyushu and southeast of the Kii Peninsula is approximately 5 months. Taking into the consideration the distance along the LM path (~500 km), the propagation speed is estimated as 3.9 cms^{-1}.

Disturbances trapped in a deep flow below the main pycnocline are thought to propagate with the propagation speed of Doppler-shifted Rossby waves:

$$c_R = \left(\beta' - \beta\right)\lambda^2 + U, \quad (4)$$

where U is the advection speed; λ, the internal Rossby radius of deformation; β, the latitudinal variation of the Coriolis parameter f; and β', the horizontal gradient of potential vorticity due to the variation of the main pycnocline depth. Positive values indicate propagations in the direction of the Kuroshio, i.e., to the east. Using the northward shoaling of the main pycnocline depth dh/dy and the mean thickness between the pycnocline to the bottom H, we can express β' as $(f/H)dh/dy$. At 30°N latitude, f and β are 7.3×10^{-5} s^{-1} and 2.0×10^{-11} m^{-1} s^{-1}, respectively. If we set H = 2,000 m and $dh/dy = 0.5 \times 10^{-3}$ ($\beta' = 1.8 \times 10^{-11}$ m^{-1} s^{-1} and λ = 75 km), the first term of the right hand side of **Eq. 4**, the intrinsic Rossby wave propagation speed, is estimated as −1.0 cms^{-1}. Thus, the advection speed should be U = 4.8 cms^{-1}, based on the previous two numbers given, for disturbances to proceed in the deep layer along the outer edge of the cyclonic eddy and reach the southeast of the Kii Peninsula in 5 months. It is a reasonable value for the Kuroshio current speed below depths of 2,000 m. To validate the hypothesis, the mechanism of enhancement of the deep cyclonic circulation in the Shikoku Basin should be examined in future works.

4 SUMMARY AND CONCLUSIONS

To the south of Japan, the Kuroshio takes either the LM or NLM paths on interannual to decadal timescales. Nagano et al. (2019) classified the LM paths into the stable and unstable types based on the stability of the current path. The Kuroshio has taken the LM path since September 2017, and the LM path is active at present as of November 2020 although the cyclonic LM eddy has been separated from the Kuroshio. The 2017–present LM path is the unstable-type LM path because the current path greatly fluctuates on the timescale of months. In this study, we examined the characteristics of the seafloor pressure variation across the continental slope off the eastern coast of Kyushu in association with the formation of the 2017–present LM path in comparison with the stable-type LM path during the period 2004–2005. Additionally, we collected the five sets of hydrographic data from 2017 to 2019 by using CTD and XCTD profilers. By using the hydrographic data, we verified the seafloor pressure change related to the LM path formation is caused not by the sensor drift but by the ocean variation.

Before the formation of the 2017–present LM path, seafloor pressure rapidly decreased from March to May 2017 by approximately 0.1 dbar over the lower continental slope between depths of approximately 3000 and 4000 m (stations P1 and P2), accompanied by an SSH depression due to the passage of the small meander. While the SSH became high again in association with the intensification of the Shikoku Basin local recirculation, the seafloor pressure continued to be low until the end of the observation period (April 2019). Beneath the unstable-type LM path, no significant pressure change was observed over the onshore mid-continental slope (stations P3 and P4) and the topographic steering of the current was not effective unlike the 2004–2005 LM path of the Kuroshio. The pressure drop over the lower continental slope caused an attenuation of the northeastward geostrophic current anomaly over the continental slope between depths of approximately 2300 and 3000 m and the magnitude of the velocity variation reached approximately 80 cms^{-1}. This is similar to that observed south of the Kii Peninsula during the formation of the 1981–1984 unstable-type LM path (Fukasawa and Teramoto, 1986) but much larger than that observed to the south of Shikoku during the formation of the 2004–2005 stable-type LM path (Nagano et al., 2018). It is suggested that the formation of the unstable-type Kuroshio LM path greatly intensifies the cyclonic deep circulation along the northern periphery of the Shikoku Basin.

Corresponding to the pressure depression over the lower continental slope, the main pycnocline was found to be substantially deepened. The pressure depression over the lower slope off the eastern coast of Kyushu was attributed to the baroclinic intensification of the Shikoku Basin local recirculation. The seafloor pressure depression from March to May 2017 in association with the deepening of the main pycnocline generated in the recirculation is hypothesized to be advected by the deep Kuroshio current and to propagate along the outer edge of the cyclonic eddy south of the Kii Peninsula. Approximately 5 months after the seafloor pressure drop in March 2017, we found a seafloor pressure decrease of approximately 0.05 dbar in early August 2017 and a subsequent low seafloor pressure from the data of the DONET OBPs deployed over the lower slope deeper than 4000 m southeast of the Kii Peninsula. The 5-months time lag is consistent with the hypothesis that the seafloor pressure depression propagates along the outer edge of the cyclonic eddy south of the Kii Peninsula as a baroclinic Rossby wave advected in the deep Kuroshio current.

The magnitude of the seafloor pressure change (~0.1 dbar) and the rate of seafloor pressure change (0.0011 dbar day^{-1}) associated with the LM formation are equivalent to or larger than those due to slow slip events near the Nankai Trough expected from numerical simulation (Ariyoshi et al., 2014) and observed by the DONET (Suzuki et al., 2016) and near the Hikurangi subduction zone (Wallace et al., 2016). The LM-related decrease in seafloor pressure possibly occurs along the periphery of the Shikoku Basin and can not be identified by the SSH change alone. Thus, in addition to SSH data, *in situ* hydrographic measurements down to depths deeper than the main pycnocline base (~1,500 m) as in the present study or full-depth acoustic observation (Nagano et al., 2018) are helpful to distinguish the seafloor pressure change due to crustal deformation from those caused by the Kuroshio and recirculation variations.

DATA AVAILABILITY STATEMENT

The OBP and hydrographic observations of Hyuga-nada were conducted as part of "Research project for compound disaster mitigation on the great earthquakes and tsunamis around the Nankai Trough region," a project of Ministry of Education, Culture, Sports, Science and Technology and the data are available on request to the corresponding author. The DONET OBP data were provided by National Research Institute for Earth Science and Disaster Prevention (NIED) and JAMSTEC. The AVISO delayed-time updated mapped data (DT-SLA-H) and

absolute SSH values were computed by adding the mean dynamic topography values (MDT_CNES-CLS13) analyzed for this study can be found in the FTP site of the CMEMS.

AUTHOR CONTRIBUTIONS

AN estimated sensor drifts of the OBP data and corrected the data, analyzed the OBP, hydrographic, altimetric SSH data, and wrote the manuscript. YY designed and performed the OBP observations. KA provided XCTD probes for the hydrographic observations. TH and HM decided the locations of hydrographic observations in cooperation with AN, YY, and KA. MS conceived and promoted this project. All coauthors collaborated with the corresponding author (AN) in the construction of the manuscript and approved the final manuscript.

FUNDING

This work was partly supported by the Japan Society for the Promotion of Science, Grant-in-Aid for Scientific Research (Grant Numbers: JP15H04228, JP16H06473, JP17K05660, JP20K04072, JP20H02236).

ACKNOWLEDGMENTS

The authors thank the scientists, technicians, and crew on board the T/V Nagasaki Maru (Nagasaki University), R/V Kaiyo Maru No.2, R/V Kaiyo Maru No. 7 (Kaiyo Engineering Co., Ltd.), and R/V Kaiko Maru No. 7 (Offshore Operation Co., Ltd.) for deployment and recovery operations of OBPs and collecting hydrographic data. The authors are deeply grateful to the editor, Ryota Hino (Tohoku University), and anonymous reviewers for constructive review comments.

SUPPLEMENTARY MATERIAL

The Supplementary Material for this article can be found online at: https://www.frontiersin.org/articles/10.3389/feart.2020.583481/full#supplementary-material.

REFERENCES

Ando, M. (1975). Source mechanisms and tectonic significance of historical earthquakes along the Nankai trough, Japan. *Tectonophysics* 27, 119–140. doi:10.1016/0040-1951(75)90102-X

Ariyoshi, K., Nakata, R., Matsuzawa, T., Hino, R., Hori, T., Hasegawa, A., et al. (2014). The detectability of shallow slow earthquakes by the Dense Oceanfloor Network system for Earthquakes and Tsunamis (DONET) in Tonankai district, Japan. *Mar. Geophys. Res.* 35, 295–310. doi:10.1007/s11001-013-9192-6

AVISO (2008). SSALTO/DUACS user handbook: (M)SLA and (M)ADT near-real time and delayed time products. Ramonville St Agnes: CLS.

Cushman-Roisin, B., and Beckers, J.-M. (2011). *Introduction to Geophysical fluid dynamics*. 2nd Edn. Cambridge, Massachusetts: Academic Press.

Fukasawa, M., and Teramoto, T. (1986). Characteristics of deep currents off Cape Shiono-misaki before and after formation of the large meander of the Kuroshio in 1981. *J. Oceanogr. Soc. Japan* 42, 53–68. doi:10.1007/BF02109192

Fukasawa, M., Teramoto, T., and Taira, K. (1987). Abyssal current along the northern periphery of Shikoku Basin. *J. Oceanogr. Soc. Japan* 42, 459–472. doi:10.1007/BF02110196

Fukasawa, M., Teramoto, T., and Taira, K. (1995). Hydrographic structure in association with deep boundary current in the north of the Shikoku Basin. *J. Oceanogr.* 51, 187–205. doi:10.1007/bf02236524

Gill, A. E. (1982). *Atmosphere-ocean dynamics*. Cambridge, Massachusetts: Academic Press.

Hasegawa, T., Nagano, A., Matsumoto, H., Ariyoshi, K., and Wakita, M. (2019). El Niño-related sea surface elevation and ocean bottom pressure enhancement associated with the retreat of the Oyashio southeast of Hokkaido, Japan. *Mar. Geophys. Res.* 40, 505–512. doi:10.1007/s11001-019-09392-8

Houston, M. H., and Paros, J. M. (1998). "High accuracy pressure instrumentation for underwater applications," in Proceedings of 1998 International Symposium on Underwater Technology, Tokya, Japan, April 17, 1998, (IEEE). doi:10.1109/UT.1998.670113

Ishibashi, K. (2004). Status of historical seismology in Japan. *Ann. Geophys.* 47, 339–368.

Kawabe, M. (1985). Sea level variations at the Izu Islands and typical stable paths of the Kuroshio. *J. Oceanogr. Soc. Japan.* 41, 307–326.

Kawabe, M. (1986). Transition processes between the three typical paths of the Kuroshio. *J. Oceanogr. Soc. Japan* 42, 174–191. doi:10.1007/BF02109352

Kawabe, M. (1987). Spectral properties of sea level and time scales of Kuroshio path variations. *J. Oceanogr. Soc. Japan* 43, 111–123.

Kawabe, M. (1995). Variations of current path, velocity, and volume transport of the Kuroshio in relation with the large meander. *J. Phys. Oceanogr.* 25, 3103–3117. doi:10.1175/1520-0485(1995)025<3103:VOCPVA>2.0.CO;2

Kawabe, M. (2005). Variations of the Kuroshio in the southern region of Japan – condition for large meander of the Kuroshio. *J. Oceanogr.* 61, 529–537. doi:10.1007/s10872-005-0060-0

Kobari, T., Honma, T., Hasegawa, D., Yoshie, N., Tsutsumi, E., Matsuno, T., et al. (2020). Phytoplankton growth and consumption by microzooplankton stimulated by turbulent nitrate flux suggest rapid trophic transfer in the oligotrophic Kuroshio. *Biogeosciences* 17, 2441–2452. doi:10.5194/bg-17-2441-2020

Kuwano-Yoshida, A., and Minobe, S. (2017). Storm-track response to SST fronts in the northwestern Pacific region in an AGCM. *J. Climate* 30, 1081–1102. doi:10.1175/JCLI-D-16-0331.1

Latif, M., and Barnett, T. (1994). Causes of decadal climate variability over the north pacific and north America. *Science* 266, 634–637. doi:10.1126/science.266.5185.634

Mizuno, K., and Watanabe, T. (1998). Preliminary results of *in-situ* XCTD/CTD comparison test. *J. Oceanogr* 54, 373–380.

Munk, W. H. (1950). On the wind-driven ocean circulation. *J. Meteor.* 7, 79–93. doi:10.1175/1520-0469(1950)007<0080:OTWDOC>2.0.CO;2

Nagano, A., Hasegawa, T., Matsumoto, H., and Ariyoshi, K. (2018). Bottom pressure change associated with the 2004–2005 large meander of the Kuroshio south of Japan. *Ocean Dynam.* 68, 847–865. doi:10.1007/s10236-018-1169-1

Nagano, A., Ichikawa, K., Ichikawa, H., Konda, M., and Murakami, K. (2013). Volume transports proceeding to the Kuroshio extension region and recirculating in the Shikoku Basin. *J. Oceanogr.* 69, 285–293. doi:10.1007/s10872-013-0173-9

Nagano, A., Ichikawa, K., Ichikawa, H., Tomita, H., Tokinaga, H., and Konda, M. (2010). Stable volume and heat transports of the North Pacific subtropical gyre revealed by identifying the Kuroshio in synoptic hydrography south of Japan. *J. Geophys. Res.* 115, 5747. doi:10.1029/2009JC005747

Nagano, A., and Kawabe, M. (2004). Monitoring of generation and propagation of the Kuroshio small meander using sea levels along the southern coast of Japan. *J. Oceanogr.* 60, 879–892. doi:10.1007/s10872-004-5780-z

Nagano, A., and Kawabe, M. (2005). Coastal disturbance in sea level propagating along the south coast of Japan and its impact on the Kuroshio. *J. Oceanogr.* 61, 885–903. doi:10.1007/s10872-006-0007-0

Nagano, A., Kizu, S., Hanawa, K., and Roemmich, D. (2016). Heat transport variation due to change of North Pacific subtropical gyre interior flow during 1993–2012. *Ocean Dynam.* 66, 1637–1649. doi:10.1007/s10236-016-1007-2

Nagano, A., Yamashita, Y., Hasegawa, T., Ariyoshi, K., Matsumoto, H., and Shinohara, M. (2019). Characteristics of an atypical large-meander path of the Kuroshio current south of Japan formed in September 2017. *Mar. Geophys. Res.* 40, 525–539. doi:10.1007/s11001-018-9372-5

Nakano, M., Hyodo, M., Nakanishi, A., Yamashita, M., Hori, T., Kamiya, S., et al. (2018). The 2016 M_W5.9 earthquake off the southeastern coast of Mie Prefecture as an indicator of preparatory processes of the next Nankai Trough megathrust earthquake. *Prog. Earth Planet Sci.* 5, 3. doi:10.1186/s40645-018-0188-3

Nishiyama, K., Konaga, S., and Ishizaki, H. (1980). Warm water regions off Shikoku associated with the Kuroshio meander. *Pap. Meteor. Geophys.* 31, 43–52.

Nishiyama, K., Konaga, S., and Ishizaki, H. (1981). Some considerations on the Kuroshio meander and the surrounding oceanographic conditions. *Pap. Meteor. Geophys.* 32, 109–117.

Nitani, H. (1972). "Beginning of the Kuroshio," in *Kuroshio-its physical aspects*, Editors. H. Stommel and K. Yoshida Tokyo, Japan: University of Tokyo Press, 129–163.

Pedlosky, J. (1987). *Geophysical fluid dynamics*. 2nd Edn. New York: Springer-Verlag. doi:10.1007/978-1-4612-4650-3

Pedlosky, J. (1996). *Ocean Circulation theory*. New York: Springer-Verlag. doi:10.1007/978-3-662-03204-6

Polster, A., Fabian, M., and Villinger, H. (2009). Effective resolution and drift of Paroscientific pressure sensors derived from long-term seafloor measurements. *Geochem. Geophys. Geosyst.* 10, 2532. doi:10.1029/2009GC002532

Rio, M. H., Guinehut, S., and Larnicol, G. (2011). New CNES-CLS09 global mean dynamic topography computed from the combination of GRACE data, altimetry, and *in situ* measurements. *J. Geophys. Res.* 116, 6505. doi:10.1029/2010JC006505

Schwartz, S. Y., and Rokosky, J. M. (2007). Slow slip events and seismic tremor at circum-pacific subduction zones. *Rev. Geophys.* 45, 208. doi:10.1029/2006RG000208

Shoji, D. (1972). "Time variation of the Kuroshio south of Japan," in *Kuroshio-its physical aspects*. Editors. H. Stommel and K. Yoshida, Tokyo, Japan: University of Tokyo Press. 217–234.

Stommel, H. (1948). The westward intensification of wind-driven ocean currents. *Trans. Am. Geophys. Union* 29, 202–206.

Suzuki, K., Nakano, M., Takahashi, N., Hori, T., Kamiya, S., Araki, E., et al. (2016). Synchronous changes in the seismicity rate and ocean-bottom hydrostatic pressures along the Nankai trough: a possible slow slip event detected by the Dense Oceanfloor Network system for Earthquakes and Tsunamis (DONET). *Tectonophysics* 680, 90–98. doi:10.1016/j.tecto.2016.05.012

Taft, B. (1972). "Characteristics of the flow of the Kuroshio south of Japan," in *Kuroshio-its physical aspects*, Editors. H. Stommel and K. Yoshida, Tokyo, Japan: University of Tokyo Press, 165–216.

Taft, B. (1978). Structure of Kuroshio south of Japan. *J. Mar. Res.* 36, 77–117.

Taira, K., and Teramoto, T. (1985). Bottom currents in Nankai Trough and sagami trough. *J. Oceanogr. Soc. Japan* 41, 388–398.

Thompson, R. (1983). Low-pass filters to suppress inertial and tidal frequencies. *J. Phys. Oceanogr.* 13, 1077–1083. doi:10.1007/BF02109033

Tian, Y., Uchikawa, K., Ueda, Y., and Cheng, J. (2014). Comparison of fluctuations in fish communities and trophic structures of ecosystems from three currents around Japan: synchronies and differences. *ICES Journal of Marine Science* 71, 19–34. doi:10.1093/icesjms/fst169

Wallace, L. M., Webb, S. C., Ito, Y., Mochizuki, K., Hino, R., Henrys, S., et al. (2016). Slow slip near the trench at the Hikurangi subduction zone, New Zealand. *Science* 352, 701–704. doi:10.1126/science.aaf2349

Watts, D. R., and Kontoyiannis, H. (1990). Deep-ocean bottom pressure measurement: drift removal and performance. *J. Atmos. Oceanic Technol.* 7, 296–306. doi:10.1175/1520-0426(1990)007<0296:DOBPMD>2.0.CO;2

Worthington, L., and Kawai, H. (1972). "Comparison between deep sections across the Kuroshio and the Florida current and gulf stream," in *Kuroshio-its physical aspects*, Editors H. Stommel and K. Yoshida Tokyo, Japan: University of Tokyo Press. 371–385.

Yoshida, S. (1964). A note on the variations of the Kuroshio during recent years. *Bull. Japan. Soc. Fish. Oceanogr.* 5, 66–69.

Conflict of Interest: The authors declare that the research was conducted in the absence of any commercial or financial relationships that could be construed as a potential conflict of interest.

The handling editor declared a past co-authorship with several of the authors (MS and KA).

frontiers in Earth Science

ORIGINAL RESEARCH
published: 15 January 2021
doi: 10.3389/feart.2020.600671

A Thirty-Month Seafloor Test of the A-0-A Method for Calibrating Pressure Gauges

William S. D. Wilcock[1], Dana A. Manalang[2], Erik K. Fredrickson[1], Michael J. Harrington[2], Geoff Cram[2], James Tilley[2], Justin Burnett[2], Derek Martin[2], Taro Kobayashi[3] and Jerome M. Paros[3]*

[1]School of Oceanography, University of Washington, Seattle, WA, United States, [2]Applied Physis Laboratory, University of Washington, Seattle, WA, United States, [3]Paroscientific, Inc., Redmond, WA, United States

Geodetic observations in the oceans are important for understanding plate tectonics, earthquake cycles and volcanic processes. One approach to seafloor geodesy is the use of seafloor pressure gauges to sense vertical changes in the elevation of the seafloor after correcting for variations in the weight of the overlying oceans and atmosphere. A challenge of using pressure gauges is the tendency for the sensors to drift. The A-0-A method is a new approach for correcting drift. A valve is used to periodically switch, for a short time, the measured pressure from the external ocean to the inside of the instrument housing at atmospheric pressure. The internal pressure reading is compared to an accurate barometer to measure the drift which is assumed to be the same at low and high pressures. We describe a 30-months test of the A-0-A method at 900 m depth on the MARS cabled observatory in Monterey Bay using an instrument that includes two A-0-A calibrated pressure gauges and a three-component accelerometer. Prior to the calibrations, the two pressure sensors drift by 6 and 2 hPa, respectively. After the calibrations, the offsets of the corrected pressure sensors are consistent with each other to within 0.2 hPa. The drift corrected detided external pressure measurements show a 0.5 hPa/yr trend of increasing pressures during the experiment. The measurements are corrected for instrument subsidence based on the changes in tilt measured by the accelerometer, but the trend may include a component of subsidence that did not affect tilt. However, the observed trend of increasing pressure, closely matches that calculated from satellite altimetry and repeat conductivity, temperature and depth casts at a nearby location, and increasing pressures are consistent with the trend expected for the El Niño Southern Oscillation. We infer that the A-0-A drift corrections are accurate to better than one part in 10^5 per year. Additional long-term tests and comparisons with oceanographic observations and other methods for drift correction will be required to understand if the accuracy the A-0-A drift corrections matches the observed one part in 10^6 per year consistency between the two pressure sensors.

Keywords: seafloor geodesy, pressure gauge calibration, MARS cabled observatory, Monterey Bay, A-0-A method

OPEN ACCESS

Edited by:
Keiichi Tadokoro, Nagoya University, Japan

Reviewed by:
Yoshihiro Ito, Kyoto University, Japan
Spahr Webb, Lamont Doherty Earth Observatory, United States

****Correspondence:***
William S. D. Wilcock
wilcock@uw.edu

Specialty section:
This article was submitted to Solid Earth Geophysics, a section of the journal Frontiers in Earth Science

Received: *30 August 2020*
Accepted: *25 November 2020*
Published: *15 January 2021*

Citation:
Wilcock WSD, Manalang DA, Fredrickson EK, Harrington MJ, Cram G, Tilley J, Burnett J, Martin D, Kobayashi T and Paros JM (2021) A Thirty-Month Seafloor Test of the A-0-A Method for Calibrating Pressure Gauges. Front. Earth Sci. 8:600671. doi: 10.3389/feart.2020.600671

INTRODUCTION

On land, dense geodetic observations from global navigation satellite systems and interferometric synthetic aperture radar have transformed our understanding of plate tectonics, earthquake cycles and volcanic processes (Bürgmann and Thatcher, 2013; Doglioni and Riguzzi, 2018). On the seafloor, geodetic observations are more challenging because seawater does not propagate electromagnetic waves, but they are nevertheless important (Bürgmann and Chadwell, 2014; Fujimoto, 2014). Most of the Earth's volcanism occurs underwater and most plate boundaries lie within the oceans or near coastlines, including subduction zones that host the largest and many of the most destructive earthquakes. To characterize and mitigate seismic and tsunami risk, seafloor geodesy is needed in subduction zones to determine where the faults are locked and where they are partially or completely slipping by steady creep or episodic slow slip (e.g., Wang and Tréhu, 2016). Seafloor geodesy is also necessary for improving our understanding of the dynamic processes at ocean spreading centers, transform faults and hotspot volcanoes (e.g., Chadwell et al., 1999; Chadwick et al., 2006; McGuire and Collins, 2013). Furthermore, along some coastlines, geodetic observations are of potential importance for monitoring the stability of submarine slopes (Blum et al., 2010).

There are several established methods for seafloor geodesy (Bürgmann and Chadwell, 2014; Fujimoto, 2014) and extensive research efforts are underway to develop new techniques (e.g., Zumberge et al., 2018; DeSanto and Sandwell, 2019). One longstanding approach is the use of seafloor pressure gauges to sense vertical changes in the elevation of the seafloor after correction for variations in the weight of the overlying oceans and atmosphere. This method was first pioneered to monitor the elevation of Axial Seamount (Fox, 1990; Fox, 1993) where the subsidence associated with an eruption in 1998 was measured (Fox, 1999). At this site continuous monitoring of the inflation and deflation associated with the eruptive cycles now spans more than 2 decades (Chadwick et al., 2012; Nooner and Chadwick, 2016). More recently, bottom pressure measurements have been used successfully in several subduction zones to detect and characterize slow slip events updip of the seismogenic zone occurring on time scales of weeks (Ito et al., 2013; Davis et al., 2015; Suzuki et al., 2016; Wallace et al., 2016), thus contributing to our understanding of megathrust coupling.

There are two primary challenges of using bottom pressure gauges for seafloor geodesy. First, the detection of slow slip events requires that the pressure records are corrected to remove oceanographic signals that can have timescales that are similar to those of slow slip events. This is most simply done by differencing nearby stations under the assumption that the oceanographic signals are largely invariant over short distances (e.g., Ito et al., 2013), but studies have also explored the use of ocean circulation models to predict the oceanographic component of bottom pressure (Inazu et al., 2012; Fredrickson et al., 2019b; Muramoto et al., 2019). Second, there is a tendency for bottom pressure gauges to drift. The highest resolution pressure sensors, manufactured by Paroscientific, Inc., are subject to long term measurement drift at typical rates of up to ~1 part in 10^4 per year (Chiswell and Lukas, 1989; Watts and Kontoyiannis, 1990; Polster et al., 2009; Matsumoto et al., 2014), which cannot be predicted from laboratory calibrations before and after a seafloor deployment or from the drift observed on previous deployments. Drift limits the utility of bottom pressure measurements for resolving long-term strain signals and if the drift rate is changing, complicates the process of identifying transient geodetic signals.

There are three observational approaches to removing pressure sensor drift. The first is to use a mobile pressure recorder carried by a submersible, usually a remotely operated vehicle (ROV), in a closed loop survey to measure the pressure on a series of concrete benchmarks (Chadwick et al., 2006). Repeat visits are then used to correct for the drift of the mobile pressure recorder before calculating the relative pressure values on each benchmark. If one benchmark is assumed to be stable, then repeat surveys can be used to remove the drift from continuous pressure records deployed at the benchmarks. The method has been shown to have a repeatability of <1 hPa (1 cm H_2O) (Chadwick et al., 2006; Nooner et al., 2014). Recent enhancements include the application of laser leveling techniques to match the depth of the mobile pressure recorder to the bottom pressure gauge without the need for a concrete benchmark (Nishida et al., 2019) and the development of a system that maintains the mobile pressure recorder between deployments at seafloor temperature and pressure hPa (Araki et al., 2019). This second enhancement allows the mobile pressure recorder to be calibrated in the laboratory against a deadweight tester (also known as a piston gauge), a laboratory apparatus that combines an accurately measured mass and a rotating oil filled piston cylinder to generate a known pressure accurate to ~1 hPa. By closing the survey loop in the laboratory, there is no need for the calibrations to be conducted on a single dive and absolute rather than relative pressure is determined.

The second approach is to incorporate a deadweight tester into the bottom pressure recorder. The self-calibrating pressure recorder (SCPR) (Sasagawa and Zumberge, 2013; Sasagawa et al., 2016) employs a redundant pair of Paroscientific pressure gauges that record ambient external pressure except for short intervals when they are connected by turning a valve to a deadweight tester that is configured to generate a pressure that closely matches the external pressure. By periodically repeating the calibrations with the deadweight tester, the drift of the sensors can again be measured to within ~1 hPa. A mobile version of this instrument, the absolute self-calibrating pressure recorder (ASCPR) has also been developed to make absolute pressure measurements on benchmarks visited by a remotely operated vehicle (Cook et al., 2017).

The third approach known as A-0-A (ambient–zero/atmospheric–ambient) is similar conceptually to the SCPR, except that the deadweight tester is replaced by the internal pressure of the instrument housing measured by an accurate

barometer. This leads to an instrument that is more compact and less complex than the SCPR at the expense of measuring relative rather than absolute pressure. The method relies on the assumption that the sensor drift is the same at low pressures as it is at high pressures, so that the span or sensitivity of the sensor do not change. Support for this approach first came from work to develop an efficient and reproducible means to calibrate pressure gauges at high pressures for short intervals (0-A-0) for industrial applications (Kajikawa and Kobata, 2014; Kajikawa and Kobata, 2016). The A-0-A approach has been tested in the laboratory using multiple pressure sensors (Sasagawa et al., 2018). Over 12 months, the drift rates for Paroscientific sensors measured by A-0-A calibrations with an uncertainty of ~2 hPa/yr, were indistinguishable from those obtained by repeated calibrations with a deadweight tester.

The Monterey Accelerated Research System (MARS) cabled observatory has been previously used to demonstrate the high resolution Paroscientific pressure sensors for tsunami warning and earthquake recording (Paros et al., 2012a; Paros et al., 2012b). In this paper, we describe a 30-months seafloor test on the MARS observatory of an instrument that incorporates a triaxial accelerometer and a pair of A-0-A calibrated pressure recorders. This test is the first multi-year seafloor test of the A-0-A calibration approach in the academic community.

MATERIALS AND METHODS

Seafloor Experiment

The instrument developed for the seafloor test, which we have named the Geodetic and Seismic Sensor Module (GSSM) (**Figure 1**), utilizes a Paroscientific Seismic and Ocean Sensors (SOS) module comprising two absolute pressure gauges with a maximum depth rating of 1,400 m, an accurate Paroscientific barometer to measure the internal pressure of the housing, a Quartz Seismic Sensors triaxial accelerometer, and Paroscientific nano-resolution processing electronics. Each of these sensors works by measuring the change in oscillation frequency of a quartz crystal that is strained under pressure- or acceleration-induced loads. Each sensors also contains an unstrained quartz crystal temperature sensor to measure and correct for thermal effects (see for example Watts and Kontoyiannis (1990) for a description of the pressure gauge).

As in the SCPR, the oil filled lines to the pressure sensor are connected to a 3-way Swagelok ball valve that is operated by a Hanbay motorized actuator to switch between the external ocean

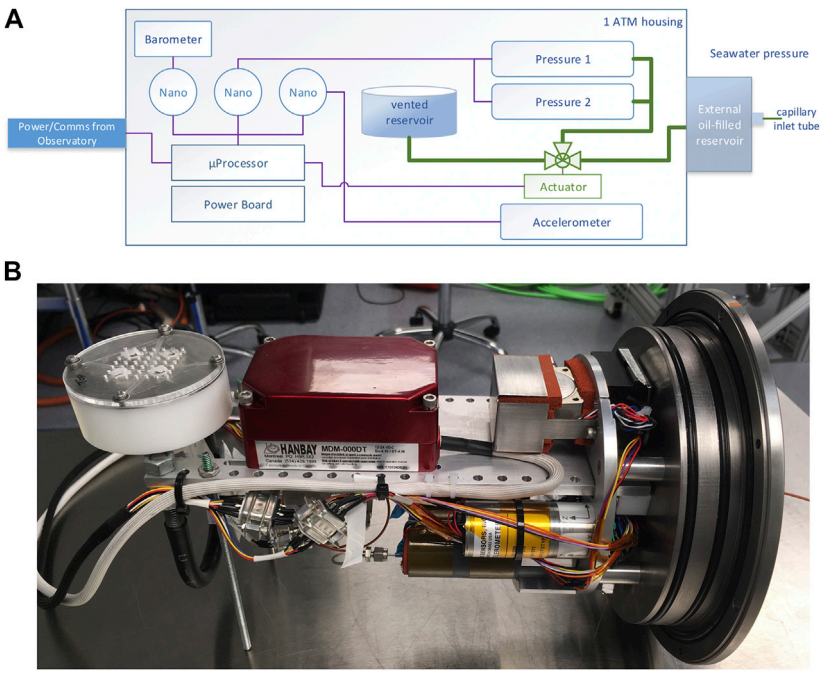

FIGURE 1 | (A) Block diagram for the Geodetic and Seismic Sensor Module (GSSM). A pair of Paroscientific pressure sensors (model 42K-101) connect to an actuator-controlled, 3-way ball valve that toggles between external seawater pressure and internal housing pressure of ~1 atm by sending commands from shore. The Paroscientific barometer (model 216B) provides an accurate reference measurement of internal housing pressure. A Quartz Seismic Sensors three-component accelerometer continuously monitors seafloor motion. Three Paroscientific Nano-Resolution electronics boards capture high resolution sensor measurements, timestamping them and passing them in real time to an onshore computer through the microprocessor. Thick green lines represent oil-filled plumbing. Thin purple lines represent data paths. **(B)** Photograph of the GSSM in the laboratory. The Paroscientific Seismic and Ocean Sensors module is on the right-hand side with the barometer on top, the accelerometer in the front on the bottom and one of the pressure sensors visible behind. The Hanbay valve actuator is in the center and the internal oil reservoir on the left. Reproduced from Wilcock et al. (2018).

pressure and the internal pressure for the A-0-A calibrations. For this experiment, the oil used was Dow Corning FS-1265 flurosilicone fluid (300 centistoke-grade kinematic viscosity), which has a density of 1,250 kg m^{-3} and is thus denser than seawater. A small amount of oil leaks through the valve into the pressure case when the valve turns, so an external oil reservoir is included to prevent the ingress of seawater to the instrument plumbing, and an internal reservoir captures the oil within the instrument housing and avoids the potential effects of surface tension if the oil is allowed to drip from the internal tubing. Based on laboratory measurements that showed ~4 cm^3 of oil would leak through the valve for 100 turns at high pressure, the external reservoir was conservatively designed with a capacity of 40 cm^3 for ~1,000 valve cycles with the expectation that the number of calibrations would not exceed 200. The external oil reservoir is a cylindrical chamber machined in plexiglass with the axis oriented horizontally (**Figure 2A**). An outlet at the bottom connects to the plumbing in the pressure housing and an outlet at the top connects to the ocean via a short length of thin horizontal peek capillary tubing. As oil leaks through the valve, seawater replaces oil at the top of the chamber. The internal fluid reservoir is a simple cup with an internal diameter of 7 cm. The wide cross-sectional area was chosen to minimize the change in oil elevation that would occur during the deployment, but the design requires the instrument orientation to be maintained within ~20° at all times during deployment to avoid oil spilling out.

The MARS cabled observatory operated by Monterey Bay Aquarium Research Institute (MBARI) provided power, communications to control the valve and retrieve the data, and precise one pulse per second timing. Custom electronics condition the incoming observatory power and custom software provide a user interface through which operators can control the internal valve and sensors in real time from shore. The GSSM was deployed at 36° 42.7481′N, 122° 11.2139′W at a depth of 887°m (**Figure 3**) on June 13, 2017 using the MBARI R/V *Rachel Carson* and ROV *Ventana*. For the deployment, the pressure housing was secured to a triangular grated platform, measuring ~80 cm on each side (**Figure 2**). Three 5-cm-diameter hollow cylindrical legs made of fiberglass extended ~30 cm beneath the platform and were designed to be driven into the soft muddy sediment to embed the instrument into the seafloor. The GSSM was attached to the junction box on the MARS cabled observatory with a 50-m-long Falmat power and ethernet cable with a wet-mate ODI connector. Data collection ended on December 14, 2019 and the instrument was recovered on December 17, 2019 by the same vessel and ROV. Prior to the recovery, the legs of the platform were inspected carefully, and no evidence of sediment scouring was observed (**Figure 2B**).

The pressure sensors and accelerometer were sampled at 40 Hz and the barometer at 1 Hz. The low-pass filter implemented by the processing electronics was initially set to 0.5 Hz for the pressure and accelerometer data, but was increased

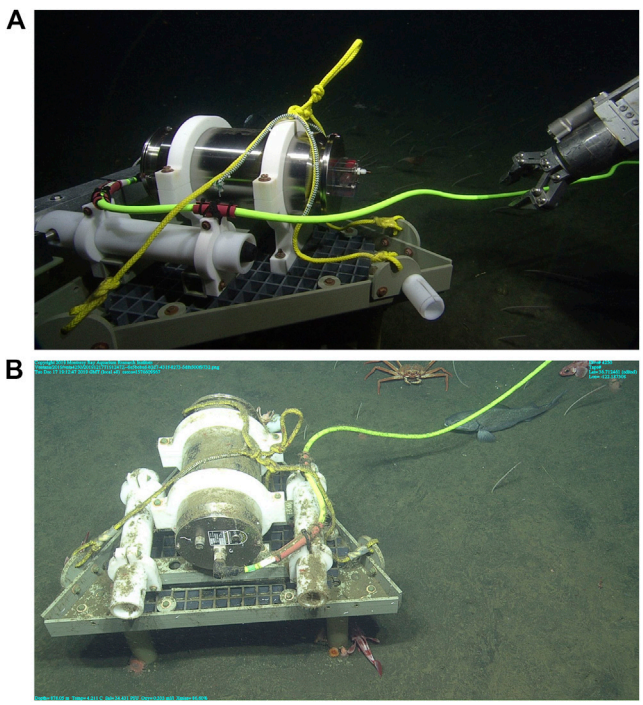

FIGURE 2 | Photographs of the GSSM **(A)** The instrument during deployment with the external oil reservoir and inlet capillary tube visible on the right-hand side of the pressure housing. **(B)** The instrument just before recovery. There is no visible scouring of sediments around the platform legs.

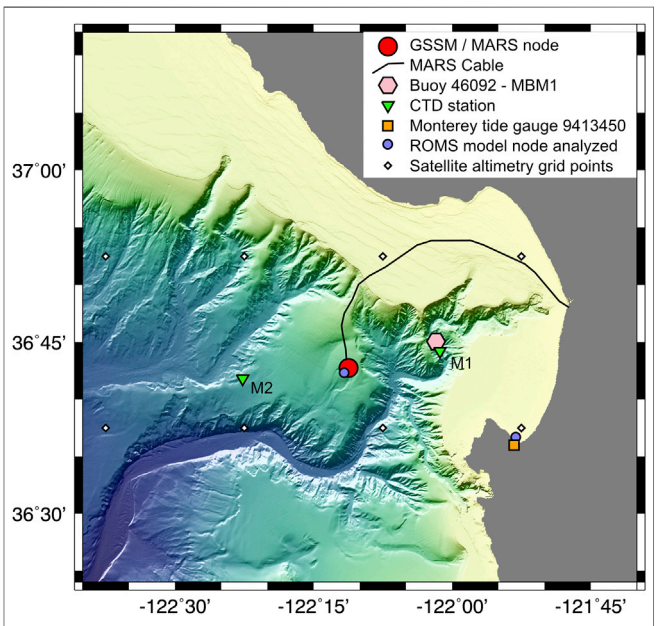

FIGURE 3 | Bathymetric map of Monterey Bay showing the location of the MARS cable (black line) and main MARS node and GSSM (red circle). Also shown are the positions MBARI buoy MBM1 (NOAA buoy 46092) (pink hexagon), MBARI CTD sites Mooring one and Mooring 2 (inverted green triangles labeled M1 and M2), the NOAA Monterey tide gauge 9413450 (orange square), nodes in the ROMS model that are used to obtain pressure time series for comparison (purple circles) and grid points for the reprocessed multi-mission altimeter satellite sea surface heights (white diamonds).

to 8 Hz on August 25, 2017. The data were streamed to a laptop in the shore station and uploaded each day to the University of Washington for analysis and archiving. A total of 154 A-0-A calibrations were performed with each lasting 5 min. The calibrations were initially spaced 1 day apart. The interval then increased incrementally to two weeks over the first year of the deployment and was held at this value for the second year. For the first 10 calibrations, the valve actuator was only turned on for the calibration interval but subsequently it was left on permanently which resulted in an increase in the internal temperature of the housing. For the final six months of the deployment, the actuator was turned on only for valve turns which decreased the internal housing temperature again. During this last period, the calibration interval was reduced to one day and then increased to one week.

Oceanographic Data

In order to enable comparisons of long-term trends in the measured bottom pressures with those predicted from physical oceanographic data, we used two approaches to obtain time series of predicted bottom pressure. First, we obtained predicted bottom pressures by combining the sea surface height (SSH) anomalies determined from satellite altimetry data with a time series of repeat conductivity, temperature and depth (CTD) profiles that are collected by MBARI approximately monthly at two mooring stations M1 and M2, that lie 15 and 17 km to the east and west of the MARS observatory, respectively (**Figure 3**). The SSH anomaly was obtained from the Global Ocean Gridded L4 Sea Surface Heights and Derived Variables Reprocessed data set that is provided by the Copernicus Program (Taburet et al., 2019). Time series of daily SSH anomaly at stations M1 and M2 were obtained from the daily quarter degree spatial grids by linear interpolation for the period June 1, 2017 to October 15, 2019, the last date for which the reprocessed data were available at the time of analysis. The CTD casts were obtained from June 2017 to December 2019 and for each cast with good data that extended from ≤5 m to at least 500 m depth (36 casts at station M1 and 28 at station M2), a vertical profile of temperature and salinity to 900 m depth was created by combining the CTD casts from the surface to 500 m, with a seasonally-dependent temperature and salinity model from the 2018 World Ocean Atlas (Locarnini et al., 2018; Zweng et al., 2018) at greater depths. These profiles were converted to density using the Gibbs Seawater Oceanographic Toolbox (McDougall and Barker, 2011) and interpolated linearly with time to obtain daily profiles at stations M1 and M2 for each day in the altimetry time series. The density was then multiplied by the acceleration of gravity and integrated vertically to 887 m plus the SSH anomaly to estimate the pressure at the depth of the GSSM.

Second, we obtained predicted bottom pressures from the West Coast Ocean Forecast System (WCOFS) ocean circulation model developed at the National Oceanic and Atmospheric Administration (NOAA) Coast Survey Development Laboratory (Kurapov et al., 2017a; Kurapov et al., 2017b). The WCOFS model is constructed using the Regional Ocean Modeling System (ROMS) framework which utilizes the Boussinesq approximation and solves for hydrostatic pressures (Shchepetkin and McWilliams, 2005). The WCOFS model domain extends from 24° to 54°N along the North American coast and has 40 vertical layers with grid nodes spaced 2 km apart horizontally. This model was not developed to predict seafloor pressure but it was previously used for comparisons with seafloor pressure gauges off the coast of the Pacific Northwest (Fredrickson et al., 2019b) where it was shown to produce many of the statistical characteristics of the observed pressure field but not necessarily individual features. Modeled daily averaged pressures were calculated at the nodes closest to the GSSM and the Monterey tide gauge (**Figure 3**) from December 17, 2016 to November 14, 2018, the last date for which model output was available at the time of analysis. Tide height data from the Monterey tide gauge (NOAA station 9413450) was also downloaded and corrected for atmospheric pressure using barometric data from the MBARI buoy MBM1 (NOAA Station 46092) (**Figure 3**).

RESULTS

Over the 914-days recording interval, the GSSM successfully collected data for all but 26 days with data gaps of up to 4 days resulting mostly from scheduled and unscheduled shutdowns of the observatory. **Figure 4A** shows power spectra for the accelerometer and pressure sensors for a typical day in the winter. The microseism peak is visible on all channels between 0.1 and 1 Hz. At lower frequencies spectral levels increase with decreasing frequency due to the effects of infragravity waves and noise levels are much higher on the horizontal accelerometer channels than the vertical accelerometer channel due to the effects of instrument tilting (Webb, 1998). At frequencies above the microseism peak, the spectral levels on the accelerometer channels increase above ~3 Hz due to the increased frequency counting noise at higher frequencies and there is a pronounced peak at ~8 Hz. Correcting the vertical channel for the tilt and compliance signals following the method of Crawford and Webb (2000) shows that this peak is a result of instrument tilting (**Figure 4A**) presumably due to a resonance with the seafloor. The relatively low noise floor of a few parts-per-billion of the full-scale range of 30 m/s^2 near 1 Hz provides a useful band in which to record seismic events (**Figures 4B,C**).

Figure 5A shows one day of pressure data from the first summer of the deployment. At this time, the external pressures on the two pressure sensors differ by ~0.3 hPa, although by the end of the deployment they are several hPa apart. Over the day, the pressures vary by over 100 hPa due to diurnal and semi-diurnal tides but the difference between the two sensors remains stable within about ±0.05 hPa. The spectrum of the pressure difference (**Figure 5B**) shows an inverse dependence on frequency at frequencies below ~0.5 Hz and have levels that are consistent with the predictions for electronic noise on the crystal oscillators of Webb and Nooner (2016). At frequencies above ~1 Hz, the differences are quite small because the two sensors share the same counting electronics and the low pass filter was set to 0.5 Hz at this point in the experiment. Over shorter

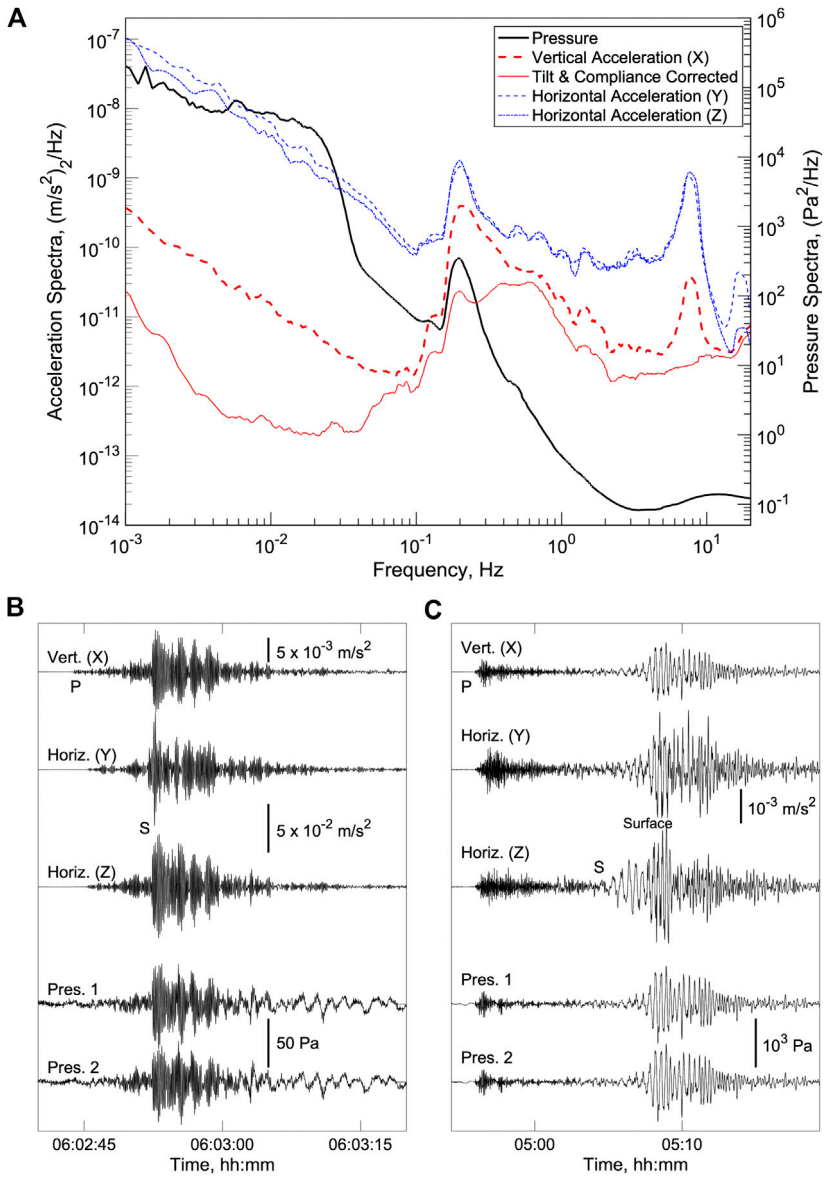

FIGURE 4 | (A) Acceleration and pressure power spectra density for January 25, 2018 obtained using Welch's method with 1-h windows, a Hamming taper, and 90% overlap. Spectral values have been smoothed by averaging samples with frequencies within ±10% of each sample. Correcting the vertical channel for compliance and tilt noise using the method of Crawford and Webb (2000) as implemented by Janiszewski et al. (2019), shows that the peak in accelerations at ~8 Hz is a result of instrument tilting **(B)** Example record section showing 40 s of data for the accelerometer and pressure sensor for a magnitude 3.6 earthquake that occurred 53 km to the northeast of the GSSM near Aromas, California on January 24, 2018 with the *P* and *S* waves labeled. The vertical accelerometer is scaled by a factor of five relative to the horizontal channels and the pressure records have been filtered with a 0.2 Hz high pass filter. The *S* waves are dominated by energy at 0.5–1 Hz and the amplitudes are suppressed on the pressure sensors because the data is narrowband because it was acquired with a 0.5 Hz low pass filter. **(C)** Example record section showing 25 min of data for the magnitude 8.1 Chiapas, Mexico earthquake on September 7, 2017 with the *P*, *S* and surface waves labeled. A 0.005–2 Hz bandpass filter has been applied to all the data. There is a marked difference between the frequency of the *P* waves and the *S* and surface waves.

intervals (**Figure 5A** inset), the pressure sensors resolve the pressure excursions due to infragravity waves with periods of ~100 s and microseisms with periods of about 5 s.

At the onset of a calibration (**Figure 6**), it takes about 3 s to fully turn the valve with two-thirds of the pressure drop occurring over 0.5 s. The measured pressure drop initially overshoots to pressure lower than atmospheric because of short term viscoelastic transients and because the adiabatic expansion of oil leads to cooling that takes some time to equilibrate. During the calibration, the pressures recover approximately exponentially, and we chose to measure the calibration pressure by averaging pressures from each gauge and the barometer from 3 to 4 min after the pressure first decreases below 1,000 hPa near the end of valve turn. The offset of each external pressure gauge from the

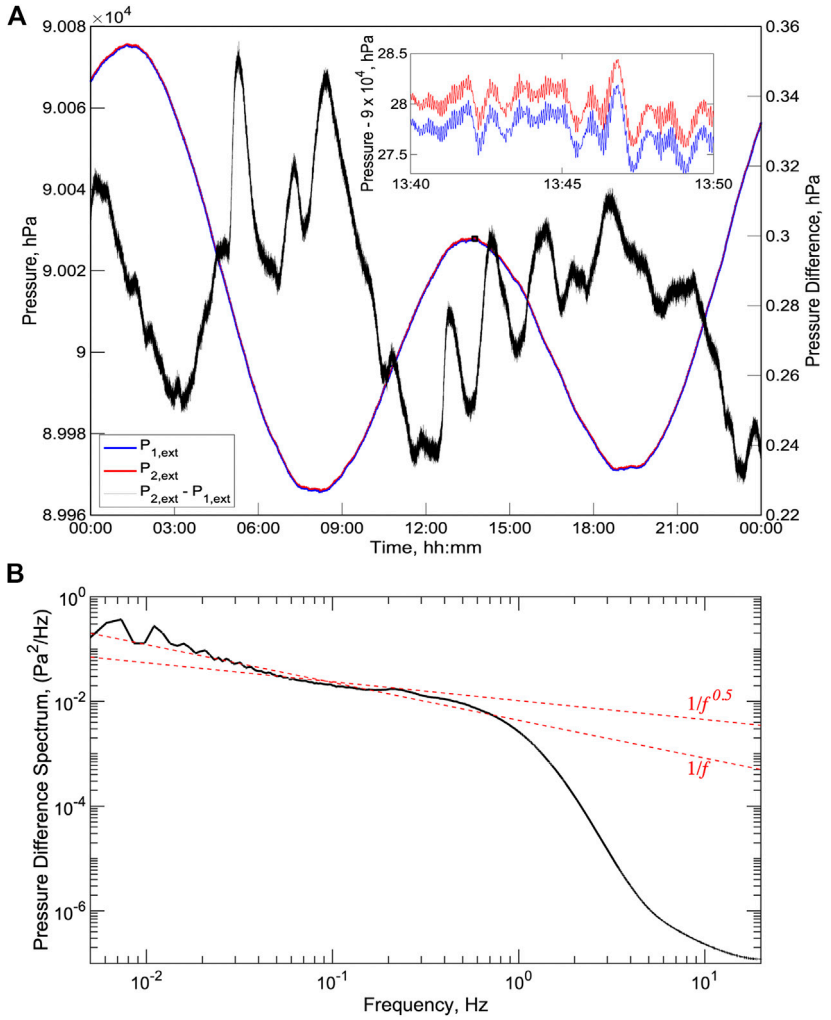

FIGURE 5 | (A) Example day of external pressure data from July 2, 2017, a day without an A-0-A calibration. The two pressure sensors (blue and red lines and left axis) track each other over the tidal cycle within a range of ~0.1 hPa (black line and right axis). (inset) Ten minutes of pressure with variations due to infragravity waves with periods of ~100 s and microseisms with periods of <10 s. **(B)** Spectrum of the difference between the two pressure sensors (black lines) together with approximate f^{-1} and $f^{-0.5}$ fits to the spectrum for frequencies below ~0.5 Hz. Note that at this point in the development the low pass filter was set to 0.5 Hz for the pressure sensors.

barometer is then recorded. It is important to obtain all calibration measurements over the same time interval relative to the time of the valve turn, but provided the calibration average is obtained starting at least 2 min after the turn and over at least 30 s, the consistency of the calibrations is not sensitive to when this is done. At the end of the calibration when the valve turns back, there is initially a small pressure drop related to the valve plumbing and the pressure then returns to its external value over a slightly longer time interval than observed for the value opening (just under half of the pressure increase occurs over 0.5 s). The effect of the calibration is to temporarily perturb the external pressure toward slightly lower values. Measured pressures are ~0.5 hPa too low 30 s after the calibration, but they essentially recover over about 10 min.

The first calibration was obtained within minutes of attachment to the MARS cabled observatory to test the valve commands while the ROV was still nearby; the results are not reliable because the GSSM had not reached thermal equilibrium with its surroundings. The remaining 153 are plotted in **Figure 7A** along with the temperature measured by one of the pressure gauges (the pressure gauge temperatures are offset from each other by ~0.06°C but are consistent with each other to ~0.002°C). For both sensors the changes in temperature which accompany changes in the valve actuator operation, result in a clear jump in measured offset. Over the course of the experiment the offset measured for the first pressure sensor increases by over 6 hPa while the offset on the second pressure sensors increases by nearly 2 hPa. Thus, the pre-calibration drift rates of the two pressure sensors was significantly better than the ~1 part in 10^4 per year (or ~10 hPa in 1,000 m of water) reported for some sensors (Polster et al., 2009).

The drift of the Paroscientific pressure sensors can be explained as the sum of two exponential terms of opposite sign (Paros and Kobayashi, 2015b). Outgassing from the

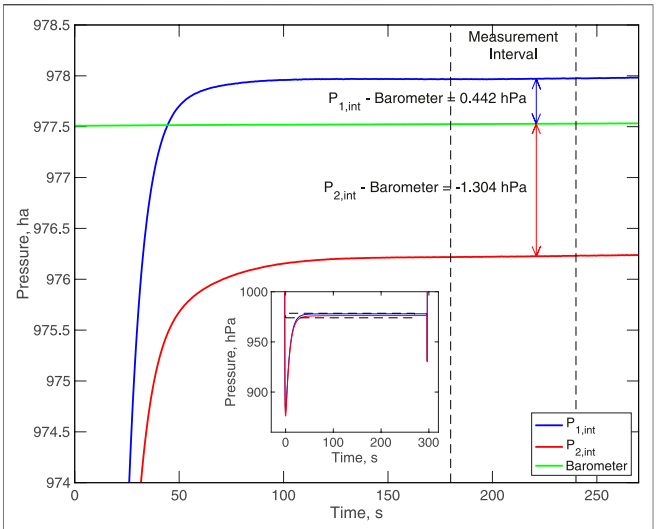

FIGURE 6 | Pressure data for an example calibration, showing all but the first and last 30 s. The calibration is obtained by averaging the pressure measurements between 180 and 240 s after the onset of the test and measuring the offset of the pressure gauges from the barometer. (inset) Pressure data for the full 5-min calibration. Initially the pressures undershoot but they then recover approximately exponentially on a timescale of ~20 s. Reproduced from Wilcock et al. (2018).

quartz crystal causes drift to higher frequencies and pressures and has a long time constant. On shorter time scales, viscoelastic creep of the quartz crystal attachments in response to the pressure history of the crystal causes drift to lower frequencies and pressures. A number of mathematical models can be used to fit the drift of Paroscientific sensors (Paros and Kobayashi, 2015a). Here, we find it adequate to follow the approach of several previous studies (Chiswell and Lukas, 1989; Watts and Kontoyiannis, 1990; Polster et al., 2009; Kajikawa and Kobata, 2019) with the addition of a temperature dependent term, and fit a function of the form

$$p(t) = a\exp(-t/t_0) + bt + c + d\left(T - T_{\mathrm{ref}}\right)$$

where $p(t)$ is the pressure offset as a function of time since the deployment, T is the temperature relative to a reference temperature T_{ref} that is set to the median of the deployment and a, t_0, b, c and d are constants. The exponential term accounts for viscoelastic creep that is observed when ambient pressure changes and the linear term is sufficient to model the effects of outgassing on the timescale of our experiment. We use a least squares linear inversion to solve for a, b, c and d for different fixed values of the exponential time constant t_0 and select the value of t_0 that gives the minimum root mean squared (RMS) residual. **Figure 7B** shows the temperature corrected offsets together with a smooth curve obtained for the remaining terms in **Eq. 1**. For pressure sensors 1 and 2, the best fitting curves have an exponential time constant of 280 and 14 days and yield an RMS misfit of 0.091 and 0.102 hPa, respectively. The early measurements for pressure sensor two are fit better if a second exponential term with a time constant of 9 days is added, which reduces the RMS residual to 0.087 hPa. Inspection of the residuals obtained from subtracting the modeled offsets from the observations, shows that they are strongly correlated between the two sensors (correlation coefficient = 0.83).

If the sensitivity or span of a pressure sensor remined constant, then the difference between repeat measurements of a fixed high and a fixed low pressure should be invariant with time. This cannot be tested with the field observations on a single sensor by comparing the pre-calibration external pressure with the internal calibration pressure. This is because the pressures are not fixed primarily because the external pressure changes with tides and other oceanographic effects. However, if the difference between the external and internal pressure is compared between two sensors, the difference should not change with time if the sensitivities of both sensors are constant. In order to assess the consistency of the calibrations between sensors, we calculate the span of the two instruments by subtracting the pressure measured during the calibration from the external pressure averaged from 65 to 5 s before the start of the calibration and then look at the difference of the two spans. After applying a linear temperature correction, the results (**Figure 8A**) show that the two sensors remain consistent with each other within just over 0.2 hPa for the 30-month deployment. After the first two months of the deployment, the two sensors drift apart approximately linearly at a rate that averages 0.08 hPa/yr. The A-0-A calibrations improve the self-consistency of the two pressure measurements by well over an order of magnitude (**Figure 8B**) and the relative drift rates of one part in 10^6 are two orders of magnitude better than the typical drift rates of uncalibrated sensors reported by Polster et al. (2009).

DISCUSSION

Applying the Pressure Calibrations

Several small corrections need to be applied to the A-0-A calibrations. Upon recovery the oil level in the external reservoir was found to have dropped by about 0.6 cm which would lead to an apparent decrease in the measured external pressures of 0.13 hPa as seawater replaced the denser oil. The measured drop requires that 8 cm^3 of oil leaked through the valve which is reasonably consistent with the prediction of 6 cm^3 obtained from laboratory testing of the valve. The oil levels in the internal reservoir are estimated to have risen by 0.2 cm. While this was not accurately measured, it was noted that the oil level in the internal reservoir changed only slightly. A 0.2 cm increase in the internal reservoir oil level would increase the internal pressure measurements by 0.25 hPa, and thus reduce the calibrated external pressures by the same amount. The net effect of the changes in levels in the two reservoirs is corrected by increasing the observed change in external pressures over the deployment by 0.38 hPa.

After the experiment, the frequency of the counting clock used to measure the frequency of the temperature and pressure sensing crystals in the pressure gauges was found to have drifted over the 30-months deployment to higher frequencies by a fraction of 1.05×10^{-6}. The equivalent annual rate of 0.42×10^{-6}, is consistent with Sasagawa et al. (2018) who reported that the

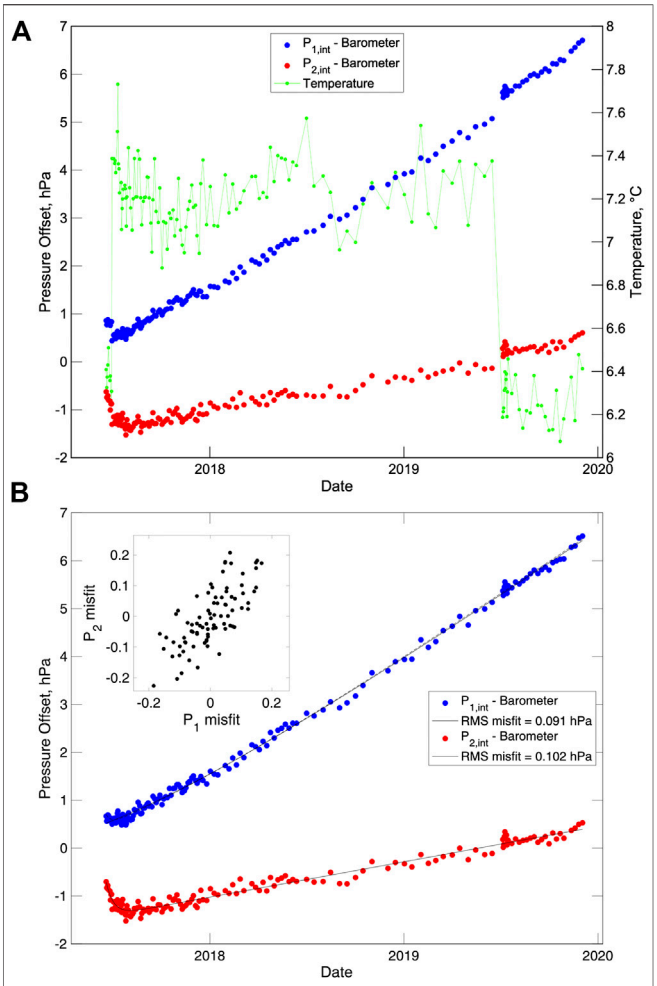

FIGURE 7 | (A) Pressure offsets (pressure gauge minus barometer) measured during the calibrations for the two pressure gauges (blue and red circles) and temperature measured inside the pressure housing by the second pressure sensor (green points connected by a thin line). The temperature increased by ~0.8°C early in the deployment when the operation of the valve actuator was changed from turning on the power just for the 5-min calibration to leaving it on permanently. The temperatures decreased by ~0.9°C for the last 6 months when the valve actuator was only turned on for the valve turns at the start and end of the calibration. **(B)** Pressure offsets after applying a linear temperature correction (see text) with smooth fits to the data (black lines). (inset) Plot of the misfits of the calibrated pressure offsets from the smooth curve for the two sensors showing that they are strongly correlated.

fractional frequency drift for 12 systems averaged 0.2×10^{-6} yr^{-1} and never exceeded 0.5×10^{-6} yr^{-1}. Using the equations presented in the manual for the counting electronics to convert frequency to temperature and pressure (Paroscientific, Inc., 2016), the resulting drift for pressure sensor one is calculated as 1.12 hPa at the external pressure of 900 MPa and 0.95 hPa for the internal pressure of 10 MPa. For the pressure 2, the corresponding values are 1.17 and 0.99 hPa. Since the A-0-A calibrations correct for the drift at internal pressures, the remaining effect of counting clock drift on external pressure is corrected by decreasing the observed change in external pressures over the deployment by 0.17 and 0.18 hPa, respectively.

Any drift of the barometer will also offset the calibrations. The Paroscientific 216B barometer is certified to drift at less than 0.01% (0.1 hPa) per year but typically drifts at about a 10th this rate. We have not recalibrated the barometer because we anticipate this to be a very small correction. For a less stable barometer, it would be important to do this.

The pressure measurements are dependent on the stability of the instrument platform. **Figures 9A and 9B** shows the smoothed change in tilt over the deployment measured using the two horizontal accelerometer channels (**Figure 10** shows the channel orientations relative to the instrument platform). The tilt rates of several milliradians per year are equivalent to about one part in 10^3 of the ±3 g measurement span and thus significantly exceed the expected drift of the accelerometer at no more than one part in 10^4. We verified the reliability of the horizontal tilts by computing the resulting change in total tilt of the platform and comparing it to an equivalent calculation from the vertical accelerometer after applying a correction for its drift determined from the change in magnitude of the total vector acceleration which, in the absence of sensor drift, should be constant (Fredrickson et al., 2019a). The results of comparison (**Figure 1C**) show that the two measurements are consistent within <0.04 mrad, confirming that the horizontal tilts are reliable. Paroscientific pressure gauges are sensitive to orientation because the pressure sensing crystal cannot be fully isolated from the effects of gravitational loading. In the Paroscientific SOS module, these corrections are automatically applied based on the output of the horizontal tilt sensors and were <0.1 hPa for the observed tilts in our experiment.

The tilting of the platform is most simply explained by platform subsidence which can be expected to be most significant in settings such the MARS observatory where the instrument is deployed on soft mud. Accounting for platform subsidence is a significant challenge in seafloor geodesy (Cook and DeSanto, 2019). We can estimate a minimum subsidence from the tilt measurements under the assumption that at any instant, not all legs are subsiding, and no legs are rising. If we ignore the first two weeks of data in June when the tilt data suggests the platform was settling unevenly and divide the tilt time series in two for this calculation at the time where the sign of the rate of change of tilt on the horizontal Z channel changed (**Figure 9B**), we estimate that the pressure sensor subsided by 3.0 mm, equivalent to an apparent pressure increase of 0.3 hPa (**Figure 10**). Performing this calculation on daily changes in smoothed tilt, predicts 4.1 mm of subsidence. In both cases most of the observed tilt can be modeled as the result of subsidence of one leg by nearly 1 cm (**Figure 10**). Performing the calculations on shorter intervals with unsmoothed data leads to higher subsidence predictions but these are likely to be unreliable given that tides and tidal currents can be expected to rock the platform back and forth on timescales of a day or less without necessarily leading to subsidence. Of course, the pressure sensor may have subsided more than calculated if all the legs subsided together, and ideally an independent means should be employed to measure this in sedimented settings (Cook and DeSanto, 2019). To account for subsidence, we chose to reduce the observed changes in external pressure over the experiment by 0.3 hPa, since this is the minimum feasible correction.

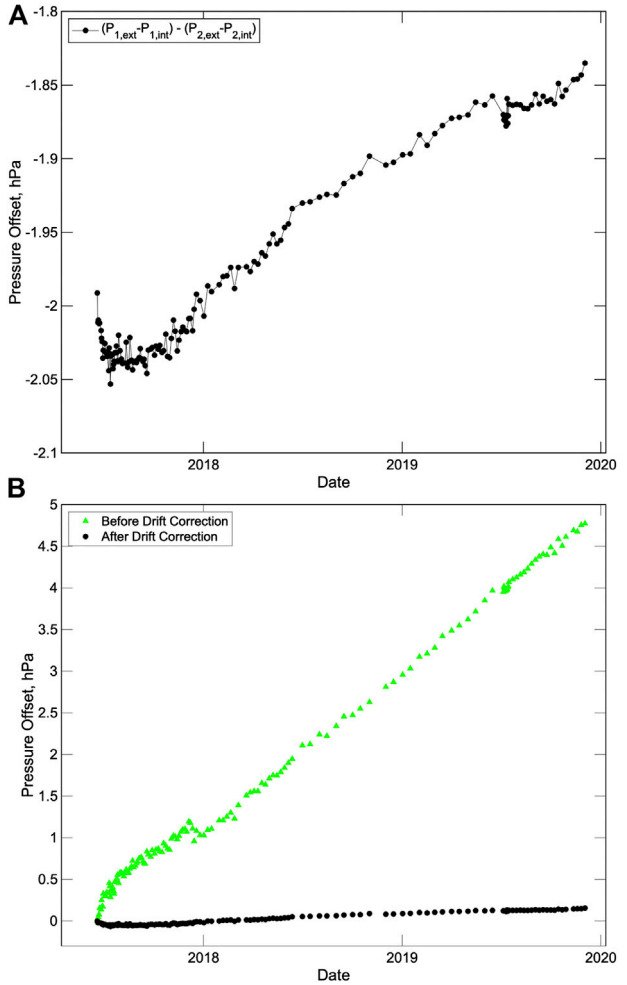

FIGURE 8 | (A) Difference in span between the two pressure sensors after applying a linear temperature correction. The span for each sensor is measured by subtracting the internal pressure measured during a calibration from the external pressure averaged for a minute just before the calibration. **(B)** Change in offset of the external pressures between the two sensors at the times of calibrations relative to the time of the first calibration shown before (green triangles) and after (black circles) applying the drift correction.

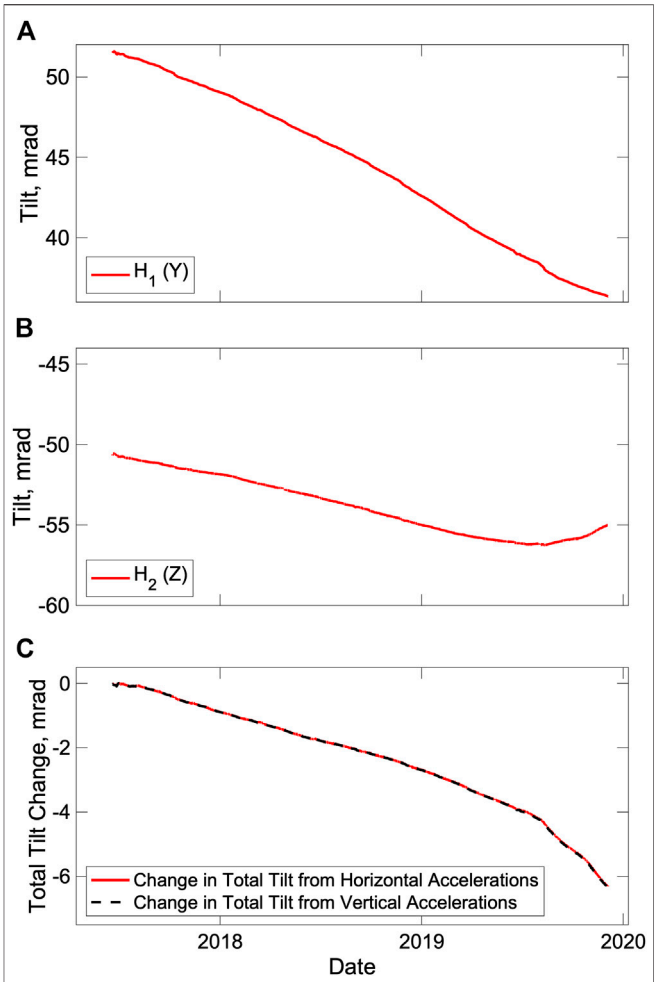

FIGURE 9 | Tilt measured by the accelerometer from June 20, 2017 to the end of the deployment after applying a 1 day running mean. **(A)** Tilt on the horizontal channel *Y*. **(B)** Tilt on the horizontal channel *Z*. **(C)** Change in total tilt relative to July 1, 2017. This was calculated from combining the horizontal tilts using the small angle approximation and from the change in vertical acceleration after correcting for the sensor drift and the resulting curves are identical at the scale of the plot.

Figure 11 shows the detided external pressure data after applying the calibration curves of **Figure 7B** with an additional correction that reduces the change in pressures over the deployment by 0.1 hPa to account for the combined effects of changes in oil reservoir levels, counting clock drift and the minimum subsidence. The two calibrated pressure sensors track each other very closely, showing an apparent tendency for higher pressures in the summer than winter. There is an apparent slope in pressure over the course of the experiment of 0.48 and 0.43 hPa/yr for the two pressure sensors, respectively.

Comparisons With Oceanographic Predictions

Because Monterey Bay is not situated in a region that is prone to vertical tectonics and the MARS observatory is located in an area with muted bathymetry that is not subject to slope instability, the measured trends of increasing pressure over the experiment must be due to oceanographic processes if they are not the result of additional platform subsidence or an unidentified systematic measurement error.

Figure 12 shows a comparison between the calibrated GSSM pressure time series and the pressures predicted at station M2 at 887 m depth by combining the SSH anomalies and time dependent water column density structure. Station M2 which lies to the west of the GSSM (**Figure 3**) was selected because it is a site of monthly CTD casts. The incorporation of the water column density structure into the pressure predictions substantially modulates the pressure variations predicted from SSH anomalies alone (blue dashed line in **Figure 12**), reducing the overall amplitude of variations, as would be expected given that the component of sea surface height anomalies associated

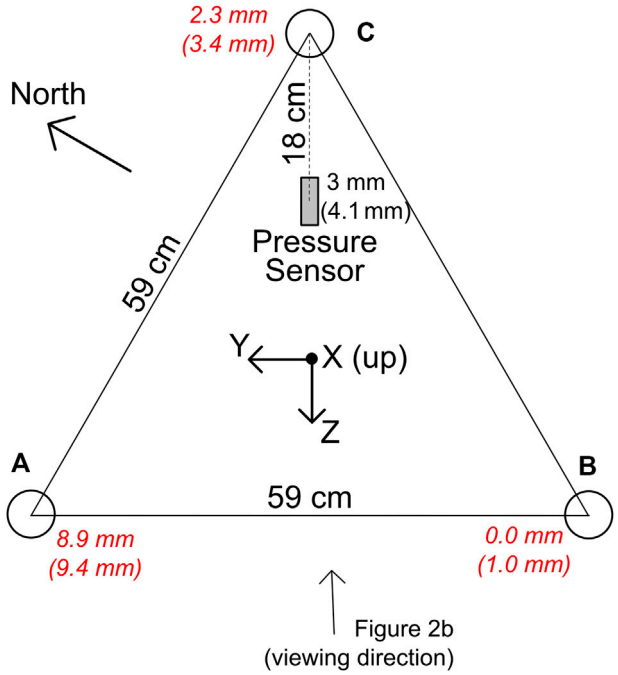

FIGURE 10 | Schematic showing the approximate relative locations of the instrument legs and the pressure sensors and the orientation of the accelerometer channels. The convention for the accelerometer is that accelerations are positive when their point away from the channel orientation so that the X channel which points up records the acceleration of gravity as a positive number. The orientation of the instrument is such that the *Z*-axis is at an azimuth of ~240° with respect to north. Labels in red italics on the sensor legs and pressure sensor give estimates of the subsidence of those components based on summing the minimum subsidence for two intervals between which the rate of change of the Z channel tilt changed sign, with a second estimate based on summing daily calculations shown in parentheses (see text).

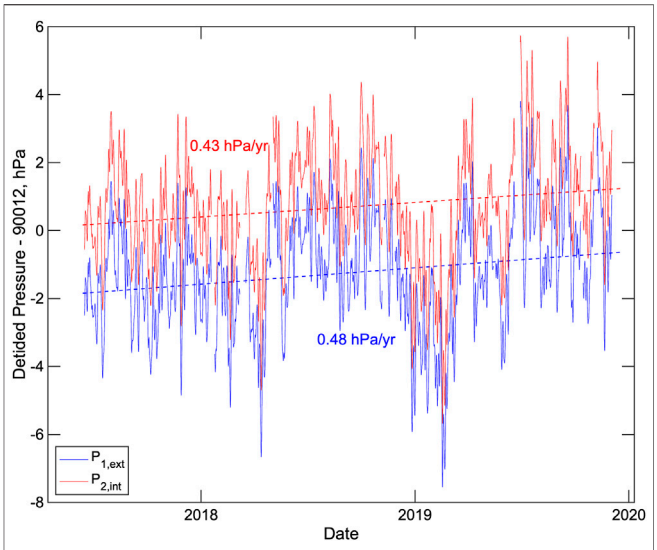

FIGURE 11 | External pressures measured by the two pressure sensors after removing tides using a low-pass Godin filter comprising successive running averages of 24, 24, and 25 h (Godin, 1972) and applying drift corrections based on the calibration curves of **Figure 7B** with an additional small correction for the combined effects of changes in the reservoir heights, counting clock drift and the minimum platform subsidence required to explain tilt changes of the instrument (see text).

with currents that do not extend to the depth of the GSSM will be compensated by density variations at depth. The predicted pressure variations are generally similar to the calibrated GSSM pressure variations showing many of the same long-period features. Only in a few instances do the curves deviate from one another during an interval when there are constraints on density from a CTD cast. Over the interval for which there is reprocessed satellite altimetry, which is all but the last two months of the GSSM deployment, the observed and predicted time series show trends in increasing pressures (0.4 hPa/yr for the pressure sensor two and 0.5 hPa/yr for the altimetry and CTD predictions) that are remarkably consistent.

Efforts to derive predicted bottom pressures at station M1, a second site with monthly CTD casts, were less successful. Here the interpolated satellite sea surface height anomalies are smaller than at station M2, and the water column density structure overcompensates many features leading to bottom pressure variations with higher amplitudes than those predicted from the satellite altimetry alone. We infer that the interpolated altimetry data are unreliable and muted at site M1 because it includes a contribution from grid points that are very close to the shore (**Figure 3**) (Cipollini et al., 2017).

Figure 13 shows comparison of the pressure predictions of the ROMS model with the Monterey tide gauge and the calibrated GSSM pressures. The ROMS model matches the seasonal variations in the pressures obtained from the Monterey tide gauge quite well (**Figure 13A**). Lower pressures are observed in the spring and early summer as is typically observed at the coast in this region (Ryan and Noble, 2002), and over the 30-months interval of the GSSM data, the tide gauge shows a trend in increasing pressures of 1.1 hPa/yr.

For the GSSM comparison (**Figure 13B**), the ROMS model has been smoothed with a 29-days running mean to remove a strong residual spring-neap tide signal with a period of 14–15 days. The comparison is limited to 16½ months from the start of the GSSM deployment and the trends obtained with a least squares linear fit are not well matched, with the GSSM data showing a slope of 1 hPa/yr and the ROMS model slope near zero. This mismatch is almost entirely a result of a large trough in predicted pressures in ROMS model in late summer and fall 2018 that is not present in the GSSM pressures. Over the first 14 months, the predictions and observations are in much better agreement and the slopes of a linear fit are similar. As Fredrickson et al. (2019b) notes, the WCOFS ROMS model predicts pressure better near the coast than in deeper water because it is primarily validated with observations from the continental shelf, and the processes that influence density structure in the deeper ocean are less deterministic. Furthermore, the bathymetry in the vicinity of the GSSM is complex because of the presence of the Monterey Canyon and the local effects of this bathymetry on circulation will not be fully simulated in a regional model with limited spatial resolution. A longer time series would be required to adequately

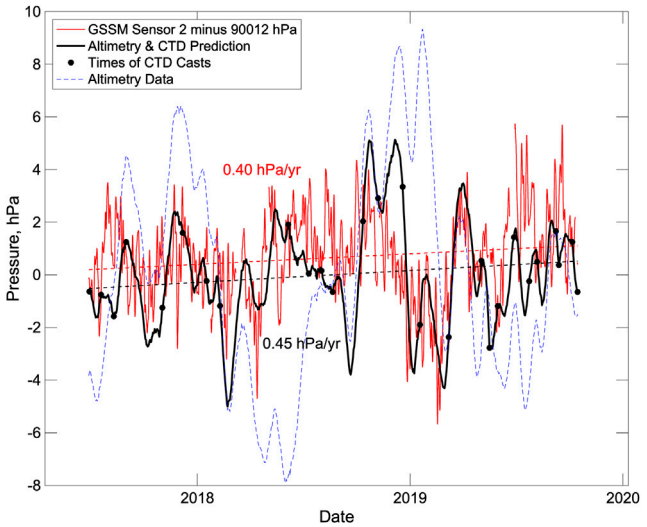

FIGURE 12 | Comparison of GSSM pressure with the bottom pressures predicted at station M2, 17 km to the west using satellite altimetry and repeat CTD casts. Calibrated detided pressure for GSSM pressure sensor 2 (red line) are compared to the pressures obtained from the altimetry data and water column density profiles (bold black line with solid circles showing the time of CTD casts) and those predicted directly from altimetry data (dashed blue line). A least squares straight lie fit labeled with the slope is shown for the first two curves (dashed lines).

compare the long-term trends in bottom pressure with those predicted by the ROMS circulation model.

The trend of increasing pressure seen in our data are consistent with the trend expected from the El Niño Southern Oscillation. Data from the San Francisco tide gauge show that during the winter months, sea surface heights at the coast are about 4 cm higher during El Niño and 4–5 cm lower during La Niña (Ryan and Noble, 2002). This effect is not a result of density structure but is related partly to variations in local wind stress moving water toward or away from the coast and partly due to the effects of coast trapped waves generated by wind stresses elsewhere (Ryan and Noble, 2002). The first winter of the GSSM deployment coincided with a weak La Niña event from October 2017–March 2018 while the latter parts of the deployment coincided with weak El Niño conditions from October 2018–June 2019 and November–December 2019. Thus, average sea surface heights, and by inference bottom pressure, would be expected to increase during the deployment.

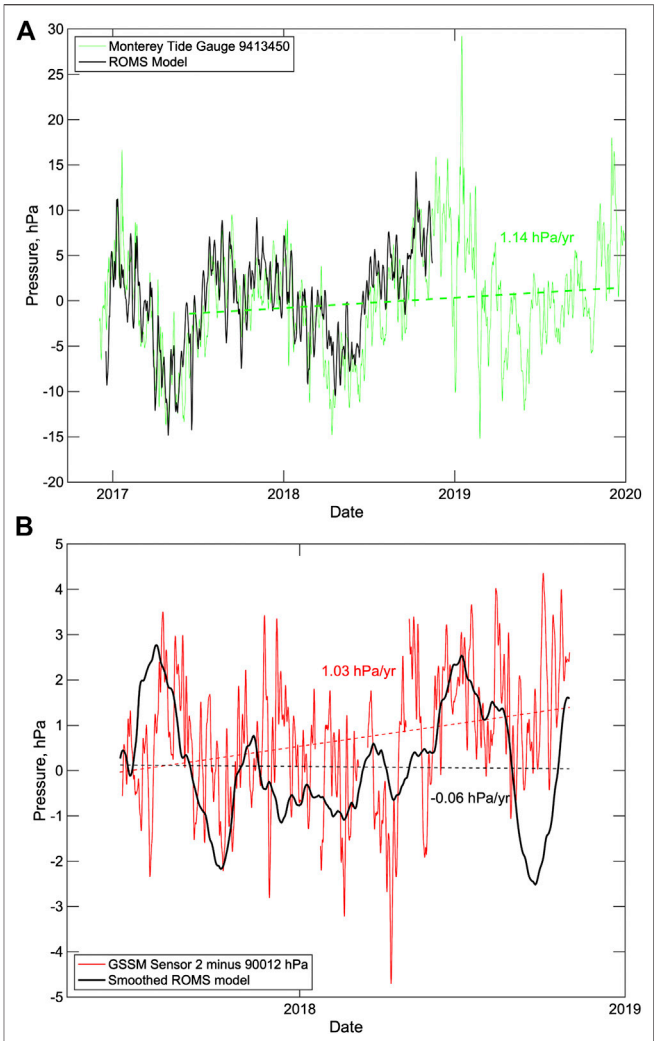

FIGURE 13 | Comparisons of observed pressures with the predictions of a ROMS circulation model (Kurapov et al., 2017a; Kurapov et al., 2017b). **(A)** Tide gauge record from Monterey (station 9413450) converted to pressure and adjusted for atmospheric pressure (green line) compared to the ROMS model at a node 1 km to the north at 10 m depth (black line). The seasonal variations and trends in the tide gauge data are well matched for the period December 17, 2016 to November 14, 2018. A least squares straight line fit (dashed line) labeled with the slope is shown for the tide gauge data for June 13, 2017 to December 14, 2019 (the interval of operation of the GSSM). **(B)** Calibrated, detided pressure for GSSM pressure sensor 2 (red line) compared with the ROMS model at a node 0.8 km to the southwest at a depth of 1,083 m (black line) for the period June 13, 2017 to November 14, 2018. A 29-days running mean has been applied to the ROMS model because the average daily solutions display a strong residual spring-neap tide signal that is only apparent in deeper waters. A least squares straight line fit (dashed line) labeled with the slope is shown for each time series.

Precision and Accuracy of the Calibrated Pressures

The remarkable agreement between the calibrations on the two sensors is consistent with a precision in correcting drift of 0.1 hPa/yr or one part in 10^6, but experiments with more sensors will be required to demonstrate that this can be achieved consistently. Because the discrepancy between the sensors is so small and there is possibly an unknown component of subsidence that was not measured by the tilt meter, it is not possible to determine whether the accuracy of the drift removal matches the precision. However, given that the observed trend in pressure of only 0.5 hPa/yr closely matches that calculated from satellite altimetry and repeat CTD casts at a nearby location, and that the sign of the trend agrees with that expected for the El Niño Southern Oscillation, it is very likely that the calibrations are accurate to much better than one part in 10^5.

The drift rates observed on Paroscientific sensors are proportional to the depth rating (Paros and Kobayashi, 2015b) so the precision observed in the GSSM experiment with 1,400 m (2000 psi) sensor would equate to a 0.5 hPa/yr for a 7,000 m (10,000 psi) full ocean depth sensor. In subduction zones, the signals from slow slip events observed to date have amplitudes of several centimeters and so may lead to resolvable permanent offsets in bottom pressure when observed with A-0-A calibrated pressure gauges. For secular strain, the magnitude of the expected signals is ≤1 hPa/yr (Fredrickson et al., 2019b) so here A-0-A calibrated pressure gauges are more likely to be successful in resolving strain when they are deployed at relatively shallow depths with the appropriate depth-rated sensors. Resolving geodetic signals will, off course, also require paying careful attention to removing oceanographic signals that also limit the resolution of seafloor pressure measurements for geodesy.

CONCLUSION

A 30-month test of the A-0-A technique for calibrating seafloor pressure gauges at 900 m in Monterey Bay, resulted in calibrated pressure records on two Paroscientific pressure gauges that are consistent with each other to one part in 10^6 per year, well over an order of magnitude improvement relative to the uncalibrated pressure gauges. The calibrated pressure gauges detected an overall trend in increasing seafloor pressure of ~0.5 hPa/yr which matches well with that predicted by combining sea surface height anomalies from satellite altimetry with CTD data at a site 17 km seaward of the test site. The trend is qualitatively consistent with the pattern expected based on sea level variations due to the El Niño Southern Oscillation. However, because there is an unknown component of platform subsidence and the deployment interval was short compared with that necessary to resolve oceanographic trends, the absolute error of the calibrations is not fully constrained.

For applications where a pressure gauge drift of one part in 10^5 is sufficiently small to resolve the signals of interest, our seafloor experiment and the laboratory tests of Sasagawa et al. (2018) show that A-0-A calibration is more than sufficient. For applications where a drift approaching one part in 10^6 is required, additional experiments are required to fully evaluate the A-0-A method. These will require long multi-year deployments in stable well-characterized settings and careful attention to characterizing platform stability and subsidence. The results should be compared with those obtained from other methods of pressure gauge drift removal and ideally with the pressure variations predicted from physical oceanographic observations.

DATA AVAILABILITY STATEMENT

The datasets presented in this study can be found in online repositories. The names of the repository/repositories and accession number(s) can be found below: he data collected by the GSSM has been archived at the University of Washington in the Research Works database and is available at http://hdl.handle.net/1773/46596 (Wilcock et al., 2020).

AUTHOR CONTRIBUTIONS

WW interacted closely with the engineering team, undertook the data analysis and wrote the manuscript. DAM was the project manager leading the engineering design, fabrication and testing of the GSSM and directed the deployment and recovery of the instrument at sea. EF contributed to the comparisons with oceanographic data. MH, GC, JT, JB, and DeM participated in the design, fabrication and testing of the GSSM. TK demonstrated how to analyze the accelerometer data for sensor tilt. JP proposed the A-0-A approach for calibrating seafloor pressure gauges and provided advice on the GSSM design and data analysis.

FUNDING

This work was supported by JP, the Jerome M. Paros Endowed Chair in Sensor Networks, and the University of Washington.

ACKNOWLEDGMENTS

We thank the engineers at Paroscientific for support with the design and fabrication of the GSSM; the captain and crew of the R/V *Rachel Carson* and the operators of the ROV *Ventana* for their assistance deploying and recovering the GSSM; Craig Dawes for help connecting and operating the GSSM on the MARS cabled observatory; Francisco Chavez and Reiko Michisaki for providing access to the MBARI CTD data; Alex Kuparov for sharing the WCOFS regional oceanographic model simulations; Susan Hautala and Parker MacCready for helpful advice and assistance with the oceanographic data analysis; and Yoshichio Ito and Spahr Webb for thoughtful reviews.

REFERENCES

Araki, E., Machida, Y., Nishida, S., Kimura, T., Yokobiki, T., and Kodaira, S. (2019). Seafloor pressure measurement to evaluate inter-plate coupling in the Nankai trough seismogenic zone. Available at: https://agu.confex.com/agu/fm19/meetingapp.cgi/Paper/513896 (Accessed August 1, 2020).

Blum, J. A., Chadwell, C. D., Driscoll, N., and Zumberge, M. A. (2010). Assessing slope stability in the Santa Barbara Basin, California, using seafloor geodesy and CHIRP seismic data. *Geophys. Res. Lett.* 37, L13308. doi:10.1029/2010GL043293

Bürgmann, R., and Chadwell, D. (2014). Seafloor geodesy. *Annu. Rev. Earth Planet Sci.* 42, 509–534. doi:10.1146/annurev-earth-060313-054953

Bürgmann, R., and Thatcher, W. (2013). Space geodesy: a revolution in crustal deformation measurements of tectonic processes. *Spec. Pap. Geol. Soc. Am.* 500, 397–430. doi:10.1130/2013.2500(12)

Chadwell, C. D., Hildebrand, J. A., Spiess, F. N., Morton, J. L., Normark, W. R., and Reiss, C. A. (1999). No spreading across the Southern Juan de Fuca Ridge axial

cleft during 1994–1996. *Geophys. Res. Lett*. 26, 2525–2528. doi:10.1029/1999GL900570

Chadwick, W. W., Nooner, S. L., Butterfield, D. A., and Lilley, M. D. (2012). Seafloor deformation and forecasts of the April 2011 eruption at axial seamount. *Nat. Geosci*. 5, 474–477. doi:10.1038/ngeo1464

Chadwick, W. W., Nooner, S. L., Zumberge, M. A., Embley, R. W., and Fox, C. G. (2006). Vertical deformation monitoring at Axial Seamount since its 1998 eruption using deep-sea pressure sensors. *J. Volcanol. Geoth. Res*. 150, 313–327. doi:10.1016/j.jvolgeores.2005.07.006

Chiswell, S. M., and Lukas, R. (1989). The low-frequency drift of paroscientific pressure transducers. *J. Atmos. Ocean. Technol*. 6, 389–395. doi:10.1175/1520-0426(1989)006<0389:TLFDOP>2.0.CO;2

Cipollini, P., Calafat, F. M., Jevrejeva, S., Melet, A., and Prandi, P. (2017). Monitoring sea level in the coastal zone with satellite altimetry and tide gauges. *Surv. Geophys*. 38, 33–57. doi:10.1007/s10712-016-9392-0

Cook, M. J., and DeSanto, J. B. (2019). Validation of geodetic seafloor benchmark stability using structure-from-motion and seafloor pressure data. *Earth and Space Science* 6, 1781–1786. doi:10.1029/2019EA000623

Cook, M. J., Sasagawa, G., Roland, E. C., Schmidt, D. A., Wilcock, W. S. D., and Zumberge, M. A. (2017). "Campaign-style measurements of vertical seafloor deformation in the Cascadia subduction zone using and absolute self-calibrating pressure recorder," in Fall Meeting 2017, New Orleans, LA, December 2017 [abstract].

Crawford, W. C., and Webb, S. C. (2000). Identifying and removing tilt noise from low-frequency (<0.1 Hz) seafloor vertical seismic data. *Bull. Seismol. Soc. Am*. 90, 952–963.

Davis, E. E., Villinger, H., and Sun, T. (2015). Slow and delayed deformation and uplift of the outermost subduction prism following ETS and seismogenic slip events beneath Nicoya Peninsula, Costa Rica. *Earth Planet Sci. Lett*. 410, 117–127. doi:10.1016/j.epsl.2014.11.015

DeSanto, J. B., and Sandwell, D. T. (2019). Meter-scale seafloor geodetic measurements obtained from repeated multibeam sidescan surveys. *Mar. Geodes*. 42, 491–506. doi:10.1080/01490419.2019.1661887

Doglioni, C., and Riguzzi, F. (2018). The space geodesy revolution for plate tectonics and earthquake studies. *Rendiconti Lincei. Sci. Fis. Nat*. 29, 29–34. doi:10.1007/s12210-017-0639-6

Fox, C. G. (1990). Evidence of active ground deformation on the mid-ocean ridge: axial seamount, juan de Fuca ridge, April-June 1988. *J. Geophys. Res. Solid Earth* 95, 12813–12822. doi:10.1029/JB095iB08p12813

Fox, C. G. (1993). Five years of ground deformation monitoring on axial seamount using a bottom pressure recorder. *Geophys. Res. Lett*. 20, 1859–1862. doi:10.1029/93GL01216

Fox, C. G. (1999). *In situ* ground deformation measurements from the summit of Axial Volcano during the 1998 volcanic episode. *Geophys. Res. Lett*. 26, 3437–3440. doi:10.1029/1999GL900491

Fredrickson, E. K., Wilcock, W. S. D., Baillard, C., Harrington, M., Cram, G., Tilley, J., et al. (2019a). "Observing and interpreting seafloor tilt at axial seamount," in Fall Meeting 2019, San Francisco, CA, December 2019 [abstract].

Fredrickson, E. K., Wilcock, W. S. D., Schmidt, D. A., MacCready, P., Roland, E., Kurapov, A. L., et al. (2019b). Optimizing sensor configurations for the detection of slow-slip earthquakes in seafloor pressure records, using the cascadia subduction zone as a case study. *J. Geophys. Res.: Solid Earth* 124, 13504–13531. doi:10.1029/2019JB018053

Fujimoto, H. (2014). Seafloor geodetic approaches to subduction zone thrust earthquakes. *Monogr. Environ. Earth Planets* 2, 23–63. doi:10.5047/meep.2014.00202.0023

Godin, G. (1972). *The analysis of tides*. 1st Edn. Toronto, ON, Canada: University of Toronto Press.

Inazu, D., Hino, R., and Fujimoto, H. (2012). A global barotropic ocean model driven by synoptic atmospheric disturbances for detecting seafloor vertical displacements from *in situ* ocean bottom pressure measurements. *Mar. Geophys. Res*. 33, 127–148. doi:10.1007/s11001-012-9151-7

Ito, Y., Hino, R., Kido, M., Fujimoto, H., Osada, Y., Inazu, D., et al. (2013). Episodic slow slip events in the Japan subduction zone before the 2011 Tohoku-Oki earthquake. *Tectonophysics* 600, 14–26. doi:10.1016/j.tecto.2012.08.022

Janiszewski, H. A., Gaherty, J. B., Abers, G. A., Gao, H., and Eilon, Z. C. (2019). Amphibious surface-wave phase-velocity measurements of the Cascadia subduction zone. *Geophys. J. Int*. 217, 1929–1948. doi:10.1093/gji/ggz051

Kajikawa, H., and Kobata, T. (2019). Evaluation and correction for long-term drift of hydraulic pressure gauges monitoring stable and constant pressures. *Measurement* 134, 33–39. doi:10.1016/j.measurement.2018.10.051

Kajikawa, H., and Kobata, T. (2016). Pressure gauge calibration applying 0-A-0 pressurization to reference gauge. *Acta IMEKO*. 5, 59. doi:10.21014/acta_imeko.v5i1.3192012

Kajikawa, H., and Kobata, T. (2014). Reproducibility of calibration results by 0-A-0 pressurization procedures for hydraulic pressure transducers. *Meas. Sci. Technol*. 25, 015008. doi:10.1088/0957-0233/25/1/015008

Kurapov, A. L., Erofeeva, S. Y., and Myers, E. (2017a). Coastal sea level variability in the US West Coast Ocean Forecast system (WCOFS). *Ocean Dynam*. 67, 23–36. doi:10.1007/s10236-016-1013-4

Kurapov, A. L., Pelland, N. A., and Rudnick, D. L. (2017b). Seasonal and interannual variability in along-slope oceanic properties off the US West Coast: inferences from a high-resolution regional model. *J. Geophys. Res.: Oceans* 122, 5237–5259. doi:10.1002/2017JC012721

Locarnini, R. A., Mishinov, A. V., Baranova, O. K., Boyer, T. P., Zweng, M. M., Garcia, H. E., et al. (2018). "Temperature," in *World Ocean Atlas 2018*. Editor A. Mishonov (Boston, MA: U.S. Government Printing Office), Vol. 1, 52.

Matsumoto, H., Araki, E., Kawaguchi, K., Nishida, S., and Kaneda, Y. (2014). "Long-term features of quartz pressure gauges inferred from experimental and *in-situ* observations," in OCEANS 2014–TAIPEI, Taipei, Taiwan, April 7–10, 2014 (Piscataway, NJ: IEEE), 1–4. doi:10.1109/OCEANS-TAIPEI.2014.6964447

McDougall, T. J., and Barker, P. M. (2011). Getting started with TEOS--10 and the gibbs seawater (GSW) oceanographic toolbox. SCOR/IAPSO. Technical Paper WG127.

McGuire, J. J., and Collins, J. A. (2013). Millimeter-level precision in a seafloor geodesy experiment at the Discovery transform fault, East Pacific Rise. *Geochem. Geophys. Geosyst*. 14, 4392–4402. doi:10.1002/ggge.20225

Muramoto, T., Ito, Y., Inazu, D., Wallace, L. M., Hino, R., Suzuki, S., et al. (2019). Seafloor crustal deformation on ocean bottom pressure records with nontidal variability corrections: application to hikurangi margin, New Zealand. *Geophys. Res. Lett*. 46, 303–310. doi:10.1029/2018GL080830

Nishida, S., Kimura, T., Machida, Y., and Araki, E. (2019). "Level adjust unit at seafloor for precise pressure measurement," in 2019 IEEE Underwater Technology (UT), Taiwan, Taiwan, April 16–19, 2019 (Piscataway, NJ: IEEE), 1–4. doi:10.1109/UT.2019.8734331

Nooner, S. L., and Chadwick, W. W. (2016). Inflation-predictable behavior and co-eruption deformation at Axial Seamount. *Science* 354, 1399. doi:10.1126/science.aah4666

Nooner, S. L., Webb, S. C., Buck, W. R., and Cormier, M.-H. (2014). Post eruption inflation of the east Pacific rise at 9°50′ N. *Geochem. Geophys. Geosyst*. 15, 2676–2688. doi:10.1002/2014GC005389

Paros, J., Migliacio, P., and Schaad, T. (2012a). "Nano-resolution sensors for disaster warning systems," in 2012 Oceans–Yeosu, Yeosu, South Korea, May 21–24, 2012 (Piscataway, NJ: IEEE), 1–5. doi:10.1109/OCEANS-Yeosu.2012.6263413

Paros, J., Migliacio, P., Schaad, T., Chadwick, W., Meinig, C., Spillane, M., et al. (2012b). "Nano-resolution technology demonstrates promise for improved local tsunami warnings on the MARS project," in 2012 Oceans–Yeosu, Yeosu, South Korea, May 21–24, 2012 (Piscataway, NJ: IEEE), 1–6. doi:10.1109/OCEANS-Yeosu.2012.6263411

Paros, J. M., and Kobayashi, T. (2015a). Mathematical models of quartz sensor stability. Available at: http://paroscientific.com/pdf/G8095_Mathematical_Models.pdf.

Paros, J. M., and Kobayashi, T. (2015b). Root causes of quartz sensor drift. Available at: http://paroscientific.com/pdf/G8101_Root_Causes_of_Quartz_Sensors_Drift.pdf.

Paroscientific, Inc. (2016). Digiquartz broadband intelligent instruments with RS-232 and RS-485 interfaces: user manual. Available at: http://paroscientific.com/pdf/8819-001_Digiquartz_Operations_Manual_for_RS_485_RS_232_Products_715_Display.pdf.

Polster, A., Fabian, M., and Villinger, H. (2009). Effective resolution and drift of Paroscientific pressure sensors derived from long-term seafloor measurements. *Geochem. Geophys. Geosyst*. 10, Q08008. doi:10.1029/2009GC002532

Ryan, H. F., and Noble, M. (2002). Sea level response to ENSO along the central California coast: how the 1997–1998 event compares with the historic record. *Prog. Oceanogr*. 54, 149–169. doi:10.1016/S0079-6611(02)00047-2

Sasagawa, G., Cook, M. J., and Zumberge, M. A. (2016). Drift-corrected seafloor pressure observations of vertical deformation at Axial Seamount 2013–2014. *Earth Space Sci*. 3, 2016EA000190. doi:10.1002/2016EA000190

Sasagawa, G. S., Zumberge, M. A., and Cook, M. J. (2018). Laboratory simulation and measurement of instrument drift in quartz-resonant pressure gauges. *IEEE Access*. 6, 57334–57340. doi:10.1109/ACCESS.2018.2873479

Sasagawa, G., and Zumberge, M. A. (2013). A self-calibrating pressure recorder for detecting seafloor height change. *IEEE J. Ocean. Eng*. 38, 447–454. doi:10.1109/JOE.2012.2233312

Shchepetkin, A. F., and McWilliams, J. C. (2005). The regional oceanic modeling system (ROMS): a split-explicit, free-surface, topography-following-coordinate oceanic model. *Ocean Model*. 9, 347–404. doi:10.1016/j.ocemod.2004.08.002

Suzuki, K., Nakano, M., Takahashi, N., Hori, T., Kamiya, S., Araki, E., et al. (2016). Synchronous changes in the seismicity rate and ocean-bottom hydrostatic pressures along the Nankai trough: a possible slow slip event detected by the Dense Oceanfloor Network system for Earthquakes and Tsunamis (DONET). *Tectonophysics* 680, 90–98. doi:10.1016/j.tecto.2016.05.012

Taburet, G., Sanchez-Roman, A., Ballarotta, M., Pujol, M.-I., Legeais, J.-F., Fournier, F., et al. (2019). Duacs DT2018: 25 years of reprocessed sea level altimetry products. *Ocean Science* 15, 1207–1224. doi:10.5194/os-15-1207-2019

Wallace, L. M., Webb, S. C., Ito, Y., Mochizuki, K., Hino, R., Henrys, S., et al. (2016). Slow slip near the trench at the Hikurangi subduction zone, New Zealand. *Science* 352, 701–704. doi:10.1126/science.aaf2349

Wang, K., and Tréhu, A. M. (2016). Invited review paper: some outstanding issues in the study of great megathrust earthquakes-The Cascadia example. *J. Geodyn*. 98, 1–18. doi:10.1016/j.jog.2016.03.010

Watts, D. R., and Kontoyiannis, H. (1990). Deep-ocean bottom pressure measurement: drift removal and performance. *J. Atmos. Ocean. Technol*. 7, 296–306. doi:10.1175/1520-0426(1990)007<0296:DOBPMD>2.0.CO;2

Webb, S. C. (1998). Broadband seismology and noise under the ocean. *Rev. Geophys*. 36, 105–142. doi:10.1029/97RG02287

Webb, S. C., and Nooner, S. L. (2016). High-resolution seafloor absolute pressure gauge measurements using a better counting method. *J. Atmos. Ocean. Technol*. 33, 1859–1874. doi:10.1175/JTECH-D-15-0114.1

Wilcock, W. S. D., Manalang, D. A., and Harrington, M. J. (2020). Pressure, barometer and acceleration data from a 30-month deployment of the Geodetic and Seismic Sensor Module in Monterey Bay from June 2017 to December 2019 [Data set]. University of Washington. doi:10.6069/X6BZ-410

Wilcock, W. S. D., Manalang, D. A., Harrington, M. J., Fredrickson, E. K., Cram, G., Tilley, J., et al. (2018). "New approaches to in situ calibration of seafloor geodetic measurements," in 2018 Oceans-Kobe, Kobe, Japan, May 28–31, 2018 (Piscataway, NJ: IEEE), 1–8. doi:10.1109/OCEANSKOBE.2018.8559178

Zumberge, M. A., Hatfield, W., and Wyatt, F. K. (2018). Measuring seafloor strain with an optical fiber interferometer. *Earth Space Sci*. 5, 371–379. doi:10.1029/2018EA000418

Zweng, M. M., Reagan, J. R., Seidov, D., Boyer, T. P., Locarnini, R. A., Garcia, H. E., et al. (2018). "Salinity," in *World Ocean Atlas 2018*. Editor A. Mishonov (Boston, MA: U.S. Government Printing Office), Vol. 2, 50.

Conflict of Interest: JP is the Founder, President and Chairman of Paroscientific, Inc., that develops and manufactures the quartz crystal sensors and the SOS module. He provided advice and support for the design of the GSSM and the best approaches for correcting sensor drift but was not directly involved in the acquisition or analysis of the data.

The remaining authors declare that the research was conducted in the absence of any commercial or financial relationships that could be construed as a potential conflict of interest.

frontiers in Earth Science

ORIGINAL RESEARCH
published: 22 January 2021
doi: 10.3389/feart.2020.600793

Characteristics of Slow Slip Event in March 2020 Revealed From Borehole and DONET Observatories

Keisuke Ariyoshi[1], Takeshi Iinuma[1], Masaru Nakano[1], Toshinori Kimura[1], Eiichiro Araki[1], Yuya Machida[1], Kentaro Sueki[1], Shuichiro Yada[1], Takehiro Nishiyama[1], Kensuke Suzuki[2], Takane Hori[1], Narumi Takahashi[1,3] and Shuichi Kodaira[1]*

[1]*Japan Agency for Marine-Earth Science and Technology, Yokohama, Japan,* [2]*Sendai Regional Headquarters, Japan Meteorological Agency, Sendai, Japan,* [3]*National Research Institute for Earth Science and Disaster Resilience, Tsukuba, Japan*

OPEN ACCESS

Edited by:
Keiichi Tadokoro, Nagoya University, Japan

Reviewed by:
Michel Campillo, Université Grenoble Alpes, France
Norio Matsumoto, National Institute of Advanced Industrial Science and Technology (AIST), Japan

***Correspondence:**
Keisuke Ariyoshi
ariyoshi@jamstec.go.jp

Specialty section:
This article was submitted to Solid Earth Geophysics, a section of the journal Frontiers in Earth Science

Received: *31 August 2020*
Accepted: *07 December 2020*
Published: *22 January 2021*

Citation:
Ariyoshi K, Iinuma T, Nakano M, Kimura T, Araki E, Machida Y, Sueki K, Yada S, Nishiyama T, Suzuki K, Hori T, Takahashi N and Kodaira S (2021) Characteristics of Slow Slip Event in March 2020 Revealed From Borehole and DONET Observatories. Front. Earth Sci. 8:600793. doi: 10.3389/feart.2020.600793

We have detected an event of pore pressure change (hereafter, we refer it to "pore pressure event") from borehole stations in real time in March 2020, owing to the network developed by connecting three borehole stations to the Dense Oceanfloor Network System for Earthquakes and Tsunamis (DONET) observatories near the Nankai Trough. During the pore pressure event, shallow very low-frequency events (sVLFEs) were also detected from the broadband seismometers of DONET, which suggests that the sVLFE migrated toward updip region along the subduction plate boundary. Since one of the pore pressure sensors have been suffered from unrecognized noise after the replacement of sensors due to the connecting operation, we assume four cases for crustal deformation component of the pore pressure change. Comparing the four possible cases for crustal deformation component of the volumetric strain change at C0010 with the observed sVLFE migration and the characteristic of previous SSEs, we conclude that the pore pressure event can be explained from SSE migration toward the updip region which triggered sVLFE in the passage. This feature is similar to the previous SSE in 2015 and could be distinguished from the unrecognized noise on the basis of *t*-test. Our new finding is that the SSE in 2020 did not reach very shallow part of the plate interface because the pore pressure changes at a borehole station installed in 2018 close to the trough axis was not significant. In the present study, we estimated the amount, onset and termination time of the pore pressure change for the SSE in 2020 by fitting regression lines for the time history. Since the change amount and duration time were smaller and shorter than the SSE in 2015, respectively, we also conclude that the SSE in 2020 had smaller magnitude that the SSE in 2015. These results would give us a clue to monitor crustal deformation along the Nankai Trough directly from other seafloor observations.

Keywords: shallow very low-frequency event (sVLFE), slow earthquake, Nankai trough, pore pressure, seafloor leveling change, crustal deformation

INTRODUCTION

In the wake of the 2004 Sumatra-Andaman earthquake (e.g., Wiseman and Bürgmann, 2011), the Japanese government has established seafloor networks of cable-linked observatories around Nankai Trough (**Figure 1**): DONET (Dense Oceanfloor Network system for Earthquakes and Tsunamis along the Nankai Trough) which has sensors of broadband seismogram, strong ground motion, and hydraulic pressure (e.g., Kaneda et al., 2015; Kawaguchi et al., 2015). DONET has been expected to monitor the propagation process of tsunami (e.g., Maeda et al., 2015) and seismic waves (Nakamura et al., 2015) as well as seismic activity (Nakano et al., 2016; 2018) in real time.

Owing to inland dense networks of seismic and geodetic observations have revealed that slow earthquakes occur along the subduction plate boundaries in the shallower and deeper extensions of megathrust earthquake source regions worldwide (e.g., Schwartz and Rokosky, 2007; Obara and Kato, 2016). Slow earthquake is assumed to be classified into several types according to the spatiotemporal scale (Ide et al., 2007). For example, low-frequency tremor and very low-frequency events (VLFEs) have dominant periods of approximately several hertz (Obara, 2002) and 10–100s (Ito et al., 2007), respectively, whereas slow slip events (SSEs) have a duration time of days to years (Dragert et al., 2001).

As a Japanese governmental organization, Earthquake Research Committee of the Headquarters for Earthquake Research Promotion (2013) has pointed out the possibility of megathrust earthquakes occurring along Nankai in the near future. Slow earthquake is more sensitive to stress change than a regular earthquake (Obara and Kato, 2016); hence, it is important to monitor slow earthquake activities close to a megathrust earthquake. Some numerical simulations have demonstrated that the recurrence interval and the moment

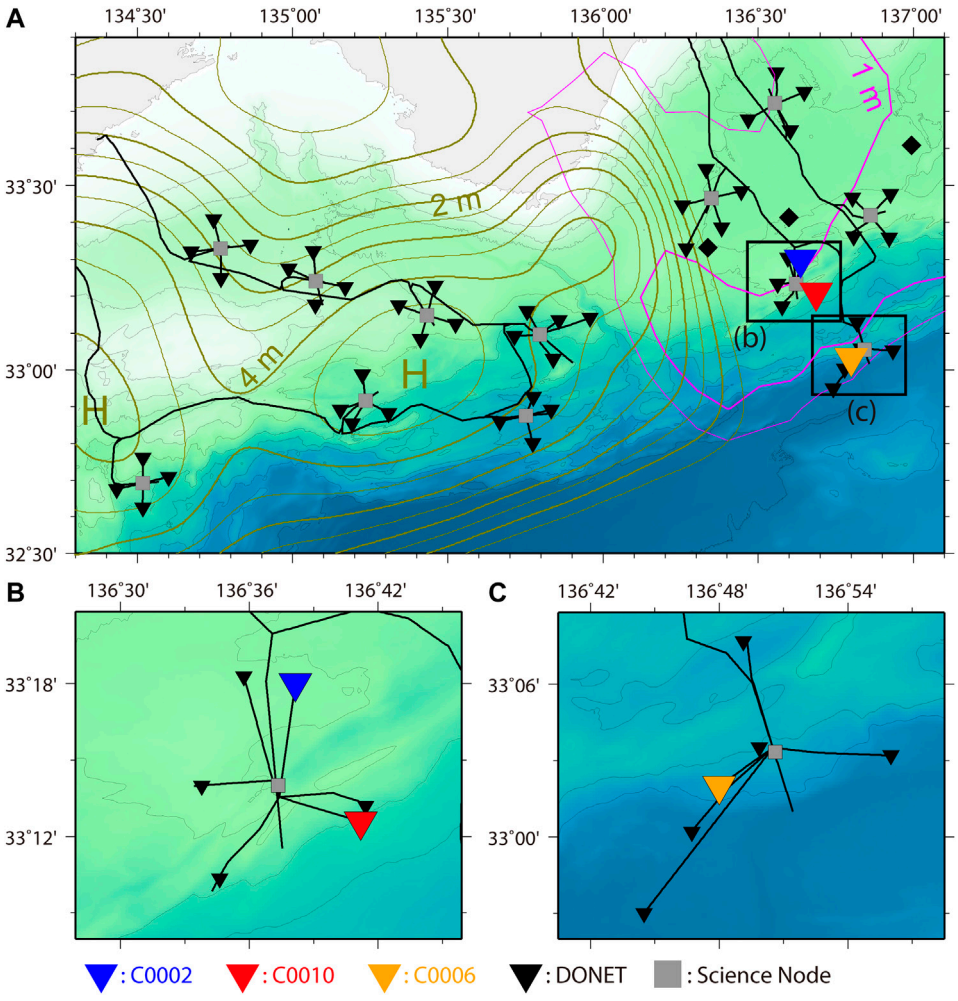

FIGURE 1 | A) Map of the borehole observatories and DONET stations along Nankai Trough. The triangle marks (▼ blue, ▼ red, ▼ yellow, and ▼ black) represent C0002, C0010, and C0006 of the borehole observatories and the DONET stations, respectively. The diamonds represent the GNSS-A stations. The magenta and olive contours represent the slip distributions of the 1944 Tonankai and 1946 Nankai earthquakes, respectively (Ichinose et al., 2003; Murotani et al., 2015). Their contour interval is 0.5 m. L and H: regions of low and high slip, respectively. **(B)** Closeup of C0002 and C0010 of the borehole observatories and D-node of the DONET station. **(C)** Closeup of C0006 and C-node.

release rate of VLFEs/SSEs become shorter and higher, respectively, in the pre-seismic stage of a megathrust earthquake (Matsuzawa et al., 2010; Ariyoshi et al., 2012).

For the shallower slow earthquakes occurred in the shallower extension, these changes are expected to be larger than those in the deeper one from numerical simulation study (Ariyoshi et al., 2014a; Ariyoshi et al., 2014b). Shallower VLFEs near the trench (sVLFE) has been detected around the Nankai Trough not only by seafloor cabled networks (Nakano et al., 2016; Nakano et al., 2018; Nishikawa et al., 2019) but also by inland seismic networks (Takemura et al., 2019). By contrast, the shallower SSE near the trench has so far been detected only from the pore pressure change of the borehole observatories (Wallace et al., 2016; Araki et al., 2017) and the seafloor global navigation satellite system-acoustic (GNSS-A) (Ishikawa et al., 2020) because the SSE can be detected by static crustal deformation with distance r^{-3} decay, which is too small for inland GNSS networks. However, the data of the borehole observatories at that time were offline. GNSS-A is also offline, and its time resolution of the SSE signal detection is 0.2 years (Yokota and Ishikawa, 2020).

Recently, the borehole observatories in holes C0002 (**Figure 2**), C0010, and C0006 were successfully connected to

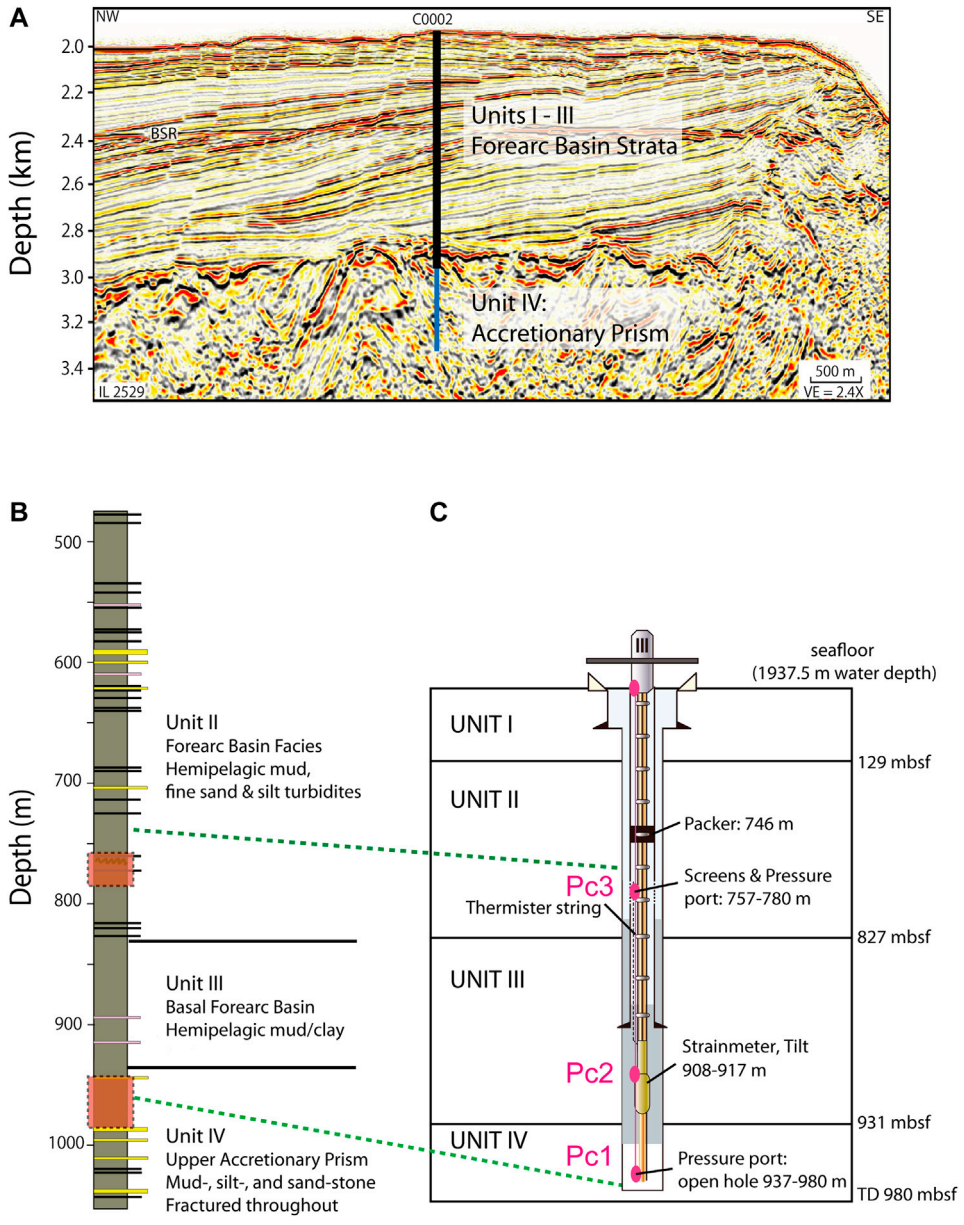

FIGURE 2 | (A) Seismic section showing the location of the borehole observatory installation at C0002. **(B)** Schematic stratigraphic column. Gray: clay and mudstone. Black: silt. Yellow: sand. Pink: ash. **(C)** Borehole completion diagram. The solid magenta ellipses indicate the pressure gauges, where the top one is a hydrostatic reference pressure sensor used to remove oceanographic signals. This figure is modified after the **Supplemental Material** of Araki et al. (2017).

DONET: C0002 in January 2013 (Kitada et al., 2013), C0010 in April 2016 (Saffer et al., 2017), and C0006 in March 2018. This operation has enabled us to monitor crustal deformation along the Nankai Trough in real time. Afterward, in the latter part of March 2020 (**Figure 3**), significant change of pore pressure (we refer to "pore pressure event") and five sVLFEs were detected by the borehole site C0002 and broadband seismometers of DONET, respectively. On the other hand, there is no signal at C0006. For C0010, there appears pore pressure change during that time, but it seems not to be stable before and after that period. This instability began after the replacement operation of the sensors, which means the possibility that the record of the pore pressure at C0010 contains both crustal deformation and other unrecognized fluctuations. Therefore, it is very important to examine whether those changes could be explained by a reasonable fault model of SSE or not. In the present study, we first reviewed the pore pressure change and sVLFE activity. Next, we investigate the time history of pore pressure change at C0002 by fitting regression lines. Using these results, we try to find reasonable fault models for the pore pressure event by considering possible cases of pore pressure change at C0010, the observed sVLFE, and the characteristics of previous SSEs when C0010 was stable. To evaluate the reliability of pore pressure record at C0010, we conduct *t*-test between the pore pressure event and the unrecognized fluctuation for yearlong data before the pore pressure event. Finally, we discussed the detectability of the seafloor crustal deformation caused by the possible fault models, toward monitoring the plate coupling around the Nankai Trough.

PORE PRESSURE CHANGE AT BOREHOLES

Three borehole observatories (i.e., C0002, C0010, and C0006) in the sedimentary wedge can be found above the subduction plate boundary in the Nankai Trough. An overview of the observatory station at C0002, which is the main target of the present study, is shown in **Figure 2**. We have continuously monitored the crustal deformations, using the pore pressure changes observed by the sensors installed in finely grained sediments with low permeability. For each observatory, two or three sensors were installed at hydraulically isolated depth intervals (C0002: 1966 m depth below sea level [mbsl], Pc1: 937–980 m depth below seafloor [mbsf], and Pc2: 908–917 mbsf, Pc3: 757–780 mbsf; C0010: 2524 mbsl, Pc1: 610 mbsf, and Pc3: 405 mbsf; C0006: 3872 mbsl, Pc1: 456 mbsf, and Pc2: 426 mbsf). We focused herein on the deepest pore pressure (Pc1) at each borehole to see the crustal deformation close to the subduction plate boundary.

The pore pressure change mainly reflects the contributions from the following components: volumetric strain change driven by the crustal deformation in the accretionary prism several kilometers above the plate interface (Davis et al., 2006), ocean tides and other oceanographic loading (Araki et al., 2017), and dynamic deformation due to the passage of seismic waves radiated from earthquakes (Katakami et al., 2020). We removed the oceanic loading using the reference pressure sensor on the seafloor co-located for each observatory (Araki et al., 2017). The value of coefficient (α) for the reference pressure is obtained by the method of least squares for R=(Pc1−α*Pc0).

If the pore pressure change is derived from elastic deformation, we can linearly convert it to the volumetric strain change. From previous studies, the conversion factors are obtained for each Pc1 at C0002 (5.7 kPa/μstrain), C0010 (4.7 kPa/μstrain), and C0006 (6.0 kPa/μstrain) (Davis et al., 2006; Wallace et al., 2016; Araki et al., 2017). Therefore, monitoring of the pore pressure change is useful to evaluate the crustal deformation.

Figure 3 shows the time history of Pc1 at each borehole from March to April in 2020 with the oceanic signals reduced, which suggests that pore pressure change at C0002 is similar to ramp function. This feature could not be explained from the oceanic loading. If this change is due to crustal deformation, the volumetric strain at C0002 had a significant dilation change (estimated as −0.14 μstrain) on March 17–26, 2020. By contrast, no significant change was observed at C0006. As mentioned in the introduction section, C0010 has already the unrecognized fluctuation before the pore pressure event. This means that we have to extract the crustal deformation component if the pore pressure event is driven by SSE, which is to be discussed in the following sections.

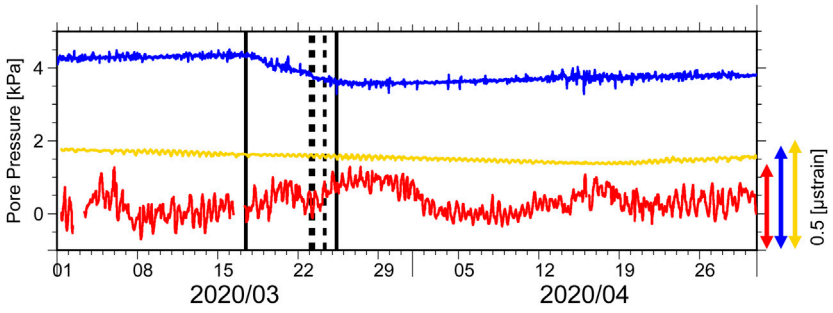

FIGURE 3 | Time history of the pore pressure at the deepest stations (Pc1) of each borehole observatory with a volumetric scale for each station (vertical double arrows). The oceanic signals are reduced by the reference hydraulic pressure gauge on the seafloor. The bold lines represent the onset/termination time of the pore pressure event. The dotted lines represent the origin times of the sVLFEs (**Table 1**).

sVLFE Activities Beneath the Borehole Observatories

Figure 4A shows past sVLFE activities off Tonankai and Nankai regions, which indicates that sVLFE is active locally around the strong coupling regions of the megathrust earthquakes. In the target area, sVLFE had occurred in the marginal part of the 1944 Tokai earthquake and the transition zone to the 1946 Nankai earthquake. From the previous results, the previous SSE source areas coincided with the sVLFE locations (Sugioka et al., 2012; Obara and Kato, 2016), and the sVLFEs were temporally excited during the SSE (Araki et al., 2017; Nakano et al., 2018).

We found the five sVLFEs between March 23 and 24, 2020 from the broadband velocity seismograms of the DONET stations along Nankai Trough. The sVLFE catalog during that period, indicating that one of them is a doublet event spatiotemporally, is shown in **Table 1**. We applied a centroid moment tensor waveform inversion to the broadband velocity seismometers at

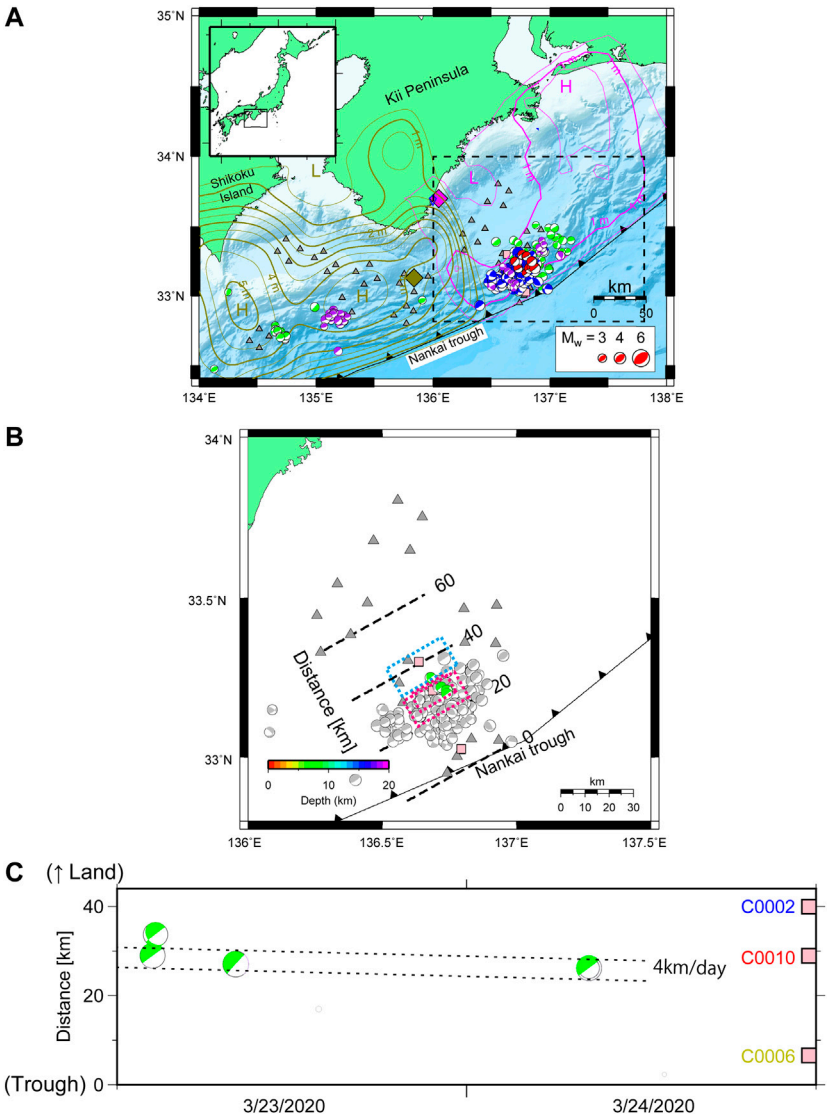

FIGURE 4 | (A) Past seismic activities in the study area. The gray triangles represent the locations of the DONET stations. The epicentral distribution of the focal mechanism for the sVLFE occurred in 2003–2004 (green: Obara and Ito, 2005; Ito and Obara 2006), 2009 (red: Sugioka et al., 2012), 2015 (purple: Nakano et al., 2016), and 2016 (blue: Nakano et al., 2018). Epicenters of the 1944 Tonankai and 1946 Nankai earthquakes are represented by magenta and olive diamonds, respectively. The magenta and olive contours are the same as **Figure 1A**. **(B)** Closeup of the rectangle region enclosed by black broken lines in **(A)**. The gray and green focal mechanisms represent the sVLFE catalog in 2016 (Nakano et al., 2018) and the latest one accompanied by the pore pressure event, respectively. The pink squares represent the borehole stations buried with the focal mechanism in **(A)**. The dotted rectangles represent the fault models of Case A-1 (cyan) and Case A-2 (magenta) (A-2 is smaller, A-2+ is larger) for the pore pressure event (**Figure 6**). **(C)** Activities of the sVLFEs in March 2020 along the dip direction from the Nankai Trough with the same color scale of the depth profile in **(B)**. The dotted lines depict the migration speed at 4 km/day estimated by Nakano et al. (2018), where the interval of the two dotted lines is 5 km as a spatial resolution for the epicenter determination.

TABLE 1 | sVLFE catalog in March 2020.

Date	Time	Latitude	Longitude	Depth (km)	Mw
03/23/2020	02:24:39	33.22	136.72	7.0	3.4
	02:32:58	33.25	136.68	6.0	3.3
	08:10:30	33.21	136.74	6.0	3.5
03/24/2020	08:19:58	33.20	136.74	7.0	2.8
(Doublet)	08:21:10	33.20	136.74	7.0	3.4

each DONET station (Nakano et al., 2018) during the pore pressure event to determine the source location, fault orientation parameters, and moment magnitude of the sVLFEs. The obtained source location and moment magnitudes are listed in **Table 1**, where horizontal and vertical resolution is 5 and 2 km, respectively.

Figure 4B shows the focal mechanisms of the sVLFEs were low-angle thrust-type faults largely along the plate interface. These results are consistent with previous sVLFE activities (**Figure 4A**). The hypocenter distribution of the sVLFEs in 2020 overlapped the source regions of past sVLFEs in part of the large slip area of the great 1944 Tonankai earthquake (Ichinose et al., 2003).

The time history of the sVLFEs along the horizontal distance from the trench is shown in **Figure 4C**. As suggested in **Figures 4B,C**, the spatiotemporal change of the five sVLFEs in 2020 appeared to be characterized by a migration from downdip to updip toward the trench (**Figure 4C**). This result is similar to the previous SSE in 2016, whose migration rate was approximately 4 km/day (Nakano et al., 2018).

These results imply that the pore pressure event is driven by SSE migrating toward the trench and the time history of pore pressure at C0010 may partly have crustal deformation component, which is discussed in the following sections.

ESTIMATION OF THE ONSET/ TERMINATION TIME AND THE PORE PRESSURE CHANGE AT C0002

The duration time of the SSE was estimated in days (Araki et al., 2017; **Table 2**), whereas the origin time of the sVLFE was estimated in seconds (or less). This might cause difficulty to investigate the relationship between the SSE and sVLFE. One of the reasons of the daily solution for the SSE duration time is that the change in rate of the pore pressure at the beginning and ending of SSEs appears insufficiently clear, which is difficult to estimate the duration time precisely. We compensated for the gap of the time precision by trying to quantitatively estimate the amount of the pore pressure change and the onset/termination time of the pore pressure event in March 2020 by fitting regression lines, focusing on C0002 because of its simple behavior.

The time history of the pore pressure change at C0002 could be separated into three periods as before, during, and after the pore pressure event (**Figure 3**). Before and after the pore pressure event, linear regression analysis is well applicable with trend negligible. During the pore pressure event, however, a temporal decrease of the pore pressure was observed (hidden in **Figure 3** because of decimation operation), which could not be explained by the regression analysis and will be discussed later.

To avoid a wrong regression estimation caused by such an unrecognized perturbation during the pore pressure event, we only estimated the two regression lines before and after the pore pressure event by treating the onset and the termination time of the pore pressure event as unknown parameters. The remaining regression line during the pore pressure event can be obtained by connecting both edges of the two regression lines before and after the pore pressure event, which gives the change amount of the pore pressure during the event. We select the input data span from March 1 to April 9, 2020 so that the periods of before, during and after the pore pressure event is comparable, where this choice of the date range is not critical for the following result. We

TABLE 2 | Updated summary of the borehole pressure signals and SSE characteristic.

Dates	Polarity	$\Delta\varepsilon_v$ C0002 (μstrain)	$\Delta\varepsilon_v$ C0010 (μstrain)	Slip (cm)	Location (km)	Slip region
*Mar 11–13, 2011	Dilation	−0.32	−0.46	2–4	<25	Updip
Feb 14–Apr 26, 2012	Contraction	0.05	0.07	1–2	>36	Downdip
Dec 5–14, 2012	Mixed	−0.08	0.15	1–2	25–36	Intermediate
Mar 6–19, 2014	Mixed	−0.07	0.13	1–2	25–36	Intermediate
Nov 19–Dec 1, 2014	Contraction	0.04	0.05	1–2	>36	Downdip
Oct 8–Nov 4, 2015	Mixed	−0.24	0.15	2–4	25–36	Intermediate
*Oct 8–Nov 4, 2015	Dilation	−0.24	−0.15	2–4	<25	Updip
*Apr 3–18, 2016	Dilation	−0.48	N/A	2–4	<25	Updip
Aug 10–24, 2016	Mixed	−0.05	0.14	1–2	25–36	Intermediate
Jul 4–16, 2017	Mixed	−0.11	0.11	1–2	25–36	Intermediate
Apr 26–May 7, 2018	Mixed	−0.07	0.30	2–4	25–36	Intermediate

$\Delta\varepsilon_v$: the compressional volumetric strain is positive, whereas the dilatational one is negative.
*Location: distance from the center for the slip region of 20–40 km width to the trench landward, as shown by the equidistant lines in **Figure 4B**.*
Shaded region: the result from Araki et al. (2017).
**SSE accompanied by sVLFEs.*

adopted the least absolute value (L1 norm) to the evaluation function for all input data of 20 min sampling, moving the onset and the termination time during the data period at a 20 min interval. Although we also investigated other methods, such as the least squares method (L2 norm) with the time sampling changed, these methods could not obtain reasonable solutions.

Table 3 shows the results of best solution for each sensor at C0002. The standard deviations of the onset/termination time and the pore pressure change are 1.0 days and 1.0 hPa (1.1 days and 1.7 hPa for Pc3), respectively. Without the temporal decrease, the standard deviations are 9 h and 0.4 hPa, respectively. The time history of the pore pressure change compared with the regression lines of the analytical solution is shown in **Figure 5**. Since the time lag from the origin time of sVLFEs to the termination time of the pore pressure event (1 day and 20 min) is larger than the standard deviation (0.375 or 1.0 days), we statistically conclude that the sVLFE occurred during the pore pressure event.

From **Table 3** and **Figures 5A–C**, the best solution of Pc3 has shorter duration time due to the later onset and the earlier termination times than Pc1/Pc2. **Figure 5C** also shows that ocean noise component for Pc3 is significantly larger than that for Pc1 and Pc2. This means that the determination of the onset/termination time of the pore pressure event for Pc3 may not be robust. **Figure 5D** shows another regression combination for Pc3, assuming the onset/termination time is the same as Pc1 and Pc2, which seems also consistent with observation data. The amounts of pore pressure changes for Pc3 in **Figures 5C,D** are −10.3 and −10.0 hPa, respectively. This result suggests that the amplitude of ΔP for Pc3 is larger than Pc1 and Pc2, which is consistent with static dislocation model (Okada, 1992) due to the free surface condition.

POSSIBILITY OF SSE FOR THE PORE PRESSURE EVENT

In **Figure 3**, the unrecognized fluctuation of pore pressure at C0010 seems to be classified into (about daily) periodic and systematic components of non-crustal deformation. The amplitude of the systematic component is sometimes greater than that of periodic one. This means that it is not reasonable to estimate the onset/termination time and the amount of pore pressure change at C0010 solely from the time history. To evaluate the amount of pore pressure change statistically, we have to classify the time history of pore pressure change at C0010 into the signal (crustal deformation component), the systematic error and periodic perturbation.

TABLE 3 | Estimation results of pore pressure change due to the SSE in 2020.

Station	Onset	Time	Termination	Time	ΔP_{C0002} (hPa)
Pc1	17 March	11:20	25 March	08:40	−8.0
Pc2	17 March	11:20	25 March	08:40	−7.9
Pc3	18 March	14:00	25 March	04:40	−10.3 (−10.0)*

() is the value in case of both the onset/termination time is the same as Pc1 and Pc2 as shown in **Figure 5D**.*

In this section, we try to find a reasonable time series of pore pressure change at C0010 and discuss the validity of identifying the pore pressure event as SSE by considering our results mentioned above and characteristics of previous SSEs.

Possible Cases of the Onset/Termination Times and Volumetric Strain Change at C0010

First, we compare the pore pressure event with previous SSEs which accompanied sVLFE. From **Table 2**, the corresponding SSEs occurred in 2011, 2015 and 2016. Unfortunately, the pore pressure record at C0010 was not obtained for SSE in 2016. Hence, we focus on the SSEs in 2011 and 2015. Since these SSEs occurred before the replacement of sensors at C0010, the quality of pore pressure record at C0010 was as good as C0002. For these SSEs, the onset and termination time of the pore pressure change is almost simultaneous between C0002 and C0010 (Araki et al., 2017). Therefore, we focus on the pore pressure records of the pore pressure event between the onset and termination times estimated in the preceding section (17 March 11:20 to 25 March 08:40; as listed in **Table 3**) as shown in **Figures 5A,B**.

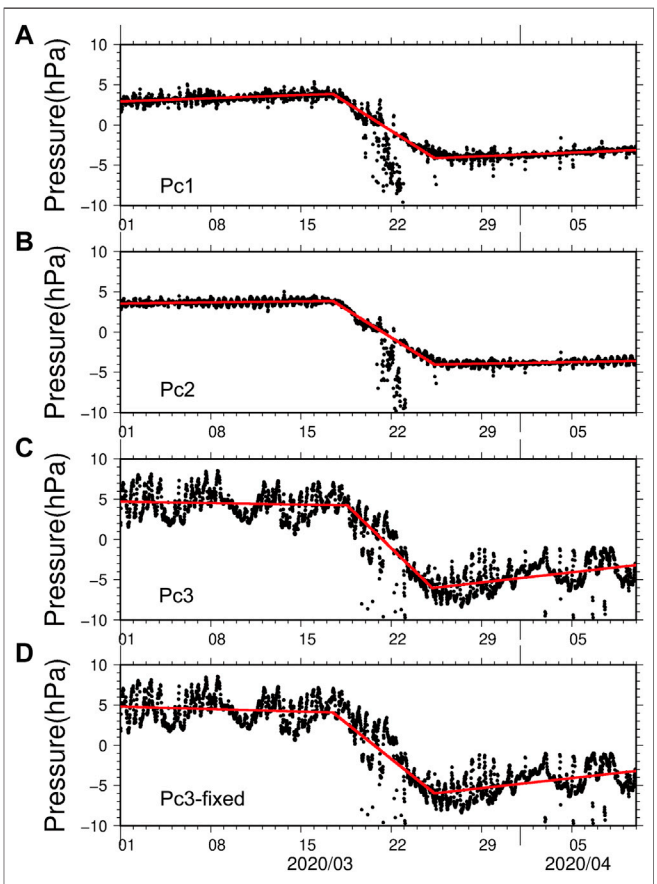

FIGURE 5 | Time history of the pore pressure (dotted black: 20 min sampling) with the fitting regression lines (red) for **(A)** Pc1, **(B)** Pc2, **(C)** Pc3, and **(D)** Pc3 under the same time of onset and termination as Pc1 and Pc2.

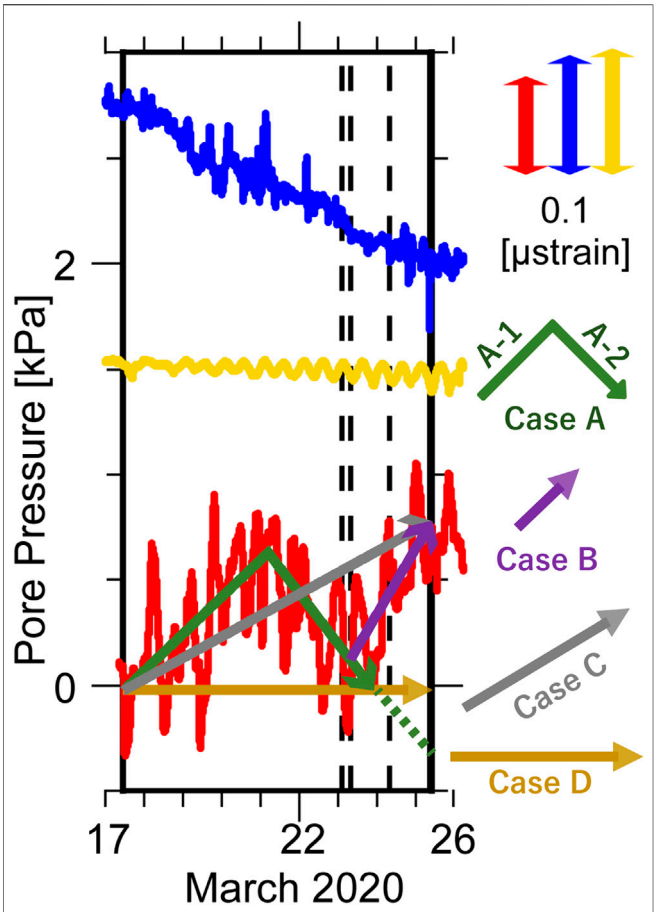

FIGURE 6 | Close up of the time history of the pore pressure (**Figure 3**) during the event, where the onset/termination time is determined by **Figures 5A,B**. Arrows indicate possible cases for the time histories of crustal deformation component at C0010 determined by regression lines (see text). The dotted lines represent additional Cases A-2+ and C+ as listed in **Table 4**.

On the basis of the time history of pore pressure at C0010 during the event, we assume four possible cases as shown by arrows in **Figure 6**. Case A is derived from the SSE in 2015, which is divided into the increase (A-1) and decrease (A-2) cases of the pore pressure. This means that the crustal deformation of SSE is composed of Cases A-1 and A-2, where the latter part of increase at C0010 in **Figure 6** is treated as unrecognized noise component. In addition, we also assume Case A-2+, whose dilation lasts for the dilation of C0002 time as shown by dotted line in **Figure 6**, in according to SSE in 2015 (Araki et al., 2017). Case B assumes that the latter part of increase is the crustal deformation component. Case C assumes that the decrease of pore pressure is the unrecognized noise and the crustal deformation is described as monotonic increase. Case D assumes that there is no signal like C0006.

To estimate the pore pressure change at C0010 for each Case and onset times for Cases A-2 and Case B, we apply the same regression analysis as **Figure 5** to C0002 by treating the error of periodic component of fluctuation approximately as a Gaussian distribution. **Figure 6** shows the best solutions of regression lines for each Case. The amounts of volumetric strain changes at C0002 and C0010 for each Case and the onset times for Case A-2 and Case B are listed in **Table 4**, where the volumetric strain changes at C0002 for Cases A-1, A-2 and B are determined by the onset/termination times under the constant decrease rate of the best regression analysis in **Figure 5**. The standard deviations of the pore pressure change at C0010 and onset time are 2.1 hPa (~0.045 μstrain) and 0.86 days, respectively.

Statistical Evaluation of Confidence for Each Case of Pore Pressure Change at C0010

As mentioned in Section *Possible Cases of the Onset/Termination Times and Volumetric Strain Change at C0010*, we assume that the pore pressure change at C0010 contains crustal deformation component between the onset and termination times estimated from C0002. However, there is still possibility that the pore pressure change at C0010 during that time span is due to unrecognized fluctuation. In this section, we try to evaluate the statistical confidence of the crustal deformation component at C0010 for each Case in **Figure 6**.

To verify the possibility of crustal deformation at C0010 due to SSE statistically, we adopt the minimum square method for the regression lines of all Cases in **Figure 6**,

$$S(i) = \left\{ y(t_i) - f_{(\mathrm{A,B,C,D})}\ (t_i) \right\}^2, \tag{1}$$

$$U = \{S(1), S(2), \ldots, S_n\}, \tag{2}$$

where t and i are time and its index, respectively. y and $f_{(\mathrm{A,B,C,D})}$ are observational data and the regression analysis in **Figure 6**, respectively. n is the number of 20 min sampling for each Case as listed in **Table 4**. For the pore pressure event (**Figure 6**), the average and standard deviation of $S(i)$ in $U_{(\mathrm{A,B,C,D})}$ are obtained as $\overline{S}$ and σ.

Since the last SSE occurred in May 2018 (**Table 2**), we can treat the yearlong data from 16 March in 2019 to 16 March in 2020 (**Figure 7**) as the reference of the unrecognized fluctuation. If the time series of pore pressure change at C0010 in **Figure 6** were due to the unrecognized fluctuation, similar change would occur in

TABLE 4 | Possible cases of the volumetric strain change due to the SSE in 2020.

	Polarity	C0002 (μstrain)	C0010 (μstrain)	Onset Time (March 2020)	Termination Time (March 2020)	Sample (n)
A-1	Mixed	−0.066	+0.14	17 11:20	21 04:00	
Case	↓	↓	↓			
A-2	Dilation	−0.074	−0.14	21 04:00	23 20:40	461*
A-2+			−0.22	21 04:00	25 08:40	569*
Case B	Mixed	−0.066	+0.14	23 06:20	25 08:40	152
Case C	Mixed	−0.14	+0.17	23 06:20	25 08:40	569
Case D	—	−0.14	0.0	23 06:20	25 08:40	569

**Total sample of Case A-1 and A-2 (+).*
Compressional volumetric strain is positive, whereas the dilatational one is negative.

the yearlong period. For the yearlong data, we calculate $\overline{S}'$ and σ' with the same number of sampling as the regression lines for each Case (**Table 4**), moving the time window by one sampling at a time from the beginning to the end of the yearlong data.

If the pore pressure change at C0010 in **Figure 6** is significantly different from the unrecognized fluctuation (**Figure 7**), there should be always significant difference between $\overline{S}$ and $\overline{S}'$ for all the time window in the yearlong period. Here, we apply two-sample t-test between ($\overline{S}$, σ) and ($\overline{S}'$, σ') for each moving time window to verify whether $\overline{S} < \overline{S}'$ or not, where the value of t statistics is described as

$$t = \frac{\overline{S}' - \overline{S}}{\sqrt{(\sigma^2 + (\sigma')^2)/n}}, \quad (3)$$

and t distribution is approximated as the standard normal distribution function because of high degree of freedom ($n-1 > 100$).

Figure 8 shows the time history of t statistics for each Case. **Figures 8A,B** show that the value of t statistics is basically positive (>5). For Case (A-1) to (A-2+), the (negative) minimum value of the t statistics is -0.84 for the time window between 27 April 08:40 and 5 May 05:40 in 2019 and -0.74 between 31 March 20:00 and 8 April 16:40 (dotted lines in **Figure 7**). These mean that the probability of $\overline{S} < \overline{S}'$ is 20% and 27%, respectively. For the other Cases, **Figure 8** shows that there are many time windows with the t statistics less than -5, where the probability of $\overline{S} < \overline{S}'$ is less than 0.01%. From these results, Cases B, C, and D could not be distinguished from the unrecognized fluctuation, and the reliability of Case (A-1) to (A-2+) for crustal deformation component is at most 20% because of low S/N ratio. In the following sections, we try to enhance the reliability of pore pressure change at C0010 by considering sVLFE activities as well as pore pressure changes at other borehole sites.

Relationship Between the Volumetric Strain Change and Fault Location of SSE

Because of the insufficient number of borehole observatories, it is practically difficult to estimate the fault parameters by inversion method. In this study, we assume that SSE occurred on the plate interface beneath the borehole observatories, according to the previous method (Wallace et al., 2016; Araki et al., 2017).

We set up the fault location, fault width, and fault displacement as unknown parameters which well explain the two volumetric strain changes at C0002 and C0010. Considering the spatial resolution due to limited observations, we assume that the epicentral location for the center point of fault is along the line between C0002 and C0010, the width is 20 or 40 km, and the displacement is 1-2 or 2–4 cm. The forward modeling assumed a simple rectangular fault model (Okada, 1992) in a homogeneous elastic medium with a Poisson's ratio of 0.35 and a rigidity of 20 GPa, which is the same condition as Araki et al. (2017). The simplified fault model assumed that the direction angles of strike, dip, and rake were 239° (along subduction direction), 6°, and 90°, respectively, where the strike direction was orthogonal to the equidistant lines from the trench in **Figure 4B**.

For the previous SSEs, the polarities of the volumetric strain changes at C0002 and C0010 reflects the relative location between the two sites and SSE (Araki et al., 2017). Following the result, we classified the polarities into three patterns: 1) Mixed pattern with a dilation at hole C0002 and a contraction at C0010 under the condition of a similar magnitude between them, 2) Dilation at both sites, and 3) Contraction at both sites. These patterns can roughly constrain the fault location relative to the two sites. We categorized the possible slip regions into three on the basis of the distance from the trench to the center for the 20–40 km-wide fault (**Table 2**): updip region (<25 km) for the Dilation polarity, intermediate region for the Mixed (25–36 km), and downdip region (>36 km) for the Contraction.

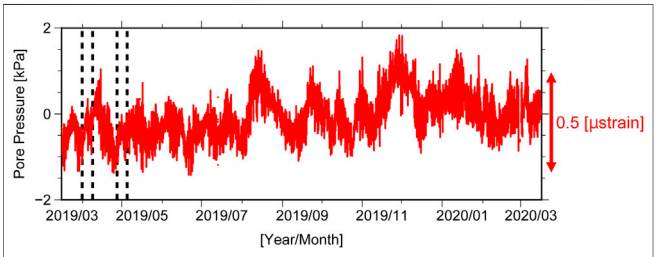

FIGURE 7 | Time history of the pore pressure at the deepest stations (Pc1) of C0010 with a volumetric scale for each station (vertical double arrows) from one year before to the one day before the onset time of the pore pressure event. Two pairs of vertical dotted lines indicate the time windows of best fitting regression lines for Case (A-1) to (A-2+) as indicated by vertical arrows in **Figure 8**.

Constraint of sVLFE Migration on the SSE Fault Models

Next, we apply the fault estimation to the volumetric strain change for each Case, where the polarity is summarized in **Table 4**. Case A has combination of the Dilation (A-1) and the Mixed (A-2) polarities. This means the fault slip migrated from the intermediate region (A-1) to updip (A-2). Case B and Case C have the Mixed polarity with the fault slip in the intermediate region. Case D has the Dilation polarity with the fault slip in the updip region.

From recent results, the sVLFEs were detected from the DONET seismic records during the SSEs in 2011 (To et al., 2015), 2015 (Nakano et al., 2016), and April 2016 (Nakano et al., 2018) [(*), **Table 2**), whereas the sVLFE has not been detected during the other SSEs. Nakano et al. (2018) suggested that whether the SSE will be accompanied by an sVLFE or not is dependent on the source location. If the SSE is in the downdip or intermediate region, sVLFE does not occur. If the SSE migrates to the updip region and reach the source regions of sVLFEs, sVLFEs occur during the SSE.

As investigated in the Section *sVLFE Activities Beneath the Borehole Observatories*, five sVLFEs were detected during the pore pressure event, migrating toward the updip region. Their focal mechanisms of the sVLFEs were on the subduction plate

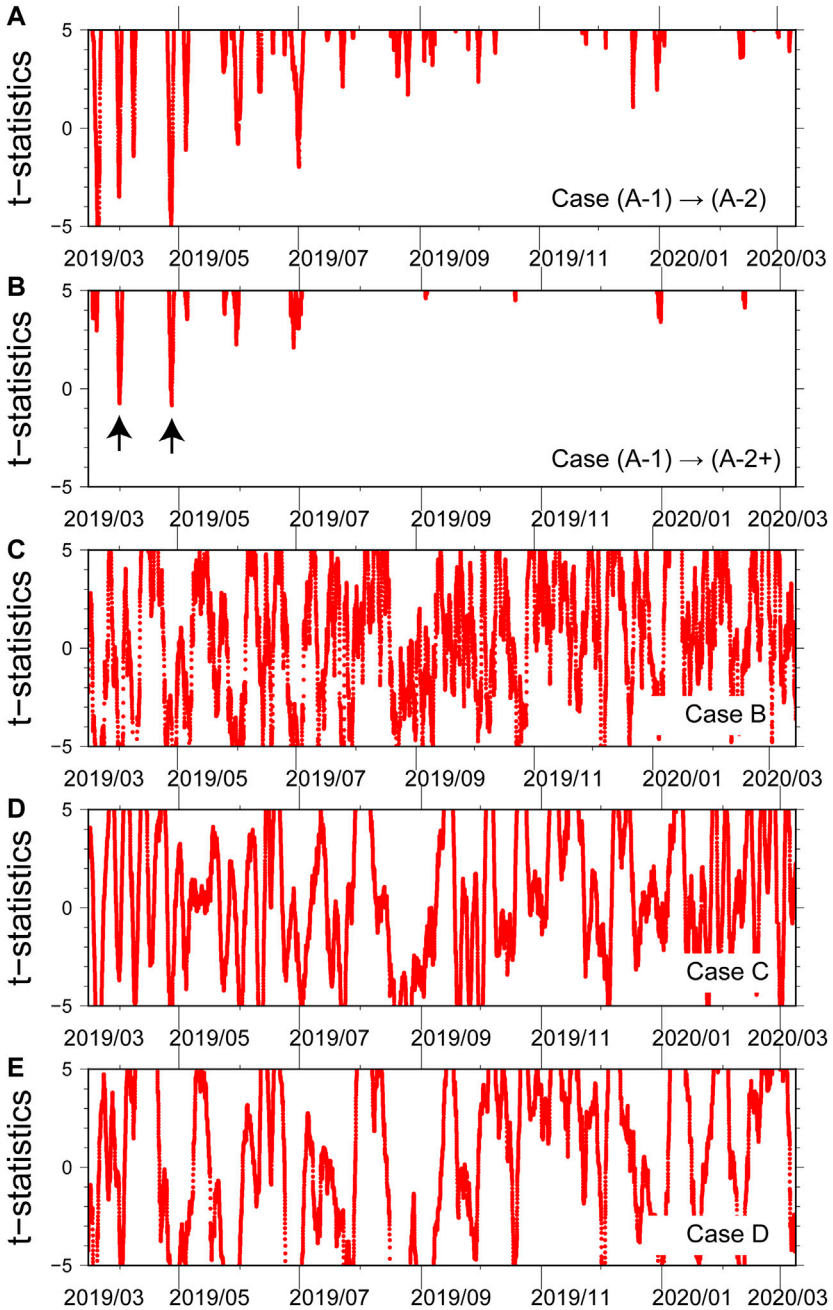

FIGURE 8 | Time history of t-statistics in **Eq. (3)** for each Case. Horizontal axis is origin time of fitting time window. Positive value of *t*-statistics means regression lines explain crustal deformation component due to SSE better than unrecognized fluctuation. Vertical arrows indicate the minimum value of *t*-statistics for Case (A-1) to (A-2+), where corresponding time windows are indicated by two pairs of vertical dotted lines in **Figure 7**.

boundary with low dip angles (**Figure 4C**), which meets the dip angle subducting there. These features are consistent with the suggestion by Nakano et al. (2018) for the previous SSEs as mentioned above.

Considering these results, Case C is not acceptable because the pore pressure event was accompanied by sVLFEs which needs slip in the updip region. In addition, since the epicentral location are of sVLFEs are close to C0010 as shown in **Figure 4**, Case D is not acceptable because no signal at C0010 contradicts the sVLFE activity during the pore pressure event (**Figure 4B**).

Estimation of the Reasonable SSE Fault Model Without Depth Fixed Condition

To investigate the validity of Cases A-C, we try to find the best fit model for each Case by adopting alternative grid search without

depth fixed on the subduction plate boundary, confirming whether the fault location is on the subduction plate boundary or not and whether its slip migration is toward the updip region or not.

In our model, the aspect ratio of the fault was assumed to be 2.0, and the directions of the strike, dip, and rake were fixed as 240°, 6°, and 90°, respectively. The other parameters were the same as those of the simplified model in the Section *Statistical Evaluation of Confidence for Each Case of Pore Pressure Change at C0010*. We adopted grid search by fitting the location, size, and depth of the fault compared with the two volumetric strain changes between each Cases A-C (**Table 4**) and the calculation. The grid intervals of the location for the fault center point, size, and depth were 0.01 time of distance between C0002 and C0010, 2 km, and 1 km, respectively. The uniform slip was assumed as purely dip of reverse type. Its amount was estimated from the least minimum square.

Fault parameters of the best fit model for Cases A-C are listed in **Table 5**. All the best fit model for each Case can quantitatively explain the observed volumetric strain changes at the two sensors (C0002 and C0010), where we do not use the information about no signal at C0006 of Pc1 as input data for the fitting. Next, we compare the best fit models for each Case with the observational results analyzed in previous sections.

The fault location for the best fit model of Case A is shown in **Figures 9**, **4B**, which suggests that Case A can also explain the slip migration toward the updip region under the free constraining condition for the focal depth. Since **Figure 4B** shows that the epicenters of sVLFE are in the fault model of Case A-2, Case A is also consistent with the timing of the sVLFE activity.

In previous SSEs accompanied sVLFE in 2011 and 2015, the rate of pore pressure change at C0010 kept constant until the termination time (Araki et al., 2017). Therefore, we also assume that condition (Case A-2+) as shown by dotted line extended from Case A-2 in **Figure 6**, where the amount of volumetric strain change at C0010 is −0.22 μstrain as listed in **Table 4**. The best fit model of Case A-2+ is shown in **Figure 9C**; **Table 5**, whose fault geometry is almost the same result as Case A-2.

Case B suggests that the volumetric strain is changed from the Dilation polarity to the Mixed on the way of Case A-2. Since the amount of the volumetric strain change for Case B is almost the same as Case A-1 (**Table 4**) due to similar rate and period (**Figure 6**), the best fit model of Case B is also the same as Case A-1. These results suggest that the fault slip migrates from the updip on the way of Case A-2 to intermediate region in Case B, which could not explain the sVLFE activity with the migration toward the updip region (**Figure 4**) during Case B. Therefore, we conclude that Case B is not acceptable.

The best fit model of Case C is shown in **Supplementary Figure S1**; **Table 5**, which has relatively large magnitude with larger slip and wider area covering epicentral locations of C0002 and C0010. This model is expected to have significant volumetric strain change at C0006 (0.042 μstrain in **Table 5**). However, **Figures 3**, **6** suggest that the observed one seems no significant signal at C0006 during the event. Therefore, we conclude that Case C is not acceptable.

From these results and *t*-test in Section *Statistical Evaluation of Confidence for Each Case of Pore Pressure Change at C0010*, assuming that crustal deformation component of the observed volumetric strain change due to SSE is treated as Case A, we can explain the migration of sVLFE toward the updip region during the SSE reasonably (hereafter, we refer to this event as the SSE in 2020). Since Case A is similar to the time history of pore pressure change for the SSE in 2015, we discuss the characteristics of the SSE in 2020 by comparing with it in the following section.

SUMMARIES AND DISCUSSIONS

First, we discuss the difference of the magnitude between the SSEs in 2020 and 2015. The amplitude of the pore pressure changes for Case A (**Table 4**) for both C0002 and C0010 sites were smaller than that of the SSE in 2015 (**Table 2**). The duration of the SSE in 2020 (10 days) was shorter than the SSE in 2015, which was 28 days. As shown in **Table 1**, five sVLFEs (Mw 2.8 to 3.4) during the SSE in 2020 were detected in 30 h. The total number of sVLFEs (Mw ≧ 3.4) during the SSE in 2015 was more than 20 over 20 days (Takemura et al., 2019), indicating that the cumulative moment magnitude of the sVLFE in 2020 should be smaller than that in 2015. These results suggest that the slip process of the SSE in 2020 is similar to the SSE in 2015 but with a smaller magnitude.

Figure 10 shows the catalog of the pore pressure and the volumetric strain transient at the C0002 and C0010 boreholes with the simplified fault models for the previous SSEs in **Table 2** and Case (A-1) to (A-2) in **Table 4** applied to the SSE in 2020 occurring between the origin and termination times as listed in **Table 3**. As depicted in **Figure 10**; **Table 2**, all the duration times for the SSEs, except in 2012, were much shorter than the time resolution of the SSE detection from GNSS-A (0.2 years; Yokota and Ishikawa, 2020). We also estimated the onset and the termination time of the SSE in 2020 in 20 min. Owing to the high time resolution, we estimate the slip process of the SSE in 2020 as migration from the intermediate to the updip regions crossing over beneath C0010.

TABLE 5 | The best fit fault model for Cases A-C.

Case	Latitude	Longitude	Depth km)	Width (km)	Slip (cm)	Mw	C0002* (μstrain)	C0010* (μstrain)	C0006 (μstrain)
A-1(B)	33.28	136.65	5	22	0.83	5.0	−0.066	+0.14	+0.001
A-2	33.20	136.69	5	14	2.0	5.0	−0.074	−0.14	+0.001
A-2+	33.18	136.70	5	20	1.7	5.2	−0.074	−0.22	+0.0002
C	33.23	136.68	7	36	4.1	5.7	−0.14	+0.17	−0.042

**Input data for the least minimum square method in grid search.*

Compressional volumetric strain is positive, whereas the dilatational one is negative.

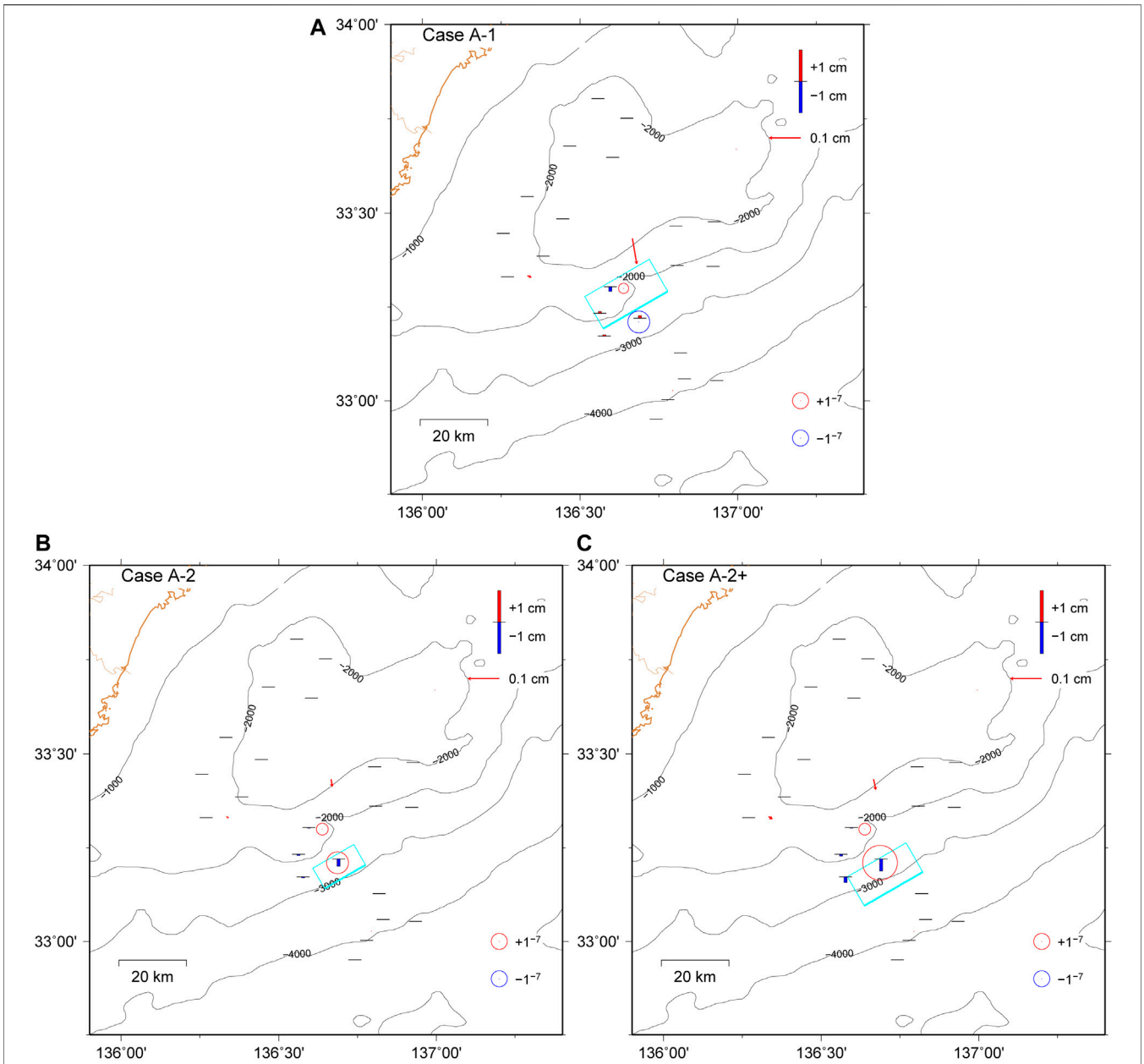

FIGURE 9 | Fault model (cyan) for **(A)** Case A-1, **(B)** Case A-2, **(C)** Case A-2+ with the observed volumetric strains (open circle) at C0002 and C0010 and a leveling change at the DONET stations (vertical scale; uplift: red; subsidence: blue). The calculated volumetric strain change at C0002 and C0010 is listed in **Table 5**. The red vectors represent the horizontal displacement at the GNSS-A stations [**Figure 1A** (almost 0 for KUM01)]. The contour shows seafloor bathymetry (meter).

Because of no significant signal at C0006, we conclude that the slip of the SSE in 2020 did not reach very shallow part of plate interface beneath C0006 as shown in **Figure 4B**. **Figure 4B** also shows that sVLFE is not active around the epicentral location of C0006, where the slip amount of the 1944 Tonankai earthquake is relatively small. These results indicate that the volumetric strain just below C0006 might not be accumulated because of stable frictional property near the trench (e.g., Scholtz, 1998), or there is strong coupling enough to refrain from sVLFE activity. This question is to be solved by long-term monitoring at C0006. The results demonstrate that monitoring the pore pressure change is a powerful tool for precisely estimating the region and duration of SSEs. If we estimate the fault model promptly during the pore pressure changes on the basis of our analysis, we can judge the possibility of sVLFE activity in advance of the occurrence.

We could not identify a significant increase in the moment release rate and shorter recurrence interval of the SSE from **Figure 10**. However, unrecognized SSEs (Katakami et al., 2020) could have possibly been buried in a large noise component. In addition, as mentioned in the Section *Estimation of the Onset/Termination Time and the Pore Pressure Change at C0002*, there

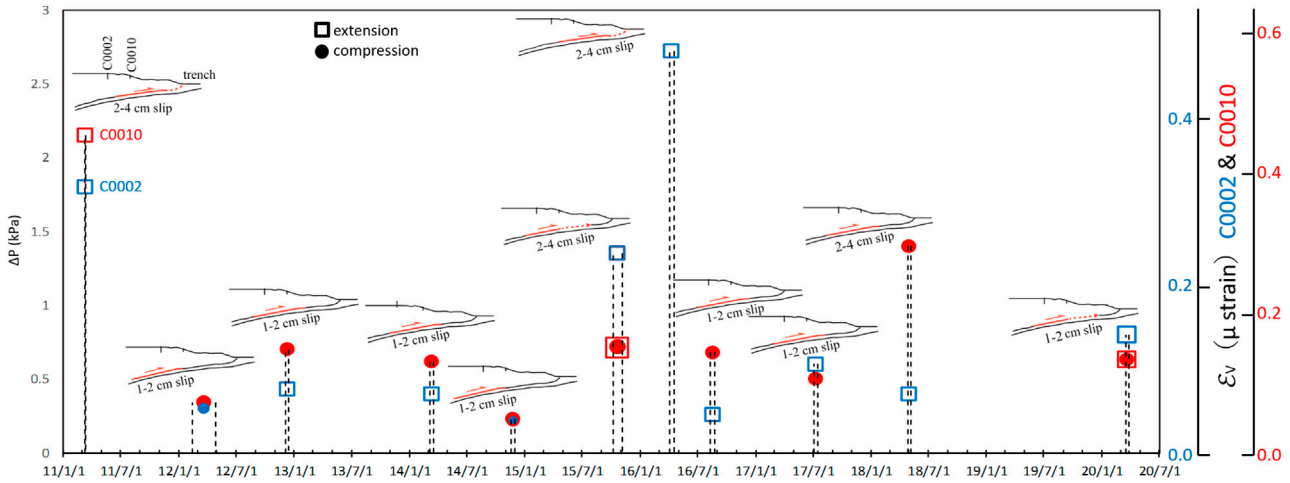

FIGURE 10 | Updated summary of the transients in pore pressure (ΔP) and volumetric strain (ε_v) at the C0002 (blue) and C0010 (red) boreholes collated after Araki et al. (2017) (**Table 2**). The SSE in 2020 is assumed to be Cases A-1 and A-2 in **Table 5**. The vertical dashed lines indicate the duration of each SSE. The open square and solid circle represent extension and compression, respectively. The schematic cross-sections for each SSE are based on the catalog (**Table 2**), where the red region represents the slip region.

is the temporal decrease of pore pressure during the SSE in 2020 in **Figure 5**. Because it lasted for several days, which could be explained from the temporal change of slip velocity during the SSE in 2020 rather than the excitation of the local sVLFE or tremors (Barbour 2015) because of the significantly longer period without a comparable increase. Therefore, the development of a noise reduction analysis using other borehole sensors and/or a combination of the nearby hydraulic pressure gauges of DONET would be important in identifying missed SSEs.

The leveling change in all DONET stations is also shown in **Figure 9**, implying that the expected leveling change was not sufficient for detection (i.e., 0.3 hPa at most). The observed noise level of the DONET pressure gauge was approximately 1–2 hPa (1–2 cm for leveling change) (Suzuki et al., 2016; Takemura et al., 2019). This small leveling change was partly due to low dip angle around the Nankai Trough (e.g., Sugioka et al., 2012).

We discussed the detectability of the horizontal displacement by showing the horizontal displacement of Case A on the seafloor at the GNSS-A stations (**Figure 1A**) (red arrows, **Figure 9**). The displacement is expected to be small (0.2 cm at most) if the fault slip is uniform. If the actual fault slip distribution changes spatiotemporally (Fukuda, 2018); thus, the SSE in 2020 can still be detected from other observations, such as GNSS-A (Yokota and Ishikawa, 2020). This will be the focus of our future work.

DATA AVAILABILITY STATEMENT

DONET observation data and the catalog of sVLFE estimated by Nakano et al. (2016) and Takemura et al. (2019) are available via the website of the National Research Institute for Earth Science and Disaster Resilience (2019) and the Slow Earthquake Database website (Kano et al., (2018); http://www-solid.eps.s.u-tokyo.ac.jp/~sloweq/), respectively. Borehole data is available from the website of the J-SEIS (JAMSTEC Ocean-bottom Seismology Database; https://join-web.jamstec.go.jp/join-portal/).

AUTHOR CONTRIBUTIONS

KA estimated the pore pressure change, onset, and termination time of the SSE in 2020. TI estimated the fault model of the Updip region for the SSE in 2020. MN estimated the focal mechanisms of the sVLFEs. TK also checked the pore pressure change independently as double check. EA led the DONET system installation. EA, TK, and YM installed the borehole observatories. TH, NT, and SK commented on improving the manuscript. TK, KS, and KS installed the real-time monitoring system of borehole observatory and DONET, making some figures automatically. SY and TN compiled the SSE catalog.

FUNDING

This work was partly supported by the Japan Society for the Promotion of Sciences (JSPS), Grant-in-Aid for Scientific Research (KAKENHI) Grant Number JP16H06477, JP17K19093, JP19H02411, and JP20H02236.

ACKNOWLEDGMENTS

Generic Mapping Tools (Wessel et al., 2013) was used to create figures. The authors would like to thank reviewers for their helpful comment to improve our manuscript, and Editor Keiichi Tadokoro for his expeditious handling.

SUPPLEMENTARY MATERIAL

The Supplementary Material for this article can be found online at: https://www.frontiersin.org/articles/10.3389/feart.2020.600793/full#supplementary-material.

REFERENCES

Araki, E., Saffer, D. M., Kopf, A. J., Wallace, L. M., Kimura, T., Machida, Y., et al. (2017). Recurring and triggered slow-slip events near the trench at the Nankai Trough subduction megathrust. *Science* 356, 1157–1160. doi:10.1126/science.aan3120

Ariyoshi, K., Matsuzawa, T., Ampuero, J.-P., Nakata, R., Hori, T., Kaneda, Y., et al. (2012). Migration process of very low-frequency events based on a chain-reaction model and its application to the detection of preseismic slip for megathrust earthquakes. *Earth Planets Space* 64, 693–702. doi:10.5047/eps.2010.09.003

Ariyoshi, K., Nakata, R., Matsuzawa, T., Hino, R., Hori, T., Hasegawa, A., et al. (2014a). The detectability of shallow slow earthquakes by the Dense Oceanfloor Network system for Earthquakes and Tsunamis (DONET) in Tonankai district, Japan. *Mar. Geophys. Res.* 35, 295–310. doi:10.1007/s11001-013-9192-6

Ariyoshi, K., Matsuzawa, T., Hino, R., Hasegawa, A., Hori, T., Nakata, R., et al. (2014b). A trial derivation of seismic plate coupling by focusing on the activity of shallow slow earthquakes. *Earth Planets Space* 66, 55. doi:10.1186/1880-5981-66-55

Barbour, A. J. (2015). Pore pressure sensitivities to dynamic strains: observations in active tectonic regions. *J. Geophys. Res. Solid Earth* 120, 5863–5883. doi:10.1002/2015JB012201

Davis, E. E., Becker, K., Wang, K., Obara, K., Ito, Y., and Kinoshita, M. (2006). A discrete episode of seismic and aseismic deformation of the Nankai Trough subduction zone accretionary prism and incoming Philippine Sea plate. *Earth Planet Sci. Lett.* 242, 73–84. doi:10.1016/j.epsl.2005.11.054

Dragert, G., Wang, K., and James, T. S. (2001). A silent slip event on the deeper Cascadia subduction interface. *Science* 292, 1525–1528. doi:10.1126/science.1060152

Earthquake Research Committee of the Headquarters for Earthquake Research Promotion (2013). Long-term evaluation of nankai trough earthquake activity. 2nd Edition. Available at: http://www.jishin.go.jp/main/chousa/13may_nankai/nankai2_shubun.pdf (Accessed October 28, 2020).

Fukuda, J. (2018). Variability of the space-time evolution of slow slip events off the Boso Peninsula, central Japan, from 1996 to 2014. *J. Geophys. Res. Solid Earth* 123, 732–760. doi:10.1002/2017JB014709

Ichinose, G. A., Thio, H. K., Somerville, P. G., Sato, T., and Ishii, T. (2003). Rupture process of the 1944 Tonankai earthquake (Ms 8.1) from the inversion of teleseismic and regional seismograms. *J. Geophys. Res.* 108, 2497. doi:10.1029/2003JB002393

Ide, S., Beroza, G. C., Shelly, D. R., and Uchide, T. (2007). A scaling law for slow earthquakes. *Nature* 447, 76–79. doi:10.1038/nature05780

Ishikawa, T., Yokota, Y., Watanabe, S., and Nakamura, Y. (2020). History of on-board equipment improvement for GNSS-A observation with focus on observation frequency. *Front. Earth Sci.* 8, 150. doi:10.3389/feart.2020.00150

Ito, Y., and Obara, K. (2006). Dynamic deformation of the accretionary prism excites very low frequency earthquakes. *Geophys. Res. Lett.* 33, L02311. doi:10.1029/2005GL025270

Ito, Y., Obara, K., Shiomi, K., Sekine, S., and Hirose, H. (2007). Slow earthquakes coincident with episodic tremors and slow slip events. *Science* 315, 503–506. doi:10.1126/science.1134454

Kaneda, Y., Kawaguchi, K., Araki, E., Matsumoto, H., Nakamura, T., Kamiya, S., et al. (2015). "Development and application of an advanced ocean floor network system for megathrust earthquakes and tsunamis?," in *Seafloor observatories*,(Chichester, United Kingdom: Springer Praxis Books), 643–663. doi:10.1007/978-3-642-11374-1_25

Kano, M., Aso, N., Matsuzawa, T., Ide, S., Annoura, S., Arai, R., et al. (2018). Development of a slow earthquake Database. *Seismol Res. Lett.* 89, 1566–1575. doi:10.1785/0220180021

Katakami, S., Kaneko, Y., Ito, Y., and Araki, E. (2020). Stress sensitivity of instantaneous dynamic triggering of shallow slow slip events. *J. Geophys. Res. Solid Earth* 125, e2019JB019178. doi:10.1029/2019JB019178

Kawaguchi, K., Kaneko, S., Nishida, T., and Komine, T. (2015). "Construction of the DONET real-time seafloor observatory for earthquakes and tsunami monitoring," in *Seafloor observatories*,(Chichester, United Kingdom: Springer Praxis Books), 211–228. doi:10.1007/978-3-642-11374-1_10

Kitada, K., Araki, E., Kimura, T., Kinoshita, M., Kopf, A., and Saffer, D. (2013). "Long-term monitoring at C0002 seafloor borehole in Nankai Trough seismogenic zone," in 2013 IEEE international underwater technology symposium (UT), Tokyo, March 5–8, 2013(IEEE), 1–3. doi:10.1109/UT.2013.6519882

Maeda, T., Obara, K., Shinohara, M., Kanazawa, T., and Uehira, K. (2015). Successive estimation of a tsunami wavefield without earthquake source data: a data assimilation approach toward real-time tsunami forecasting. *Geophys. Res. Lett.* 42, 7923–7932. doi:10.1002/2015GL065588

Matsuzawa, T., Hirose, H., Shibazaki, B., and Obara, K. (2010). Modeling short- and long-term slow slip events in the seismic cycles of large subduction earthquakes. *J. Geophys. Res.* 115, B12301. doi:10.1029/2010JB007566

Murotani, S., Shimazaki, K., and Koketsu, K. (2015). Rupture process of the 1946 Nankai earthquake estimated using seismic waveforms and geodetic data. *J. Geophys. Res.* 120, 5677–5692. doi:10.1002/2014JB011676

Nakamura, T., Takenaka, H., Okamoto, T., Ohori, M., and Tsuboi, S. (2015). Long-period ocean-bottom motions in the source areas of large subduction earthquakes. *Sci. Rep.* 5, 16648. doi:10.1038/srep16648

Nakano, M., Hori, T., Araki, E., Kodaira, S., and Ide, S. (2018). Shallow very-low-frequency earthquakes accompany slow slip events in the Nankai subduction zone. *Nat. Commun.* 9, 984. doi:10.1038/s41467-018-03431-5

Nakano, M., Hori, T., Araki, E., Takahashi, N., and Kodaira, S. (2016). Ocean floor networks capture low-frequency earthquake event. *Eos*. doi:10.1029/2016EO052877

National Research Institute for Earth Science and Disaster Resilience (2019). *NIED DONET*. Tokyo: National Research Institute for Earth Science and Disaster Resilience. doi:10.17598/NIED.0008

Nishikawa, T., Matsuzawa, T., Ohta, K., Uchida, N., Nishimura, T., and Ide, S. (2019). The slow earthquake spectrum in the Japan Trench illuminated by the S-net seafloor observatories. *Science* 365, 808–813. doi:10.1126/science.aax5618

Obara, K., and Ito, Y. (2005). Very low frequency earthquakes excited by the 2004 off the Kii peninsula earthquakes: A dynamic deformation process in the large accretionary prism. *Earth Planets Space* 57, 321–326. doi:10.1186/BF03352570

Obara, K., and Kato, A. (2016). Connecting slow earthquakes to huge earthquakes. *Science* 353, 253–257. doi:10.1126/science.aaf1512

Obara, K. (2002). Nonvolcanic deep tremor associated with subduction in southwest Japan. *Science* 296, 1679–1681. doi:10.1126/science.1070378

Okada, Y. (1992). Internal deformation due to shear and tensile faults in a half-space. *Bull. Seismol. Soc. Am.* 82, 1018–1040.

Saffer, D., Kopf, A., and Toczko, S. (2017). "The expedition 365 scientists," in Proceedings of the international ocean discovery program, 365, November 23, 2017. Available at: publications.iodp.org (Accessed November 23, 2017). doi:10.14379/iodp.proc.365.103.2017

Scholtz, C. H. (1998). Earthquakes and friction laws. *Nature* 391, 37–42. doi:10.1038/34097

Schwartz, S. Y., and Rokosky, J. M. (2007). Slow slip events and seismic tremor at circum–pacific subduction zones. *Rev. Geophys*, 45, RG3004. doi:10.1029/2006RG000208

Sugioka, H., Okamoto, T., Nakamura, T., Ishihara, Y., Ito, A., Obana, K., et al. (2012). Tsunamigenic potential of the shallow subduction plate boundary inferred from slow seismic slip. *Nat. Geosci.* 5, 414–418. doi:10.1038/ngeo1466

Suzuki, K., Nakano, M., Takahashi, N., Hori, T., Kamiya, S., Araki, E., et al. (2016). Synchronous changes in the seismicity rate and ocean-bottom hydrostatic pressures along the Nankai Trough: a possible slow slip event detected by the Dense Oceanfloor Network system for Earthquakes and Tsunamis (DONET). *Tectonophysics* 680, 90–98. doi:10.1016/j.tecto.2016.05.012

Takemura, S., Noda, A., Kubota, T., Asano, Y., Matsuzawa, T., and Shiomi, K. (2019). Migrations and clusters of shallow very low frequency earthquakes in the regions surrounding shear stress accumulation peaks along the Nankai Trough. *Geophys. Res. Lett.* 46, 11830–11840. doi:10.1029/2019GL084666

To, A., Obana, K., Sugioka, H., Araki, E., Takahashi, N., and Fukao, Y. (2015). Small size very low frequency earthquakes in the Nankai accretionary prism, following the 2011 Tohoku-Oki earthquake. *Phys. Earth Planet. In*. 245, 40–51. doi:10.1016/j.pepi.2015.04.007

Wallace, L. M., Araki, E., Saffer, D., Wang, X., Roesner, A., Kopf, A., et al. (2016). Near-field observations of an offshore Mw 6.0 earthquake from an integrated seafloor and subseafloor monitoring network at the Nankai Trough, southwest Japan. *J. Geophys. Res. Solid Earth* 121, 8338–8351. doi:10.1002/2016JB013417

Wessel, P., Smith, W. H. F., Scharroo, R., Luis, J., and Wobbe, F. (2013). Generic mapping tools: improved version released. *Eos Trans. AGU* 94 (45), 409. doi:10.1002/2013EO450001

Wiseman, K., and Bürgmann, R. (2011). Stress and seismicity changes on the sunda megathrust preceding the 2007 M_w 8.4 earthquake. *Bull. Seismol. Soc. Am*. 101 (1), 313–326. doi:10.1785/0120100063

Yokota, Y., and Ishikawa, T. (2020). Shallow slow slip events along the Nankai Trough detected by GNSS-A. *Sci. Adv*. 6, eaay5786. doi:10.1126/sciadv.aay5786

Conflict of Interest: The authors declare that the research was conducted in the absence of any commercial or financial relationships that could be construed as a potential conflict of interest.

frontiers in Earth Science

ORIGINAL RESEARCH
published: 10 February 2021
doi: 10.3389/feart.2021.601138

A Decade of Global Navigation Satellite System/Acoustic Measurements of Back-Arc Spreading in the Southwestern Okinawa Trough

Horng-Yue Chen[1], Ryoya Ikuta[2], Ya-Ju Hsu[1], Toshiaki Tsujii[3], Masataka Ando[2], Yoko Tu[1], Takeru Kohmi[2], Kiyomichi Takemoto[2], Koto Mizuno[2], Hsin Tung[1], Chin-Shang Ku[1] and Cheng-Horng Lin[1]*

[1]Institute of Earth Science, Academia Sinica, Taipei, Taiwan, [2]Faculty of Science, Shizuoka University, Sakai, Japan, [3]Department of Aerospace Engineering, Graduate School of Engineering, Osaka Prefecture University, Sakai, Japan

Long-term seafloor geodetic measurements are important for constraining submarine crustal deformation near plate boundaries. Here we present an integrated analysis of a decade of GNSS/acoustic data collected at a site 60 km to the east of northeast Taiwan near the axis of the Okinawa Trough back-arc basin. We obtained a time-series of horizontal and vertical positions based on 18 measurements from 2009 to 2019. These data reveal a southeastward movement at a rate of 43 ± 5 mm/yr since 2012 with respect to the Yangtze Plate. The horizontal motion can be explained by the clockwise rotation of the Yonaguni Block and northern Central Range. In addition, the vertical displacement of the transponder array shows rapid subsidence of 22 ± 9 mm/yr from 2012 to 2019. The fast subsidence rate and negative free-air gravity anomaly in this region indicate that crustal thinning is compensated mainly by surface deformation rather than upward migration of the Moho. Taking into account the offset in 2012 owing to the replacement of the transponder array, the horizontal position time series of our site are best explained by two linear lines with a slope change in July 2013. The timing of the velocity change coincides broadly with a change in the nearby seismicity rate and dike intrusion 150 km away from the site. Our results highlight the potential of seafloor geodesy in assessing temporal changes in deformation near the spreading center of the Okinawa Trough, which cannot be one using data from onland GNSS stations.

Keywords: GNSS/acoustic, okinawa trough opening, ryukyu arc, yilan basin, ryukyu trench-arc system, crustal thinning, yonaguni block

OPEN ACCESS

Edited by:
Ryota Hino,
Tohoku University, Japan

Reviewed by:
Tadashi Ishikawa,
Japan Coast Guard, Japan
Valérie Ballu,
UMR7266 Littoral, Environnement Et Sociétés (LIENSs), France

****Correspondence:***
Ryoya Ikuta
ikuta.ryoya@shizuoka.ac.jp

Specialty section:
This article was submitted to Solid Earth Geophysics, a section of the journal Frontiers in Earth Science

Received: *31 August 2020*
Accepted: *07 January 2021*
Published: *10 February 2021*

Citation:
Chen H-Y, Ikuta R, Hsu Y-J, Tsujii T, Ando M, Tu Y, Kohmi T, Takemoto K, Mizuno K, Tung H, Ku C-S and Lin C-H (2021) A Decade of Global Navigation Satellite System/Acoustic Measurements of Back-Arc Spreading in the Southwestern Okinawa Trough. Front. Earth Sci. 9:601138. doi: 10.3389/feart.2021.601138

INTRODUCTION

The Okinawa Trough is an active back-arc basin (Sibuet et al., 1987). The axis of the basin has its southwestern end in the Yilan Plain of Taiwan and extends to the Beppu–Shimabara rift zone in Japan. The spreading rate is fastest (60 mm/yr) around the Yaeyama rift in the southwestern Okinawa Trough (Nishimura et al., 2004; **Figure 1**). Episodic opening of the rift has been reported around the Yaeyama rift. For example, dike intrusion was detected north of Yonaguni Island in 2002 (Nakamura and Kinjo, 2018), beneath the Yilan Plain in 2005 (Lai et al., 2009), and north of Iriomote Island in 2013 (Ando et al., 2015). In contrast to the episodic rifting, onland Global Navigation

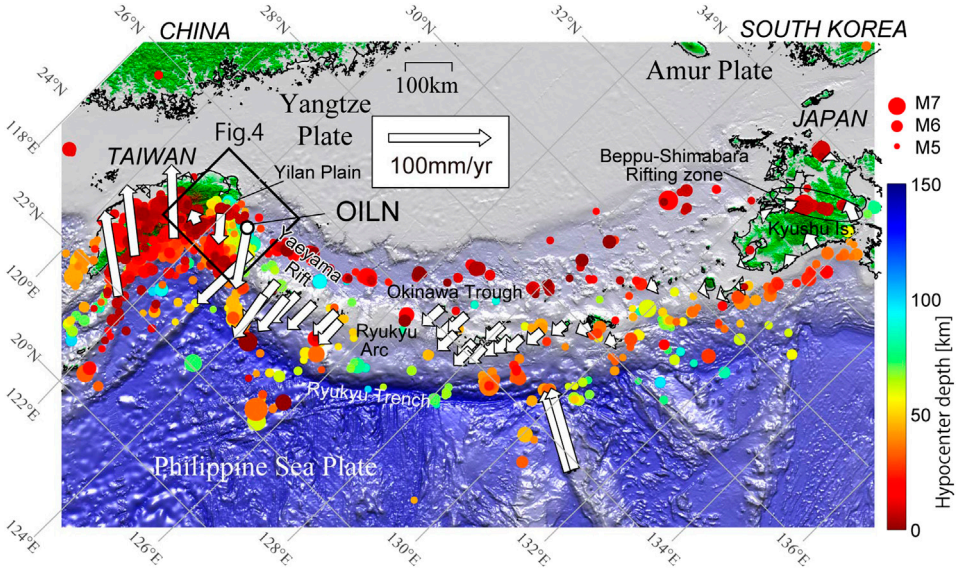

FIGURE 1 | Tectonic setting of the Okinawa Trough. GNSS velocity vectors relative to the Yangtze Plate during January 2009 to January 2016 are shown as white arrows. The Euler vector between ITRF2005 and the Yangtze Plate is from DeMets et al. (2010). Hypocenters of earthquakes larger than M5 in the same period are shown as solid circles and are color-coded according to depth. Earthquake source parameters were determined by the Japan Meteorological Agency (JMA) and Central Weather Bureau (CWB). The black box encloses the study area of **Figure 4**. The location of the OILN site is shown as a white circle. The velocity at the OILN site was estimated from the data acquired over a 4-years period in Chen et al. (2018). The vectors of the on-land GNSS stations were calculated from the daily time series by linear fitting after removing offsets caused by large earthquakes, antenna maintenances, and offsets over 30 mm even if the cause is not clear.

Satellite System (GNSS) measurements of the Ryukyu Arc (Lallemand and Liu, 1998; Nishimura et al., 2004) have shown an almost constant southward velocity. To investigate episodic opening of the Okinawa Trough, Chen et al. (2018) conducted GNSS/acoustic seafloor geodetic measurements immediately south of the spreading center for four years from 2012 to 2016, and suggested episodic opening of the rift valley occurred between the most active site of rifting and the Yilan Plain.

In this study, we analyzed data obtained using the seafloor benchmark unit installed by Chen et al. (2018) for three additional years (i.e., 2016–2019). In addition, we retrieved data from 2012 and earlier years that were discarded previously because of the replacement of transponders due to battery exhaustion, making it impossible to compare these data with later transponder data. Using these data acquired over the past decade, we determined the vertical and horizontal motions at this site and the associated uncertainties.

DATA AND METHODS

We carried out 18 series of GNSS/acoustic geodetic measurements using a fishing boat or buoys (**Figures 2A–C**) from 2009 to 2019 at the seafloor site OILN (**Figure 1**), which includes the 8 series of measurements reported in Chen et al. (2018). We used the drifting measurement strategy proposed by Ikuta et al. (2008), in which the vessel drifts with the sea current and wind for hours with the boat engine shut down during the transmission and reception of acoustic signals. We repeated the drifting measurement with different initial vessel locations until the coverage was sufficient. The observation period for each campaign varied from 11 to 62 h, depending on the weather and sea conditions.

History of the Site

The OILN site comprises a triplet or quartet of mirror-response transponders that were installed at a depth of about 1300 m. The site was first built in October 2008 with a triplet of transponders equipped with short-lived batteries (Units 3, 4, and 9 in **Table 1** and **Figure 2E**). In 2010, we deployed an additional transponder (Unit 12). Three more transponders were installed in 2012 (Units 15, 17, and 18) to replace the transponder triplet installed in 2008, as their batteries were exhausted between 2010 and 2012. Only Unit 12 was in operation before July 2012. The number of available seafloor transponders was three and four prior to and after 2012, respectively. The detailed history of the transponder replacement is listed in **Table 1**.

Data Acquisition

For 15 of the 18 field campaigns, measurements were conducted using the fishing boat Yilonglu-VI, whereas the other 3 campaigns were carried out using two towed buoys (**Table 1**; **Figure 2**). Each vessel was equipped with a transducer, a GNSS antenna for determining the position of the transducer, and a GNSS antenna triplet (the boat and buoy I) or a gyrocompass (buoy II) for determining the attitude of the vessel (**Figure 2**). The positions of the seafloor transponders were measured by acoustic

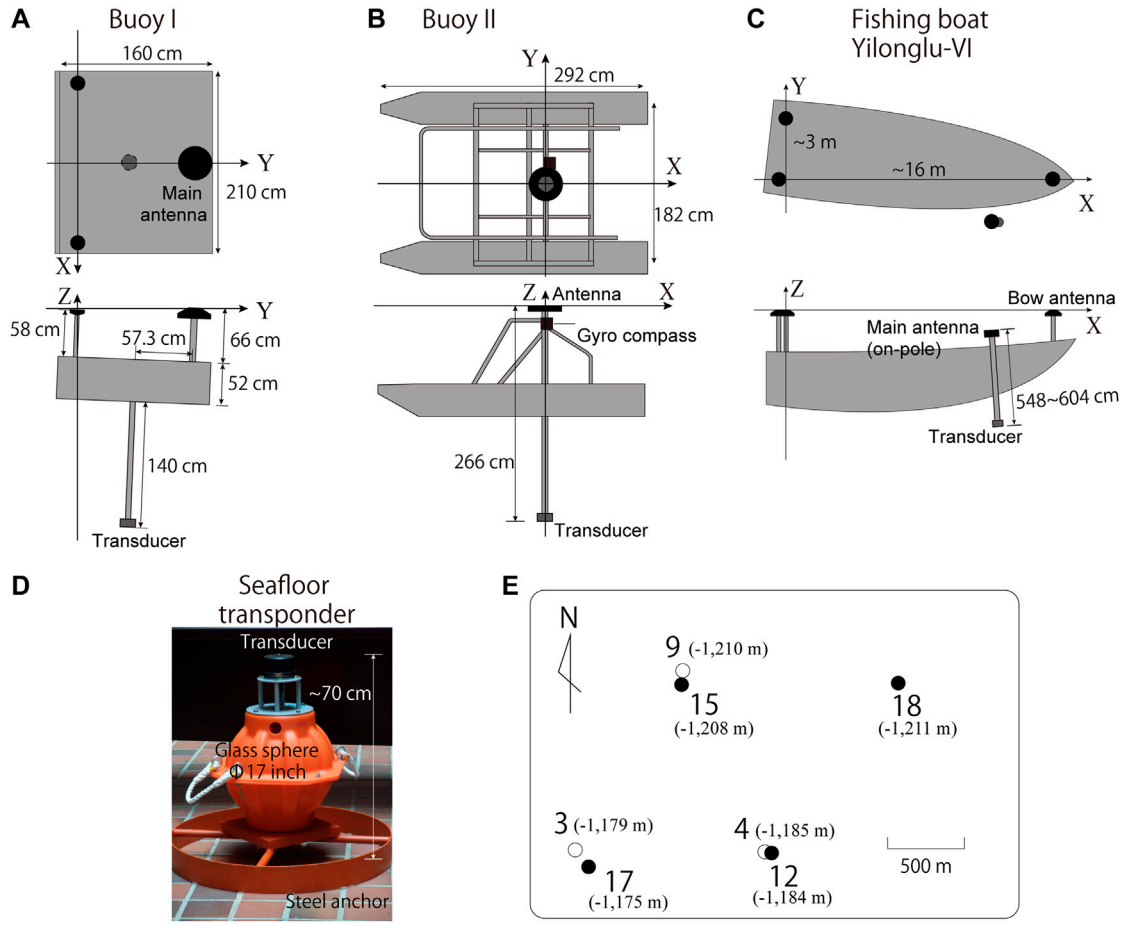

FIGURE 2 | Onboard configuration and seafloor transponders. **(A)** Schematic illustration of the onboard configuration of Buoy I used in the June 2010 measurement. The onboard XYZ coordinates were defined by the GNSS antenna triplet. All antenna phase centers are on the XY plane. **(B)** Buoy II used in the April and July 2012 measurements. The onboard XYZ coordinates were defined by the gyrocompass. **(C)** The fishing boat Yilonglu-VI. The onboard coordinates were defined by the GNSS antenna triplet. **(D)** A seafloor transponder installed at the OILN site. **(E)** Relative location of the seafloor transponders. The inactive and active transponders are shown as open and solid circles, respectively. The values in parentheses are the ellipsoidal heights of the transponders.

ranging from the onboard transducer, whose position was determined by combining the GNSS antenna position and attitude of the vessel. We solved the kinematic 3D position of the GNSS antenna every 0.2 s using GrafNav Ver.8.60. Two onshore GNSS stations, SCHN and S101, located 110 km SW and 90 km W of the OILN site, respectively, were used as fiducial sites to solve the kinematic GNSS antenna position. Given the signal condition of the GNSS antenna on the top of the transducer pole was sometimes not optimal, owing to obstruction by onboard structures above the antenna, on several campaigns Chen et al. (2018) used a GNSS antenna at the bow of the vessel as the main antenna instead of the on-pole antenna (**Figure 2C**). In this study, we improved the kinematic positioning of the on-pole antenna by using the bow antenna as a nearby moving fiducial site. This very short baseline analysis improved the yield of kinematic solutions significantly and allowed the on-pole antenna to always be used as a reference to calculate the onboard transducer position. The length between the antenna and transducer was determined with an accuracy of 1 cm. As a result, the repeatability of the estimated vertical position was improved relative to the result of Chen et al. (2018).

According to Chen et al. (2018), the error propagation from the unbiased observation error to the benchmark location is approximately $\sqrt{\{\mathbf{\Delta G}^2 + (\mathbf{\Delta\theta} \times \mathbf{r})^2 + \Delta t^2\}/N}$, where $\mathbf{\Delta G}$ represents the error on the kinematic GNSS positioning, $\mathbf{\Delta\theta}$ is the uncertainty of the vessel attitude in 3D orthogonal coordinates, $\mathbf{r}$ is the relative position of the onboard transducer with reference to the onboard GNSS antenna, Δc is the travel-time error measured as a distance, and N is the number of acoustic shots. $\mathbf{\Delta G}$ is 8 cm in the vertical direction and 2 cm in the horizontal direction (Ikuta et al., 2008). $\mathbf{\Delta\theta \times r}$ is 2 × 2.7 m for Buoy II, 0.8 × 2.6 m for Buoy I, and 0.4 × 6.0 m for the fishing boat (Chen et al., 2018). Δt is 0.04 ms for all systems (Ikuta et al., 2008). Based on these values, the resulting error varies from 1.3 to 2.0 mm for a number of acoustic measurements between 3000–12,000. This error is much smaller than the actual repeatability of the estimated seafloor benchmark positions. The error on the benchmark positioning is

TABLE 1 | Details of the transponders used in this study.

Campaign no	Date	Vessel	Period [hr]	Acoustic data number for each transponder							RMS traveltime residual [ms]	[a]Northing [cm]	[a]Easting [cm]	[a]Ascending [cm]	Measured TD pole length L [m]	Estimated horizontal TD position to GNSS antenna [x, y] [cm]
				Unit 3	Unit 4	Unit 9	Unit 12	Unit 15	Unit 17	Unit 18						
1	May 12, 2009	Yilonglu-VI	16	1,315	703	1,449	-	-	-	-	0.123	-	-	-	5.51	[126.8, 89]
2	July 01, 2009	Yilonglu-VI	20	1,281	1,154	1,384	-	-	-	-	0.114	–7.30	–3.11	3.12	5.59	[122.5, 17.5]
3	June 19, 2010	Buoy-I	17	389	19	439	336	-	-	-	0.082	–14.75	–4.85	6.69	2.58	[0, 0][b]
4	Aug. 24, 2011	Yilonglu-VI	19	1,500	-	104	1,607	-	-	-	0.035	-23.37	20.04	–26.16	5.51	[109.8, 33.2]
5[c]	July 02, 2012	Buoy-II	11	-	-	-	826	795	636	731	0.095	–41.06	17.09	–27.62	2.66	[–4.3, 5.4]
6	Sept. 06, 2012	Buoy-II	16	-	-	-	769	774	575	722					2.66	
7	Apr. 16, 2013	Yilonglu-VI	35	-	-	-	2,692	2,679	2,088	2,333	0.065	–37.40	22.45	–34.83	5.51	[64.4, 13.2]
8	July 24, 2013	Yilonglu-VI	40	-	-	-	2,359	2,218	1,642	1,859	0.115	–42.07	27.24	–29.16	5.51	[117.8, 26.1]
9	Sept. 12,2013	Yilonglu-VI	34	-	-	-	2,259	2,176	1,667	1,912	0.077	–36.96	27.65	–23.92	5.50	[116.3, 36.4]
10	Apr. 23, 2014	Yilonglu-VI	12	-	-	-	589	477	197	347	0.053	-47.86	29.10	-31.26	5.50	[112.9, 10.1]
11	Sept. 26,2014	Yilonglu-VI	40	-	-	-	3,074	2,848	2,125	2,119	0.080	–43.70	26.65	–25.27	5.48	[120.4, 30.2]
12	June 27, 2015	Yilonglu-VI	26	-	-	-	1,370	1,157	1,185	854	0.053	–54.88	36.93	–35.49	5.54	[115.9, 24.9]
13	Sept. 1, 2015	Yilonglu-VI	48	-	-	-	2,413	1,883	1,598	2,361	0.098	-51.49	36.64	-34.21	5.53	[117.3, 31.4]
14	May 12, 2016	Yilonglu-VI	48	-	-	-	2,269	2,681	2,035	2,394	0.067	–50.84	41.41	–40.99	5.59	[105.6, 46.1]
15	Aug. 17, 2016	Yilonglu-VI	30	-	-	-	2,190	2,026	1,669	1,754	0.101	–56.90	41.60	–52.90	5.59	[118.6, 16.3]
16	July 17, 2017	Yilonglu-VI	40	-	-	-	2,744	2,491	2,298	2,430	0.067	-58.61	44.87	–32.29	5.55	[125.9, 42.2]
17	Sept. 04, 2018	Yilonglu-VI	62	-	-	-	3,693	3,352	1,401	1,368	0.047	–71.54	47.97	–36.41	6.04	[82.7, –60.1]
18	Oct. 02, 2019	Yilonglu-VI	56	-	-	-	3,195	3,459	2,621	2,687	0.087	–77.32	49.79	–43.40	5.54	[126.3, 46.3]

[a]*Difference from the first measurement with reference to ITRF2005 coordinates.*

[b]*Onboard transducer position relative to the GPS antenna fixed to the value for Buoy I.*

[c]*Data for the two campaigns in 2012 were merged, because the number of data for each campaign was small.*

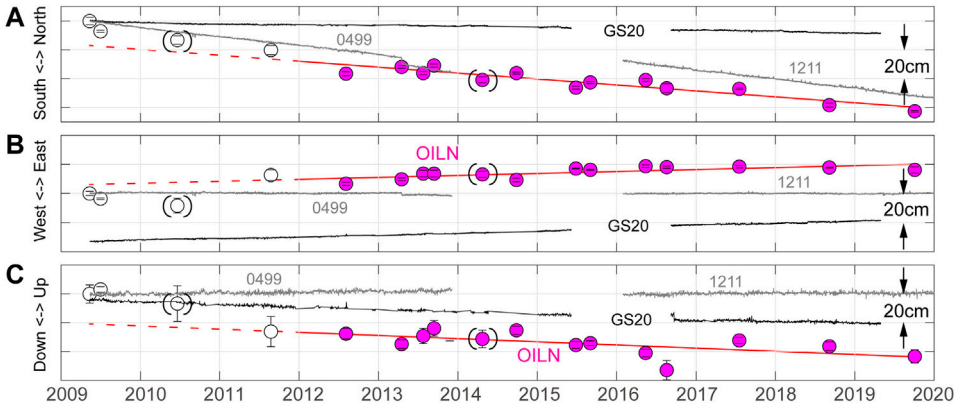

FIGURE 3 | Three-dimensional time-series of the position of the OILN site relative to the Yangtze Plate. **(A)** N–S component. The error bars for individual campaigns were defined by Chen et al. (2018). Thin black and gray lines show the positions of the GNSS sites on Gueishang (GS20) and Yonaguni (0499, 1211) islands, respectively. Station 1211 on Yonaguni Island was built ~800 m from site 0499 in March 2014, and its absolute position on the diagram is not meaningful. Open and solid purple circles show the campaigns before and after transponder replacement, respectively. Circles with brackets show the positions estimated from acoustic data with <3000 shots. **(B)** E–W component. **(C)** Up–down component.

larger than that expected from the unbiased observation error, which may be due to unexpected biased error in the observations, including kinematic GNSS positioning, as well as a discrepancy between the observational model and actual signal propagation.

ANALYTICAL METHODS

We solved the position of the seafloor transponders using a tomographic technique based on Chen et al. (2018). The position of the seafloor transponders, as well as the sound speed variation and onboard configuration, were solved using the penalized least squares method. We used the following equation:

$$\sum_{j}^{17}\left\{\sum_{i}^{N_j}\left(T_i - f\left(\boldsymbol{r}_{0j}, \boldsymbol{r}_i, a\left(t_i\right)\right)\right)^2 + \mu_j^2\int\left(\frac{\partial a\left(t\right)}{\partial t}\right)^2 dt\right\} \rightarrow min \quad (1)$$

where T_i is the ith acoustic travel-time (ms) obtained at time t_i (s), $f(\boldsymbol{r_0}, \boldsymbol{r_i}, a(t_i))$ is the travel-time predicted by ray tracing from the position of the seafloor transponders $\boldsymbol{r_{0j}}$ in the jth campaign and the onboard transducer $\boldsymbol{r_i}$, $a(t)$ is the temporal varying coefficient (no units) of the speed of sound in seawater represented by superposition of cubic B-spline functions (Barnhill and Riesenfeld, 1974), and μ_j is the hyper parameter that balances the smoothness of $a(t)$ with the travel-time residual. We selected the best hyper parameter for each campaign using the Akaike's Bayesian information criterion (ABIC), based on Chen et al. (2018). The resulting hyper parameters range from $10^{4.00}$ to $10^{4.16}$, although the values of Chen et al. (2018) ranged from $10^{3.67}$ to $10^{4.00}$. Hyper parameter dependence of the seafloor benchmark position solutions is evaluated in **Appendix**. The total number of campaigns in this study was 17, because two measurements conducted in 2012 were merged into one campaign because of the limited amount of data.

To solve **Eq. 1**, we used two realistic assumptions. Firstly, in estimating $\boldsymbol{r_0}$, we assumed that all the transponders were fixed on a rigid body that does not rotate, and moved from campaign to campaign in the same geometric configuration. This rigid body assumption allows us to estimate the motion of the rigid body between campaigns, even if some of the transponders are different, provided there was at least one common transponder in each campaign. Secondly, the temporal variation of the speed of sound was assumed to be controlled by a horizontal layered structure:

$$V\left(z,t\right) = a\left(t\right)V_0\left(z\right) \quad (2)$$

where z is the depth and $V_0(z)$ is the speed of sound obtained by the CTD measurements.

The configuration between the onboard GNSS antenna and transducer was not measured accurately, but was solved from the acoustic ranging because it was difficult to keep the same instrument configuration on the fiberglass fishing boat between the different campaigns. Although the acoustic ranging has an approximately linear trade-off between the vertical component of the seafloor transponder and the vertical position of the onboard transducer relative to the GNSS antenna, the horizontal onboard configuration of the transducer can be estimated robustly by the acoustic ranging. Given that the onboard GNSS antenna is on top of the transducer pole, we measured the length of the pole L with an accuracy of <1 cm. When the horizontal distance of the transducer from the GNSS antenna is solved as h_0, the vertical distance is $\sqrt{L^2 - h_0^2}$. We first solved **Eq. 1** by assuming the pole length L, and then resolved it iteratively. This improvement in the on-pole antenna solution allowed us to obtain more accurate vertical seafloor position than Chen et al. (2018).

RESULTS

Figure 3 shows a time-series of the 3D position of the OILN site relative to the Yangtze Plate from 2009 to 2019. The horizontal components show a southeastward motion, but there is a

discontinuity between the initial four and the latter campaigns. The campaigns prior to and post-2012 have only one common transponder (Unit 12). Furthermore, the amount of data from the third and fourth campaigns (June 2010 and August 2011), which were measured using the common transponder (Unit 12) before 2012, is limited (**Table 1**). For this reason, we first focused on the post-2012 results without considering the pre-2012 data. In addition, we discarded the positions from the two campaigns conducted in 2010 and April 2014, due to the limited acoustic data (<3,000), as compared with the other campaigns (average = 7,597).

The average rate of movement since 2012 is 41.2 ± 4.8 and 13.5 ± 3.7 mm/yr in the southward and eastward direction, respectively (**Figures 3A,B**). This result is considerably different from the average velocities of 50.3 ± 11.2 and 34.8 ± 7.2 mm/yr in the southward and eastward directions, respectively, obtained by Chen et al. (2018) from measurements over 4 years (2012–2016). This discrepancy is significant, even taking into account the 1σ error, and may reflect a temporal change in the motion (*Temporal Variation in Horizontal Motion*). The position of the benchmark for each campaign also differs in the present and previous studies. The vertical positions reveal there has been 22.0 ± 8.9 mm/yr of subsidence over 7 years (**Figure 3C**). The scatter of data from the individual campaigns from a linear trend is 33 and 59 mm, which is expressed as the root-mean-square (rms) deviation of the horizontal and vertical components, respectively.

DISCUSSION

Observation Errors

The horizontal velocity of the OILN site from 2012 to 2019 has an accuracy of <5 mm/yr, and the positions of the individual campaigns have a scatter of 35.6 and 27.6 mm (rms deviations from the linear trends of the N–S and E–W components, respectively). This error is comparable with the value of 20–30 mm obtained by the Japan Coast Guard (JCG) group (e.g., Yokota et al., 2016). Although the errors result from a combination of numerous factors, our observations appear to have some limitations compared with those of the JCG group. One involves the uncertainty on the position of the acoustic transducer relative to the GNSS antenna, which changed slightly from campaign to campaign. The fishing boat used in this study is made of fiberglass and, as such, rigging is not possible. This caused difficulties in setting the sensor jigs at the same positions with centimeter accuracy. As a result, the configuration between the onboard GNSS antenna and transducer also needed to be solved from the acoustic ranging. This led to an increase in the number of unknown parameters, which resulted in a reduction of the accuracy of the transponder array positioning. A further disadvantage of our data is the uneven ship track coverage over the transponder array. Due to the noise from the engine and crew, we had to cease boat operations and allow the boat to drift during the acoustic measurements. Sato et al. (2013) developed a hull-mounted onboard system, in which the transducer is installed on the bottom of the vessel, and this enables the vessel to sail along predetermined track lines. This improved the positioning repeatability and decreased the observation time for a single site from 2 to 4 days to 16–24 h (Ishikawa et al., 2020). Although our method had some disadvantages compared with that of the JCG group, we compensated for these disadvantages with long observation periods.

Average Rate of Back-Arc Rifting

Although the transponder array motion appears to have some temporal variations in both the horizontal and vertical components (**Figure 3**), we first consider the average motion (i.e., linear fitting without offsets) during 2012–2019. As proposed by Chen et al. (2018), if we assume the rigid Yonaguni Block is the western end of the Ryukyu arc, the Euler pole calculated from the 0499 (Yonaguni Island) and OILN sites is located off the eastern coast of Taiwan (**Figure 4**). The velocity predicted from the rotation of the Yonaguni Block at onland GNSS sites in the northern part of the Central Range is consistent with the observed GNSS velocities within ±15 mm/yr (**Figure 4B**). This suggests that clockwise rotation of the Ryukyu arc is the main driving mechanism for deformation of the Yilan Plain, which is consistent with evidence from earthquake focal mechanisms (e.g., Huang et al., 2012). Most of the earthquakes shallower than 25 km beneath the Yilan Plain and the Okinawa Trough show normal faulting mechanisms (**Figure 4B**). In addition, the GNSS velocities in northern Taiwan (**Figure 4A**), with respect to the stable Yangtze Plate, also exhibit a small eastward velocity of up to 10 mm/yr, associated with the clockwise rotation of the Yonaguni Block (**Figure 4C**). The velocity generally increases toward the trough axis. This E–W extension suggests that this area is also affected by back arc spreading. Schellart and Moresi (2013) used a 3D lithospheric deformation and mantle flow simulation to show that slab-rollback-induced toroidal and poloidal mantle flows are responsible for back-arc spreading. The overriding plate is extended by the basal shear of the asthenosphere, which flows into the space vacated by the rollback of the sinking slab. The E–W extension off the northern coast of Taiwan behind the spreading center may reflect the mantle flow beneath this region (**Figure 4D**), which has been predicted from a numerical mantle flow simulation based on the specific slab geometry (Lin and Kuo, 2016).

Large Subsidence Rate

Chen et al. (2018) did not discuss the vertical motion of the OILN site because of its large uncertainty. However, we estimated the vertical motion more accurately, with the improved onboard configuration of the main GNSS antenna on top of the transducer pole. The total subsidence during 2012–2019 was ~150 mm (**Figure 3C**). The average subsidence rate was 22.0 ± 8.9 mm/yr.

One possible interpretation of the high subsidence rate of the OILN site is sinking of the seafloor transponders into thick sediments. Taking into account that the transponder is ~70 cm high and comprises a glass sphere that is 43 cm in diameter (**Figure 2D**), the transponders should have sunk fastest just after installation. However, after the installation of the new transducers in 2012, there was no acceleration in the subsidence. Another possibility for the high subsidence rate is a submarine landslide.

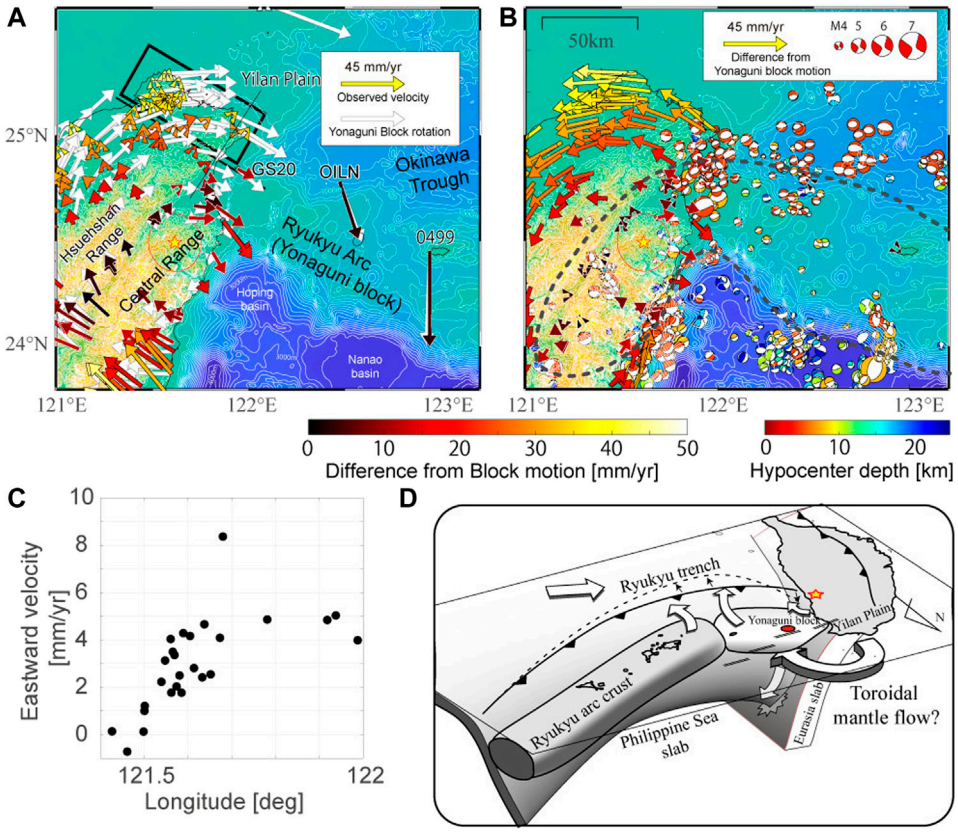

FIGURE 4 | (A) Observed horizontal velocities with reference to the stable Yangtze Plate. Colored vectors represent observed velocities and white vectors show the predicted rotation of the Yonaguni Block estimated from the OILN and onland 0499 sites. The vectors on Taiwan were calculated from daily coordinates for variable periods from 1 to 15 years. The 95% confidence interval for the OILN horizontal velocity are shown as the black ellipse, while the errors for the onland sites are not visible at this same scale. The yellow star marks the estimated Euler pole of the Yonaguni Block, with the 95% confidence interval shown as a red ellipse. The black rectangle shows the area of the GNSS stations shown in **(C)**. **(B)** Residual observed velocity vectors with reference to the motion of the Yonaguni Block. The dashed line is the 15 mm/yr contour. Beach balls show the centroid moment tensor (CMT) solutions for earthquakes between March 1999 and May 2020 with depths of <25 km. The CMT solutions were provided by F-net, National Research Institute for Earth Science and Disaster Prevention (NIED). **(C)** Eastward velocity of the onland GNSS stations in the rectangular area outlined in **(A)**. **(D)** Schematic illustration of the tectonics around northeastern Taiwan taken from Chen et al. (2018), but also showing toroidal mantle flow.

The slope of the seafloor around this site is 1.5° to the north. When a landslide occurs, we would expect a large horizontal northward displacement compared with the subsidence. However, no such northward displacement was observed in the study period.

The other possibility is that subsidence is occurring due to crustal thinning at the margin of the back-arc basin, which is supported by the similar subsidence rate observed at the onland site on Gueishang Island (GS20; **Figures 3C**, **5A**). In addition, onland sites in the Yilan Plain also show subsidence with rates of 5–10 mm/yr (**Figure 5A**). The subsidence rate of the OILN site is much faster than in active rift basins. For example, Steckler et al. (1988) showed from borehole profile data that the fastest tectonic subsidence rate in the central–southern Gulf of Suez was a few mm/yr in the late Burdigalian. This discrepancy may be explained by the unusual geological setting around the OILN site and Yilan Plain. The crust beneath the Okinawa Trough around the Yaeyama rift is continental, and the trough is in a transitional stage from continental rifting to seafloor spreading (Arai et al., 2017). If crustal thinning had a major role in the back-arc rifting around the OILN site, the thinning rate would be controlled by crustal thickness, spreading rate, and width of the trough. Assuming there is no change in the volume of the crust due to extension, the estimated thinning rate for a crustal thickness of 15–25 km (Arai et al., 2017) is 25–42 mm/yr, based on an average spreading rate of 50 mm/yr over a 30-km-wide trough. If isostasy is being attained, then thinning of the continental crust should be compensated by upward migration of the Moho discontinuity and seafloor subsidence. The ratio of the subsidence to thinning rate is governed by the density ratio between seawater, crust, and mantle according to the following equation:

$$\Delta h_c \rho_c = \Delta d \rho_w + (\Delta h_c - \Delta \mathrm{d}) \rho_m \quad (3)$$

where Δh_c is the crustal thinning rate and Δd is the seafloor subsidence rate. ρ_w, ρ_c, and ρ_m are the densities of seawater, continental crust, and mantle, respectively. In this case, when typical density values of 1.0, 2.7, and 3.3 g/cm^3 are adopted for ρ_w,

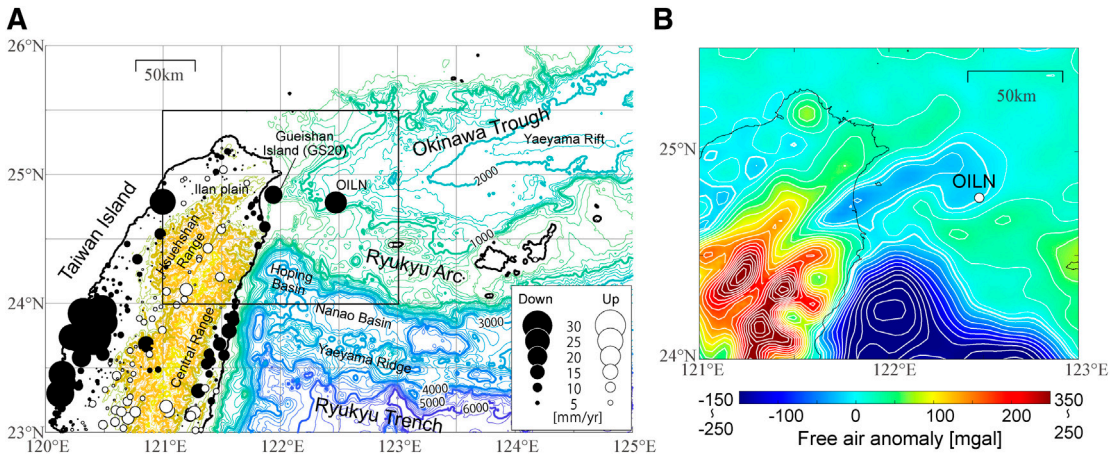

FIGURE 5 | Vertical motion of northern Taiwan. **(A)** Observed vertical velocity at onland GNSS sites and the OILN seafloor site. Solid and open circles show subsidence and uplift, respectively. The rectangle shows the area of **(B)**. The colored depth contour intervals are 200 and 1000 m for the thin and thick lines, respectively. The vertical velocity at on-land GNSS stations were calculated from the daily time series in the same manner with **Figures 1**, **4**, in which offsets by large earthquakes, antenna maintenances, and offsets over 100 mm even if the cause is not clear were removed before fitting. **(B)** Free-air gravity anomaly around the OILN site. The contour interval is 20 mgal. A large negative anomaly around the Hoping and Nanao forearc basins corresponds to flexure of the subducted Philippine Sea Plate. There is a narrow depression that extends from the Yilan Plain to the OILN site along the trough axis.

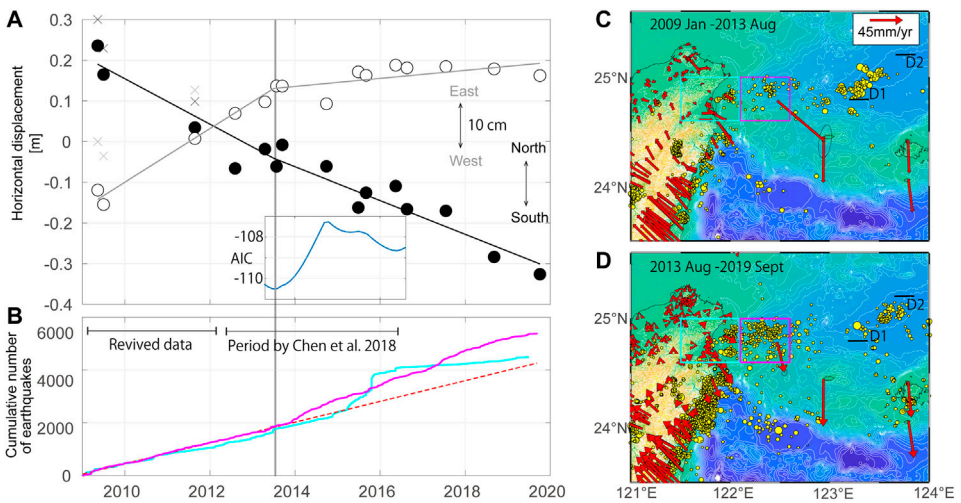

FIGURE 6 | Time-series of the OILN site position relative to the stable part of the Yangtze Plate. **(A)** Same as **Figures 3A,B**. N–S (solid circles) and E–W (open circles) components. The coordinates for the data prior to 2012 were modified by **Eq. 4**. The original N–S and E–W coordinates are shown as black and gray crosses, respectively. Each time-series is fitted with linear lines with a break at July 2, 2013 (vertical line), which was determined by AIC. Data for the middle eight campaigns are from Chen et al. (2018), but were treated with our new procedure. **(B)** Cumulative seismicity (>M2.0) detected within the corresponding colored rectangles shown in **(C,D)**. The red dashed line is a fit to the seismicity from January 2009 to July 2013. **(C)** Horizontal velocity vectors and seismicity (>M3.0) from Jan 1, 2009 to July 2, 2013. D1 and D2 show the location of dike intrusion modeled by Nakamura and Kinjo (2018), which occurred at the end of 2002 and in April 2013, respectively. **(D)** Horizontal velocity vectors and seismicity from July 3, 2013 to September 30, 2019.

ρ_c, and ρ_m, the expected subsidence rate Δd is 6.5–11.0 mm/yr for an estimated thinning rate Δh_c of 25–42 mm/yr.

The observed subsidence rate of 22 mm/yr at the OILN site is higher than expected from isostasy. In fact, there is a narrow, negative, free-air gravity anomaly region that extends from the Yilan Plain to the OILN site along the trough axis (WGM2012 Earth Gravity Model; Bonvalot et al., 2012), which does not correlate with the bathymetry. This suggests that gravitational mantle flow cannot compensate for the rapid deformation within the narrow region around the western end of the rift axis. Given the small negative free-air gravity anomaly to the east of the OILN site in the Okinawa Trough, this rapid subsidence should be

limited to this westernmost area in the initial stages of back-arc rifting.

Temporal Variation in Horizontal Motion

We estimated an average velocity in *Average Rate of Back-Arc Rifting*, but Chen et al. (2018) reported that the transponder array position of the OILN site from 2012 to 2016 can be explained by intermittent motion, based on Akaike Information Criteria (AIC). We examined if intermittent rifting of the Okinawa Trough axis as occurred using a longer observation period from 2009 to 2019.

Chen et al. (2018) modeled the horizontal transponder array position from 2012 to 2016 with a linear fit and an offset in 2013. They suggested that the offset was associated with an acceleration of seismic activity around the OILN site in 2013. **Figure 6A** shows an enlargement of the horizontal transponder array motion from **Figure 3**, excluding the campaigns with limited acoustic data (<3,000 shots). When including the new campaigns since 2016, no offset is recognized between the sixth (July 2013) and seventh (September 2013) campaigns.

However, the site appears to have moved at different rates before and after 2013. We estimated the time of the rate change and the offset due to transponder array replacement by least squares regression as the follows:

$$\boldsymbol{x}(t) = \begin{cases} \boldsymbol{V}_1 (t - t_0) + \boldsymbol{x}_0 & t < 2012 \\ \boldsymbol{V}_1 (t - t_0) + \boldsymbol{x}_1 & 2012 \le t \le t_0 \\ \boldsymbol{V}_2 (t - t_0) + \boldsymbol{x}_1 & t_0 < t \end{cases} \quad (4)$$

where $\boldsymbol{x}$ is the horizontal position vector at time t, $\boldsymbol{V_1}$ and $\boldsymbol{V_2}$ are the horizontal velocities before and after the bending time t_0, respectively; and $\boldsymbol{x_0}$ and $\boldsymbol{x_1}$ are the intercepts before and after the transponder array replacement, respectively. The appropriate t_0 value was determined based on AIC. Note that we did not include the vertical component in this regression because uncertainty of the vertical component is much larger compared to the horizontal components.

The best-fit result is shown in **Figure 6A**, and yielded a t_0 of July 2, 2013. The minimum AIC value is −110.5. The offsets caused by the replacement of the transponder array are estimated as 5.6 and 12.7 cm for the south and west components, respectively. When fitting by a line instead of bending lines, the AIC value is −103.9. The relative likelihood of the linear fitting with respect to the bending-line fitting is calculated as exp {(103.9–110.5)/2} = 0.037. Consequently, it is plausible that the velocity of OILN changed in July 2013. The estimated t_0 value based on the horizontal motion of the OILN site is consistent with the timing of the change in seismicity. The seismicity rate around the OILN site increased abruptly at the end of 2013 (**Figure 6B**), which was at the time of dike intrusion in the Yaeyama rift (D2 in **Figure 6C**) reported by Nakamura and Kinjo (2018). Nakamura and Kinjo (2018) analyzed onland GNSS coordinate data and seismicity around Iriomote Island and showed that the shear strain rate changed around the time of dike intrusion, which was also associated with a seismicity change in the forearc region of Iriomote Island. Our results show that these changes also coincided with the seismicity and crustal deformation changes 150 km away from the Yaeyama rift. However, the motion of the OILN site does not show an acceleration in rifting, but instead exhibits a deceleration of rotation associated with an increase of seismicity, which appears to be counterintuitive. One possible explanation for this is activation of a normal fault to the south of the OILN site, which separates the Okinawa Trough from the Ryukyu arc. Arai et al. (2017) described a high-angle normal fault that separates the trough from the arc ~100 km east of the OILN site, which appears to continue to the south of the OILN site, based on the bathymetry. The increased seismicity may reflect not only the opening of the Okinawa Trough, but also normal faulting south of the OILN site.

Chadwell et al. (1999) conducted a 2-years-long acoustic ranging experiment over a distance of 1 km across the Juan de Fuca ridge axis, and found that the ridge axis was not rifting. Chadwell and Spiess (2008) subsequently studied the plate motion using GNSS/acoustic methods at a location 25 km away from the same ridge axis, and found a motion indicative of constant seafloor spreading. They suggested that the crust between 0.5–25 km from the ridge axis accommodates the transient deformation by normal faults on the ridge slope and elastic strain accumulation. Our site is located 10 km away from the trough axis, and also shows a transient velocity change. Although we did not observe intermittent rifting, the velocity changes almost perpendicular to the rifting direction. The timing of the near-axis velocity change coincides with a change in the strain rate (Nakamura and Kinjo, 2018) and the inter-plate slow slip event (SSE) occurrence rate (Tu and Heki, 2017). The unique location of the OILN site close to the rifting center allows changes in the deformation field to be detected over time, which is not possible with land-based stations.

Differences From the Study of Chen et al. (2018)

Figure 7 shows the horizontal positions determined by Chen et al. (2018) superimposed on the result of the present study. There are significant differences of up to 10 cm in the N–S positions of campaigns conducted in 2012 and 2014. In 2012, the position accuracy of Chen et al. (2018) is degraded because of the limited acoustic data (<3,000). In this study, we merged the data from the campaigns in April 2012 and July 2012 that were previously discarded by Chen et al. (2018) due to lack of data, in order to increase the available data to 5,828. Despite the absence of such differences in the 2014 acoustic data, there are significant differences in the estimated benchmark position. The difference between the results of Chen et al. (2018) and this study for the 2014 campaign reflect the KGPS analysis. Chen et al. (2018) solved for the GNSS antenna position using Interferometric Translocation software (IT; Colombo, 1998), whereas we solved for the same antenna using the bow antenna as the fiducial site with GrafNav software (NovAtel Inc, 2014). As a result, the positions of the onboard transducer estimated in this study differ from those in Chen et al. (2018). On average, the positions determined in this study differ from Chen et al. (2018) by 0.7 ± 5.0 cm in a westward direction, 3.8 ± 3.3 cm in a northward direction (**Figure 8A**), and

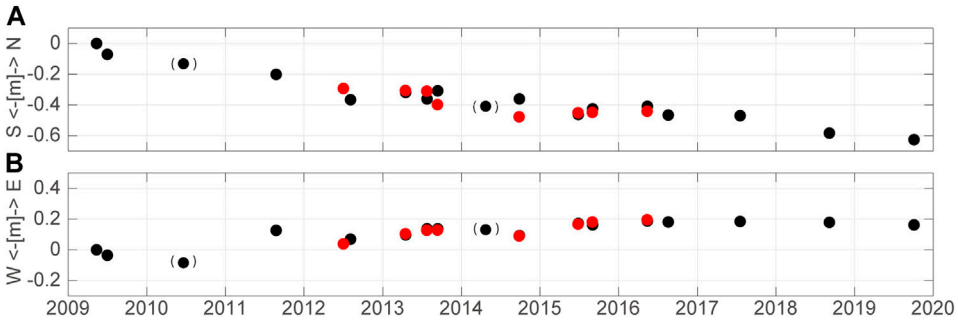

FIGURE 7 | Time-series of the OILN site position relative to the stable part of the Yangtze Plate. **(A)** N–S component. Black circles show the results of this study. Circles with parentheses show the positions estimated from acoustic data with <3000 shots. Red circles are the results of Chen et al. (2018). **(B)** E–W component.

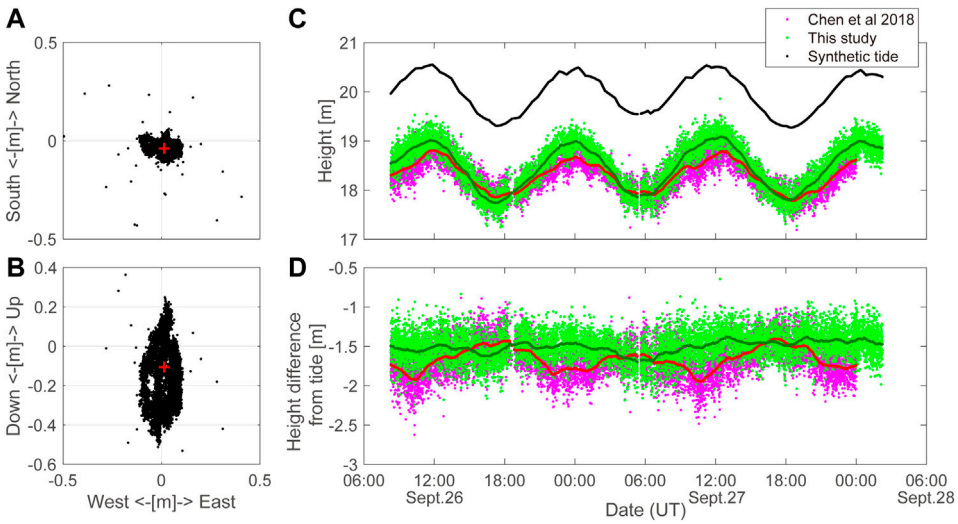

FIGURE 8 | Differences in the onboard transducer positions between this study and Chen et al. (2018). **(A)** Relative horizontal positions from Chen et al. (2018). The red cross shows the average position. **(B)** E–W cross-section. **(C)** Time-series of the vertical transducer position. Positions from Chen et al. (2018) and this study are shown as purple and light green dots. One-hour running averages are shown as green and red dots. The predicted astronomical tide is shown as black dots. **(D)** Height difference between the transducer position and the astronomical tide level.

15.6 ± 15.7 cm in a downward direction (**Figure 8B**). We compared the elevation with the theoretical sea level in order to evaluate which result is more reliable (**Figures 8C,D**). The results show that the elevations obtained in this study are more consistent with sea level than those of Chen et al. (2018). This trend is also evident in some other campaigns, but is especially large in April 2014. It is possible that the coordinates of the seafloor position might have been influenced by this unexpected bias in the kinematic GNSS positioning of Chen et al. (2018).

In the time-series obtained by low-frequency campaigns, the temporal changes are heavily biased by the results of only a few campaigns (e.g., 2012 and 2014 in Chen et al. 2018). This is also the case for our study. It should be noted that the estimated motion before 2012 obtained in this study was determined mainly by the location of the campaign in 2011. However, irrespective of the pre-2011 coordinate values, the eastward velocity appears to have decreased over time, at least when comparing 2012–2016 with 2016–2019 (**Figure 6**).

CONCLUSION

We measured seafloor movement near the rift axis of the Okinawa Trough back-arc basin over a 10-years-long period using a GNSS/acoustic technique. We deployed a seafloor site that is 60 km east of northeastern Taiwan in 2009, and conducted 18 measurement campaigns until 2020. Chen et al. (2018) reported the results for campaigns from 2012 to 2016 and found possible temporal variations in the rifting velocity of the Okinawa Trough. In this study, we extended the measurement period to 2019, in order to obtain more reliable estimates of

velocity. The seafloor transponder array has undergone southeastward movement at an average velocity of 43 mm/yr from 2012 to 2019, which is 18 mm smaller than the results of Chen et al. (2018) for 2012–2016. This horizontal movement can be explained by clockwise block rotation of the Yonaguni Block and Central Range, which form the Yilan Plain, by back-arc rifting. In addition to the horizontal motion, the transponder array revealed fast subsidence in the 7 years from 2012 to 2019, with an average velocity of 22 mm/yr. The rapid subsidence and negative gravity anomaly suggest that rapid crustal thinning is not being fully compensated for by upward migration of the Moho, but is being accommodated by surface deformation. We also attempted to retrieve the acoustic ranging data obtained from 2009 to 2012, which were initially discarded because of replacement of the seafloor transponders. By fitting the decadal horizontal motion with two linear lines with a break and an offset due to the transponder replacement, the break is estimated to have occurred in July 2013. This timing coincides with a change in the seismicity rate around the site, as well as dike intrusion 150 km away from the site.

DATA AVAILABILITY STATEMENT

The raw data supporting the conclusions of this article will be made available by the authors, without undue reservation.

AUTHOR CONTRIBUTIONS

H-YC designed the on-board system and took responsibility for all the experiments and data. RI designed acoustic data analysis. Y-JH constructed model to explain the result collaborating with RI. TT provided analysis tool to determine attitude of the vessel from GNSS tripret. MA designed the seafloor geodesy system and deployed the transponders in OILN site. YT managed all the measurements and analyzed the acoustic data.before 2014. TK established a model strategy to determine the benchmark position accurately. KT improved the quality of poor GNSS data obtained in 2010. KM developed the analysis strategy to solve data with offset by benchmark replacement. HT developed analysis to solve vertical position of the benchmark accurately. C-SK managed all the measurements since 2014 to keep high data quality. C-HL determined the location of seafloor site and analyzed the hypocenters distribution.

ACKNOWLEDGMENTS

3D coordinates of the onland GNSS stations in Japan were downloaded from the Geospatial Information Authority of Japan (https://terras.gsi.go.jp/). GNSS station position in Taiwan and GPS phase data for fiducial stations were provided by the Institute of Earth Science, Academia Sinica (http://gps.earth.sinica.edu.tw/). Hypocenter data around Japan was provided by Japan Meteorological Agency (JMA). We thank R. Watanabe for assistance in revisiting the previously discarded data. We also thank Hsin-I Chen, Suan-Han Su, Yi-lin Jiang, and I-Chuen Tsai for assistance with fieldwork and data analyses. T. Kawamoto improved this manuscript through insightful discussions. The bathymetry was downloaded from the Japan Oceanographic Data Center. This research was funded by Ministry of Science and Technology in Taiwan (MOST109-2116-M-001–009 and MOST108-2116-M-001–022) and Institute of Earth Sciences Academia Sinica. We thank two anonymous reviewers for their critical and constructive comments.

REFERENCES

Ando, M., Ikuta, R., Tu, Y., Chen, H. Y., and Lin, C. H. (2015). "The Apr 2013 earthquake swarm and dyke intrusion in the Okinawa trough, abstract for, 2015," in Japan Geoscience Union Meeting, Makuhari, chiba, May 24–28, 2015, SCG62–SCG07.

Arai, R., Kodaira, S., Kaiho, Y., Takahashi, T., Miura, S., and Kaneda, Y. (2017). Crustal structure of the southern Okinawa Trough: symmetrical rifting, submarine volcano, and potential mantle accretion in the continental back-arc basin. *J. Geophys. Res. Solid Earth.* 122 (1), 622–641. doi:10.1002/2016jb013448

R. R. Barnhill and R. F. Riesenfeld (Editors) (1974). *Computer aided geometric design*. New York: Academic, 326.

Bonvalot, S., Balmino, G., Briais, A., Kuhn, M., Peyrefitte, A., Vales, N., et al. (2012). *World gravity map. Commission for the geological map of the world*. Paris: BGI-CGMW-CNES-IRD.

Chadwell, C. D., Hildebrand, J. A., Spiess, F. N., Morton, J. L., Normark, W. R., and Reiss, C. A. (1999). No spreading across the southern Juan de Fuca ridge axial cleft during 1994-1996. *Geophys. Res. Lett.* 26 (16), 2525–2528. doi:10.1029/1999gl900570

Chadwell, C. D., and Spiess, F. N. (2008). Plate motion at the ridge-transform boundary of the south Cleft segment of the Juan de Fuca Ridge from GPS-Acoustic data. *J. Geophys. Res.* 113 (B4), B04415. doi:10.1029/2007JB004936

Chen, H. Y., Ikuta, R., Lin, C.-H., Hsu, Y.-J., Kohmi, T., Wang, C.-C., et al. (2018). Back-arc opening in the western end of the Okinawa Trough revealed from GNSS/Acoustic Measurements. *Geophys. Res. Lett.* 45 (1), 137–145. doi:10.1002/2017GL075724

Colombo, O. L. (1998). "Earth Sciences and Geography," in *GPS for geodesy*. 2nd Edn, Editors A. Kleusberg, P. Teunissen, and J. G. Peter (Berlin: Springer), 537–567.

DeMets, C., Gordon, R., and Argus, D. (2010). Geologically current plate motions. *Geophys. J. Int.* 181 (1), 1–80. doi:10.1111/j.1365-246X.2009.04491.x

Huang, H. H., Shyu, J. B. H., Wu, Y. M., Chang, C. H., and Chen, Y. G. (2012). Seismotectonics of northeastern Taiwan: kinematics of the transition from waning collision to subduction and postcollisional extension. *J. Geophys. Res.* 117 (B1), B01313. doi:10.1029/2011JB008852

Ikuta, R., Tadokoro, K., Ando, M., Okuda, T., Sugimoto, S., Takatani, K., et al. (2008). A new GPS-acoustic method for measuring ocean floor crustal deformation: application to the Nankai Trough. *J. Geophys. Res.* 113 (B2), B02401. doi:10.1029/2006JB004875

Ishikawa, T., Yokota, Y., Watanabe, S., and Nakamura, Y. (2020). History of on-board equipment improvement for GNSS-A observation with focus on observation frequency. *Front. Earth Sci.* 8, 150. doi:10.3389/feart.2020.00150

Lai, K. Y., Chen, Y. G., Wu, Y. M., Avouac, J. P., Kuo, Y.-T., Wang, Y., et al. (2009). The 2005 Ilan earthquake doublet and seismic crisis in northeastern Taiwan: evidence for dyke intrusion associated with on-land propagation of the Okinawa Trough. *Geophys. J. Int.* 179 (2), 678–686. doi:10.1111/j.1365-246X.2009.04307.x

Lallemand, S., and Liu, C. S. (1998). Geodynamic implications of present-day kinematics in the southern Ryukyus. *J. Geol. Soc. China.* 41 (4), 551–564

Lin, S. C., and Kuo, B. Y. (2016). Dynamics of the opposite-verging subduction zones in the Taiwan region: insights from numerical models. *J. Geophys. Res. Solid Earth.* 121 (3), 2174–2192. doi:10.1002/2015JB012784

Nakamura, M., and Kinjo, A. (2018). Activated seismicity by strain rate change in the Yaeyama region, south Ryukyu. *Earth Planets Space.* 70 (1), 154. doi:10.1186/s40623-018-0929-y

Nishimura, S., Hashimoto, M., and Ando, M. (2004). A rigid block rotation model for the GPS derived velocity field along the Ryukyu arc. *Phys. Earth Planet. In.* 142 (3-4), 185–203. doi:10.1016/j.pepi.2003.12.014

NovAtel Inc (2014). GrafNav 8.60: user guide OM-20000147 rev 3. Available at: https://hexagondownloads.blob.core.windows.net/public/Novatel/assets/Documents/Waypoint/Downloads/NavNet860_Manual/NavNet860_Manual.pdf (Accessed January 26, 2021).

Sato, M., Fujita, M., Matsumoto, Y., Ishikawa, T., Saito, H., Mochizuki, M., et al. (2013). Interplate coupling off northeastern Japan before the 2011 Tohoku-oki earthquake, inferred from seafloor geodetic data. *J. Geophys. Res. Solid Earth.* 118 (7), 3860–3869. doi:10.1002/jgrb.50275

Schellart, W. P., and Moresi, L. (2013). A new driving mechanism for backarc extension and backarc shortening through slab sinking induced toroidal and poloidal mantle flow: results from dynamic subduction models with an overriding plate. *J. Geophys. Res. Solid Earth.* 118 (6), 3221–3248. doi:10.1002/jgrb.50173

Sibuet, J. C., Letouzey, J., Barbier, F., Charvet, J., Foucher, J. P., Hilde, T. W. C., et al. (1987). Back arc extension in the Okinawa trough. *J. Geophys. Res.* 92 (B13), 14041–14063. doi:10.1029/JB092iB13p14041

Steckler, S. M., Berthelot, F., Lyberis, N., and Le Pichon, X. (1988). Subsidence in the gulf of suez: implications for rifting and plate kinematics. *Tectonophysics.* 153 (1–4), 249–270. doi:10.1016/0040-1951(88)90019-4

Tu, Y., and Heki, K. (2017). Decadal modulation of repeating slow slip event activity in the southwestern Ryukyu Arc possibly driven by rifting episodes at the Okinawa Trough. *Geophys. Res. Lett.* 44 (18), 9308–9313. doi:10.1002/2017GL074455

Yokota, Y., Ishikawa, T., Watanabe, S., Tashiro, T., and Asada, A. (2016). Seafloor geodetic constraints on interplate coupling of the Nankai Trough megathrust zone. *Nature.* 534 (7607), 374–377. doi:10.1038/nature17632

Conflict of Interest: The authors declare that the research was conducted in the absence of any commercial or financial relationships that could be construed as a potential conflict of interest.

APPENDIX: HYPER PARAMETER DEPENDENCE

We selected the appropriate hyper parameters μ based on the minimum ABIC. **Figure A1** shows how the time-series site position changes with different hyper parameters. When varying the hyper parameters within a range from $10^{3.5}$ to $10^{4.5}$, which covers the range of both Chen et al. (2018); ($10^{3.67}$–10^{4}) and this study (10^{4}–$10^{4.16}$), the horizontal and vertical positions change <1.5 cm and <3.0 cm, excluding the campaign with limited acoustic data (<3000; **Figure A1E**). The different hyper parameters within this range effect the velocity estimates by < 0.6 mm/yr in a N–S direction, <1.2 mm/yr in an E–W direction, and <2.1 mm/yr in a vertical direction (**Figure A1F**).

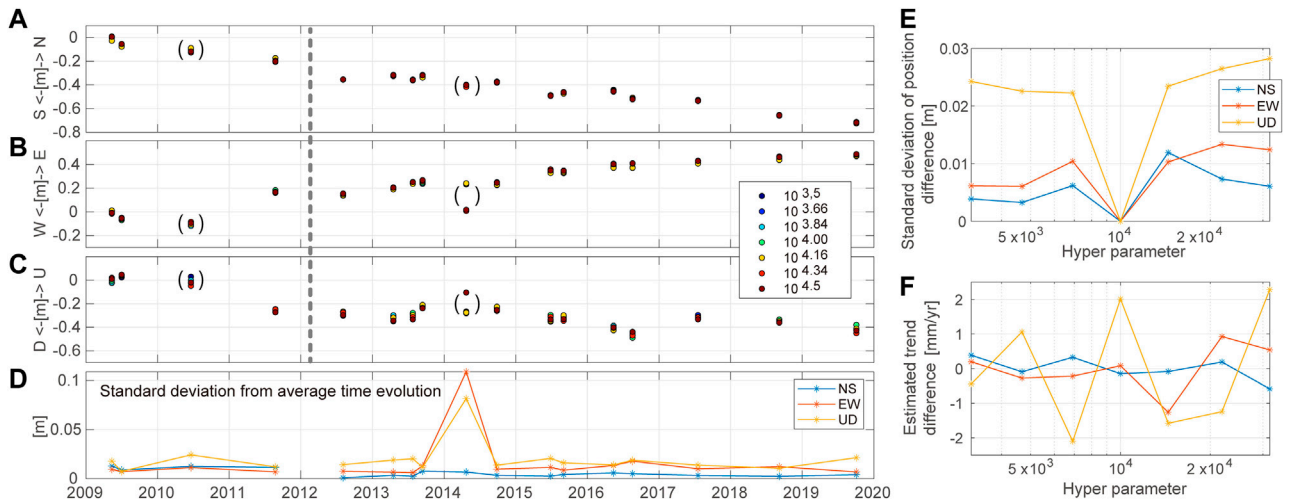

FIGURE A1 | Time-series of the OILN site position solved with different hyper parameters ranging from $10^{3.5}$ to $10^{4.5}$. **(A)** N–S component. Circles with parentheses show the positions estimated from limited acoustic data (<3,000 shots). **(B)** E–W component. **(C)** Up–down component. **(D)** Differences in the estimated site positions using different hyper parameters, showing the standard deviation for all hyper parameters between $10^{3.5}$ to $10^{4.5}$. The horizontal and vertical motion ranges between ±1.5 and ±3 cm, respectively, excluding the campaigns with limited data. The standard deviation was calculated for the deviation from the temporal variation trend obtained by averaging all hyper parameters. The campaigns before and after 2012 were evaluated separately. **(E)** Standard deviation of the site position difference from the value estimated with a hyper parameter of 10^{4}. The two campaigns with limited data (campaigns with brackets in the left panels) were not included in this evaluation. **(F)** Differences in the trend estimated using various hyper parameters in this study.

frontiers in Earth Science

ORIGINAL RESEARCH
published: 10 February 2021
doi: 10.3389/feart.2021.600732

Application of Phase-Only Correlation to Travel-Time Determination in GNSS-Acoustic Positioning

Chie Honsho[1], Motoyuki Kido[2], Toshihito Ichikawa[3], Toru Ohashi[3], Taichi Kawakami[3] and Hiromi Fujimoto[1]*

[1]Research Center for Prediction of Earthquakes and Volcanic Eruptions, Graduate School of Science, Tohoku University, Sendai, Japan, [2]International Research Institute of Disaster Science, Tohoku University, Sendai, Japan, [3]Kaiyo Denshi Co., Ltd., Tsurugashima, Japan

The GNSS-acoustic technique is a geodetic method for oceanic areas that combines GNSS positioning of a sea-surface platform and acoustic ranging of seafloor stations. Its positioning accuracy is typically a few and several centimeters for the horizontal and vertical positions, respectively. For further accuracy enhancement, we examined the errors in travel time, the most fundamental data in acoustic ranging. The reference signal used in our observations is a series of sinusoidal waves modulated by binary phase-shift keying with a maximal length sequence whose auto-correlation has a clear main peak at zero lag. However, cross-correlation between the actual returned signal and reference signal is often accompanied by many large sidelobes and looks very different from the synthetic auto-correlation. As a practical measure, we have chosen empirically one peak among several comparable peaks in the cross-correlation, though that is likely to lead to systematic errors in travel time. In this study, we revealed that a variety of cross-correlation waveform primarily depends on the incident angle of acoustic paths and that sidelobes were significantly reduced by substituting phase-only correlation (POC) for conventional cross-correlation. We therefore developed a template-matching technique using POC for the peak detection. POC templates were prepared by stacking actual POCs with certain ranges of the incident angle for each campaign. In the application of this method to actual data, we achieved successful results of our numerous campaign data to date. We consider that POC is advantageous in identifying the main peak uniquely and performing template matching more robustly, because POC enhances short-period components and thus highlights the timing of phase changes further than conventional cross-correlation.

Keywords: seafloor geodesy, acoustic ranging, travel-time determination, phase-only correlation, template matching

OPEN ACCESS

Edited by:
Keiichi Tadokoro, Nagoya University, Japan

Reviewed by:
Tadashi Ishikawa, Japan Coast Guard, Japan
Chau-Chang Wang, National Applied Research Laboratories, Taiwan

****Correspondence:***
Chie Honsho
chie.honsho.b7@tohoku.ac.jp

Specialty section:
This article was submitted to Solid Earth Geophysics, a section of the journal Frontiers in Earth Science

Received: *31 August 2020*
Accepted: *06 January 2021*
Published: *10 February 2021*

Citation:
Honsho C, Kido M, Ichikawa T, Ohashi T, Kawakami T and Fujimoto H (2021) Application of Phase-Only Correlation to Travel-Time Determination in GNSS-Acoustic Positioning. Front. Earth Sci. 9:600732. doi: 10.3389/feart.2021.600732

INTRODUCTION

The GNSS-acoustic (GNSS-A) technique is a geodetic method for ocean areas that combines GNSS positioning of a sea-surface platform and acoustic ranging of seafloor stations (Spiess, 1985). The accuracy of GNSS-A positioning has been enhanced with advances in observation technology and is reaching a few and several centimeters for horizontal and vertical positions, respectively (e.g., Ishikawa, 2016; Yokota et al., 2018). The positioning error arises mainly from undersea acoustic

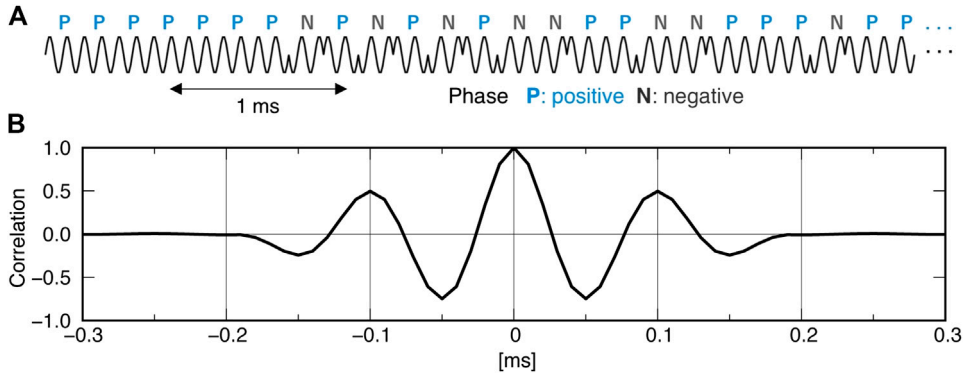

FIGURE 1 | Reference acoustic signal used for our GNSS-A observations. **(A)** Waveform of the beginning 5 ms of the entire, 25.4 ms-long signal. The carrier wave frequency is 10 kHz. **(B)** Auto-correlation of the reference signal.

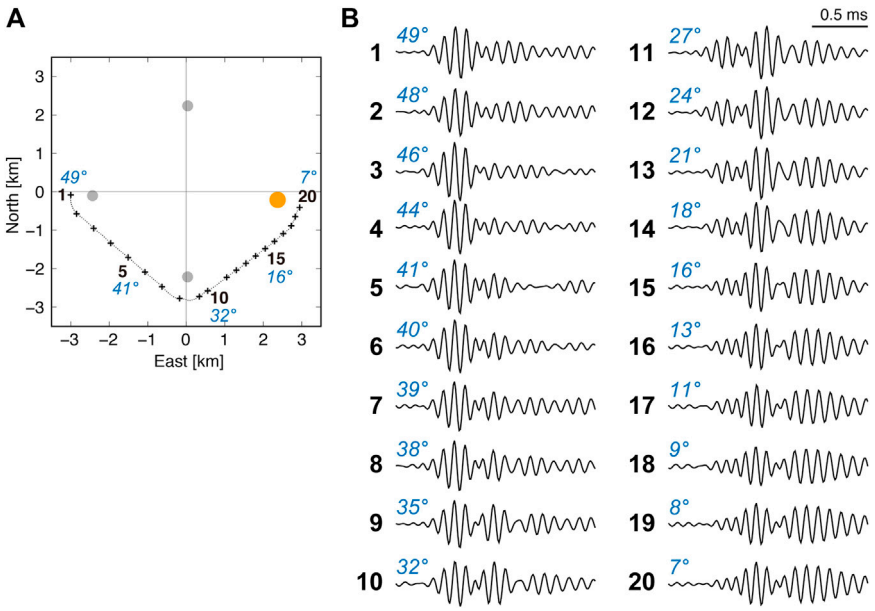

FIGURE 2 | Examples of actual cross-correlation between the reference and returned signals. **(A)** Part of ship tracks (small gray dots) of a campaign in a benchmark, which is settled on the seafloor at ~4.8 km water depth and consists of four transponders (gray or orange circles) forming a ~3.3 km square. **(B)** Cross-correlations of the reference and returned signals from the eastern transponder (orange). The numbers in black bold indicate ship's positions shown by crosses in **(A)**. The figures in blue indicate incident angles of acoustic waves to the transponder (a vertical acoustic path has 0° incident angle).

ranging rather than the GNSS positioning of a sea-surface platform. The slant range is calculated from the two-way travel time of the acoustic wave and the sound speed of seawater along the ray path. Although the both can have significant errors, the scope of this study is the former, that is, the error in travel time.

Two-way travel times are determined with a resolution of a few microseconds by calculating the cross-correlation between a reference waveform generated by an onboard transducer and a signal returned from a seafloor transponder. A series of sinusoidal waves modulated by binary phase-shift keying with a maximal length sequence (MLS) is often used as the reference signal because its auto-correlation has a clear main peak at zero lag. The cross-correlation between the actual returned signal and the reference signal is, however, often accompanied by large sidelobes and looks very different from the synthetic auto-correlation. Possible causes for the distortion of the cross-correlation are the degradation of the signal due to the frequency and phase characteristics of acoustic devices through electro-acoustic transformation, distortion of the returned signal caused by frequency-dependent absorption in seawater, and reflected waves from the surface of a glass sphere of the seafloor transponder or the ship bottom.

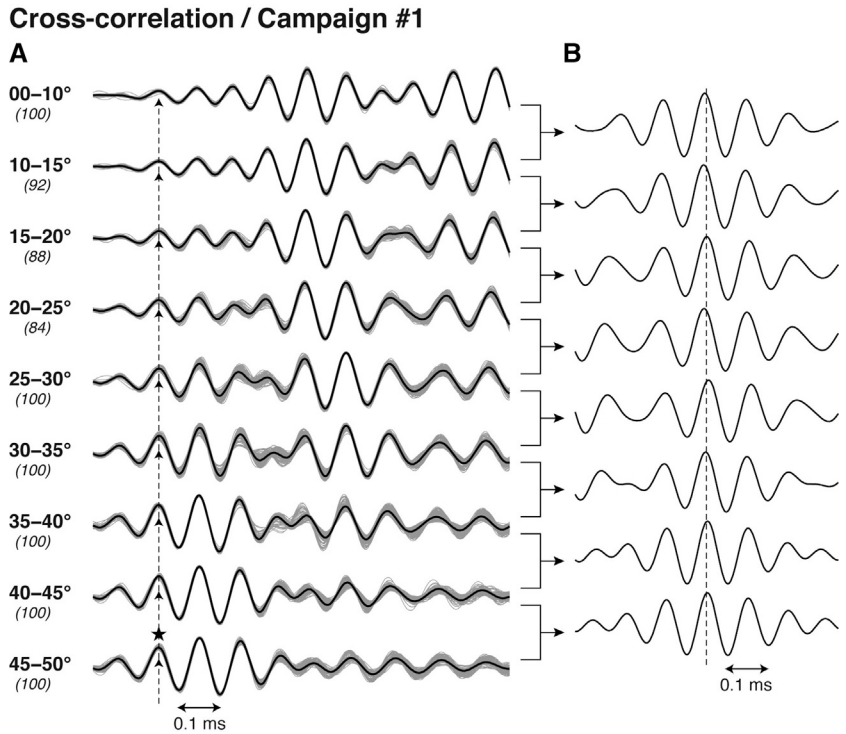

FIGURE 3 | Example of cross-correlation templates created from the data of the same campaign as shown in **Figure 2**. **(A)** Templates (bold lines) obtained by stacking ~100 cross-correlation waveforms (gray thin lines) for each zone of incident angle. Figures in bold and italics indicate incident angle ranges and the number of stacked lines, respectively. The main peak was first chosen for the template at the highest incident angle zone (a star on the bottom template). Dashed upward arrows indicate the corresponding peak in the other templates determined in order from higher to lower incident angle zones. **(B)** Cross-correlation between the adjacent templates. A vertical dashed line indicates position of the zero lag.

To cope with such ill-distorted cross-correlations, we had to take a semi-empirical approach to the detection of the main peak as follows (Azuma et al., 2016). A variety of cross-correlation waveforms are first classified using the K-means algorithm, and then a representative cross-correlation is chosen as a template for each group. Although several comparable peaks commonly exist in the template waveform, the main peak is chosen empirically from among them. Subsequently, the main peak in other cross-correlations is determined by template matching for each group. Although this approach was developed as a practical measure, the arbitrary and individual choice of the main peak is a serious problem, meaning that the correspondence of the main peak among the groups is not ensured. If a wrong peak is chosen as the reference of a certain group, the same error would arise in the travel times determined from cross-correlations in the group, leading to systematic errors depending on the waveform.

In this study, we revised the present method to determine the main peak more objectively and identically. First, we show that the cross-correlation waveform primarily depends on the incident angle of an acoustic wave to a transponder. This means that various waveforms can be the generality and scope of the method sorted out and related to each other systematically. Second, we demonstrate that the phase-only correlation (POC) has much simpler waveform than the conventional cross-correlation and present a peak detection method based on a template matching technique using POC. Finally, we discuss the generality and scope of the presented method.

ANALYSIS METHOD

Characteristics of Actual Cross-Correlation

We used a series of sinusoidal waves modulated by binary phase-shift keying with a 7-th order MLS of 2^7-1 bins for the reference signal (**Figure 1A**). There are two sinusoids at a frequency of 10 kHz per bin; the signal length thus becomes 25.4 ms. The auto-correlation of the reference signal has a clear maximum peak and a moderate second peak on each side corresponding to the two sinusoids per bin (**Figure 1B**).

As previously mentioned, the actual cross-correlation between the synthetic reference signal and a returned signal is severely distorted and has large sidelobes. However, it has been found that the cross-correlation waveform is strongly related to the incident angle of an acoustic wave to a transponder. **Figure 2** shows examples of the cross-correlation of actual signals returned from one seafloor transponder (shown by an orange circle in **Figure 2A**), obtained while the ship was approaching from

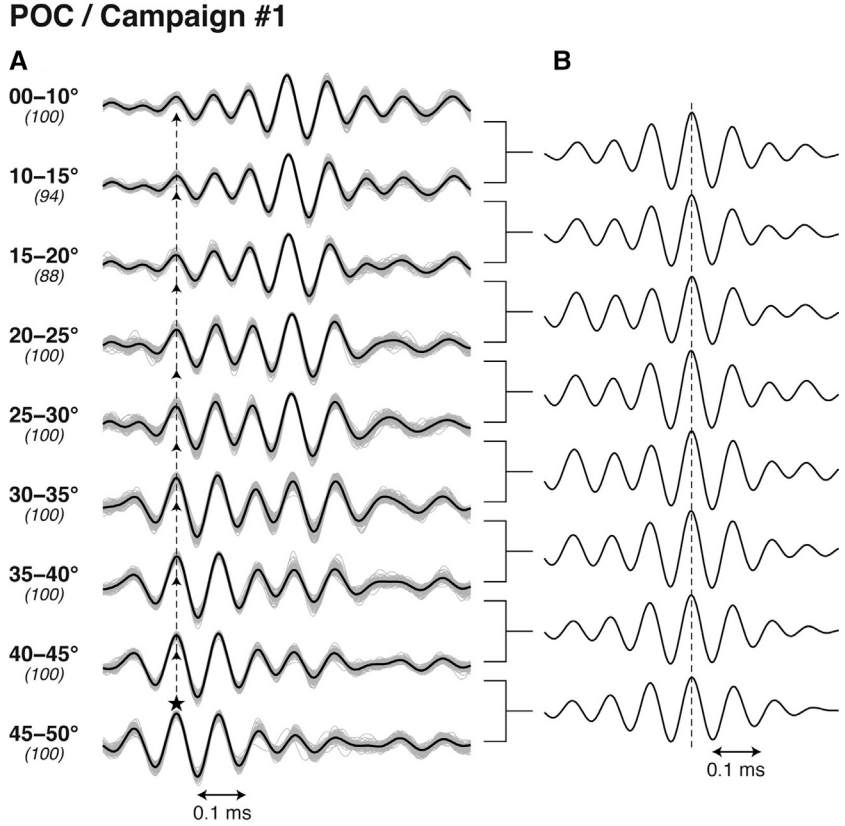

FIGURE 4 | POC templates created from the data of the same campaign as shown in **Figures 2** and **3**. **(A)** Templates for each zone of incident angle. A vertical dashed line indicates the position of the main peak. **(B)** Cross-correlation between the adjacent templates. A vertical dashed line indicates position of the zero lag.

a distance (cross labeled "1" in **Figure 2A**) to above the transponder (labeled "20"). The incident angle, indicated by blue figures, denotes the angle of ship-transponder straight path to the vertical. Although actual ray paths draw a curve according to the structure of the sound speed in seawater, the change of angles due to ray bending is less than 2° and does not affect the classification significantly. When the ship is far and the incident angle is high (>~40°), cross-correlation has a relatively simple waveform similar to the synthetic auto-correlation (correlogram #1–5 in **Figure 2B**). However, the subsequent wave groups grow as the incident angle decreases, and become even larger than the first main peak group when the incident angle becomes lower than 30° (correlogram #11 in **Figure 2B**); they continue to grow as the incident angle decreases further.

We examined the cross-correlation of a number of actual returned signals obtained from different transponders or different onboard transducers and confirmed that the cross-correlation waveform primarily depends on the incident angle in general, although it also depends on the ship (transducer) or water depth to a certain degree. This means that although there are a variety of waveforms, they vary continuously with gradually varying incident angles, and thus the same peak can be tracked from one waveform to another.

Preparation of Cross-Correlation Templates

As the cross-correlation waveform primarily depends on the incident angle of acoustic waves, we first prepared the templates by stacking cross-correlations with certain incident angle ranges. **Figure 3A** shows an example set of templates; five-degree bins of incident angle were adequate for our data but the lowest bin was taken 10° wide. A hundred cross-correlations were stacked to form a template for each incident angle zone; however, in some zones, less than 100 data were available. Signals from all the transponders were used without distinction because no significant difference in waveform among transponders was recognized.

As recognized in **Figure 2**, cross-correlation has a relatively simple waveform at high (>~40°) incident angles. First, we chose the first prominent peak in the waveforms at high angles as the true peak to be detected (star on the bottom correlogram in **Figure 3A**). Then, the corresponding peaks were determined in order from highest to lowest angles (dashed upward arrows in **Figure 3A**) by calculating the cross-correlation between adjacent templates (**Figure 3B**). Although it is not the main subject, one may find it strange that the highest peaks slightly deviate from the zero lag in **Figure 3B**. This is because the templates were finally aligned so that the main peak, which is

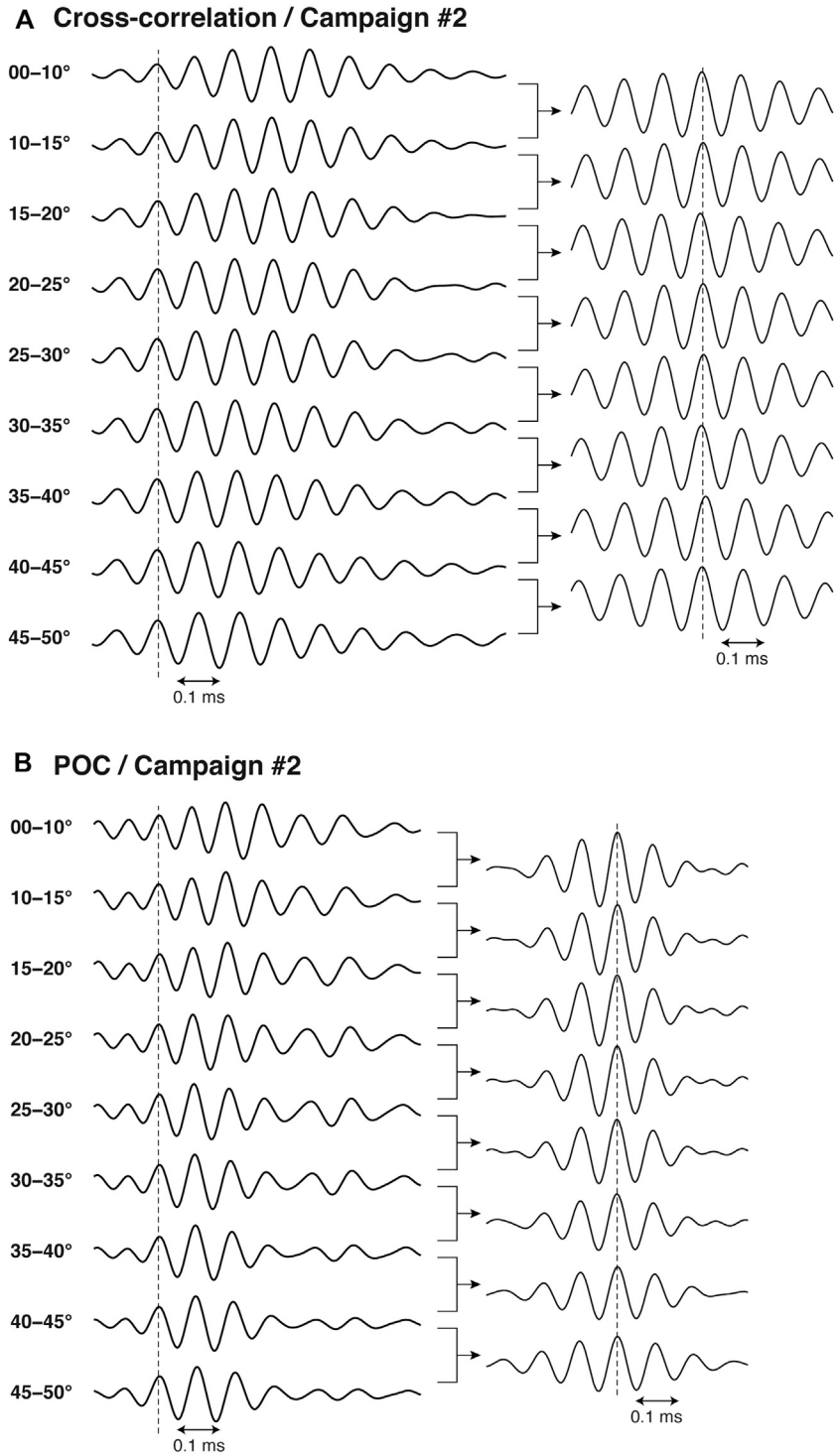

FIGURE 5 | Another example of templates using **(A)** conventional cross-correlation or **(B)** POC, created for a campaign conducted in a benchmark off the northeast Japan, located ~2,050 m in water depth. Graphs in the left and right columns are the templates and the cross-correlation between adjacent templates, respectively.

not necessarily large, should be exactly lined up, while the highest correlation generally occurs at a lag between largest peaks. Generally in our data, the main peak is prominent at high incident angles but diminishes as the incident angle decreases, where, instead, a few subsequent peaks grow at low incident angles. If the continuous variation of

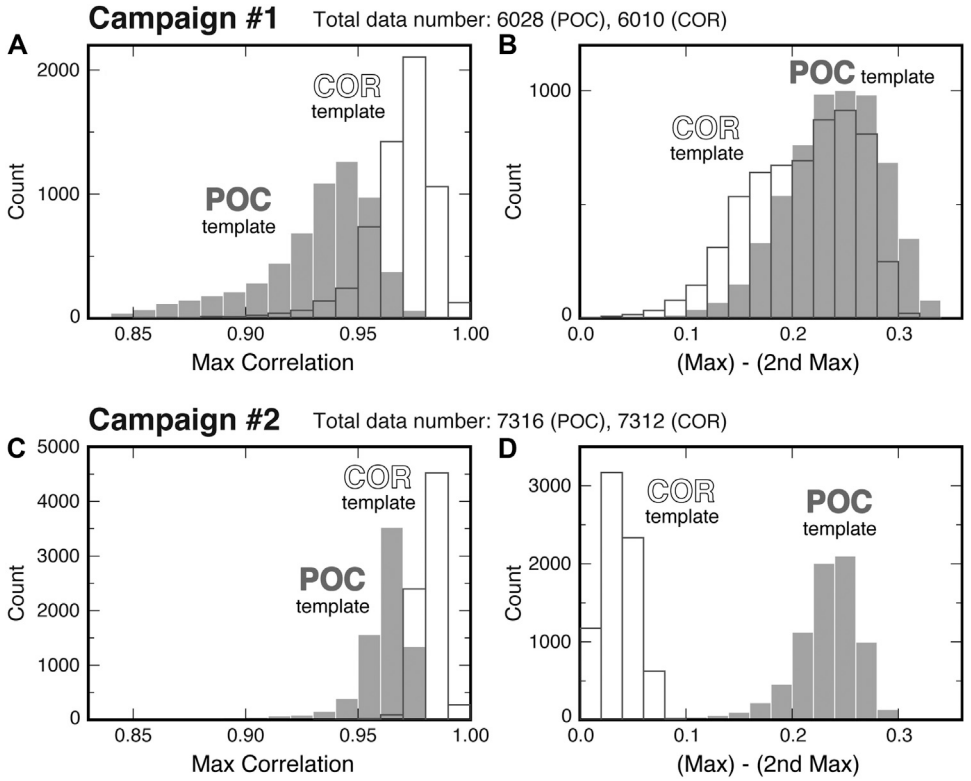

FIGURE 6 | Results of template matching for the two campaigns. **(A)** Histograms of values of the maximum peak of normalized correlation obtained using the POC template (gray bars) or the conventional cross-correlation template (white bars) for Campaign #1. **(B)** Histograms of differences between the maximum and second maximum peak values for Campaign #1. Bar colors mean the same as **(A)**. **(C)** and **(D)** show the same as **(A)** and **(B)**, respectively, but for Campaign #2.

waveforms by the incident angle is not correctly considered, a prominent peak behind the true main peak may be wrongly chosen when the incident angle is low. Such systematic error in travel times depending on the incident angle can significantly affect positioning.

When a set of templates is prepared, the main peak in the POC of each returned signal is determined by a template-matching technique for each zone of the incident angle. We prepared a template set for each campaign, that is, for each benchmark and cruise, thereby enhancing the results of template matching. As shown in **Figure 3A**, the POC waveform is highly similar if the incident angle is similar. Consequently, generally high (>0.9) maxima of the normalized cross-correlation were obtained between a template and an individual POC. The results of template matching are shown in the next section in comparison with those using conventional cross-correlation.

Introducing Phase-Only Correlation

Herein, we introduce the POC, which is widely used as a high-accuracy image matching technique (e.g., Ito et al., 2004) and also came into use in seismic wave identification (Moriya, 2011). Letting $g*h$ denote the cross-correlation of functions g and h, the Fourier transform is written as follows:

$$\mathcal{F}[g*h] = \mathcal{F}[g]\overline{\mathcal{F}[h]}, \quad (1)$$

where $\mathcal{F}$ denotes the Fourier transform and $\overline{\mathcal{F}[h]}$ denotes the complex conjugate of $\mathcal{F}[h]$. The POC of g and h, represented here as $g\bigstar h$, is written in the Fourier domain as follows:

$$\mathcal{F}[g\bigstar h] = \frac{\mathcal{F}[g]\overline{\mathcal{F}[h]}}{\left|\mathcal{F}[g]\overline{\mathcal{F}[h]}\right|}. \quad (2)$$

POC only has information on the phase difference between $\mathcal{F}[g]$ and $\mathcal{F}[h]$, and in general, short-period variations are more emphasized in POC than in conventional cross-correlation. **Equation 2** becomes 1 when $g = h$, indicating that the auto-correlation of any function becomes the delta function in the framework of POC.

We examined the POCs of the reference and returned acoustic signals and found that its waveform also strongly depends on the incident angle, as it is with the cross-correlation. Therefore, templates of POC can be prepared following the same procedure. **Figure 4** shows the resulting POC templates (**Figure 4A**) and the cross-correlation between the adjacent templates (**Figure 4B**). Similar to the case of cross-correlation, POC templates also show simpler waveforms at higher incident angles, although they still greatly differ from the delta function, which is expected as a phase-only auto-correlation of any function.

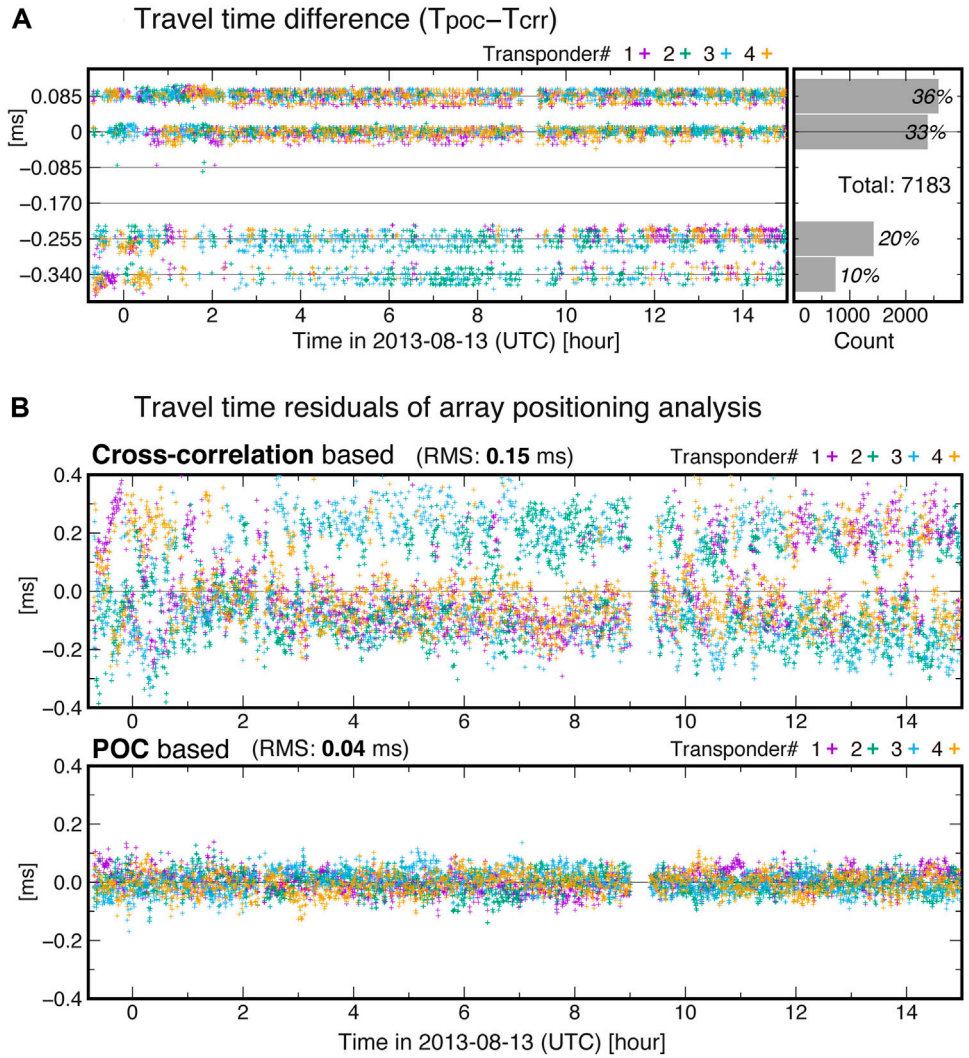

FIGURE 7 | Comparison of travel times determined using the cross-correlation and POC templates. **(A)** Difference of travel times, shown in a time series during the ~15 h observation period of Campaign #2 (left) and in a histogram (right). There were 4 transponders in the array, which are indicated by color. **(B)** Travel-time residuals (vertically normalized values) resulting from the array positioning analysis using the travel-time data determined with the cross-correlation (upper) or those with the POC (lower). Color indicates the transponder number.

Nevertheless, the POC waveform is obviously more compact than the conventional cross-correlation waveform (**Figure 3A**), which has a large later phase growing in middle-to-low (<~25°) incident angles and forming a long-winded signal lasting for >1 ms after the true peak. Because it was confirmed that POC is more advantageous for identifying the main peak uniquely than cross-correlation, as will be shown in the next section, we decided to adopt POC for the peak detection.

When a set of templates is prepared, the main peak in the POC of each returned signal is determined by a template-matching technique for each zone of the incident angle. We prepared a template set for each campaign, that is, for each benchmark and cruise, thereby enhancing the results of template matching. As shown in **Figure 4A**, the POC waveform is highly similar if the incident angle is similar. Consequently, generally high (>0.9) maxima of the normalized cross-correlation were obtained between a template and an individual POC. The results of template matching are shown in the next section in comparison with those using conventional cross-correlation.

RESULTS AND DISCUSSION

Comparison With Conventional Cross-Correlation

In our data, the waveform of conventional cross-correlation is generally more distorted and less compact than that of POC. Nevertheless, the cross-correlation templates also worked well regarding that campaign; cross-correlation between adjacent templates has a clear peak (**Figure 3B**) and thus can uniquely

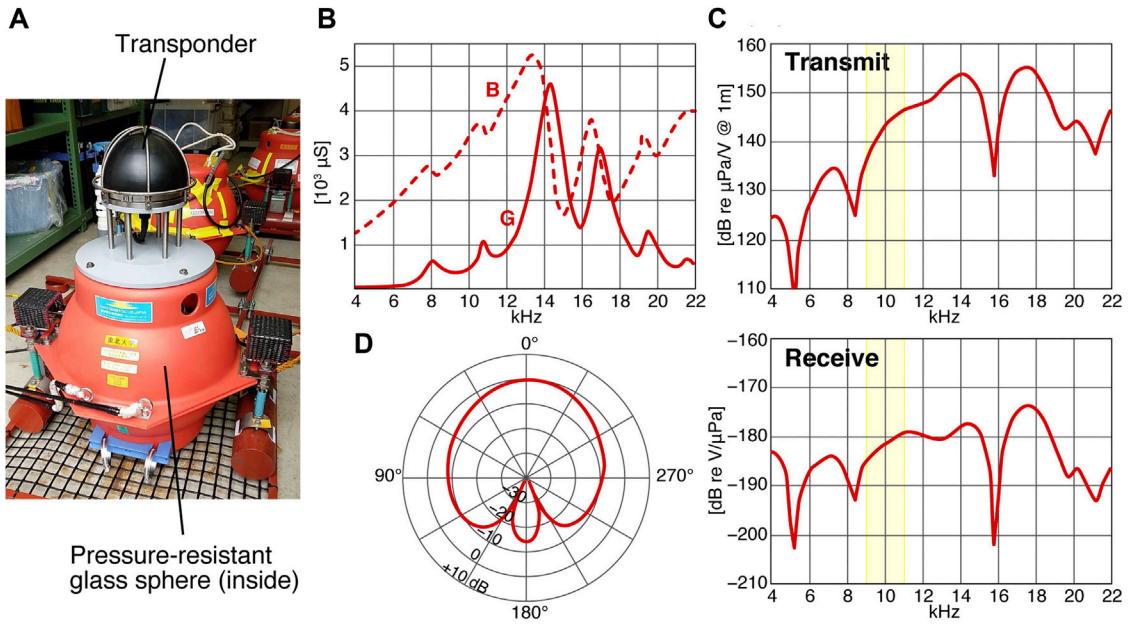

FIGURE 8 | Appearance of the seafloor station **(A)** and product specifications of the transponder: in-water admittance (G: conductance; **B**: susceptance) vs. frequency **(B)**, transmitting (top) and receiving (bottom) sensitivity **(C)**, and directivity pattern at 10 kHz **(D)**.

identify the true peak. Nearly the same results of travel-time determination could be obtained regardless of whether cross-correlation or POC was used for the campaign. However, in the analyses of other campaigns, we often experienced a serious problem utilizing cross-correlation: templates have so many (and large) sidelobes that several comparable peaks occur when taking the cross-correlations between templates. **Figure 5A** shows an example of such problematic templates created using data from another campaign. The templates (the left column) generally have a succession of large peaks, and consequently, the cross-correlation between the templates (the right column) also has several comparable peaks. The maximum peak is not readily apparent because several peaks have nearly the same height. This means that there is uncertainty in matching adjacent templates and that it is less confident whether an identical peak is chosen among the templates. If a wrong peak is chosen for a certain template, this would lead to systematic errors in the travel time obtained with a corresponding incident angle. The same problem also arises in template matching, which brings uncertainty in peak identification by an integral multiple of the wave period. It turned out that such a troublesome waveform of cross-correlation, having successive large peaks, occurred commonly for particular cruises or for benchmarks with relatively small water depths (<~2,000 m).

An exceptional advantage of POC is that its waveform remains simple enough to uniquely identify the main peak, even for the previously mentioned cruises or shallow benchmarks. **Figure 5B** shows the POC templates for the same campaign as **Figure 5A**; sidelobes are generally reduced in the templates, and the cross-correlation between adjacent templates exhibits a remarkable peak, which ensures that an identical peak is chosen among the templates despite its variation in waveform. Consequently, POC works more stably in template matching. **Figure 6** shows the results of template matching for the two campaigns mentioned thus far: the histograms of the maximum peak value of the normalized correlation (left panels: **Figures 6A and C**) and its difference from that of the second maximum peak (right panels: **Figures 6B and D**). In general, the maximum correlation using POC templates becomes slightly lower than that using conventional cross-correlation templates (**Figures 6A and C**), probably because a larger number of sidelobes are likely to result in higher cross-correlation. However, the maximum correlation of POC templates is still high (>~0.90) enough for template matching. The major advantage of POC is that template matching can be performed more robustly with a higher uniqueness; the differences in normalized correlation between the maximum and 2nd maximum peaks are generally large (>~0.2) when POC is used (**Figures 6B and D**) even for Campaign #2, in which nearly comparable (<0.1 in difference) peaks generally appeared when the conventional cross-correlation was used (**Figure 6D**).

In **Figure 7A**, we compared travel times of Campaign #2 determined using the cross-correlation templates (**Figure 5A**) and POC templates (**Figure 5B**). The differences took discrete values, indicating that different peaks were chosen. It was found that the dominant periods in the cross-correlation or POC were generally 0.08–0.09 ms, though the period of the carrier wave of the reference signal was to be 0.1 ms. Accordingly, the difference took values every ~0.085 ms. Nearly the same (within 0.03 ms difference) travel times were obtained for only 33% of the total data (**Figure 7A**). The remaining 67% had differences of −0.4 to +0.1 ms, which correspond to the difference of 1–4 periods. The travel-time difference apparently depends on the transponders (shown by color), indicating that slight difference in the cross-correlation

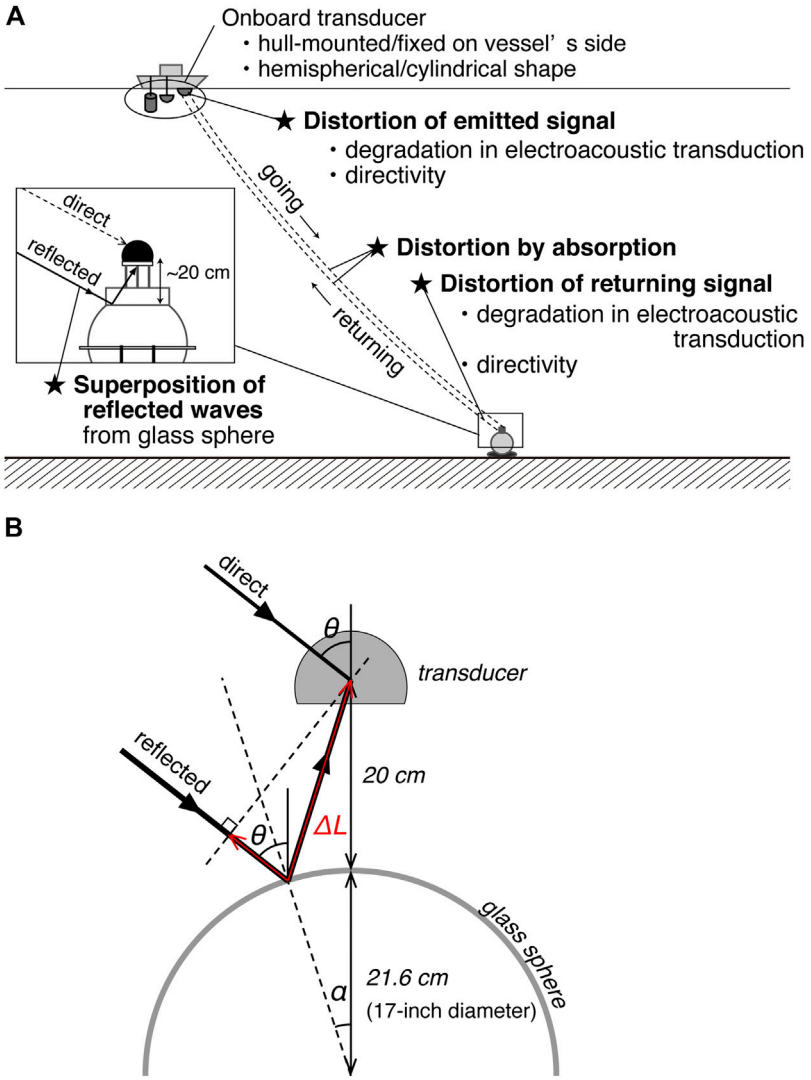

FIGURE 9 | Schematic drawing of acoustic ranging. **(A)** Possible causes for the distortion of acoustic signals. **(B)** The path of reflected waves from the glass sphere surface. The path length difference ΔL can be calculated for the incident angle θ of the incoming waves.

waveform by transponders seriously affected the results of peak detection. Using these two sets of travel-time data, we performed the array positioning analysis (Kido et al., 2006; Honsho and Kido, 2017) and compared the results. **Figure 7B** shows the resulting travel-time residuals in a time series. When the travel-time data determined with the cross-correlation templates were used (upper panel of **Figure 7B**), it results in large and scattered residuals as much as ~0.3 ms (0.15 ms in RMS). On the other hand, when the data determined with the POC templates were used (lower panel), the residuals were greatly reduced to less than ~0.1 ms (0.04 ms in RMS). This indicates that the travel times determined by the POC were correct. The obtained array positions also differ by 5–6 cm both in the horizontal and vertical components. This example demonstrates that a simple waveform of POC has the advantage of reducing systematic and random errors in travel time arising from the wrong choice of main peak in templates and errors in template matching.

Generality and Scope of Application of the Method

We have applied the method presented in this study to our data in numerous (>100) campaigns to date and achieved successful results of peak detection. The method is based on the two characteristics actually confirmed: the dependency of cross-correlation or POC waveform on the incident angle, and the superiority of POC to conventional cross-correlation. In this section, we consider their possible reasons to discuss the generality and scope of the method.

Our transponders installed in the seafloor unit are the identical product type, manufactured by Kaiyo Denshi Co., Ltd. (**Figure 8**).

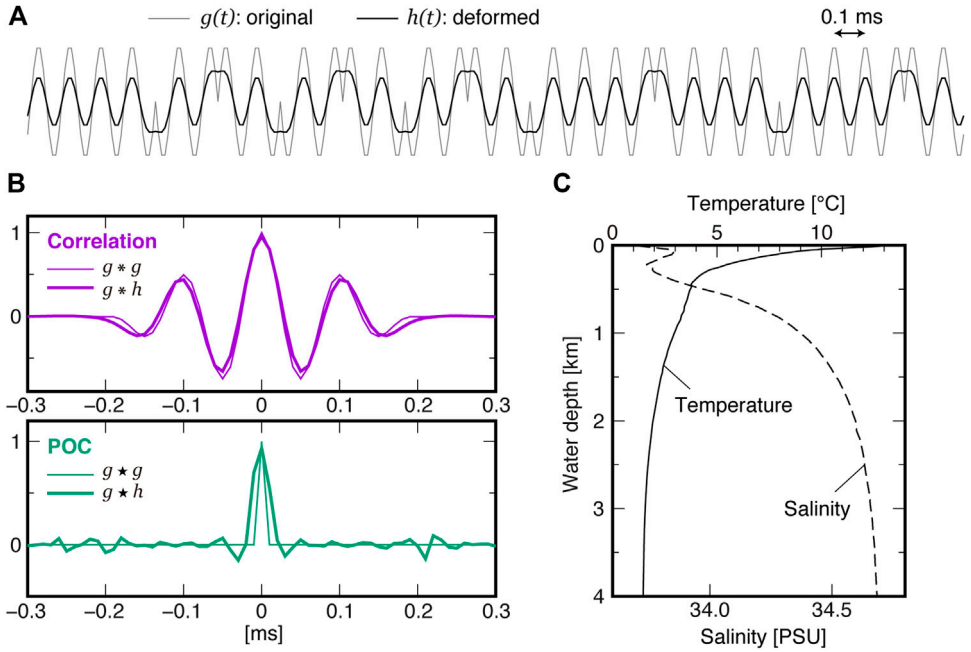

FIGURE 10 | Effect of the frequency-dependent signal attenuation by absorption in seawater. **(A)** A part of the deformed reference signal through a round trip to a depth of 4 km along a vertical path. **(B)** The cross-correlation (top) and POC (bottom) between the original and deformed signals (bold lines). The auto-correlation of the reference signal is shown by thin lines. **(C)** Depth-profile of temperature and salinity used for the calculation of the signal attenuation by absorption.

The in-water admittance vs. frequency plot (**Figure 8B**) shows that the resonance frequency is ~14.3 kHz, keeping sufficient sensitivity around 10 kHz (**Figure 8C**: zones 9–11 kHz are shown by yellow filled boxes). On the other hand, onboard transducers were different both in its shape (hemispherical or cylindrical element) and installation (hull-mounted or fixed on the vessel's side) among campaigns, because we have used several vessels. We summarized possible causes for the distortion of acoustic waves in **Figure 9A**: distortion of emitted (or returning) signals due to degradation of an input signal in electroacoustic transduction and its directivity for the onboard transducer (or seafloor transponder) side, the frequency-dependent attenuation by viscous and chemical absorption in sea water, and superposition of reflected waves from a glass sphere of the seafloor unit. Geometric attenuation is not considered here, because it lessens the signals uniformly without changing the waveform. As measures against the transmission loss, the recording gain of onboard transducers was adjusted according to the water depth at each site, and seafloor transponders were designed to fully amplify acoustic signals when mirroring, and thereby achieving measurable slant ranges up to ~9 km. Among those causes for the distortion, attenuation through absorption is a general, device-independent process. We simulated deformation of the reference signal through a round trip to a depth of 4 km along a vertical path (**Figure 10A**), using the equation presented by Ainslie and McColm (1998). Typical depth-profiles of temperature and salinity (**Figure 10C**), obtained from our oceanographic observations off the northeast Japan, were tentatively used as input to the equation. The result did not significantly differ from the one calculated using the simpler equation by Thorp (1967) which depends only on frequency. Because acoustic waves at higher frequency are more attenuated through absorption, it results in a smoother waveform (black line in **Figure 10A**) than the original one (gray line). However, it turned out that the correlation was little affected by absorption; the cross-correlation between the original and deformed reference signals (a bold purple line in **Figure 10B**) differs only slightly from the auto-correlation of the reference signal (a thin purple line). This indicates that the attenuation through absorption does not have a negative effect on its own. However, it may contribute to the deformation of the POC waveform from a spike of the theoretical delta function (a thin green line) to a peak of some width (a bold green line).

We also examined the effect of reflected waves, because our transponder has wide directivity extending to backward (**Figure 8D**). We calculated the path of acoustic waves coming with a certain incident angle θ, reflected from the glass sphere surface, and then entering the transponder, as illustrated in **Figure 9B**. The phase center of the transponder lies 20 cm above the 17-inch glass sphere, and the position on the glass sphere surface where the acoustic wave reflects, represented by an zenith angle α, and the difference in the path length between the reflected and direct waves ΔL were calculated. Simply assuming total reflection with no phase change, we simulated the acoustic wave superimposed by the reflected wave and its cross-correlation and POC with the reference for incident angles θ = 0°, 15°, 30°, 45°, 60° (**Figure 11**). When the wave comes right above the transponder (**Figure 11B**), the path difference is 40.0 cm long, corresponding to ~0.27 ms in traveltime and thus to ~2.7 times the wave period. As the incident angle increases, the

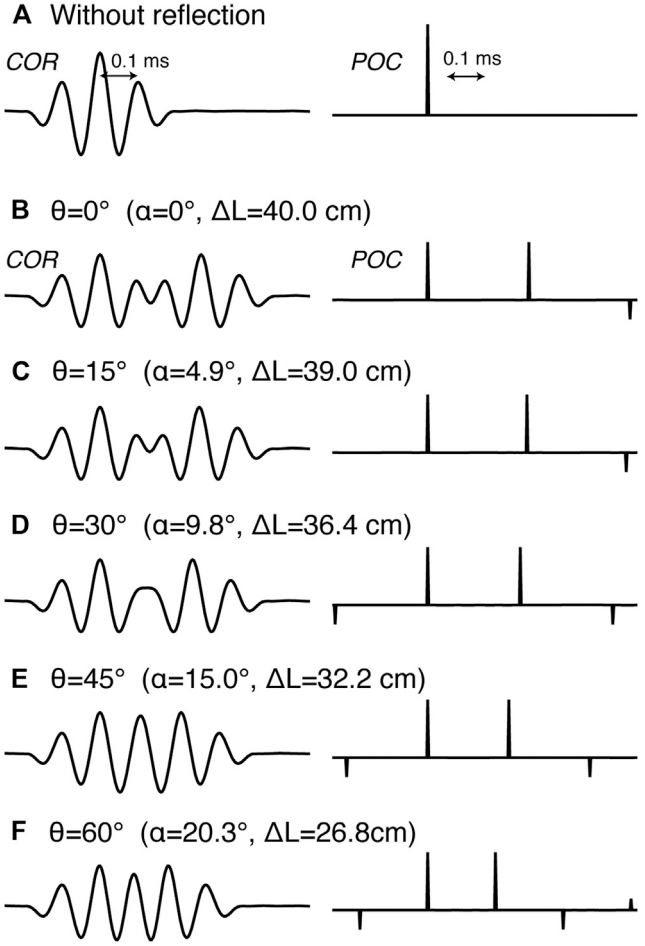

FIGURE 11 | Cross-correlation (left) and POC (right) between the reference signal and simulated signals superimposed by reflected waves, calculated for incident angles θ = 0°, 15°, 30°, 45°, 60°.

path difference decreases and the waveform changes accordingly. The incident angle rarely exceed 45° in our observations, and the path difference when θ = 45° becomes 32.2 cm in length and ~0.21 ms in traveltime (**Figure 11E**). Although a simple model of total reflection without phase change is assumed, the result indicates that the superposition of reflected waves may partly explain the existence of many sidelobes and the dependency of the cross-correlation or POC waveform on the incident angle. However, it cannot enough reproduce the actual wide variety of the cross-correlation or POC waveform by the incident angle (**Figures 3–5**). Moreover, the sensitivity of the transponder is much lower (<~1/10) on the backside than the front side (**Figure 8D**), and therefore reflected waves from the backside are expected to be received with much lower sensitivity. It is considered that the dependency on the incident angle would arise from the directivity, which affects not only the intensity but also the phase, of the seafloor transponder and/or the onboard transducer, as well as the effect of reflected waves. Even if the directivity of the onboard transducer has a significant effect, the classification by the incident angle is still valid because pitching and rolling of the ship are generally less than 5°. Because the directivity differs depending on acoustic devices, it is difficult to simulate the phenomenon with generalities. However, any type of transducer necessarily has its own directivity of intensity and phase, which would result in a particular dependency of the waveform on the incident angle.

We have demonstrated from the actual application examples that POC generally works more effectively than the conventional cross-correlation for peak detection. The formulation of POC (**Eq. 2**) can be rewritten as

$$\mathcal{F}[g \bigstar h] = \mathcal{F}[g^{\dagger}]\overline{\mathcal{F}[h^{\dagger}]}, \tag{3}$$

where $\mathcal{F}[g^{\dagger}]$ represents what is obtained by equalizing the amplitudes of all period components of $\mathcal{F}[g]$ (to be 1), that is,

$$\mathcal{F}[g^{\dagger}] = \frac{\mathcal{F}[g]}{|\mathcal{F}[g]|}. \tag{4}$$

This means that POC is a cross-correlation of $g^{\dagger}$ and $h^{\dagger}$. In **Figure 12**, $g^{\dagger}$ and g are compared as for the reference signal (shown by red) and an example of actual returned signal (blue). The equalization of amplitudes results in the relative amplification of short-period components and, consequently, phase shifts where short-period variation stands out are strongly emphasized in $g^{\dagger}$ of the reference signal (red arrows). The results of the above examinations indicate that the conventional cross-correlation would be practical enough even if affected by absorption and reflected waves. However, we suppose that device-dependent degradation of returning signals may be significant especially at the phase shifts, because resonance-aided transducers have been used for the seafloor stations. We consider that matching the reference signal to the actual returning signals can be performed more robustly by using POC and thereby focusing more on the timing of phase shift in a MLS. Although specific and quantitative examination of those device-dependent effects is difficult, it can be said that the effectiveness of POC which highlights the timing of phase shift would be general as long as utilizing acoustic signals of pulse compression by phase shift.

CONCLUSION

We examined numerous actual cross-correlations of the reference and returned acoustic signals and revealed that the waveform of cross-correlation strongly depends on the incident angle of the acoustic waves. By following gradual changes in the waveform with continuously varying incident angles, an identical peak can be detected among a variety of waveforms. It is supposed that device-dependent directivity as well as superposition of reflected waves result in the dependency of cross-correlation waveform on the incident angle. We also demonstrated that sidelobes were significantly reduced by taking advantage of the phase-only correlation (POC) instead of the conventional cross-correlation. The simpler waveform of POC gives us the advantage of identifying the main peak uniquely and performing template matching more robustly. Although the distortion of cross-correlation waveform is probably caused by device-dependent degradation of signals, the effectiveness of POC which emphasizes the timing of phase

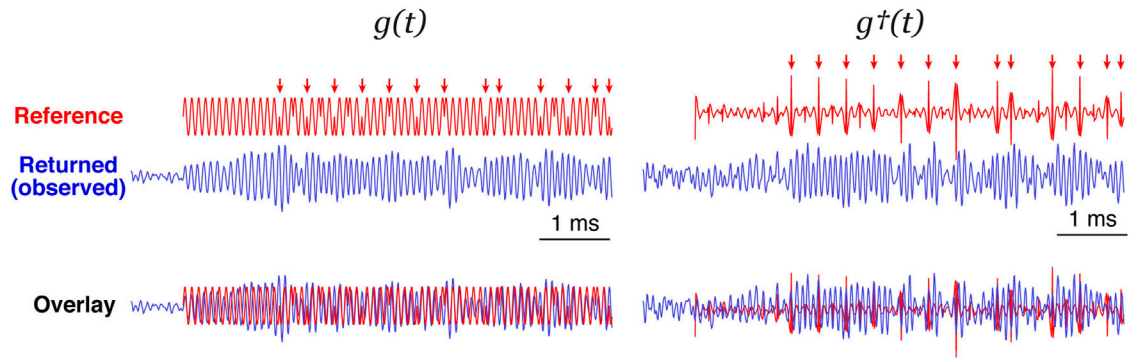

FIGURE 12 | Comparison of the original signal g(t) (left) and the transformed one g†(t) obtained by equalizing amplitudes of all period components (right). The reference signal and an example of actual returned signal are shown by red and blue, respectively (the beginning ~6 ms-long part is shown). Phase shifts in the reference signal are indicated by red arrows. The reference signal is overlaid on the returned signal (bottom) according to the peak detection results.

shift would be general as long as employing phase-shift keying pulse compression.

DATA AVAILABILITY STATEMENT

The raw data supporting the conclusions of this article will be made available by the authors, without undue reservation.

AUTHOR CONTRIBUTIONS

CH and MK designed the study and wrote the manuscript. TI and TO suggested the key idea of utilizing POC. TK and HF continuously supported the study and participated in discussion.

FUNDING

CH acknowledge financial support from JSPS KAKENHI Grant Number JP19H05596: "Head and tail of massive earthquakes: Mechanism arresting growth of interplate earthquakes". The research was funded by activity of the Core Research Cluster of Disaster Science in Tohoku University (a Designated National University).

ACKNOWLEDGMENTS

We thank F. Tomita for providing us fundamental data of the GNSS-A observations used in this study. All the figures in the manuscript were produced using GMT software, developed by P. Wessel and W. H. F. Smith.

REFERENCES

Ainslie, M. A., and McColm, J. G. (1998). A simplified formula for viscous and chemical absorption in sea water. *J. Acoust. Soc. Am.* 103 (3), 1671–1672. doi:10.1121/1.421258

Azuma, R., Tomita, F., Iinuma, T., Kido, M., and Hino, R. (2016). Development and examination of new algorithms of traveltime detection in GPS/acoustic geodetic data for precise and automated analysis. *Earth Planets Sp.* 68, 143. doi:10.1186/s40623-016-0521-2

Honsho, C., and Kido, M. (2017). Comprehensive analysis of traveltime data collected through GPS-acoustic observation of seafloor crustal movements. *J. Geophys. Res. Solid Earth* 122, 8583–8599. doi:10.1002/2017JB014733

Ishikawa, T. (2016). Statistical method for accuracy evaluation of seafloor geodetic observatio [in Japanese with English abstract]. *Rep. Hydrogr. Oceanogr. Res.* 53, 57–81. doi:10.1534/genetics.104.031153

Ito, K., Nakajima, H., Kobayashi, K., Aoki, T., and Higuchi, T. (2004). A fingerprint matching algorithm using phase-only correlation. *IEICE Trans. Fundam.* E87-A3, 682–691. doi:10.1016/j.cviu.2015.09.004

Kido, M., Fujimoto, H., Miura, S., Osada, Y., Tsuka, K., and Tabei, T. (2006). Seafloor displacement at Kumano-nada caused by the 2004 off Kii Peninsula earthquakes, detected through repeated GPS/acoustic surveys. *Earth Planets Sp.* 58 (7), 911–915. doi:10.1186/BF03351996

Moriya, H. (2011). Phase-only correlation of time-varying spectral representations of microseismic data for identification of similar seismic events. *Geophysics* 76 (6), 21. doi:10.1190/geo2011-0021.1

Spiess, F. N. (1985). Suboceanic geodetic measurements. *IEEE Trans. Geosci. Rem. Sens. GE-* 23 (4), 502–510. doi:10.1109/TGRS.1985.289441

Thorp, W. H. (1967). Analytic description of the low-frequency attenuation coefficient. *J. Acoust. Soc. Am.* 42, 270. doi:10.1121/1.381574

Yokota, Y., Ishikawa, T., and Watanabe, S. (2018). Seafloor crustal deformation data along the subduction zones around Japan obtained by GNSS-A observations. *Sci. Data* 5, 180182. doi:10.1038/sdata.2018.182

Conflict of Interest: Authors TI, TO, and TK were employed by the company Kaiyo Denshi Co., Ltd.

The remaining authors declare that the research was conducted in the absence of any commercial or financial relationships that could be construed as a potential conflict of interest.

frontiers in Earth Science

BRIEF RESEARCH REPORT
published: 22 February 2021
doi: 10.3389/feart.2021.600993

Optimal Transponder Array and Survey Line Configurations for GNSS-A Observation Evaluated by Numerical Simulation

Yuto Nakamura[1]*, *Yusuke Yokota*[2], *Tadashi Ishikawa*[1] and *Shun-ichi Watanabe*[1]

[1]Hydrographic and Oceanographic Department, Japan Coast Guard, Tokyo, Japan, [2]Institute of Industrial Science, University of Tokyo, Tokyo, Japan

The Global Navigation Satellite System-Acoustic ranging combination technique (GNSS-A) has enabled us to measure seafloor crustal deformation in the precision of centimeters, leading to numerous discoveries of subseafloor tectonic phenomena. The moving observation conducted by our research group allows us to measure both the horizontal and vertical absolute positions of a reference point on the seafloor. However, the observation frequency of our GNSS-A observation system is still insufficient to observe short-term phenomena. This paper focused on the possibility to reduce the observation time per a seafloor site by shrinking the seafloor transponder array size and the survey line radius, which were empirically defined to be equal to the seafloor site depth in the early research. We evaluated the effects of changing these sizes on the GNSS-A positioning accuracy by conducting a series of numerical experiments. The results of the numerical experiments indicated that for a seafloor site with a depth of 3,000 m, the positioning accuracy is rapidly degraded as the transponder array size and the survey line radius are reduced to less than 3,000 m. Additional experiments done for transponder array sizes and survey line radii around 2,000–4,000 m revealed that shrinking the survey line radius has a dominant effect on the decrease in positioning accuracy. Thus, shrinking the transponder array size and the survey line radius is not a suitable option for reducing observation time, and the empirically defined observation configurations are concluded to be quite optimal when regarding both the positioning accuracy and the observation time.

Keywords: seafloor geodesy, simulator, transponder array, survey line, GNSS-A

OPEN ACCESS

Edited by:
Keiichi Tadokoro, Nagoya University, Japan

Reviewed by:
Fumiaki Tomita, Japan Agency for Marine-Earth Science and Technology (JAMSTEC), Japan
Pierre Sakic, German Research Center for Geosciences, Helmholtz Center Potsdam, Germany

***Correspondence:**
Yuto Nakamura
ynakamura@jodc.go.jp

Specialty section:
This article was submitted to Solid Earth Geophysics, a section of the journal Frontiers in Earth Science

Received: *31 August 2020*
Accepted: *14 January 2021*
Published: *22 February 2021*

Citation:
Nakamura Y, Yokota Y, Ishikawa T and Watanabe S (2021) Optimal Transponder Array and Survey Line Configurations for GNSS-A Observation Evaluated by Numerical Simulation. Front. Earth Sci. 9:600993. doi: 10.3389/feart.2021.600993

INTRODUCTION

The Global Navigation Satellite System-Acoustic ranging combination technique (GNSS-A) has realized the precise measurement of a reference point on the seafloor, expanding the crustal observation network into the ocean (Spiess, 1985; Asada and Yabuki, 2001; Fujita et al., 2006). In the GNSS-A observation of the Japan Coast Guard (JCG), the precise position of a survey vessel sailing along a survey line is measured using kinematic GNSS positioning, and the distances between the onboard transducer and the mirror transponders installed on the seafloor are measured using acoustic ranging (**Figure 1A**). Combining these data with the vessel attitude data and XBT/XCTD observations, the global coordinates of the virtual reference point (the centroid of the transponders)

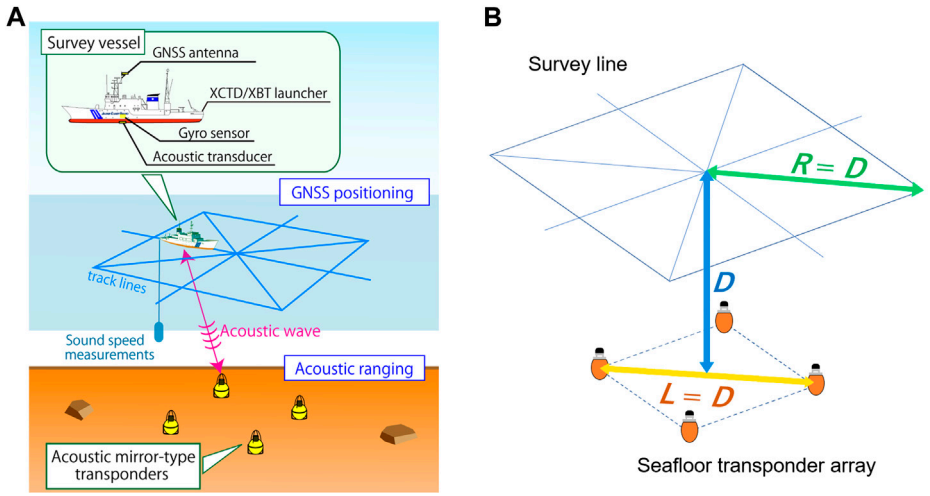

FIGURE 1 | Schematic images of the current GNSS-A observation system conducted by the Japan Coast Guard. **(A)** is the overview of the entire GNSS-A observation system, and **(B)** indicates the configurations of the transponder array and the survey line. As shown in **(B)**, the seafloor site depth (D), transponder array size (L), and survey line radius (R) are set to be equal.

is precisely determined in the centimeter level. GNSS-A observation has revealed numerous tectonic phenomena such as the coseismic and postseismic movements of the 2011 Tohoku-oki earthquake (M_w 9.0) (Sato et al., 2011; Watanabe et al., 2014), interplate coupling in the Nankai Trough region (Yokota et al., 2016a), and shallow slow slip events that occurred near the Nankai Trough axis (Yokota and Ishikawa, 2020).

The observation frequency has been a crucial matter for GNSS-A observation over the past 20 years, and we have been making significant efforts to improve the observation frequency. Despite the increase in the number of our seafloor sites, the observation frequency of the JCG group has improved from approximately one time per year per site in the early 2000s to 4 times per year per site by 2018 (Ishikawa et al., 2020). However, this frequency is still inadequate for observing tectonic phenomena with time scales less than few months (e.g. shallow short-term slow slip events).

One of the key factors that affects the observation efficiency is the size of the transponder array and the survey line, as shown in **Figure 1B**. In the early research by Spiess (1985), the proposed stationary observation system required at least three transponders, and the transponder array size has been defined that the circumdiameter of the transponder array should be approximately equal to the depth of the seafloor site.

However, the stationary system using a triangular transponder array proposed by Spiess (1985) was unable to detect the vertical displacement. To overcome this problem of detecting the vertical displacement, our research group has taken a different approach. We have developed an observation system that uses a vessel to perform a moving survey (**Figure 1A**), which is capable to detect both the horizontal and vertical displacements. In our system, although it is possible to detect the movement of only a single transponder, we deploy four transponders to form a square array as shown in **Figure 1A** to increase the positioning accuracy and stability. The transponder array size in our observation system is configured to be equal to the site depth, as done in Spiess (1985).

Regarding the survey line, theoretical studies by a research group in China have indicated that the optimal survey line radius is $\sqrt{2}$ times the depth of the seafloor site, which is the radius when the smallest geometric dilution of precision (GDOP) is achieved (Zhao et al., 2016). In the current observation system of our group, the survey line radius is set to be approximately equal to the depth of the seafloor site. Taking in account of the effects of vessel attitude and the seawater turbulence on the acoustic ranging, the maximum speed of the survey vessel during an observation is limited to approximately 6–7 knots. Therefore, deeper sites which have longer survey lines tend to take relatively longer observation times, and it is difficult to reduce the observation times of the deeper sites by increasing the vessel speed.

One possible approach to reduce the observation time for the deep sites is by reducing the transponder array size and the survey line radius which were empirically defined in the early studies (e.g. Spiess 1985). However, the effects of changing the transponder array size and the survey line radius on the accuracy of GNSS-A positioning have not been clearly investigated. In this study, we evaluated the effects of changing the transponder array size and the survey line radius on the accuracy of GNSS-A observation, by analyzing synthetically generated datasets.

We created a series of synthetic datasets with different transponder array sizes and survey line radii by using a numerical simulator (Yokota et al., 2016b) to evaluate the effects of changing these sizes on the positioning accuracy. In

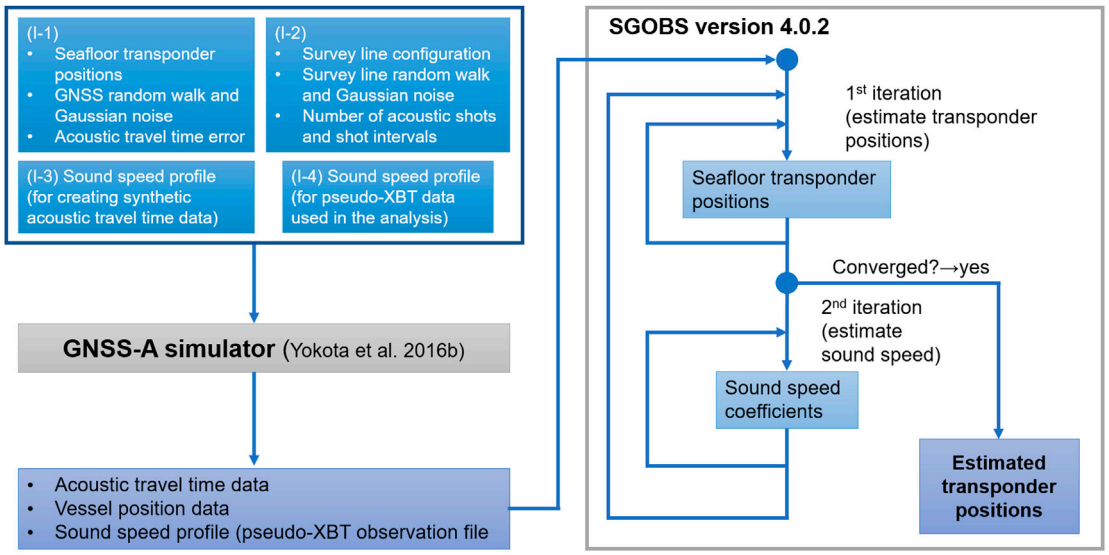

FIGURE 2 | The flow chart of our numerical experiment. The input files (I-1), (I-2), (I-3), and (I-4) are used for the configurations of the numerical simulation by the GNSS-A simulator. The outputs of the GNSS-A simulator (the synthesized GNSS-A data) are analyzed using the analysis software SGOBS version 4.0.2, in which the linearized inversion method by Fujita et al. (2006) is implemented (right side of the figure).

our numerical experiments, we assumed a simple square transponder array and assigned a symmetrical survey line. To focus only on the effects of changing the geometry of the observation system, we configured a simple sound speed structure with no horizontal and temporal variations. We analyzed these datasets like the actual GNSS-A datasets using the conventional linearized inversion method (Fujita et al., 2006).

METHODS

The GNSS-A Simulator

We used a numerical simulator that has been developed to create synthetic GNSS-A observation datasets (Yokota et al., 2016b). In the GNSS-A simulator, the synthetic travel times are calculated between the synthetic vessel positions and the preconfigured transponder positions, and the outputs are formatted to be analyzed like an actual GNSS-A observation dataset. The GNSS-A simulator requires the following input files (also shown in **Figure 2**):

(I-1) Transponder position and error configuration file
(I-2) Survey line configuration file
(I-3) Sound speed profile configuration file (for synthetic acoustic travel time data)
(I-4) Sound speed profile configuration file (as pseudo-XBT data used in analysis)

In our simulation, the three-dimensional position is expressed by local East-North-Up (ENU) coordinates, with the origin at the sea surface directly above the centroid of the transponder array. Configuration file (I-1) contains the three-dimensional positions of the transponders, which are written in the local ENU coordinates. The acoustic travel time error, pseudo-random walk of the GNSS, and Gaussian noise of the GNSS are also configured in this file. Survey line configuration file (I-2) contains the survey line geometry and size, number of acoustic shots and shot interval for each survey line, and the pseudo-random walk and Gaussian noises of the survey line (which express random distortions of the survey line geometry). In the sound speed profile configuration file for the theoretical ray path calculation (I-3), the spatiotemporal variation of the sound speed profile can be configured. There is also a sound speed profile configuration file (I-4) for the pseudo-XBT data used in the analysis. The sound speed profile in (I-3) and (I-4) are configured at several depth layers; the sound speed at depths between these configured depth layers are either linearly interpolated or extrapolated. Settings for the vessel attitude and the offset between the GNSS antenna and the transducer are not implemented in this simulator; thus, the calculated vessel positions are equivalent to the transducer positions.

The resulting outputs of the calculated data are the acoustic travel time file, vessel position file, and the sound speed observation file. These output files can be analyzed like an actual GNSS-A dataset using the method of Fujita et al. (2006), as described in **Figure 2** and *Analysis of the Synthetic Datasets*.

Configurations of the Numerical Experiments

In our study, we mainly edited input files (I-1) and (I-2) to configure the transponder positions and the survey line radius for

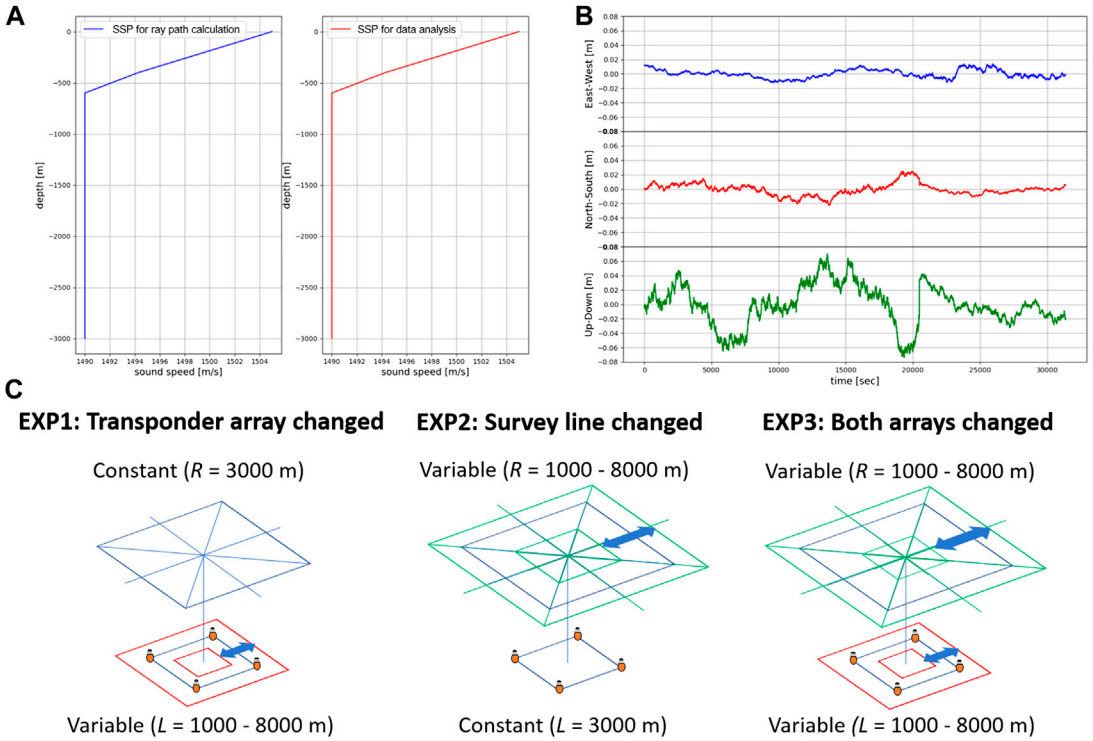

FIGURE 3 | The configurations of our numerical experiment. **(A)** shows the vertical sound speed profile (SSP) configured for the ray path calculation (left, blue line) and the vertical SSP used in the data analysis (right, red line). Note that the difference between these two profiles is so small that the difference cannot be distinguished in this figure (see *Configurations of the Numerical Experiments* for details). **(B)** indicates sample waveforms of the GNSS pseudo-random walk added to the synthesized data (from top to bottom, the east-west, north-south, and up-down components). **(C)** is the schematic diagram of the settings of EXP1, EXP2, and EXP3, from left to right (see *Configurations of the Numerical Experiments* for details).

each experimental run, and kept the settings in files (I-3) and (I-4) constant throughout all of the numerical experiments.

Since the focus of our study is on the possibility to reduce the observation times for the deep sites, we have set the depth of the seafloor site in file (I-1) to 3,000 m, which is a representative depth of the deepest seafloor sites installed by our research group. In our numerical experiments, the depths of all transponders were set to 3,000 m. This value was kept constant for all of the experimental runs. The transponder positions were set so that the transponders form a square array, with the centroid at position (0 m, 0 m, −3,000 m) in local ENU coordinates. For example, when we set the transponder array size to L, we assigned the transponders at (L/2, 0 m, −3,000 m) (−L/2, 0 m, −3,000 m) (0 m, L/2, −3,000 m), and (0 m, −L/2, 3,000 m), in local ENU coordinates. The transponder array size was changed depending on the experimental run.

In the survey line configuration file (I-2), a symmetrical survey line configuration currently adopted in our GNSS-A observation, as shown in **Figure 1B**, is configured. Like the transponder positions, the survey line radius was also changed depending on the type of the experimental run. For each trial of data synthesis and analysis, a total of four sets with each having 784 acoustic shots were simulated to create a single GNSS-A dataset with a total of 3,136 shots. The acoustic shots were created at a constant time interval, to synthesize a geometrically well-balanced data, as we do in the actual observations. The number of acoustic shots per line and the shot intervals were tuned so that the total simulated acoustic shots is 3,136 for each trial, regardless of the survey line radius.

We configured a simple sound speed structure in files (I-3) and (I-4) that has no horizontal sound speed gradient nor temporal variation. Such a simplified sound speed structure was used instead of a more realistic model (e.g. Munk, 1974), since our focus is on how the GNSS-A positioning accuracy is affected by changing the transponder array size and the survey line radius. The configured values for the ray path calculation in (I-3) were 1,505.00 m/s at 0 m, 1,494.30 m/s at 400 m, and 1,490.00 m/s at depths below 600 m, as shown in the left of **Figure 3A**. The acoustic shots calculated using these values have round-trip travel times ranging roughly 4–10 s and takeoff angles ranging roughly from 100° – 180°, depending on the transponder array size and the survey line radius. As shown in the right of **Figure 3A**, we configured values in (I-4) for the XBT data used in the analysis that were almost identical to the values configured in (I-3). Since the temporal variation estimated in SGOBS ver. 4.0.2 is much larger in magnitude compared to the XBT measurement errors, our settings of the XBT measurement errors should not affect the outcome of the simulation.

We created high-rate pseudo-GNSS noises using the Box-Muller's method (Box and Muller, 1958). For the pseudo-GNSS

noise, we assigned a Gaussian noise and a random walk for the vertical and horizontal components. Gaussian noise and random walk were empirically known to be included in the GNSS noises (Bilich et al., 2008). The values of 1σ of the pseudo-GNSS noises, implemented in file (I-1), were 0.5 cm for the horizontal Gaussian noise, 1.5 cm for the vertical Gaussian noise, 2.5 cm for the horizontal random walk, and 7.5 cm for the vertical random walk. Sample waveforms of the random walk are shown in **Figure 3B**. To focus on how the transponder array size and the survey line radius affect the GNSS-A positioning accuracy, we have only added the pseudo-GNSS noises, and did not configure the travel time errors in our experiments.

We performed a series of experimental runs as shown in **Figure 3C** to evaluate the individual and the combined effects of changing the transponder array size and the survey line radius on the GNSS-A positioning accuracy. In our first experiment, only the transponder array size was changed from 1,000 m to 8,000 m at 1,000 m intervals, and the survey line radius was fixed to 3,000 m (EXP1 in **Figure 3C**). In our second experiment, only the survey line radius was changed from 1,000 m to 8,000 m at 1,000 m intervals, and the transponder array size was fixed to 3,000 m (EXP2 in **Figure 3C**). In the third experiment (EXP3 in **Figure 3C**), both the transponder array size and the survey line radius were simultaneously changed from 1,000 m to 8,000 m at 1,000 m intervals (e.g. when the transponder array size is configured to 8,000 m, the survey line radius is also configured to 8,000 m). Additionally, we have also performed an experiment with a transponder array size of 2,000 m and a survey line radius of 4,000 m, and another experiment with a transponder array size of 4,000 m and a survey line radius of 2,000 m, to closely examine the effects of transponder array sizes and survey line radii around 2,000–4,000 m. As stated above in this section, note that the site depth is fixed to 3,000 m for all experimental runs.

To evaluate the positioning accuracy, we conducted 300 trials of data synthesis and analysis for each experimental run. For each trial, we created pseudo-GNSS noises as assigned in file (I-1), and added the noises to the synthetic data, to create data variation among the trials.

Analysis of the Synthetic Datasets

For the analysis of the synthetic datasets, we used the analysis software SGOBS version 4.0.2, in which the method developed by Fujita et al. (2006) is implemented. SGOBS version 4.0.2 is regularly used in the observation and analysis routine of our group. In the method of Fujita et al. (2006), the sound speed structure and the three-dimensional transponder positions are alternately estimated using Bayesian inversion. As shown in the right of **Figure 2**, this algorithm first iterates to determine the positions of the seafloor transponders using the initial sound speed profile, and then the resulting residuals of the first loop are used in the second loop to determine the sound speed coefficient. Then, the transponder positions are determined again using the newly estimated sound speed coefficients, and so on. These iterations are repeated until both the sound speed and the transponder positions satisfy the convergence criteria. The centroid of the transponder positions is calculated from the final estimations of the transponder positions.

In the actual GNSS-A observations, acoustic shots with extremely small takeoff angles may be due to fake return signals, such as echoes from the seafloor. In order to remove such acoustic shots that may not be responses from the transponders, acoustic shots with takeoff angles less than 120° are removed in the algorithm of SGOBS version 4.0.2.

To evaluate the GNSS-A positioning accuracy, we defined three criteria as listed below:

(1) The average horizontal error of the centroid (μ_{Ch})
(2) The average horizontal error of the four transponders ($\mu_{\overline{M}}$)
(3) The average vertical error of the centroid (μ_{Cv})

The average horizontal error of the centroid (μ_{Ch}) is defined as the average displacement of the horizontal centroid positions of the N trials from the "true" horizontal position of the centroid $\boldsymbol{C}_0$. As explained in *Configurations of the Numerical Experiments*, the horizontal centroid position $\boldsymbol{C}_0$ is always at (0 m, 0 m) regardless of the transponder array size. Let $\boldsymbol{C}_i$ be the estimated horizontal position of the centroid of the ith trial, and μ_{Ch} can be calculated as follows:

$$\mu_{Ch} = \frac{1}{N}\sum_{i=1}^{N}|\boldsymbol{C}_i - \boldsymbol{C}_0|.$$

$\mu_{\overline{M}}$ is calculated by averaging the horizontal errors of the four transponders numbered j (j = 1, 2, 3, 4, corresponding to the transponder in the east, west, north, and south of the centroid). Let $\boldsymbol{M}_i^j$ be the estimated horizontal position of the jth transponder in the ith trial, and $\boldsymbol{M}_0^j$ be the "true" horizontal position of the jth transponder configured in file (I-1), and the average horizontal error of the four transponders for the ith trial $\overline{M}_i$ is expressed as:

$$\overline{M}_i = \frac{1}{4}\sum_{j=1}^{4}\left|\boldsymbol{M}_i^j - \boldsymbol{M}_0^j\right|.$$

Thus, the average horizontal error of the four transponders for N trials, $\mu_{\overline{M}}$ can be simply calculated as the average of $\overline{M}_i$ for all trials:

$$\mu_{\overline{M}} = \frac{1}{N}\sum_{i=1}^{N}\overline{M}_i.$$

The average vertical error of the centroid σ_{Cv} is calculated by averaging the absolute value of the anomaly of the N trials from the "true" vertical position of the centroid, d, configured in file (I-1), which is constantly $d = 3,000$ m for all trials in all experimental runs. Thus, when the vertical position of the centroid for the ith trial is defined as u_{C_i}, μ_{Cv} is simply calculated as below:

$$\mu_{Cv} = \frac{1}{N}\sum_{i=1}^{N}\left|u_{C_i} - d\right|.$$

In *Results and Discussion*, the results will be evaluated by calculating and plotting the values of μ_{Ch}, $\mu_{\overline{M}}$, μ_{Cv} of each experimental run. Since 300 trials were performed for each run, N = 300 in these equations above for this study.

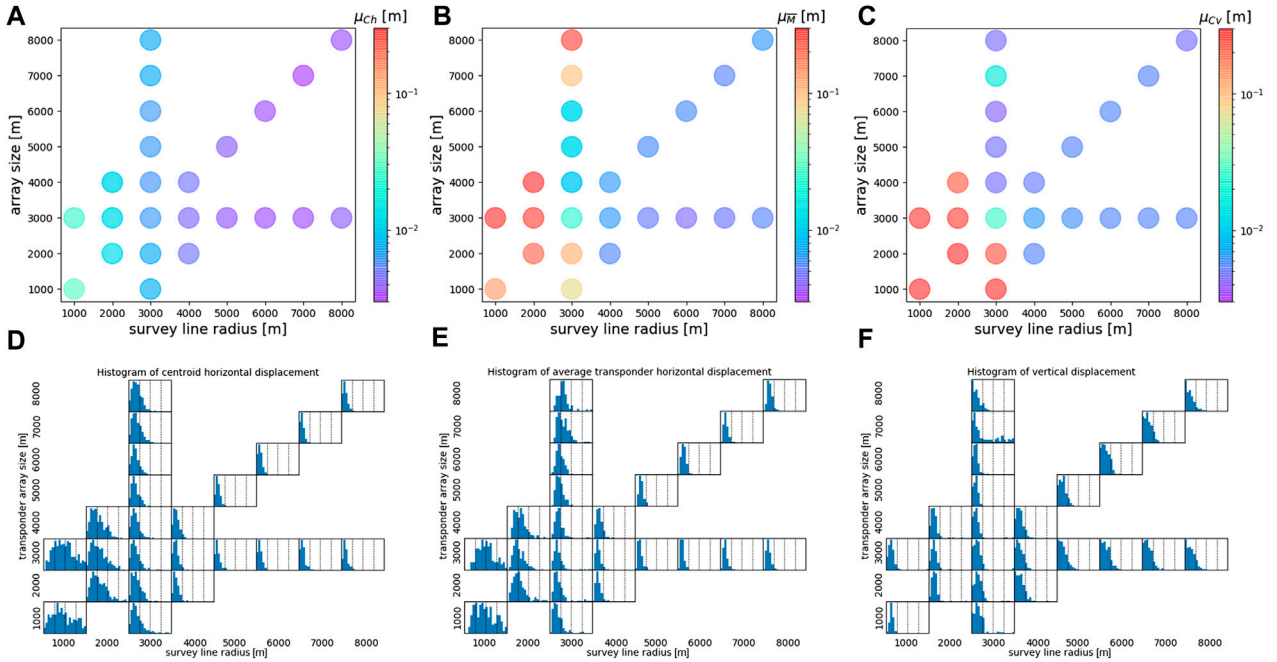

FIGURE 4 | The results of the numerical experiments. Figure **(A)** is the plot of the average horizontal error of the centroid μ_{Ch}, **(B)** is the plot of the average horizontal error of the four transponders $\mu_{\overline{M}}$, **(C)** is the plot of the average vertical error of the centroid μ_{Cv}. Figure **(D)** is the histogram of the horizontal error of the centroid obtained from 300 trials for each experimental run, **(E)** is the histogram of the average horizontal error of the four transponders, and **(F)** is the histogram of the vertical error of the centroid. The range of these histograms are from 0 cm to 4 cm, and the dashed lines indicate 1 cm intervals. Note that Figures **(D)**, **(E)**, and **(F)** have outliers that exceed 4 cm.

RESULTS

Figures 4A–C indicate the values of μ_{Ch}, $\mu_{\overline{M}}$, and μ_{Cv} obtained from the numerical experiments, respectively. **Figure 4A** indicates that the horizontal positioning accuracy of the centroid decreases when the survey line radius is shrunk to less than 3,000 m. When the survey line radius is fixed to 3,000 m, the change in the values of μ_{Ch} is small, regardless of the transponder array size. Overall, the values of μ_{Ch} fluctuate within the range of few centimeters, indicating that changing the transponder array size and the survey line radius do not significantly affect the horizontal positioning accuracy of the centroid.

Meanwhile, the values of $\mu_{\overline{M}}$ (**Figure 4B**) shows that the horizontal positioning accuracies of the individual transponders fluctuate in the order of decimeters. This indicates that unlike the centroid, the positioning accuracy of each transponder is clearly affected by changing the transponder array size and/or the survey line radius. $\mu_{\overline{M}}$ is approximately 2 cm for an array size of 3,000 m, but when the transponder array size is shrunk to less than 3,000 m, $\mu_{\overline{M}}$ becomes greater than 10 cm. The positioning accuracy is degraded even more when the survey line radius is shrunk to less than 3,000 m; $\mu_{\overline{M}}$ becomes greater than 20 cm $\mu_{\overline{M}}$ also increases when the survey line radius is fixed to 3,000 m and the transponder array size is greater than 6,000 m, exceeding 20 cm when the transponder array size is 8,000 m.

Figure 4C shows that the average error of the vertical position μ_{Cv} generally increases as the transponder array size and/or the survey line radius decrease. When the transponder array size and/or the survey line radius become smaller than 3,000 m, μ_{Cv} rapidly increases, and the values exceed 20 cm. This result indicates that the vertical positioning becomes inaccurate and unstable as these sizes decrease. However, when the transponder array size and the survey line radius become larger than 3,000 m, μ_{Cv} rapidly converges to values less than 1 cm.

Figures 4D–F shows the histograms of the horizontal error of the centroid, the average horizontal error of the four transponders, and the vertical error of the centroid, respectively. All histograms indicate the frequency of errors in the range of 0–4 cm. **Figures 4D,E** show that the distribution peaks of the horizontal errors become generally sharper, and the peak gradually shifts to 0 cm as the transponder array size and the survey line radius increase. This indicates that the horizontal positioning accuracy generally improves as these sizes increase. In **Figure 4F**, the histograms of the vertical error, the distribution peak shifts toward 0 cm as the transponder array size and the survey line radius increase. This result shows that the vertical positioning accuracy also improves by increasing these sizes.

DISCUSSION

Effects of Changing the Transponder Array Size

Figure 4B indicates that $\mu_{\overline{M}}$ increases rapidly as the transponder array size becomes greater than 6,000 m, when the survey line

radius is fixed to 3,000 m. Histograms in **Figure 4E** show that when the survey line radius is fixed to 3,000 m and the transponder array size becomes greater than 6,000 m, the distribution peak becomes wider and shifts away from 0 cm. These results imply that the horizontal positioning errors of each transponder becomes larger when the transponder array size becomes wider than the survey line radius. When the transponder array is larger than the area covered by the survey line, most of the acoustic shots will be taken from the inside of the transponder array. Since a geometrically well-balanced acoustic data is necessary for GNSS-A observation, such poorly balanced data would degrade the positioning accuracy, leading to the results shown in **Figure 4B**.

The values of $\mu_{\overline{M}}$ also increase when the transponder array size is shrunk to less than 3,000 m, as well as the vertical error μ_{Cv} (**Figure 4C**). Shrinking the transponder array size would eventually converge as observing a single transponder at the centroid. The position obtained by observing only a single transponder is unstable compared to the position of the centroid obtained by observing a square array of four transponders, which may be the cause of the decrease in positioning accuracy when the transponder array size is decreased.

However, the values of μ_{Ch} remain relatively stable throughout all array sizes when the survey line radius is kept constant at 3,000 m, each ranging between 6 and 10 mm (**Figure 4A**). The results of μ_{Ch} imply that the horizontal positioning of the centroid is not significantly affected by shrinking the transponder array size, despite the fact that $\mu_{\overline{M}}$ significantly increases by shrinking the array. This indicates that rather than determining the position of an individual transponder as the position of a seafloor site, determining the centroid of a square transponder array is an effective method for reducing observation errors and stably positioning a seafloor site.

Effects of Changing the Survey Line Radius

In general, larger survey line radius enhances the variation of the takeoff angles of the acoustic shots, which leads to improved positioning accuracy, as shown in **Figure 4**. This is analogous to a good constellation geometry in GNSS positioning; it is better that the GNSS satellites spread out evenly across the sky rather than being confined in a very small area.

Shrinking the survey line radius would eventually converge as a stationary observation at the sea surface directly above the centroid. The takeoff angle variation of the acoustic shots decreases since the survey range is confined to a smaller area. Unlike the transponder arrangement proposed by Tomita et al. (2019), our square transponder array cannot determine the vertical displacement by stationary observation. Our results shown in **Figure 4C** indicate that μ_{Cv} rapidly increases as the survey line radius is decreased below 3,000 m. The histogram (**Figure 4F**) also shows that the distribution peak gradually shifts away from 0 cm as the survey line radius decrease, implying the decrease in the positioning accuracy. $\mu_{\overline{M}}$ (**Figure 4B**) and the histograms (**Figure 4E**) indicate that the horizontal positioning of the individual transponders is degraded as well by decreasing the survey line radius. Nevertheless, the values of μ_{Ch} when the survey line radius is less than 3,000 m are much smaller compared to the values of $\mu_{\overline{M}}$. This indicates that positioning the centroid of the seafloor transponders forming a square array is an effective method to reduce the horizontal positioning error.

When the survey line radius is increased, all of the errors tend to become very small. However, it must be noted that the availability of the acoustic data in the analyses for a very large survey line radius is very poor. For example, when the survey line radius is 8,000 m, the data availability is around 30–50%. This is due to the takeoff angle limitation in our GNSS-A observation to exclude acoustic signals transmitted from takeoff angles that are less than 120°, as explained in *Analysis of the Synthetic Datasets*. Thus, although very large survey line radii seem to perform well regarding the positioning accuracies, these radii are not suitable for the actual observation routine. Also, the improvement of the positioning accuracy when configuring a survey line radius larger than 3,000 m is small, improving only in order of millimeters, compared to the significant increase in the observation time, making the observation inefficient.

The Optimal Transponder Array Size and Survey Line Radius

We can imply from **Figure 4** that when regarding the horizontal and vertical positioning accuracies, the transponder array size and the survey line radius should be as large as possible. However, due to the takeoff angle limitation explained in *Effects of Changing the Survey Line Radius*, the optimal transponder array size and survey line radius for our observation system is limited to approximately 3,000–4,000 m. When regarding both the observation time and the positioning accuracy, the transponder array size and survey line radius of 3,000 m, which is equal to the empirically defined sizes for a depth of 3,000 m, seems to be quite optimal. When the sizes are less than 3,000 m, the positioning errors become too large for crustal monitoring. When the sizes are greater than 3,000 m, the improvement of the positioning accuracy is small compared to the significant increase in the observation time. It can be concluded that the trade-off between the positioning accuracy and the observation time is well balanced at our empirically defined sizes. Also, it must be noted that in the real world, increasing the transponder array size and the survey line radius would increase errors due to the spatial variability of the sound speed structure.

Figure 4A has indicated that the horizontal positioning error of the centroid of the transponders remains stable when the transponder array size and/or the survey line radius is changed. This result implies that it is possible to obtain the horizontal positions of a site with a transponder array size and a survey line radius that is smaller than our empirically defined sizes. One of the limitations when installing a site is the seafloor topography; there are cases where we cannot install a site with the empirically defined transponder array size, due to the lack of a smooth seafloor. When regarding only the horizontal positioning accuracy, we can shrink the transponder array size to some degree, which would give us more valuable options when installing a site. Also, the result that the horizontal positioning

is not significantly affected by shrinking the survey line radius indicates a possibility that we can reduce the observation time. By reducing the observation time and increasing the observation frequency, we can improve the accuracy of the time series of the horizontal positions. An improved time series of the horizontal positions would provide us valuable information on the temporal variation of the seafloor crustal deformation.

Our simulation results may also be applied to the observations of other institutions, with different survey line geometry. As explained in *Effects of Changing the Survey Line Radius*, assigning a large survey line radius enables us to obtain acoustic data with larger variation of takeoff angles, which is necessary for achieving high positioning accuracies for both the horizontal and the vertical components. Thus, it may be possible that the optimal sizes indicated in our study can be applied to other types of survey line geometry, if the survey line geometry is configured to obtain acoustic data with large variation of the takeoff angles.

Future Works

The results of the numerical experiments indicated that the positioning accuracy is degraded rapidly assuming transponder array size and survey line radius of less than 3,000 m for a site with 3,000 m of depth. Thus, shrinking the transponder array size and the survey line radius is not a suitable solution for improving observation frequency. In fact, the empirically defined sizes, which is equal to 3,000 m in the experiments of our study, are quite optimal values when regarding both the positioning accuracy and observation efficiency.

GNSS-A observation has numerous error sources other than those focused in this study. One of the main error sources is the spatiotemporal variation of the sound speed structure, which has been investigated in numerous studies (e .g. Yasuda et al., 2017; Honsho et al., 2019; Yokota et al., 2019). Assessing the effects of the temporal change of the sound speed structure and the horizontal sound speed gradient on the GNSS-A accuracy is one of the main topics for our future research using the GNSS-A simulator. Numerical experiments using different transponder arrangements such as those proposed by Tomita et al. (2019) is an important topic as well, since there is a possibility that the positioning accuracy may improve by changing the arrangement of the transponders. Also, a new analysis software that directly estimates the sound speed structure using a Bayesian approach is being developed (Watanabe et al., 2020). We can utilize the simulator to validate the capability of this new software to accurately determine the transponder positions and to properly estimate the sound speed structure. We plan to further investigate the GNSS-A observation errors by taking the approach using numerical simulation, as done in this study.

DATA AVAILABILITY STATEMENT

The raw data supporting the conclusions of this article will be made available by the authors, without undue reservation.

AUTHOR CONTRIBUTIONS

YN designed the study and wrote this manuscript. YY developed and tuned the GNSS-A simulator. YN, YY, TI, SW discussed about the simulation configurations and the results, and commented to improving the manuscript.

FUNDING

The submission of this manuscript was funded by the Japan Coast Guard.

ACKNOWLEDGMENTS

We thank the many staff members from the Hydrographic and Oceanographic Department, Japan Coast Guard, including the crew of the survey vessels Takuyo, Shoyo, Meiyo, and Kaiyo for their support in our observations and technological developments. We especially thank the active senior staff members from the Geodesy and Geophysics Office, Hydrographic and Oceanographic Department, Japan Coast Guard, for their devoted maintenance and management of the equipment.

REFERENCES

Asada, A., and Yabuki, T. (2001). Centimeter-level positioning on the seafloor. *Proc. Jpn. Acad. Ser. B* 77, 7–12. doi:10.2183/pjab.77.7

Bilich, A., Larson, K. M., and Axelrad, P. (2008). Modeling GPS phase multipath with SNR: case study from the salar de Uyuni, boliva. *J. Geophys. Res.* 113, B04401. doi:10.1029/2007JB005194

Box, G. E. P., and Muller, M. E. (1958). A note on the generation of random normal deviates. *Ann. Math. Stat.* 29 (2), 610–611. doi:10.1214/aoms/1177706645

Fujita, M., Ishikawa, T., Mochizuki, M., Sato, M., Toyama, S., Katayama, M., et al. (2006). GPS/acoustic seafloor geodetic observation: method of data analysis and its application. *Earth Planets Space* 58, 265–275. doi:10.1186/BF03351923

Honsho, C., Kido, M., Tomita, F., and Uchida, N. (2019). Offshore postseismic deformation of the 2011 Tohoku earthquake revisited: application of an improved GPS-acoustic positioning method considering horizontal gradient of sound speed structure. *J. Geophys. Res. Solid Earth* 124. doi:10.1029/2018JB017135

Ishikawa, T., Yokota, Y., Watanabe, S., and Nakamura, Y. (2020). History of on-board equipment improvement for GNSS-A observation with focus on observation frequency. *Front. Earth Sci.* 8, 150. doi:10.3389/feart.2020.00150

Munk, W. H. (1974). Sound channel in an exponentially stratified ocean, with application to SOFAR. *J. Acoust. Soc. Am.* 55, 220. doi:10.1121/1.1914492

Sato, M., Ishikawa, T., Ujihara, N., Yoshida, S., Fujita, M., Mochizuki, M., et al. (2011). Displacement above the hypocenter of the 2011 Tohoku-oki earthquake. *Science* 332, 1395. doi:10.1126/science.1207401

Spiess, F. N. (1985). Suboceanic geodetic measurements. IEEE Trans. Geosci. Remote Sensing, GE-23, 502–510. doi:10.1109/TGRS.1985.289441

Tomita, F., Kido, M., Honsho, C., and Matsui, R. (2019). Development of a kinematic GNSS-Acoustic positioning method based on a state-space model. *Earth Planets Space* 71, 102. doi:10.1186/s40623-019-1082-y

Watanabe, S., Ishikawa, T., Yokota, Y., and Nakamura, Y. (2020). GARPOS: analysis software for the GNSS-A seafloor positioning with simultaneous estimation of sound speed structure. *Front. Earth Sci.* 8, 597532. doi:10.3389/feart.2020.597532

Watanabe, S., Sato, M., Fujita, M., Ishikawa, T., Yokota, Y., Ujihara, N., et al. (2014). Evidence of viscoelastic deformation following the 2011 Tohoku-oki earthquake revealed from seafloor geodetic observation. *Geophys. Res. Lett.* 41, 5789–5796. doi:10.1002/2014GL061134

Yasuda, K., Tadokoro, K., Taniguchi, S., Kimura, H., and Matsuhiro, K. (2017). Interplate locking condition derived from seafloor geodetic observation in the shallowest subduction segment at the Central Nankai Trough, Japan. *Geophys. Res. Lett.* 44, 3572–3579. doi:10.1002/2017GL072918

Yokota, Y., and Ishikawa, T. (2020). Shallow slow slip events along the Nankai Trough detected by GNSS-A. *Science Advances* 6, eaay5786. doi:10.1126/sciadv.aay5786

Yokota, Y., Ishikawa, T., and Watanabe, S. (2019). Gradient field of undersea sound speed structure extracted from the GNSS-A oceanography. *Mar. Geophys. Res.* 40 (4), 493–504. doi:10.1007/s11001-018-9362-7

Yokota, Y., Ishikawa, T., Watanabe, S., Tashiro, T., and Asada, A. (2016a). Seafloor geodetic constraints on interplate coupling of the Nankai Trough megathrust zone. *Nature* 534, 374–377. doi:10.1038/nature17632

Yokota, Y., Tashiro, T., Ishikawa, T., and Watanabe, S. (2016b). Development of numerical simulator for seafloor geodetic observation system [in Japanese]. *Rep. Hydrogr. Oceanogr. Researches* 53, 90–97.

Zhao, J., Zou, Y., Zhang, H., Wu, Y., and Fang, S. (2016). A new method for absolute datum transfer in seafloor control network measurement. *J. Mar. Sci. Technol.* 21, 216–226. doi:10.1007/s00773-015-0344-z

Conflict of Interest: The authors declare that the research was conducted in the absence of any commercial or financial relationships that could be construed as a potential conflict of interest.

frontiers in Earth Science

BRIEF RESEARCH REPORT
published: 11 March 2021
doi: 10.3389/feart.2021.600946

GNSS-Acoustic Observations of Seafloor Crustal Deformation Using a Wave Glider

Takeshi Iinuma[1], Motoyuki Kido[2,3], Yusaku Ohta[3], Tatsuya Fukuda[4], Fumiaki Tomita[1] and Iwao Ueki[5]*

[1]Research Institute for Marine Geodynamics, Japan Agency for Marine-Earth Science and Technology (JAMSTEC), Yokohama, Japan, [2]International Research Institute of Disaster Science, Tohoku University, Sendai, Japan, [3]Graduate School of Science, Tohoku University, Sendai, Japan, [4]Institute for Marine-Earth Exploration and Engineering, Japan Agency for Marine-Earth Science and Technology (JAMSTEC), Yokosuka, Japan, [5]Research Institute for Global Change, Japan Agency for Marine-Earth Science and Technology (JAMSTEC), Yokosuka, Japan

Crustal deformation of the seafloor is difficult to observe solely using global navigation satellite system (GNSS). The GNSS-acoustic (GNSS-A) technique was developed to observe seafloor crustal deformation, and it has produced a steady series of successful observations with remarkable results related to crustal deformation associated with huge earthquakes around the Japanese Islands. However, utilizing GNSS-A incurs very large financial and human costs as it requires the use of a research vessel as a surface platform and has a limited observation frequency, which is less than once a year at seafloor stations along the Japan Trench. To conduct frequent observations, an automatic GNSS-A data acquisition system was developed that operates via an unmanned surface vehicle (wave glider). The first observations using this system were performed at a seafloor station off Aomori Prefecture in July 2019. The wave glider was equipped with two GNSS antennas, an acoustic transducer, a microelectromechanical system gyroscope, and associated control and logging units. Data acquisition and autonomous activation of the seafloor stations were successfully executed by controlling the power supply to the payload via satellite communication with the wave glider. The glider rarely strayed off the configured course and the solar panels generated sufficient power to perform the observations although the weather was mostly cloudy. The GNSS-A data processing results show that the position of the station was determined with the same accuracy and precision as in previous observations performed using a research vessel.

Keywords: seafloor crustal deformation, GNSS-acoustic technique, wave glider, unmanned surface vehicle, 2011 tohoku-oki earthquake, Japan trench

OPEN ACCESS

Edited by:
Keiichi Tadokoro,
Nagoya University, Japan

Reviewed by:
Yusuke Yokota,
The University of Tokyo, Japan
Ryoya Ikuta,
Shizuoka University, Japan

****Correspondence:***
Takeshi Iinuma
iinuma@jamstec.go.jp

Specialty section:
This article was submitted to Solid Earth Geophysics, a section of the journal Frontiers in Earth Science

Received: *31 August 2020*
Accepted: *02 February 2021*
Published: *11 March 2021*

Citation:
Iinuma T, Kido M, Ohta Y, Fukuda T, Tomita F and Ueki I (2021) GNSS-Acoustic Observations of Seafloor Crustal Deformation Using a Wave Glider. Front. Earth Sci. 9:600946. doi: 10.3389/feart.2021.600946

INTRODUCTION

While terrestrial crustal deformation has been monitored using global navigation satellite system (GNSS) observations since the 1990s, crustal deformation of submarine offshore regions is difficult to detect using satellite geodetic methods as the electromagnetic waves cannot penetrate the deep ocean to reach the seafloor. The GNSS-acoustic (GNSS-A) technique was developed to overcome this difficulty in observing seafloor crustal deformation (Spiess, 1985; Spiess et al., 1998; Asada and Yabuki, 2001; Fujita et al., 2006). Recent results related to crustal deformation associated with huge

earthquakes around the Japanese Islands have shown the usefulness of the GNSS-A technique (e.g., Kido et al., 2011; Sato et al., 2011; Sun et al., 2014; Watanabe et al., 2014; Yokota et al., 2016).

Conventional GNSS-A requires large financial and human costs because a research vessel that functions as a surface platform is exclusively necessary. Therefore, increasing the observation frequency at the seafloor stations along the Japan Trench is quite difficult. Tohoku University installed 20 seafloor GNSS-A stations in 2012 following the 2011 Tohoku-oki earthquake to detect post-seismic deformation due to the earthquake (Kido et al., 2015). However, repeated observations at all stations have not been conducted frequently (i.e., less than once a year), especially after 2017 due to financial difficulties as usage of a research vessel costs several tens of thousands of dollars per day (cf. Tomita et al., 2017).

Another issue associated with using a research vessel is the accessibility to the hull-mounted acoustic transducer. A hull-mounted system enables us to perform the GNSS-A observations along ideal well-balanced track lines and increases observation frequency (Ishikawa et al., 2020). However, once the hull-mounted transducer fails, it cannot be repaired until the vessel is dry-docked. Easier maintenance access is desirable for continuous observations over an extended period (years to decades).

To conduct frequent observations and ensure easy maintenance, we have developed an automatic GNSS-A data acquisition system using a wave glider (WG), which is an unmanned surface vehicle. As Chadwell et al. (2016) demonstrated, the WG has the capability for GNSS-A observations. The WG can navigate from station to station on autopilot without an external power supply or fuel consumption. The solar panels on the WG generate sufficient power to change course, manage satellite communications, and perform the GNSS-A observations. The deployment and recovery operations are also easy such that we can handle the WG from small vessels as long as they are equipped with a derrick or crane capable of lifting the WG whose weight and length are about 250 kg and 3 m, respectively.

Herein, we report on the developed GNSS-A system installed in the WG, initial sea trial conducted in July 2019, and results of data processing from the trial deployment of the WG. We also present planned future work regarding the development of the system.

METHODS

Automatic GNSS-A Data Acquisition System

In the automatic GNSS-A data acquisition system, the WG transits to a seafloor station, initiates the GNSS-A observation, and remains at the station for several hours (up to ~20 h) to record the GNSS-A observation data. These actions should be performed automatically and as autonomously as possible. It is also desirable that the WG remains offshore and continues recording observations for as long as possible. Thus, the required functions of the system are as follows:

(1) Autonomous transit according to a pre-configured course or target waypoints while avoiding other ships
(2) Automatic control of the GNSS-A system, consisting of the GNSS receiver, acoustic unit, and microelectromechanical system (MEMS) gyroscope
(3) Power generation using the solar panels and internal batteries, whose capacity is sufficient to carry out the cruise and observations
(4) Satellite communication for configuring the course or target waypoints and for monitoring power generation and the battery status

The SV3 WG (manufactured by Liquid Robotics, Inc., CA, United States) has the capability for functions 1 and 4. We then constructed a system that would accomplish function 2 and considered power needs (function 3). Note that the observation includes waking-up the seafloor transponders, transmitting the acoustic ranging signals, receiving/recording the replies from the transponders, and storing GNSS and gyroscope data.

Figure 1A shows the block diagram of the GNSS-A data acquisition system developed for this study. It consists of two GNSS antennas, a GNSS receiver, an acoustic transducer, an acoustic unit, an MEMS gyroscope, a controlling and recording single board computer (SBC), a wired/wireless router, band filters to filter out Iridium satellite signals, and power supply units (a DC/DC converter, a supercapacitor, and a charge–discharge relay board to the supercapacitor). The supercapacitor is necessary to supply the acoustic unit with instantaneous high current to transmit a wake-up signal to the seafloor transponder. The GNSS antennas and the acoustic transducer are mounted on the float, while the other instruments are installed inside a waterproof container (**Figures 1B,C**). The router has a wireless port that allows for access after the waterproof container is sealed. We can modify the controlling script installed in the SBC, configure the GNSS receiver setting, and check the recording status of acoustic ranging and gyroscope data via the wireless port on the deck before deployment.

The power supply to the payload can be remotely turned on and off (i.e., the S1 and S3 ports on the WG (**Figure 1A**) from land via communication from an Iridium satellite. The power supply for the acoustic unit is started when the S3 port is turned on. Once the S1 port is turned on, the GNSS receiver and the gyroscope are activated, and the SBC is booted up. The GNSS receiver itself records the raw data. The startup script in the SBC checks the current geographic location through the GNSS output. If the location is found sufficiently close to a certain GNSS-A observation site, it starts recording GNSS National Marine Electronics Association (NMEA) 0183 sentence output and raw gyroscope data, as well as starts sending a sequence of acoustic commands of wake-up and delay setting to the corresponding seafloor transponders at the site. After confirming that all the transponders have woken-up based on their reply messages, the acoustic ranging session is initiated. The

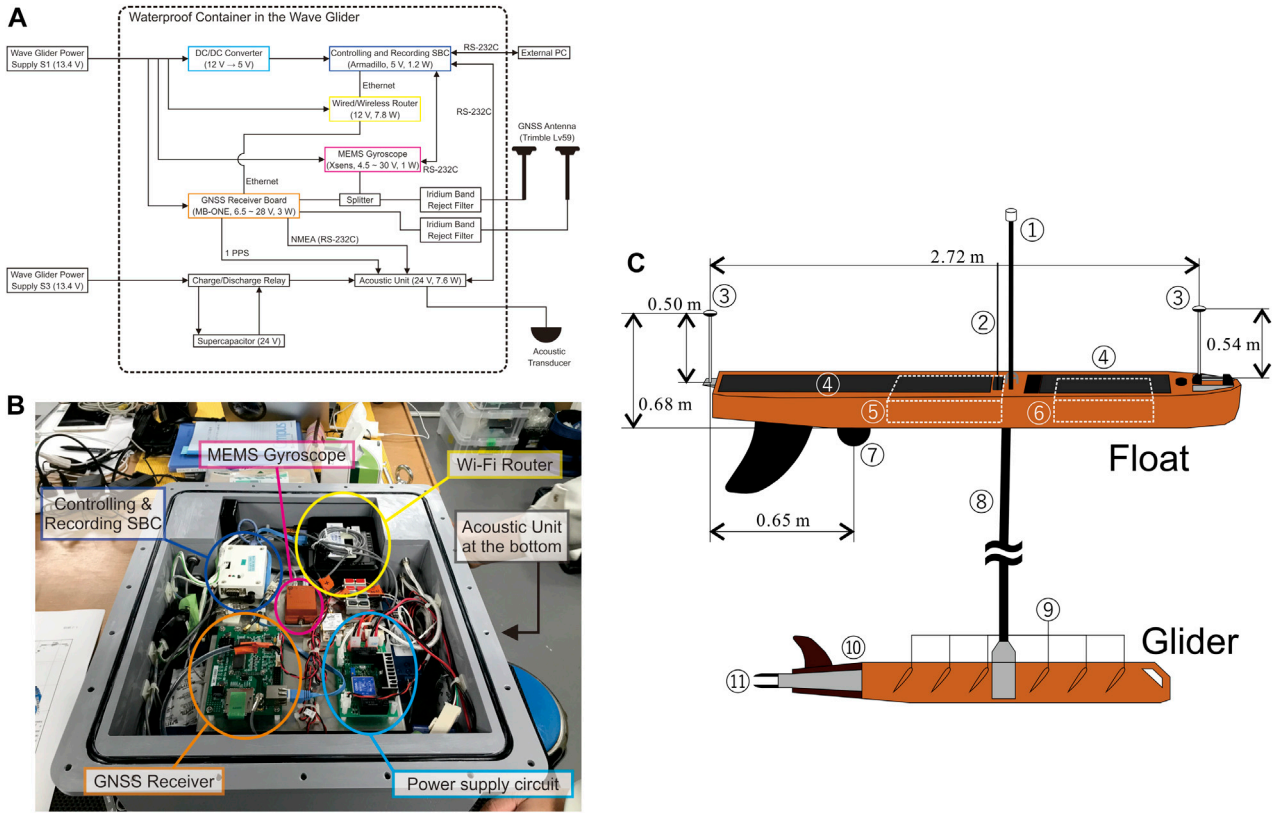

FIGURE 1 | (A) Block diagram of the GNSS-A data acquisition system. Items within a rounded rectangle with dashed line are installed inside a water-proof container as shown in **(B)**. PPS and NMEA are pulse per second and NMEA (National Marine Electronics Association) 0183 sentences, respectively. **(B)** The waterproof container prior to sealing. Its internal dimensions are 342 mm (width) × 380 mm (length) × 174 mm (maximum depth). **(C)** Schematic diagram of the WG. ① to ⑪ indicate the parts and equipment as follows: ①: weather sensor, ②: AIS antenna, ③: GNSS antennas, ④: solar panels, ⑤: command and controlling unit and batteries inside the float, ⑥: water-proof container shown in **Figure 1B** inside the float, ⑦: acoustic transducer, ⑧: umbilical cable (~8 m), ⑨: wings, ⑩: rudder, and ⑪: thruster.

acoustic ranging signal is transmitted every minute, and the replies from the seafloor transponders are recorded by the acoustic unit. When the WG leaves the site at a threshold distance, acoustic ranging and data recording of GNSS NMEA and gyroscope are automatically stopped, and the SBC halts and is ready to turn off the S1 port. In this experiment, data processing to estimate the position of the site, which is defined as the center of the array of seafloor transponders, is performed after the cruise ends. However, it can be estimated onboard in semi-real time and the position of the site can be transmitted to shore via satellite communication. Effecting such semi-real time observations is the next step in the development of this system.

Trial Observations at Sea and Data Processing

We conducted GNSS-A observations at a seafloor station off the coast of Aomori Prefecture in July 2019 during a survey cruise (KS-19-12) using the research vessel *Shinsei-maru* (Joint Usage/Research Center for Atmosphere and Ocean Science and Japan Agency for Marine-Earth Science and Technology, 2019). **Figure 2** shows the tracks of the *Shinsei-maru* and the WG throughout the cruise. **Table 1** shows the extracted time schedule with respect to the GNSS-A observations made by the WG during the survey cruise. *Shinsei-maru* deployed the WG at site G02 on July 4. After conducting the GNSS-A observation by means of its own system parallel with the WG for about 3 h, *Shinsei-maru* moved toward northeast to install observation instruments at other sites. On July 7, it returned to the retrieval point ER4 to recover the WG. Note that the activation of the seafloor transponders at site G02 was performed using the GNSS-A observation equipment mounted on the *Shinsei-maru* before the deployment of the WG, and the GNSS-A observation by *Shinsei-maru* was suspended and resumed at 23:36 on July 3 and 00:05 on July 4 in order to confirm that the WG was transducing the acoustic ranging signal as shown in **Table 1**.

The items tested during the trial observations were as follows:

(1) Data acquisition from the sensors, namely, the GNSS carrier phase, attitude of the float (heading, roll, and pitch), and acoustic waveforms from the transponders
(2) Autonomous activation of the seafloor transponders by turning the power supply to the payload on or off from shore via satellite communication
(3) Autonomous transit between the sites and tracing a pre-configured course at each site

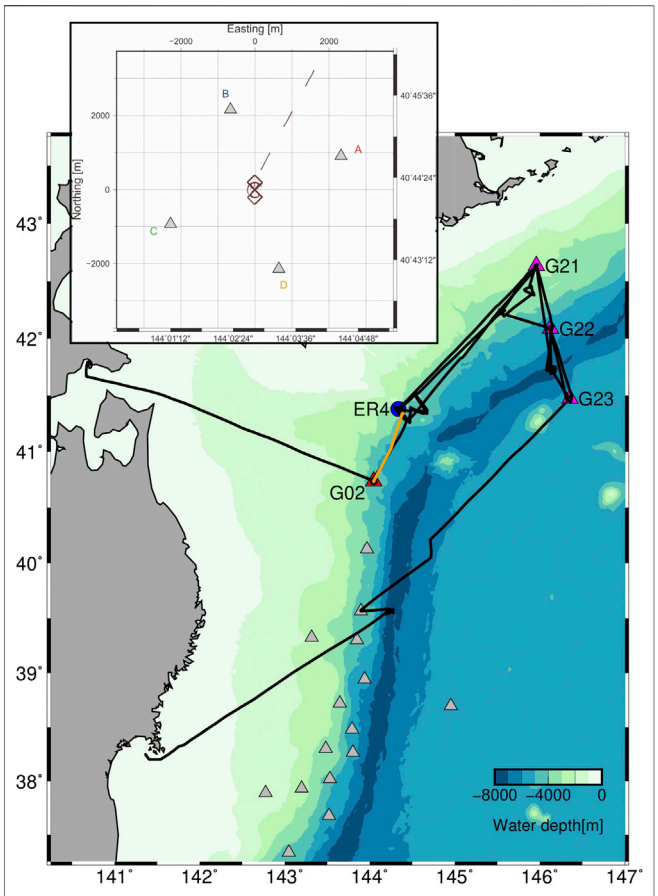

FIGURE 2 | Cruise tracks of the research vessel *Shinsei-maru* (black line) and the WG (orange line) during survey cruise KS-19-12 (Joint Usage/Research Center for Atmosphere and Ocean Science and Japan Agency for Marine-Earth Science and Technology, 2019). A red triangle and a blue circle point the sites G02 and ER4, respectively. Gray and magenta triangles indicate the seafloor sites that were installed in 2012 and during this cruise, respectively. The inset shows the track of the WG at site G02 with the locations of the seafloor acoustic transponders.

To examine these items, in the initial plan, the WG was deployed at a site (G02), performed GNSS-A observations with tracing a figure-eight course that was centered at the center of the array of seafloor transponders (**Figure 2**), and then was ordered to transit to another site (G03), which is located just south of site G02 (item 3), and GNSS-A observations were initiated at site G03 (item 2). However, as the weather forecast stated that the state of the sea will become worse from the south, we altered the recovering point of the WG (G03) to site ER4, where a long-term ocean bottom seismograph was installed during the same survey cruise. Therefore, item 2 was examined at site G02 by suspending GNSS-A observations for a period of time. One hour after the final acoustic shot is received, the seafloor transponders go into a "sleep mode." Thus, we suspended and resumed the GNSS-A observations at 08:17 and 23:00 by turning off and on the S1 port, respectively, to test whether the autonomous activation of the seafloor transponders was successful. We could ascertain whether the data acquisition was successful (item 1) only after we recovered the WG on deck.

After the recovery of the WG, we analyzed the collected GNSS-A data by applying the method devised by Kido et al. (2006). We estimated the translational horizontal displacements of the seafloor transponder array relative to the pre-defined position and net sound velocity change for each shot by combining the absolute position of the surface transducer and its distances to the seafloor transponders under the condition of a stratified sound velocity structure. The pre-defined array geometry and its position were estimated by Honsho et al. (2019) in the past using vessel-based moving observations. The positions of the surface transducer at timings of transmission and reception in a global coordinate system are derived based on the position of GNSS antenna and the WG's attitude. The GNSS NMEA and MEMS gyroscope data provide information about the attitude of the WG, which is defined by the heading, pitch, and roll angles. The heading angle was estimated based on the dual antenna GNSS, while the pitch and roll angles were observed directly by the MEMS gyroscope. The relative position between the GNSS antenna and surface transducer in the body-fixed frame is also regarded as an unknown that can be solved by minimizing travel time residuals throughout the campaign. Once the relative position is solved, we can finally estimate the position of the array and temporal change in the average sound velocity for each acoustic shot to evaluate the temporal stability of the estimated array positions.

RESULTS

Data Acquisition and Power Management

The data acquisition from the sensors performed well at site G02. **Figure 3A** shows the time series of the pseudo ranges between the acoustic transducer mounted on the WG and the seafloor acoustic transponders. Note that the pseudo ranges include apparent distances due to artificial response delays of seafloor transponders. Owing to a bug in the controlling script of the acoustic unit, the wake-up sequence, in which the acoustic commands to wake-up the seafloor transponder and configure the artificial delay were sent for each transponder, and an acoustic ranging session that was composed of 20 acoustic signal transmissions at the rate of 1 shot/min were repeated. The wake-up sequence and acoustic ranging session took ~35 min and 20 min, respectively. Therefore, the acoustic ranging data is discontinuous. Although the total amount of the acoustic ranging data was reduced by this script error, the acquired data are sufficient to estimate the position of the seafloor transponder array. The wake-up sequence succeeded in activating the seafloor stations when the power supply to the payload was turned on from the shore via satellite communication after the observations were suspended. This proved that the WG can autonomously perform observations from a site on another site.

The solar panels generated sufficient power to perform the GNSS-A observations although the weather was mostly cloudy during the deployment. **Figure 3B** shows the time series of the battery power. During the periods when GNSS-A observations were performed, the total operation consumed approximately 24 Wh per hour at night. However, the total consumption rate was almost balanced or was exceeded by the power generation rate during the day.

TABLE 1 | Itinerary of the research vessel *Shinsei-maru* and the WG during survey cruise KS-19-12.

Time (in UTC)	*Shinsei-maru*		Wave glider	
	Location	Event	Location	Event
July 3, 05:00	Hakodate	Departure	On the deck	
July 3, 19:50	G02	Arriving at G02 Activation of the seafloor stations and starting GNSS-A observation	On the deck	
July 3, 23:36	G02	Suspension of GNSS-A observation	On the deck	Preparation for the deployment
July 3, 23:50	G02	Deployment of the WG	G02	Starting GNSS-A observation
July 4, 00:02	G02	Confirming that the WG was transducing the acoustic ranging signal	G02	GNSS-A observation
July 4, 00:05	G02	Resumption of GNSS-A observation	G02	GNSS-A observation
July 4, 02:43	G02	Stopping GNSS-A observation	G02	GNSS-A observation
July 4, 03:00	G02	Leaving G02	G02	GNSS-A observation
July 5, 08:17			G02	Suspension of the observation Seafloor stations went into "sleep mode" after 1 h
July 5, 23:00			G02	Resumption of the observation Activation of the seafloor stations was automatically executed
July 6, 04:32			G02	The WG left G02
July 7, 03:19			On the way G02 to ER4	Starting the usage of the auxiliary thruster
July 7, 16:00			ER4	The WG arrived at the retrieval point ER4
July 7, 19:20	ER4	Arrival at the retrieval point ER4	ER4	
July 7, 19:40	ER4	Discovery of the WG	ER4	
July 7, 23:00	ER4	Retrieval operation began	ER4	
July 7, 23:58	ER4	Retrieval operation completed	On the deck	

Results of the GNSS-A Data Processing

The GNSS data were processed by IT (interferometric translocation) software (Colombo et al., 2000). The quality of the GNSS data has no significant problem considering the temporal stability of the vertical positions which was evaluated using the technique provided by Fujita and Yabuki (2003).

An example of the recorded acoustic raw waveform and the time series of cross-correlation between the transmitted and received signals is shown in **Figure 3C**. The raw waveform shows that the background noise is high, and the signal-to-noize ratio is low, while the cross-correlation time series exhibits clear correlation peaks that correspond to the arrival of reply signals from the four seafloor transponders. The correlation waveforms are similar to those obtained using a research vessel (e.g., Azuma et al., 2016), and the differences in the correlation waveforms of individual seafloor transponders are not significant. Thus, the quality of the acoustic data is equivalent to that obtained using a research vessel. We obtained the travel time of the acoustic wave between the acoustic transducer mounted on the WG and the seafloor transponders by applying the detection method devised by Azuma et al. (2016) to the cross-correlation time series for the estimation of the position of the seafloor transponder array. Note that an ingenious method to obtain the travel time is necessary because the correlation peak sometimes does not correspond with the direct arrival of the reply signal from the seafloor transponder in the correlation waveform (Azuma et al., 2016).

Figure 3D shows the position of the center of the array estimated for each acoustic shot. The scatter in the WG-derived positions (red points) is not larger than the positions estimated from observations made using a research vessel (blue points). The precision of the estimated position of the center of the array for this campaign is less than 10 cm; that is, the standard deviations of the scatter for each acoustic shot are 7.0 cm and 6.1 cm for both N–S and E–W components, respectively.

To estimate the seafloor displacement rate with high precision, both precision and accuracy (i.e., repeatability between observation campaigns) are required. **Figure 3E** shows the time series of the average array position of site G02. The array position estimated from the WG data is consistent with past observations. This indicates that negligible systematic bias is included in the estimated position. Therefore, we can directly compare the results from the WG data with past observations that were performed using research vessels and expect to estimate displacement rates as large as the plate convergence rate (i.e., ~8 cm/year) along the Japan Trench with the observations at least once a year for a couple of years. For instance, we can estimate the displacement rate with the estimation error of less than 5 cm/year based on three observations with the observation error at 7.0 cm during 3 years at even intervals.

DISCUSSION

The WG GNSS-A observation system worked well during the first trial cruise. The tested items performed satisfactorily encouraging us to proceed to the next step of undertaking a long observation cruise and real-time data processing.

As there are more than 20 GNSS-A sites located along the Japan Trench, a cruise of more than one month will be required to

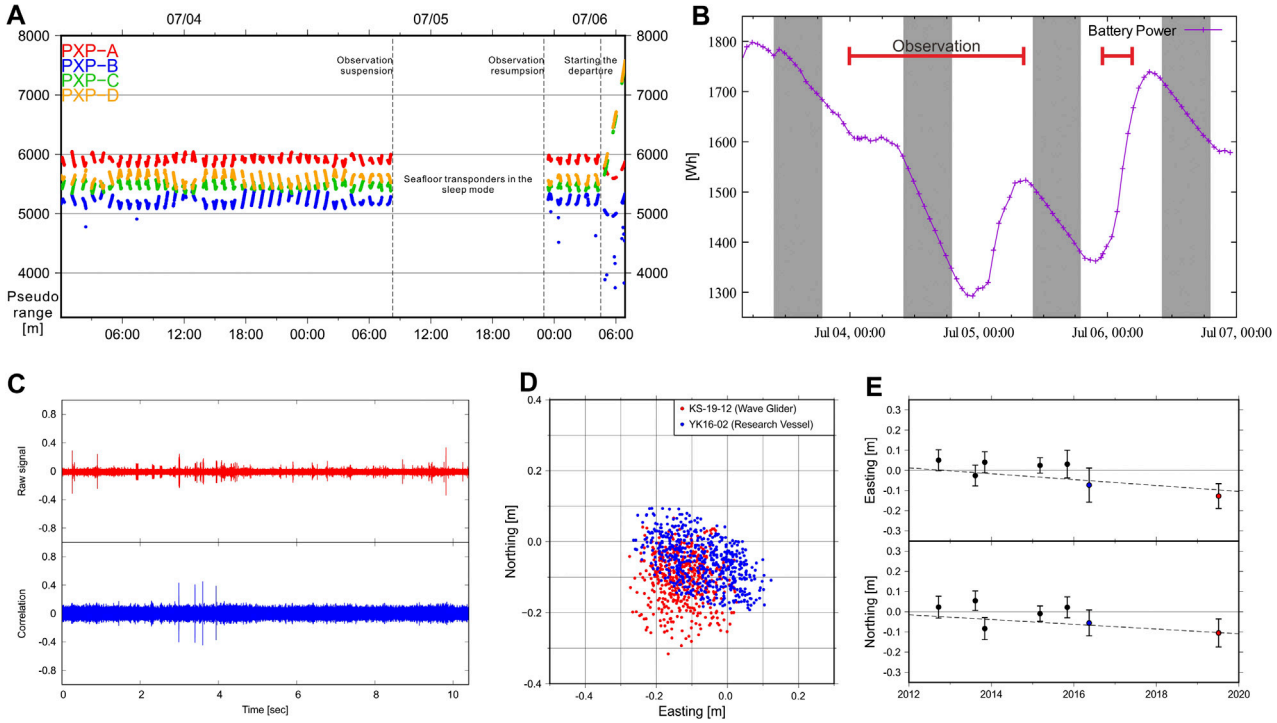

FIGURE 3 | (A) Time series of the slant ranges between the acoustic transducer mounted on the WG and the seafloor acoustic transponders (PXPs). Red, blue, green, and orange dots correspond to the pseudo ranges (in m) with respect to transponder A (northeast), B (northwest), C (southwest), and D (southeast), respectively (see the inset of **Figure 2**). The horizontal axis is the time in UTC. **(B)** Time series of the battery power. Gray areas correspond to nighttime. Red bars indicate the periods when the GNSS-A observations were performed. The horizontal axis is the time in UTC. **(C)** An example of the raw acoustic waveform (upper panel) and the correlation waveform between the transmitted code and the recorded signal (lower panel) The horizontal axis shows time of the whole recording duration of up to 10 s for a single shot. The vertical axes are normalized pressure level for the upper panel and correlation coefficient for the lower panel. **(D)** The position of the center of the array estimated for each acoustic shot. Red and blue dots indicate the positions based on the data obtained by the WG and the research vessel *Yokosuka* in 2016 (Tomita et al., 2017). **(E)** Time series of the average array center positions of site G02 estimated by utilizing the method of Kido et al. (2006). The upper and lower panels correspond to the E–W and N–S components, respectively. The dashed lines correspond to the displacement rate estimated from the array center position data obtained before 2017 (Honsho, et al., 2019).

visit all the sites and perform GNSS-A observations. One of the next steps is to conduct an observation cruise that is longer than a month. The stability, robustness, and reliability of the entire system during this month-long cruise will be tested. It will enable us to detect not only secular and transient seafloor crustal deformation.

Recently, Uchida et al. (2016) revealed the periodic changes in interplate locking along the northeastern Japan subduction zone based on the activity of small repeating earthquakes and terrestrial crustal deformation data. They found that slow slip along the plate interface has occurred repeatedly at intervals of 2–6 years depending on the location. In the northern part of the Japan Trench, a tsunami-generating earthquake occurred and ruptured the shallow plate boundary in 1896; however, it is not known whether the coseismic slip fully released the interseismic slip deficit, and whether periodic slow slip events occur near the trench or not. To investigate the interplate locking state in this region, more frequent GNSS-A observations are essential. Such repeated observations could be carried out by a WG system.

Furthermore, the development of the WG GNSS-A system is to perform real-time data processing. If we can estimate the position of the transponder array for each seafloor site in real time, and if the WG transmits the positioning results to shore via satellite communications, the WG can remain offshore depending on our preference. The WG system will enable us to perform more frequent GNSS-A observations and monitor the interplate locking state in real time. Moreover, flexible operations will be possible such that we can arrange the observation schedule depending on the results of the real-time data processing. Although the real-time GNSS-A positioning has been investigated using a moored buoy (e.g., Kido et al., 2018), further improvements of the processing system are required. One of the obstacles in performing real-time positioning is the detection of accurate travel time for acoustic ranging. Detection of accurate travel time presupposes post-processing as the highest correlation peak is not always the true arrival time (e.g., Azuma et al., 2016). Therefore, automating this procedure is required for real-time processing.

Some limitations are observed in utilizing the WG for collecting GNSS-A observations. The most significant issue is the speed of the WG. Using the WG in areas where ocean currents are strong may be difficult. The effect of the heterogeneity of the acoustic velocity structure in the sea water is difficult to eliminate owing to the slow

speed of the WG. We generally assume that the velocity structure is laterally stratified when analyzing the GNSS-A data. However, if a horizontal gradient in the acoustic velocity structure exists, the position of an acoustic transponder on the slower (faster) side of the gradient is mis-determined as a farther (closer) position (Tomita et al., 2019). As a result, a horizontal gradient in acoustic velocity structure adds critical systematic biases to the estimates (i.e., horizontal positions) of the GNSS-A measurements. Recent studies have successfully eliminated the influence of a long-term (over 12 h) horizontal gradient in acoustic velocity structure by simultaneously solving the gradients and positions (Yasuda et al., 2017; Honsho et al., 2019; Yokota et al., 2019). Note that these methods are applicable only when one set of moving survey (e.g., a single circling) can be completed within a time much shorter than the duration of the gradient structure. The WG with a typical speed of 1–1.5 knot takes 5–7 h to complete a square course around four transponders, whose sides are 1.8 nautical miles each at G02 site (**Figure 2**). This speed is not sufficient to stably solve the gradient. Therefore, while we examine the practical limits of the moving survey using the WG along the Japan Trench for solving the gradient, depending on ocean conditions and the purpose of the observations, a research vessel that has a hull-mounted system and the WG should be used.

DATA AVAILABILITY STATEMENT

The raw data supporting the conclusions of this article will be made available by the authors, without undue reservation.

AUTHOR CONTRIBUTIONS

TI directed the project and wrote this manuscript; MK developed the system to control the acoustic unit and to perform data acquisition from the sensors; YO directed the survey cruise (KS-19-12) and oversaw the GNSS observations; TF designed and produced the circuits, container, and jigs to mount all of the equipment on the WG; FT participated in the survey cruise to collect data and analyzed the data to estimate the station positions; IU managed the usage of the WG.

FUNDING

A part of this study and the submission of the manuscript were supported by JSPS KAKENHI Grant Number JP19H05596. The development of the observation system and operation of the WG were supported by Japan Agency for Marine-Earth Science and Technology and Tohoku University.

ACKNOWLEDGMENTS

The figures were generated using Generic Mapping Tools software. The observation data were obtained using the Research Vessel *Shinsei-maru*, which was supported by the Collaborative Research Program of Atmosphere and Ocean Research Institute, University of Tokyo.

REFERENCES

Asada, A., and Yabuki, T. (2001). Centimeter-level positioning on the seafloor. *Proc. Jpn. Acad. Ser. B* 77, 7–12. doi:10.2183/pjab.77.7

Azuma, R., Tomita, F., Iinuma, T., Kido, M., and Hino, R. (2016). Development and examination of new algorithms of traveltime detection in GPS/acoustic geodetic data for precise and automated analysis. *Earth Planet. Space* 68, 143. doi:10.1186/s40623-016-0521-2

Chadwell, C. D., Webb, S., and Nooner, S. (2016). "Campaign-style GPS-Acoustic with wave gliders and permanent seafloor benchmarks," in Proceedings of the Subduction Zone Observatory Workshop, Boise Center, Boise, ID, (Sep 29–Oct 1, 2016).

Colombo, O. L., Evans, A. G., Vigo-Aguiar, M. I., Ferrandiz, J. M., and Benjamin, J. J. (2000). *Long-baseline (>1000 km), sub-decimeter kinematic positioning of buoys at sea, with potential application to deep sea studies*. Salt Lake City, Utah: ION GPS 2000 Meeting, 19–22 Sep.

Fujita, M., Ishikawa, T., Mochizuki, M., Sato, M., Toyama, S., Katayama, M., et al. (2006). GPS/Acoustic seafloor geodetic observation: method of data analysis and its application. *Earth Planet. Space* 58, 265–275. doi:10.1186/BF03351923

Fujita, M., and Yabuki, T. (2003). A way of accuracy estimation of K-GPS results in the seafloor geodetic measurement. *Tech. Bull. Hydrogr. Oceanogr.* 21, 62–66. (in Japanese).

Honsho, C., Kido, M., Tomita, F., and Uchida, N. (2019). Offshore postseismic deformation of the 2011 Tohoku earthquake revisited: application of an improved GPS-acoustic positioning method considering horizontal gradient of sound speed structure. *J. Geophys. Res. Solid Earth* 124, 5990–6009. doi:10.1029/2018JB017135

Ishikawa, T., Yokota, Y., Watanabe, S., and Nakamura, Y. (2020). History of on-board equipment improvement for GNSS-A observation with focus on observation frequency. *Front. Earth Sci.* 8, 150. doi:10.3389/feart.2020.00150

Joint Usage/Research Center for Atmosphere and Ocean Science and Japan Agency for Marine-Earth Science and Technology (2019). *Shinsei-maru KS-19-12 cruise data*. Yokosuka: JAMSTEC. doi:10.17596/0002041

Kido, M., Fujimoto, H., Hino, R., Ohta, Y., Oasda, Y., Iinuma, T., et al. (2015). "Progress in the project for development of GPS/acoustic technique over the last 4 years," in *International symposium on geodesy for earthquake and natural hazards (GENAH)*. Editor M. Hashimoto (Cham: Springer), 3–10. doi:10.1007/1345_2015_127

Kido, M., Fujimoto, H., Miura, S., Osada, Y., Tsuka, K., and Tabei, T. (2006). Seafloor displacement at Kumano-nada caused by the 2004 off Kii Peninsula earthquakes, detected through repeated GPS/Acoustic surveys. *Earth Planet. Space* 58, 911–915. doi:10.1186/BF03351996

Kido, M., Imano, M., Ohta, Y., Fukuda, T., Takahashi, N., Tsubone, S., et al. (2018). Onboard realtime processing of GPS-acoustic data for moored buoy-based observation. *J. Disaster Res.* 13 (3), 472–488. doi:10.1007/1345_2015_127

Kido, M., Osada, Y., Fujimoto, H., Hino, R., and Ito, Y. (2011). Trench-normal variation in observed seafloor displacements associated with the 2011 Tohoku-Oki earthquake. *Geophys. Res. Lett.* 38, L24303. doi:10.1029/2011GL050057

Sato, M., Ishikawa, T., Ujihara, N., Yoshida, S., Fujita, M., Mochizuki, M., et al. (2011). Displacement above the hypocenter of the 2011 tohoku-oki earthquake. *Science* 332, 1395. doi:10.1126/science.1207401

Spiess, F. N., Chadwell, C. D., Hildebrand, J. A., Young, L. E., Purcell, G. H., Jr., and Dragert, H. (1998). Precise GPS/Acoustic positioning of seafloor reference points for tectonic studies. *Phys. Earth Planet. Inter.* 108, 101–112. doi:10.1016/S0031-9201(98)00089-2

Spiess, F. N. (1985). Suboceanic geodetic measurements. *IEEE Trans. Geosci. Remote Sens. Ge-* 23, 502–510. doi:10.1109/TGRS.1985.289441

Sun, T., Wang, K., Iinuma, T., Hino, R., He, J., Fujimoto, H., et al. (2014). Prevalence of viscoelastic relaxation after the 2011 Tohoku-oki earthquake. *Nature* 514, 84–87. doi:10.1038/nature13778

Tomita, F., Kido, M., Ohta, Y., Iinuma, T., and Hino, R. (2017). Along-trench variation in seafloor displacements after the 2011 Tohoku earthquake. *Sci. Adv.* 3, e1700113. doi:10.1126/sciadv.1700113

Tomita, F., Kido, M., Honsho, C., and Matsui, R. (2019). Development of a kinematic GNSS-Acoustic positioning method based on a state-space model. *Earth Planet. Space* 71, 102. doi:10.1186/s40623-019-1082-y

Uchida, N., Iinuma, T., Nadeau, R. M., Bürgmann, R., and Hino, R. (2016). Periodic slow slip triggers megathrust zone earthquakes in northeastern Japan. *Science* 351, 488–492. doi:10.1126/science.aad3108

Watanabe, S., Sato, M., Fujita, M., Ishikawa, T., Yokota, Y., Ujihara, N., et al. (2014). Evidence of viscoelastic deformation following the 2011 Tohoku-Oki earthquake revealed from seafloor geodetic observation. *Geophys. Res. Lett.* 41, 5789–5796. doi:10.1002/2014GL061134

Yasuda, K., Tadokoro, K., Taniguchi, S., Kimura, H., and Matsuhiro, K. (2017). Interplate locking condition derived from seafloor geodetic observation in the shallowest subduction segment at the Central Nankai Trough. *Jpn. Geophys. Res. Lett.* 44, 3572–3579. doi:10.1002/2017GL072918

Yokota, Y., Ishikawa, T., Watanabe, S., Tashiro, T., and Asada, A. (2016). Seafloor geodetic constraints on interplate coupling of the Nankai Trough megathrust zone. *Nature* 534, 374–377. doi:10.1038/nature17632

Yokota, Y., Ishikawa, T., and Watanabe, S. (2019). Gradient field of undersea sound speed structure extracted from the GNSS-A oceanography. *Mar. Geophys. Res.* 40, 493–504. doi:10.1007/s11001-018-9362-7

Conflict of Interest: The authors declare that the research was conducted in the absence of any commercial or financial relationships that could be construed as a potential conflict of interest.

frontiers in Earth Science

TECHNOLOGY AND CODE
published: 16 March 2021
doi: 10.3389/feart.2021.608381

Deep-Sea DC Resistivity and Self-Potential Monitoring System for Environmental Evaluation With Hydrothermal Deposit Mining

Takafumi Kasaya[1]*, *Hisanori Iwamoto*[2] *and Yoshifumi Kawada*[1]

[1]*Submarine Resources Research Center, Research Institute for Marine Resources Utilization, Japan Agency for Marine–Earth Science and Technology, Yokosuka, Japan,* [2]*Nippon Marine Enterprises, Ltd., Yokosuka, Japan*

Environmental impact assessment has become an important issue for deep-sea resource mining. The International Seabed Authority has recently developed recommendations for guidelines on environmental assessment of resource mining effects. Several research and development groups have been organized to develop methods for environmental assessment of the seafloor and sub-seafloor under the "Zipangu in the Ocean program," a part of the Cross-ministerial Strategic Innovation Promotion Program managed by the Cabinet Office of the Japanese government. One attempt planned for long-term environment and sub-seafloor structure monitoring uses a cabled observatory system. To support this observatory plan, we began development of a system to monitor the sub-seafloor resistivity and self-potential reflecting the physicochemical properties of ore deposits and the existence of hydrothermal fluid. The system, which mainly comprises an electro-magnetometer and an electrical transmitter, detects spatio-temporal changes in subseafloor resistivity and in self-potential. Because of the project's policy changes, cabled observatory system development was canceled. Therefore, we tried to conduct an experimental observation using only a current transmitter and a voltmeter unit. Data obtained during three and a half months show only slight overall apparent resistivity variation: as small as 0.005 Ω-m peak-to-peak. The electrode pair closest to the hydrothermal mound shows exceptionally large electric field variation, with a semidiurnal period related to tidal variation. Results indicate difficulty of explaining electric field variation by seawater mass migration around the hydrothermal mound. One possibility is the streaming potential, i.e., fluid flow below the seafloor, in response to tides. However, we have not been able to perform rigorous quantitative analysis, and further investigation is required to examine whether this mechanism is effective. The system we have developed has proven to be capable of stable data acquisition, which will allow for long-term monitoring including industrial applications.

Keywords: DC resistivity, environmental impact assessment, long term monitoring, self-potential, streaming potential

OPEN ACCESS

Edited by:
Keiichi Tadokoro,
Nagoya University, Japan

Reviewed by:
Andre Revil,
Center National de la Recherche Scientifique (CNRS), France
Peter Kannberg,
University of California, San Diego, La Jolla, CA, United States

***Correspondence:**
Takafumi Kasaya
tkasa@jamstec.go.jp

Specialty section:
This article was submitted to Solid Earth Geophysics, a section of the journal Frontiers in Earth Science

Received: *20 September 2020*
Accepted: *02 February 2021*
Published: *16 March 2021*

Citation:
Kasaya T, Iwamoto H and Kawada Y (2021) Deep-Sea DC Resistivity and Self-Potential Monitoring System for Environmental Evaluation With Hydrothermal Deposit Mining. Front. Earth Sci. 9:608381. doi: 10.3389/feart.2021.608381

INTRODUCTION

Environmental impact assessment has persisted as an important issue for on-land and marine mining activities. Constructing normative rules for undersea mining was a main topic of the "Zipangu in the Ocean program" (Yamamoto, 2020), a part of the Strategic Innovation Promotion Program (SIP) managed by the Cabinet Office of the government of Japan. The program was launched to meet expectations of recent national requirements for marine natural resources in Japan, and to develop survey technology necessary to discover those resources. Recently, the International Seabed Authority (ISA) developed recommendations for guidelines on environment assessment to evaluate the effects of resource mining. The ISA recommendations suggest long-term observations of more than one year to assess physical characteristics of the seafloor and to elucidate the distribution and activity of benthos in the baseline surveys before and after mining. Under the ISA recommendations, pre-environmental surveys and post-exploration impact assessments were conducted by the Japan Oil, Gas and Metals National Corporation (JOGMEC) during hydrothermal metal deposit mining trials (METI, 2018).

Instruments are being developed for long-term monitoring. For example, the "Edokko" monitoring system was developed. The main observation device of this system is a high-resolution time-lapse camera system to record variations of surrounding ecosystem at deep sea bottom; many practical observations have been conducted (Miwa et al., 2016). The key feature of the "Edokko" is that it does not require a special vessel for deploy and recovery operations. Fukuba et al. (2018) developed another large lander system that can accommodate a video camera system, a turbidity sensor, a conductivity-and-temperature sensor, a dissolved oxygen sensor, a flow meter, and a heat-flow meter. However, these systems are insufficient to detect temporal and spatial alterations occurring below the seafloor associated with the mining of submarine ore deposits, which are often accompanied by active hydrothermal areas with subseafloor upward fluid flow.

Electric and electromagnetic methods, which are sensitive to changes in the subseafloor structure, probably show superior performance in detecting such variations. Kaieda et al. (2018) conducted self-potential (SP) and resistivity monitoring around shore area in Scotland to detect some changes with the controlled sub-seabed CO_2 release experiment for Carbon capture and storage (CCS). They observed clear anomalous changes of positive SP and electrical resistivity and concluded that CO_2 migration under the seabed caused these electrical variations. MacAllister et al. (2016) detected clear semidiurnal responses using SP monitoring in a borehole nearshore, and imply that their responses are driven by ocean tidal processes in the aquifer. Soueid Ahmed et al. (2016) considered the effectivity of SP data with harmonic pumping tests using 3D inversion technique. Results suggest that the electric and electromagnetic methods for monitoring are effective for changes in the subsurface structure and conditions. Therefore, we consider adoption of a monitoring instrument based on electric and electromagnetic methods to detect environmental changes in hydrothermal activities related to mining. In the marine environment, SP survey, as well as electrical and electromagnetic explorations, has been attracting attention for hydrothermal deposit exploration (Kawada and Kasaya, 2017; Safipour et al., 2017). Constable et al. (2018) and Kawada and Kasaya (2018) carried out SP surveys using autonomous undersea vehicles (AUVs) and successfully detected negative anomalies associated with hydrothermal deposits.

Kasaya et al. (2009) detected precursory electric potential changes associated with seismically generated turbidity flows by connecting electro-magnetometers and pressure gauges to cables laid off Hatsushima. Goto et al. (2007) connected an electro-magnetometer to an intelligent node (Asakawa et al., 2009) of a cabled observatory system off Toyohashi city. They attempted continuous resistivity monitoring by current transmission. As described herein, we review our electromagnetic observation system developed under the SIP project and discuss the results of long-term data acquired at a hydrothermal deposit area. The system mainly comprises an electro-magnetometer and an electrical transmitter, which detect changes in subseafloor resistivity and the SP both in time and space. The system currently works as a stand-alone system, but it was developed originally as a component of a cable-connected observatory for seafloor environment monitoring of the Japan Agency for Marine–Earth Science and Technology (JAMSTEC), which uses the technologies of a JAMSTEC cabled observatory system for seismic disaster prevention, called the DONET system (Kimura et al., 2013; Kawaguchi et al., 2015). Because of SIP project policy changes, the cabled observatory system development was canceled. Herein, before explaining the current system, we explain the original version of the system presumed for development. We also discuss the results of a field test conducted in the Izena hole in the middle Okinawa Trough, at which the existence of hydrothermal ore deposits has been indicated by JOGMEC (METI, 2018). A deep sulfide layer was found at depths greater than 30 m below the seafloor by drilling operations conducted by D/V CHIKYU (Totsuka et al., 2019).

INSTRUMENTS

The backbone cable system which was to be built under the SIP project was based on an existing cable system constructed under the DONET project (Kawaguchi et al., 2015). Two junction boxes equipped with optical/electrical wet mate connectors were to be deployed at two locations on the seafloor. All observational instruments are connected to each junction box using electrical wet mate connectors. Our electromagnetic observation system, which was designed to detect changes in subsurface electrical/electromagnetic features associated with mining, would be connected to one of the junction boxes. To detect temporal and spatial changes in the subseafloor environment, both measurement of the electric field in multiple channels and transmission of the electric current

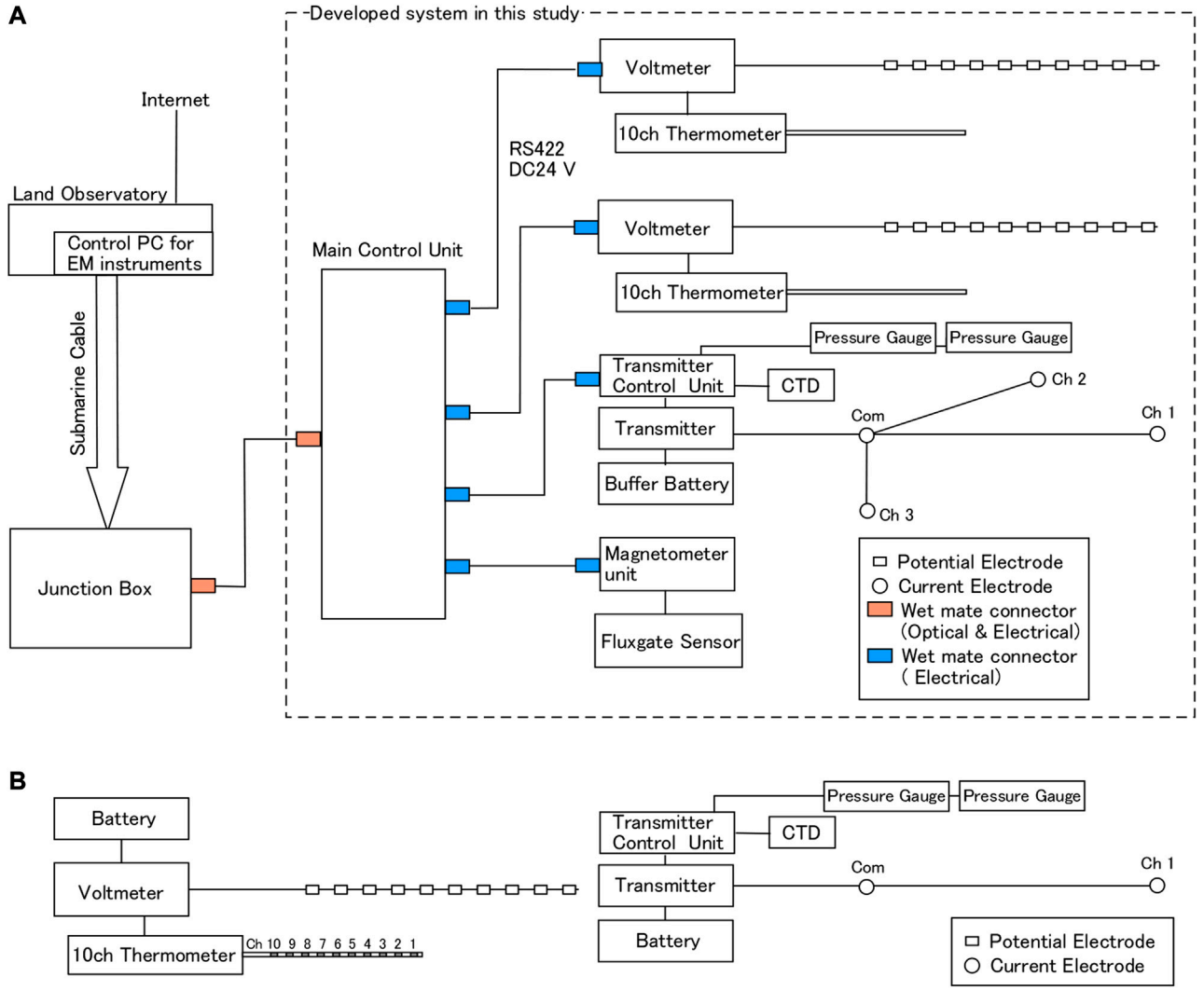

FIGURE 1 | (A) Original system configuration of the monitoring resistivity and self-potential (surrounded by the dashed square) planned for connection with the cabled observatory system. The main control unit connects to the junction box of the backbone cable system via an electrical/optical wet mate underwater connector. The main control unit has four electrical wet mate connectors to communicate with observation units. **(B)** Modified system configuration for a stand-alone experimental observation.

source are necessary. Consequently, our system has a main control unit, which governs individual observation units, and which communicates with the land observatory through the backbone cable system (**Figure 1A**).

The main control unit, which has a CPU unit with an atomic clock and a power supply circuit, receives data from each observational unit. It then sends the data to the control computer in the land observatory through the junction box of the backbone cable system. The main control unit synchronizes with the land-based communication server using a standard network time protocol. It also synchronizes with each observation unit by serial communication using the RS-422 protocol, in which case the main unit functions as a time server. The main control unit can supply 24 V DC power to each observational unit, but the planned power supply from the junction box is limited to 250 W per external port. For that reason, all the instruments must have low power consumption.

The observation system used for investigation of electromagnetic field variations comprises four units (**Figure 1A**): two 10-channel voltmeters, a three-channel current transmitter, and a three-component magnetometer. Each unit has a CPU and an atomic clock, which work independently. The IGBT-controlled transmitter is based on the circuit of the towed electromagnetic survey system developed in Kasaya et al. (2018). Because the transmitter requires more electrical power than any other system component, a buffer battery was added to the transmitter unit to store electricity continuously. The voltmeter and the magnetometer are based on the relevant components of the

TABLE 1 | Specifications of observation instruments.

Receiver unit	
Voltmeter	
Channel number	10 channels
Sampling rate	20 Hz
A/D converter	24 bits
Dynamic range	±1 mV, ±2 mV, ±10 mV (selectable)
Communication port	RS-422
Thermometer	
Channel number	10 channels
Sampling rate	1 Hz (multiplexer)
A/D Converter	24 bits
Transmitter unit	
Transmitter	
Channel number	3 channels
Transmit control	IGBT
A/D Converter	24 bits
Communication port	RS-422
Maximum current	50 A
Buffer battery	Li-ion battery (56 cells)
CTD (Valeport mini CTD)	
Conductivity	
Range	0–80 mS/cm
Resolution	0.001 mS/cm
Accuracy	±0.01 mS/cm
Temperature	
Range	−5 to +35°C
Resolution	0.001°C
Accuracy	±0.01°C
Pressure	
Range	5, 10, 30, 50, 100, 300 or 600 bar
Resolution	0.001%
Accuracy	±0.05%
Pressure gauge (Valeport miniIPS)	
Type	Temperature compensated piezo-resistive
Range	5, 10, 30, 50, 100, 300 or 600 bar
Resolution	0.001%
Accuracy	±0.05%
Magnetometer unit	
Magnetometer type	Fluxgate (3 components)
Sampling rate	20 Hz
A/D Converter	24 bits
Dynamic range	±70,000 nT
Communication port	RS-422

OBEM system of Kasaya et al. (2009) with 20 Hz sampling and 24-bit A/D recording circuitry. The amplifier gain of the voltmeter can be chosen externally on three levels. The receiving electrode is an Ag-AgCl non-polarizing electrode. The transmitting electrode is a copper rod of 1 cm diameter and 30 cm length.

A 1-m-long ground thermometer equipped with 10 thermistors at a 10 cm interval was developed based on a stand-alone thermometer of Kinoshita et al. (2006). This thermometer was attached to each voltmeter unit to measure the subsurface temperature gradient with a 10 s sampling rate.

In addition, a conductivity–temperature–depth (CTD) meter is attached to the transmitter unit for environmental observation. Two pressure gauges were motivated to take differential pressure measurements below the seafloor. The CTD and pressure meters take observations only when the electric current is transmitted. **Table 1** presents specifications of the respective instruments.

INSTALLATION AND RECOVERY OPERATION

We conducted experimental observation using the modified version of the developed system at the Izena hole (**Figure 2**), which is a known hydrothermal deposit area (METI, 2018). A hydrothermal mound called the Dragon Chimney site is in the northeastern part of the observation area (**Figure 2C**). Because of cancellation of the cabled observatory system, we modified the transmitter and the voltmeter (receiver) units for stand-alone operation (**Figure 1B**). For this observation, the current transmission occurs in only one component with an electrode pair equipped with a 30-m-long cable (**Figure 3A**). A potential electrode array is also a 30-m-long cable with 10 potential electrodes and a common electrode (**Figure 3A**). Each electrode array was bundled on the base frame of the corresponding unit for deployment (**Figure 3B** for the receiver unit).

The system installation operation was conducted in January 2018 using a remotely operated vehicle (ROV, HAKUYO 2000; Fukada Salvage and Marine Works Co. Ltd.). The receiver unit (**Figure 3B**) and the transmitter unit (**Figure 3C**) were deployed on the seafloor using a winch system. Operations were monitored by the ROV via HD cameras. After landing, we released each unit from the winch via acoustic release (**Figure 4**). These units were located eastward of the sulfide mound designated as the North site (**Figure 2C**). The potential electrode array was extended westward of the receiver unit, and the transmit electrode cable was extended eastward of the transmitter unit (**Figure 3A**). Both cables were in almost inline in the east-west direction. The distances between each unit was 90.5 m, and that between the westernmost source electrode and the easternmost potential electrode (ch. 1) was 97.5 m. After installation operation, we carried out the acoustic ranging using an ROV Homer (Type 7835, Sonardyne Inc.). The absolute error of the ROV Homer is as small as 0.1 m according to the catalog specifications. The ROV held its position and measured the distance using the ROV Homer. However, the error in the acoustic positioning of the ROV from the mother ship may be within 1 m, which determines the overall accuracy of the positioning.

Data acquisition started on January 17, 2018. The voltmeter (receiver) recorded data continuously with a 20 Hz sampling rate. Due to the limitation of the battery size, the transmitter sent two rectangular-wave sets every hour with a 20 Hz sampling rate, which consisted of a 2-s-long transmission of the positive current followed by a 2-s-long suspend and a 2-s-long transmission of the negative current. The CTD and the two pressure gauges also recorded the data at the time of signal transmission. The recovery operation was conducted on May 4, 2018 using JAMSTEC's R/V KAIMEI. Data were acquired perfectly from deployment until recovery.

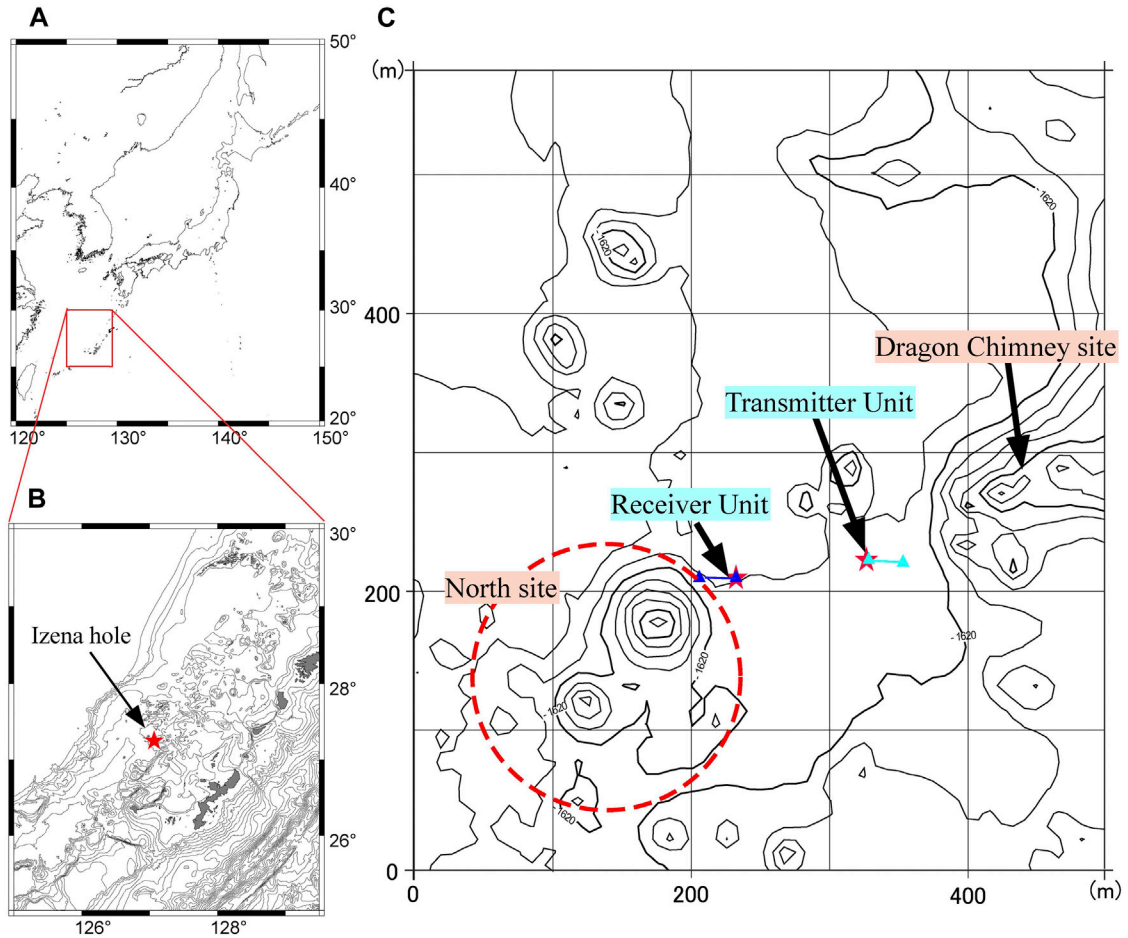

FIGURE 2 | Maps of the survey area: **(A)** regional map around Japan, **(B)** map of the mid-Okinawa Trough with the location of the Izena hole, and **(C)** map of the survey area in the Izena hole. Known hydrothermal mounds are marked. Locations of the receiver and transmitter units are marked by stars, with blue (for receiver) and light blue (for transmitter) triangles indicating the nearest and furthest electrodes of these units. The distance between each unit was 90.5 m, and that between the westernmost source electrode and the easternmost potential electrode (ch. 1) was 97.5 m.

OBSERVED SPATIO-TEMPORAL VARIATION OF ELECTRIC SIGNAL

The voltmeter measured the electric potential difference of each electrode relative to the common electrode. The offset value of each electrode relative to the common electrode was calculated using the 10-minute-long data during the period after landing the instrument and before the cable extension operation. For each electrode, the offset value is assumed to be time-independent and is subtracted from the raw data. **Figures 5A–D** present the time series of the electric field on April 30, 2018, obtained for four electrode pairs with an electrode span of 7–8 m. The electric field is calculable by any pair of potential electrodes being divided by the distance between the pair. Many spike-like waveforms are signals from the transmitter. The sweep-wave-like waveforms from 0:00 to 4:00 in **Figures 5A–D** are also signals from a transmitter loaded on an AUV during a different experimental geophysical survey using two AUVs (Kasaya et al., 2020). The variation of electric field calculated from the electrode pair closest to the mound (ch. 8 and 10) was exceptionally large. The period of this large variation was almost semidiurnal. Other pairs' data also show semidiurnal variation. **Figure 5E** is a further enlarged view of the waveforms, clearly depicting two pairs of positive and negative rectangular waves from the transmitter and signals from the AUV. Signals from the AUV change in the amplitude and polarity, reflecting that the AUV approaches close to the voltmeter within the time window of **Figure 5E**.

Figure 6A Presents the spatial distribution of electric potential relative to the common electrode, averaged over the entire observation period after the installation, with error bars. **Figures 6B–K** show the time series of the 1-h averaged electric potentials relative to the common electrode. The pattern of this spatial distribution is kept thought observation term, and the potential values of ch. 8 and ch. 10 are negative and positive, respectively (**Figures 6I,K**). Small fluctuations in these channels correspond to the temporal variations of the electric field shown in **Figure 5A**. The cause of the positive value of ch. 10 will be considered in the Discussion.

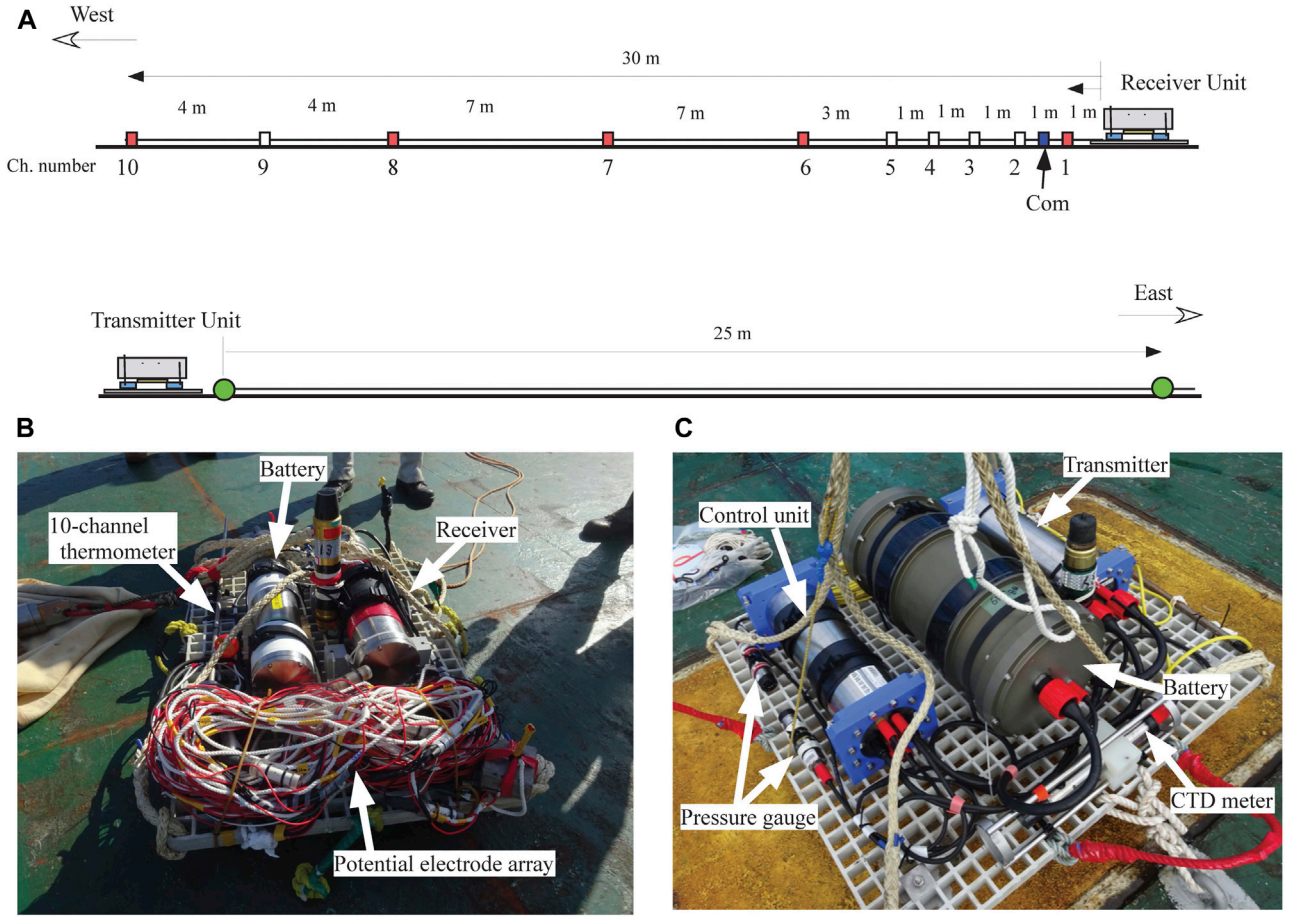

FIGURE 3 | (A) Electrode configuration of the receiver unit and the transmitter unit. Electrode cables have length of 30 m. **(B)** Photograph of the receiver unit. **(C)** Photograph of the transmitter unit.

RESISTIVITY DATA

To estimate the apparent resistivity, we first split the time series data into every two transmission cycles (16-s-long). For each set of divided data, we remove a long period trend, stack two transmission cycles, and cut 0.15 s before and after the rectangular wave to remove chargeability effects. Then, we calculated V/I for each electrode pair from the measured potential difference and the recorded electric current via linear approximation between the voltage and the current. Here, I is the source current amplitude (in A); V represents the received voltage (in V). The apparent resistivity was calculated using the geometry of the current transmitter electrodes and the receiver electrodes. These apparent resistivity estimations followed the procedure explained by Kasaya et al. (2020). The absolute values of apparent resistivity, however, have uncertainly because we were unable to carry out the resistivity calibration using data acquired in the middle sea layer.

Figures 7A–D show the relative variations for the calculated daily mean apparent resistivity with error bars for the same four electrode pairs as those presented in **Figure 5**, minus the averaged value of the whole observation term. **Figures 7E–H** also show the calculated relative variations of 1 h mean apparent resistivities for April 30, 2018, which is the same data window as those used in **Figures 5A–D**. In all pairs in both time windows, the error bars are extremely small. The overall variation of the apparent resistivity is as small as 0.005 Ω-m peak-to-peak. The apparent resistivity shows temporal variations, but these are random among the electrodes. Therefore, these variations may contain information of local subsurface fluctuations near the electrodes.

OTHER SENSOR DATA

For the observation of environmental conditions, CTD and pressure meters were attached to the transmitter unit. A 10-channel ground thermometer was attached to the receiver unit. **Figures 8A–C** show time series of the ambient temperature and electrical conductivity measured using the CTD meter, with depth measured by the pressure gauges. The ambient temperature, measured at the transmitter location, was stable. The variations are only about 0.11°C throughout the observation

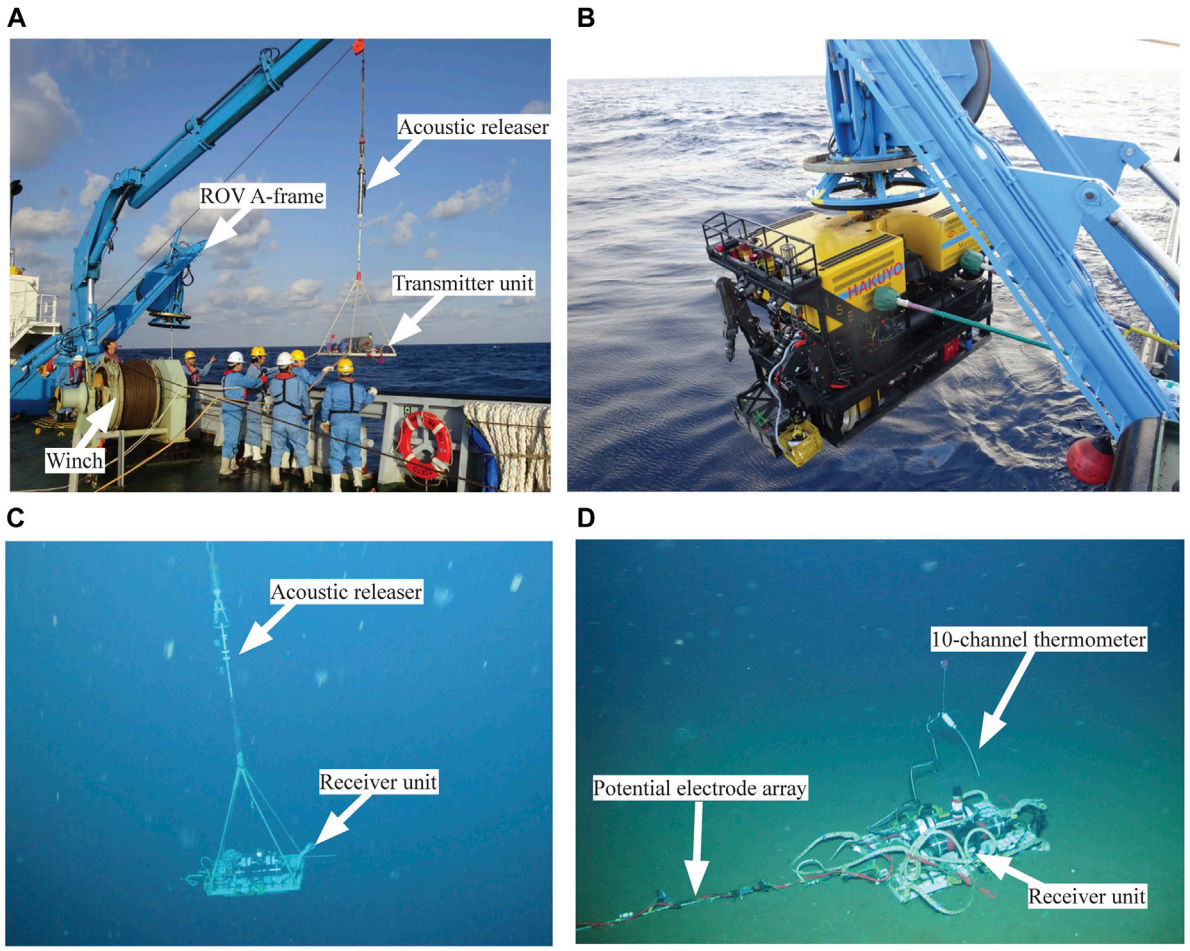

FIGURE 4 | (A) Photograph of the install operation. Each unit was deployed using a winch system. Before installation, the ROV dove and waited for the instrument near the deployment location. **(B)** Photograph of the ROV, HAKUYO 2000. **(C)** Receiver unit descending by a winch system. **(D)** Photograph of the installed receiver unit, the potential electrode array, and the 10-channel thermometer.

period (**Figure 8B**). The pressure time series, taken from one of the two pressure sensors, shows clear tidal variations of the 12 h period. No clear correlation was found between the ambient temperature/electrical conductivity and tidal variations throughout the observation period. **Figures 8D–F** show the enlarged time series during april 30, exhibiting very small changes (about 0.02°C). There is less clear correlation between the tidal variations and the ambient seawater temperature or electrical conductivity.

Figure 9 presents the time series of the 10-channel ground thermometer, which was deployed near the receiver unit and which complements the CTD meter deployed near the transmitter. The sensor probe of the thermometer penetrated only 60 cm, about the middle of its length; it then bent (**Figure 4D**). Perhaps a hard layer existed at that depth below the seafloor. The uppermost four sensors measure the ambient seawater temperature because these sensors were above the seafloor, whereas the other six sensors are expected to measure the subsurface temperature. However, all sensors except for the lowermost sensor (ch. 1) seem to record the ambient temperature for all periods of the observation. The nine sensors aside from ch. 1 give almost identical temperature changes to those of the ambient temperature measured using the CTD meter. Consequently, the data of the ground thermometer might be used as a reference for the ambient temperature of the deployment location. Except for ch. 1, the data of a 10-channel ground thermometer, which measures the ambient temperature of the receiver, presents a similar pattern to that measured using the CTD meter for ambient temperature (compare **Figure 9A** with **Figure 7B**). Daily temperature variation (April 30) is as little as about 0.02°C. The temperature of ch. 1 has a higher value and less variability than the data of other channels. Since the test data obtained in the laboratory and in a shallow water area verified to show the same trend for all channels, the cause of the observed variations in ch. 1 requires further investigation.

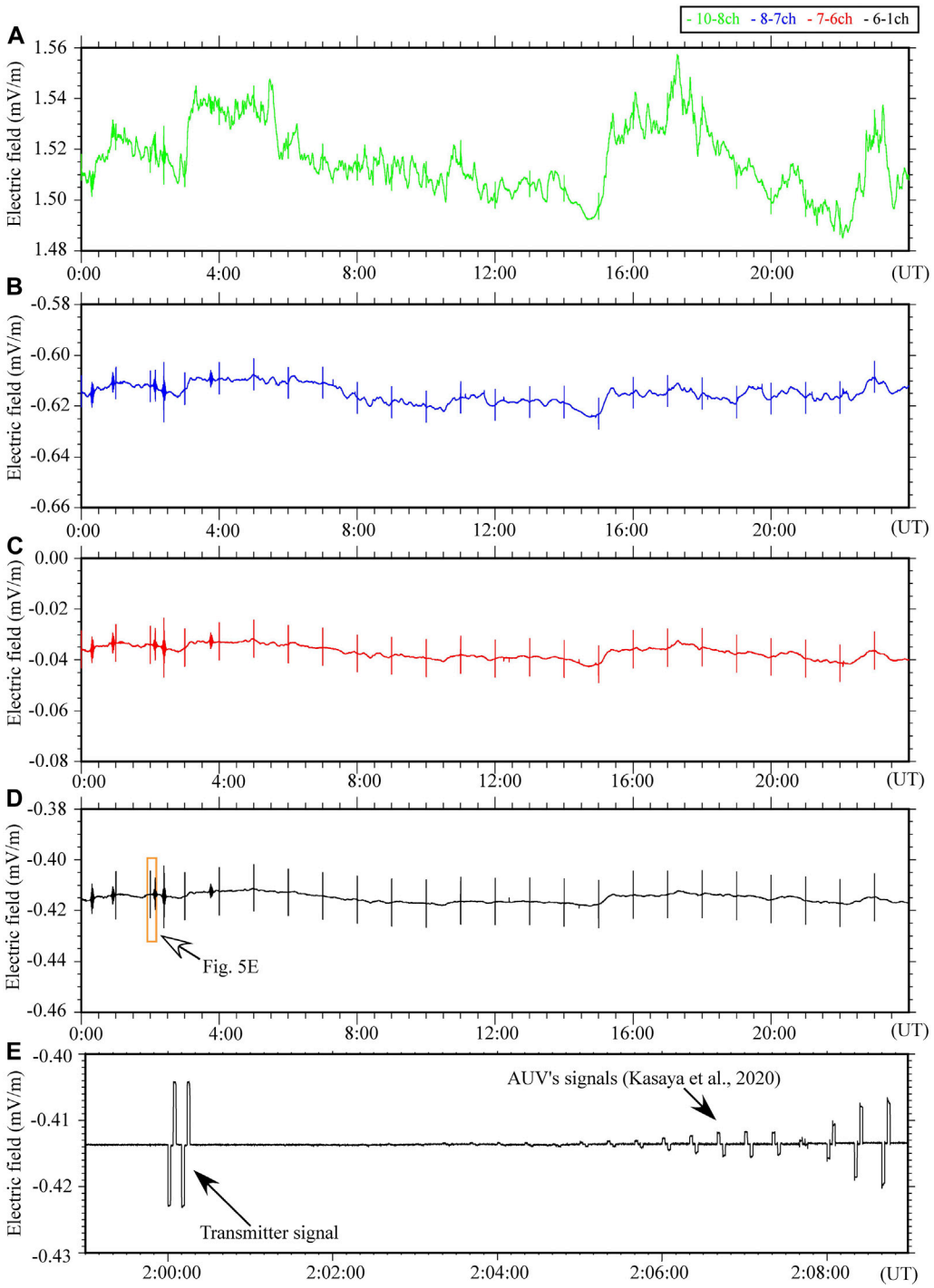

FIGURE 5 | (A–D) Time series of the electric field calculated by four almost equally spaced electrode pairs on April 30, 2018. Locations of these electrodes are denoted by red squares in **Figure 3A**. **(E)** Enlarged (10 min) time series obtained the electrode pair (ch. 6–1) recording the responses of rectangular waveforms from the transmitter unit used for the present study and a transmitter loaded on an AUV during another survey (Kasaya et al., 2018; Kasaya et al., 2020).

DISCUSSION

We conducted continuous electric potential and DC resistivity monitoring near a hydrothermal deposit area and acquired stable data for three and a half months. First, we discuss the apparent resistivity variations. The absolute values of apparent resistivities are comparable to those of other data obtained by AUVs at and near this site (Kasaya et al., 2020). However, we

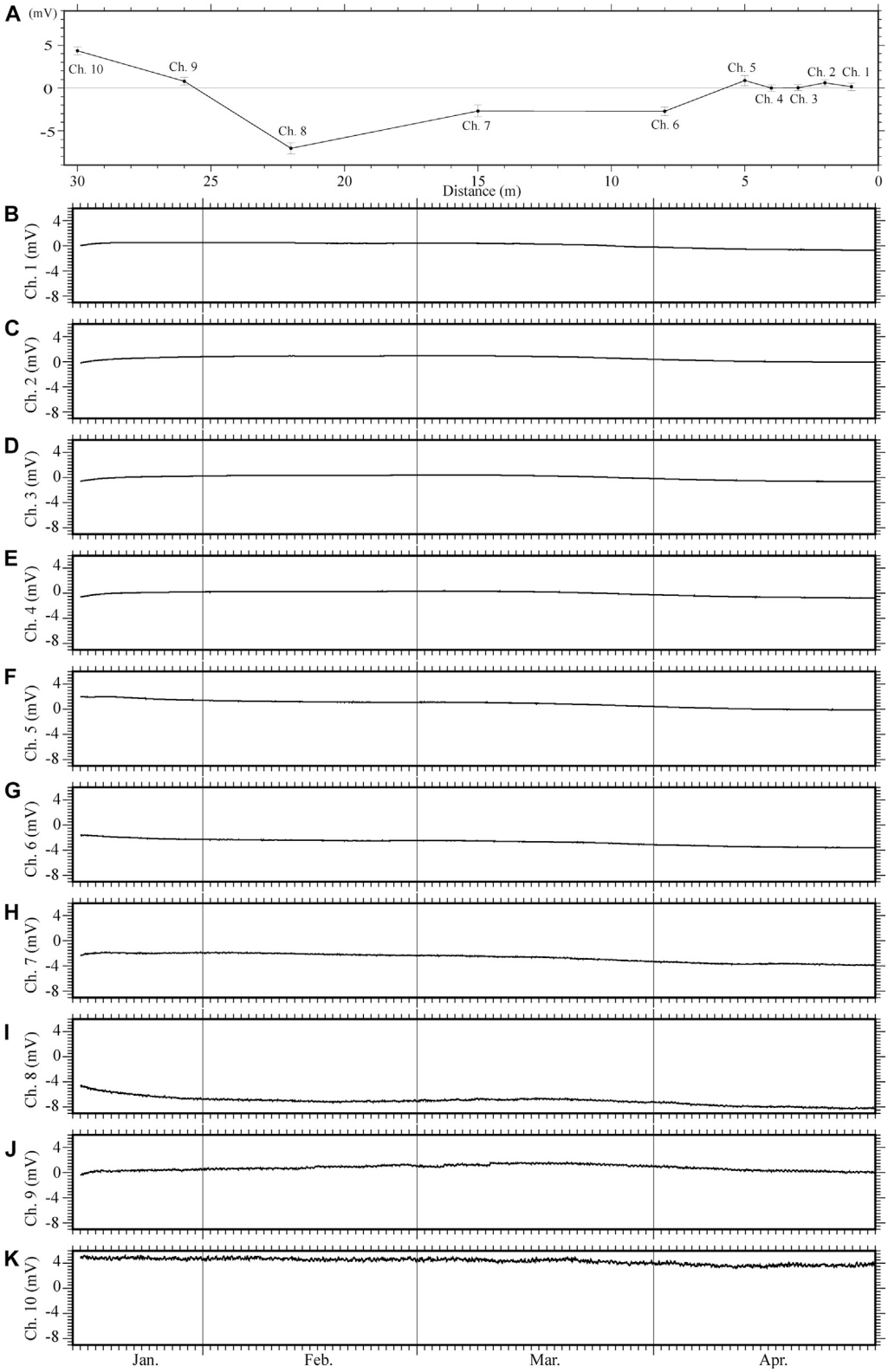

FIGURE 6 | (A) Spatial variation of the electric potential relative to the common electrode (averaged over the entire observation period). **(B–K)** Time series of 1 h average values for each electric potential relative to the common electrode throughout the observation period. For each electrode, the value immediately before installation was set to zero (the value measured in the period before installation was subtracted from the raw data).

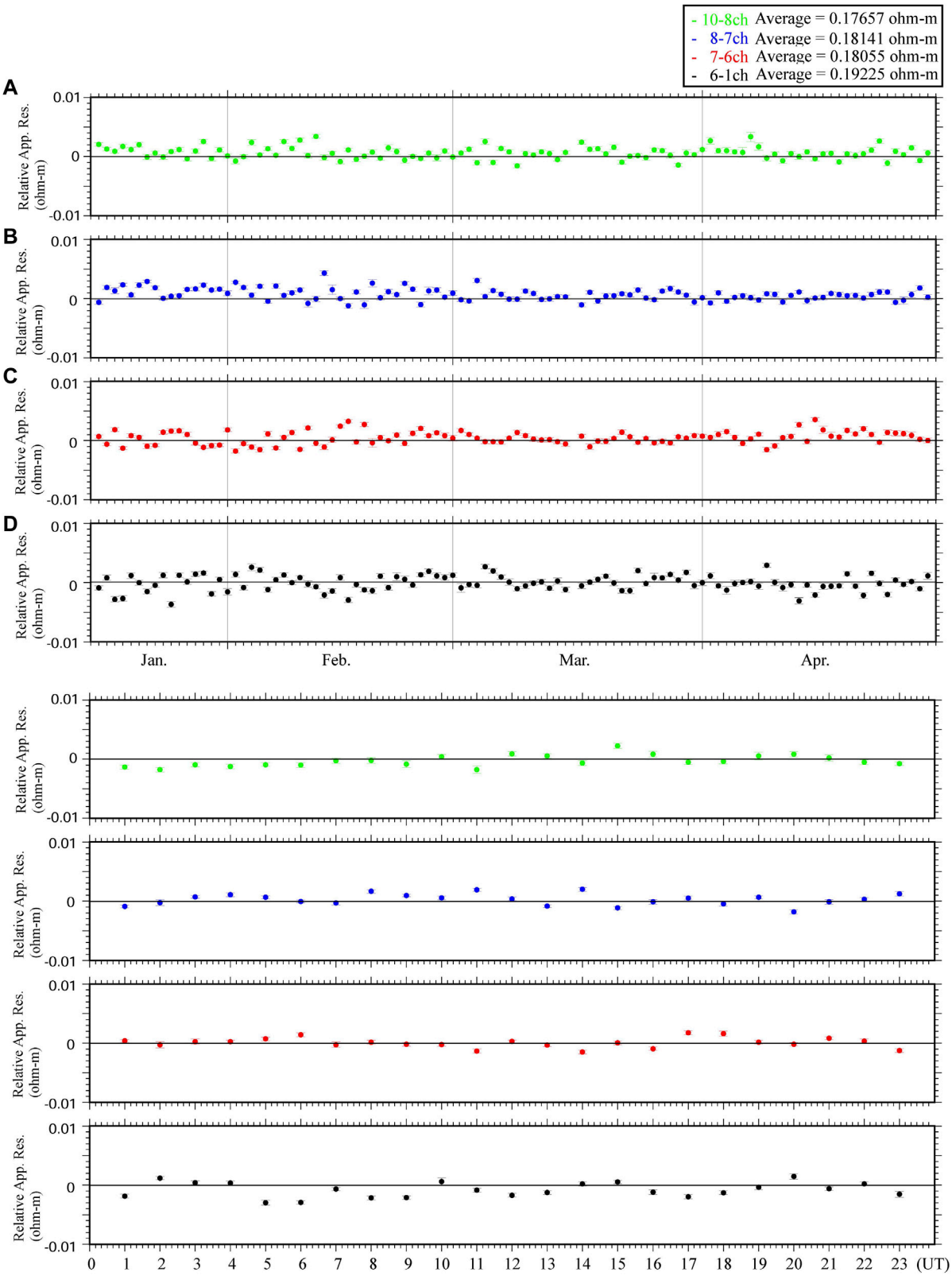

FIGURE 7 | Time series of the relative apparent resistivity calculated from four electrode pairs shown in the legend. Each averaged value is also shown in the legend. **(A–D)** Daily mean values throughout the observation period. **(E–H)** One-hour mean value of the relative apparent resistivity on april 30, 2018. Electric signals were transmitted twice each hour.

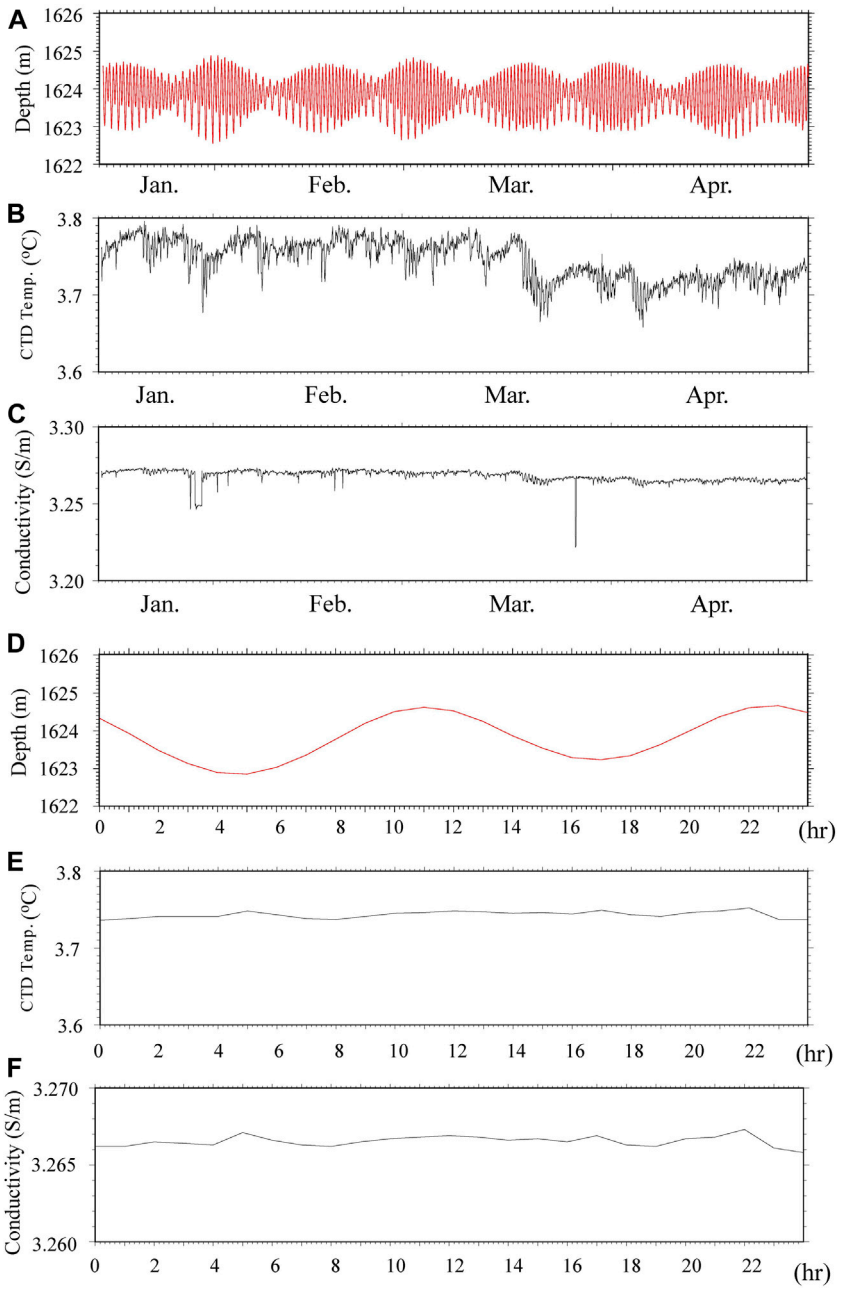

FIGURE 8 | Time series of **(A)** the pressure meter (depth) and **(B,C)** the ambient temperature and electrical conductivity throughout the observation period **(D–F)** Same as **(A–C)**, but with data for April 30, 2018.

were unable to carry out the calibration in the middle layer as in the towed DC resistivity survey. Therefore, only relative values are discussed herein. The relative apparent resistivity calculated from four almost equally spaced electrode pairs was stable throughout the observation period (**Figures 7A–D**). Its peak-to-peak variation is less than 0.005 Ω-m. The relative apparent resistivity in April 30 also shows no clear daily or semidiurnal variation (**Figures 7E–H**). The ambient conductivity was also stable (**Figures 8C,F**), with variation of less than 0.001 S/m (0.0001 Ω-m). The obtained apparent resistivities are very low values, which are smaller than the ambient seawater conductivity recorded by the CTD meter attached to the transmitter unit. For the analyses described above, the apparent resistivity is calculated using the dipole–dipole electrode configuration, for which the sensitivity is high in a region near each electrode. Consequently, the time variation of the calculated apparent resistivity might be caused mainly by local pore conditions

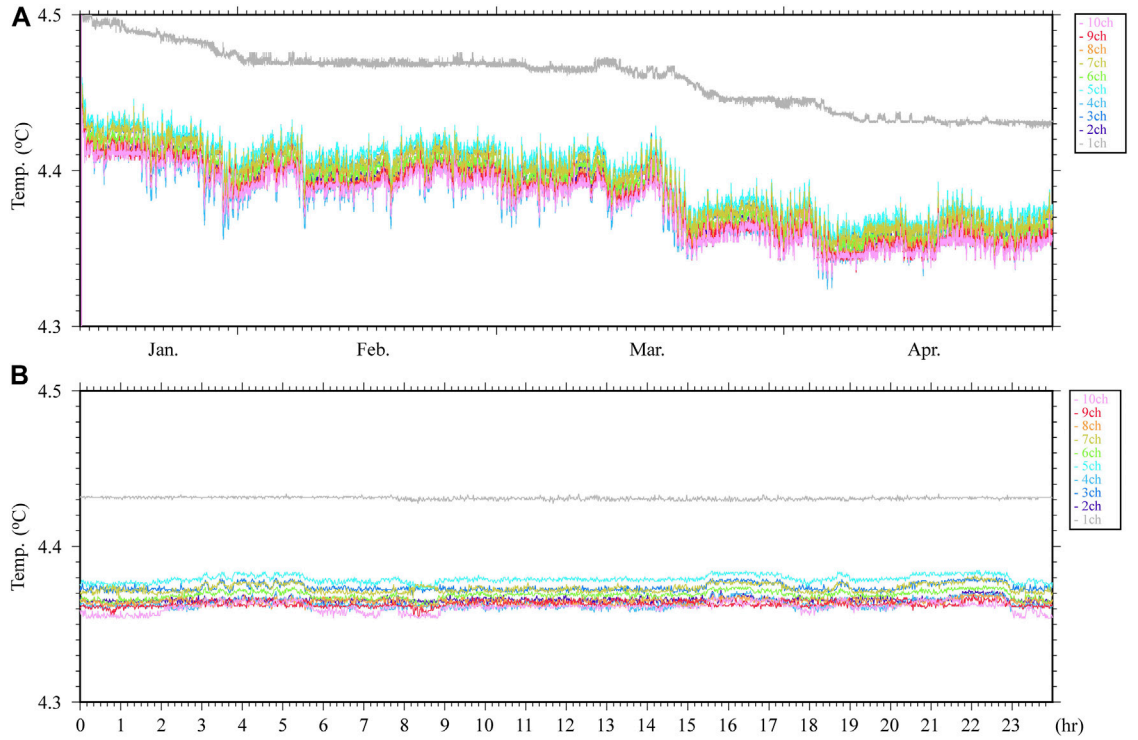

FIGURE 9 | (A) Time series of the temperature variation measured using a 10-channel thermometer during the whole observation period **(B)** Same as A, but with data of April 30, 2018.

changing around each electrode, not the change of deeper subsurface structures.

Next, we briefly describe the spatial distribution of the electric potential relative to the common electrode (**Figure 6**). The overall spatial distribution pattern is not changed throughout the whole observation period (**Figure 6A**), although small short-term fluctuations that are probably excited locally persist in the sensors near the hydrothermal mound (e.g., **Figure 6K**). The region near the North site including the observed area is a zone of a large negative SP anomaly down to −50 mV, the value of which was obtained from deep-tow observations at altitude of 5 m (Kawada and Kasaya, 2017). This negative SP anomaly distribution around the ore deposit area is probably caused by the oxidation–reduction potential (Sato and Mooney, 1960). Its range spans approximately 300 m (Kawada and Kasaya, 2017; Kubota et al., 2020). Consequently, the spatial distribution observed by the 30-m-long potential electrode array in the present study should be interpreted as a relative spatial distribution within the large negative anomaly.

We discuss the time-dependent behavior of the observed signals. The electric field calculated from four electrode pairs with an electrode span of 7–8 m shows variations of natural origin as well as signals of the current transmission (**Figures 5A–D**). The electrode pair closest to the mound (ch. 8 and 10) represents the largest variation with a semidiurnal period. **Figure 10** presents the power spectrum of electric field of the four electrode pairs calculated by FFT analysis. The entire time series was divided into 31 segments of 532,488 s in length with no gaps. Each segment was subjected to FFT analysis using a rectangular window, and the output was averaged in the frequency domain. All of these pairs have the largest power spectrum at 12 h as well as peaks at 6 h and 8 h. A 24-h peak is also found, although it is weaker than the others. The peaks at 6 and 8 h are probably due to diurnal response, since they are respectively the second and third harmonics of the tidal components. MacAllister et al. (2016) also detected signals at about 6, 8, 12, and 24 h responses influenced by tides in their near shore long-term SP observation. These variations are apparently correlated with and/or induced from tides. Consequently, the electrical signal might detect some responses influenced by subsurface variations.

From now on, we discuss possible mechanisms of the temporal electrical variations for each electrode pair (**Figure 5**). We first consider the migration of seawater mass around a hydrothermal mound caused by tides. Kasaya et al. (2018) detected precursory electric potential changes associated with seismically generated turbidity flow by an electromagnetic meter connected to a cabled observatory system. The maximum height and horizontal velocity of the turbidity flow were over 30 m and about 100 mm/s. The maximum temperature change caused by the arrival of turbidity flow was 1.5°C. These results are much larger than those observed during the present study (temperature change are 0.11°C). However, the amplitude of potential changes observed using the electro-magnetometer with 20 m electrode distance is less than 0.15 mV (about 0.0075 mV/m in an electric field). This value is less than one-tenth of our observation results (about 0.07 mV/

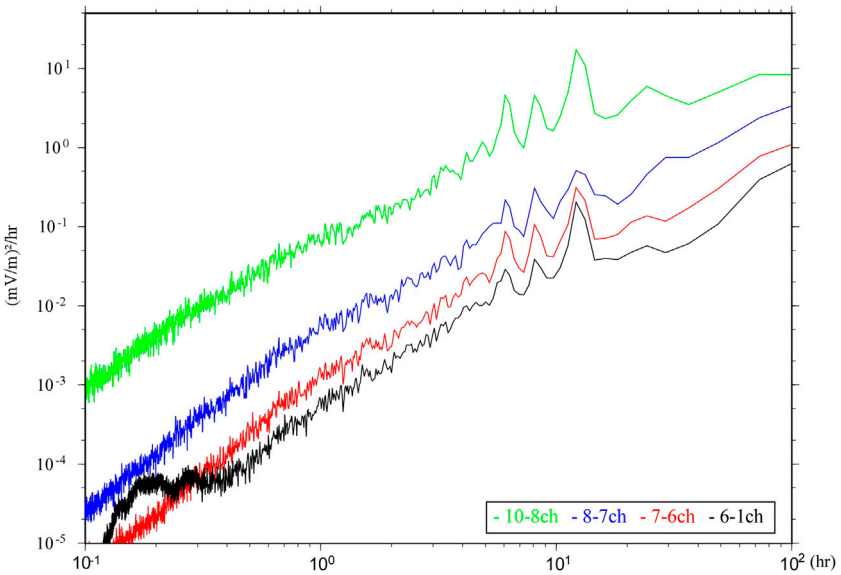

FIGURE 10 | Power spectra of electric fields of four electrode pairs calculated by FFT analysis. Colors are the same as those used for **Figure 5**.

m). Therefore, with static water temperatures during the present observation, it is difficult to explain these variations caused by the migration of seawater mass around a hydrothermal mound.

A change in the depth of the redox front around an orebody would change the distribution of the negative SP anomaly (Sato and Mooney, 1960). In the context of the present study, the source of this anomaly must be close to the seafloor because the detected variations were observed in a short, 30-m-long electrode array. More importantly, the electric field responses differ among electrode pairs (**Figure 5**). After removing the offset between electrodes using the pre-extending operation data, temporal changes in each electrode after installation are gradual (**Figures 6B–K**). They are extremely large in the closest electrode pair to the hydrothermal mound. For that reason, we do not believe that changes in the redox potential are the main reason. The possibility of induced electric current exists because of variation in the geomagnetic field to affect the electric potential variations (Ward and Hohmann, 1987). However, the geomagnetic induction phenomenon should affect the wide area more or less simultaneously. This mechanism cannot account for the local variation found within a 30 m electrode array.

Bearing in mind that the temporal variation of the electric field is strongest with the electrode pair closest to the vent field, streaming potential (e.g., Jouniaux and Ishido, 2012; Revil and Jardani, 2013) in response to tides is another candidate for the observed temporal variation in the electric field. Tides might alter the sub-seafloor rock and sediment pore structure by poroelasticity, which might cause changes in the flow rate of upwelling hydrothermal fluid (e.g., Jupp and Schultz, 2004). MacAllister et al. (2016) also pointed out that some SP signals are periodic responses to changes in fluid pressure and chemical concentration gradients within the coastal aquiferthat are driven by ocean tides. If the electrical current source related to the streaming potential is generated by variation in the upwelling flow rate, then its response is greater near the area of an active hydrothermal system. The observed result is consistent with this idea because the response of potential variation to tides becomes stronger toward the hydrothermal mound of the North site (**Figure 5**). To verify this supposition, we must conduct flow rate measurements and determine the *in situ* electrokinetic coefficient, which represents the relation between the flow rate and the electrical variation.

CONCLUSION

For this study, we planned an integrated electromagnetic long-term monitoring system connecting to a cabled observatory system. We also conducted an experimental observation near the hydrothermal deposit area using only a developed current transmitter and a voltmeter unit. We were able to detect the controlled source signal. We obtained very stable apparent resistivity with no significant change through all observation terms. The electrical data exhibited characteristic changes over time. The electric field variation of the electrode pair closest to the hydrothermal mound is exceptionally large. In fact, the period of this large variation is almost semidiurnal. We conclude that explaining the electric field variations by the migration of a seawater mass around a hydrothermal mound is difficult. We inferred that this variation results from the effects of streaming potential, i.e., fluid flow below the seafloor, in response to tides. The cause for obtained electric potential variations, however, demands further investigation. As established for the electromagnetic observation technique, these observations are expected to be adaptable to other purposes of sub-surface structure monitoring such as CCS and environmental monitoring. During this study, we were unable to observe connection of a cabled observatory because of cancellation of a cable deployment plan. Nevertheless, we completed the

development of all instruments. By connecting our system to a cable system, if a cabled observatory is constructed, we will be able to carry out long-term monitoring.

DATA AVAILABILITY STATEMENT

The raw data supporting the conclusions of this article will be made available by the authors, without undue reservation.

AUTHOR CONTRIBUTIONS

TK designed and developed all instruments. HI analyzed the time series data and contributed to the system revision and testing. YK interpreted self-potential variation. TK and HI conducted a deployment and recovery operation. All authors contributed to the article and approved the submitted version.

FUNDING

This study was supported by the Cross-ministerial Strategic Innovation Promotion Program "Next-generation technology for ocean resources exploration" launched by the Council for Science, Technology and Innovation (CSTI) by the Cabinet Office of the Japanese government.

ACKNOWLEDGMENTS

We thank the respective captains and crews of R/V SHINSEI-MARU and R/V KAIMEI and marine technicians for assisting the observation during deployment and recovery cruise. We are grateful to the operation team for HAKUYO 2000 and KM-ROV. Comments from reviewers were valuable in improving the manuscript. We drew many figures using Generic Mapping Tools (Wessel et al., 2013).

REFERENCES

Asakawa, K., Yokobiki, T., Goto, T-n., Araki, E., Kasaya, T., Kinoshita, M., et al. (2009). New scientific underwater cable system tokai-SCANNER for underwater geophysical monitoring utilizing a decommissioned optical underwater telecommunication cable. *IEEE J. Oceanic Eng.* 34, 539–547. doi:10.1109/JOE.2009.2026987

Constable, S., Kowalczyk, P., and Bloomer, S. (2018). Measuring marine self-potential using an autonomous underwater vehicle. *Geophys. J. Int.* 215, 49–60. doi:10.1093/gji/ggy263

Fukuba, T., Choi, J. K., Furushima, Y., Miwa, T., and Yamamoto, H. (2018). "Lander observatory with non-contact power supply and communication interfaces for long-term ecosystem monitoring in deep-sea, in The 28th international ocean and polar engineering conference, Sapporo, Japan, June 10–15, 2018, International Society of Offshore and Polar Engineers.

Goto, T-N., Kasaya, T., Kinoshita, M., Araki, E., Kawaguchi, K., Asakawa, K., et al. (2007). "Scientific survey and monitoring of the off-shore seismogenic zone with Tokai SCANNER: submarine cabled network observatory for nowcast of earthquake recurrence in the Tokai region, Japan," in 2007 symposium on underwater technology and workshop on scientific use of submarine cables and related technologies. Tokyo, Japan, April 17–20, 2007, 670–673. doi:10.1109/UT.2007.370818

Jouniaux, L., and Ishido, T. (2012). Electrokinetics in earth sciences: a tutorial. *Int. J. Geophys.* 2012, 286107. doi:10.1155/2012/286107

Jupp, T. E., and Schultz, A. (2004). A poroelastic model for the tidal modulation of seafloor hydrothermal systems. *J. Geophys. Res.* 109 (B3), B03105. doi:10.1029/2003JB002583

Kaieda, H., Suzuki, K., and Jomori, A. (2018). "Electrical survey results in a sub-seabed CO2 release experiment," in 14th international conference on greenhouse gas control technologies. Melbourne, Australia. 21–26 October, 2018 (GHGT-14). doi:10.2139/ssrn.3365998

Kasaya, T., Mitsuzawa, K., Goto, T. N., Iwase, R., Sayanagi, K., Araki, E., et al. (2009). Trial of multidisciplinary observation at an expandable sub-marine cabled station "off-hatsushima island observatory" in Sagami Bay, Japan. *Sensors.* 9, 9241–9254. doi:10.3390/s91109241

Kasaya, T., Goto, T-n., Iwamoto, H., and Kawada, Y. (2018). "Development of multi-purpose electromagnetic survey instruments," in The 13th SEGJ international symposium, Tokyo, Japan, November 12–14, 2018. doi:10.1190/segj2018-042.1

Kasaya, T., Iwamoto, H., Kawada, Y., and Hyakudome, T. (2020). Marine DC resistivity and self-potential survey in the hydrothermal deposit areas using multiple AUVs and ASV. *Terr. Atmos. Ocean. Sci.* 31, 579–588. doi:10.3319/TAO.2019.09.02.01

Kawada, Y., and Kasaya, T. (2017). Marine self-potential survey for exploring seafloor hydrothermal ore deposits. *Sci. Rep.* 7, 13552. doi:10.1038/s41598-017-13920-0

Kawada, Y., and Kasaya, T. (2018). Self-potential mapping using an autonomous underwater vehicle for the Sunrise deposit, Izu-Ogasawara arc, southern Japan. *Earth, Planets Space.* 70, 142. doi:10.1186/s40623-018-0913-6

Kawaguchi, K., Kaneko, S., Nishida, T., and Komine, T. (2015). "Construction of the DONET real-time seafloor observatory for earthquakes and tsunami monitoring", in *Seafloor Observatories*, ed. P. Favali, L. Beranzoli, and A. D. Santis (Berlin: Springer), 211–228. doi:10.1007/978-3-642-11374-1_10

Kimura, T., Araki, E., Takayama, H., Kitada, K., Kinoshita, M., Namba, Y., et al. (2013). Development and performance tests of a sensor suite for a long-term borehole monitoring system in seafloor settings in the Nankai Trough, Japan. *IEEE J. Oceanic Eng.* 38, 383–395. doi:10.1109/JOE.2012.2225293

Kinoshita, M., Kawada, Y., Tanaka, A., and Urabe, T. (2006). Recharge/discharge interface of a secondary hydrothermal circulation in the Suiyo Seamount of the Izu-Bonin arc, identified by submersible-operated heat flow measurements. *Earth Planet. Sci. Lett.* 245 (3–4), 498–508. doi:10.1016/j.epsl.2006.02.006

Kubota, R., Ishikawa, H., Okada, C., Matsuda, T., and Kanai, Y. (2020). Marine deep-towed self-potential and DC resistivity explorations for seafloor massive sulfide deposits (in Japanese with English abstract and figure captions). *BUTSURI-TANSA (Geophys. Explor.)* 7 (1), 3–13. doi:10.3124/segj.73.3

MacAllister, D. J., Jackson, M. D., Butler, A. P., and Vinogradov, J. (2016). Tidal influence on self-potential measurements. *J. Geophys. Res. Solid Earth* 121, 8432–8452. doi:10.1002/2016JB013376

METI (2018). *Final report of the development of deep-sea mineral resource program (in* Japanese), 158. Available at: http://www.jogmec.go.jp/content/300359550.pdf (Accessed March 1, 2021).

Miwa, T., Iino, Y., Tsuchiya, T., Matsuura, M., Takahashi, H., Katsuragawa, M., et al. (2016). "Underwater observatory lander for the seafloor ecosystem monitoring using a video system", in *2016 Techno-Ocean (Techno-Ocean).* Kobe, Japan, October 6–8, 2016, 333–336. doi:10.1109/Techno-Ocean.2016.7890673

Revil, A., and Jardani, A. (2013). *The self-potential method: theory and applications in environmental geosciences*. New York: Cambridge University Press. doi:10.1017/CBO9781139094252

Safipour, R., Hölz, S., Jegen, M., and Swidinsky, A. (2017). On electric fields produced by inductive sources on the seafloor. *Geophysics* 82 (6), E297–E313. doi:10.1190/geo2016-0700.1

Sato, M., and Mooney, H. M. (1960). The electrochemical mechanism of sulfide self-potentials. *Geophysics* 25, 226–249. doi:10.1190/1.1438689

Soueid Ahmed, A., Jardani, A., Revil, A., and Dupont, J. P. (2016). Joint inversion of hydraulic head and self-potential data associated with harmonic pumping tests. *Water Resour. Res.* 52, 6769–6791. doi:10.1002/2016WR019058

Totsuka, S., Shimada, K., Nozaki, T., Kimura, J-I., Chang, Q., and Ishibashi, J-I. (2019). Pb isotope compositions of galena in hydrothermal deposits obtained by drillings from active hydrothermal fields in the middle Okinawa Trough determined by LA-MC-ICP-MS. *Chem. Geology.* 514, 90–104. doi:10.1016/j.chemgeo.2019.03.024

Ward, S. H., and Hohmann, G. W. (1987). "Electromagnetic theory for geophysical applications," *Electromagnetic methods in applied Geophysics*, Editor. M. N. Nabighian (Tulsa: Society of Exploration Geophysicists), Vol. 1, 130–311. doi:10.1190/1.9781560802631.ch4

Wessel, P., Smith, W. H. F., Scharroo, R., Luis, J., and Wobbe, F. (2013). Generic mapping tools: improved version released. *EOS Trans. AGU.* 94, 409–410. doi:10.1002/2013EO450001

Yamamoto, H. (2020). Survey, monitoring and assessment of marine communities conducted by new technology (in Japanese with English abstract and figure captions). *BUTSURI-TANSA (Geophys. Explor.)* 73, 53–63. doi:10.3124/segj.73.53

Conflict of Interest: HI is employed by the company Nippon Marine Enterprises, Ltd.

The remaining authors declare that the research was conducted in the absence of any commercial or financial relationships that could be construed as a potential conflict of interest.

frontiers in Earth Science

ORIGINAL RESEARCH
published: 17 March 2021
doi: 10.3389/feart.2020.599810

Tilt Observations at the Seafloor by Mobile Ocean Bottom Seismometers

Hajime Shiobara[1], Aki Ito[2], Hiroko Sugioka[3], Masanao Shinohara[1] and Toshinori Sato[4]*

[1]Earthquake Research Institute, The University of Tokyo, Tokyo, Japan, [2]Research Institute for Marine Geodynamics, Japan Agency for Marine-Earth Science and Technology, Yokosuka, Japan, [3]Kobe Ocean-Bottom Exploration Center, Kobe University, Kobe, Japan, [4]Graduate School of Science, Chiba University, Chiba, Japan

We have developed a broadband ocean bottom seismometer (BBOBS) and its new generation (BBOBS-NX) with the penetrator sensor system since 1999. With them, we performed many practical observations to create a new research category of ocean bottom broadband seismology. As the next step in seafloor geophysical observation, the BBOBS and the BBOBS-NX can be a breakthrough in realizing a geodetic observation network on the seafloor. Although vertical displacement observation by the absolute pressure gauge has been widely conducted in recent years, other geodetic observations are rarely performed. A few trials to measure the seafloor tilt were performed, but those looked inadequate for practical observations. Note that the broadband sensor in our BBOBSs has a mass position signal output, which can be used to measure the tilt change. As the horizontal component noise level of the BBOBS-NX is good at a long period range, we expected it to be adequate for the tilt measurement. At the first evaluation, we performed a comparison with a water-tube tiltmeter. The result was comparable with a resolution of better than 1 μ radian. A practical observation at the south of Boso Peninsula (KAP3 site) was conducted as the *in-situ* study from April, 2013. In January, 2014, a slow slip event (SSE) occurred near this site. The tilt data were processed by removing steps, mechanical relaxation, and tides. The results show a clear peak started from late December 2013. Two more 2 year-long tilt observations began in 2015: one was at the KAP3 site and another was off the Miyagi Prefecture at the slope to the Japan Trench. The latter was recovered in 2017 with about 1.5 years of data, which indicate a large continuous tilt up to several tens of μ radian. This amount of tilt can be explained by a similar already estimated SSE. Mobile tilt measurement at the seafloor can be a powerful tool to study SSEs, as they can be located above the source area and also possible to build an observation array for a practical study because of its low cost and ease of deployment compared with a seafloor borehole site.

Keywords: geodesy, ocean bottom seismometer, tilt observation, broadband seismometer, earth tide, bottom current, slow slip event

OPEN ACCESS

Edited by:
Ryota Hino,
Tohoku University, Japan

Reviewed by:
Tolulope Morayo Olugboji,
University of Rochester, United States
Hiromi Fujimoto,
Tohoku University, Japan

****Correspondence:***
Hajime Shiobara
shio@eri.u-tokyo.ac.jp

Specialty section:
This article was submitted to Solid Earth Geophysics, a section of the journal Frontiers in Earth Science

Received: *28 August 2020*
Accepted: *28 December 2020*
Published: *17 March 2021*

Citation:
Shiobara H, Ito A, Sugioka H, Shinohara M and Sato T (2021) Tilt Observations at the Seafloor by Mobile Ocean Bottom Seismometers. Front. Earth Sci. 8:599810. doi: 10.3389/feart.2020.599810

INTRODUCTION

To understand the Earth from a geophysical point of view, observations on the seafloor are very important due to the fact that the seafloor encompasses a large percentage of the Earth's surface, as well as several phenomena in the oceanic area, such as seafloor spreading at the oceanic ridge and oceanic slab subduction at the trench, which cause earthquakes and magma source production by

water and chemical cycling. Slow slip events (SSEs) have been found from land networks (e.g., Hirose et al., 1999; Obara, 2002), which are also key to understanding usual earthquakes (Ide et al., 2007). Most SSE sources are beneath the land area, but some shallow SSEs occur between the trench and the coast, below the seafloor (e.g. Sugioka et al., 2012; Ozawa, 2014).

Several kinds of geophysical observations at the seafloor have been attempted since the 1960s. After the 1990s, seismic studies using ocean bottom seismometers (OBS) became common for temporal observations (Shinohara et al., 2012), as well as those using a cable system for real-time monitoring (e.g. Kaneda et al., 2015). For researchers in this field, it is natural to try to expand the observation coverage in many aspects and also to adopt the same kind of observations performed on the land, for a better understanding of the natural phenomena through seafloor observations. A broadband seismic observation at the seafloor was attempted by Suyehiro et al. (1995), and it has already become a common tool in several countries as the broadband ocean bottom seismometer (BBOBS), which is explained in Suetsugu and Shiobara (2014). With the BBOBS, shallow very low frequency seismic activity near the trench was revealed clearly by Sugioka et al. (2012), and a non-volcanic SSE was recently found around the ridge off Chile (Sáez et al., 2019) by Japanese OBS array data.

To achieve more coverage in longer, geodetic periods, as shown in this special issue, the GNSS (GPS)/Acoustic method has become a common tool to measure horizontal displacements at the seafloor after the success by Spiess et al. (1998). In addition, absolute pressure observation to measure the vertical displacement of the seafloor (e.g. Hino et al., 2009; Ito et al., 2013) has been widely performed with several technical improvements (e.g. Kajikawa and Kobota, 2014). However, other geodetic observation methods at the seafloor have not become common yet.

Tilt observation at the seafloor has been tried since the 1980s in an effort to investigate the ridge center volcanism or subduction dynamics. Sakata and Shimada (1984) developed an ocean bottom tiltmeter (OBT) that was tested in shallow water in offshore Japan, as it was of an on-line cabled type. Shimamura and Kanazawa (1988) seemed the first off-line OBT observation. Two OBTs were deployed at the top of the Erimo seamount (3,930 m depth) in the Kuril Trench using the manned French submersible vessel, *Nautile*. This OBT system was considered well, but was designed with too advanced specifications as there was no precise positioning system (such as GPS) at that time, which was important for data recovery by the acoustic link within a short distance. Other OBT developments were of the free-fall and self pop-up type (Tolstoy et al., 1998; Sato and Kasahara, 1999). Another type of OBT, a long-baseline OBT (LBT), was also tried at the Juan de Fuca ridge by Anderson et al. (1997). In the same project, several short-baseline OBTs (Tolstoy et al., 1998) were also used, which were based on Scripp's OBS with a bubble tilt sensor (Westphal et al., 1983). The LBT had a length of 100 m, which was deployed with the dynamic deployment technique by Webb et al. (1985), like a deep-tow system, not by using a remotely operated vehicle (ROV). Fabian and Villinger (2007, 2008) made the first long-term tilt observation with their original OBT which was operated with a ROV at the Mid-Atlantic Ridge. Although those OBTs were designed to be deployed on the seafloor, there were some tilt observations in seafloor boreholes even in the 1980s, when the geophone was used as a seismic sensor. Duennebier et al. (1987) obtained continuous tilt data in a seafloor borehole in the northwestern Pacific for 64 days. Sacks et al. (2000) deployed two seafloor borehole geophysical observatories on the deep-sea terrace of the Japan Trench, and the data obtained were examined by Araki et al. (2004). Those were stand-alone systems, but recently, an online borehole observatory with a tilt sensor near the Nankai Trough has begun operation (Araki, 2017).

This paper introduces our new approach of the simultaneous broadband seismic and tilt observation by Japanese BBOBSs, not only regarding the instrumentation, but also offering some results of the feasibility long-term observations at the landside slope of the Japan Trench.

MATERIALS AND METHODS

Base of the Instrumentation

Broadband Ocean Bottom Seismometer

The BBOBS in Japan has been developed since 1999 (e.g. Suetsugu and Shiobara, 2014). This BBOBS (**Figure 1**) contains all necessary components in its titanium alloy sphere housing of 650 mm in diameter, which was designed as a free-fall and self pop-up type. The CMG-3T of 360 s (Guralp systems, United Kingdom) was chosen as the broadband sensor with special orders for its weight and power consumption. This sensor was installed on our original leveling unit to keep it in level within ±0.2°, during the observation. During more than 170 deployments of the BBOBS, we obtained noise models (Incorporated Research Institutions for Seismology (IRIS), 1994) that show the averaged noise spectrum without known earthquakes in short, for almost all sites. An example is shown in **Figure 2A**, with the new high noise model (NHNM) and the new low noise model (NLNM) by Peterson (1993). Because of the low gravity center and the rigid connection between the sphere housing and the anchor, the noise level of the vertical component (Z) is between the NHNM and the NLNM, which means it is comparable to land seismic sites. However, those of the horizontal components (H1 and H2) are around or above the NHNM, due to the effect of the bottom current with the housing above the seafloor. Even with this situation, the lowest noise level of the horizontal component would be near the NLNM (**Figure 2B**), probably when the bottom current is weak.

New Generation BBOBS With a Penetrator Sensor

To improve the noise level of the horizontal components, a burial sensor system seems effective as land seismic stations and at the seafloor, which was well demonstrated in Collins et al. (2001). We started the development of a BBOBS with a penetrator sensor unit in 2003, based on an original CMG-3T equivalent broadband sensor and our BBOBS system. The first-generation system,

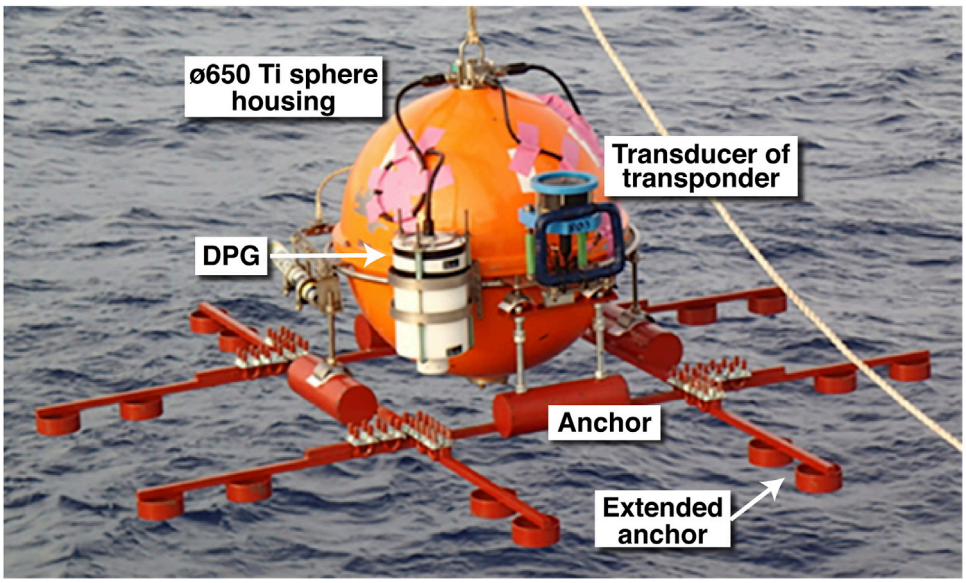

FIGURE 1 | Japanese broadband ocean bottom seismometer (BBOBS). The most recent design of the Japanese BBOBS originally developed in 1999. The broadband sensor inside is the CMG-3T (360 s) mounted on the original leveling system. The anchor base size was 1 m × 1 m. To achieve more stable coupling to the sediment, the "extended anchor" is attached to a 2 m × 2 m base. The DPG (differential pressure gauge) is now standard equipment. The maximum observation period is now 2 years, and it can be deployed at up to 6,000 m.

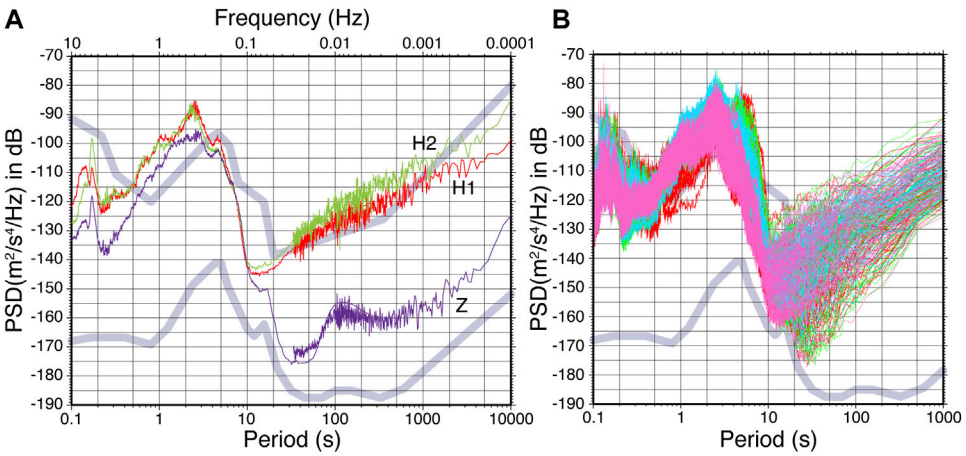

FIGURE 2 | Noise model of the BBOBS. **(A)** One example of the noise model (NM) of the BBOBS using the IRIS standard procedure, which indicates the observation performance of the site including the instrument. The vertical component NM (Z) is usually between the NHNM and the NLNM (thick curves), but horizontal ones (H1 and H2) are around or above the NHNM in the long period range, more than 30 s. **(B)** Stack of the noise spectra used to calculate the H1 component NM in **Figure 2A**. Colors indicate four seasons: cyan (January-March), pink (April-June), red (July-September), and green (October-December). Although the H1's NM is high, the lowest noise level could be near the NLNM in a 10–30 s period.

BBOBS-NX, was used at an *in-situ* test in 2009, which was operated by a ROV (Shiobara et al., 2013). The broadband sensor is separated into three component units without the leveling mechanism to minimize the height and diameter of the pressure case for each component, which makes it easier to penetrate into the sediment layer using gravity (**Figures 3A**,**B**). The noise model of the test showed more than 20 dB of noise reduction in the horizontal components (**Figure 3C**). This effect was obvious in more than 10 s periods, which reflects the fact that a smaller part of the sensor was exposed to the bottom current (Shiobara et al., 2013).

The advantage of the penetrator sensor system is apparent, but the necessity of a ROV limits the opportunity of observations because of availability and cost issues. If the data quality of the BBOBS-NX was obtained with a high-mobility operation like our BBOBS, it would be a breakthrough in the broadband seismology at the seafloor. This second-generation system, NX-2G, is now in its final evaluation stage

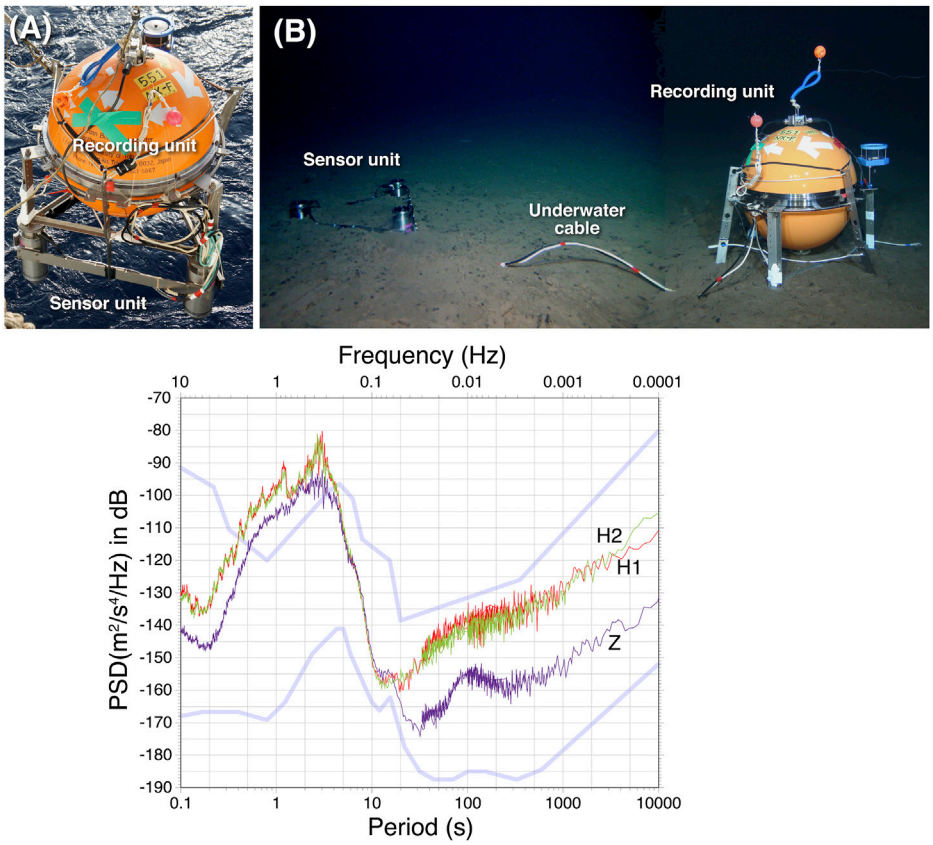

FIGURE 3 | The BBOBS-NX. The BBOBS with the penetrator sensor system using gravity. ROV operation is required in deployment and recovery. The broadband sensor has the same performance of the BBOBS. **(A)** The sensor unit and the recording unit are temporally attached, and free-fallen from the sea surface. Descending speed is about 1.5 m/s. **(B)** They are detached and the recording unit is moved a few meters away from the sensor unit by the ROV. The observation period can be more than 2 years. **(C)** An NM example of the BBOBS-NX. Because of the penetration of the sensor unit, all three component NMs are between the NHNM and the NLNM.

(Shiobara et al., 2019). As shown in **Figure 4**, it is almost based on the BBOBS-NX, and functions of the NX-2G's operation were tested on the deep seafloor in 2017 and 2018.

Method for Simultaneous Broadband Seismic and Tilt Measurement

The broadband sensor equipped in the BBOBS and the BBOBS-NX has a mass position signal output, which are the low-pass filtered (cut-off at 360 s of the eigen period) acceleration data, which can be used to measure the tilt change in time after the mass centering (and the mass unlocking) operation from the two horizontal components data. This is because these mass position signals indicate the fraction of the gravitational acceleration according to the tilt change of the BBOBS or the sensor unit of the BBOBS-NX at the seafloor. As the horizontal component noise level of the BBOBS-NX is more than 10 times better than the BBOBS in a long period range (more than 10 s), and because the penetrator sensor system has good coupling to the sediment layer and is influenced less by bottom currents, we expected the BBOBS-NX to be adequate for tilt measurement. Here, we refer to the BBOBS-NX with the tilt measurement function as the BBOBST-NX. This additional tilt measurement requires a small modification in the system (new wiring and two more input channels of the data recorder). Even for the BBOBS deployed on the seafloor, this tilt measurement is possible with a limitation of the noise level, which relates with conditions of the site, such as the bottom current.

The largest advantage of the tilt observation at the seafloor by the BBOBST-NX (or the BBOBS) exists at the location above or close to the source area of the event with a short horizontal distance. Because tilt is a spatial differentiate of vertical displacement, we can expect large tilt change around the source area. In addition, with these mobile observation instruments, it is possible to build a dense array to cover the target area, because of its low cost and ease of deployment compared with a seafloor borehole site.

RESULTS

Test at the Land Vault

As the first evaluation test of this method, we performed a comparison test in 2010 between the sensor unit of the BBOBST-NX and the water-tube tiltmeter (WTT) at the land vault (at Nokogiri-yama, Chiba Prefecture) near Tokyo Bay (Ishii

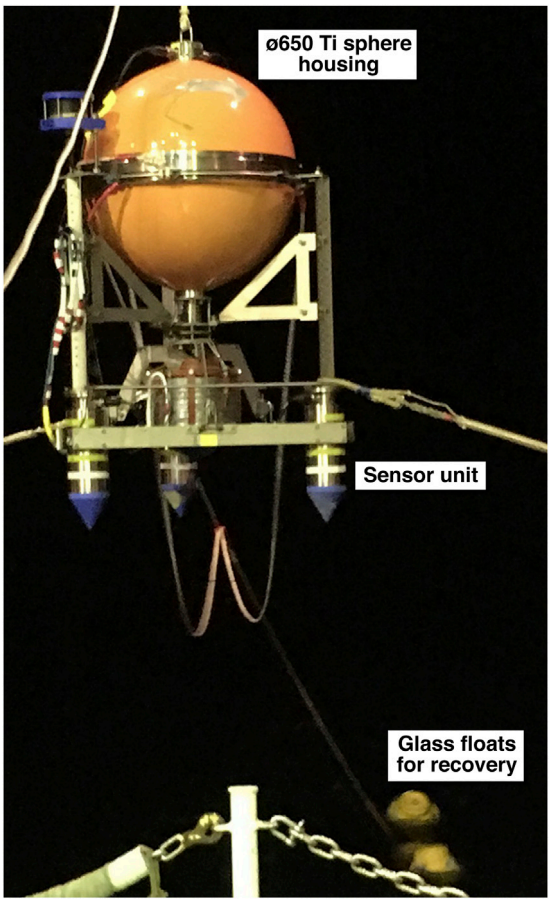

FIGURE 4 | The NX-2G, autonomous type of the BBOBS-NX. To achieve the same performance of the BBOBS-NX without aid of submersibles, the autonomous type is in the final feasibility test.

et al., 1992), about 600 m from the shore. The tilt data were resampled in 1 min intervals at first to match with the WTT data, and were high-pass-filtered with 100,000 s of the cut-off period to remove longer fluctuations than those of 1-day length. The result (**Figure 5**) shows tilt changes comparable to that of the WTT with a resolution of better than 1 μ radian, which shows clear signals by tides. Our sensor was placed inside the seismometer room in the vault, but several tests were ongoing simultaneously with some human operation (performed on May 6 and 9) during our test. As the WTT is located in the tunnel of the same vault separated by two doors from the seismometer room, no human noise was recognized. One problem was a large drift (a few μ radian per day) in the raw tilt data, which is the same as that often seen in our BBOBS as several automatic mass centering operations occurred soon after the deployment lasting for a few weeks. Usually, this kind of drift in our BBOBS becomes smaller, and only a few times of the mass centering operation were observed during the 1 year-long observation period after 1 month of the mass unlocking operation of the broadband sensor. Thus, it was necessary to investigate the mass position stability of the broadband sensor at the seafloor environment in terms of whether it is adequate for tilt measurement.

Here, it is worth mentioning the difference of mass centering function of the broadband sensor used in the BBOBS and the BBOBS-NX. The CMG-3T in the BBOBS has a fixed threshold level to start the mass centering at about 10% to the full-scale (FS), when the mass centering command is received by the sensor's controller. But the original broadband sensor for the BBOBS-NX, based on the borehole type of the CMG-3T, has a user definable threshold level (0–100% FS) by a command. Therefore, we can set a large value (such as 50%) to expect continuous mass position (tilt) change with a trade-off of an adequate operation condition as the seismic sensor because, as mentioned above, it is better to keep a small mass position value like that of the BBOBS.

First Test Observation at the Seafloor

Before the application of the BBOBST-NX for a practical observation, such as SSE monitoring, we performed a test to measure the resolution and instrumental noise level in this tilt observation at an empirically known quiet site (T08) that was previously used for tests of the BBOBS-NX, at the Shikoku Basin (4,930 m depth) of the Philippine Sea Plate (**Figure 6A**), in 2012–2013 for about 2 months. As this test also aimed to undertake preparation experiments of the NX-2G development, the large Ti sphere housing (recording unit) and the gray colored tube were located close to the sensor unit (**Figure 6B**), unlike in **Figure 3B**. This was done to examine the effect of objects closely located to the sensor unit on the long period noise level. Same as for the BBOBS-NX, the deployment of the BBOBST-NX was performed by free falling from the sea surface, then the ROV (KAIKO 7000II, JAMSTEC) was used to untie the connection between the sensor unit and the recording unit, and to move the recording unit beside the sensor unit without any mechanical connection except the underwater cable. The recovery was also done by the same ROV. In this observation, an ocean bottom Doppler current profiler (OBDC), which is based on our long-term OBS, was also deployed with a distance of 100 m.

The tilt data were resampled in 1 h intervals at first, and were processed to remove the large drift that is considered as the mechanical relaxation effect. This effect is assumed to be empirically expressed by a combination of logarithmic function and linear trend, so that the best-fit parameters were searched using a curve fitting function built-in the gnuplot program, and these parameters were used to substitute the drift from the tilt data. Finally, the Baytap08 program (Tamura et al., 1991) was applied to remove tidal components, and a moving averaging of 7 days window length was also applied to observe stability in long periods. The result (**Figure 6C**) indicates a small tilt fluctuation at about 0.6 μ radian peak-to-peak throughout the observation period. The bottom current speed and seawater temperature obtained by the OBDC are shown too. As we cannot control the azimuth of the OBS landing, two horizontal components are expressed as H1 and H2, which are the NS and EW outputs of the broadband sensor, respectively.

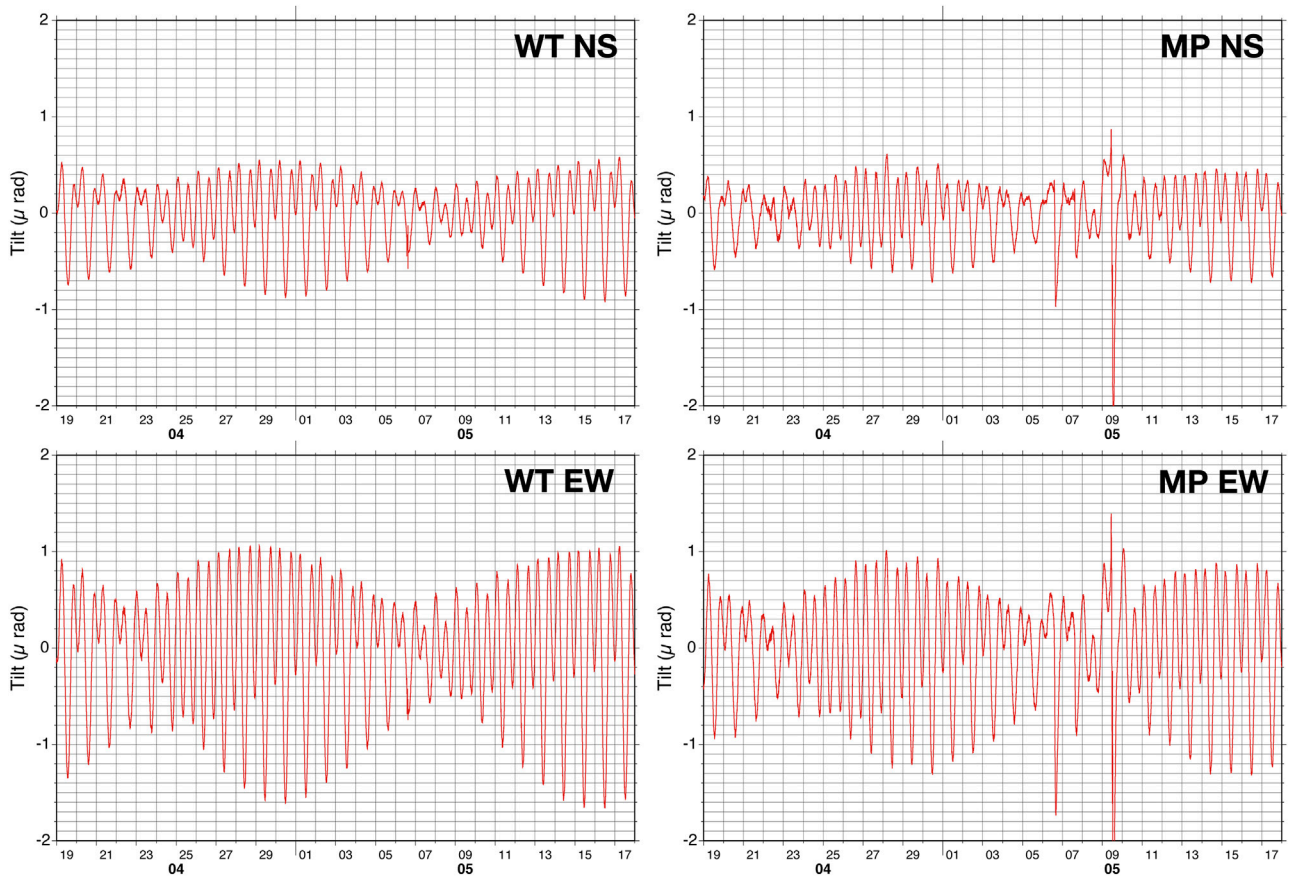

FIGURE 5 | The land vault test of this method. A 2 month test of the broadband sensor for the BBOBST-NX (MP) compared with the water tube tilt-meter (WT) in the same vault. The two large disturbances on May 6 and 9 were due to other human works in the same seismometer room that we used.

Feasibility Observations

Next, more practical observation at the seafloor south of Boso Peninsula (close to the KAP3 site, 1,370 m depth) was performed as an *in-situ* feasibility study from April 2013 for 1 year. In this observation, the BBOBST-NX was deployed and recovered using the ROV (Hyper DOLPHIN, JAMSTEC). As this site is near the Kuroshio current axis, the OBDC was deployed near the BBOBST-NX (**Figures 7A**,**B**) to monitor the environment condition. Between December 28, 2013 and January 4, 2014, a slow slip event (SSE) occurred near this site (Ozawa, 2014), which is indicated as a yellow rectangle in **Figure 7C**. The tilt data were resampled in 1 h intervals at first, then several steps in the mass centering operations were removed. Other processes were the same as mentioned in *First Test Observation at the Seafloor*. The result shows a clear peak of about 6 μ radian in the H2 components, which started from late December 2013, but the tilt did not persist after the SSE ended. In the H1 component, it is difficult to recognize the existence of the similar peak, due to a large disturbance in the whole observation period. As additional information, the azimuth of the H1 component, the dominant bottom current, and the seafloor topography were almost matched with each other in the NE-SW direction (**Figures 7B,D**).

As the 1 year-long data were thought to be too short to examine the tilt data of the BBOSBT-NX, which seemed to contain an annual fluctuation, two more tilt observations were started from 2015 for 2 year-long observations. One was at the KAP3 site, which is shallower and has no special topography, from July and another one was east off Miyagi Prefecture at the slope to the Japan Trench (AoA40 site, 5,430 m depth) from September, as shown in **Figures 7B**, **8A**. They were deployed by the ROVs, Hyper DOLPHIN and KAIKO 7000II, respectively. The latter was recovered in April 2017 with about 1.5 years worth of data, because of the ship schedule. The raw data were processed with the same method used for the 2013 data near the KAP3 site. The result indicates large continuous tilt changes up to several tens of μ radian in both components from the middle of the observation period, which started around June 10 and October 20, 2016, respectively (two purple thick lines in **Figure 8B**). From our experiences of the same type of broadband sensors in BBOBSs, this is not due to an internal sensor problem, because the mass position is usually more stable. It is difficult to judge whether gradual changes in both the components for 7 months before the start of the large and sudden change are annual or not. Another BBOBST-NX at the KAP3 site was recovered in October 2020 by SHINKAI 6500, because of no

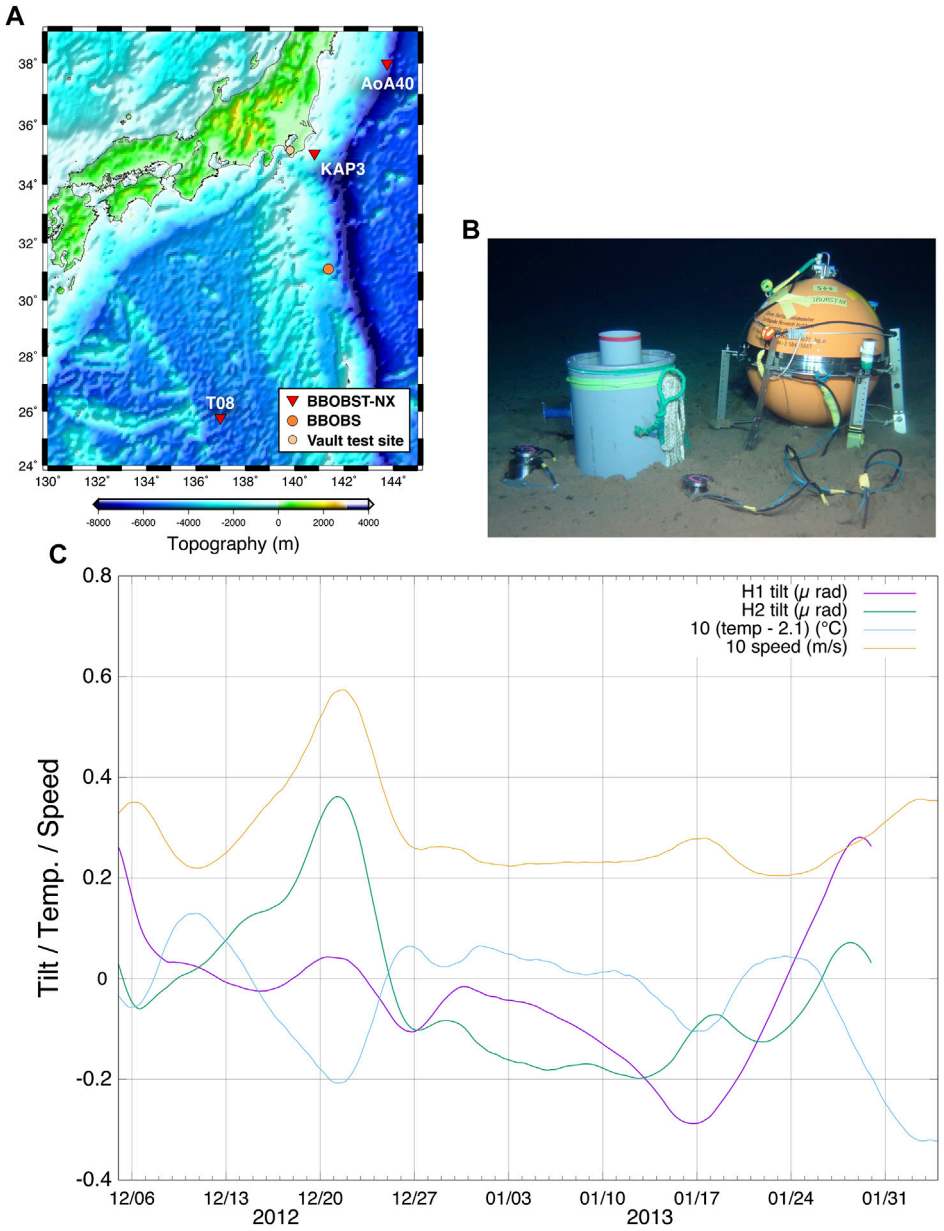

FIGURE 6 | The first seafloor test of the BBOBST-NX. **(A)** The map shows all five sites mentioned in this paper. At the T08 site, where we have performed several observations, the first test was conducted. **(B)** The recording unit and a large gray tube were located close to the sensor unit for the preparation of NX-2G development, to examine influence on the data by these objects. The tube was originally designed as the base for the recording unit, but we failed to place the unit on the tube. The OBDC was also deployed at a 100 m distance. **(C)** Results of the tilt change for 2 months by the BBOBST-NX and water temperature and bottom current speed by the OBDC. All data were resampled with 1 h intervals and moving-averaged (1 week). The tilt data were processed using the Baytap08 program.

ROV dive being performed in 2017 and 2019 due to a strong surface sea current and bad sea conditions, respectively. This newly obtained full 2 years worth of data are still being initially processed.

Tilt Data Using the BBOBS on the Seafloor

We also tried to perform tilt observations using the (standard) BBOBS, free-fall and self-popup type, with mass position data recording on the seafloor, four times at three sites. Compared with the tilt data obtained by the BBOBST-NX using the penetrator sensor system, the effective resolution was generally larger at more than 10 μ radian, which should correspond to the horizontal noise level difference between the BBOBS and the BBOBS-NX as show in Shiobara et al. (2013). However, one case of the BBOBS deployed near the Izu-Ogasawara Trench (5,430 m depth) showed stable and high signal to noise ratio tilt data (**Figure 9**), especially in the H1 component with less mass centering operations. **Figure 9A** shows a kind of a "RAW" tilt

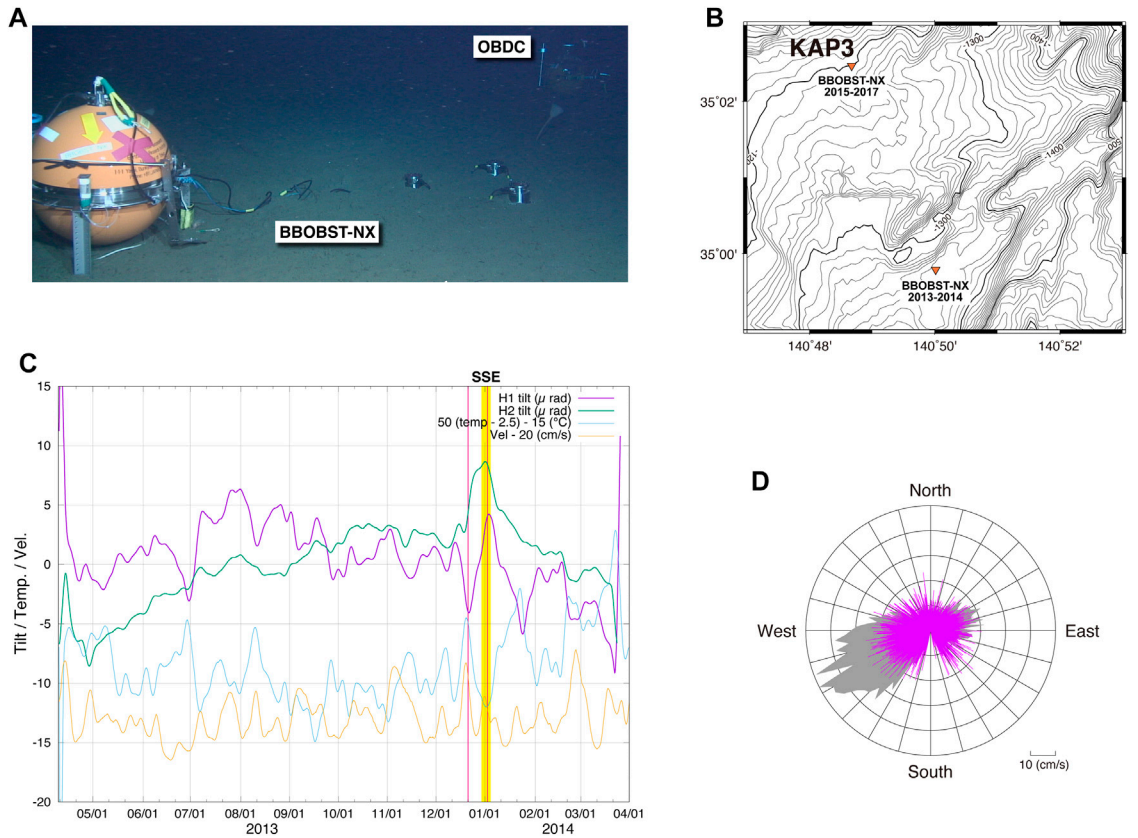

FIGURE 7 | The first feasibility test off the Boso Peninsula. The first long-term observation of the BBOBST-NX was performed at the source area of the SSE with 3–4 years intervals. **(A)** The BBOBST-NX and the OBDC deployed in April 2013 for 1 years-long observation. **(B)** The location map of two sites in 2013–2014 and 2015–2017 (recovered in October 2020). The former site was near the cliff with an NE-SW strike. **(C)** Results of this test observation. In December 28, 2013–January 4, 2014 (yellow rectangle), the SSE was detected (Ozawa, 2014). The data were processed as in **Figure 6C**, after removing the steps at mass centering operations. Two purple vertical lines show two earthquakes mentioned in *SSE Estimations* **(D)** The rose histogram (normalized) of the bottom current direction (gray shade) and the current velocity (purple) from the 1 h averaged OBDC data. In spite of the surface current by Kuroshio, the dominant current direction was toward N245°E, similar to the seafloor topography trend.

data without any process that effects the waveform. Several jumps after July 2015 reflected mass centering operations, when the tilt value exceeded about ±10 μ radian. From the relatively stable period between September 2015 and March 2016, the tilt data were applied to the Baytap08 program and were moving-averaged. The result is in **Figure 9B**, which shows a similar result to that of the BBOBST-NX in **Figure 6C**. So, the possibility of tilt measurement even using the BBOBS exists, if the ambient noise at the site is low enough in the long period range that we want to use for analyses. Nevertheless, there is a limitation in the continuity of the tilt data due to the narrow range of the mass position, as mentioned in *Test at the Land Vault*.

DISCUSSION AND CONCLUSION

Effective Resolution of This Method

The tilt fluctuation shown in **Figure 6C** is about 1 μ radian through the observation period for 2 months, and more stable in a shorter time window. The speed of bottom currents and water temperature measured by the OBDC are also indicated in **Figure 6C**. It shows a clear relation between the speed of bottom currents and the tilt, and also between the temperature and the tilt, which show opposite relation patterns. As the temperature change seems to be caused mainly by the movement of the water block, it would be a secondary indicator by bottom currents, the first importance in the tilt should be the speed of the bottom current. From the tidal deformation model calculation by GOTIC2 (Matsumoto et al., 2001), the tilt change by the Earth tide that includes the oceanic tide loading at this site is less than 0.1 μ radian and mostly contain M_2, S_2, K_1, and O_1 tidal components which occur in approximate 12 or 24 h cycles. Thus, we assumed that a fluctuation of about 1 μ radian at this site was mainly due to the bottom current and the mechanical instability of the broadband sensor.

Although, in the first feasibility test near the KAP3 site, the H1 component of the tilt data showed a fluctuation of a few μ radian order after the tide reduction process by the Baytap08 program as shown in **Figure 7C**. And, as this fluctuation only occurred in the H1 component, this indicates a clear relation with the

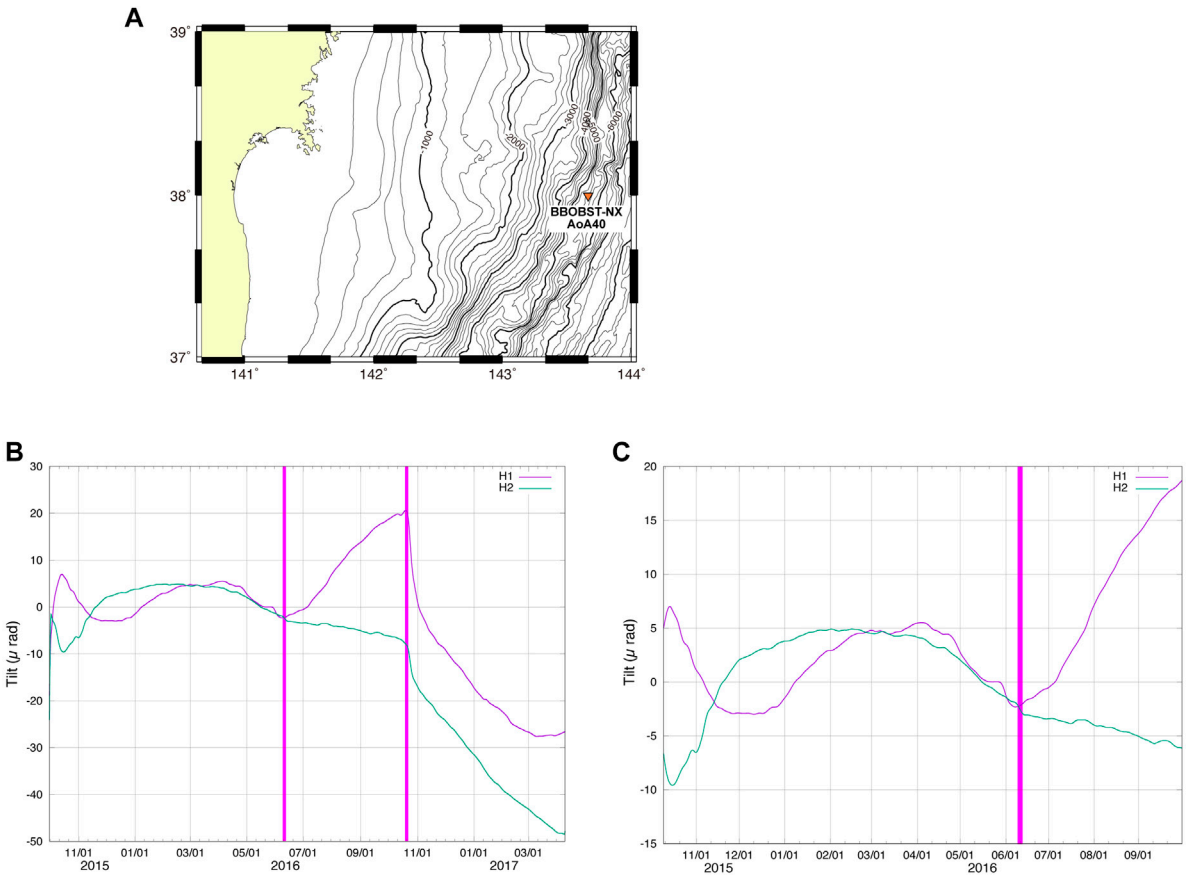

FIGURE 8 | The long-term test off the Miyagi Prefecture. For more detail validation of the BBOBST-NX, a test lasting more than 1 years was conducted at the landward terrace near the Japan trench. **(A)** The location map of the site, AoA40, 5,430 m depth. No bottom current observation was conducted in this time. **(B)** Results of whole observation period of 18 months (earlier recovery due to the ship schedule). The data processing was the same as in **Figure 7C.** The H1 component had a similar direction matched with the maximum gradient (6°) of the seafloor. Two thick purple lines show the starting points of the large tilt change mentioned in *Feasibility Observations* **(C)** Same as **(B)** but re-scaled in both axes as in **Figure 7C** for easier comparison.

temperature change that occurred about 30 h offset of the advance, but not always with the speed of the bottom current, in contrast to that in **Figure 6C**. This H1 component had an azimuth of NE-SW (N63°E) determined by the video picture and the magnetic compass value of the ROV superimposed at the seafloor, which is matched with the dominant bottom current direction (N245°E, SW going current) as shown in **Figure 7D** and the seafloor topography trend (**Figure 7B**). If the temperature affected the broadband sensor, it seems difficult to explain why there was no large fluctuation in the H2 component like that of the H1 component. This means that the temperature change should indicate the move of the water block like in **Figure 6C**, and affected the tilt measurement less. To make it clear, we deployed the next BBOBST-NX in 2015 near the site of the 2013–2014 observation at the KAP3 site with a relatively flat topography (**Figure 7A**). So, it is better to wait for this new data that were recovered in October 2020 for a detailed discussion, but if the SSE may cause a tilt change of more than a few μ radian within a few days, it seems that the BBOBST-NX can resolve it. This detection level looked similar to the case at the AoA40 site (**Figure 8B**). For an easier comparison, this graph is re-scaled with the same range of **Figure 6C** in both axes (**Figure 8C**). Generally, except for the H1 component of **Figure 7C** which had a large (almost monthly) fluctuation, they showed a similar long-term change of a few μ radian per month. If the tilt event is in a short time and the background noise level is low enough, we may resolve the tilt change well less than 1 μ radian as shown in **Figure 9B** even at the seafloor by the BBOBS, but it is better to measure below the seafloor as results of the BBOBST-NX demonstrated.

From these results, the effective resolution of this method is a few μ radian per week or smaller under better conditions of the observation site. If the tilt change is in a shorter time span, it becomes easier to detect. These values look large compared with a tiltmeter on the land, but this method has an inherent advantage in the tilt signal level because of the short distance between the source and the site. To perform better tilt signal detection from the noisy data, the analysis technique in Sato et al. (2017) will be useful. In addition, if the NX-2G with the same broadband sensor of the BBOBST-NX is available, we can deploy the dense array without the use of a submersible vessel near the source area of the SSE in the near future. As mentioned already, tilt measurement in a seafloor borehole is ideal to obtain precise data of a nano radian

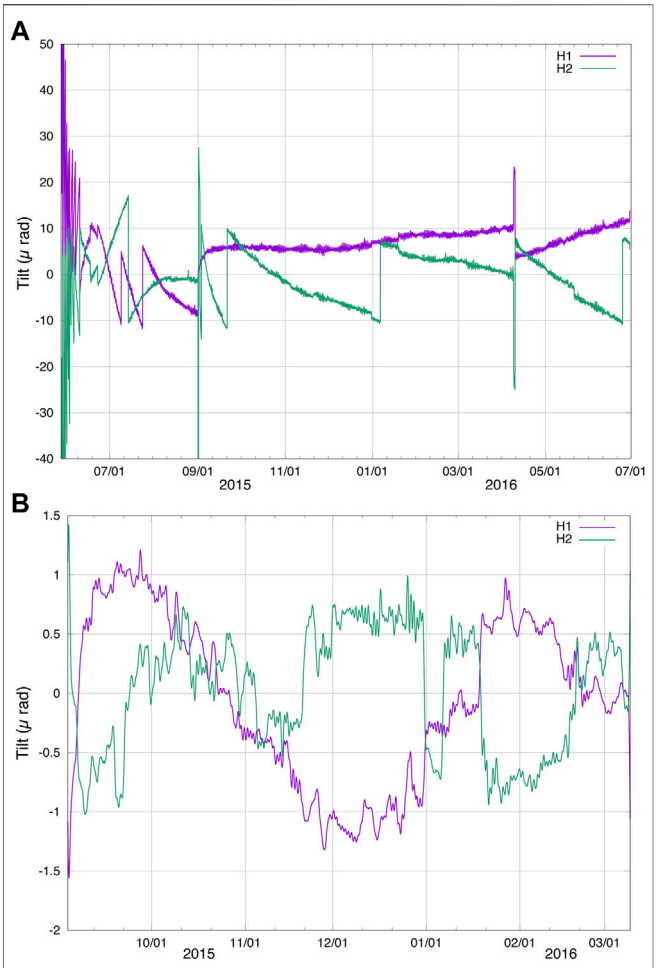

FIGURE 9 | An example of the tilt measurement using the BBOBS. The BBOBS may be used for tilt measurement in the same method as the BBOBST-NX. One example is shown here, which was obtained by the BBOBS deployed near the Izu-Ogasawara trench (**Figure 6A**). **(A)** The whole "RAW" tilt data were only converted from the mass position data, which includes several mass centering steps. However, the H1 component in the middle part seemed stable for 7 months. **(B)** The stable period mentioned above was processed with the same method as in **Figure 6C**. Except for a few parts of mass centering operations in the H2 component, usual tilt fluctuation remained smaller than 1 μ radian.

order, but it requires high cost and drilling ship availability. Instead, this method has high mobility and a lower cost. Therefore, a combination of both the tilt measurement types will be a good solution to achieve the best quality and quantity data for our scientific goals.

SSE Estimations

As SSE observation is the first target of this method, we examined the tilt observed at two sites, whether these tilt values were adequate with that estimated by a ground deformation model. Here, we used an interactive tool, Coulomb3.3 (Toda et al., 2011) based on Okada (1992), and also the method of Sato et al. (2017) for one case, to estimate the tilt from the elevation output of the tool and the method.

In the case of the near KAP3 site (**Figure 7**), the SSE in January 2014 was detected by land sites and ocean bottom pressure gauges (OBPs), and the slip distributions were already analyzed (Sato et al., 2017). For the tilt calculation, the fault plane geometry and slip parameters were almost adjusted to that of Sato et al. (2017) for the Coulomb3.3. The shape of the fault plane was simplified into a rectangle (60 km × 60 km) to cover the main slip region of Sato et al. (2017), and the maximum slip was set as 6.5 cm at the center and gradually decreased toward the edge of the rectangle as shown in **Figure 10A**. The shallowest depth, the dip, and rake angle of the reverse fault plane were assumed as 9.3 km (bsf), 12.0° toward northwest (N315°), and 90°, respectively. The position of the BBOBST-NX was at the origin, and the calculated tilt values were rotated to the H2 component direction (N153°E) (**Figure 10A**). The color shows the vertical displacement distribution obtained by the tool. As this result reflects the tilt when the SSE had ended, the tilt at the site was −2.4 μ radian and the maximum was +3 μ radian in the calculated area, which was about half of the peak value observed in the H2 component (**Figure 7C**). And, we also obtained the calculated H2 tilt value as −0.43 μ radian by the method and the slip distribution of Sato et al. (2017), which was about one sixth smaller than that in **Figure 10A**. Reasons for this difference probably come from the roughness of slip distributions applied for the tool and the method, and also a small difference in the BBOBST-NX position in both models, which were located near the ridge / peak of the elevation distribution (**Figure 10A**). If the tilt observation was far from the source area, the tilt record was a simple increase or decrease pattern. However, above the source area, the polarity of the tilt may change according to the slip propagation, as we observed in **Figure 7C**. As for the seismic activity obtained at the same site and the broadband sensor, even around the time period of the SSE detected (December 28, 2013-January 4, 2014), no significant continuous change was seen in signal strength in the longer period range of 400–10 s for the CMG-3T sensor (**Figure 10B**). There was an intensity change in higher frequency (2–40 Hz) on about December 21, 2013, which was related the earthquake (M_{JMA} 5.5) and its aftershocks occurred at the northwestern edge of this SSE source area. On January 2, 2014, three earthquakes, the largest one of M_{JMA} 5.0, occurred at the western edge, too. These two earthquakes are indicated as purple lines in **Figure 7C** and also as purple arrows in **Figure 10B**. The high intensity at the microseism range (around 0.2 Hz) and longer period on about December 21 were due to high wave height by the low pressure from the meteorological record.

In another case of the AoA40 site, no SSE was detected by other observations at land sites. However, this area is far from any land observatories, more than 130 km, Ito et al. (2013) suggested the possible SSE in 2008 (Mw 6.8), which was based on analysis of the OBPs and the volumetric strain meter data on land. The fault plane was close to the AoA40 site, less than 10 km from its eastern edge. For the tilt calculation, we used similar fault parameters estimated by Ito et al. (2013), as 100 km length in N-S, 40 km width in E-W, and 1 m slip toward east as a reverse fault (rake angle = 90°). The depth and the dip were determined as 5.1 km to the top of the fault plane and 7.0°, respectively, based on the result of the crustal structure study (Miura et al., 2005) nearby. As shown in

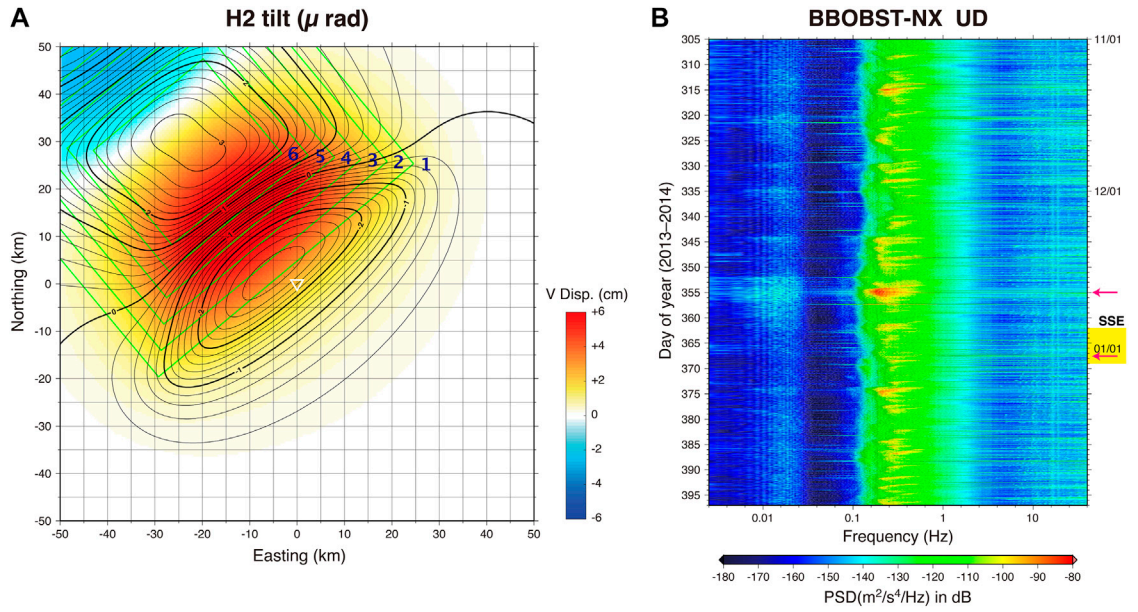

FIGURE 10 | The SSE in 2013–2014 off Boso Peninsula. **(A)** Calculated result of H2 tilt (contour lines in μ radian) based on the fault parameters by Sato et al. (2017). The red-blue color scale shows the vertical displacement by the tool, Coulomb3.3 (Toda et al., 2011). The outline size of the fault plane rectangle is 60 km × 60 km, and it is divided as 6 gradually shrinking rectangles (green, 1–6) with different slip values, 2.0, 2.5, 3.0, 4.5, 5.5, and 6.5 cm, respectively. The inverted triangle (white) shows the BBOBST-NX position, which is at the H2 tilt of −2.4 μ radian. **(B)** The running spectrum of the vertical (UD) component of the broadband sensor's ground velocity signal, before and after the SSE (December 28, 2013–January 4, 2014; indicated as a yellow rectangle). The time (vertical axis) resolution is 1 h. There was no significant change in signal level in the <0.1 Hz frequency range during the SSE. Some earthquakes around the SSE source area occurred, as shown in the >2 Hz frequency range. Two purple arrows indicate the two earthquakes mentioned in *SSE Estimations*.

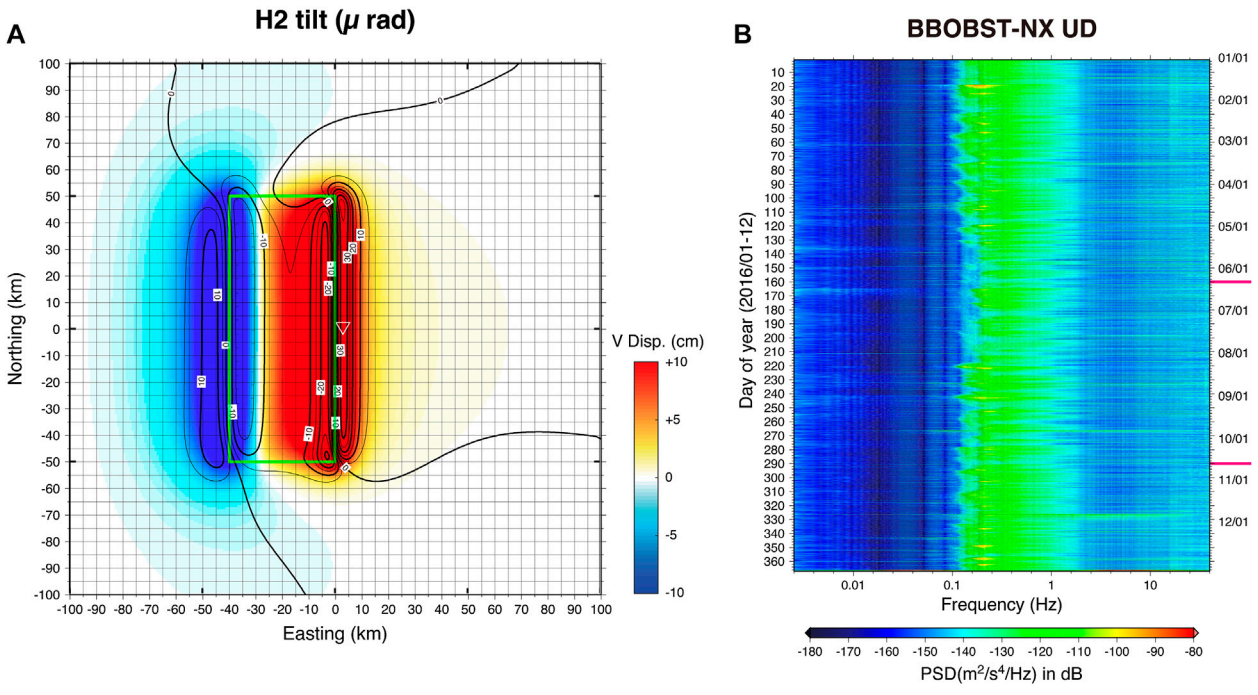

FIGURE 11 | A possible SSE for the large tilt change at the AoA40 site. **(A)** Similar result of **Figure 10A**, but for the assumed SSE based on Ito et al. (2013). The green rectangle shows the fault plane (100 km × 40 km), and the slip amount is 1 m. In this case, the position of the BBOBST-NX is unknown. However, the calculated tilt range is between −20 and +30 in μ radian. **(B)** The running spectrum of the vertical (UD) component is the same as in **Figure 10B**, but for the AoA40 site in 2016, including two starting points of the large tilt change at about June 10 and October 20, which are shown as two thick purple lines.

Figure 11A, the range of the tilt was between several tens of μ radian of plus and minus, which was a same order of the tilt observed, but the location of the AoA40 site was unknown relative to this assumed fault and the tilt was only estimated when the fault slip had ended. Seafloor pressure gauges of the S-net (Uehira et al., 2018) in this area did also not show large change. One explanation for this large tilt change may be an event in the shallow sediment, such as a land slide. The azimuth of the H1 component (N140°E) was close to the maximum gradient of the seafloor (6°) from the fine topography data. Regarding the positions of the BBOBST-NX in deployment and recovery, there were no clear differences, and the condition of the instrument and the seafloor in the recovery ROV dive had no remarkable change. So that, it was still difficult to find a reason for the large tilt change observed. In the seismic data of the BBOBST-NX, there were no significant change in the signal strength in the whole frequency range according to two tilt changes around June 10 and October 20, 2016 (**Figure 11B**), as in **Figure 10B**, except for aftershocks mostly of the 2011 off-Tohoku earthquake shown in higher frequency (2–20 Hz).

In both cases, the necessity of the tilt array observation and a dynamic analysis of tilt source modelling became essential to further study of the SSE process. And, it is highly recommended that the tilt and absolute pressure are simultaneously observed as a geodetic measurement site on the seafloor.

DATA AVAILABILITY STATEMENT

The datasets used in **Figures 2, 3, 5–11** can be found in the OHP-DMC (http://ohpdmc.eri.u-tokyo.ac.jp) and in a cloud data folder (https://www.icloud.com/iclouddrive/0MlBeQ0auaB6Yng6bnfbY5GIw#Frontiers_in_Seafloor_Geodesy).

AUTHOR CONTRIBUTIONS

HSH and MS initiated the concept of the method. HSH, AI, and HSU performed several test observations. HSH, HSU and TS analyzed the data. All the authors wrote the manuscript and contributed to the interpretation of results.

FUNDING

This research was supported by JSPS (Japan Society for the Promotion of Science) KAKENHI, Grant-in-Aid for Scientific Research (B) of JP19340121 for the BBOBS-NX and (C) of JP23540489 for the BBOBST-NX. It was also partly supported by the Ministry of Education, Culture, Sports, Science, and Technology (MEXT) of Japan, under its The Second Earthquake and Volcano Hazards Observation and Research Program (Earthquake and Volcano Hazard Reduction Research).

ACKNOWLEDGMENTS

The authors thank the captains, crews, ROV operation teams, and land support staff of the Japan Agency for Marine-Earth Science and Technology and Nippon Marine Enterprises Ltd. for their great help in several research cruises for this study. Drs. R. Hino and T. Isse and technical staff T. Yagi, helped us in several tests on land and during cruises. We also express our appreciation to the editor and two reviewers for their comments which were valuable for improving this manuscript.

REFERENCES

Anderson, G., Constable, S., Staudigel, H., and Wyatt, F. K. (1997). A seafloor long-baseline tiltmeter. *J. Geophys. Res.* 102 (B9), 20269–20285. doi:10.1029/97JB01586

Araki, E. (2017). Long-term seafloor borehole observation in the Nankai Trough. *Report of the Coordinating Committee for Earthquake Prediction, Japan* 98, 12–19, 502–506 [in Japanese].

Araki, E., Shinohara, M., Sacks, S., Linde, A., Kanazawa, T., Shiobara, H., et al. (2004). Improvement of seismic observation in the ocean by use of seafloor boreholes. *Bull. Seism. Soc. Am.* 94, 678–690. doi:10.1785/0120020088

Collins, J. A., Vernon, F. L., Orcutt, J. A., Stephen, R. A., Peal, K. R., Wooding, F. B., et al. (2001). Broadband seismology in the oceans: lessons from the ocean seismic network pilot experiment. *Geophys. Res. Lett.* 28, 49–52. doi:10.1029/2000GL011638

Duennebier, F. K., Cessaro, R. K., and Harris, D. (1987). Temperature and tilt variation measured for 64 Days in hole 581C. *Init. Repts.* 88, 161–166. doi:10.2973/DSDP.PROC.88.112.1987

Fabian, M., and Villinger, H. (2008). Long-term tilt and acceleration data from the logatchev hydrothermal vent field, mid-atlantic ridge, measured by the bremen ocean bottom tiltmeter. *Geochem. Geophys. Geosyst.* 9, Q07016. doi:10.1029/2007GC001917

Fabian, M., and Villinger, H. (2007). The Bremen ocean bottom tiltmeter (OBT) – a technical article on a new instrument to monitor deep sea floor deformation and seismicity level. *Mar. Geophys. Res.* 28, 13–26. doi:10.1007/s11001-006-9011-4

Hino, R., Ii, S., Iinuma, T., and Fujimoto, H. (2009). Continuous long-term seafloor pressure observation for detecting slow-slip interplate events in Miyagi-Oki on the landward Japan Trench Slope. *J. Disaster Res.* 4, 72–82. doi:10.20965/jdr.2009.p0072

Hirose, H., Hirahara, K., Kimata, F., Fujii, N., and Miyazaki, S. (1999). A slow thrust slip event following the two 1996 Hyuganada earthquakes beneath the Bungo Channel, southwest Japan. *Geophys. Res. Lett.* 26 (21), 3237–3240. doi:10.1029/1999GL010999

Ide, S., Beroza, G. C., Shelly, D. R., and Uchide, T. (2007). A scaling law for slow earthquakes. *Nature* 447, 76–79. doi:10.1038/nature05780

Incorporated Research Institutions for Seismology (IRIS). (1994). *Estimation of seismic noise," in federation of digital seismograph networks: station book*. Washington, DC: IRIS data management system.

Ishii, H., Matsumoto, S., Suzuki, K., Hitara, Y., Takahashi, T., Wakasugi, T., et al. (1992). Development of a new water-tube tiltmeter (ERI-90 type): float type without mechanical suspension. *Bull. Eartq. Res. Inst. Univ. Tokyo* 67, 79–87.

Ito, Y., Hino, R., Kido, M., Fujimoto, H., Osada, Y., Inazu, D., et al. (2013). Episodic slow slip events in the Japan subduction zone before the 2011 Tohoku-Oki earthquake. *Tectonophys* 600, 14–26. doi:10.1016/j.tecto.2012.08.022

Kajikawa, H., and Kobata, T. (2014). Reproducibility of calibration results by 0-A-0 pressurization procedures for hydraulic pressure transducers. *Meas. Sci. Technol.* 25, 1. doi:10.1088/0957-0233/25/1/015008

Kaneda, Y., Kawaguchi, K., Araki, E., Matsumoto, H., Nakamura, T., Kamiya, S., et al. (2015). Development and application of an advanced ocean floor network system for megathrust earthquakes and tsunamis, seafloor observatories. *Springer Praxis Books* 643–662. doi:10.1007/978-3-642-11374-1_25

Matsumoto, K., Takanezawa, T., and Ooe, M. (2001). GOTIC2: a program for computation of oceanic tidal loading effect. *J. Geod. Soc. Japan* 47, 243–248. doi:10.11366/sokuchi1954.47.243

Miura, S., Takahashi, N., Nakanishi, A., Tsuru, T., Kodaira, S., and Kaneda, Y. (2005). Structural characteristics off Miyagi forearc region, the Japan Trench

seismogenic zone, deduced from a wide-angle reflection and refraction study. *Tectonophysics* 407, 165–188. doi:10.1016/j.tecto.2005.08.001

Obara, K. (2002). Nonvolcanic deep tremor associated with subduction in southwest Japan. *Science* 296, 1679–1681. doi:10.1126/science.1070378

Okada, Y. (1992). Internal deformation due to shear and tensile faults in a half-space. *Bull. Seismol. Soc. Am.* 82, 1018–1040.

Ozawa, S. (2014). Shortening of recurrence interval of Boso slow slip events in Japan. *Geophys. Res. Lett.* 41, 2762–2768. doi:10.1002/2017GL060072

Peterson, J. (1993). *Observations and modeling of seismic background noise*. Reston, VA: USGS Open File Report, 93–322.

Sacks, I. S., Suyehiro, K., Acton, G. D., et al. (2000). Proc. ODP, Initial Reports. 186: College Station, TX (Ocean Drilling Program). doi:10.2973/odp.proc.ir.186.2000

Sakata, S., and Shimada, S. (1984). Development of the ocean bottom tiltmeter (2). *J. Geodetic Soc. Japan*. 30 (1), 50–58 [in Japanese].

Sato, T., Hasegawa, S., Kono, A., Shiobara, H., Yagi, T., Yamada, T., et al. (2017). Detection of vertical motion during a Boso slow-slip event by ocean-bottom pressure gauges. *Geophys. Res. Lett.* 44, 2710–2715. doi:10.1002/2017GL072838

Sato, T., and Kasahara, J. (1999). Development of free-fall and pop-up ocean bottom tiltmeters. *Abstract of jpgu*.

Sáez, M., Ruiz, S., Ide, S., and Sugioka, H. (2019). Shallow nonvolcanic tremor activity and potential repeating earthquakes in the Chile triple junction: seismic evidence of the subduction of the active nazca–antarctic spreading center. *Seis. Res. Lett.* 90, 5. doi:10.1785/0220180394

Shimamura, H., and Kanazawa, T. (1988). Ocean bottom tiltmeter with acoustic data retrieval system implanted by a submersible. *Marine Geophys. Res.* 9, 237–254.

Shinohara, M., Suyehiro, K., and Shiobara, H. (2012). "CHAPTER 7.5 Marine seismic observation," in *New manual of seismological observatory practice (NMSOP-2)*. Editor P. Bormann, Potsdam: IASPEI, GFZ German Research Centre for Geosciences. doi:10.2312/GFZ.NMSOP-2_ch7

Shiobara, H., Ito, A., Sugioka, H., and Shinohara, M. (2019). New era of ocean bottom broadband seismology with penetrator system of the autonomous BBOBS-NX (NX-2G). Abstract of IUGG2019. MONTREAL, JUL. 16, S05A, IUGG19-0453.

Shiobara, H., Kanazawa, T., and Isse, T. (2013). New step for broadband seismic observation on the sea floor: BBOBS-NX. *IEEE-JOE.* 38. 2, 396–405. doi:10.1109/JOE.2012.2222792

Spiess, F. N., Chadwell, C. D., Hildebrand, J. A., Young, L. E., Purcell, G. H., Jr., and Dragert, H. (1998). Precise GPS/Acoustic positioning of seafloor reference points for tectonic studies. *Phys. Earth Planet. Int.* 108, 101–112. doi:10.1016/S0031-9201(98)00089-2

Suetsugu, D., and Shiobara, H. (2014). broadband ocean bottom seismology. *Annu. Rev. Earth Planet Sci.* 42, 27–43. doi:10.1146/annurev-earth-060313-054818

Sugioka, H., Okamoto, T., Nakamura, T., Ishihara, Y., Ito, A., Obana, K., et al. (2012). Tsunamigenic potential of the shallow subduction plate boundary inferred from slow seismic slip, *Nature Geosci.* 5 (6), 414–418. doi:10.1038/ngeo1466

Suyehiro, K., Kanazawa, T., Hirata, N., and Shinohara, M. (1995). Ocean downhole seismic project. *J. Phys. Earth* 43, 599–618.

Tamura, Y., Sato, T., Ooe, M., and Ishiguro, M. (1991). A procedure for tidal analysis with a Bayesian information criterion. *Geophys. J. Internat.* 104, 507–516. doi:10.1111/j.1365-246X.1991.tb05697.x

Toda, S., Stein, R. S., Sevilgen, V., and Lin, J. (2011). Open-File Report 2011–1060. Coulomb 3.3 Graphic-rich deformation and stress-change software for earthquake, tectonic, and volcano research and teaching—user guide: *U.S. Geological Survey*, 63. Available at https://pubs.usgs.gov/of/2011/1060/

Tolstoy, M., Constable, S., Orcutt, J., Staudigel, H., Wyatt, F. K., and Anderson, G. (1998). Short and long baseline tiltmeter measurements on axial seamount, Juan de Fuca Ridge. *Phys. Earth Planet. Int.* 108, 129–141.

Uehira, K., Kunugi, T., Shiomi, K., Aoi, S., Takahashi, N., Chikasada, N. Y., et al. (2018). Ground motion noises observed by Seafloor observation network for earthquakes and tsunamis along the Japan Trench (S-net). American Geophysical Union, Fall Meeting 2018, OS21E-1612.

Webb, S. C., Constable, S. C., Cox, C. S., and Deaton, T. K. (1985). A seafloor electric field instrument. *J. Geornagn. Geoelectr.* 37, 1115–1130. doi:10.5636/jgg.37.1115

Westphal, J. A., Carr, M. A., and Miller, W. F. (1983). Expendable bubble tiltmeter for geophysical monitoring. *Rev. Sci. Instrum.* 54 (4), 415–418.

Conflict of Interest: The authors declare that the research was conducted in the absence of any commercial or financial relationships that could be construed as a potential conflict of interest.

frontiers in Earth Science

ORIGINAL RESEARCH
published: 06 April 2021
doi: 10.3389/feart.2021.636156

Geodetic Seafloor Positioning Using an Unmanned Surface Vehicle—Contribution of Direction-of-Arrival Observations

Pierre Sakic[1], *Clémence Chupin*[2], *Valérie Ballu*[2]*, *Thibault Coulombier*[2], *Pierre-Yves Morvan*[3], *Paul Urvoas*[3], *Mickael Beauverger*[4] *and Jean-Yves Royer*[4]

[1] GFZ German Research Centre for Geosciences, Helmholtz-Zentrum Potsdam, Potsdam, Germany, [2] Littoral Environnement et Sociétés, CNRS and University of La Rochelle, La Rochelle, France, [3] iXBlue, Acoustic Positioning Division, Brest, France, [4] Laboratoire Géosciences Océan, CNRS and University of Brest, Brest, France

Precise underwater geodetic positioning remains a challenge. Measurements combining surface positioning (GNSS) with underwater acoustic positioning are generally performed from research vessels. Here we tested an alternative approach using a small Unmanned Surface Vehicle (USV) with a compact GNSS/Acoustic experimental set-up, easier to deploy, and more cost-effective. The positioning system included a GNSS receiver directly mounted above an Ultra Short Baseline (USBL) module integrated with an inertial system (INS) to correct for the USV motions. Different acquisition protocols, including box-in circles around transponders and two static positions of the USV, were tested. The experiment conducted in the shallow waters (40 m) of the Bay of Brest, France, provided a data set to derive the coordinates of individual transponders from two-way-travel times, and direction of arrival (DOA) of acoustic rays from the transponders to the USV. Using a least-squares inversion, we show that DOAs improve single transponder positioning both in box-in and static acquisitions. From a series of short positioning sessions (20 min) over 2 days, we achieved a repeatability of ∼ 5 cm in the locations of the transponders. Post-processing of the GNSS data also significantly improved the two-way-travel times residuals compared to the real-time solution.

Keywords: seafloor geodesy, GNSS/acoustics, underwater positioning, unmanned surface vehicle, direction of acoustic ray arrivals, direction of arrival

OPEN ACCESS

Edited by:
Keiichi Tadokoro, Nagoya University, Japan

Reviewed by:
Motoyuki Kido, Tohoku University, Japan
Horng-Yue Chen, Institute of Earth Sciences, Academia Sinica, Taiwan
Huimin Liu, Qingdao National Laboratory for Marine Science and Technology, China

***Correspondence:**
Valérie Ballu
valerie.ballu@univ-lr.fr

Specialty section:
This article was submitted to Solid Earth Geophysics, a section of the journal Frontiers in Earth Science

Received: *01 December 2020*
Accepted: *01 March 2021*
Published: *06 April 2021*

Citation:
Sakic P, Chupin C, Ballu V, Coulombier T, Morvan P-Y, Urvoas P, Beauverger M and Royer J-Y (2021) Geodetic Seafloor Positioning Using an Unmanned Surface Vehicle—Contribution of Direction-of-Arrival Observations. Front. Earth Sci. 9:636156. doi: 10.3389/feart.2021.636156

1. INTRODUCTION

In plate tectonics, precise positioning of points on the seafloor is a key for applications ranging from precise *in situ* plate motion to local-fault loading assessment. Since Spiess et al. (1998), numerous studies have demonstrated that combining surface GNSS positioning with underwater acoustic positioning, known as the GNSS/A approach, is an adequate methodology for this purpose.

GNSS/A positioning is generally performed from research vessels, which are precisely positioned by GNSS, offer facilities to deploy acoustic transponders on the seafloor, and are often equipped with an acoustic modem and an inertial system to monitor the ship's motions. However, such vessels may generate unwanted acoustic noise, particularly when maintaining a fixed position above transponders; in addition, the offsets between the GNSS antennas on a mast, the underwater acoustic modem and the inertial system may not be known accurately enough to correct for the

lever arms between them. Since GNSS/A data usually need to be simultaneously acquired for several hours above a network of transponders (e.g., Gagnon et al., 2005; Yasuda et al., 2017; Ishikawa and Yokota, 2018), using a large vessel may also not be cost-effective.

To palliate these inconveniences, we tested a GNSS/A experiment with a small Unmanned Surface Vehicle (USV). Such devices are now commonly used in marine surveys, to retrieve data from seafloor instruments or to directly acquire data (e.g., Berger et al., 2016; Chadwell et al., 2016; Penna et al., 2018; Foster et al., 2020). Our USV was equipped with a GNSS antenna mounted directly above an Ultra Short Baseline System (USBL) integrated with an inertial system (INS). So, we combined a silent vehicle (electrical propulsion) with a compact GNSS/A system with a lever arm reduced to ∼1 m. Here we report the results from an experiment conducted with this autonomous system in shallow waters to position transponders laid on the seafloor. The acquired data allowed us to test and improve a method for positioning a single transponder that takes advantage of the use of an USBL instead of a simple acoustic modem, the former providing more information than just two-way-travel times.

2. EXPERIMENTAL SETUP

The principle of a GNSS/A experiment is to use a surface platform as a relay between surface positioning relative to satellites and underwater acoustic positioning relative to transponders fixed on the seafloor. In this experiment, carried out in the Bay of Brest, France, in July 2019, we tested a set of new instruments:

- four CANOPUS transponders developed by iXblue company (section 2.1);
- a small USV catamaran designed by L3 Harris—ASV company, equipped with a GNSS receiver and a GAPS integrated USBL/INS system also from iXblue (section 2.2).

2.1. The Underwater Transponders

The CANOPUS transponders (Complex Acoustic Network for Offshore Positioning and Underwater Surveillance) are a new generation of acoustic transponders developed by iXblue. These new transponders handle underwater acoustic communication, signal processing and algorithms and offer improved performances for acoustic positioning of submarine vehicles or for geodetic experiments. The CANOPUS transponders were developed with a long autonomy (up to 3–4 years) and operate up to 4,000 m depth.

In July 2019, four CANOPUS transponders were deployed in the shallow waters of the Bay of Brest from R/V Albert Lucas (**Figures 1**, **2**). The transponders were mounted on tripods, placing the acoustic heads 1.5m above the seabed, and immersed at an average depth of 38 m. The initial objective was to form a 30 m quadrilateral, but unfortunately one of tripod tipped over during deployment and the final geometry ended up being a nearly isosceles triangle of 30 m side.

The CANOPUS transponders are omni-directional, and measure inter-transponder two-way travel times. This

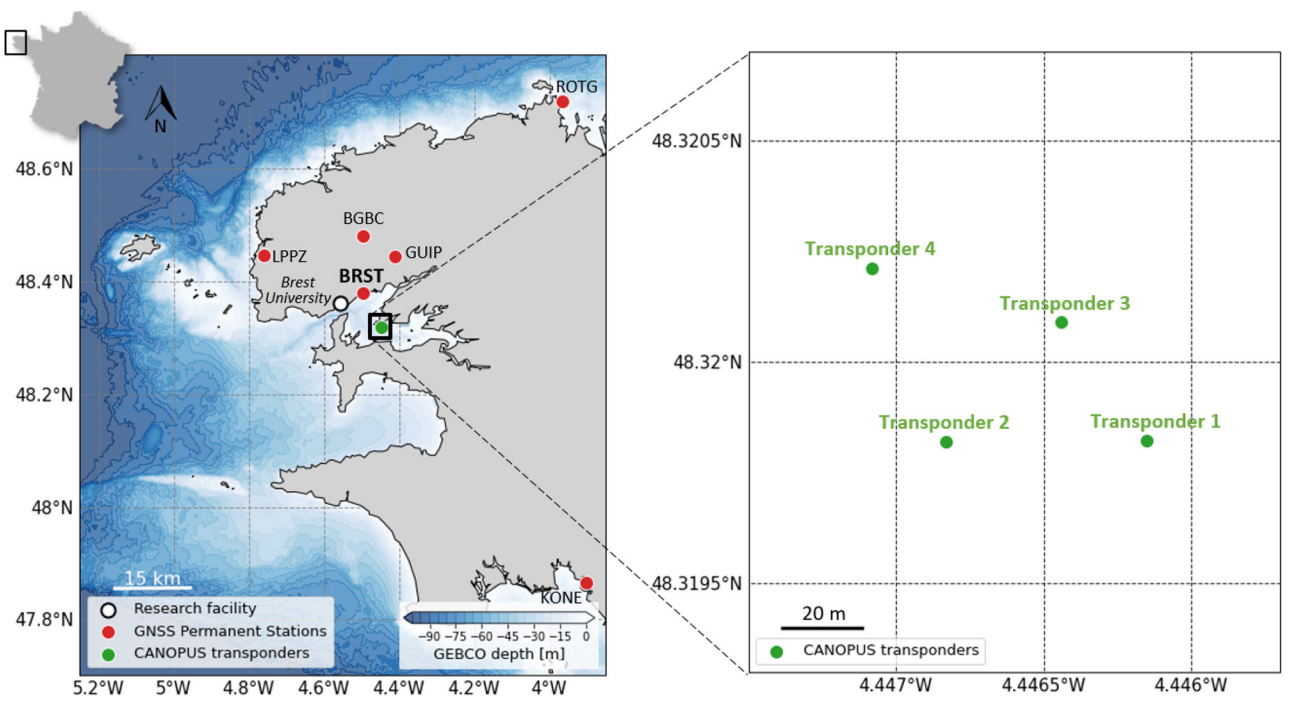

FIGURE 1 | Study area. (Left) The Bay of Brest and the permanent GNSS network (red dots); (Right) Geographic locations of the transponders during the experiment.

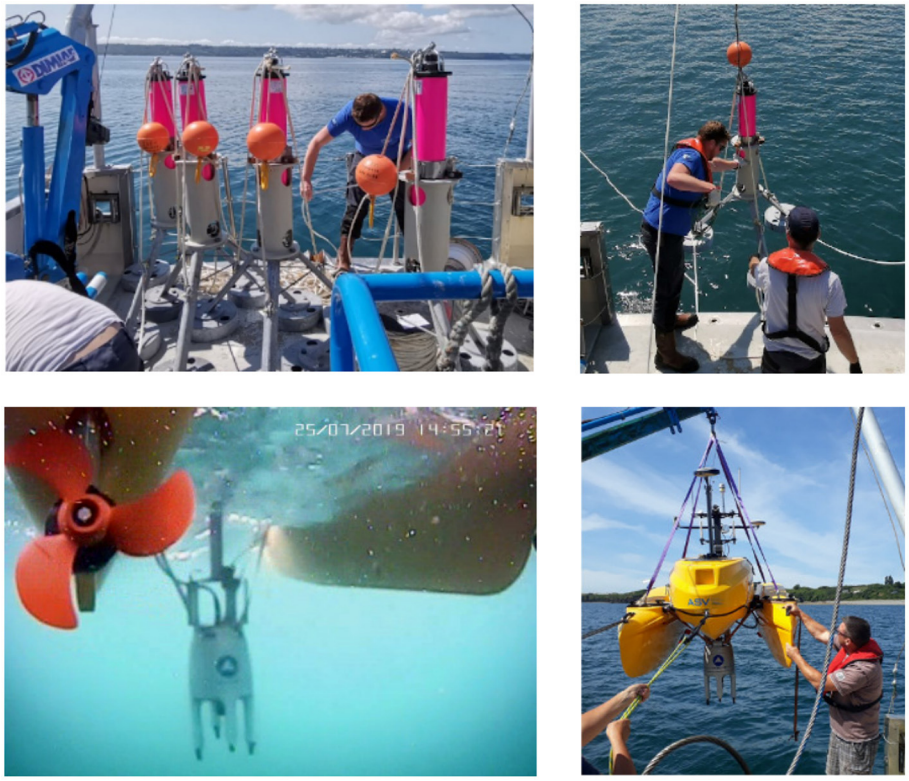

FIGURE 2 | (Upper left and upper right) Preparation and deployment of the CANOPUS transponders mounted on tripods. The fourth one was not used in this study; (Lower left) iXblue integrated USBL/INS system (GAPS) mounted on PAMELi adjustable daggerboard; (Lower right) Deployment of PAMELi USV from R/V Albert Lucas. Note the installation of the GNSS antenna on the daggerboard, directly above the GAPS.

information can be used to measure relative displacements between transponders (e.g., Sakic et al., 2016; Lange et al., 2019; Petersen et al., 2019) or to constrain GNSS/A multi-transponder array positioning (e.g., Sweeney et al., 2005; Sakic et al., 2020). They can also communicate with the surface for telemetry or positioning purposes using an USBL or an acoustic modem. The transponders were equipped with temperature and pressure sensors, but this information was not used here, since we collected sound-speed profiles during the acquisition sessions. The transponder inclinometers showed that the tripods remained stable throughout the experiment.

2.2. The Surface Platform and Positioning Systems

An innovative aspect of this experiment was to mount the GNSS/A positioning system on an Unmanned Surface Vehicle (USV) named PAMELi (*Plateforme Autonome Multicapteurs pour l'Exploration du Littoral*—Autonomous Multisensor Platform for Coastal Exploration). The PAMELi project was developed by La Rochelle University for repeated and multidisciplinary monitoring of shallow coastal areas (Chupin et al., 2020). The vehicle, built by ASV, is a small battery-powered catamaran (3 m-long, 1.6 m-wide, weighting 300 kg), remotely controlled from a mother-ship or land through Wi-Fi, GSM, or VHF communications. Capable of cruising at 3–4 kn, it has an autonomy of about 8 h. Profiles can be pre-programmed or set-up interactively by remote control; in addition, with a propeller on each of its floats, the USV can maintain a stationary position within a radius given by the operator. Data from the mounted sensors can be telemetered to the operator and/or stored internally.

The GNSS receiver was a Spectra SP80, able to track and record signals from several GNSS constellations. The sampling rate was set at 1 Hz during the whole experiment. The Real-Time Kinematic (RTK) positioning mode was used to provide real-time positions to the GAPS system. The GNSS antenna was mounted directly above the underwater acoustic system on the keel of the USV (**Figure 2**).

The acoustic system was a GAPS (Global Acoustic Positioning System) M7 integrated USBL/INS device, manufactured by iXblue. Such devices are commonly used on oceanographic vessels for precise positioning of underwater devices or vehicles. The GAPS is a 64 cm-high and 30 cm-wide cylinder with four legs (**Figure 2**). The acoustic signal is emitted by a central acoustic head and received by an antenna made of four hydrophones ca. 21 cm apart. This design allows to measure both the two-way travel times and the direction of the return signal from the interrogated underwater device, here the transponders. In an optimal configuration, i.e., for a SNR $\geq$ 20 dB, the GAPS

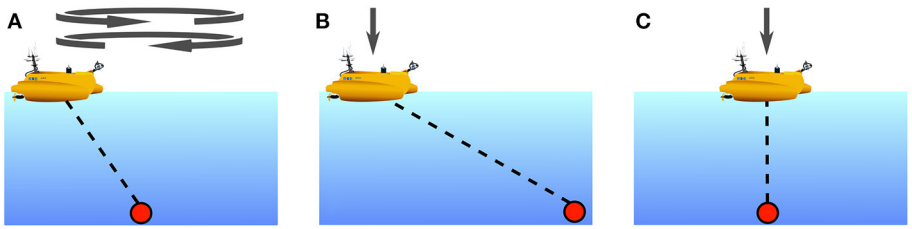

FIGURE 3 | Different data acquisition modes: **(A)** *Box-in*, with clockwise and anti-clockwise circles around and centered on the transponder (red dot), **(B)** *Static-slanted*, and **(C)** *Static-above* the transponder.

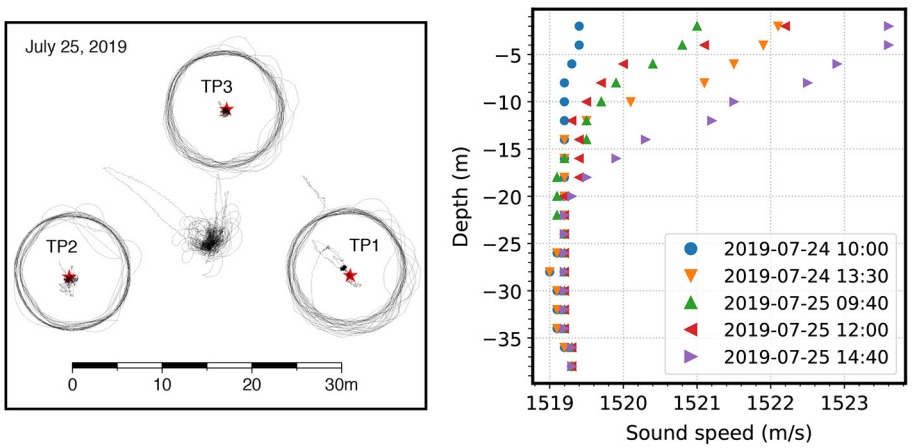

FIGURE 4 | (Left) Data acquisition trajectories of the USV during Day 2, including box-in circles and stations above or slanted relative to the transponders (TP, red stars). **(Right)** Sound-speed profiles acquired during the experiment.

has a range accuracy of 2 cm and a bearing accuracy of 0.03°. The signal uses a frequency-shift keying modulation carried by a 26 kHz-signal. The GAPS is able to range every 0.8 s. For this experiment, it was configured to range the transponders every 2 s. Ship's motion are corrected for by the GAPS' inertial system (INS), which also filters out spurious real-time GNSS positions. This INS has an accuracy of 0.01° on the heading, roll and pitch components. With a GNSS receiver connected to the GAPS, vertical and horizontal displacements of the selected center of mass of the system (acoustic head or INS center) were thus fully constrained (pitch, roll, latitude, longitude, heading). The acoustic system, quasi weightless in sea-water, was immersed in the front of the USV, away from the propellers, at $\sim$ 1 *m* depth (**Figure 2**). Despite such keel, the USV remained very maneuverable, and operated smoothly in winds up to 12 kn. The GNSS and GAPS data acquisition were monitored in real-time from R/V Albert Lucas. The recorded noise was most of the time below 60 dB re $\mu Pa/\sqrt{Hz}$, whereas, on a regular vessel, the noise would range between 70 and 85 dB.

2.3. Experimental Protocols

The GNSS/A experiment was carried out from July 23 to 25, 2019 in the Bay of Brest during the GEODESEA-2019 experiment (Royer et al., 2021). Its goals were (1) to test the CANOPUS transponders and their auxiliary sensors, and (2) to test the feasibility of GNSS/A positioning from an USV. The Bay of Brest provided a convenient area, close to port and sheltered from the open-sea swell. The nearest permanent GNSS station (BRST) was only 8 km away from the deployment area (see also section 3.2). Five vertical sound-velocity profiles were acquired during the experiment using a CTD probe. The profiles are shown in **Figure 4**. To avoid strong tidal currents, the experience took place during a neap tide period (coefficients 50 to 44)[1] and weather conditions were sunny and calm. The tides had a 2–3 m amplitude (i.e., the depth of the transponders varied by that amount about an average depth of 38 m).

During deployment, transponder TP#4 tipped over, but despite its transducer on the ground, operated at nominal capacity. Still, this transponder will not be considered here. For the absolute positioning test, three different acquisition protocols were tested (**Figures 3**, **4**):

- In a *Box-in mode*, the USV navigated for about 20–30 min along repeated circles of 10 m diameter (about 1/4th the water depth) centered on the transponder of interest. Thus, the shooting angle w.r.t. to the vertical was $\sim$12° and the average

[1]The French Navy's hydrographic and oceanographic service (SHOM) defines the amplitude of the tides for the French coasts on a scale ranging from 20 to 120.

slant range was equal to the depth. The circles were traveled both clockwise and anti-clockwise;
- In a *Static-above mode*, the USV remained stationary for 10–15 min within a 3 m circle centered at the apex of the considered transponder;
- In a *Static-slanted mode*, the USV remained stationary during 1 h within a 3 m circle centered at the apex of the barycenter of the triangle made by the three vertical transponders. Acoustic rays were then slanted by about ∼20°. In this mode, the GAPS ranged each transponder in turn.

3. DATA PROCESSING

3.1. Inputs and Outputs

The ultimate objective of GNSS/A positioning is to determine the coordinates of seafloor transponders. For each transponder i, we note its coordinates $\mathbf{X}_{R_i} = [x_{R_i}, y_{R_i}, z_{R_i}]$. We assume these coordinates fixed and stable during the whole experiment, since the transponders are installed on rigid and ballasted metal tripods. These coordinates will be derived from the following observations (represented in **Figure 5**):

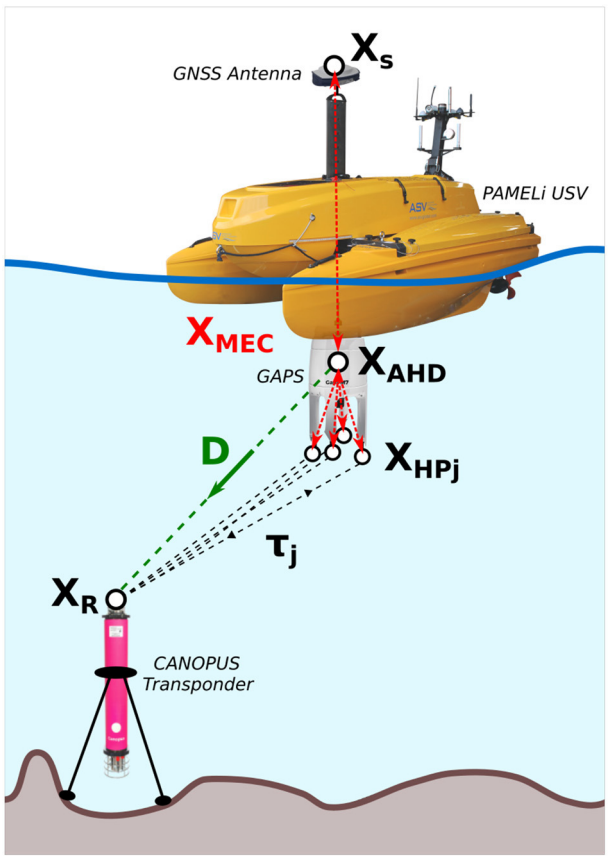

FIGURE 5 | Components and vector representation of the GNSS/A system (description in section 3.1).

- The positions of the embarked surface devices $\mathbf{X}_S = [x_S, y_S, z_S]$, provided by GNSS observations. Since the USV is moving, $\mathbf{X}_S$ is a function of time and thus we have, for each epoch t of the experiment, $\mathbf{X}_S(t)$. The embarked devices are, namely:
  - the GNSS antenna whose position is $\mathbf{X}_{GNSS}(t)$.
  - the GAPS acoustic head emitting the acoustic pings, whose position is $\mathbf{X}_{AHD}(t)$.
  - and the GAPS four-hydrophones receiving the returned pings, whose positions are $\mathbf{X}_{HPj}(t)$, where $j \in [1, 4]$.
- The tie vectors $\mathbf{X}_{MEC}$ (also known as lever arms), that link the different surface devices in the mechanical frame *MEC* of the USV. These vectors were measured manually on-shore before the USV deployment;
- The attitude of the USV, i.e., the heading α, pitch β, and roll γ angles recorded by the Inertial Motion Unit (IMU) integrated in the GAPS. So for each epoch t, $\mathbf{R}(t) = [\alpha(t), \beta(t), \gamma(t)]$ is acquired;
- The two-way-travel times τ_i (called TWTT hereinafter) between the GAPS and the seafloor transponders for each acoustic ping i. Each TWTT is received at instant $t_{TWTT,rec,i}$. The emission instant $t_{TWTT,emi,i}$ of the corresponding ping is determined by the relation $t_{TWTT,rec,i} = t_{TWTT,emi,i} + \tau_i + \tau_{TAT}$. The τ_{TAT} (for *Turn Around Time*) is a preset delay before the transponder replies to an interrogating signal. Since there are four hydrophones recording separately, for one emitted ping i, there are four TWTT values $\tau_{i,j}$ and four distinct reception instants $t_{TWTT,rec,i,j}$;
- The direction of arrival (also known as direction cosines, called DOA hereinafter), corresponding to the vectors between the GAPS and each transponder. Here, we used the DOA values directly estimated by the GAPS interface. In addition to the TWTTs, for each ping i, the DOA vector is defined as $\mathbf{D}_i = [d_{x,i}, d_{y,i}, d_{z,i}]$, which we assumed normalized;
- And a sound-speed profile (SSP) made of two vectors $\mathbf{Z}$ and $\mathbf{C}$, respectively the depth and corresponding sound speed. Since this experiment took place in shallow waters over a short-time period, we here assumed that the sound velocity field was homogeneous (Sakic et al., 2018). From the sound-speed profile, an harmonic mean value can be determined: $c_{ref} = \frac{z_{max} - z_0}{\int_{z_0}^{z_{max}} c(z)^{-1} dz}$. This simplification allowed us to estimate a correction δc to this mean value. When processing each acquisition mode, described hereafter, we applied the nearest available SSP.

To simplify the calculations, the coordinates of the transponders will be determined in a local topocentric reference frame with North, East, and Down axes, hereafter called *NED*. We arbitrarily chose the *NED* frame origin $[x_0, y_0, z_0]$ as the center of gravity of the three vertical transponder array.

3.2. GNSS Processing

To determine the GAPS position at the emission and reception times in a terrestrial reference frame, the GNSS position of the USV must be transferred to the acoustic system. During the experiment, the former was determined from real-time kinematic

(RTK) positioning. Through the cellular network, the SP80 receiver downloaded the real-time corrections from the French TERIA network and achieved a centimetric positioning accuracy (Chambon, 2019). This method is commonly used in geodetic field experiments, whenever the RTK network is accessible. The transfer of accurate real-time positions from GNSS to the GAPS also allowed the INS to be realigned and limit the effects of the USV drift.

To test the quality of our RTK real-time positioning, the GNSS data were post-processed with the RTKLIB software, using the double-difference method (Takasu and Yasuda, 2009). We use the BRST permanent station as the reference base (**Figure 1**); this station, located at ∼8 km from our working area, is part of the French permanent RGP-GNSS network managed by IGN (the French national mapping agency). Since real-time coordinates were given in the French national reference system RGF93 (Duquenne, 2018), for the sake of consistency, we computed all post-processed coordinates in this reference system. We considered the GPS data only (hereinafter called "GPS-only mode"), and all the available data including those of the Galileo and GLONASS constellations (hereinafter called "multi-GNSS mode"). In the absence of operational IGS multi-GNSS products so far (Mansur et al., 2020; Sośnica et al., 2020), we used the GFZ multi-GNSS products for orbit and clock corrections (Deng et al., 2017; Männel et al., 2020). The other GNSS processing parameters are summarized in **Table 1**.

3.3. Transfer of the GNSS Position to the GAPS

The objective is to determine the GAPS position at the emission and reception instants. This is the reason why it is necessary to transfer the GNSS-antenna position to the different GAPS components (emitter and receivers).

The input data involved in this operation are:

- The positions of a main GNSS antenna in a global Earth-centered, Earth-fixed reference frame *ECEF*, either geocentric (x_i, y_i, z_i) or geographic $(\varphi_i, \lambda_i, h_i)$, at sampling times $t_{GNSS,i}$. We call them $\mathbf{X}_{ECEF,GNSS}(t_{GNSS,i})$;
- The heading α, pitch β, and roll γ angles of the USV at the sampling time $t_{INS,i}$;
- The tie vectors between these devices in the USV internal mechanical frame *MEC*. If we consider the GAPS IMU reference point as the origin of this frame, then $\mathbf{X}_{MEC,IMU} = [0, 0, 0]$. The coordinates of the GNSS-antenna reference point ($\mathbf{X}_{MEC,GNSS}$), that of the acoustic head ($\mathbf{X}_{MEC,AHD}$) and those of the four hydrophones ($\mathbf{X}_{MEC,HPj}$) are thus expressed with respect to the IMU reference point. To simplify the notation, $\mathbf{X}_{MEC,AHD}$ and $\mathbf{X}_{MEC,HPj}$ are hereinafter assimilated to the same vector $\mathbf{X}_{MEC,S}$.

TABLE 1 | GNSS post-processing parameters.

Mode	GPS-only	Multi-GNSS
Constellations	GPS	GPS, GLONASS, Galileo
Frequency	L1 + L2	L1 + L2
Elevation mask	10°	10°
Ionospheric correction	Broadcast IGS	Broadcast IGS
Tropospheric correction	Saastamoinen	Saastamoinen
Tide corrections	Off	Off
GNSS phase center	ANTEX NGS14	ANTEX NGS14
Ephemeris	MGEX GFZ products	MGEX GFZ products
Ambiguity resolution	Fix and hold	Fix and hold
Dynamic mode	On	On

Thus, the objective is to get, in the *NED* topocentric reference frame, the coordinates of the GAPS ($\mathbf{X}_{NED,S}(t)$) at the ping emission $t_{emi,i}$ and reception $t_{rec,i}$ instants. The USV position $\mathbf{X}_{ECEF,GNSS}$ is transferred into the *NED* frame using the formula described, for instance, by Grewal et al. (2007), and thus we have $\mathbf{X}_{NED,GNSS}$ for any sampling instant $t_{GNSS,i}$. We then performed a linear interpolation to obtain the exact positions of the platform at the ping emission and reception instants ($t_{emi,i}$ and $t_{rec,i}$).

Meanwhile, the USV on-board device coordinates in the *MEC* frame are transferred to the "instantaneous topocentric frame" *iNED*. It corresponds to a transformation of the *MEC* frame where its axes are co-linear to the *NED* ones, i.e., by applying the USV attitude $\mathbf{R}$ to the tie vectors. To do so, we associated a quaternion $\mathbf{q}(t_{INS,i})$ to each record of the IMU, $\mathbf{R}(t_{INS,i})$ (Großekatthöfer and Yoon, 2012). We renamed t_i the instants $t_{emi,i}$ and $t_{rec,i}$ since the procedure is the same for the emission and reception instants. Then, using the *Slerp* attitude interpolation method (Kremer, 2008), we determine the attitude of the platform at instant t_i represented by the quaternion $\mathbf{q}_i$.

From this operation, the positions of the GNSS and of the GAPS acoustic head and hydrophones in the *iNED* frame at the transmission and reception instants are determined by:

$$\mathbf{X}_{iNED,S}(t_i) = \mathbf{q}_i \begin{bmatrix} 0 \\ \mathbf{X}_{MEC,S}(t_i) \end{bmatrix} \mathbf{q}_i^{-1} \tag{1}$$

$$\mathbf{X}_{iNED,GNSS}(t_i) = \mathbf{q}_i \begin{bmatrix} 0 \\ \mathbf{X}_{MEC,GNSS}(t_i) \end{bmatrix} \mathbf{q}_i^{-1} \tag{2}$$

It comes that the vector $\mathbf{T}_i$ between the *iNED* positions of the GNSS and the GAPS is:

$$\mathbf{T}_i = \overrightarrow{GNSS\ ,\ S} = \mathbf{X}_{iNED,S} - \mathbf{X}_{iNED,GNSS} \tag{3}$$

Then, the *NED* position of the GNSS can be transferred to the GAPS by translation:

$$\mathbf{X}_{NED,S}(t_i) = \mathbf{X}_{NED,GNSS}(t_i) + \mathbf{T}_i \tag{4}$$

3.4. Least-Squares Model

Finally, we used a least-squares (LSQ) inversion (e.g., Strang and Borre, 1997; Ghilani, 2011) to estimate the desired parameters, namely the transponder coordinates $\mathbf{X}_{R_i}$ and the sound speed correction δc. The observable, in the least-squares sense, are the

TWTTs τ_i and the DOAs $\mathbf{D}_i$. Thus, the associated observation functions f_{TWTT} and f_{DOA} are:

$$f_{TWTT} : (\mathbf{X}_R, \delta c) \quad \longmapsto \quad \tau \tag{5}$$

$$f_{DOA} : (\mathbf{X}_R) \quad \longmapsto \quad \mathbf{D} \tag{6}$$

We have:

$$f_{TWTT} : \frac{\left\|\mathbf{X}_R - \mathbf{X}_{AHD}(t_{emi})\right\| + \left\|\mathbf{X}_R - \mathbf{X}_{HPj}(t_{rec})\right\|}{c + \delta c} + \tau_{TAT} = \tau \tag{7}$$

$$f_{DOA} : \frac{\mathbf{X}_R - \mathbf{X}_{AHD}(t_{rec})}{\left\|\mathbf{X}_R - \mathbf{X}_{AHD}(t_{rec})\right\|} = \mathbf{D} \tag{8}$$

To establish the Jacobian matrix $\mathbf{A}$, we need the partial derivatives of f_{TWTT} and f_{DOA}:

$$\frac{\partial f_{TWTT}}{\partial \mathbf{X}_R} = \frac{1}{c + \delta c} \cdot \left(\frac{\mathbf{X}_R - \mathbf{X}_{AHD}(t_{emi})}{\left\|\mathbf{X}_R - \mathbf{X}_{AHD}(t_{emi})\right\|} + \frac{\mathbf{X}_R - \mathbf{X}_{HPj}(t_{rec})}{\left\|\mathbf{X}_R - \mathbf{X}_{HPj}(t_{rec})\right\|} \right) \tag{9}$$

$$= \begin{bmatrix} \frac{1}{c+\delta c} \cdot \left(\frac{x_R - x_{AHD}(t_{emi})}{\left\|\mathbf{X}_R - \mathbf{X}_{AHD}(t_{emi})\right\|} + \frac{x_R - x_{HPj}(t_{rec})}{\left\|\mathbf{X}_R - \mathbf{X}_{HPj}(t_{rec})\right\|} \right) \\ \frac{1}{c+\delta c} \cdot \left(\frac{y_R - y_{AHD}(t_{emi})}{\left\|\mathbf{X}_R - \mathbf{X}_{AHD}(t_{emi})\right\|} + \frac{y_R - y_{HPj}(t_{rec})}{\left\|\mathbf{X}_R - \mathbf{X}_{HPj}(t_{rec})\right\|} \right) \\ \frac{1}{c+\delta c} \cdot \left(\frac{z_R - z_{AHD}(t_{emi})}{\left\|\mathbf{X}_R - \mathbf{X}_{AHD}(t_{emi})\right\|} + \frac{z_R - z_{HPj}(t_{rec})}{\left\|\mathbf{X}_R - \mathbf{X}_{HPj}(t_{rec})\right\|} \right) \end{bmatrix}^{\mathsf{T}} \tag{10}$$

$$\frac{\partial f_{TWTT}}{\partial \delta c} = \frac{-\left\|\mathbf{X}_R - \mathbf{X}_{AHD}(t_{emi})\right\| - \left\|\mathbf{X}_R - \mathbf{X}_{HPj}(t_{rec})\right\|}{(c + \delta c)^2} \tag{11}$$

$$\frac{\partial f_{DOA}}{\partial \mathbf{X}_R} = \begin{bmatrix} -\frac{(y_R - y_S)^2 + (z_R - z_S)^2}{\left\|\mathbf{X}_R - \mathbf{X}_{AHD}(t_{rec})\right\|^3} & -\frac{(x_R - x_S)(y_R - y_S)}{\left\|\mathbf{X}_R - \mathbf{X}_{AHD}(t_{rec})\right\|^3} & -\frac{(x_R - x_S)(z_R - z_S)}{\left\|\mathbf{X}_R - \mathbf{X}_{AHD}(t_{rec})\right\|^3} \\ -\frac{(y_R - y_S)(x_R - x_S)}{\left\|\mathbf{X}_R - \mathbf{X}_{AHD}(t_{rec})\right\|^3} & -\frac{(x_R - x_S)^2 + (z_R - z_S)^2}{\left\|\mathbf{X}_R - \mathbf{X}_{AHD}(t_{rec})\right\|^3} & -\frac{(y_R - y_S)(z_R - z_S)}{\left\|\mathbf{X}_R - \mathbf{X}_{AHD}(t_{rec})\right\|^3} \\ -\frac{(z_R - z_S)(x_R - x_S)}{\left\|\mathbf{X}_R - \mathbf{X}_{AHD}(t_{rec})\right\|^3} & -\frac{(z_R - z_S)(y_R - y_S)}{\left\|\mathbf{X}_R - \mathbf{X}_{AHD}(t_{rec})\right\|^3} & -\frac{(x_R - x_S)^2 + (y_R - y_S)^2}{\left\|\mathbf{X}_R - \mathbf{X}_{AHD}(t_{rec})\right\|^3} \end{bmatrix} \tag{12}$$

Then, the problem is solved with an approach similar to the one described by Sakic et al. (2020). The adjustment $\boldsymbol{\delta X}$ on the *a priori* values $\mathbf{X_0}$ of the transponder coordinates and the sound speed correction are given by the relation:

$$\boldsymbol{\delta X} = (\mathbf{A}^{\mathsf{T}} \mathbf{P}\, \mathbf{B})^{-1} \mathbf{A}^{\mathsf{T}} \mathbf{P}\, \mathbf{B} \tag{13}$$

where $\mathbf{A}$ is the Jacobian in the neighborhood of $\mathbf{X_0}$. $\mathbf{B}$ and $\mathbf{P}$ is the weight matrix. If the DOA are ignored, $\mathbf{P}$ is equal to the identity and corresponds to the differences between the observations and the theoretical quantities determined by $f_{TWTT}(\mathbf{X_0})$ and $f_{DOA}(\mathbf{X_0})$. In the end, the observation residuals are given by:

$$\mathbf{V} = \mathbf{B} - \mathbf{A}(\mathbf{X_0} + \boldsymbol{\delta X}) \tag{14}$$

Since the algorithm needs several steps k to converge, we used an iterative process where the estimated values become the new *a priori* values at step $k+1$, so that $\mathbf{X_0}_{,k} + \boldsymbol{\delta X}_k = \mathbf{X_0}_{,k+1}$. The iterations stop when the convergence criterion is met, in our case when $\|\boldsymbol{\delta X}\|_k < 10^{-5}\, m$. It generally occurs after the fourth or fifth iteration.

3.5. Outlier Detections

To eliminate the outliers, both in the TWTTs and the DOAs, we use the MAD (*Median Absolute Deviation*) method (Leys et al., 2013).

For a set of observation $\mathbf{L}$, the MAD is defined as:

$$\text{MAD} = \text{median}\left(\left| \mathbf{L} - \text{median}(\mathbf{L}) \right| \right) \tag{15}$$

Then, for each observation l_i (where $l_i \in \{\tau_i, d_{x,i}, d_{y,i}, d_{z,i}\}$), we have M_i so as :

$$M_i = \frac{b\left(l_i - \text{median}\,(\mathbf{L})\right)}{\text{MAD}} \tag{16}$$

where b is a coefficient related to the statistical distribution of the data considered (Rousseeuw and Croux, 1993). If the distribution is normal, $b \approx 0.67449$. Then, if $M_i > s$, l_i is eliminated as an outlier for the next iteration, s is a threshold and typically we take $s = 3$ if the distribution is normal.

4. DATA ANALYSIS

4.1. Parameterization

The data acquired during the experiment were processed with the model described in the previous sections. The observed TWTTs were weighted by an *a priori* standard deviation $\varsigma_{TWTT} = 2 \times 10^{-5}$ s, corresponding to the time precision described in the GAPS data-sheet. We tested different configurations where the sound-speed correction δc is estimated and where it is not. We also tested the contribution of the DOAs in the precision and repeatability of the transponder position. We thus processed the DOAs in three different ways: (1) not used in the inversion, (2) taken into account with a loose *a priori* standard deviation $\varsigma_{DOA,l} = 10^{-2}$ or (3) considered as fully constraint $\varsigma_{DOA,c} = 10^{-3}$. Like the DOAs, ς_{DOA} are unitless and were chosen based on the direction cosine variations for signal's direction of arrival uncertainties $\delta\theta$ at $\approx 45°$. For $\delta\theta = 1$ and $0.1°$, we found $\varsigma_{DOA} = \cos(45° + \delta\theta) - \cos(45°) \approx 10^{-2}$ and 10^{-3}, respectively.

4.2. Test of Different Parameterizations in a Box-In Mode

To test whether the DOAs improve the positioning accuracy, we first exploited the observations made in box-in modes on Day 2. As we focused on the acoustic positioning algorithm, we used the post-processed GPS-only data as the surface positioning solution. We processed each box-in with the six parameterizations described in section 4.1, made up of three ς_{DOA} and two δc modes (estimated or not). The acquisition duration were in the order of ∼25 min, as summarized in **Table 2A** along with the number of recorded TWTTs and the percentage of TWTT outliers.

TABLE 2 | Acquisition duration, number of pings, and percentage of outlier pings for each transponder in the different acquisition modes.

	TP	Dura. (min)	TWTTs (#)	Outliers (%)
(A) IN BOX-IN MODE				
1	1	26.60	2320.00	5.78
2	2	24.90	2260.00	1.59
3	3	22.20	2176.00	1.84

	TP	Mode	Dura. (min)	TWTTs (#)	Outliers (%)
(B) IN STATIC MODES					
1	1	Above	17.20	1,616	15.22
2	1	Slanted (AM)	50.50	1,131	32.18
3	1	Slanted (PM)	30.10	670	32.69
4	2	Above	16.40	1,846	0.11
5	2	Slanted (AM)	50.70	1,300	27.85
6	2	Slanted (PM)	30.20	831	24.31
7	3	Above	12.20	1,304	0.31
8	3	Slanted (AM)	50.70	1,045	36.36
9	3	Slanted (PM)	30.20	778	17.35

	TP	Mode	Day	Dura. (min)	TWTTs(#)	Outliers (%)
(C) IN CLOCKWISE AND ANTICLOCKWISE MODE						
1	1	CW	1	11.00	984	0.81
2	1	ACW	1	10.20	1,015	0.39
3	1	CW + ACW	1	21.90	1,999	0.45
4	1	CW	2	17.00	1,484	8.83
5	1	ACW	2	9.60	832	0.84
6	1	CW + ACW	2	26.60	2,320	5.86
7	3	CW	1	7.70	716	0.00
8	3	ACW	1	13.20	1,136	0.26
9	3	CW + ACW	1	23.90	1,852	4.37
10	3	CW	2	11.50	1,096	2.01
11	3	ACW	2	10.60	1,080	1.67
12	3	CW + ACW	2	22.20	2,176	2.25

When errors are independent from epoch to epoch and follow a Gaussian distribution, having more data will reduce the final position error. However, noise in GNSS positioning is known to be colored (Williams, 2004), and the ocean properties, such as current, salinity, or temperature, do not evolve with a white noise either. Therefore, subsampling the data from the experiment may give results that are highly sensitive to the selected subsampled windows. To test the accuracy (or appropriateness) of the model used in the least-squares inversion, we extracted successive and non-overlapping subsets from the experimental dataset and observed how the resulting transponder position changed between subsets. We can then derive a standard deviation for each parameterization. For each transponder, we divided the total acquisition period into five data subsets, each containing the same number of USV circles around the transponder.

Figure 6 shows the resulting locations for the three transponders. Each parameterization is represented in a different color and symbol. The "tripod" symbols (≻, ≺, ≺) represent runs where the δc estimation is disabled, and the triangles (►, ▲, ▼) represent runs where δc is estimated. The light tripods and empty triangles represent the LSQ inversion result for each of the five data subsets, and the bold/thick equivalent symbols represent the arithmetic mean of the five subsets, with their standard deviations. Star filled-symbols (★) in matching colors represent the results of the LSQ inversion for the entire period, with their formal standard deviation. Standard deviations for each parameterization are listed in **Table 3**.

First of all, solutions where δc is estimated and DOAs are not used or loosely constrained (► and ▲) yield high standard deviations and a poor compatibility with their complete period counterpart. This is due to a complete trade-off between the TWTTs and the sound speed. Such parameterization should thus be avoided. Solutions where δc is not estimated while the DOAs are either unused or loosely constrained (≻ and ≺) give almost equal values (within a millimeter). In a box-in mode, we can conclude that using loose or no constraints from the DOAs yields equivalent results, if δc is not estimated. It is worth noting that when DOAs are constrained (≺ and ▼), standard deviations are smaller compared to the two previous solutions. However, compatibility with the solution based on the whole period is also smaller, which shows the best stability among these parameterizations.

When DOAs are constrained, we note a difference for transponders 1 and 3 between solutions whether δc is estimated or not, even if the subset standard deviations are slightly higher when δc is estimated. This dispersion may be due to the relatively small number of TWTTs in each data subset ($\sim$ 440), which prevents a reliable estimation of the δc parameter. Nevertheless, the residual sum of squares remains smaller by about 2–10% (which is expected since adjusting an additional parameter reduces the residuals). Thus, in a box-in mode, a solution with constrained DOAs and estimated δc is considered as the most optimal parameterization.

Note that even if the horizontal standard deviation is mostly below 10 cm, the standard deviation on the depth can reach the meter level. This is due to the high dependence of depth on sound velocity. Nevertheless, the parameterization with constrained DOAs and estimated δc also tends to reduce the dispersion on the vertical component.

4.3. Repeatability in Static Mode

The repeatability of the different parameterizations in a static mode can be evaluated from the data collected Day 2, where two sessions in a static-slanted mode were recorded, in the morning (AM) and in the afternoon (PM) (**Figure 3B**), along with a station above each transponder (**Figure 3C**). **Table 2B** summarizes the acquisition sessions, the number of recorded TWTTs and the outlier ratio. The results are presented in **Figure 7** and **Table 4**.

The three sub-figures in **Figure 7** show the resulting locations for the three transponders in static mode. Symbols represent different parameterizations and colors, different static acquisition modes. The horizontal and vertical bars give the LSQ formal standard deviations. The black star (★) shows the position estimated from the box-in mode in section 4.2.

Parameterizations where δc is estimated and DOAs are loosely constrained yield a repeatability of several decimeters between the three sessions, up to a meter when DOAs are not used and δc is estimated. The dispersion of the solutions decreases

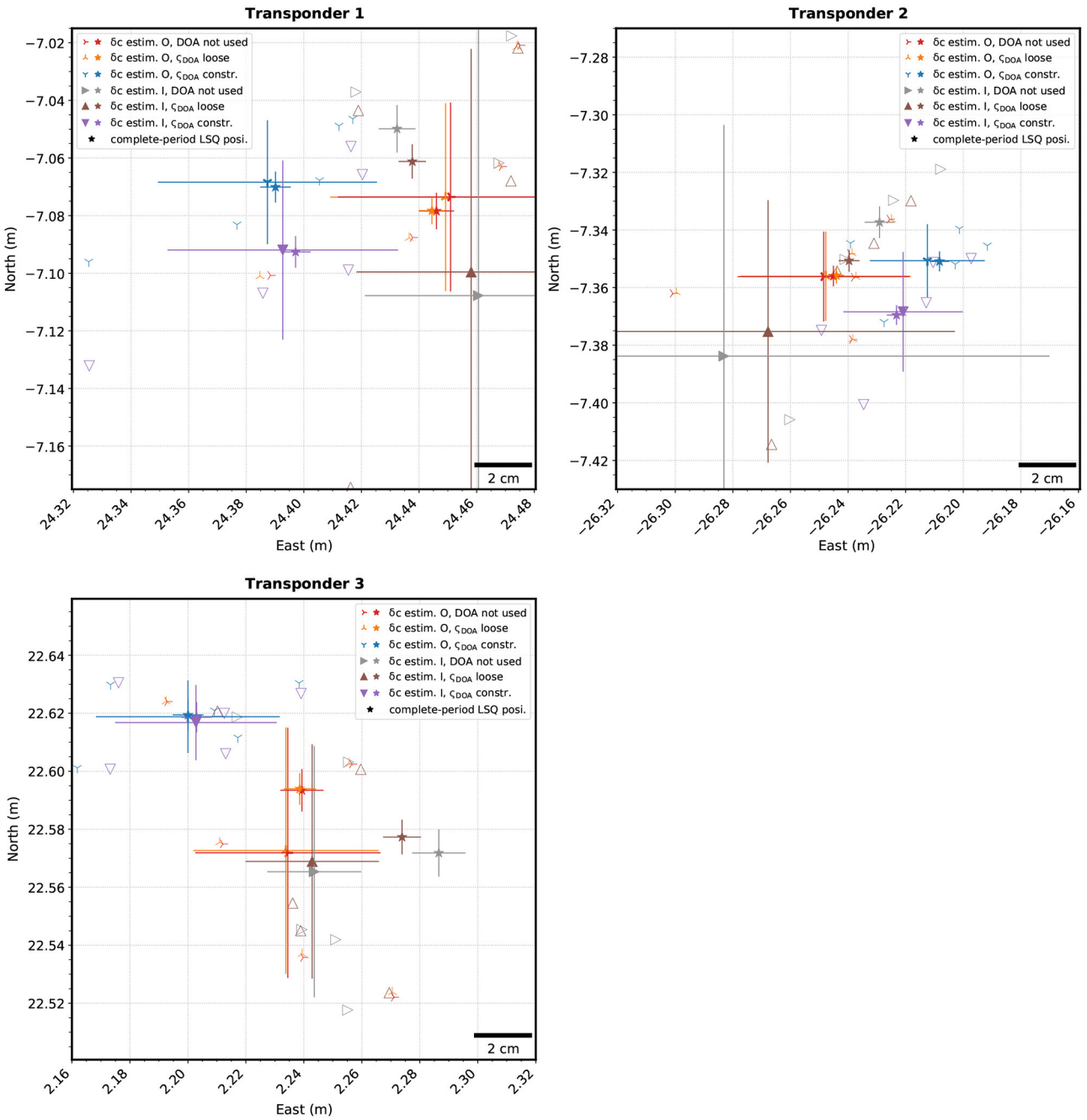

FIGURE 6 | Positions of the three transponders based on the box-in acquisitions, in a local topocentric reference frame. The thin tripod symbols (⊁, ⅄, ϒ) and empty triangles (, △, ▽) represent the LSQ inversion results for each of the five data subsets. The equivalent bold/thick symbols represent the arithmetic means of the five subset-derived positions with their standard deviations. The colored-star (★) represents the result of the LSQ inversion and its formal standard deviation, based on the entire dataset; colors correspond to the different parameterizations used. For the δc estimation, "I" stands for used, and "O" for not used. Few outlier solutions are outside the frame.

depending on whether DOAs are not used, loosely or fully constrained, showing that taking DOAs into account improves the position determination. The best repeatability is obtained with constrained DOAs but δc not estimated. The dispersion then ranges between 1 and 6.5 cm on the North component and 6 and 13.4 cm on the East component. Moreover, these solutions are the most consistent with the best solution obtained in a box-in mode (section 4.2). The dispersion with constrained DOAs is

TABLE 3 | Standard deviations of the North, East, Depth, and Celerity components, for each parameterizations (δ_c and ς_{DOA} columns) and each transponders (TP column) in box-in mode.

	TP	δ_c	ς_{DOA}	σN (cm)	σE (cm)	σD (cm)	σC (m/s)
1	1	False	Constr.	2.15	3.80	1.08	N/A
2	1	False	Loose	3.26	4.00	0.78	N/A
3	1	False	False	3.28	3.91	0.77	N/A
4	1	True	Constr.	3.11	4.00	24.05	9.32
5	1	True	Loose	7.74	3.98	72.50	26.81
6	1	True	False	9.57	3.94	98.17	36.23
7	2	False	Constr.	1.27	1.99	0.66	N/A
8	2	False	Loose	1.55	2.96	0.67	N/A
9	2	False	False	1.56	2.98	0.67	N/A
10	2	True	Constr.	2.08	2.08	29.24	10.64
11	2	True	Loose	4.56	6.49	63.47	22.83
12	2	True	False	8.03	11.30	135.58	48.95
13	3	False	Constr.	1.25	3.17	1.45	N/A
14	3	False	Loose	4.25	3.20	1.88	N/A
15	3	False	False	4.32	3.20	1.88	N/A
16	3	True	Constr.	1.30	2.79	23.49	8.40
17	3	True	Loose	4.04	2.30	53.84	19.74
18	3	True	False	4.33	1.62	100.07	36.81

two to three times greater when estimating δc. Thus, in a static mode, estimating the sound speed is not optimal, as it does not improve the solution. Moreover, the solutions without DOAs are constrained only by the small USV displacements induced by the waves and the currents (a perfectly still USV on a perfectly flat sea would lead to a singular design matrix and thus to an under-determined problem). In general, a static acquisition is not optimal for geodetic applications due to the lack of constrain on the vertical component in the USV motion; the addition of a depth sensor (echosounder or pressure sensor) would be needed.

4.4. Repeatability of Box-In Mode

To further test the repeatability of the box-in mode, we compared the sessions between Day 1 and 2, and particularly the effects of the USV direction when circling the transponders. Thus, we processed separately, for both days and for transponders 1 and 3, periods when the USV was rotating clockwise (CW) or anticlockwise (ACW), and when clockwise + anticlockwise (CW + ACW) acquisitions were combined (**Table 2C** and **Figure 8**). Unfortunately, the raw GNSS observations are not available for the first day (and thus could not be reprocessed), so all these tests use the Real-Time RTK positions of the USV.

Despite the short duration of each session, the results display a very good repeatability between Days 1 and 2 for the combined CW + ACW sessions (**Table 5B**). The differences are smaller than 3 cm on the North and East components, except for Transponder 3 which shows a difference of 7.2 cm on the East component. This difference could be explained by the poor repeatability of the ACW rotation. As expected, the CW + ACW solution is located in the middle of the individual CW and ACW solutions. It is also worth noticing that the rotation direction seems to influence the repeatability of the box-in (**Table 5A**). The horizontal difference is about 5 cm, and up to 8.5 cm for transponder 3 on Day 1. This difference may be due to changes in the water column between successive CW and ACW acquisitions or to an unidentified bias in the lever arms; both effects would averaged out in combining CW and ACW sessions.

4.5. Influence of the GNSS Solution on Seafloor Positioning

To evaluate the effects of GNSS positioning (section 3.2), namely real-time RTK, GPS-only and multi-GNSS, on the overall solution, we analyzed the TWTT residuals after the least-square inversion. We considered the three transponder box-in modes presented in section 4.2 and tested the three different GNSS solutions. The inversion is based on constrained DOAs and an adjusted δc. The results are shown in **Figure 9** and **Table 6**. For a better readability, the TWTT residuals are converted into distances using the estimated sound speed.

We can see that the GNSS solution has an effect on the TWTT residuals. The standard deviation difference for transponders 1 and 3 are respectively ∼3.5 and ∼4.5 cm smaller for post-processed solution compared to the real-time one. The multi-GNSS solution also yields slightly smaller residuals than the GPS-only solution but the improvement is not significant. For transponder 2, the post-processed vs. real-time difference is less prominent (∼5 mm) and the GPS-only solution gives smaller residuals. Overall, the post-processed solutions provide smaller TWTT residuals than the real-time solution.

5. DISCUSSION

In line with previous experiments (Chadwell et al., 2016; Iinuma et al., 2021), this study confirms the feasibility of GNSS/A positioning from an USV. In addition to an easier implementation at a reduced cost, the size of USV avoids any complex topometric survey to determine the lever arms of the system (eg. Chadwell, 2003). Here, the lever arms were measured directly on-shore with a simple ruler with an optimal accuracy. Nevertheless, an *a posteriori* adjustment of the lever arms in the LSQ model can be valuable (Chen et al., 2019). Regarding the absolute positioning, we used a simple linear interpolation to determine the USV's position at the ping emission and reception epochs. This approach is sufficient for the static modes since the GNSS position sampling rate is high (1 Hz) and the USV displacements relatively small (sub-meter level). Nevertheless, a Lagrangian interpolation would be more appropriate when the USV is moving (box-in mode).

USV platforms may revolutionize seafloor geodesy in the near future. In addition to more frequent and spatially denser GNSS/A observations, combining multiple platforms (USVs and a ship) can allow a simultaneous monitoring of the sound-speed field in the ocean (Matsui et al., 2019; Ishikawa et al., 2020). This parameter undoubtedly remains the most critical for an accurate underwater geodetic positioning.

Using an USBL (here a GAPS) instead of a simple acoustic modem allow to measure DOAs in addition

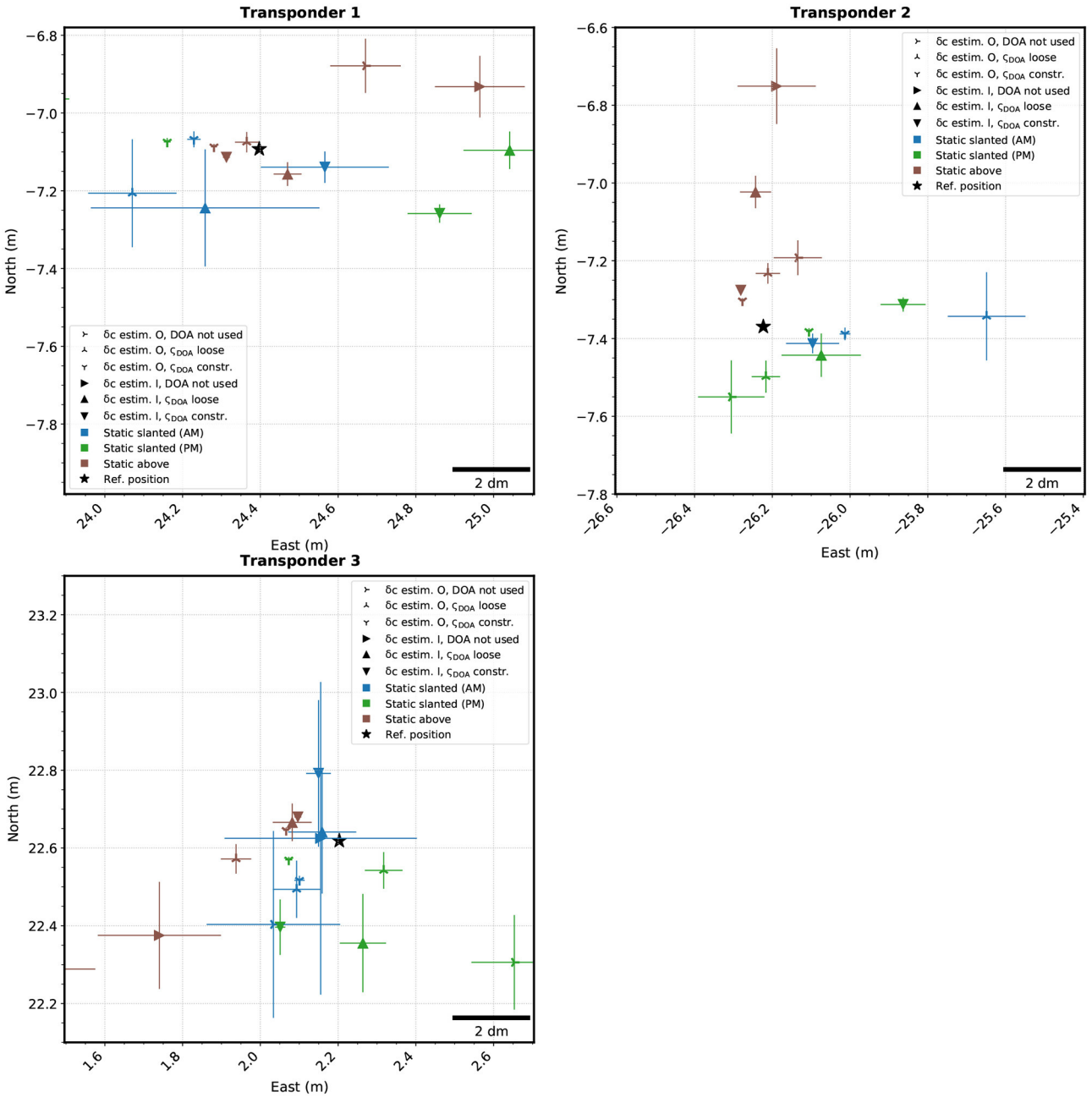

FIGURE 7 | Positions of the three transponders based on the static acquisitions. The symbols represent the different parameterizations and the colors the acquisition modes (static-slanted in the morning or the afternoon, and static-above). The horizontal and vertical bars are LSQ formal standard deviations. The black stars (★) represent the real-time solutions provided by the USBL/INS system after box-in (see section 4.2). For δc estimation, "I" stands for used, and "O" for not used. Few outlier solutions are outside the frame.

to TWTTs. Integrating these observations in the least-squares inversion improve the transponder positioning accuracy. We have shown that, both in box-in and static acquisitions, taking the DOAs into account improves the repeatability of the estimated positions between different sessions.

This experiment in shallow water (∼40 m) is a proof-of-concept. The repeatability of the sessions in box-in mode is about 5 cm. Such accuracy is not sufficient to measure plate motions or fault-slips which are in the order of few mm/year to cm/year (e.g., Bürgmann and Chadwell, 2014), unless measurements are repeated very often and over half a decade

TABLE 4 | Standard deviations of the North, East, Depth, and Sound-speed components, for each parameterizations (δ_c and ς_{DOA} columns) and each transponders (TP column) in static modes.

	TP	δ_c	ς_{DOA}	σN (cm)	σE (cm)	σD (cm)	σC (m/s)
1	1	False	Constr.	0.98	6.03	126.81	N/A
2	1	False	Loose	12.14	24.93	135.63	N/A
3	1	False	False	67.47	72.11	156.22	N/A
4	1	True	Constr.	7.72	27.46	130.55	11.05
5	1	True	Loose	7.45	40.52	80.88	32.48
6	1	True	False	112.04	823.36	410.85	271.00
7	2	False	Constr.	4.75	13.39	124.11	N/A
8	2	False	Loose	13.34	32.63	129.54	N/A
9	2	False	False	51.20	123.61	172.84	N/A
10	2	True	Constr.	7.07	20.93	33.19	40.96
11	2	True	Loose	44.23	136.97	316.54	159.19
12	2	True	False	240.75	753.49	424.65	234.84
13	3	False	Constr.	6.46	1.82	128.07	N/A
14	3	False	Loose	3.94	19.09	128.38	N/A
15	3	False	False	6.19	59.13	133.35	N/A
16	3	True	Constr.	20.38	4.94	114.18	94.51
17	3	True	Loose	17.26	9.12	406.69	211.90
18	3	True	False	163.59	23.40	418.76	227.25

TABLE 5 | (A) Differences on East, North, and Down components between clockwise and anti-clockwise box-in rotations. **(B)** Differences in the East, North, and Down components between days 1 and 2 for clockwise (CW), anti-clockwise (ACW), and complete (CW + ACW) box-in circles.

	TP	Day/Rotation mode	ΔN (cm)	ΔE (cm)	Δ2D (cm)	ΔD (cm)
(A) DIFFERENCE BETWEEN CW and ACW ROTATIONS						
1	1	1	−4.56	−1.82	4.91	65.65
2	1	2	−1.67	−5.76	6.00	77.32
3	3	1	1.71	−8.29	8.46	74.73
4	3	2	3.66	−3.63	5.16	57.38
(B) DIFFERENCE BETWEEN DAYS 1 AND 2						
1	1	CW	−2.34	2.64	3.53	235.62
2	1	ACW	0.55	−1.30	1.41	247.28
3	1	CW + ACW	0.54	1.98	2.06	229.81
4	3	CW	0.19	4.98	4.98	166.81
5	3	ACW	2.14	9.64	9.87	149.46
6	3	CW + ACW	−0.74	7.21	7.25	160.37

or more. Despite the significant contribution of the DOAs, longer acquisition sessions (i.e., continuous over few hours) would be necessary in a true experiment. The effect would be to average out the GNSS positioning and acoustic propagation errors along with internal wave effects. Moreover, the poor repeatability of static acquisitions clearly shows that additional observations like depth are required to efficiently estimate the sound speed.

Since the DOA accuracy is a function of the water depth, DOAs in deep waters may not be as critical as in shallow waters for the precision of seafloor positioning. Further investigations are needed to assess their actual contribution in the deep ocean. In any case, one of the objectives of this work was to explore the contribution of such information, and we believe that DOAs would improve seafloor positioning accuracy, for instance, in an experiment using a single seafloor transponder and several ranging mobile-platforms. They could also be of value to observe fast and/or repeated co-seismic displacements of the seafloor (in the order of several centimeters within few days), where active tectonics occurs in shallow waters, as for instance, off the Vanuatu Islands (e.g., Ballu et al., 2013) or near the Saintes Archipelago (West Indies) (e.g., Bazin et al., 2010).

In this paper, we chose to adjust the sound speed by a simple constant since the acquisition sessions were short (15 min to 1 h). The sound speed variability between the beginning and end of a session could thus be neglected at first approximation. However, for longer sessions, adjusting this parameter with a sine, polynomial, or spline function should be preferred (Fujita et al., 2006; Yasuda et al., 2017; Chen et al., 2018; Liu et al., 2019). Moreover, in deeper waters, more accurate ray-tracing should also replace the straight-ray approximation (Chadwell and Sweeney, 2010; Sakic et al., 2018).

6. CONCLUSION

This experiment in the Bay of Brest, France, was meant to be a proof-of-concept for underwater geodetic positioning from an Unmanned Surface Vehicle. The experimental set-up comprised three acoustic transponders on the seafloor and an integrated USBL/INS system coupled with a GNSS receiver mounted on a USV. The locations of the transponders were derived from the recorded two-way-travel times between the USV and the transponders, and from the direction of arrival of the returned signals. The GNSS receiver, supplemented by the inertial system, provided the surface positioning. During the experiment and this study, different acquisition trajectories were compared: box-in circles and stations above or slanted relative to the transponders.

This paper describes a method to calculate the position of the USBL acoustic head from GNSS observations and attitude measurements. A least-squares model is developed to determine the transponder positions from TWTT and DOA observations, and from an estimation of the acoustic signal propagation speed. Using DOAs improve the repeatability of transponder positioning in box-in and static acquisitions. For a single transponder localization, box-in provides better results than a static acquisition. Over all the sessions spanning 2 days, the resulting repeatability of positioning is 5 cm, despite the short duration of the GNSS/A sessions (∼ 20 min each). We also demonstrated a smaller dispersion of TWTTs residuals when a post-processed GNSS solution is used instead of the real-time

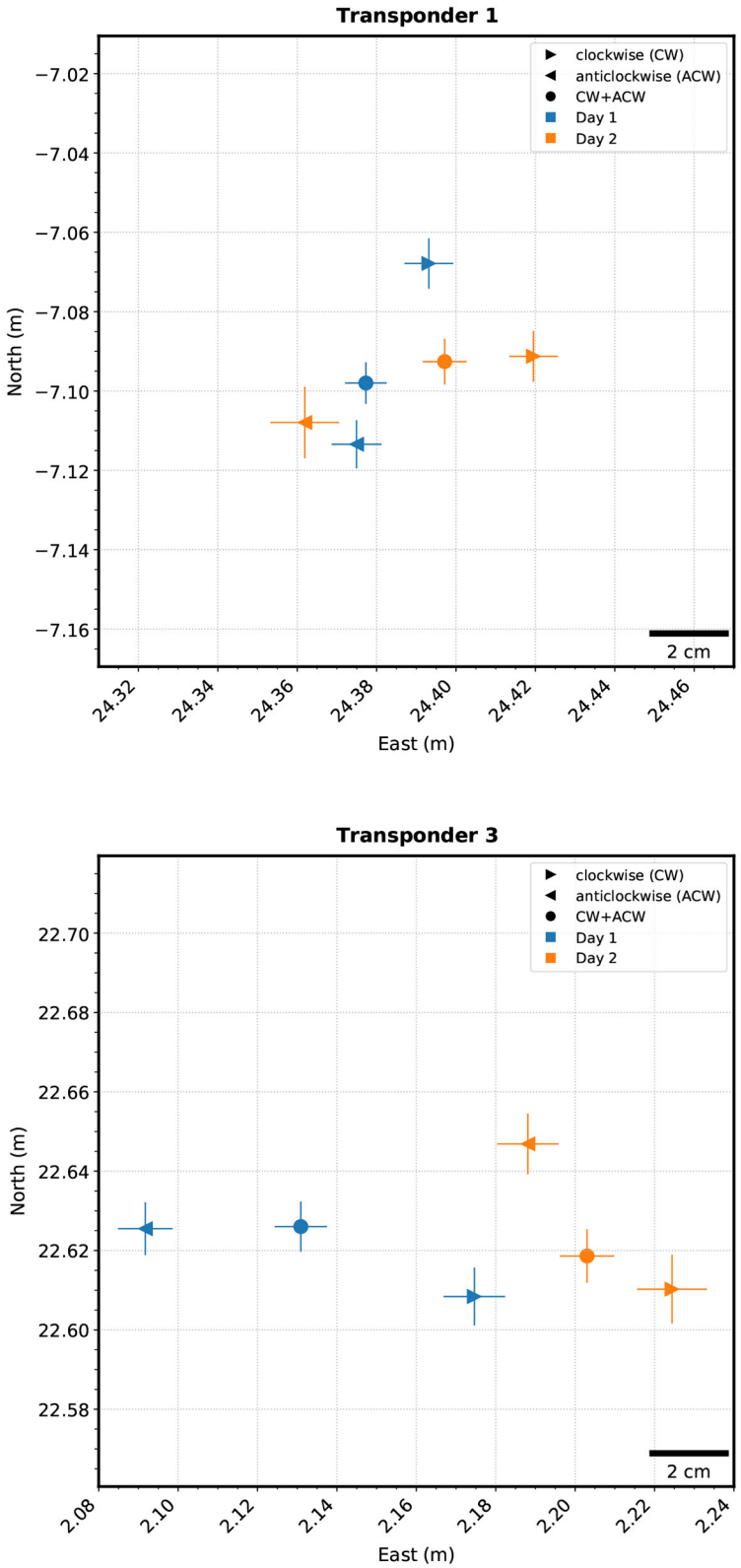

FIGURE 8 | Positions of transponders 1 and 3 based on a clockwise box-in (▶) and anticlockwise box-in (◀) for Day 1 and 2, compared to the result combining CW and ACW box-ins (●).

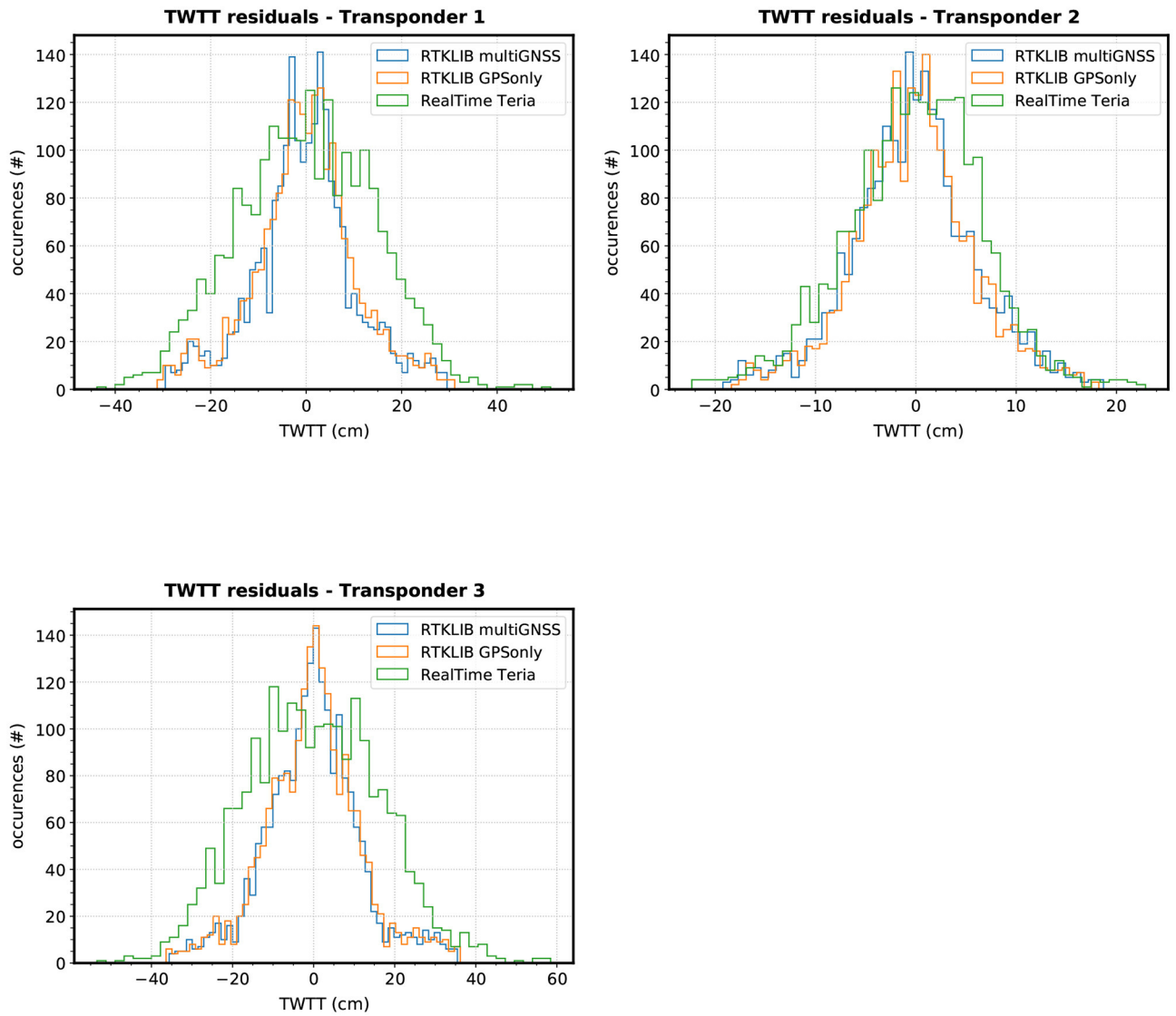

FIGURE 9 | Histograms of the TWTT residuals (converted to distance) based on the different GNSS solutions for the three transponders in box-in mode.

TABLE 6 | Standard deviation in centimeters of the TWTT residuals converted to distance using different GNSS solution type for the three transponders (TP) in box-in mode.

TP	RTKLIB multiGNSS	RTKLIB GPS only	RTK Real-time
1	10.55	10.78	14.34
2	6.20	5.90	6.78
3	11.73	11.88	16.50

RTK solution. This work could set the basis for operational USV-based GNSS/A campaigns for geophysical monitoring in the near future.

DATA AVAILABILITY STATEMENT

The datasets used in this study can be found in the SEANOE database (www.seanoe.org/data/00674/78593/, doi: 10.17882/78593. *Python 3* source codes developed for this article are freely available at an online GitHub git repository upon request to the corresponding author.

AUTHOR CONTRIBUTIONS

J-YR and VB conceived, organized, and conducted the experiment. J-YR, VB, TC, MB, CC, P-YM, and PU participated to the data acquisition at sea. PS, VB, and CC elaborated the processing strategy. PS designed and implemented the model, and produced the results. CC post-processed the GNSS data

and pre-processed the acoustic data. TC was in charge for setting-up and piloting the USV PAMELi. MB designed the transponder lay-out and acquired the sound-speed profiles. P-YM and PU provided the advice and expertise on the GAPS and CANOPUS transponders. J-YR, VB, PS, CC, P-YM, and PU discussed the results, contributed to, and edited the article. All authors contributed to the article and approved the submitted version.

FUNDING

The CANOPUS transponders were funded by the ERC FOCUS project (2019-2023, PI M.-A. Gutscher at LGO). This GNSS/A experiment (GEODESEA-2019) was funded by the French Oceanographic Fleet, LGO, and LIENSs, with support from the iXblue company for the preparation of the transponders and the implementation of their equipment. Funding for CC's Ph.D. was provided by the Direction Générale de l'Armement (DGA) and the Nouvelle Aquitaine Region.

ACKNOWLEDGMENTS

The authors would like to thank Charles Poitou (LGO) for his assistance in the deployment and recovery of the equipment. The authors also wish to thank the crew, Frank Quéré and Robin Carlier, of R/V Albert Lucas, LGO's director Marc-André Gutscher for the scientific and administrative support, and the iXblue team members Yoann Caudal and Corinne Le Guicher.

SUPPLEMENTARY MATERIAL

The Supplementary Material for this article can be found online at: https://www.frontiersin.org/articles/10.3389/feart.2021.636156/full#supplementary-material

REFERENCES

Ballu, V., Bonnefond, P., Calmant, S., Bouin, M.-N., Pelletier, B., Laurain, O., et al. (2013). Using altimetry and seafloor pressure data to estimate vertical deformation offshore: Vanuatu case study. *Adv. Space Res.* 51, 1335–1351. doi: 10.1016/j.asr.2012.06.009

Bazin, S., Feuillet, N., Duclos, C., Crawford, W., Nercessian, A., Bengoubou-Valérius, M., et al. (2010). The 2004–2005 Les Saintes (French West Indies) seismic aftershock sequence observed with ocean bottom seismometers. *Tectonophysics* 489, 91–103. doi: 10.1016/j.tecto.2010.04.005

Berger, J., Laske, G., Babcock, J., and Orcutt, J. (2016). An ocean bottom seismic observatory with near real–time telemetry. *Earth Space Sci.* 3, 68–77. doi: 10.1002/2015EA000137

Bürgmann, R., and Chadwell, D. (2014). Seafloor geodesy. *Annu. Rev. Earth Planet. Sci.* 42, 509–534. doi: 10.1146/annurev-earth-060313-054953

Chadwell, C. D. (2003). Shipboard towers for global positioning system antennas. *Ocean Eng.* 30, 1467–1487. doi: 10.1016/S0029-8018(02)00141-5

Chadwell, C. D., and Sweeney, A. D. (2010). Acoustic ray-trace equations for seafloor geodesy. *Mar. Geod.* 33, 164–186. doi: 10.1080/01490419.2010.492283

Chadwell, C. D., Webb, S. C., and Nooner, S. L. (2016). "Campaign-style GPS-acoustic with wave gliders and permanent seafloor benchmarks," in *Proceedings of the Subduction Zone Observatory Workshop* (Boise, ID: Boise Center).

Chambon, P. (2019). Du NRTK vers le PPP-RTK, un exemple avec TERIA. *XYZ J. French Topogr. Assoc.* 159, 44–49.

Chen, G., Liu, Y., Liu, Y., Tian, Z., Liu, J., and Li, M. (2019). Adjustment of transceiver lever arm offset and sound speed bias for GNSS-acoustic positioning. *Rem. Sens.* 11, 1–12. doi: 10.3390/rs11131606

Chen, H. Y., Ikuta, R., Lin, C. H., Hsu, Y. J., Kohmi, T., Wang, C. C., et al. (2018). Back-arc opening in the western end of the Okinawa trough revealed from GNSS/acoustic measurements. *Geophys. Res. Lett.* 45, 137–145. doi: 10.1002/2017GL075724

Chupin, C., Ballu, V., Testut, L., Tranchant, Y. T., Calzas, M., Poirier, E., et al. (2020). Mapping sea surface height using new concepts of kinematic GNSS instruments. *Rem. Sens.* 12:2656. doi: 10.3390/rs12162656

Deng, Z., Nischan, T., and Bradke, M. (2017). *Multi-GNSS Rapid Orbit-, Clock- and EOP-Product Series*. doi: 10.5880/GFZ.1.1.2016.003

Duquenne, F. (2018). Les systèmes de référence terrestre et leurs réalisations Cas des territoires français. *XYZ J. French Topogr. Assoc.* 154, 46–54.

Foster, J. H., Ericksen, T. L., and Bingham, B. (2020). Wave glider–enhanced vertical seafloor geodesy. *J. Atmos. Ocean. Technol.* 37, 417–427. doi: 10.1175/JTECH-D-19-0095.1

Fujita, M., Ishikawa, T., Mochizuki, M., Sato, M., Toyama, S., Katayama, M., et al. (2006). GPS/Acoustic seafloor geodetic observation: method of data analysis and its application. *Earth Planets Space* 58, 265–275. doi: 10.1186/BF03351923

Gagnon, K., Chadwell, C. D., and Norabuena, E. (2005). Measuring the onset of locking in the Peru-Chile trench with GPS and acoustic measurements. *Nature* 434, 205–208. doi: 10.1038/nature03412

Ghilani, C. (2011). Adjustment computations: spatial data analysis. *Int. J. Geograph. Inform. Sci.* 25, 326–327. doi: 10.1080/13658816.2010.501335

Grewal, M. S., Weill, L. R., and Andrews, A. P. (2007). *Global Positioning Systems, Inertial Navigation, and Integration*. Hoboken, NJ: John Wiley and Sons, Inc.

Großekatthöfer, K., and Yoon, Z. (2012). *Introduction Into Quaternions for Spacecraft Attitude Representation*. Berlin: TU Berlin.

Iinuma, T., Kido, M., Ohta, Y., Fukuda, T., Tomita, F., and Ueki, I. (2021). GNSS-acoustic observations of seafloor crustal deformation using a wave glider. *Front. Earth Sci.* 9:600946. doi: 10.3389/feart.2021.600946

Ishikawa, T., and Yokota, Y. (2018). Detection of seafloor movement in subduction zones around Japan using a GNSS–a seafloor geodetic observation system from 2013 to 2016. *J. Disaster Res.* 13, 511–517. doi: 10.20965/jdr.2018.p0511

Ishikawa, T., Yokota, Y., Watanabe, S. I., and Nakamura, Y. (2020). History of on-board equipment improvement for GNSS–a observation with focus on observation frequency. *Front. Earth Sci.* 8:150. doi: 10.3389/feart.2020.00150

Kremer, V. (2008). *Quaternions and SLERP*. Technical report, University of Saarbrücken, Department for Computer Science.

Lange, D., Kopp, H., Royer, J.-Y., Henry, P., Çakir, Z., Petersen, F., et al. (2019). Interseismic strain build-up on the submarine North Anatolian Fault offshore Istanbul. *Nat. Commun.* 10:3006. doi: 10.1038/s41467-019-11016-z

Leys, C., Ley, C., Klein, O., Bernard, P., and Licata, L. (2013). Detecting outliers: do not use standard deviation around the mean, use absolute deviation around the median. *J. Exp. Soc. Psychol.* 49, 764–766. doi: 10.1016/j.jesp.2013.03.013

Liu, H., Wang, Z., Zhao, S., and He, K. (2019). Accurate multiple ocean bottom seismometer positioning in shallowwater using GNSS/acoustic technique. *Sensors* 19:1406. doi: 10.3390/s19061406

Männel, B., Brandt, A., Bradke, M., Sakic, P., Brack, A., and Nischan, T. (2020). "Status of IGS reprocessing activities at GFZ," in *International Association of Geodesy Symposia* (Berlin; Heidelberg: Springer). doi: 10.1007/1345_2020_98

Mansur, G., Sakic, P., Männel, B., and Schuh, H. (2020). Multi-constellation GNSS orbit combination based on MGEX products. *Adv. Geosci.* 50, 57–64. doi: 10.5194/adgeo-50-57-2020

Matsui, R., Kido, M., Niwa, Y., and Honsho, C. (2019). Effects of disturbance of seawater excited by internal wave on GNSS-acoustic positioning. *Mar. Geophys. Res.* 40, 541–555. doi: 10.1007/s11001-019-09394-6

Penna, N. T., Morales Maqueda, M. A., Martin, I., Guo, J., and Foden, P. R. (2018). Sea surface height measurement using a GNSS wave glider. *Geophys. Res. Lett.* 45, 5609–5616. doi: 10.1029/2018GL077950

Petersen, F., Kopp, H., Lange, D., Hannemann, K., and Urlaub, M. (2019). Measuring tectonic seafloor deformation and strain-build up with acoustic direct-path ranging. *J. Geodyn.* 124, 14–24. doi: 10.1016/j.jog.2019.01.002

Rousseeuw, P. J., and Croux, C. (1993). Alternatives to the median absolute deviation. *J. Am. Stat. Assoc.* 88, 1273–1283. doi: 10.1080/01621459.1993.10476408

Royer, J. Y., Ballu, V., Beauverger, M., Coulombier, T., Morvan, P. Y., Urvoas, P., et al. (2021). *Geodesea-2019 An Experiment of Seafloor Geodesy in the Bay of Brest*. doi: 10.17882/78593

Sakic, P., Ballu, V., Crawford, W. C., and Wöppelmann, G. (2018). Acoustic ray tracing comparisons in the context of geodetic precise off-shore positioning experiments. *Mar. Geod.* 41, 315–330. doi: 10.1080/01490419.2018.1438322

Sakic, P., Ballu, V., and Royer, J. Y. (2020). A multi-observation least-squares inversion for GNSS-acoustic seafloor positioning. *Rem. Sens.* 12:448. doi: 10.3390/rs12030448

Sakic, P., Piété, H., Ballu, V., Royer, J.-Y., Kopp, H., Lange, D., et al. (2016). No significant steady state surface creep along the North Anatolian Fault offshore Istanbul: Results of 6 months of seafloor acoustic ranging. *Geophys. Res. Lett.* 43, 6817–6825. doi: 10.1002/2016GL069600

Sośnica, K., Zajdel, R., Bury, G., Bosy, J., Moore, M., and Masoumi, S. (2020). Quality assessment of experimental IGS multi-GNSS combined orbits. *GPS Solut.* 24:54. doi: 10.1007/s10291-020-0965-5

Spiess, F. N., Chadwell, C. D., Hildebrand, J. A., Young, L. E., Purcell, G. H., and Dragert, H. (1998). Precise GPS/Acoustic positioning of seafloor reference points for tectonic studies. *Phys. Earth Planet. Interiors* 108, 101–112. doi: 10.1016/S0031-9201(98)00089-2

Strang, G., and Borre, K. (1997). *Linear Algebra, Geodesy, and GPS*. Wellesley, MA: Wellesley-Cambridge Press.

Sweeney, A. D., Chadwell, C. D., Hildebrand, J. A., and Spiess, F. N. (2005). Centimeter-level positioning of seafloor acoustic transponders from a deeply-towed interrogator. *Mar. Geod.* 28, 39–70. doi: 10.1080/01490410590884502

Takasu, T., and Yasuda, A. (2009). "Development of the low-cost RTK-GPS receiver with an open source program package RTKLIB," in *International Symposium on GPS/GNSS* (Jeju).

Williams, S. D. P. (2004). Error analysis of continuous GPS position time series. *J. Geophys. Res.* 109, 1–19. doi: 10.1029/2003JB002741

Yasuda, K., Tadokoro, K., Taniguchi, S., Kimura, H., and Matsuhiro, K. (2017). Interplate locking condition derived from seafloor geodetic observation in the shallowest subduction segment at the Central Nankai Trough, Japan. *Geophys. Res. Lett.* 44, 3572–3579. doi: 10.1002/2017GL072918

Conflict of Interest: The authors declare that the research was conducted in the absence of any commercial or financial relationships that could be construed as a potential conflict of interest.

frontiers in Earth Science

ORIGINAL RESEARCH
published: 21 April 2021
doi: 10.3389/feart.2021.614088

Sensitivity Analysis for Seafloor Geodetic Constraints on Coseismic Slip and Interseismic Slip-Deficit Distributions

Sota Murakami[1], Tsuyoshi Ichimura[1], Kohei Fujita[1], Takane Hori[2] and Yusaku Ohta[3]*

[1]Earthquake Research Institute and Department of Civil Engineering, The University of Tokyo, Bunkyo, Japan, [2]R and D Center for Earthquake and Tsunami, Japan Agency for Marine-Earth Science and Technology, Yokohama, Japan, [3]Research Center for Prediction of Earthquakes and Volcanic Eruptions, Graduate School of Science, Tohoku University, Sendai, Japan

Estimating the coseismic slip distribution and interseismic slip-deficit distribution play an important role in understanding the mechanism of massive earthquakes and predicting the resulting damage. It is useful to observe the crustal deformation not only in the land area, but also directly above the seismogenic zone. Therefore, improvements in terms of measurement precision and increase in the number of observation points have been proposed in various forms of seafloor observation. However, there is lack of research on the quantitative evaluation of the estimation accuracy in cases where new crustal deformation observation points are available or when the precision of the observation methods have been improved. On the other hand, the crustal structure models are improving and finite element analysis using these highly detailed crustal structure models is becoming possible. As such, there is the real possibility of performing an inverted slip estimation with high accuracy via numerical experiments. In view of this, in this study, we proposed a method for quantitatively evaluating the improvement in the estimation accuracy of the coseismic slip distribution and the interseismic slip-deficit distribution in cases where new crustal deformation observation points are available or where the precision of the observation methods have been improved. As a demonstration, a quantitative evaluation was performed using an actual crustal structure model and observation point arrangement. For the target area, we selected the Kuril Trench off Tokachi and Nemuro, where M9-class earthquakes have been known to occur in the past and where the next imminent earthquake is anticipated. To appropriately handle the effects of the topography and plate boundary geometry, a highly detailed three-dimensional finite element model was constructed and Green's functions of crustal deformation were calculated with high accuracy. By performing many inversions via optimization using Green's functions, we statistically evaluated the effect of increase in the number of observation points of the seafloor crustal deformation measurement and the influence of measurement error, taking into consideration the diversity of measurement errors. As a result, it was demonstrated that the observation of seafloor crustal deformation near the trench axis plays an extremely important role in the estimation performance.

Keywords: seafloor observation, inversion of fault slip, sensitivity analysis, crustal deformation, finite element analysis, Tokachi-oki earthquake

OPEN ACCESS

Edited by:
Laura Wallace, University of Texas at Austin, United States

Reviewed by:
Eric Lindsey, University of New Mexico, United States
William B Frank, Massachusetts Institute of Technology, United States

****Correspondence:***
Sota Murakami
souta@eri.u-tokyo.ac.jp

Specialty section:
This article was submitted to Solid Earth Geophysics, a section of the journal Frontiers in Earth Science

Received: *05 October 2020*
Accepted: *05 February 2021*
Published: *21 April 2021*

Citation:
Murakami S, Ichimura T, Fujita K, Hori T and Ohta Y (2021) Sensitivity Analysis for Seafloor Geodetic Constraints on Coseismic Slip and Interseismic Slip-Deficit Distributions. Front. Earth Sci. 9:614088. doi: 10.3389/feart.2021.614088

1 INTRODUCTION

1.1 Background

At most of the plate convergent margins, the denser oceanic plates subduct beneath the continental plates and due to the subduction, topographic depressions, trenches or troughs, are created and filled with sea water. Since plate subduction proceeds under the seafloor, the seismogenic zone of a large interplate earthquake would also be located in the offshore region. This type of earthquake may generate a tsunami due to the crustal deformation on the seafloor resulting from the coseismic displacement. In previous M9-class earthquakes (e.g., the Tohoku, Sumatra, Cascadia, and Chile earthquakes), the induced tsunami run-up has stretched as far as several kilometers from the coastline, causing great damage. After the 2011 earthquake that occurred off the Pacific coast of Tohoku (M9, hereafter the 2011 Tohoku-Oki earthquake), the Geospatial Information Authority of Japan (GSI) and Tohoku University jointly developed the real-time analysis system to accurately estimate the moment magnitude of the huge earthquake using real-time Global Navigation Satellite System (GNSS) data (Ohta et al., 2012b; Ohta et al., 2015; Kawamoto et al., 2016; Kawamoto et al., 2017). This system is called REGARD (the REal-time Geonet Analysis system for Rapid Deformation monitoring). Accurately estimating the moment magnitude is possible with the REGARD system since the GNSS provides unsaturated magnitude values for large events. In fact, this information is used by the Japan Meteorological Agency as supporting information to issue tsunami warnings/advisories (e.g., Ohta et al., 2018). The main observable of the REGARD system is the permanent ground displacement deduced from the real-time onshore GNSS data in Japan (GEONET).

However, it is difficult to estimate the coseismic slip behavior in the offshore regions simply based on the onshore GNSS data. In fact, the 2011 Tohoku-Oki earthquake highlighted the importance of the seafloor geodetic technique, such as the GNSS-acoustic coupling method (here in after, GNSS-A) and the seafloor pressure sensors, for understanding the slip characteristics close to the trench axis (e.g., Ito et al., 2011; Iinuma et al., 2012). Here, the techniques clearly indicated the existence of the large slip on the shallowest part of the subducting plate interface (e.g., Iinuma et al., 2012). In addition, whether such a coseismic fault slip reaches the trench axis or not can significantly affect the crustal deformation as well as the coastal height and the run-up distribution of the accompanying tsunami (e.g., Ichimura et al., 2017). It is thus crucial to improve the accuracy of coseismic slip distribution estimation including within the vicinity of the trench axis, for improving the prediction accuracy of the tsunami inundation immediately after a huge earthquake. Here, it is desirable to observe the real-time crustal deformation above the source area and to input the data into an estimation system such as REGARD.

In recent years, it has been confirmed that the fault slip during an earthquake involves a process of releasing the elastic strain energy stored underground, and the state of energy accumulation can be estimated via analysis of the crustal deformation data (e.g., Hashimoto et al., 2012). In this way, it is possible to estimate the possible slip distribution of future earthquakes by estimating the slip-deficit distribution based on the crustal deformation data. While it is difficult to predict how much of the accumulated elastic strain energy will be released by an imminent earthquake, we can, to a certain extent, estimate the fault slip distribution, the accompanying crustal deformation, and the potential hazards, which include tsunami height and run-up distribution, when assuming that all of the accumulated energy will be released. In such cases, the information related to the accumulation of the slip-deficit near the trench axis is important for improving the prediction accuracy. Due to the progress in the seafloor geodetic techniques, it has been confirmed that slip-deficit has accumulated also near the trench axis (Gagnon et al., 2005). As such, it is clear that the crustal deformation measurement at both the land area away from the source and at the seafloor above the source area, especially near the trench axis, plays an important role in improving the estimation accuracy of both the slip-deficit distribution and the fault slip distribution during an earthquake.

Satellite geodesy based on electromagnetic waves (microwaves) has resulted in significant progress in the field of land-related crustal deformation studies. However, as the microwaves do not penetrate through seawater due to the rapid attenuation, the observation of any geodetic deformation on the seafloor requires using alternative methods such as acoustic ranging. The currently used seafloor-related crustal deformation measurement methods include the vertical crustal deformation measurement using ocean bottom pressure (OBP) sensors, the horizontal and vertical crustal deformation measurement using the GNSS-A acoustic technique (combination of GNSS and acoustic ranging), and strain measurement based on the acoustic distance measurement between different observation sites on seafloor. Here, specific analysis has been performed on the data obtained by these methods after the observation. In recent years, the real-time measurement of OBP data using submarine cable networks (e.g., Mochizuki et al., 2018) and the quasi real-time analysis of GNSS-A data using marine platforms (e.g., Imano et al., 2019; Kinugasa et al., 2020) have been undergoing continuous development. Monitoring of vertical crustal deformation by the submarine cable network OBP system is expected to contribute to improving the accuracy of real-time estimation of coseismic slip distribution. In addition, the precision of interseismic crustal deformation measurement, and thus the accuracy of slip-deficit estimation, can be improved by increasing the observation frequency of GNSS-A.

As yet, few studies have sufficiently focused on the quantitative evaluation of the improvement in the accuracy of coseismic slip distribution and interseismic slip-deficit distribution estimations following the incorporation of such observational data. Previous studies that assess the detection ability enhancement through increasing the number of observation points do exist (e.g., Suito, 2016; Sathiakumar et al., 2017; Agata et al., 2019), while the effect of the model error in terms of the underground structure assumed in the data analysis on the estimation results has also

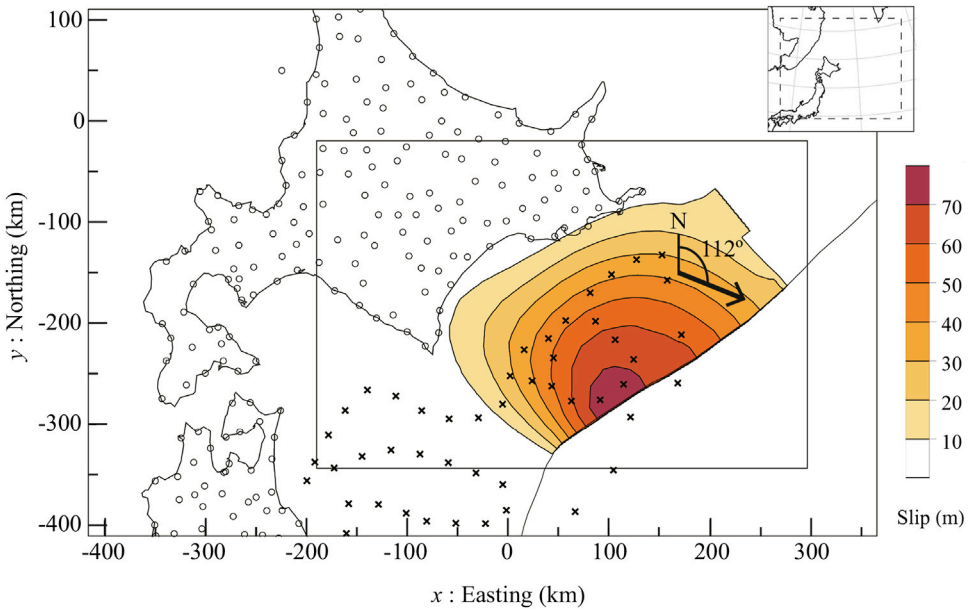

FIGURE 1 | Reference spatial distribution of coseismic fault slip is shown as color contour. The direction of the slip was uniform in the 112° clockwise from north direction. The rectangle (solid line) is the target area for estimating the fault slip distribution. The curved thin solid line indicates the trench axis. The GNSS observation points are represented by circles, and the S-net and PG observation points are represented by crosses. The target range of the finite element model is indicated with dotted lines in the inset figure.

been evaluated (Yamaguchi et al., 2017a; Yamaguchi et al., 2017b). However, few studies have quantitatively evaluated the effect of observation error on the estimation results of plate interface slip distribution focusing on the observation of the seafloor crustal deformation. Kimura et al. (2019) estimated the slip-deficit distribution at the subducting plate interface, including in terms of block motion, using Markov chain Monte Carlo methods for the Nankai Trough using data from onshore GNSS and offshore GNSS-A measurements. However, discussions on observation methods other than GNSS-A and on the variety of errors involved are lacking. Therefore, in this study, we assume the case where several types of seafloor crustal deformation observation methods are mixed and propose a method for quantitatively evaluating the effect of observation error on the estimation of coseismic slip and interseismic slip-deficit distribution. Furthermore, we aim to quantitatively demonstrate via numerical experiments the improvement in the accuracy of the slip distribution estimation when new crustal deformation observation points are available or when the precision of the observation methods are improved. Specifically, we focus on how the understanding of the slip characteristics near the trench axis, which are difficult to grasp using onshore GNSS data alone, can be improved by adding the seafloor crustal deformation observations. On the other hand, to determine how many observation points are required for this improvement, which is done by Sathiakumar et al. (2017), is out of scope in this study. The structure of this paper is as follows. In the following subsection, we explain the problem setting of the numerical experiment, provide some background information, and explain the setting of the observation error. Following this, the adopted methodology is outlined before the results and the considerations of the numerical experiments are described and subsequently summarized in the concluding section.

1.2 Problem Setting

The purpose of this study is to propose a method that will allow us to quantitatively evaluate the effect of adding offshore geodetic data in view of improving the accuracy of coseismic slip distribution and interseismic slip-deficit distribution estimations near the trench axis. We use a numerical experiment to demonstrate the approach.

The target area is the offshore region of Tokachi and Nemuro, the southwestern part of the Kuril Trench where 9M-class earthquakes have been known to occur in the past, and where the next imminent earthquake is anticipated (**Figure 1**). In the following, we first review the previous studies on the large earthquakes that occurred in the southwestern part of the Kuril Trench before outlining the framework of our numerical experiments based on these studies.

Much like with the Japan Trench, the Kuril Trench is an area where the Pacific plate subducts. Based on the distribution of tsunami deposits, it has been proposed that both segments off of Tokachi and Nemuro ruptured in the Seventeenth century (Nanayama et al., 2003). It has also been noted that the slip characteristics of this earthquake were similar to those of the 2011 Tohoku-Oki earthquake, which may have led to an 9M-class earthquake with a large slip in the shallow part of the plate interface (Ioki and Tanioka, 2016). In fact, traces of 15 tsunami deposits that span the past 6,000 years have been found (Sawai, 2020), and given the interval between the event of the Seventeenth

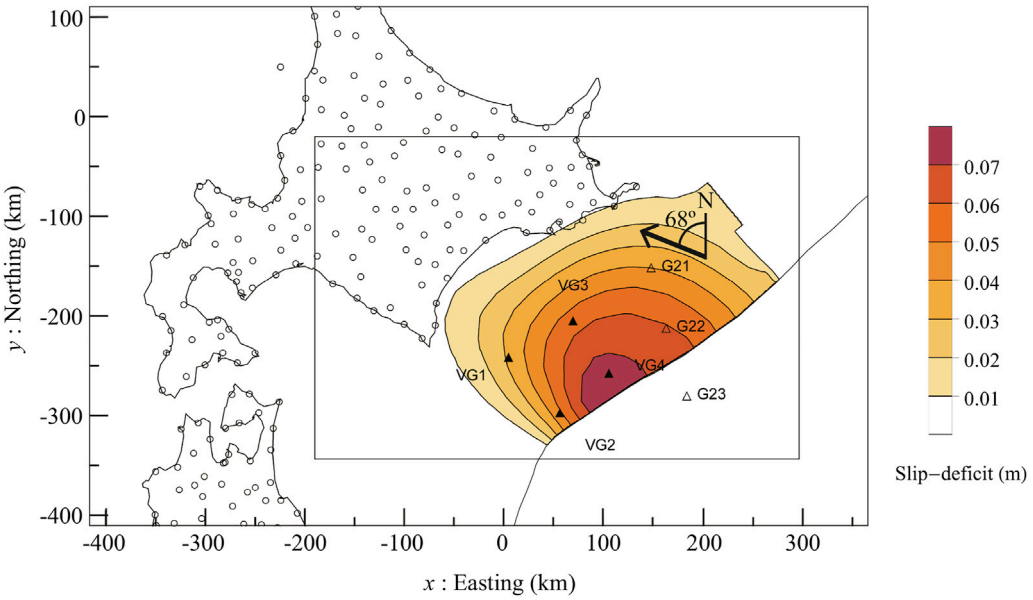

FIGURE 2 | Reference spatial distribution of interseismic slip-deficit in one year is shown as color contour. The direction of the slip-deficit was uniform in the 68° counter-clockwise from north direction. The curved thin solid line indicates the trench axis. The position of GNSS observation points, GNSS-A observation points (G21, G22, G23), and the virtual GNSS-A observation points (VG1–VG4) are represented by circles, empty triangles, and filled triangles, respectively.

century and the preceding event (some point in the 12th or 13th century), and the interval since the previous event, the indications are that a similar largest-class tsunami is imminent (Cabinet Office, 2020b). Furthermore, from the crustal deformation data on the land area, it is estimated that the slip-deficit that corresponds with the past source area is expanding (Hashimoto et al., 2012), and a seismic gap off the coast of Nemuro with low microseismic activity was noted by Takahashi and Kasahara (2013). It is possible that the plate interface at this region, including the shallow part of the plate interface, is strongly locked and has accumulated some slip-deficit. As part of an observation network in the area, submarine cable pressure sensors have been operational at two points off Kushiro for a long period, while the S-net system installed after the 2011 Tohoku-Oki earthquake covers the entire source area. Furthermore, to directly measure the seafloor deformation in the interseismic period, Tohoku University and Hokkaido University have jointly established a seafloor geodetic observation network with the aim of measuring the current interplate locking at the Kuril Trench off Nemuro. Specifically, three GNSS-A observation points and one seafloor acoustic ranging observation point were installed during the joint cruise KS-19-12 of the Tohoku Marine Ecosystem Research Vessel 'Shinseimaru', conducted in July 2019. As such, the Kuril Trench was considered to be the most suitable area for conducting the current research.

We use the geometry of the plate interface used in the tsunami hazard scenario from the Cabinet Office (Disaster Management) as announced in 2019 (Yokota et al., 2017) and the coseismic slip distribution data (Cabinet Office, 2020a, page 4), respectively, which are both based on an array of scientific knowledge. However, as the Cabinet Office's disaster management scenario assumes the occurrence of the largest possible tsunami, the slip distributes not only in the target area off Tokachi and Nemuro but also in the eastward area, where no real-time onshore nor off shore observation stations. Thus, to exclude the area outside of the observation network from the target analysis area, we use the slip distribution contained in the digital data provided by the Cabinet Office but with the eastern part removed for the reference slip distribution (see **Figure 1**). In terms of the plate interface geometry and topography, the digital elevation model data provided by the Cabinet Office is used. To appropriately handle the effects of the topography and plate interface geometry, a detailed finite element (FE) model is constructed, and the crustal deformation is calculated with high accuracy, as described in the next section. The reference interseismic slip-deficit distribution per year (**Figure 2**) was adjusted such that the maximum value will be 8 cm, as the relative velocity between the plates in this region is around 8 cm/year (Itoh et al., 2019), in the opposite direction at the time of the earthquake as back-slip method in Savage (1983) (i.e., the direction in which the slip-deficit occurs).

Since the purpose of this study is to quantitatively investigate the effect of observation error on the estimation of slip distribution, it was necessary to calculate the crustal deformation for the aforementioned reference slip distribution at each observation point, and then to provide a prescribed pseudo error for the observation data. In terms of observation data, we assume the measurement of crustal deformation via onshore GNSS, the measurement of vertical crustal deformation via OBP sensors (S-net, PG1, PG2), and the measurement of horizontal and vertical crustal deformation via GNSS-A. The

TABLE 1 | Precision of the detection level of the crustal deformation for each sensor in coseismic and interseismic time.

	Coseismic (real-time)	Interseismic (post-processed)
OBP (S-net)	V: 20 mm	NA
OBP (PG1, PG2)	V: 30 mm	NA
GNSS-A	NA	H: 20 mm/year
High-precision GNSS-A	NA	H: 5 mm/year
Onshore GNSS	H: 30 mm, V: 70 mm	H: 4 mm/year, V: 8 mm/year

H and V indicate horizontal and vertical components, respectively.

measurement precision when using crustal deformation observation in terms of both land and seafloor for coseismic (precision available in real-time) and interseismic (precision obtained by post analysis) periods are shown in **Table 1**. Here, the covariance is assumed to be zero. Detailed information on the estimation of error for each observation sensor is included in Appendix section

2 METHODOLOGY

2.1 Computation of Green's Functions Considering Three-Dimensional Crust Structure

We can expect improvement to the accuracy of fault slip distribution estimation when using Green's functions that reflect the three-dimensional (3D) crust structure with the surface topography (e.g., Williams and Wallace, 2018). Here, we used the finite-element method (FEM) with unstructured elements to compute Green's functions for the crustal deformation due to fault slip, since this method is suitable for solving problems with complex geometries and analytically satisfies the traction-free boundary condition at the surface (Ichimura et al., 2016). The fault slip could be evaluated using the split-node technique devised by Melosh and Raefsky (1981) and a clamped boundary condition was applied at the sides and bottom of the FE model. In general, it is difficult to generate large-scale 3D FE models that reflect the complex crust structure with high fidelity. Here, we generated such a model that was comprised of second-order tetrahedral elements using the automatic and robust meshing method devised by Ichimura et al. (2016). As the computational cost of FE analyses with large-scale models can be potentially huge, which was the case with this paper, FE solvers that can reduce the computation costs were proposed (Ichimura et al., 2016). The FE solver developed in Ichimura et al. (2016) enabled fast analysis on CPU-based systems. For conducting further large-scale analysis, we ported this FE solver to GPUs using OpenACC, which is a programming model with high portability.

2.2 Inversion Analysis Based on Green's Functions

We estimated the fault slip distribution using geodetic data observed at N points on the surface using Green's functions computed via the FE analysis method. We can represent the spatial distribution of fault slip $\boldsymbol{s}(\boldsymbol{x})$ using a linear combination of M basis functions $\boldsymbol{X}_m(\boldsymbol{x})$

$$\boldsymbol{s}(\boldsymbol{x}) = \sum_{m=1}^{m} a_m X_m(\boldsymbol{x}), \tag{1}$$

where $\boldsymbol{a}$ is the set of model parameters. The crustal deformation during fault slip is considered to be linear elastic. We can describe the equation representing the displacement response at the observation points on the ground surface $\boldsymbol{g}_m$ for a unit fault slip $\boldsymbol{X}_m$ as

$$\boldsymbol{d} = \boldsymbol{G}\boldsymbol{a} + \boldsymbol{e}, \tag{2}$$

where $\boldsymbol{d}$ is the vector of the surface displacements at the observation points, $\boldsymbol{G}$ is the observation matrix that is comprised of the g_i components of Green's functions, and $\boldsymbol{e}$ is the normally distributed errors with mean $\boldsymbol{0}$ and covariance matrix $\sum$. When computing slip distribution in high resolution, the inverse problem may become indeterminate (the number of model parameters M may become larger than the number of observation channels N), and even if $M < N$, the system may become unstable and the solution may become highly sensitive in terms of noise. For the stabilization of these issues, it is essential to regularize the solution using prior information of the slip distribution. One approach to this involves minimizing an objective function such as

$$\Phi(\boldsymbol{a}) = (\boldsymbol{d} - \boldsymbol{G}\boldsymbol{a})^T \sum^{-1} (\boldsymbol{d} - \boldsymbol{G}\boldsymbol{a}) + \lambda r \tag{3}$$

with,

$$r = \int \nabla^2 s(x) \mathrm{d}x, \tag{4}$$

where r is a roughness parameter used to penalize slip distribution with unrealistic oscillation in high frequencies. When using discretization based on finite difference approximations, the roughness can be represented as $r = \boldsymbol{a}^T \boldsymbol{L}\boldsymbol{a}$, with a positive-semidefinite matrix $\boldsymbol{L}$. The slip distribution of fault slip $\boldsymbol{s}$ can be determined such that the objective function is minimized, given a specific value for λ. One common method used to determine λ is the k-fold cross validation method. Here, the observation dataset was split into k subsets, and the model parameters $\boldsymbol{a}$ were estimated using the data in the $k-1$ subsets, with the remaining subset used to compute the validation error. The λ with the smallest total validation error is used in the final solution.

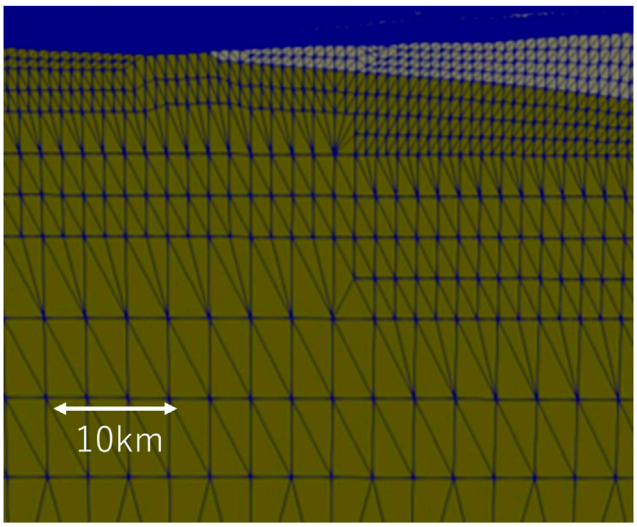

FIGURE 3 | Overview and close-up view of the FE model.

3 NUMERICAL EXPERIMENTS

We estimated the coseismic slip distribution and the interseismic slip-deficit distribution off Tokachi and Nemuro using the proposed inversion method. To verify the effect of the precision of the observation data and the presence of various observation points on the estimation accuracy, a reference solution must be generated for comparison with the estimated solutions. We obtained artificial observation data by applying the FE analysis to the reference slip distribution and adding the assumed noise to it. Using these artificial observation data, we estimated the slip distribution at the fault plane via the developed inversion method. To evaluate the difference in estimation accuracy with/without observation points and with varying observation precision, we introduced a Monte Carlo approach involving the inversion for 4,000 artificial observation datasets with different noise patterns for each case. From each inversion result, we verified the error distribution and the uncertainty in the estimated seismic slip and slip-deficit.

For the crustal structure data, we used the surface topography and the plate boundary set by the Cabinet Office's disaster prevention division (Yokota et al., 2017), as described in **Section 1.2**. The crustal structure data were projected onto the 13th system of the Japanese plane orthogonal coordinate system, with the target domain set between coordinates of $-1{,}053\ \mathrm{km} \leq x \leq 1{,}332\ \mathrm{km}$ in the east-west direction, $-1{,}048\ \mathrm{km} \leq y \leq 922\ \mathrm{km}$ in the north-south direction, and $-1{,}500\ \mathrm{km} \leq z \leq 0\ \mathrm{km}$ in the vertical direction. Since the Cabinet Office disaster prevention model assumes a homogeneous medium, the crustal structure was modeled as two layers with the same physical properties (rigidity is 40 GPa and Poisson's ratio is 0.25), with the plate boundary in between. **Figure 3** shows the FE model generated by discretizing the target model with minimum element size ds = 1,620 m. The FE model consisted of 12,118,109 second-ordered tetrahedral elements with 50,050,911 degrees of freedom.

The area of the fault plane for which Green's functions were calculated was $-189\ \mathrm{km} \leq x \leq 297\ \mathrm{km}$ and $-344\ \mathrm{km} \leq y \leq 20\ \mathrm{km}$. As a basis function of the fault slip distribution, we introduced a unit fault slip, which was designated as a bicubic B-spline curve of the grid. The grid points were set 32.4 km apart inside the target area, and the points outside the fault plane were excluded. Since the number of fitting points was 117 and the slip distribution in the x and y directions on the fault plane was considered, $2 \times 117 = 234$ Green's functions were calculated. The roughness used as regularization was provided via finite difference method using values on grid points. At this time, a virtual grid point with zero values was placed on the outer circumference of the area and regularization was applied to the range that included these points. To calculate the 234 Green's functions, two IBM Power System AC922 compute nodes with dual 16-core IBM POWER9 2.60 GHz CPUs and 4 NVIDIA Tesla V100 GPUs were used. Thus, in total, eight GPUs were used in parallel with eight MPI processes. While the computation of the 234 Green's functions via 50 million degrees of freedom 3D FE models would generally require huge computational costs, the analysis time was significantly reduced through using a suitable analysis algorithm with GPU implementation, which allowed for computing each Green's function in less than 10 s.

In the following subsections, we estimate the coseismic slip and the interseimic slip-deficit distributions using the observation points shown in **Figures 1**, **2** and discuss the obtained analysis results.

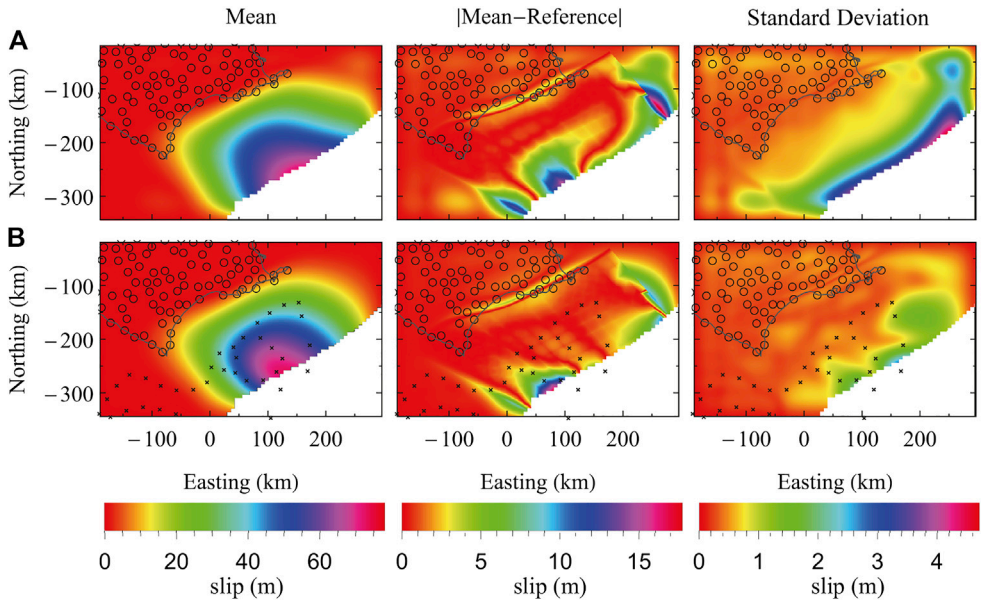

FIGURE 4 | Mean, absolute error between mean and reference solution, and standard deviation of coseismic fault slip distribution with 4,000× Monte Carlo inversions using **(A)** GNSS data and **(B)** GNSS and OBP data. The average standard deviation is **(A)** 0.847 m and **(B)** 0.439 m, respectively. The position of GNSS and OBP stations are represented by circles and cosses, respectively.

3.1 Results and Discussion for Coseismic Slip

We conducted estimations using two sets of observation data: 1) land GNSS, and 2) land GNSS and OBP. For the fault slip estimation immediately after the occurrence of an earthquake (within around 5 min), only GNSS results is used. Compared with the reference solution (**Figure 1**), the overall picture, including larger slip (>60 m) near the trench axis, is captured only by the land data (**Figure 4A** left). However, the residual near the trench axis was locally 10 m or more (several tens of percent or more) at $x \sim 100$ km (**Figure 4A**, middle). Here is near the peak of the reference slip and results in an underestimation, while the east side where the slip decreases ($x > 250$ km) results in an overestimation. The result demonstrated that it is difficult to accurately attain the heterogeneous slip distribution near the trench axis using land-based GNSS data alone, and that the estimation accuracy of the initial wave source of the resulting tsunami is low in this region. On the other hand, when we include the OBP data, the estimation accuracy of the slip distribution near the trench axis becomes much higher (**Figure 4B**). Hence, if the OBP data are inputted into the REGARD system, this is expected to improve the accuracy of estimating the tsunami height and its inundation distribution, which is of great social importance. When using the OBP data of an earthquake to measure the crustal deformation, noise such as the dynamic water pressure fluctuations associated with the seismic waves and the fluctuations associated with the tsunami will be included in the measurement data. To estimate the crustal deformation accurately in a short period of time, it is important to appropriately remove such noise. By using the proposed method, it is possible to quantify the effects of these forms of noise.

The above results are the cases where model errors are ignored. If model errors are taken into account, we can imagine that the recovery to the reference model will be worse in any case. However, the important question here is how the effect of addition of offshore observation points changes when model errors are considered. Based on the results in a previous study (Yamaguchi et al., 2017a), the standard deviation in slip estimation at the area away from the observation points is twice or more comparing with that below the observation point when P and S wave velocity varies in 10 and 20% and density varies in 15% for the 3D heterogeneous structure. This means that the advantage of addition of observation points in the offshore area is expected to be more pronounced with model error than illustrated in **Figure 4**. Additionally, the analyses with model error requires plenty number of calculations for Green's functions of various 3D heterogeneous structures with model error but we think it is possible to demonstrate with GPU application as in this study and also Yamaguchi et al. (2017a), Yamaguchi et al. (2017b).

3.2 Results and Discussion for Interseismic Slip-Deficit

The cable OBP data, which is useful for measuring coseismic seafloor deformation as shown in **Section 3.1**, is not used in interseismic slip estimations since it is difficult to correct any sensor specific drifts. Here, GNSS-A plays an important role. As noted in Appendix, the GNSS-A observation error can be significantly reduced by increasing the frequency of observations (Yokota et al., 2016). Here we conducted four cases using different types of observation data: 1) land GNSS, 2) land GNSS and GNSS-A, 3) land GNSS and high-precision GNSS-A, and 4) land GNSS and high-precision GNSS-A with additional GNSS-A points that

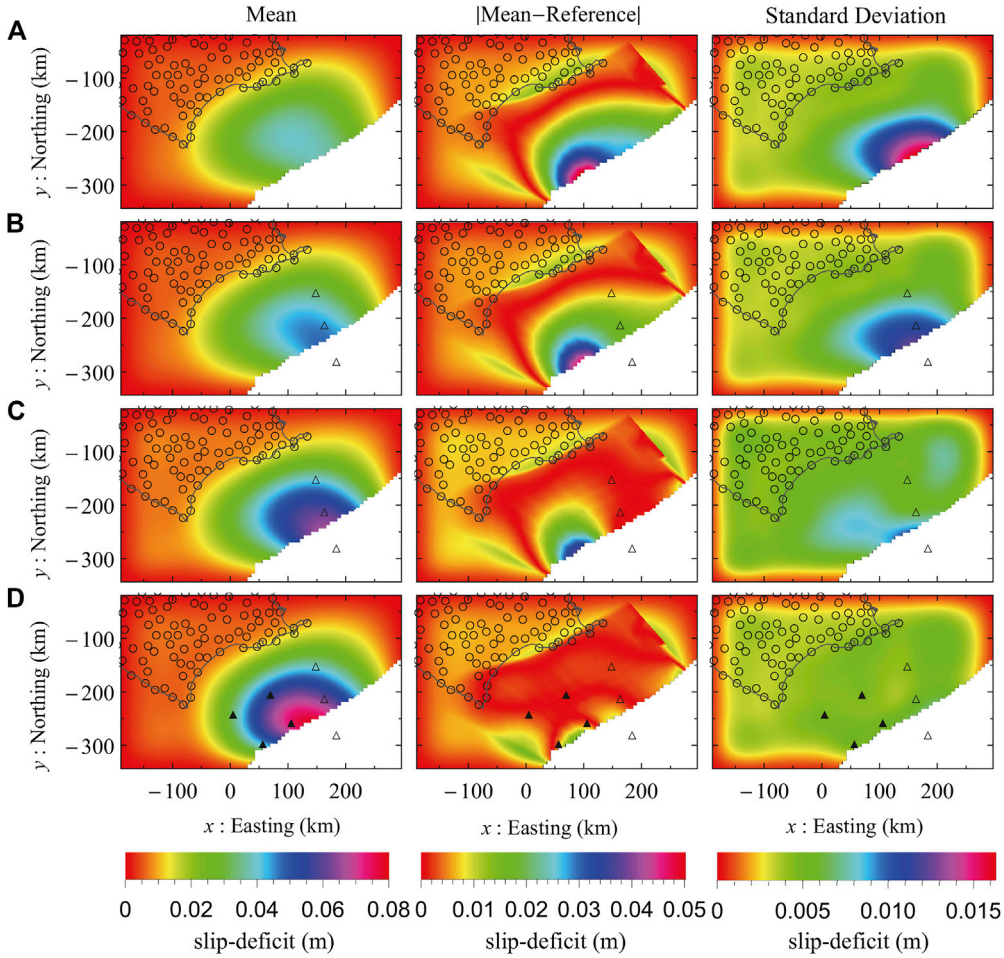

FIGURE 5 | Mean, absolute error between mean and reference solution, and standard deviation of interseismic fault slip-deficit distribution with 4,000× Monte Carlo inversions using **(A)** GNSS data, **(B)** GNSS and GNSS-A data, **(C)** GNSS and high-precision GNSS-A data, and **(D)** GNSS and high-precision GNSS-A data with additional GNSS-A observation points. The average standard deviation for each case was **(A)** 0.0040 m, **(B)** 0.0041 m, **(C)** 0.0046 m, and **(D)** 0.0034 m, respectively. The position of GNSS, GNSS-A, and the virtual GNSS-A stations are represented by circles, empty triangles, and filled triangles, respectively.

are not presently installed in the target area. The result of the land GNSS only shows that larger slip-deficit toward the trench axis cannot be recovered with considerable underestimation (**Figure 5A**). The result differs significantly from the coseismic slip case only with the land data in **Section 3.1**, even though the relative distribution is the same. This is probably because the signal-to-noise ratio is an order of magnitude smaller in the case of slip-deficit in one year than in the case of large slip caused by the 9M earthquake, and it is not possible to constrain the larger slip-deficit away from the observation points as indicated clearly in **Figure 5A**. Currently, GNSS-A observations along the Kuril Trench are conducted around once a year by Tohoku University and other institutions (Honsho et al., 2019). The error of the displacement velocity obtained is expected to be around 20 mm/year, which is large compared to the cases using GNSS-A observations with higher frequency. The estimation results for the land GNSS and GNSS-A in offshore area are shown in **Figure 5B**. Even when using such seafloor observations with the relatively large error, it is clear that the slip-deficit rate is recovered better near the trench axis than when using land observations alone. Furthermore, if high frequency observations (more than several times a year, as in regions such as southwest Japan) could be realized, the error in the magnitude of the slip-deficit rate would be quantitatively suppressed to several tens of percent or less (**Figure 5C**). In particular, the error is less than 10% just below the GNSS-A observation point. On the other hand, the part of $x = 0 - 100$ km, where there is no observation point and the peak of the slip-deficit is located, is still underestimated. While it is difficult to carry out observations with high frequency using ships, the development of automatically repeated observations using wave gliders (Iinuma et al., 2012, submitted to this issue) are in progress, which means we can expect the realization of such high accuracy estimations in the near future. Finally, the results of the slip estimation when adding four virtual GNSS-A observation points in the segments off Tokachi are shown in **Figure 5D**. The estimation accuracy of the heterogeneity of the plate coupling in the strike direction of the plate subduction is clearly improved by adding the observation points just above the peak slip-deficit area. The intervals of additional GNSS-A points are around 70 km

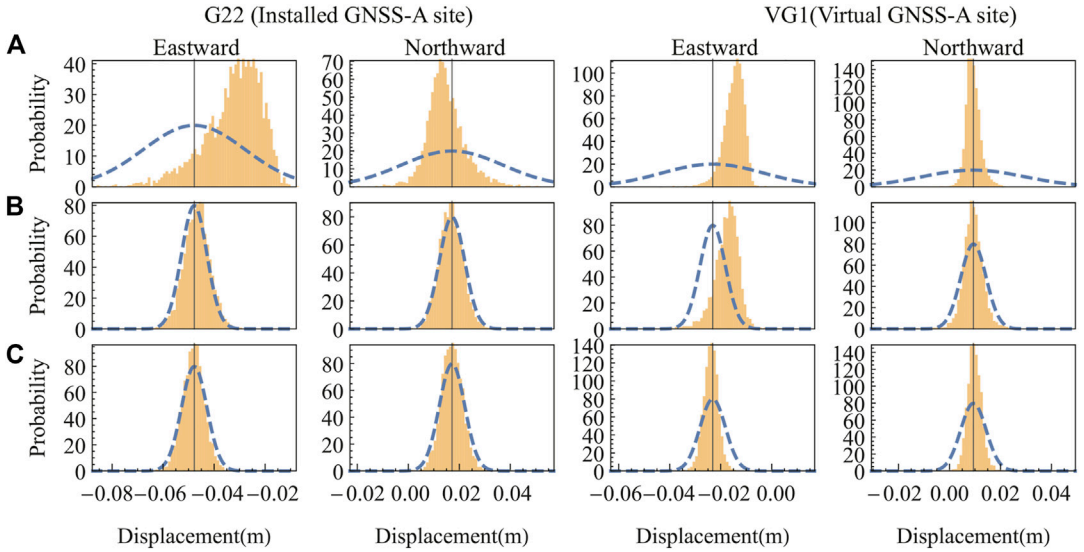

FIGURE 6 | Horizontal displacement distribution at observation points G22 and VG1 (see **Figure 2** for the position of the observation points). True predicted distribution (dotted line), true observed value (solid vertical line, as variance is zero), and predicted distribution obtained from the optimization results (histogram). **(A)** GNSS and GNSS-A **(B)** GNSS and high-precision GNSS-A, **(C)** GNSS and high-precision GNSS-A with additional GNSS-A observation points.

(similar to the existing ones). As a result, there are observation points within a horizontal distance of about 50 km from each source of the slip-deficit, and the estimation error becomes less than 10% for the whole offshore area. When adding GNSS-A observation points in the future, it will be important to determine the installation position after performing such a quantitative accuracy evaluation for a more effective estimation of the slip-deficit distribution. For this purpose, we can apply the present method to various combinations of possible distributions of slip-deficit rates and additional observation points of feasible number with a brute-force search or with a non-linear optimization method (e.g., Sathiakumar et al., 2017).

To examine the effect of the improvement in observation precision and the addition of observation points in more detail, a pointwise evaluation was performed at the installed GNSS-A observation point G22 and the virtual GNSS-A observation point VG1 (**Figure 2** shows the position of the observation points and **Figures 6**, **7** show the results). In **Figure 6**, the solid vertical line represents the true response value for the reference fault slip, while the broken line represents the modeled probability distribution when considering the observation errors listed in **Table 1**. The histogram represents the predicted response values obtained by the inversion of the pseudo observation data with the aforementioned 4,000 patterns of noise. In the case of the current GNSS-A observation measurement method, the observation precision is 20 mm/year, which is comparable with the magnitude of the horizontal crustal deformation caused by the slip-deficit of 80 mm/year. Thus, the weight of the observed value is considered to be small and the regularization is deemed to have performed strongly during the optimization process. As such, the predicted distribution obtained from the estimated slip-deficit had a large deviation from the modeled distribution (**Figure 6A**, G22 and VG1). However, when the observation precision was improved to 5 mm/year, the spatial distribution that reproduces the observed displacement was obtained (**Figure 5C**), which resulted in obtaining an almost identical probability distribution among the predicted and modeled distributions (**Figure 6B**, G22). Note that the predicted distribution for the virtual GNSS-A site (VG1), which is not included in the inversion, still shows deviation from the modeled distribution (**Figure 6C**, VG1). Furthermore, by adding virtual GNSS-A observation points, the spatial distribution of the slip-deficit was reproduced more accurately and the standard deviation became smaller (**Figure 5D**). Thus, a probability distribution with a slightly smaller variance than the modeled probability distribution was obtained for both of the observation points (**Figure 6C**, G22 and VG1).

Conventionally, the measurement of the horizontal position was the main purpose of GNSS-A; however, in recent years, methods for realizing high-precision measurement in the vertical direction have

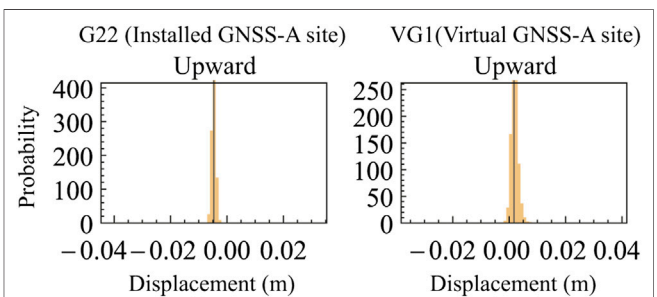

FIGURE 7 | Vertical displacement distribution at observation points G22 and VG1 (see **Figure 2**) for the case of GNSS and high-precision GNSS-A and additional GNSS-A observation points. True observed value (solid vertical line, as variance is zero) and the predicted distribution obtained from the optimization results (histogram) are shown.

been developed. Thus, it is meaningful to consider how much precision is required in the vertical displacement measurement to improve interseismic slip-deficit estimations. For a low-angle fault, the vertical displacement is smaller than the horizontal displacement, which means the difference and variance between the true value and the predicted value becomes smaller. Therefore, if the results of this study as shown in **Figure 7** are accepted, the vertical displacement of GNSS-A is unlikely to contribute to the improvement in the accuracy of interseismic slip-deficit distribution estimations, unless a high observation precision within several millimeters is realized. However, based on the discussion about model error in **Section 3.1**, it is highly possible that the use of the correct Green's function (without model error) has led to the good reproduction of vertical displacement using horizontal component observation constraints alone. If we introduce model error, horizontal component becomes not enough to constrain the slip distribution and the contribution of the vertical component becomes larger.

4 CONCLUSION

The purpose of this manuscript is to quantify the effectiveness of the offshore data for the slip estimation especially near the trench axis. Our results demonstrate the effectiveness of the observation of seafloor crustal deformation near the trench axis, as well as the advancement in the modeling, including in terms of topography and plate geometry. For the coseismic slip, the heterogeneous distribution near the trench axis can be reproduced when we include the cable OBP data, which cover whole the offshore source area. Furthermore, it was demonstrated that the interseismic slip-deficit distribution in the shallow part of the subducting plate interface can be reproduced with high accuracy by improving the precision of the seafloor crustal deformation observations (i.e., increasing the observation frequency of GNSS-A). It was also demonstrated that the estimated resolution of the slip-deficit in the strike direction in this area can be improved and the estimation error becomes less than 10% for the whole offshore area by adding four GNSS-A observation points off Tokachi to the currently installed off Nemuro with about 70 km interval. However, the cost of increasing the number of observation points will involve not only the installment costs but also the additional costs for conducting the measurements on each occasion. Thus, obtaining the maximum effect with the minimum number of additional observation points is crucial, and the proposed method applying various combinations of possible distributions of slip-deficit and additional observation points is expected to be useful for this purpose. Meanwhile, it was shown that higher observation precision than that for the horizontal components is required for the vertical components of the observations to become useful for the improvement of the estimation of slip-deficit distribution. However, it is highly possible that this finding was due to the use of exact Green's functions, and it is thus necessary to conduct additional research by extending the proposed method for the consideration of model error and to conduct appropriately extended evaluations. In addition, a numerical experiment was conducted with assuming a slip-deficit distribution that would suit a preparation process for a large 9M-class earthquake. However, seismic events at a plate interface can occur on a smaller scale (e.g., Honsho et al., 2019). In recent years, seafloor acoustic observations that range over the trench axis at the shallowest plate interface have also been performed by various researchers (e.g., Yamamoto et al., in preparation). Here, an improvement to the structure model is an expected requirement for the accurate reproduction of smaller plate interface events and the reproduction of the phenomena on a scale of around 10 km or less that straddle the trench axis. It is expected that the understanding of the phenomena that occur at the plate interface will be further advanced by improving both the modeling and the observation. It should be noted that our analysis used the exact solution as the Green's function, which meant the analysis was performed with a model error of zero. In the case of actual data analysis, such level of estimation accuracy cannot be expected since there is an error in the underground crustal structure model. However, it is expected that such analyses with model error will enable a quantitative examination of the improvement in the accuracy of the results through the improvement in observation precision and addition of observation points, even for actual data. Furthermore, we consider that the quantification procedure is applicable to other slip and slip-deficit distribution patterns and other subduction zones as well.

DATA AVAILABILITY STATEMENT

The original contributions presented in the study are included in the article/Supplementary Material, further inquiries can be directed to the corresponding author.

AUTHOR CONTRIBUTIONS

SM, TI, TH, and YO formulated the investigation. SM, TI, and KF developed the finite-element method, SM and TI developed the inversion method, and SM conducted the numerical experiments. TH and YO provided information and discussion related to the observation methods. All authors contributed to the article.

FUNDING

This work was supported by the Ministry of Education, Culture, Sports, Science and Technology of Japan (MEXT) as "Program for Promoting Researches on the Supercomputer Fugaku" (Large-scale numerical simulation of earthquake generation, wave propagation and soil amplification: hp200126) and by JSPS KAKENHI (JP18H05239).

ACKNOWLEDGMENTS

We thank the two anonymous reviewers for constructive comments. Digital data of surface topography, plate boundary

and coseismic slip distribution are given by Cabinet Office, Disaster Management. This work was supported by the Ministry of Education, Culture, Sports, Science and Technology of Japan (MEXT) as "Program for Promoting Researches on the Supercomputer Fugaku" (Large-scale numerical simulation of earthquake generation, wave propagation and soil amplification: hp200126) and by JSPS KAKENHI (JP18H05239). This work was partly supported by MEXT, under its Earthquake and Volcano Hazards Observation and Research Program.

REFERENCES

Agata, R., Hori, T., Ariyoshi, K., and Ichimura, T. (2019). Detectability analysis of interplate fault slips in the nankai subduction thrust using seafloor observation instruments. *Mar. Geophys. Res.* 40, 453. doi:10.1007/s11001-019-09380-y

Baba, T., Hirata, K., Hori, T., and Sakaguchi, H. (2006). Offshore geodetic data conducive to the estimation of the afterslip distribution following the 2003 Tokachi-oki earthquake. *Earth Planet. Sci. Lett.* 241, 281–292. doi:10.1016/j.epsl.2005.10.019

Cabinet Office, D. M. (2020a). *Figures and tables for megathrust earthquake models along the Japan Trench and the Kuril Trench*. Tokyo: Cabinet Office.

Cabinet Office, D. M. (2020b). *Report for megathrust earthquake models along the Japan Trench and the Kuril Trench*. Tokyo: Cabinet Office.

Gagnon, K., Chadwell, C. D., and Norabuena, E. (2005). Measuring the onset of locking in the Peru-Chile trench with GPS and acoustic measurements. *Nature* 434, 205–208. doi:10.1038/nature03412

Hashimoto, C., Noda, A., and Matsuura, M. (2012). The Mw 9.0 northeast Japan earthquake: total rupture of a basement asperity 189. *Geophys. J. Int.* 1–5. doi:10.1111/j.1365-246X.2011.05368.x

Hino, R., Inazu, D., Ohta, Y., Ito, Y., Suzuki, S., Iinuma, T., et al. (2014). Was the 2011 Tohoku-Oki earthquake preceded by aseismic preslip? Examination of seafloor vertical deformation data near the epicenter. *Mar. Geophys. Res.* 35, 181–190. doi:10.1007/s11001-013-9208-2

Honsho, C., Kido, M., Tomita, F., and Uchida, N. (2019). Offshore postseismic deformation of the 2011 Tohoku earthquake revisited: application of an improved GPS-acoustic positioning method considering horizontal gradient of sound speed structure. *J. Geophys. Res. Solid Earth* 124, 5990–6009. doi:10.1029/2018JB017135

Ichimura, T., Agata, R., Hori, T., Hirahara, K., Hashimoto, C., et al. (2016). An elastic/viscoelastic finite element analysis method for crustal deformation using a 3-D island-scale high-fidelity model. *Geophys. J. Int.* 206, 114–129. doi:10.1093/gji/ggw123

Ichimura, T., Agata, R., Hori, T., Satake, K., Ando, K., Baba, T., et al. (2017). Tsunami analysis method with high-fidelity crustal structure and geometry model. *J. Earthquake Tsunami* 11, 1750018. doi:10.1142/S179343111750018X

Iinuma, T., Hino, R., Kido, M., Inazu, D., Osada, Y., Ito, Y., et al. (2012). Coseismic slip distribution of the 2011 off the Pacific Coast of Tohoku Earthquake (M9.0) refined by means of seafloor geodetic data. *J. Geophys. Res.* 117, 18–91. doi:10.1029/2012JB009186

Imano, M., Kido, M., Honsho, C., Ohta, Y., Takahashi, N., and Fukuda, T. (2019). Assessment of directional accuracy of GNSS-Acoustic measurement using a slackly moored buoy. *Prog. Earth Planet. Sci.* 6, 1–14. doi:10.1186/s40645-019-0302-1

Ioki, K., and Tanioka, Y. (2016). Re-estimated fault model of the 17th century great earthquake off Hokkaido using tsunami deposit data. *Earth Planet. Sci. Lett.* 433, 133–138. doi:10.1016/j.epsl.2015.10.009

Ito, Y., Tsuji, T., Osada, Y., Kido, M., Inazu, D., Hayashi, Y., et al. (2011). Frontal wedge deformation near the source region of the 2011 Tohoku-Oki earthquake. *Geophys. Res. Lett.* 38, 35–83. doi:10.1029/2011GL048355

Itoh, Y., Nishimura, T., Ariyoshi, K., and Matsumoto, H. (2019). Interplate slip following the 2003 tokachi-oki earthquake from ocean bottom pressure gauge and land GNSS data. *J. Geophys. Res. Solid Earth* 124, 4205–4230. doi:10.1029/2018JB016328

Kawamoto, S., Hiyama, Y., Ohta, Y., and Nishimura, T. (2016). First result from the GEONET real-time analysis system (REGARD): the case of the 2016 kumamoto earthquakes. *Earth Planets Space* 68. doi:10.1186/s40623-016-0564-4

Kawamoto, S., Ohta, Y., Hiyama, Y., Todoriki, M., Nishimura, T., Furuya, T., et al. (2017). REGARD: a new GNSS-based real-time finite fault modeling system for GEONET. *J. Geophys. Res. Solid Earth* 122, 1324–1349. doi:10.1002/2016JB013485

Kimura, H., Tadokoro, K., and Ito, T. (2019). Interplate coupling distribution along the Nankai Trough in southwest Japan estimated from the block motion model based on onshore GNSS and seafloor GNSS/A observations. *J. Geophys. Res. Solid Earth* 124, 6140–6164. doi:10.1029/2018JB016159

Kinugasa, N., Tadokoro, K., Kato, T., and Terada, Y. (2020). Estimation of temporal and spatial variation of sound speed in ocean from GNSS-A measurements for observation using moored buoy. *Prog. Earth Planet. Sci.* 7, 1–14. doi:10.1186/s40645-020-00331-5

Kubota, T., Saito, T., and Suzuki, W. (2020). Millimeter-scale tsunami detected by a wide and dense observation array in the deep ocean: fault modeling of an Mw 6.0 interplate earthquake off Sanriku, NE Japan. *Geophys. Res. Lett.* 47, 1–11. doi:10.1029/2019GL085842

Melosh, H. J., and Raefsky, A. (1981). A simple and efficient method for introducing faults into finite element computations. *Bull. Seismol. Soc. Am.* 71, 1391–1400.

Mochizuki, M., Uehira, K., Kanazawa, T., Kunugi, T., Shiomi, K., Aoi, S., et al. (2018). "S-net project: performance of a large-scale seafloor observation network for preventing and reducing seismic and tsunami disasters," in OCEANS - MTS/IEEE Kobe Techno-Oceans (OTO), Kobe, Japan, May 29–31 (IEEE),1–4. doi:10.1109/OCEANSKOBE.2018.8558823

Nanayama, F., Satake, K., Furukawa, R., Shimokawa, K., Atwater, B. F., Shigeno, K., et al. (2003). Unusually large earthquakes inferred from tsunami deposits along the Kuril trench. *Nature* 424, 660–663doi:10.1038/nature01864

Ohta, Y., Hino, R., Inazu, D., Ohzono, M., Ito, Y., Mishina, M., et al. (2012a). Geodetic constraints on afterslip characteristics following the March 9, 2011, Sanriku-oki earthquake, Japan, *Geophys. Res. Lett.* 39, 430. doi:10.1029/2012GL052430

Ohta, Y., Kobayashi, T., Tsushima, H., Miura, S., Hino, R., Takasu, T., et al. (2012b). Quasi real-time fault model estimation for near-field tsunami forecasting based on RTK-GPS analysis: application to the 2011 Tohoku-Oki earthquake (Mw9.0). *J. Geophys. Res.* 117, 750. doi:10.1029/2011JB008750

Ohta, Y., Inoue, T., Koshimura, S., Kawamoto, S., and Hino, R. (2018). Role of real-time GNSS in near-field tsunami forecasting. *J. Disaster Res.* 13, 453–459. doi:10.20965/jdr.2018.p0453

Ohta, Y., Kobayashi, T., Hino, R., Demachi, T., and Miura, S. (2015). "Rapid coseismic fault determination of consecutive large interplate earthquakes: the 2011 Tohoku-Oki sequence", in International Association of Geodesy Symposia, 143 (New York: *Springer*), 467–475. doi:10.1007/13452015109

Sato, T., Hasegawa, S., Kono, A., Shiobara, H., Yagi, T., Yamada, T., et al. (2017). Detection of vertical motion during a slow-slip event off the Boso Peninsula, Japan, by ocean bottom pressure gauges. *Geophys. Res. Lett.* 44, 2710–2715. doi:10.1002/2017GL072838

Savage, J. C. (1983). A dislocation model of strain accumulation and release at a subduction zone. *J. Geophys. Res.* 88, 4984–4996. doi:10.1029/jb088ib06p04984

Sawai, Y. (2020). Subduction zone paleoseismology along the Pacific coast of northeast Japan - progress and remaining problems. *Earth-Science Rev.* 208, 103261. doi:10.1016/j.earscirev.2020.103261

Sathiakumar, S., Barbot, S. D., and Agram, P. (2017). Extending resolution of fault slip with geodetic networks through optimal network design. *J. Geophys. Res. Solid Earth* 122, 538–610. doi:10.1002/2017JB014326

Suito, H. (2016). Detectability of interplate fault slip around Japan, based on GEONET daily solution F3. *J. Geodetic Soc. Jap.* 62, 109–120. 10.10072Fs11001-019-09380-y

Takahashi, H., and Kasahara, M. (2013). "Spatial relationship between interseismic seismicity, coseismic asperities and aftershock activity in the southwestern kuril islands," in *Volcanism and subduction: the Kamchatka region, geophysical monograph series 172*. Editors

J. Eichelberger, E. Gordeev, P. Izbekov, M. Kasahara, and J. Lees (American Geophysical Union), 153–164.

Williams, C. A., and Wallace, L. M. (2018). The impact of realistic elastic properties on inversions of shallow subduction interface slow slip events using seafloor geodetic data. *Geophys. Res. Lett.* 45, 7462–7470. doi:10.1029/2018GL078042

Yamaguchi, T., Fujita, K., Ichimura, T., Hori, T., Hori, M., and Wijerathne, L. (2017a). Fast finite element analysis method using multiple GPUs for crustal deformation and its application to stochastic inversion analysis with geometry uncertainty. *Proced. Comp. Sci.* 108, 765–775. doi:10.1016/j.procs.2017.05.223

Yamaguchi, T., Ichimura, T., Yagi, Y., Agata, R., Hori, T., and Hori, M. (2017b). Fast crustal deformation computing method for multiple computations accelerated by a graphics processing unit cluster. *Geophys. J. Int.* 210, 787–800. doi:10.1093/gji/ggx203

Yokota, T., Nemoto, M., Matsusue, K., Takase, S., Takata, K., and Ikeda, M. (2017). Study on the plate model of the Pacific plate. *JpGU-AGU Jt. Meet. SSS13–P04*

Yokota, Y., Ishikawa, T., Watanabe, S. I., Tashiro, T., and Asada, A. (2016). Seafloor geodetic constraints on interplate coupling of the Nankai Trough megathrust zone. *Nature* 534, 374–377. doi:10.1038/nature17632

Conflict of Interest: The authors declare that the research was conducted in the absence of any commercial or financial relationships that could be construed as a potential conflict of interest.

APPENDIX

Here, we explain the characteristics of each observation method and the estimation of observation precision used in this study.

Cable OBP

OBP systems present observation sensors that allow us to continuously measure vertical crustal displacements and tsunami heights through measuring the pressure of the water column with a water pressure gauge installed on the seafloor. In recent years, cable OBP observations have been deployed mainly for the purpose of the immediate prediction of tsunamis in Japan. The obtained OBP data contain not only the crustal deformation but also the other contributions, including those of the tidal component, the non-tidal component, and the sensor-specific drift component. However, it is particularly difficult to remove the sensor-specific drift component, which means it is currently difficult to capture the slow crustal deformation in the interseismic period using OBP data. This form of data was thus not used for the interseismic slip-deficit estimation in this study. Meanwhile, the observation of coseismic crustal deformation, postseismic crustal deformation, and unsteady crustal deformation, which are phenomena with shorter time scales, has been carried out by numerous researchers (e.g., Baba et al., 2006; Ito et al., 2011; Ohta et al., 2012a; Hino et al., 2014; Sato et al., 2017; Kubota et al., 2020). Here, Baba et al. (2006) estimated the postseismic slip distribution of the 2003 Tokachi-Oki earthquake using two OBP sensors (PG1, PG2) installed off the coast of Tokachi and onshore GNSS data, with the authors assuming that the standard deviation of the daily OBP data after correcting with the thermometer data was 2 hPa (around 2 cm in terms of crustal deformation). Meanwhile Kubota et al. (2020) used the OBP data obtained from the S-net laid in the Japan Trench and the southern part of the Kuril Trench to analyze the millimeter-scale micro tsunami to estimate the fault model of the Mw6.0 earthquake that occurred off Sanriku. Here, the short-term stability of the S-net OBP data before and after the earthquake was 1 hPa (around 1 cm in terms of crustal deformation). To understand the crustal deformation that occurs during an earthquake, it is necessary to calculate the difference before and after the earthquake. Therefore, the error before and after the earthquake was propagated to obtain the estimation error of the displacement during the earthquake. As a result, estimation errors of 30 mm for PG1 and PG2 off Tokachi and 20 mm for S-net were used in terms of the displacement that occurs during earthquakes obtained in real-time (**Table 1**). In reality, the accuracy is likely to be degraded due to the effects of tsunami, but for simplicity, we used this value here.

GNSS-A

GNSS-A presents a technology that estimates the relative position of the reference station installed on the seafloor according to the acoustic distance measurement from the sea surface platform, with the position of the sea surface platform obtained via GNSS. The seafloor crustal deformation is then measured by combining these results. Here, we considered the precision of estimating the displacement in the interseismic period via GNSS-A. Honsho et al. (2019) estimated the postseismic crustal deformation of the 2011 Tohoku-Oki earthquake in detail from the data of 20 GNSS-A stations installed in the Japan Trench. Here, the estimation precision of the displacement velocities at 20 points based on the data covering a four-year period was found to be around 13 mm/year for both the east-west and the north-south components. Therefore, in this study, the current observation error was rounded up to 20 mm/year. In addition, Yokota et al. (2016) observed the GNSS-A seafloor observation network that is installed in the Nankai Trough more than several times a year, and estimated the horizontal velocity with high precision (around 4 mm/year). The estimation error of these displacement velocities depended on the observation frequency and the precision of individual campaign observations. From these results, we assumed 5 mm/year for the errors of high-precision interseismic horizontal velocity observation via frequent GNSS-A measurements.

Onshore GNSS

In recent years, many attempts have been made to immediately estimate the magnitude of a large earthquake using real-time GNSS data (e.g., Ohta et al., 2012a; Kawamoto et al., 2016; Kawamoto et al., 2017). Here, Ohta et al. (2012a) demonstrated that the crustal deformation can be grasped relatively accurately even in real-time using RTK-GNSS data. Here, the authors clarified that the accuracy of the RTK-GNSS positioning depended upon the baseline length, and that the horizontal and vertical precision was around 20 and 50 mm, respectively, at the 500 km baseline. Similarly, Kawamoto et al. (2017) calculated the daily coordinate value stability at 146 points of the GEONET system, and obtained a standard deviation value of 10–15 mm for the horizontal component and 42 mm for the vertical component. Since the difference of the data before and after the earthquake was used to estimate the amount of permanent displacement due to the earthquake, the horizontal and vertical precision of the coseismic displacements in real time were assumed to be 30 and 70 mm, respectively.

Next, we considered the precision of interseismic displacement measurement using land-based GNSS. Itoh et al. (2019) discussed the crustal deformation following the 2003 Tokachi-Oki earthquake using onshore GNSS and OBP data. Here, the authors removed the step-like fluctuations due to yearly peripheral components and equipment replacement from the daily GEONET coordinate values, obtained the monthly coordinate values by down sampling them, and evaluated the quartile deviation of the coordinate values within the month. As a result, the horizontal and vertical measurement error was found to be 2 and 8 mm, respectively. Elsewhere, Suito (2016) evaluated GEONET's fault slip detection capability. Here, the author estimated the average trend and the annual and semiannual components from the coordinate time series for each year from January 1, 2006 to December 31, 2010 and from January 1, 2010 to December 31, 2010. Computing the residual by subtracting the average trend, annual, and semiannual components from the observation data, average 1σ of the residual was computed for the two periods. As a result, the horizontal and vertical average deviation of all GEONET points were found to be 3.34 and 7.35 mm, respectively. Based on these results, the precision of land-based GNSS data was assumed to be 4 mm/year for the horizontal component and 8 mm/year for the vertical component.

frontiers in Earth Science

ORIGINAL RESEARCH
published: 30 April 2021
doi: 10.3389/feart.2021.600930

Effect of Ocean Fluid Changes on Pressure on the Seafloor: Ocean Assimilation Data Analysis on Warm-Core Rings off the Southeastern Coast of Hokkaido, Japan on an Interannual Timescale

Takuya Hasegawa[1,2]*, *Akira Nagano*[3], *Keisuke Ariyoshi*[4], *Toru Miyama*[5], *Hiroyuki Matsumoto*[4], *Ryoichi Iwase*[4] and *Masahide Wakita*[6]

[1]Faculty of Environmental Earth Science, Hokkaido University, Sapporo, Japan, [2]Graduate School of Science, Tohoku University, Sendai, Japan, [3]Research Institute for Global Change, Japan Agency for Marine-Earth Science and Technology (JAMSTEC), Yokosuka, Japan, [4]Research Institute for Marine Geodynamics, JAMSTEC, Yokohama, Japan, [5]Research Institute for Value-Added-Information Generation, JAMSTEC, Yokohama, Japan, [6]Mutsu Institute for Oceanography, JAMSTEC, Mutsu, Japan

OPEN ACCESS

Edited by:
Laura Wallace,
University of Texas at Austin,
United States

Reviewed by:
Nariaki Hirose,
Japan Meteorological Agency, Japan
Fumiaki Kobashi,
Tokyo University of Marine Science and Technology, Japan

***Correspondence:**
Takuya Hasegawa
takuya.hasegawa@ees.hokudai.ac.jp

Specialty section:
This article was submitted to Solid Earth Geophysics, a section of the journal Frontiers in Earth Science

Received: 31 August 2020
Accepted: 19 January 2021
Published: 30 April 2021

Citation:
Hasegawa T, Nagano A, Ariyoshi K, Miyama T, Matsumoto H, Iwase R and Wakita M (2021) Effect of Ocean Fluid Changes on Pressure on the Seafloor: Ocean Assimilation Data Analysis on Warm-Core Rings off the Southeastern Coast of Hokkaido, Japan on an Interannual Timescale. Front. Earth Sci. 9:600930. doi: 10.3389/feart.2021.600930

The relationship between sea surface height (SSH) and seawater density anomalies, which affects the pressure on the seafloor (PSF) anomalies off the southeastern coast of Hokkaido, Japan, was analyzed using the eddy-resolving spatial resolution ocean assimilation data of the JCOPE2M for the period 2001–2018. On an interannual (i.e., year-to-year) timescale, positive SSH anomalies of nearly 0.1 m appeared off the southeastern coast of Hokkaido, Japan, in 2007, associated with a warm-core ring (WCR), while stronger SSH anomalies (~0.2 m) related to a stronger WCR occurred in 2016. The results show that the effects of such positive SSH anomalies on the PSF are almost canceled out by the effects of negative seawater density anomalies from the seafloor to the sea surface (SEP; steric effect on PSF) due to oceanic baroclinic structures related to the WCRs, especially in offshore regions with bottom depths greater than 1000 m. This means that oceanic isostasy is well established in deep offshore regions, compared with shallow coastal regions. To further verify the strength of the oceanic isostasy, oceanic isostasy anomalies (OIAs), which represent the barotropic component of SSH anomalies, are introduced and analyzed in this study. OIAs are defined as the sum of the SSH anomalies and SEP anomalies. Our results indicate that the effect of oceanic fluid changes due to SSH and seawater density anomalies (i.e., OIAs) on PSF changes cannot be neglected on an interannual timescale, although the amplitudes of the OIAs are nearly 10% of those of the SSH anomalies in the offshore regions. Therefore, to better estimate the interannual-scale PSF anomalies due to crustal deformation related to slow earthquakes including afterslips, long-term slow slip events, or plate convergence, the OIAs should be removed from the PSF anomalies.

Keywords: sea surface height, seawater density, warm-core ring, oceanic mesoscale eddy, ocean assimilation data, ocean isostasy anomaly, pressure on the seafloor, steric effect on pressure on the seafloor

1 INTRODUCTION

Along the eastern coast of Japan, ocean trenches such as the Japan Trench and Kuril Trench are found (**Figure 1A**). Along the slopes of trenches, megathrust earthquakes often occur, such as the 2011 Pacific Coast of Tohoku Earthquake. It has been reported that slow slip events (SSEs) frequently occur in these regions (Shelly et al., 2007; Obara and Kato, 2016; Uchida et al., 2016; Araki et al., 2017). Recently, Nishikawa et al. (2019) pointed out that SSEs play a role in limiting the occurrence of megathrust earthquakes. Therefore, better monitoring of SSEs is useful to understand the mechanism of the occurrence of megathrust earthquakes and improve the prediction of megathrust earthquakes.

In contrast to conventional earthquakes, slow earthquakes including SSEs (e.g., Ide et al., 2007) do not emit seismic waves. A useful tool for monitoring slow earthquakes is the ocean bottom pressure gauge. Itoh et al. (2019) reported that crustal deformation caused by the afterslip of the 2003 Tokachi-oki earthquake occurred for 7.5 years from 2003 to 2011, using inland Global Positioning System (GPS) data in Hokkaido, Japan, and pressure on the seafloor (PSF; see **Table 1** for the abbreviations and corresponding full names and units of the variables used in this study) data obtained off the southeastern coast of Hokkaido, Japan. They showed that the crustal deformation increased by approximately 2×10^{-1} m (i.e., 2×10^{-1} dbar) from 2003 to 2011. Thus, a precision of 1×10^{-2} dbar of the PSF data is required to identify such changes. In this study, we focus on the oceanic fluid changes off the southeastern coast of Hokkaido, Japan, which can affect the PSF changes in this region, and briefly discuss their relationships after the occurrence of the 2003 Tokachi-oki earthquake. As described in **Section 2.3**, the observed PSF data used in this study are of sufficient precision to evaluate this relationship.

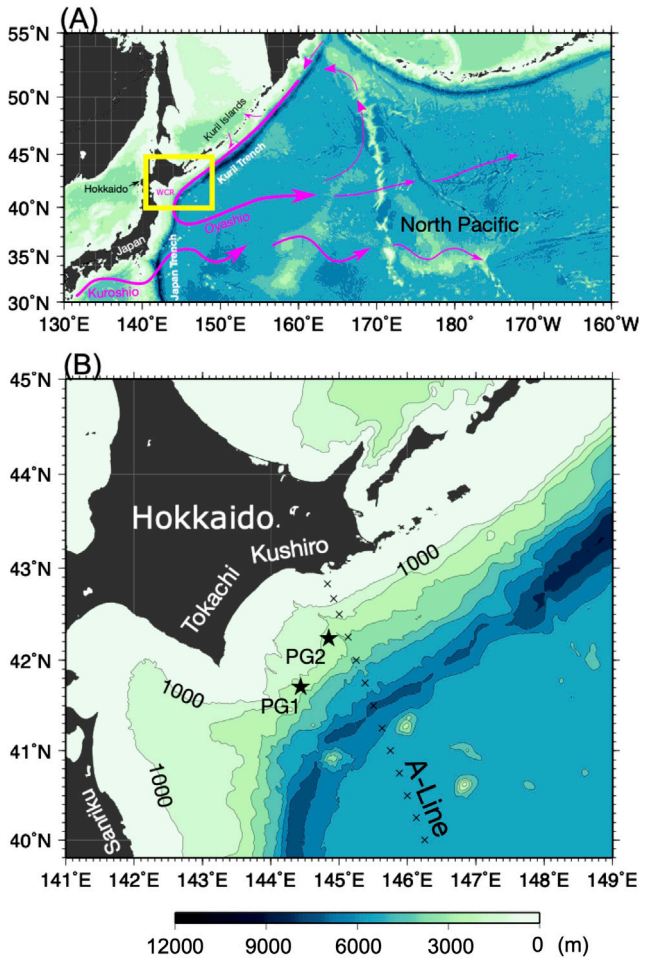

FIGURE 1 | (A) Map of the western North Pacific. Sea surface currents (Kuroshio and Oyashio) are schematically shown by purple arrows. **(B)** Map for the analysis area off Tokachi and Kushiro (off the southeastern coast of Hokkaido) marked by a yellow square in **(A)** with bottom topography. Contour interval is 1000 m. On the contour of 1000 m depth, a contour label is shown. The ocean bottom pressure gauges (PG1 and PG2) are marked by black stars and the CTD stations at A-line by black crosses.

Observed PSF data include both the pressure changes due to crustal deformation as well as those due to oceanic fluid changes (Ariyoshi et al., 2016). The area off the east coast of Japan facing the North Pacific is one of the most active areas of ocean fluid variations in the global oceans owing to the very strong Kuroshio (e.g., Nitani, 1972; Kawabe, 2005; Nagano et al., 2018, 2019) and Oyashio currents (e.g., Kono, 1997; Joyce and Dunworth-Baker, 2003; Ito et al., 2004; Kuroda et al., 2015), and numerous oceanic mesoscale eddies (e.g., Tai and White, 1990; Qiu et al., 1991; Ichikawa and Imawaki, 1994; Aoki et al., 1995; Ebuchi and Hanawa, 2000; Sugimoto et al., 2017). Thus, the oceanic fluid changes related to such phenomena can affect the PSF in the areas around the Japan Trench and Kuril Trench. Therefore, to more accurately estimate the crustal deformations related to the SSEs and other slow crustal deformations such as plate motions by use of the PSF, PSF changes caused by the oceanic fluid variabilities should be removed from the PSF data.

In our previous study (Hasegawa et al., 2019), we investigated the effect of oceanic fluid change on the PSF change off the southeastern coast of Hokkaido, Japan, using observational data, as an interdisciplinary study with solid Earth science and fluid Earth science. In the previous study, we analyzed PSF data obtained by the ocean bottom pressure gauges at the PG1 and PG2 stations (**Figure 1B**) that were recorded by the Long-Term Deep Sea Floor Observatory off Kushiro-Tokachi in the Kuril Trench deployed by the Japan Agency for Marine-Earth Science and Technology (JAMSTEC) (Kawaguchi et al., 2000), repeated observations of conductivity-temperature-depth (CTD) data along the A-line (**Figure 1B**) by the Fisheries Research Agency, and altimetric sea surface height (SSH) data provided by the Archiving, Validation and Interpretation of Satellite Oceanographic data (AVISO). We focused on the effect of oceanic fluid changes related to substantially baroclinic anticyclonic eddies, called warm-core rings (WCRs), which are of the similar kind to oceanic mesoscale eddies observed along the east coast of Japan and other regions of the world (e.g., Tomosada, 1986; Itoh and Sugimoto, 2002), on PSF changes on an interannual (i.e., year-to-year) timescale.

The impact of the WCRs on the PSF in 2007–2008 and 2012–2013 was studied by Hasegawa et al. (2019). It was

TABLE 1 | Abbreviations, their full names or explanation, units, and corresponding equations and figures of the variables used in this study.

Abbreviation	Full name/Explanation	Unit	Corresponding Eq./Fig.
PSF	Pressure on the seafloor	dbar	**Fig. 9**
SSH	Sea surface height	m	**Fig. 3**
SEP	Steric effect on pressure on the seafloor	m	**Eq. (1)/Fig. 5**
OIA	Ocean isostasy anomaly	m	**Eq. (2)/Fig. 6**
PSF′	PSF anomaly after the removal of the OIA from the original PSF anomaly	dbar	**Eq. (3)/Fig. 9**
POIA	Proxy of the ocean isostasy anomaly	m	**Eq. (5)/Fig. 10**

found that the WCRs with large positive SSH anomalies lead to retreats of the Oyashio Current after El Niño events (e.g., Trenberth, 1997; Hasegawa and Hanawa, 2003a; McPhaden et al., 2006). Hasegawa et al. (2019) also showed that although the large positive SSH anomalies due to the WCR appeared at PG2 in 2007 (i.e., the seawater volume above PG2 was larger than usual), the effect of positive SSH anomalies on the PSF change was canceled out by the effect of the negative seawater density anomalies due to the WCR (i.e., the density of seawater was reduced due to the WCR compared to the usual value), which resulted in very small changes in the PSF. Therefore, to better understand the effects of oceanic fluid changes on the PSF, a more comprehensive description of the relationship between SSH anomalies and seawater density anomalies on an interannual timescale is required.

The observational CTD data used in Hasegawa et al. (2019) do not cover the wide areas off the southeastern coast of Hokkaido, Japan, because of the limited number of *in-situ* observations obtained using such instrument. Instead, analyses using numerical models are useful, as demonstrated by Inazu et al. (2012) and Muramoto et al. (2019). These studies investigated the effect of oceanic fluid changes on PSF on a timescale of 2–20 days. They used a non-linear, single-layer barotropic ocean model, which is very useful for simulating oceanic barotropic variations on timescale of 2–20 days (Inazu et al., 2012). In addition to such a short timescale, interannual-timescale variations have also been found in crustal deformations related to long-term SSEs (e.g., Hirose and Obara, 2005; Ide et al., 2007; Uchida et al., 2016; Nakata et al., 2017; Kobayashi and Tsuyuki, 2019), afterslip (e.g., Miyazaki et al., 2004; Ide et al., 2007; Itoh et al., 2019), silent earthquakes (e.g., Franco et al., 2005; Ide et al., 2007), and plate convergence (e.g., Miyashita, 1987; DeMets et al., 1990). While the non-linear, one-layer barotropic ocean model is effective for the shorter timescale of 2–20 days, it is less effective for representing baroclinic ocean changes on timescales longer than 20 days (Inazu et al., 2012). To analyze the oceanic fluid variations on the interannual timescale related to the WCRs, continuously stratified ocean models accounting for both barotropic and baroclinic components are more suitable.

Our final goal is to quantitatively estimate the effects of SSH and seawater density anomalies on PSF anomalies related to the slow earthquakes (e.g., Ide et al., 2007) on an interannual timescale. To reach this aim, as the next step of our previous observational study (Hasegawa et al., 2019), the purpose of this study is to investigate the relationship between SSH and seawater density anomalies over the entire area off the southeastern coast of Hokkaido, Japan, with a special reference to WCRs, using the ocean assimilation data of the eddy-resolving ocean assimilation data (JCOPE2M; Miyazawa et al., 2017; 2019). The JCOPE2M estimates the optimal solution by using observational data and a continuously stratified numerical ocean model. In this study, we used SSH data and vertical profiles of temperature and salinity from the seafloor to the sea surface of the JCOPE2M to explore the relationship between SSH and oceanic density anomalies on an interannual timescale. In addition, we briefly discuss the effect of the ocean fluid changes estimated from the JCOPE2M assimilation data on changes in PSF observed by the ocean bottom pressure gauges at PG1 and PG2 on an interannual timescale. The analysis method used in this study for the SSH anomalies and vertical profiles of temperature and salinity of the JCOPE2M is applicable to observational data, i.e., altimetric SSH data, temperature and salinity vertical profiles obtained by shipboard-CTD, Argo profiling floats (Argo Science Team, 1998; Argo Science Team, 2001), eXpendable Conductivity Temperature Depth profilers (XCTDs), moorings, etc., not only in the region off the southeastern coast of Hokkaido, Japan, but also in other places where both interannual-scale crustal deformations caused by slow earthquakes and oceanic fluid variations exist.

The remainder of this article is organized as follows. In **Section 2**, the assimilation data of the JCOPE2M, observed altimetric SSH data, and observed PSF data used in this study are described. In **Section 3**, the relationship between the SSH and seawater density anomalies on an interannual timescale is investigated with a special reference to the WCRs. Discussions are given in **Section 4**, and concluding remarks are presented in **Section 5**.

2 DATA

2.1 Ocean Assimilation Data

The assimilation data analyzed in this study were obtained from a reanalysis experiment of the eddy-resolving spatial resolution ocean assimilation model developed by JAMSTEC (JCOPE2M; Miyazawa et al., 2017; Miyazawa et al., 2019). JCOPE2M is based on the Princeton Ocean Model, which adopts the vertical discretization of sigma coordinates (Mellor et al., 2002). The model domain is the western North Pacific (10.5°N to 62°N, 108°E to 180°E). The horizontal resolution is 1/12° in both zonal and meridional directions, and the model has 46 vertical levels from the ocean bottom to the sea surface. It is forced by surface wind stress and heat and salt fluxes derived from the NCEP/NCAR reanalysis data (Kalnay et al., 1996). The experimental period is

January 1993 to the present. The multiscale 3D-VAR assimilation scheme is used in the JCOPE2M. Observation data of the SSH anomaly, sea surface temperature, and vertical profile data of temperature and salinity are assimilated in the JCOPE2M. SSH data provided by the JCOPE2M do not include the atmospheric pressure change effect (i.e., the IB component; Ponte and Gaspar, 1999). In this study, we used the outputs of the SSH data and vertical profiles of temperature and salinity from the JCOPE2M reanalysis experiment.

We analyzed monthly SSH anomalies and other variables on an interannual timescale in this study. The analysis period for the JCOPE2M outputs from January 2001 to December 2018 was chosen to cover the analysis period of the observed PSF data at PG1 and PG2. The monthly anomalies were calculated as follows. First, daily vertical profiles of the potential density of seawater from the seafloor to the sea surface at each grid point were calculated using the daily outputs of vertical profiles of the temperature and salinity from January 1, 2001, to December 31, 2018. Subsequently, monthly averaged vertical profiles of the potential density were calculated from the daily vertical profiles of the potential density at each grid point from January 2001 to December 2018. Additionally, monthly SSH data were also calculated using the daily outputs of the SSH data at each grid point for the same period. Subsequently, the monthly climatologies (i.e., long-term average) of these variables were calculated by averaging the monthly variables for the individual calendar months from January 2001 to December 2018. Thereafter, the monthly anomalies of these variables were calculated by subtracting the monthly climatologies from the monthly averaged data. A 15-months running mean filter was adopted for the monthly anomalies to highlight the interannual-scale variations of these variables.

2.2 Altimetric Sea Surface Height (SSH) Data

To evaluate the SSH anomalies of the JCOPE2M, satellite altimeter data (i.e., observed altimetric SSH data) provided by AVISO were used in this study. Daily SSH anomalies of the 1/4° × 1/4° gridded delayed-time updated mapped data (DT-SLA-H) (AVISO, 2008) from January 1, 2001, to December 31, 2018, were analyzed. Monthly SSH anomalies from January 2001 to December 2018 were calculated in the same way as the JCOPE2M SSH anomalies. A 15-months running mean filter was also adopted for the altimetric SSH data.

2.3 Pressure on the Seafloor (PSF) Data

The PSF data obtained by the ocean bottom pressure gauges at PG1 and PG2 on the Long-Term Deep Sea Floor Observatory off Kushiro–Tokachi in the Kuril Trench (Kawaguchi et al., 2000) were used to discuss the PSF anomalies and effect of oceanic fluid changes on the PSF. The locations of PG1 (41.7040° N, 144.4375° E) and PG2 (42.2365° N, 144.8454° E) are shown as black stars in **Figure 1B**. The PSF gauges were deployed at depths of 2218 m and 2210 m for PG1 and PG2, respectively (also see the website of the Submarine Cable Data Center of JAMSTEC, http://www.jamstec.go.jp/scdc/top_e.html, for detailed information and data usage). The ocean bottom pressure gauges of this system are digiquartz pressure transducers (Model 2813 E) manufactured by Hewlett-Packard. The accuracy and resolution of the sensors were 7×10^{-2} dbar and 5×10^{-3} dbar, respectively. The original data were observed at a sampling rate of 8 kHz.

The PSF data for PG1 and PG2 were analyzed in our previous study (Hasegawa et al., 2019) from 2003 to 2014. In this study, we extended the data length, and PSF data from October 8, 2003, to December 31, 2018, were used. The raw data were averaged to hourly data. Subsequently, the daily mean data were calculated after removing tides from the hourly data by using the tide-eliminating filter proposed by Thompson (1983). Then, the sensor drift components were removed from the detided daily mean data by exponential and linear functions as done in our previous study (Hasegawa et al., 2019). In this study, the data length for calculating the drift component was from October 13, 2003, to December 26, 2018, which is extended compared to that of Hasegawa et al. (2019). The parameters used to estimate the sensor drift in this study are shown in **Table 2**, and are slightly changed from those used in Hasegawa et al. (2019). After the drift component was removed from the daily PSF data, monthly averaged PSF data were obtained from the residual daily data. The PSF monthly climatologies were calculated for the period from January 2004 to December 2018. Then, the monthly PSF anomalies from January 2004 to December 2018 were calculated by subtracting the monthly climatologies from the monthly PSF data. Afterward, a 15-months running mean filter was adopted for the monthly PSF anomalies to highlight the interannual-scale variations such as SSH anomalies.

As described in **Section 1**, based on previous studies (Uchida et al., 2016; Itoh et al., 2019) a precision of 1×10^{-2} dbar of the PSF data is required for analysis on interannual-scale PSF anomalies in this study. Assuming a Gaussian error distribution, the random errors of the 15-months running mean filtered PSF anomalies were estimated to be approximately 1.5×10^{-6} dbar. This is much smaller than the required precision for PSF and the amplitudes of the 15-months running mean filtered PSF anomalies at PG1 and PG2 (approximately 1×10^{-2} dbar), as shown in **Section 4.1**.

3 RESULTS

3.1 Positive Peaks of SSH Anomalies at PG1 and PG2

First, we detected the periods in which SSH anomalies showed positive peaks of during the analysis period at PG1 and PG2, respectively. As shown in previous studies (e.g., Hasegawa et al., 2019), the WCRs were accompanied by positive SSH anomalies around PG1 and PG2. Black thick solid lines in **Figures 2A,B** show the timeseries of SSH anomalies from the JCOPE2M data at the grid point closest to PG1 (41.625° N, 144.375° E) and PG2 (42.125°N, 144.875° E), respectively. It is shown that the SSH anomalies of the JCOPE2M at both PG1 and PG2 show positive SSH anomalies (approximately 5×10^{-2}) in the year 2007, which is consistent with our previous study using observed altimetric SSH data (Hasegawa et al., 2019). Additionally, much stronger positive peaks (approximately 1.5×10^{-1}) were found in the year 2016, both at PG1 and PG2. These two positive SSH anomalies

TABLE 2 | Regression coefficients A (dbar), B (d^{-1}), C (dbar d^{-1}), and D (dbar) for the exponential and linear functions to estimate the sensor drift component (p_d) of the detided daily PSF data at PG1 and PG2. p_d is represented by the equation; $p_d = A \exp(B\,t) + C\,t + D$, where t is the time (days). These parameters were calculated for the period from October 13, 2003, to December 26, 2018.

	A	*B*	*C*	*D*
PG1	6.01	0.0000385	−0.00023	2273.19
PG2	6.08	0.0000338	−0.00023	2226.95

were also observed in the observed altimetric SSH (AVISO-SSH) anomalies (red thick solid lines in **Figures 2A,B**).

The standard deviations calculated during August 2001–May 2018 (i.e., both the start and end periods of the 15-months running mean filter, in which the data cannot be adequately filtered by the running mean filter, were eliminated from the original analysis period) of the JCOPE2M-SSH and AVISO-SSH anomalies at PG1 (PG2) were approximately 5.5×10^{-2} (5.6×10^{-2}) m and 4.9×10^{-2} (3.9×10^{-2}) m, respectively. Thus, the difference in the standard deviation between the JCOPE2M and AVISO-SSH anomalies at PG1 (PG2) is approximately 6.0×10^{-3} (1.7×10^{-2}) m for this period.

Therefore, the gross features of the JCOPE2M SSH data represent the strong positive SSH anomalies at these locations. In the following subsections, we focus on oceanic fluid changes in the years 2007 and 2016 as case studies.

3.2 SSH and Seawater Density Anomalies Related to the WCRs in 2007 and 2016

Figure 3A shows the spatial pattern of the yearly averaged SSH anomalies in 2007. As shown in **Figure 3A**, a WCR existed in this period around PG1 and PG2. This WCR shows a relatively large positive SSH anomaly of approximately 0.1 m around its center. In 2016 (**Figure 3B**), a much stronger WCR was distributed over a wide area off the southeastern coast of Hokkaido, Japan, including the locations of PG1 and PG2, with large positive SSH anomalies of approximately 0.2 m around its center. Since a 1-m increase in SSH can lead to a nearly 1-dbar increase in the PSF, the SSH anomalies had the potential to increase the PSF by nearly 0.1 dbar and 0.2 dbar around the center of these WCRs in 2007 and 2016, respectively.

Subsequently, we investigated the vertical profiles of seawater density related to the WCRs in the two cases. **Figure 4A** shows the depth-longitude diagram of the yearly averaged σ_θ (σ_θ is defined as follows: $\sigma_\theta = \rho - 1000$ [kg/m^3], where ρ [kg/m^3] is the potential density of seawater) and the yearly averaged σ_θ anomaly along a horizontal line at 41.5° N from 143° E to 147° E, which is across the center of the WCR, in 2007 (**Figure 3A**). As shown in **Figure 4A**, relatively large negative σ_θ anomalies appear centered at 145° E, where the center of the WCR is located (**Figure 3A**), from the sea surface to a depth of approximately 900 m. Along the line, associated with the negative σ_θ anomalies, the isopycnal depths shown by black contours in **Figure 4A** display a slightly downward lens-like shape, showing the oceanic baroclinic structure due to the WCR. It is expected that such a negative anomaly of σ_θ generates a low seawater mass in the WCR area, when compared with the normal condition, resulting in a reduction of the PSF in this area. For the year 2016, in which much stronger positive SSH anomalies appeared (**Figure 3B**), negative σ_θ anomalies and downward lens-like shape (i.e., the oceanic baroclinic structure) were also much stronger than those in 2007 (**Figure 4B**). Thus, it is suggested that the effect of the positive SSH anomalies on the PSF can be canceled out by the effect of the negative seawater density anomalies on the PSF in both 2007 and 2016.

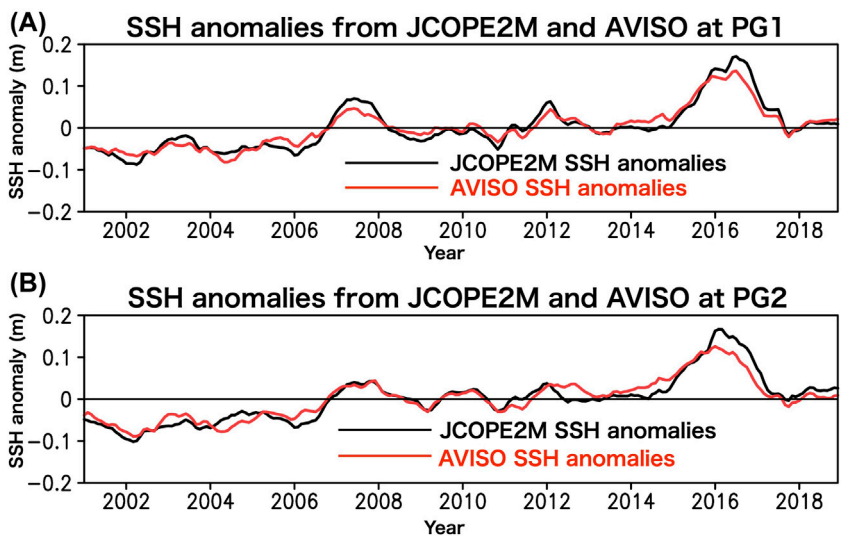

FIGURE 2 | (A) Timeseries of the JCOPE2M SSH anomalies (black thick solid line) and the observe altimetric AVISO-SSH anomalies (red thick solid line) at PG1 (indeed, the closest grid point to the location of PG1, i.e., 41.625° N, 144.375° E). The unit is m. **(B)** Same as **(A)** but at PG2 (indeed, the closest grid point to the location of PG2, i.e., 42.125° N, 144.875° E).

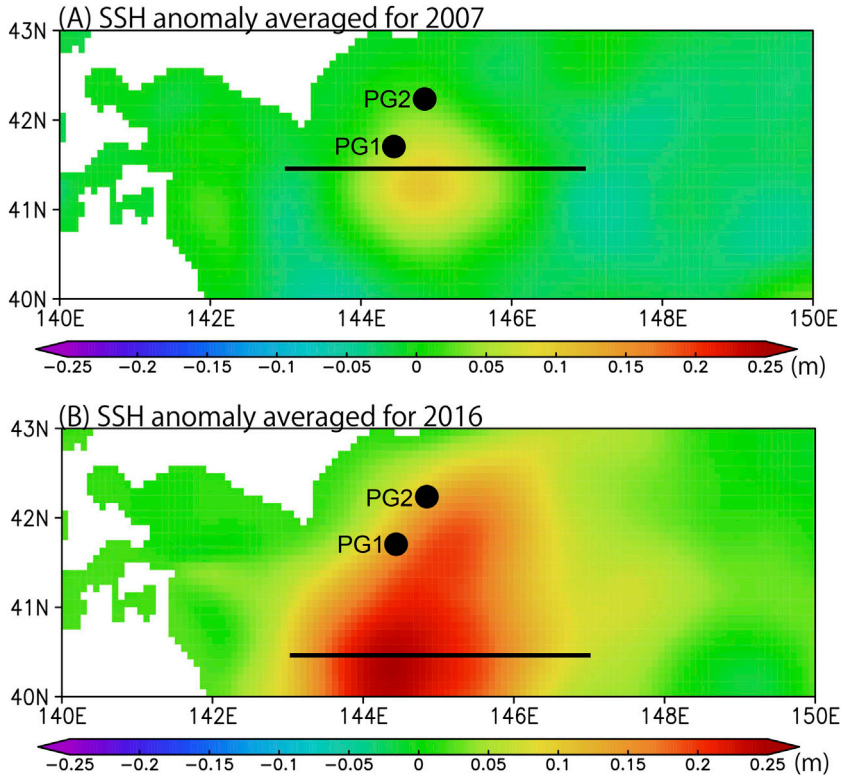

FIGURE 3 | (A) Spatial distribution of the yearly averaged SSH anomaly for the year 2007. The unit is m. The black horizontal line along 41.5° N denotes the longitude range for the longitude-depth diagram of σ_θ in **Figure 4A**. Black circles denote the location of PG1 and PG2. **(B)** Same as **(A)** but for the year 2016. The black horizontal line along 40.5° N denotes the longitude range for the longitude-depth diagram of σ_θ in **Figure 4B**.

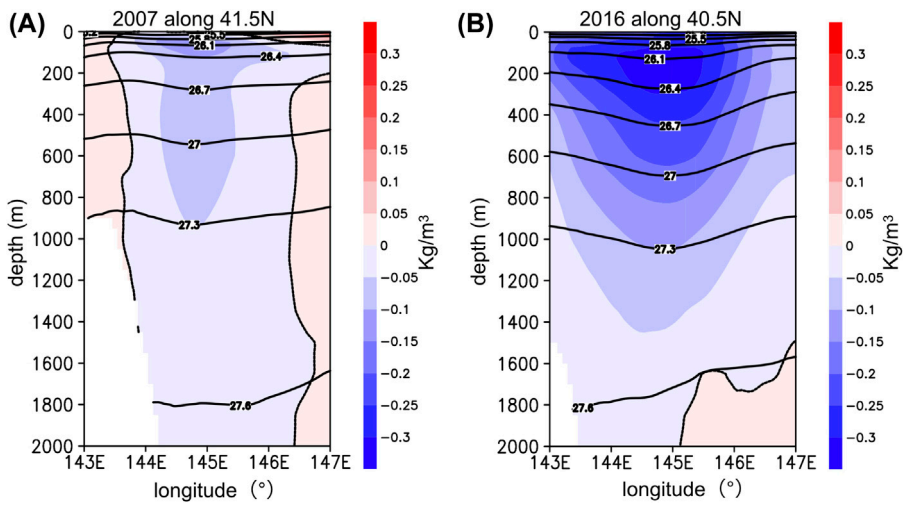

FIGURE 4 | (A) Longitude-depth diagram of the yearly averaged σ_θ (contour) and σ_θ anomaly (shaded color) for the year 2007, along the 41.5° N-horizontal line from 143° E to 147° E which is indicated by the black line in **Figure 3A**. The unit is kg/m^3. **(B)** Same as **(A)** but for the year 2016 along 40.5° N-horizontal line from 143° E to 147° E which is indicated by the black line in **Figure 3B**.

To evaluate the effect of seawater density anomalies on the PSF quantitatively and compare it with that of the SSH anomalies, we introduced a "steric effect on pressure on the seafloor" (hereafter SEP). The SEP was calculated at each grid point using daily vertical profiles of potential temperature and salinity from the ocean bottom to the sea surface of the JCOPE2M assimilation

data. The SEP between the seafloor and the sea surface along the vertical pressure axis is defined as

$$SEP = -\frac{1}{g}\int_{p1}^{p2} \delta \, dp, \quad (1)$$

where g = 9.81 m/s^2 is the gravitational acceleration; p is the pressure (Pa); $p1$ is the pressure at the sea surface, that is, $p1$ is fixed to 0 Pa; $p2$ is the pressure close to the seafloor (if the ocean bottom depth is H m, $p2$ is set to $H \times 10^4$ Pa); and δ is the specific volume anomaly (m^3/kg). The SEP has a unit of m in this definition. The definition of the SEP is similar to that of the steric height and geopotential distance anomaly, which are widely used in physical oceanography (see **Supplementary Material 1**). In this study, the monthly averaged SEP anomaly was calculated from the daily SEP, and a 15-months running mean filter was adopted for the monthly SEP anomaly. If the seawater density increases (decreases) from the mean value, that is, the seawater density anomaly is positive (negative), the vertically integrated δ will decrease (increase) from the mean value. This leads to a negatively smaller (larger) SEP value compared to the mean value, that is, a positive (negative) SEP anomaly. The positive (negative) SEP anomaly leads to an increase (decrease) in the PSF from the mean value. For example, an SEP anomaly of +1 m can lead to a +1 dbar (i.e., +1 × 10^4 Pa) PSF anomaly. **Figure 5A** shows the spatial pattern of the yearly averaged SEP anomaly in 2007. The SEP anomaly pattern is very similar to that of the SSH anomaly (black contours in **Figure 5A**; also see **Figure 3A**), but with opposite anomaly signs. In 2016, the spatial pattern of the SEP anomaly (**Figure 5B**) was also similar to that of the SSH anomaly (black contours in **Figure 5B**; also see **Figure 3B**) with opposite anomaly signs. Thus, in both cases, the effects of positive SSH anomalies related to WCRs on the PSF were partly canceled out by the negative SEP anomalies due to the negative seawater density anomalies of the WCRs.

3.3 Introduction of Ocean Isostasy Anomaly (OIA)

To evaluate the total effect of the SSH anomaly and seawater density anomalies on the PSF anomaly, we introduced a variable called the ocean isostasy anomaly (OIA) in this study. The OIA is defined as,

$$OIA = SSH\ anomaly + SEP\ anomaly. \quad (2)$$

The OIA represents the component of the SSH anomaly associated with the vertically uniform fluid motion with the same velocity as the bottom current, called the barotropic component in this study (see **Supplementary Material 1**). If the value of OIA is zero, it implies that the effect of the SSH anomaly on the PSF anomaly is perfectly canceled out by the SEP anomaly; that is, ocean isostasy is perfectly established when the OIA is zero. In this case, the total effect of the SSH and seawater density anomalies does not change the PSF. If the value of OIA is +1 m, that is, ocean isostasy is not perfectly established, the total effect of the SSH and seawater density anomalies will change the PSF anomaly by nearly +1 dbar.

Figure 6A shows the spatial pattern of the yearly averaged OIA in 2007. A relatively large positive OIA of approximately +0.025 m appeared around 41°N, 145°E during this period. In 2016, a relatively large OIA of approximately +0.025 m appeared at 40.5°N, 144.5°E (**Figure 6B**). Large positive anomalies were also found along the coast of Sanriku (around 40.5° N, 141.5° E; see **Figure 1B** for the location of Sanriku). It is also shown that relatively large negative OIAs of approximately −0.025 m appeared east of the positive OIA areas in 2007 and 2016. It is expected that strong negative SEP anomalies around the WCR area in 2016 (**Figure 5B**), related to the strong negative seawater density anomalies (**Figure 4B**), can effectively cancel out the strong positive SSH anomalies (black contours in **Figure 5B** represent SSH anomalies; also see **Figure 3B**). Due to such canceling effects of the SEP anomalies, the amplitudes of the OIA in 2016 were similar to those in 2007 (**Figure 6**), although the positive SSH anomalies were stronger in 2016 than in 2007 (black contours in **Figures 5A,B**; also see **Figures 3A,B**). As shown in **Figures 3**, **6**, the amplitudes of the OIAs are nearly 10% of those of the SSH anomalies in large areas off the southeastern coast of Hokkaido, Japan.

Here, we discuss the relationship between OIAs and SSH anomalies related to the WCRs. The OIAs exhibited non-homogeneous patterns in the WCR area, indicated by relatively large positive SSH anomaly regions (black contours in **Figures 6A,B**; also see **Figures 3A,B**), in both 2007 and 2016. In 2007, a relatively large positive OIAs appeared around 40.5°N, 145°E in the southern part of the WCR (**Figure 6A**), while, in most parts of the WCR region, the OIA values were positive but small. In 2016, a large positive OIA existed within a large part of the WCR area, as illustrated by the strong positive SSH anomalies exceeding 0.15 m (**Figure 6B**). However, at the eastern limb of the WCR centered at 41°N, 145.5°E, the positive OIA values were less than those in the other areas of the WCR. Large OIAs were found to be localized at the regions of water depths greater than 3000 m (see **Figure 1B**), where ocean isostasy was not perfectly established or the barotropic flow component remained in the WCR structure, as observed by Owens and Warren (2001). In the other small-OIA areas, ocean isostasy was thought to be established more completely.

3.4 Regression and Correlation Relationships Between SSH and SEP Anomalies

In the previous subsections, case studies focusing on the WCRs that occurred in 2007 and 2016 were conducted. In this subsection, we explore both the regression and correlation relationships between SSH and SEP anomalies over a long period, from August 2001 to May 2018. **Figure 7A** shows the spatial pattern of regression coefficients between SSH and SEP anomalies calculated for the period from August 2001 to May 2018. The regression coefficients represent the ratio of SEP anomalies to SSH anomalies. **Figure 7A** shows that large negative regression coefficients of nearly −0.9 are distributed in the offshore regions with bottom depths greater than 1000 m. This

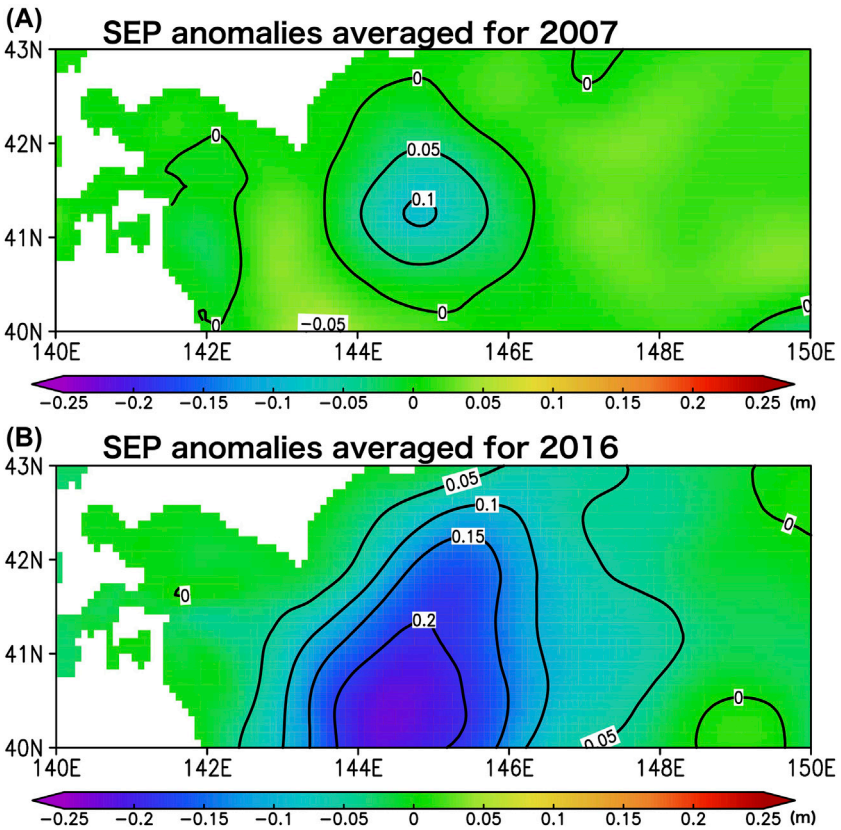

FIGURE 5 | (A) Spatial distribution of the yearly averaged SEP anomaly for the year 2007 (color shades). The yearly averaged SSH anomalies for the year 2007 are shown by black contours. The unit is m. **(B)** Same as **(A)** but for the year 2016.

result implies that nearly 90% of the effect of the SSH anomaly on the PSF anomaly is canceled out by the SEP anomaly (i.e., seawater density anomaly) in those regions. In other words, the amplitudes of the OIAs are nearly 10% of those of the SSH anomalies due to the canceling effect of the seawater density anomalies in those regions. That is, the barotropic component of the SSH anomalies are nearly 10% of the total SSH anomalies in the offshore region on an interannual timescale, in general, supporting the results shown in **Figures 3–6**. In contrast to the offshore region, negative regression coefficients are small in coastal regions with bottom depths less than 1000 m, that is, shallower than the main pycnocline in the region. Thus, ocean isostasy is better established in the deep offshore region with bottom depths greater than 1000 m rather than in the shallow coastal areas with bottom depths less than 1000 m.

Figure 7B shows the spatial pattern of correlation coefficients between the SSH and SEP anomalies during the analysis period. Large negative correlation coefficients of approximately −0.95 appeared in offshore areas and small negative values in coastal areas (**Figure 7B**), similar to the regression coefficients (**Figure 7A**). This means that the SSH and SEP anomalies are negatively in-phase in offshore regions. For example, in **Figure 8A**, scatter plots between SSH and SEP anomalies at PG1, which located in the offshore region (see **Figure 7B** and **Figure 1B** for the location of PG1), show clear negative correlation and regression relationships. The negative correlation and regression relationships between SSH and SEP anomalies are also shown by the timeseries of SSH and SEP anomalies at PG1 (black and red solid lines in **Figure 8B**). The correlation and regression coefficients are −0.9983 and −0.9167, respectively at PG1. Such negative correlation and regression relationships indicate that the effect of the SSH anomaly on the PSF is almost canceled out by the seawater density anomaly (i.e., SEP anomaly). As a result, the amplitude of the OIA (green solid line in **Figure 8B**) is much smaller than those of the SSH and SEP anomalies, which is in line with the results shown in **Figures 3–6**. At PG2, similar result is obtained (not shown here) and the correlation and regression coefficients are −0.9980 and −0.9153, respectively.

4 DISCUSSIONS

4.1 Comparison Between the OIA and Observed PSF Anomalies at PG1 and PG2

In this subsection, we compare the OIA with the observed PSF anomalies at PG1 and PG2. **Figures 9A,B** show the OIAs from

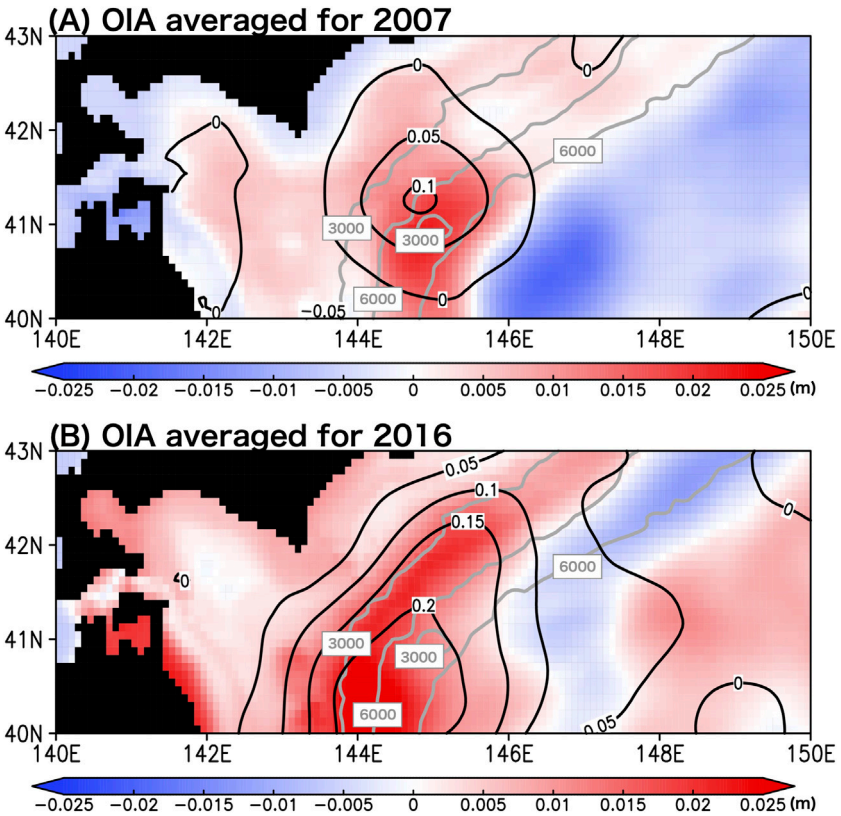

FIGURE 6 | (A) Spatial distribution of the yearly averaged OIA for the year 2007 (shaded color). The yearly averaged SSH anomalies for the year 2007 are shown by black contours. The unit is m. The bottom depths of 3000 and 6000 m are shown by the gray solid contours. **(B)** Same as **(A)** but for the year 2016.

the JCOPE2M (gray solid line) and observed PSF anomalies (black solid line) at PG1 and PG2, respectively. During the analysis period, the OIAs range from approximately -1×10^{-2} to $+1 \times 10^{-2}$ m for PG1 and PG2. Although the PSF anomalies are nearly $+5 \times 10^{-2}$ dbar in 2007 at PG1 (**Figure 9A**), the PSF anomalies at PG1 and PG2 ranged from -2×10^{-2} to $+2 \times 10^{-2}$ dbar for almost the entire period except for 2007 (**Figures 9A,B**).

The standard deviations of the OIAs and PSF anomalies were calculated from August 2004 to May 2018 at PG1 and PG2. At PG1, the standard deviations of the OIAs and PSF anomalies were 5.0×10^{-3} m and 1.9×10^{-2} dbar, respectively. At PG2, the standard deviations of the OIAs and PSF anomalies were 3.9×10^{-3} m and 8.6×10^{-3} dbar, respectively. As described in **Section 3.3**, a +1-m change in OIA will change the PSF anomaly by nearly +1 dbar. Thus, the standard deviations of the OIAs account for approximately 26 and 45% of those of the PSF anomalies, at PG1 and PG2, respectively. Therefore, it can be said that although the amplitude of the OIAs is approximately 10% of the SSH anomalies as described in the previous subsections, the amplitudes of the OIAs are not much less than those of the PSF anomalies at PG1 and PG2.

To discuss the effect of the OIAs on PSF anomalies at PG1 and PG2 after the 2003 Tokachi-oki earthquake, we calculated the PSF anomalies after the removal of the OIAs from the original PSF anomalies (hereafter PSF′) as follows,

$$PSF' = PSF - OIA. \quad (3)$$

The timeseries of PSF′ at PG1 and PG2 are shown as color shades of red and blue in **Figures 9A,B**, respectively. After the 2003 Tokachi-oki earthquake, both the PSF and PSF′ anomalies showed increasing tendencies from 2004 to 2007 at PG1 (**Figure 9A**). The PSF anomalies at PG1 increased from nearly -2.0×10^{-2} to $+5.0 \times 10^{-2}$ dbar during this period. On the other hand, positive values of PSF′ around 2007 were nearly $+3.0 \times 10^{-2}$ to 4.5×10^{-2} dbar in 2007, weaker than those of PSF around 2007 by approximately 1.0×10^{-2} dbar, due to the positive OIAs in this period (**Figure 9A**). During 2004–2005, negative values of PSF′ at PG1 were almost the same as those of PSF, since the OIAs were nearly zero during this period (**Figure 9A**). As a result, the increasing tendency of PSF′ from 2004 to 2007 was weak compared with that of PSF. At PG2, relatively large positive values of PSF (nearly $+5.0 \times 10^{-3}$ dbar) appeared around 2007, while PSF′ showed nearly zero due to positive OIAs in this period (**Figure 9B**). As a result, at PG2, PSF′ showed an increasing tendency from the late 2005 to mid-2006, although an increasing tendency of PSF is found from the late 2005 to early 2007.

As described in **Section 3.1**, the standard deviation from the JCOPE2M SSH anomalies is greater by approximately 6.0×10^{-3} (1.7×10^{-2}) m than that from the AVISO-SSH anomalies at PG1

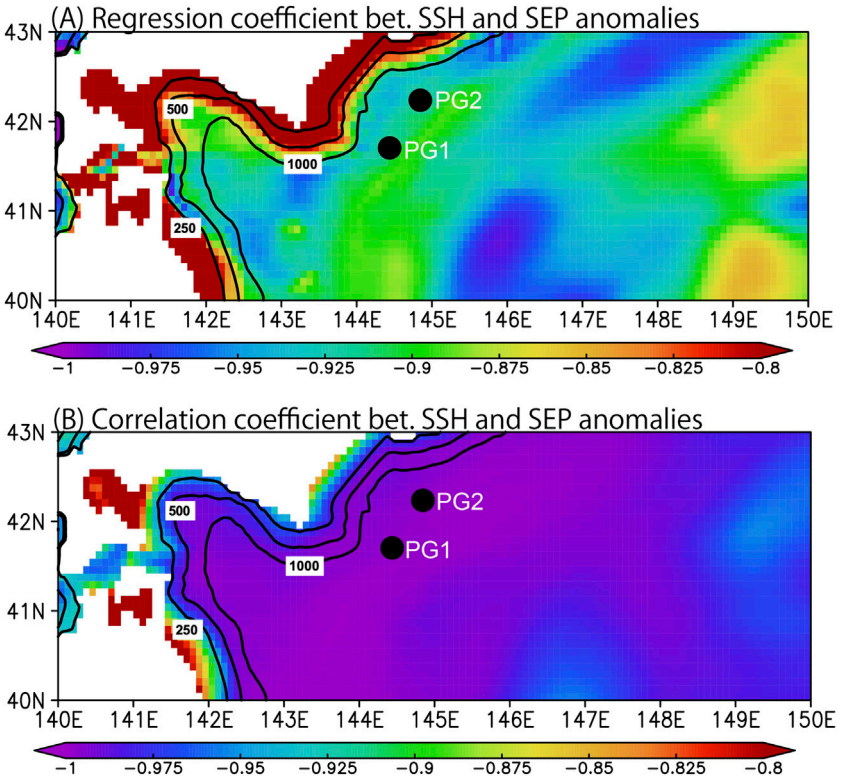

FIGURE 7 | (A) Spatial distribution of the regression coefficient between SSH and SEP anomalies. The period for the calculation of the regression coefficient is from August 2001 to May 2018. That is, both the start and end periods of the 15-months running mean filter, in which the data cannot be adequately filtered by the running mean filter, were eliminated from the original analysis period. Black solid lines show contours of bottom depths of 250, 500, and 1000 m. Black circles denote the locations of PG1 and PG2. **(B)** Same as **(A)** but for the correlation coefficient.

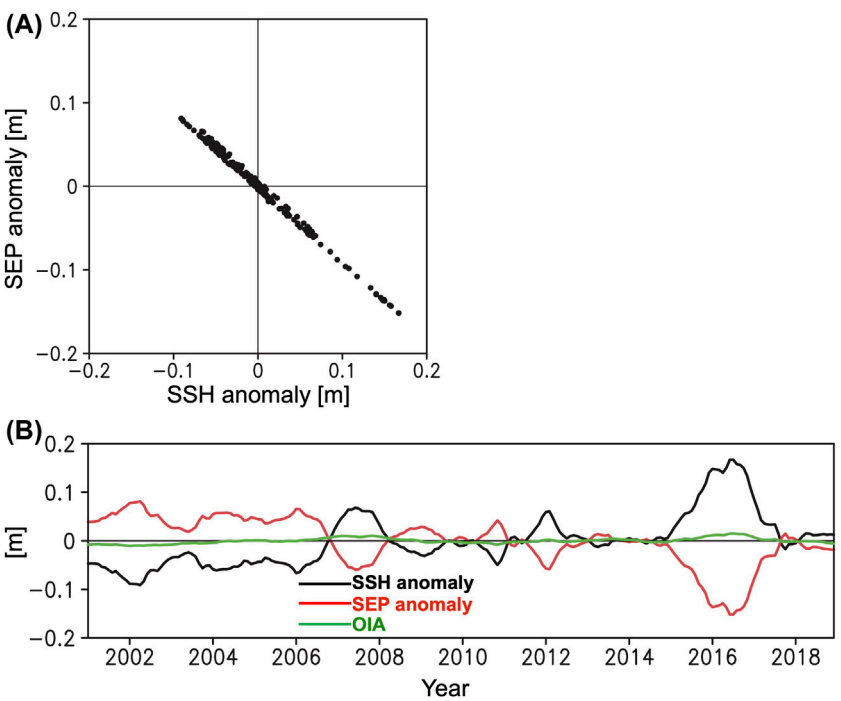

FIGURE 8 | (A) Scatter plots between SSH and SEP anomalies at the closest grid point to PG1 for the period from January 2001 to December 2018. The unit is m. **(B)** Timeseries of the SSH anomaly (black thick solid line), SEP anomaly (red thick solid line), and OIA (green thick solid line) at PG1. The unit is m.

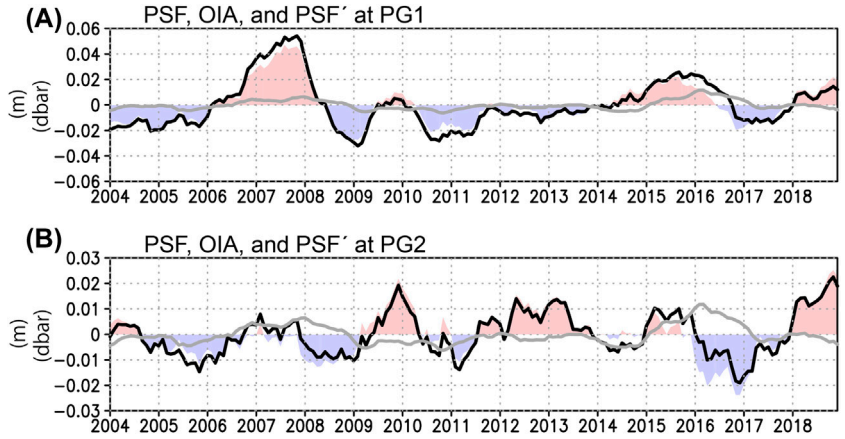

FIGURE 9 | (A) Timeseries of OIA (in m; gray solid line), PSF anomalies (in dbar; black solid line), PSF anomalies after the OIAs were subtracted from the original PSF anomalies (PSF′) at PG1 (color shades of red and blue colors). A 1-m change in OIA is almost equal to 1-dbar change in PSF. Here, we assumed that a 1-m change in OIA is perfectly equal to 1-dbar change in PSF for calculating PSF′. OIAs were re-calculated using monthly climatologies from January 2004 to December 2018, to match the data length of the PSF at PG1 and PG2. **(B)** Same as **(A)** but for PG2.

(PG2). The amplitudes of the OIAs at PG1 and PG2 were nearly 10% of those of the SSH anomalies, due to the canceling effect of the seawater density (i.e., SEP) against the effect of the SSH anomalies on the PSF changes on an interannual timescale, as described in **Section 3.4**. When it is assumed that the difference in the standard deviation between the JCOPE2M and AVISO SSH anomalies (hereafter, SDdif) is perfectly equivalent to the errors in the SSH anomalies of the JCOPE2M, the errors in the OIA can be estimated to be approximately 10% of the SDdif (see **Supplementary Material 2**). In this case, the OIA errors (PSF′ errors) at PG1 and PG2 are estimated to be approximately $\pm 6.0 \times 10^{-4}$ and $\pm 1.7 \times 10^{-3}$ m (dbar), respectively. Thus, there is a possibility that the OIA (PSF′) would be overestimated or underestimated by approximately 6.0×10^{-4} m (dbar) at PG1 and by approximately 1.7×10^{-3} m (dbar) at PG2, respectively. The error in PSF′ at PG1 (approximately $\pm 6.0 \times 10^{-4}$ dbar) is less than one tenth of the differences in the amplitude between PSF and PSF′ (i.e., amplitude of the OIA) around the year 2007 at PG1, as described above. At PG2, the error in PSF′ (approximately $\pm 1.7 \times 10^{-3}$ dbar) is approximately one third of the differences in amplitude between PSF and PSF′ around 2007, also as described above. Therefore, the difference in SSH anomalies between the JCOPE2M assimilation data and the AVISO observational data could not strongly affect the result for the year 2007 in **Figure 9**, especially at PG1. Additionally, it should be noted that observational errors were included in the observational AVISO-SSH data. The data assimilation could reduce the observational errors by use of the numerical ocean model simulation, if the numerical ocean model simulation adequately reproduced the real oceanic variations. Thus, the SDdif might not perfectly represent the error of the JCOPE2M SSH data; there is a possibility that the SDdif partly reflects the improvement in the SSH data accuracy by the JCOPE2M assimilation. Therefore, the error of the OIA (PSF′) would be less than the values estimated above. In future, improvement of data accuracies of both the assimilation data and the observed SSH data would provide more accurate estimations for the SSH, OIA and PSF′.

This result does not disprove the existence of the crustal deformations due to the afterslip related to the 2003 Tokachi-oki earthquake showing PSF increases of approximately 2.0×10^{-1} m from 2003 to 2011 (Itoh et al., 2019) and the periodic SSE with an amplitude of approximately 5.0×10^{-2} m (Uchida et al., 2016) around PG1 and PG2. It can be argued that subtracting OIAs from PSF anomalies on an interannual timescale would be useful to estimate interannual-scale PSF changes related to the slow earthquakes more precisely. In future, further studies focusing on the comparison between OIAs and PSF anomalies will be conducted.

In 2016, the OIAs showed an increasing tendency, while the PSF anomalies showed a decreasing tendency both at PG1 and PG2 (**Figures 9A,B**). The reason for this difference in tendency between the OIAs and PSF is unclear. It might be due to i) errors of temperature and salinity of the JCOPE2M assimilation data, associated with the ocean fluid structures in the 2016 WCR, ii) a remaining sensor drift component of the ocean bottom pressure gauges that was not removed by the linear and exponential functions used in this study (see **Section 2.3**), and iii) unknown interannual-scale seismic activities during this period. To explore the reason for this difference is beyond the scope of this study. In **Section 4.5**, the factors that are not considered in the JCOPE2M are described.

The results of the present study suggest that the OIAs should be estimated and compared with the PSF anomalies not only along the southeastern coast of Hokkaido, Japan, but also in other regions where oceanic currents and/or oceanic mesoscale eddies are dominant on an interannual timescale. These include areas such as the Dense Ocean floor Network system for Earthquakes and Tsunamis (DONET1 and DONET2) including the Kuroshio area, the Seafloor Observation Network for Earthquakes and Tsunamis along the Japan Trench (S-net) including the Kuroshio-Oyashio Confluence region, the Nankai Trough

Seafloor Observation Network for Earthquakes and Tsunamis (N-net) including Kuroshio area, and other areas showing strong seismic activity and strong oceanic fluid variations in the world (e.g., Ariyoshi et al., 2016). If the amplitudes of OIA cannot be neglected, compared to PSF anomalies in such areas, the OIAs should be removed from the PSF anomalies to better detect the PSF changes due to crustal deformation related to SSEs and other slow crustal movements on an interannual timescale.

4.2 OIA Proxy

To calculate the OIAs, SSH and SEP anomalies are needed, as shown in **Eq. (2)**. SSH anomalies can be calculated using the altimetric SSH anomaly data obtained from the AVISO website or other similar public institutions, instead of the SSH anomalies of the ocean assimilation data. The SEP is calculated using the vertical profile of the potential density from the seafloor to the sea surface, as shown in **Eq. (1)**. To create the vertical profile of potential density, vertical profiles of the temperature and salinity data from the sea floor to the sea surface are required. Such data can be obtained from CTD observations by research vessels, XCTDs, mooring buoys, Argo floats, etc., as well as the ocean assimilation data and outputs of continuously stratified ocean numerical model hindcast simulations. Therefore, the analysis method used in this study, using the SSH anomalies and vertical profiles of temperature and salinity of the JCOPE2M, can be applied to such observational data and outputs of continuously stratified ocean numerical models. If vertical profiles of temperature and salinity data from the sea floor to the sea surface are not available for the analysis period, the SEP cannot be calculated directly. In this case, we can approximately estimate the OIA indirectly from the regression coefficient between the SSH and SEP anomalies, calculated using the data observed during a period before (or after) the analysis period in the analysis area. In this study, the estimated OIA using such a method is called the "proxy of OIA" (POIA). The POIA is calculated as follows: Using the regression coefficient between the SSH and SEP anomalies, the SEP anomaly is estimated as

$$SEP\ anomaly = RC \times SSH\ anomaly, \tag{4}$$

where, *RC* is the regression coefficient between the SSH and SEP anomalies (i.e., *RC* is the ratio of the SEP anomaly to the SSH anomaly), as shown in **Figure 7A**. From **Eqs. (2)** and **(4)**, POIA is calculated as

$$POIA = (1 + RC) \times SSH\ anomaly. \tag{5}$$

If *RC* is -0.9, as seen in the offshore area off the southeastern coast of Hokkaido as described in **Section 3.4**, POIA can simply be estimated from **Eq. (5)** as follows:

$$POIA = 0.1 \times SSH\ anomaly. \tag{6}$$

To demonstrate the POIA method using **Eq. (5)**, POIA was calculated by use of the regression coefficient between the SSH and SEP anomalies from the JCOPE2M (**Figure 7A**), and the observed altimetric SSH anomaly (AVISO SSH anomaly) at each grid point on an interannual timescale (**Figure 10**). **Figure 10A** shows the spatial pattern of the POIA averaged for the year 2007. It is shown in **Figure 10A** that the positive POIAs distributed in the WCR area with the positive SSH anomalies centered at 41.5°N, 145°E. It is also shown in **Figure 10A** that negative POIAs distributed along the coast of Sanriku and south of Hokkaido, Japan. Such spatial pattern of the POIA in 2007 is similar to that of the OIA in 2007 (**Figure 6A**). However, the POIAs in the south part of the WCR area show negative values (**Figure 10A**), while the OIAs in this area show positive values (**Figure 6A**). In the year 2016, both the POIAs (**Figure 10B**) and OIAs (**Figure 6B**) show relatively strong positive values in the WCR area and the areas along the coast of Sanriku and south of Hokkaido, Japan. However, positive POIA distributed around 41°N, 147°E and around 42.5°N, 148°E (**Figure 10B**), while the OIAs in these areas displayed negative values in 2016 (**Figure 6B**). Along the south coast of Hokkaido, the positive values of the POIA (**Figure 10B**) is stronger by approximately 0.01 m than those of the OIA (**Figure 6B**). It is also shown that the amplitudes of POIA (**Figure 10A**) near the center of the WCR (around 41.5°N, 145°E) were smaller by approximately 0.005 m than those of OIA (**Figure 6A**). The differences in the spatial pattern and the amplitudes between the POIA and OIA would be caused by the error in the observed altimetric SSH anomalies used in calculation of the POIA, and that in the assimilation data used in the calculations for the OIA and for the regression coefficient between SSH and SEP anomalies. It should be also noted that the effective spatial resolution at midlatitude of the observed altimetric SSH data is estimated to be approximately 200 km (Ballarotta et al., 2019), although the horizontal grid interval of the AVISO-SSH dataset is 1/4° × 1/4° (i.e., approximately 25 km × 25 km in midlatitude). Therefore, the differences in the spatial pattern and in the amplitudes between the POIA and OIA include the error due to the low spatial resolution of the AVIOS-SSH data compared to the 1/12° × 1/12° spatial resolution of the JCOPE2M assimilation data. To evaluate quantitatively each error is beyond the scope of this study. The result in this study suggests that the POIA method could be more useful in the areas near the center of the WCRs and along the coast of the Sanriku and south of Hokkaido compared to the other areas in the analysis area, while there is a difference of approximately 0.005–0.01 m in amplitude between the POIA and OIA. It can be said that the next-generation of the observed SSH anomalies could provide more accurate POIA in the future.

Note that the definition of POIA requires that the regression relationship between SSH and SEP does not change significantly from the period in which the *RC* is calculated for the analysis period. For the area off the southeastern coast of Hokkaido, Japan, the regression coefficient on an interannual timescale does not seem to change significantly in the analysis period as shown in **Figures 8A,B**. However, there are oceanic variations longer than interannual timescales, namely, longer than the timescale of the El Niño–Southern Oscillation (ENSO), such as quasi-decadal ENSO-like variations (e.g., Luo and Yamagata, 2001; Hasegawa and Hanawa, 2003b; White et al., 2003; Hasegawa et al., 2007a, 2013), interdecadal or multidecadal variations (e.g., Tanimoto et al., 1993; Mantua et al., 1997; Minobe, 1999; Hasegawa et al., 2007b), and climate regime shifts (e.g., Nitta and Yamada, 1989; Trenberth, 1990; Yasunaka and Hanawa, 2003) in the global

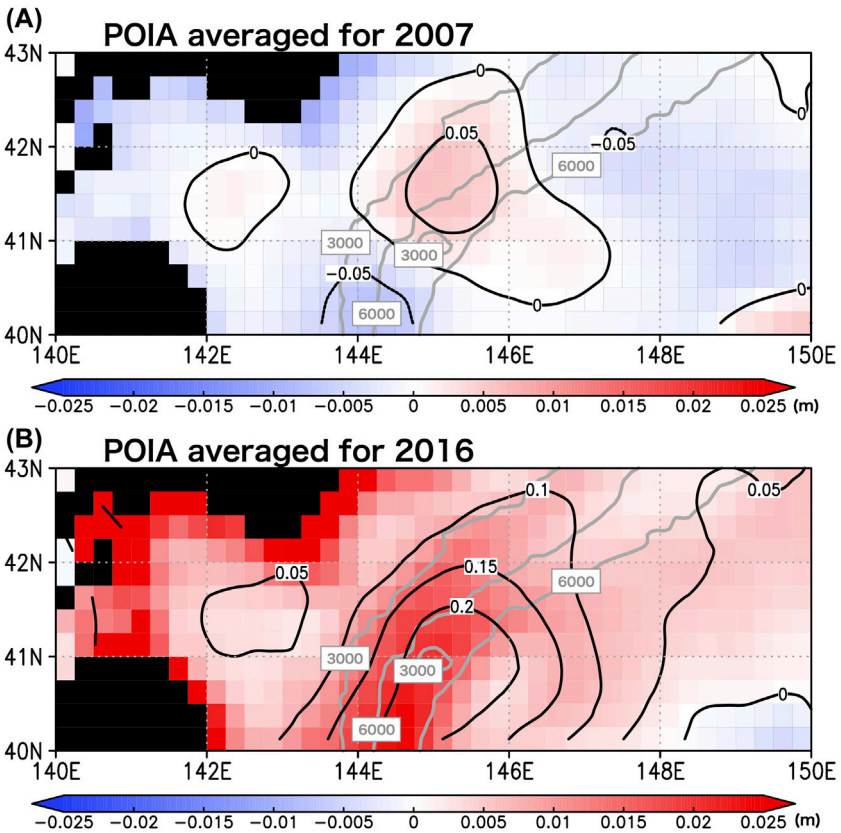

FIGURE 10 | (A) Spatial distribution of the yearly averaged POIA that were calculated by use of the regression coefficient between the SSH and SEP anomalies from the JCOPE2M (**Figure 7A**), and the observed altimetric SSH anomalies (AVISO SSH anomalies) at each grid point on an interannual timescale for the year 2007 (shaded color). The yearly averaged the AVISO SSH anomalies for the year 2007 are shown by black contours. The unit is m. The bottom depths of 3000 and 6000 m are shown by the gray solid contours. To make the POIA, the regression coefficient between SSH and SEP anomalies from the JCOPE2M with the 1/12° × 1/12° grid were re-gridded to match the spatial grid point of the AVISO SSH anomalies with the 1/4° × 1/4° grid by use of a spatial averaging of the regression coefficient using a 0.1° spatial window centered at each grid point of the AVISO SSH anomalies. **(B)** Same as **(A)** but for the year 2016.

ocean. Thus, when the POIA is used, it is suitable to consider a possible long-term change in the regression relationship between the SSH and SEP anomalies. It should also be noted that this method should be adopted in regions where the SSH and SEP anomalies are negatively in-phase; that is, the regions in which the correlation coefficient between the SSH and SEP anomalies is negatively high. For example, **Eq. (5)** can be applied to the deep offshore area off the southeastern coast of Hokkaido, Japan, where the correlation coefficients between the SSH and SEP anomalies are negatively high (nearly −0.95), as shown in **Figure 7B**.

4.3 Increasing Trend of SSH Anomaly at PG1 and PG2

Figure 2 shows an increasing trend in the SSH anomalies of both the JCOPE2M and observational data for the analysis period. As shown in **Figure 8**, the positive trend of the SSH anomalies at PG1 is almost canceled by the negative SEP anomalies (i.e., negative seawater density anomalies). In addition, **Figure 9** shows that the OIAs do not show strong linear trends. Thus, it can be said that linear OIA trends could be neglected on an interannual timescale in this region. Moreover, it could be speculated that if the increasing trend of the SSH anomalies in this area is generated by global warming, global warming could also cause a warming trend of the seawater. Thus, the increasing trend of SSH could be, at least partly, canceled out by the decreasing trend of seawater density (i.e., decreasing trend of SEP) due to the warming trend of seawater. To explore the linear trends and their relationship to the global warming will be further investigated in future works.

4.4 Relationship Between the Strong WCR in 2016 and the Preceding Strongest El Niño

Hasegawa et al. (2019) indicated a possible relationship between ENSO and WCRs off the southeastern coast of Hokkaido, Japan, using observational data from 2003 to 2014. They showed that positive SSH anomalies related to WCRs appeared in this region approximately 30 months after the onset of El Niño events. Thus, it is suggested that the preceding El Niño events could be used as prediction indicators for WCRs in this region. In this study, as

shown in **Figures 2**, **3**, very large positive SSH anomalies related to the strong WCR appeared in this region in 2016. It has been reported that the tropical Pacific showed the pre-condition for an El Niño event in 2014, followed by a very strong El Niño event from 2015 to 2016 (Hu and Fedorov, 2017). This El Niño event is the strongest event during the observational record. It can be speculated that the strong El Niño event leads to the strong WCR with the strong SSH anomalies off the southeastern coast of Hokkaido, Japan, in 2016. In future work, the generation mechanism of strong WCRs by strong El Niño events will be further investigated to improve the prediction skill of WCRs with a lead time longer than one year.

4.5 Factors Not Considered in the JCOPE2M

Several factors were not adequately considered in the JCOPE2M. First, the ocean model used in the JCOPE2M assimilation scheme does not include a sea ice model. Therefore, the oceanic volume changes due to sea ice change were not directly calculated in the ocean model of the JCOPE2M. The lack of such seawater volume changes could lead to uncertainties in the SSH anomalies of the JCOPE2M. Nevertheless, the changes in seawater temperature and salinity due to sea ice changes were included in the observational temperature and salinity data (CTD data) that were assimilated into the JCOPE2M. Thus, temperature and salinity data of the JCOPE2M contained the effect of sea ice changes to some degree. It would be useful to include a sea ice model in the ocean model to produce more accurate assimilation data in the future. Secondly, in the JCOPE2M, basin-wide and seasonal cycle steric effects are removed from SSH anomalies in order to effectively represent oceanic mesoscale eddies (Kagimoto et al., 2008). Thus, when seasonal cycle changes of SSH and OIA are investigated, this point should be considered. In the present study, as described in **Section 2**, seasonal cycle changes (i.e., monthly climatologies) of SSH data and other variables were removed from the anomalies to focus on the interannual-scale variations. The JCOPE2M does not include a tide model in its ocean model. The lack of a tide model in the JCOPE2M is favorable for this study, as we did not intend to analyze the oceanic fluid changes due to tides, as described in **Section 2**. Such factors may be considered in the future assimilation systems depending on the analysis target and purpose.

4.6 Future Interdisciplinary Studies

In this study, it was shown that ocean isostasy is better established in the offshore regions with ocean bottom depths greater than 1000 m. It can be speculated that the ocean bottom shape along with the bottom depth might also affect the ocean current and ocean structure that can affect ocean isostasy. In future, collaboration with theoretical studies of ocean fluid dynamics focusing on the bottom depth and shape (e.g., Uehara and Miyake, 1999; Kubokawa, 2008; Miyama et al., 2018) will be conducted to further explore the relationship between ocean bottom depth/bottom shape and degree of ocean isostasy.

In this study, we focused on ocean fluid changes due to the WCRs found off the southeastern coast of Hokkaido, Japan. It has been reported that the WCRs also play an important role in marine biogeochemical changes and fisheries resources changes (e.g., Imanaga and Hirano, 1984; Chiang and Taniguchi, 2000; Kaeriyama et al., 2013). In addition, recently Sugimoto et al. (2017) pointed out that the warm sea surface temperatures of the WCRs off Sanriku, Japan, have an impact on the local atmospheric changes in the region. The WCRs off the southeastern coast of Hokkaido, Japan, may have a similar impact on atmospheric changes. Thus, interdisciplinary studies focusing on the WCRs among seismology, physical oceanography, marine biogeochemistry, fisheries science, atmospheric science, etc. may lead to new approaches of science activities, including the promotion of joint use of various data, collaboration on *in-situ* observations in this area, and developing of ocean and atmosphere assimilation models including such new data. Additionally, such interdisciplinary studies would be conducted in the future, not only for the area off the southeastern coast of Hokkaido, Japan, but also for the coastal areas of Sanriku (i.e., areas including the S-net) along which WCRs propagate northward to the southeastern coast of Hokkaido, Japan, the Kuroshio area (i.e., areas including the N-net and DONET1/DONET2), and other areas in the world where seismic activity is strong, and oceanic currents and mesoscale eddies are dominant.

5 CONCLUDING REMARKS

In this study, we explored the relationship between the SSH and sea water density anomalies (i.e., SEP anomalies), with a special reference to the WCRs off the southeastern coast of Hokkaido, Japan, on an interannual (i.e., year-to-year) timescale from January 2001 to December 2018, using eddy-resolving ocean assimilation data of the JCOPE2M based on a continuously stratified numerical model. We show that positive SSH anomalies with amplitudes in the order of 0.1 m appeared off the southeastern coast of Hokkaido, Japan, in the years 2007 and 2016 in association with WCRs. During this period, negative SEP anomalies with amplitudes similar to those of the SSH anomalies but with opposite signs, related to the oceanic baroclinic structures of WCRs with negative seawater density anomalies, also appeared in this region. We further show that nearly 90% of the effect of the positive SSH anomalies on the PSF anomalies are canceled out by negative SEP anomalies (i.e., negative seawater density anomalies), especially in offshore regions with ocean bottom depths deeper than 1000 m. The results of this study support our previous observational study (Hasegawa et al., 2019) that showed that the PSF anomalies are nearly zero when large positive SSH anomalies and oceanic baroclinic structures with negative seawater density anomalies due to a WCR appeared at PG2 in 2007.

To evaluate the total effect of the SSH and seawater density (i.e., SEP) anomalies on the PSF anomalies, the OIA was introduced in this study. The results show that the amplitudes of OIAs are nearly 10% of those of SSH anomalies, ranging from −0.025 m to +0.025 m in 2007 and 2016. This is because nearly 90% of the effect of SSH anomalies on the PSF is canceled out by the seawater density anomalies in deep offshore areas with water depths greater than 1000 m. Thus, it can be said that ocean

isostasy is better established in deep offshore regions than in shallow coastal regions.

The results of this study suggest that the effect of OIAs, that is, ocean fluid changes, on PSF anomalies cannot be neglected on an interannual timescale in the areas off the southeastern coast of Hokkaido, Japan. In past studies, ocean barotropic effects on PSF were explored using a non-linear, single-layer barotropic ocean model on a shorter timescale (Inazu et al., 2012; Muramoto et al., 2019). Based on the case studies concerning the WCRs off the southeastern coast of Hokkaido, Japan, including the Kuril Trench, the results of the present study suggest that the effect of the OIA changes on PSF anomalies on an interannual timescale should be taken into consideration as well as the shorter-timescale barotropic changes. Moreover, the results indicate that the effect of OIA changes should be estimated when PSF anomalies due to crustal deformation related to slow earthquakes, including long-term SSEs, are explored on an interannual timescale. Accordingly, if an OIA change is not negligible, compared with the PSF anomaly change, the OIA should be removed from the PSF change to better evaluate the PSF anomaly change due to crustal deformations, not only in the region off the southeast coast of Hokkaido, Japan, but also in other regions.

DATA AVAILABILITY STATEMENT

The JCOPE2M assimilation data were provided by the Application Laboratory of JAMSTEC. The data can be distributed to any interested person. To use the JCOPE2M assimilation data, it is required to contact the member of the Application Laboratory via email (jcope@jamstec.go.jp). For details of the usage of the JCOPE2M assimilation data, please see the website of the Application Laboratory of JAMSTEC (http://www.jamstec.go.jp/jcope/htdocs/e/distribution/index.html). The altimetric SSH data were provided by AVISO. The AVISO SSH data is available for download from the FTP website of the Copernicus Marine and Environment Monitoring Service (CMEMS). PSF data at PG 1 and PG 2 were obtained as a part of the JAMSTEC observational project of the "Long-Term Deep Sea Floor Observatory off Kushiro -Tokachi in the Kuril Trench". The PSF data is available on the JAMSTEC website for this project (http://www.jamstec.go.jp/scdc/top_e.html).

AUTHOR CONTRIBUTIONS

TH calculated monthly anomalies of the assimilation data from the daily data, analyzed them, made figures, and wrote this manuscript. TH also calculated the observed monthly PSF anomalies at PG1 and PG2 from the hourly data and analyzed the observed altimetric SSH data. AN calculated the coefficients used for the removal of sensor drift of PSF at PG1 and PG2, gave important comments about the definitions of SEP and OIA, barotropic and baroclinic component of the WCRs, variabilities of Kuroshio, Oyashio, and WCRs, and made a prototype of Fig 1. KA gave important comments about the OIA, the afterslip related to the 2003 Tokachi-oki earthquake, SSEs, other crustal deformations on an interannual timescale. TM conducted an initial check of the SSH and seawater density vertical profiles of JCOPE2M in the analysis region and confirmed that JCOPE2M suitably reproduces the ocean structures related to WCRs. TM also provided the important comments about the factors not considered by the JCOPE2M. TM and KA also gave important comments concerning the idea of POIA. HM made hourly PSF data from the raw data at PG1 and PG2 and performed their initial checks and provided important comments about the data procedure for making the hourly PSF data at PG 1and PG2 and the increasing trends of SSH anomalies at PG1 and PG2. RI checked and provided the raw PSF data for PG1 and PG2. MW gave important comments about the marine biogeochemical studies related to the WCRs off the southeastern coast of Hokkaido, Japan. All coauthors collaborated with the corresponding author (TH) in the construction of the manuscript and approved the final manuscript.

FUNDING

This work was partly supported by the Japan Society for the Promotion of Science (JSPS), Grant-in-Aid for Scientific Research (KAKENHI) Grant Nos. JP15H02835, JP15H04228, JP17K05660, JP17K19093, JP18H03726, JP19H02411, JP20H04349, JP20H2236, and JP20K04072.

ACKNOWLEDGMENTS

The satellite altimeter data were provided by AVISO. The authors wish to express their sincere thanks to Ruochao Zhang for help with the FTP of the JCOPE2M assimilation data. The authors would also like to thank Youichi Tanimoto, Atsushi Kubokawa, Takeshi Horinouchi, Kay I. Ohshima, Kimio Hanawa, Yosuke Fujii, Masanori Konda, Kazuyuki Uehara, Yoshimi Kawai, Fumiaki Kobashi, Shusaku Sugimoto, Toshio Suga, Takane Hori, members of the Faculty of Environmental Earth Science/Graduate School of Environmental Science at Hokkaido University, members of the Physical Oceanography Laboratory at Tohoku University, and members of the Research Institute for Maine Geodynamics at JAMSTEC for their helpful discussions, suggestions, comments, support, and encouragements. The authors would also like to thank Editage (www.editage.com) for English language editing. The authors are deeply grateful to the editor, Dr Laura Wallace (University of Texas), and two reviewers for their constructive comments during the review process.

SUPPLEMENTARY MATERIAL

The Supplementary Material for this article can be found online at: https://www.frontiersin.org/articles/10.3389/feart.2021.600930/full#supplementary-material.

REFERENCES

Aoki, S., Imawaki, S., and Ichikawa, K. (1995). Baroclinic disturbances propagating westward in the Kuroshio Extension region as seen by a satellite altimeter and radiometers. *J. Geophys. Res.* 100, 839–855. doi:10.1029/94JC02255

Araki, E., Saffer, D. M., Kopf, A. J., Wallace, L. M., Kimura, T., Machida, Y., et al. IODP (2017). Expedition 365 shipboard scientist. *Science* 356, 1157–1160. doi:10.1126/science.aan3120

Argo Science Team, (1998). On the design and implementation of Argo: an initial plan for a global array of profiling floats. *GODAE report*. 5, Melbourne, VIC: GODAE Internal Project Office.

Argo Science Team, (2001). "Argo: the global array of profiling floats," in *Observing the oceans in the 21st century*. Editors C. J. Koblinsky and N. R. Smith (Melbourne: GODAE Project Office, Bureau of Meteorology), 248–258.

Ariyoshi, K., Matsumoto, H., Inoue, T., Nagano, A., Hasegawa, T., Kido, M., et al. (2016). "Extraction of crustal deformations and oceanic fluctuations from ocean bottom pressures," in OCEANS 2016 MTS/IEEE Monterey, San Francisco, CA, September 19–22, 2016, 1–5.

AVISO (2008). Technical Reports. SSALTO/DUACS user handbook: (M)SLA and (M)ADT near-real time and delayed time products. CLS, ramonville st agnes. Available at: https://icdc.cen.uni-hamburg.de/fileadmin/user_upload/icdc_Dokumente/AVISO/hdbk_duacs.pdf (Accessed October 3, 2008).

Ballarotta, M., Ubelmann, C., Pujol, M.-I., Taburet, G., Fournier, F., Legeais, J.-F., et al. (2019). On the resolutions of ocean altimetry maps. *Ocean Sci.* 15, 1091–1109. doi:10.5194/os-15-1091-2019

Chiang, K.-P., and Taniguchi, A. (2000). Distribution and modification of diatom assemblages in and around a warm core ring in the western North pacific Frontal zone east of Hokkaido. *J. Plankton Res.* 22, 2061–2074. doi:10.1093/plankt/22.11.2061

DeMets, C., Gordon, R., Argus, D., and Stein, S. (1990). Current plate motion. *Geophys. J. Int.* 101, 425–478. doi:10.1111/j.1365-246X.1990.tb06579.x

Ebuchi, N., and Hanawa, K. (2000). Mesoscale eddies observed by TOLEX-ADCP and TOPEX/POSEIDON altimeter in the Kuroshio recirculation region south of Japan. *J. Oceanogr.* 56, 43–57. doi:10.1023/A:1011110507628

Franco, S., Kostoglodov, V., Larson, K., Manea, V., Manea, M., and Santiago, J. (2005). Propagation of the 2001–2002 silent earthquake and interplate coupling in the Oaxaca subduction zone, Mexico, *Earth Planet. Sp.* 57, 973–985. doi:10.1186/BF03351876

Hasegawa, T., Ando, K., Ueki, I., Mizuno, K., and Hosoda, S. (2013). Upper-ocean salinity variability in the tropical Pacific: case study for quasidecadal shift during the 2000s using TRITON buoys and Argo floats. *J. Clim.* 26, 8126–8138. doi:10.1175/JCLI-D-12-00187.1

Hasegawa, T., and Hanawa, K. (2003a). Heat content variability related to ENSO events in the Pacific. *J. Phys. Oceanogr.* 33, 407–421. doi:10.1175/1520-0485(2003)033<0407:HCVRTE>2.0.CO;2

Hasegawa, T., and Hanawa, K. (2003b). Decadal-scale variability of upper ocean heat content in the tropical Pacific. *Geophys. Res. Lett.* 30, 1272. doi:10.1029/2002GL016843

Hasegawa, T., Nagano, A., Matsumoto, H., Ariyoshi, K., and Wakita, M. (2019). El Niño-related sea surface elevation and ocean bottom pressure enhancement associated with the retreat of the Oyashio southeast of Hokkaido, Japan. *Mar. Geophys. Res.* 40, 505–512. doi:10.1007/s11001-019-09392-8

Hasegawa, T., Yasuda, T., and Hanawa, K. (2007a). Generation mechanism of quasidecadal variability of upper ocean heat content in the equatorial Pacific Ocean. *J. Geophys. Res.* 112, C08012. doi:10.1029/2006JC003755

Hasegawa, T., Yasuda, T., and Hanawa, H. (2007b). Multidecadal variability of the upper ocean heat content anomaly field in the North Pacific and its relationship to the Aleutian Low and the Kuroshio transport. *Pap. Meteor. Geophys.* 58, 155–166. doi:10.2467/mripapers.58.155

Hirose, H., and Obara, K. (2005). Repeating short- and long-term slow slip events with deep tremor activity around the Bungo channel region, southwest Japan. *Earth Planet. Sp.* 57, 961–972. doi:10.1186/BF03351875

Hu, S., and Fedorov, A. V. (2017). The extreme El Niño of 2015–2016 and the end of global warming hiatus. *Geophys. Res. Lett.* 44, 3816–3824. doi:10.1002/2017GL072908

Ichikawa, K., and Imawaki, S. (1994). Life history of a cyclonic ring detached from the Kuroshio Extension as seen by the Geosat altimeter. *J. Geophys. Res.* 99, 15953–15966. doi:10.1029/94JC01139

Ide, S., Beroza, G., Shelly, D., and Uchide, T. (2007). A scaling law for slow earthquakes. *Nature* 447, 76–79. doi:10.1038/nature05780

Imanaga, D., and Hirano, T. (1984). Horizontal distribution of the Japanese sardine in relation to oceanic front at the purse seine fishing grounds southeast of Hokkaido. *Null. Jap. Soc. Sci. Fish.* 50, 577–589.

Inazu, D., Hino, R., and Fujimoto, H. (2012). A global barotropic ocean model driven by synoptic atmospheric disturbances for detecting seafloor vertical displacements from *in situ* ocean bottom pressure measurements. *Mar. Geophys. Res.* 33, 127–148. doi:10.1007/s11001-012-9151-7

Ito, S., Uehara, K., Miyao, T., Miyake, H., Yasuda, I., Watanabe, T., et al. (2004). Characteristics of SSH anomaly based on TOPEX/POSEIDON altimetry and *in situ* measured velocity and transport of Oyashio on OICE. *J. Oceanogr.* 60, 425–438. doi:10.1023/B:JOCE.0000038059.54334.6b

Itoh, S., and Sugimoto, T. (2002). Behavior of warm-core rings in a double-gyre wind-driven ocean circulation model. *J. Oceanogr.* 58:651–660. doi:10.1023/A:1022838205678

Itoh, Y., Nishimura, T., Ariyoshi, K., and Matsumoto, H. (2019). Interplate slip following the 2003 Takashi-oki earthquake from ocean bottom pressure gauge and land GNSS data. *J. Geophys. Res.* 124, 4205–4230. doi:10.1029/2018JB016328

Joyce, T. M., and Dunworth-Baker, J. (2003). Long-term hydrographic variability in the northwest pacific ocean. *Geophys. Res. Lett.* 30, 1043. doi:10.1029/2002GL015225

Kaeriyama, H., Ambe, D., Shimizu, Y., Fujimoto, K., Ono, T., Yonezaki, S., et al. (2013). Direct observation of 134Cs and 137Cs in surface seawater in the western and central North Pacific after the Fukushima Dai-ichu nuclear power plant accident. *Biogeosciences* 10, 4287–4295. doi:10.5194/bg-10-4287-2013

Kagimoto, T., Miyazawa, Y., Guo, X., and Kawajiri, H. (2008). "High resolution Kuroshio forecast system: description and its applications," in *High resolution numerical modelling of the atmosphere and ocean*. Editors K. Hamilton and W. Ohfuchi (New York, NY: Springer).

Kalnay, E., Kanamitsu, M., Kistler, R., Collins, W., Deaven, D., and Gandin, L. (1996). The NCEP/NCAR 40-year reanalysis project. *Bull. Am. Meteorol. Soc.* 77, 437–471. doi:10.1175/1520-0477(1996)077<0437:TNYRP>2.0.CO;2

Kawabe, M. (2005). Variations of the Kuroshio in the southern region of Japan—condition for large meander of the Kuroshio. *J. Oceanogr.* 61, 529–537. doi:10.1007/s10872-005-0060-0

Kawaguchi, K., Hirata, K., Mikada, H., Kaiho, Y., and Iwase, R. (2000). "An expendable deep seafloor monitoring system for earthquake and tsunami observation network," in OCEANS 2000 MTS/IEEE Conference and Exhibition, San Francisco, CA, September 11–14, 2000, 3, 1719–1722.

Kobayashi, A., and Tsuyuki, T. (2019). Long-term slow slip event detected beneath the Shima Peninsula, central Japan, from GNSS data. *Earth Planet. Sp.* 71, 60. doi:10.1186/s40623-019-1037-3

Kono, T. (1997). Modification of the Oyashio water in the Hokkaido and Tohoku areas. *Deep Sea Res.* 44, 669–688. doi:10.1016/S0967-0637(96)00108-2

Kubokawa, A. (2008). Quasigeostrophic planetary waves in a two-layer ocean with one-dimensional periodic bottom topography. *Geophys. Astrophys. Fluid Dyn.* 102, 119–137. doi:10.1080/03091920701614334

Kuroda, H., Wagawa, T., Shimizu, Y., Ito, S.-I., Kakehi, S., and Okunishi, T. (2015). Interdecadal decrease of the Oyashio transport on the continental slope off the southeastern coast of Hokkaido, Japan. *J. Geophys. Res.* 120, 2504–2522. doi:10.1002/2014JC10402

Luo, J., and Yamagata, T. (2001). Long-term El niño-southern oscillation (ENSO)-like variation with special emphasis on the south pacific. *J. Geophys. Res.* 106, 22211–22227. doi:10.1029/2000JC000471

Mantua, N. J., Hare, S. R., Zhang, Y., and Wallace, J. M., and Francis, R. C. (1997). A Pacific interdecadal climate oscillation with impacts on salmon production. *Bull. Amer. Meteor. Soc.* 78, 1069–1079. doi:10.1175/1520-0477(1997)078<1069:APICOW>2.0.CO;2

McPhaden, M. J., Zebiak, S. E., and Glantz, M. H. (2006). ENSO as an integrating concept in earth science. *Science* 314, 1740–1745. doi:10.1126/science.1132588

Mellor, G. L., Hakkinen, S., Ezer, T., and Patchen, R. (2002). "A generalization of a sigma coordinate ocean model and an inter comparison of model vertical

grids," in *Ocean forecasting: conceptual basis and applications*. Editors N. Pinardi and J. D. Woods (New York: Springer), 55–72.

Minobe, S. (1999). Resonance in bidecadal and pentadecadal climate oscillations over the North Pacific: role in climate regime shifts. *Geophys. Res. Lett.* 26, 855–858. doi:10.1029/1999GL900119

Miyama, T., Mitsudera, H., Nishigaki, H., and Furue, R. (2018). Dynamics of a quasi-stationary jet along the subarctic front in the North pacific ocean (the western isoguchi jet): an ideal two-layer model. *J. Phys. Oceanogr.* 48, 807–830. doi:10.1175/jpo-d-17-0086.1

Miyashita, K. (1987). A model of plate convergence in southwest Japan, inferred from leveling data associated with the 1946 Nanaimo Earthquake. *J. Phys. Earth.* 35, 449–467. doi:10.4294/jpe1952.35.449

Miyazaki, S., Segall, P., Fukuda, J., and Kato, T. (2004). Space time distribution of afterslip following the 2003 Takashi-oki earthquake: implications for variations in fault zone frictional properties. *Geophys. Res. Lett.* 31, L06623, doi:10.10129/2003GL019410

Miyazawa, Y., Kuwano-Yoshida, A., Doi, T., Nishikawa, H., Narazaki, T., Fukuoka, T., et al. (2019). Temperature profiling measurements by sea turtles improve ocean state estimation in the Kuroshio-Oyashio Confluence region. *Ocean Dyn.* 69, 267–282. doi:10.1007/s10236-018-1238-5

Miyazawa, Y., Varlamov, S. M., Miyama, T., Guo, X., Kiyomatsu, K., Kachi, M., et al. (2017). Assimilation of high-resolution sea surface temperature data into an operational nowcast/forecast system around Japan using a multi-scale three-dimensional variational scheme. *Ocean Dyn.* 67, 713–728. doi:10.1007/s10236-017-1056-1

Muramoto, T., Ito, Y., Inazu, D., Wallace, L. M., Hino, R., Suzuki, S., et al. (2019). Seafloor crustal deformation on ocean bottom pressure records with nontidal variability corrections: Application to Hikurangi margin, New Zealand. *Geophys. Res. Lett.* 46, 303–310. doi:10.1029/2018GL080830

Nagano, A., Hasegawa, T., Matsumoto, H., and Ariyoshi, K. (2018). Bottom pressure change associated with the 2004–2005 large meander of the Kuroshio south of Japan. *Ocean Dyn.* 68, 847–865. doi:10.1007/s10236-018-1169-1

Nagano, A., Yamashita, Y., Hasegawa, T., Ariyoshi, K., Matsumoto, H., and Shinohara, M. (2019). Characteristics of an atypical large-meander path of the Kuroshio current south of Japan formed in September 2017. *Mar. Geophys. Res.* 40, 525–539. doi:10.1007/s11001-018-9372-5

Nakata, R., Hino, H., Kuwatani, T., Yoshioka, S., Okada, M., and Hori, T. (2017). Discontinuous boundaries of slow slip events beneath the Bungo Channel, southwest Japan. *Sci. Rep.* 7, 6129. doi:10.1038/s41598-017-06185-0

Nishikawa, T., Matsuzawa, T., Ohta, K., Uchida, N., Nishimura, T., and Ide, S. (2019). The slow earthquake spectrum in the Japan Trench illuminated by the S-net seafloor observatories. *Science* 365, 808–813. doi:10.1126/science.aax5618

Nitani, H. (1972). "Beginning of the Kuroshio," in *Kuroshio-its physical aspects*. Editors H. Stommel and K. Yoshida (Tokyo: University of Tokyo Press), 129–163.

Nitta, T., and Yamada, S. (1989). Recent warming of tropical sea surface temperature and its relationship to the Northern Hemisphere circulation. *J. Meteorol. Soc. Jpn.* 67, 375–383. doi:10.2151/jmsj1965.67.3_375

Obara, K., and Kato, A. (2016). Connecting slow earthquakes to huge earthquakes. *Science* 353, 253–257. doi:10.1126/science.aaf1512

Owens, W. B., and Warren, B. A. (2001). Deep circulation in the northwest corner of the Pacific Ocean. *Deep Sea Res.* 48, 959–993. doi:10.1016/S0967-0637(00)00076-5

Ponte, R. M., and Gaspar, P. (1999). Regional analysis of the inverted barometer effect over the global ocean using TOPEX/POSEIDON data and model results. *J. Geophys. Res.* 104, 15587–15601. doi:10.1029/1999JC900113

Qiu, B., Kelly, K., and Joyce, T. (1991). Mean flow and variability of the Kuroshio Extension from the Geosat altimetry data. *J. Geophys. Res.* 96, 18491–18507. doi:10.1029/91JC01834

Shelly, D., Beroza, G., and Ide, S. (2007). Non-volcanic tremor and low-frequency earthquake swarms. *Nature* 446, 305–307. doi:10.1038/nature05666

Sugimoto, S., Aono, K., and Fukui, S. (2017). Local atmospheric response to warm mesoscale ocean eddies in the Kuroshio-Oyashio Confluence region. *Sci. Rep.* 7, 11871, doi:10.1038/s41598-017-12206-9

Tai, C.-K. and White, W. B. (1990). Eddy variability in the Kuroshio Extension as revealed by Geosat Altimetry: energy propagation away from the Jet, Reynolds stress, and seasonal cycle. *J. Phys. Oceanogr.* 20, 1761–1777. doi:10.1175/1520-0485(1990)020<1761:EVITKE>2.0.CO;2

Tanimoto, Y., Iwasaka, N., Hanawa, K., and Toba, Y. (1993). Characteristic variations of sea surface temperature with multiple time scales in the North Pacific. *J. Clim.* 6, 1153–1160. doi:10.1175/1520-0442(1993)006<1153:CVOSST>2.0.CO;2

Thompson, R. (1983). Low-pass filters to suppress inertial and tidal frequencies. *J. Phys. Oceanogr.* 13, 1077–1083. doi:10.1175/1520-0485(1983)013<1077:LPFTSI>2.0.CO;2

Tomosada, A. (1986). Generation and decay of Kuroshio warm-core rings. *Deep Sea Res.* 33, 1475–1486. doi:10.1016/0198-0149(86)90063-4

Trenberth, K. E. (1990). Recent observed interdecadal climate changes in the Northern Hemisphere. *Bull. Amer. Meteor. Soc.* 71, 988–933. doi:10.1175/1520-0477(1990)071<0988:ROICCI>2.0.CO;2

Trenberth, K. E. (1997). The definition of El Niño. *Bull. Amer. Meteor. Soc.* 78, 2771–2778. doi:10.1175/1520-0477(1997)078<2771:TDOENO>2.0.CO;2

Uchida, N., Iinuma, T., Nadeau, R. M., Bürgmann, R., and Hino, R. (2016). Periodic slow slip triggers megathrust zone earthquakes in northeastern Japan. *Science* 351, 488–492.doi:10.1126/science.aad3108

Uehara, K., and Miyake, H. (1999). Deep flows on the slope inshore of the kuril–kamchatka trench southeast off cape erimo, Hokkaido. *J. Oceanogr.* 55, 559–573. doi:10.1023/A:1007828517317

White, W. B., Tourre, Y. M., Barlow, M., and Dettinger, M. (2003). A delayed action oscillator shared by biennial, interannual, and decadal signals in the Pacific basin. *J. Geophys. Res.* 108, 1–18. doi:10.1029/2002JC001490

Yasunaka, S., and Hanawa, K. (2003). Regime shifts in the Northern Hemisphere SST field: revisited in relation to tropical variations, *J. Meteorol. Soc. Jpn.* 81, 415–424. doi:10.2151/jmsj.81.415

Conflict of Interest: The authors declare that this study was conducted in the absence of any commercial or financial relationships that could be construed as a potential conflict of interest.

frontiers in Earth Science

ORIGINAL RESEARCH
published: 13 May 2021
doi: 10.3389/feart.2021.667666

Seafloor Geodesy From Repeated Multibeam Bathymetric Surveys: Application to Seafloor Displacement Caused by the 2011 Tohoku-Oki Earthquake

Toshiya Fujiwara [1,2]*

[1]Research Institute for Marine Geodynamics, Japan Agency for Marine-Earth Science and Technology (JAMSTEC), Yokosuka, Japan, [2]Graduate School of Integrated Arts and Sciences, Kochi University, Kochi, Japan

Repeated multibeam bathymetric surveys played an important role for understanding the distribution of coseismic seafloor displacement caused by the March 11, 2011 Mw 9.0 Tohoku-oki earthquake. After the earthquake, we collected bathymetric data along the same tracks obtained before the earthquake. The selected tracks were crossing the trench and extending from the landward to seaward trench slopes. We examined the seafloor displacement on the landward relative to the seaward by means of the difference in bathymetry before and after the earthquake. The multibeam bathymetric survey has the advantage of areal coverage. The repeated surveys clarified the areal distribution of the coseismic seafloor displacement. In the main rupture area, very large seafloor displacement was observed. Sharp bathymetric change at the trench axis provided solid evidence that the fault slip on the shallowest part of the megathrust reached the trench axis and peaked at the trench axis. The very large displacement is limited to the particular area. Smaller seafloor displacements were observed in the area tens of kilometers away from the main rupture area. We present methods and results of the repeated multibeam bathymetric surveys and an application to the seafloor displacement caused by the 2011 Tohoku-oki earthquake in the northern Japan Trench. Less than several meters in seafloor vertical displacements and less than 20 m in seafloor horizontal displacement were estimated in the northern Japan Trench. The estimated smaller displacements are comparable in magnitude to error of the seafloor displacement observation from our bathymetric survey. Nevertheless, three adjacent survey tracks showed coherent relative differences in seafloor elevation, which suggests the relative difference enables us to discuss the along-track variation in seafloor displacement in the area. However, our survey was affected by uncertainties of roll and pitch biases and sound velocity errors. Well-prepared repeated multibeam bathymetric survey for the purpose of seafloor geodesy could lead to a higher resolution and more accurate result. Repeated acquisition of high resolution and accuracy bathymetric data using state-of-the-art technology will be important to quantitative discussion of the seafloor displacements caused by even smaller magnitude earthquakes and tsunamis.

Keywords: repeated bathymetric survey, multibeam bathymetry, Japan trench, 2011 tohoku-oki earthquake tsunami, seafloor displacement

OPEN ACCESS

Edited by:
Laura Wallace,
University of Texas at Austin,
United States

Reviewed by:
John DeSanto,
University of Washington,
United States
Dan Bassett,
GNS Science, New Zealand

***Correspondence:**
Toshiya Fujiwara
toshi@jamstec.go.jp

Specialty section:
This article was submitted to Solid Earth Geophysics, a section of the journal Frontiers in Earth Science

Received: *14 February 2021*
Accepted: *29 April 2021*
Published: *13 May 2021*

Citation:
Fujiwara T (2021) Seafloor Geodesy From Repeated Multibeam Bathymetric Surveys: Application to Seafloor Displacement Caused by the 2011 Tohoku-Oki Earthquake. Front. Earth Sci. 9:667666. doi: 10.3389/feart.2021.667666

INTRODUCTION

Repeated multibeam bathymetric surveys played an important role for understanding the areal distribution of coseismic displacement caused by the March 11, 2011 Mw 9.0 Tohoku-oki earthquake. Comparison of bathymetry collected after the earthquake with data acquired before the earthquake revealed and quantified the seafloor displacement on the landward trench slope across the Japan Trench. The seafloor on the outermost landward slope moved ~50 m toward the trench and up to 10 m upward (Fujiwara et al., 2011). The result provided solid evidence that the very large fault slip on the shallowest part of the megathrust reached the trench axis and peaked at the trench axis (Fujiwara et al., 2011; Kodaira et al., 2012; Sun et al., 2017).

In other instances, Maksymowicz et al. (2017) observed coseismic horizontal displacements of ~8 m and uplift of ~3 m caused by the February 27, 2010 Mw 8.8 Chile Maule earthquake by using repeated multibeam bathymetric data. And they estimated the up-dip limit of fault rupture during the giant earthquake. The rupture of the shallowest part of the megathrust and the following seafloor deformation has an important implication for tsunami generation.

However, deep-sea multibeam bathymetric surveys are generally supposed to map hundreds meter-scale seafloor morphological features for the purposes of marine geology and geophysics, therefore, very high accuracy measurements have rarely been required yet. The magnitudes of seafloor displacements become smaller in areas far away from the 2011 Tohoku-oki earthquake epicentral area (Fujiwara et al., 2017; Kodaira et al., 2020; Nakamura et al., 2020). In the case of the surveys to detect small seafloor displacements, the uncertainties in the bathymetric surveys are not negligible.

We present methods and results of the repeated multibeam bathymetric survey and an application to the seafloor displacement caused by the 2011 Tohoku-oki earthquake in the northern Japan Trench (**Figure 1**). In order to explain the tsunami caused by the 2011 Tohoku-oki earthquake, some papers have introduced an additional tsunami source in this area (e.g., Satake et al., 2013; Tappin et al., 2014; Romano et al., 2014; Hossen et al., 2015; Dettmer et al., 2016; Yamazaki et al., 2018). Fujiwara et al. (2017) described the smaller magnitudes of seafloor displacement in this area where the tsunami source was assumed. In this paper, two survey tracks were newly added to evaluate the methods and to refine the results (**Figure 1**). One is a repeated survey conducted before and after the earthquake. In the other survey, both of the cruises were carried out after the earthquake. Because the post seismic displacements are quite small (Watanabe et al., 2014; Tomita et al., 2017) as compared with the coseismic displacements shown by seafloor geodetic measurements (Kido et al., 2011; Sato et al., 2011), a noticeable change in the bathymetry is presumed to be absent for the survey that both two cruises conducted after the earthquake and a short time interval. Therefore, this post-earthquake survey enables us to evaluate repeatability of our survey. Then, we will present refinement of the results of Fujiwara et al. (2017), and also point out uncertainties about our surveys. Finally, we note strategies of the repeated multibeam bathymetric survey for seafloor geodesy.

METHOD

Bathymetric Data Collection

The Japan Agency for Marine-Earth Science and Technology (JAMSTEC) had carried out multibeam bathymetric surveys in June 2007 and in November 2010 aboard the R/V *Kairei* (KR07-08 and KR10-12 cruises), and in February 2008 aboard the R/V *Mirai* (MR07-07 Leg 3 cruise). These bathymetric data were collected using SeaBeam 2112 echo sounders. The operating

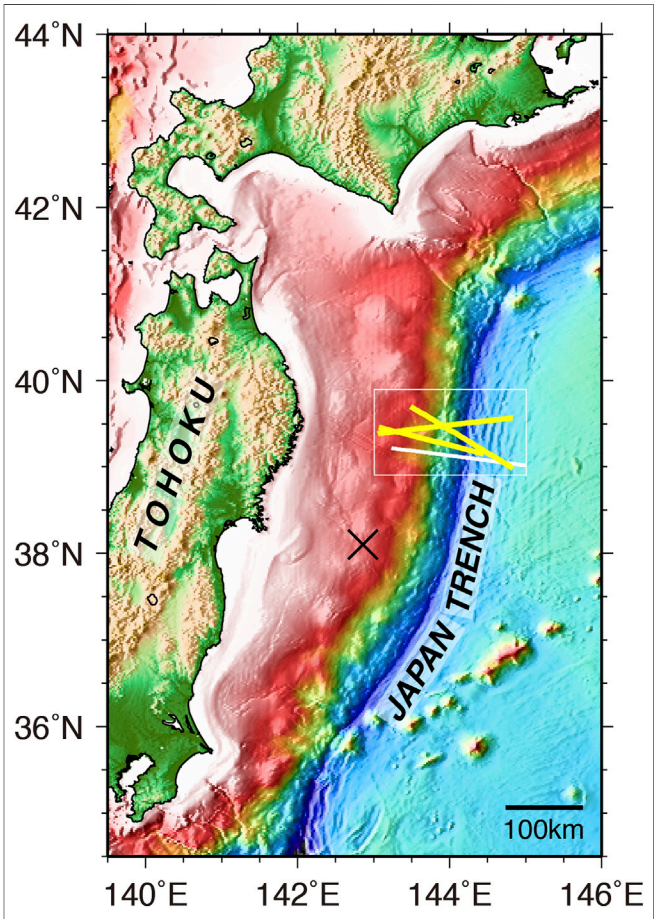

FIGURE 1 | Location map of the repeated bathymetric surveys. The white box marks the location in **Figure 2**. Survey tracks of comparison of bathymetry before and after the March 11, 2011 Tohoku-oki earthquake are indicated by yellow lines. The white line traces the survey track of comparison of bathymetry both after and after the earthquake. The black cross shows the epicenter of the earthquake. The background bathymetry is from compilation of pre-earthquake multibeam bathymetry (Hydrographic and Oceanographic Department, Japan Coast Guard and JAMSTEC, 2011).

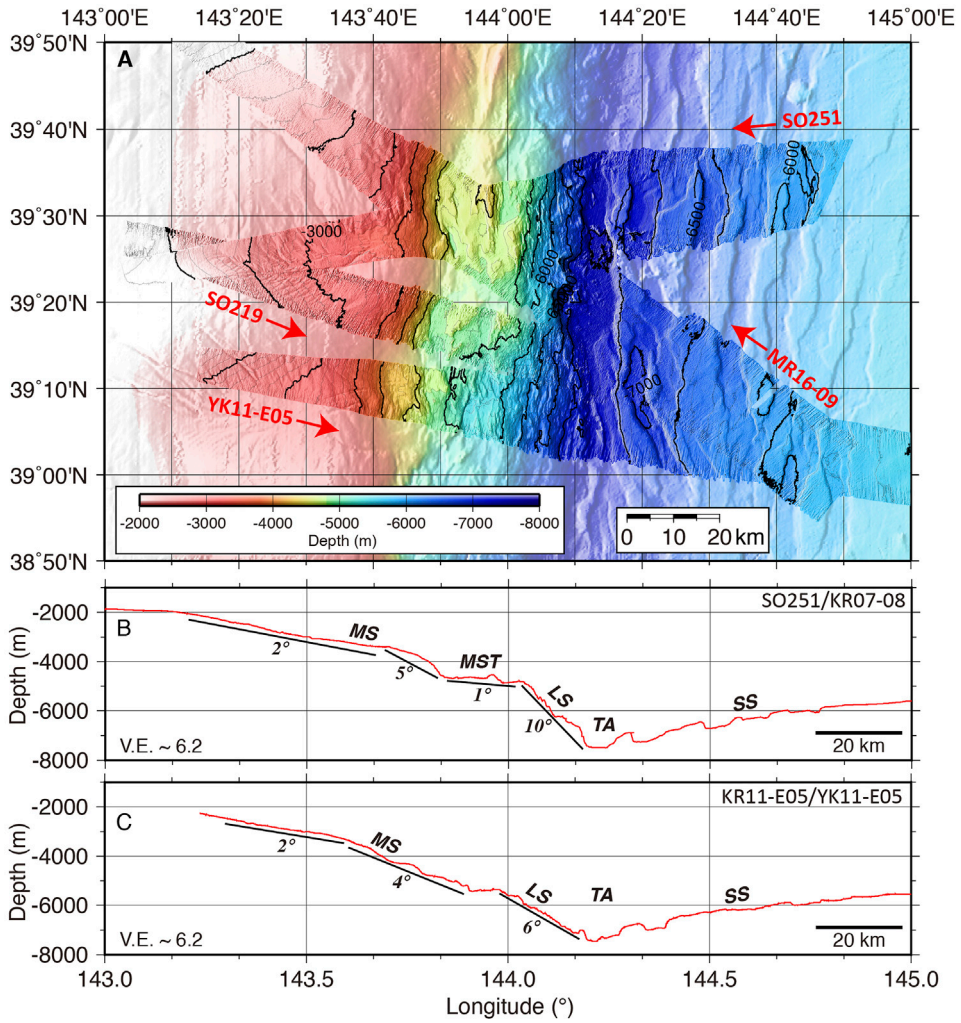

FIGURE 2 | (A) Multibeam bathymetry in the northern Japan Trench collected in 2011 (YK11-E05), 2012 (SO219A), 2016 (SO251A), and 2017 (MR16-09 Leg 4). The contour interval is 100 m, and the relief is illuminated from the northwest. Red arrows point survey ship's traveling directions. Along track bathymetric profiles using center-beam depths of **(B)** SO251A and **(C)** YK11-E05. SS: Seaward slope, LS: Lower slope, MST: Mid-slope terrace, MS: Mid slope, and TA: Trench axis. The vertical exaggeration is 6.2.

frequency was 12 kHz and a beam width was 2° × 2°. In the R/V *Kairei* cruises, the ship was traveling at speeds of 16 knots in both surveys, which yielded the along-track sampling interval of ~170 m in the deepest trench axial area. In the R/V *Mirai* cruise, the ship was traveling at speeds of 12 knots, which yielded the along-track sampling interval of ~120 m in the deepest trench axial area.

After the earthquake, the German R/V *Sonne* performed surveys along the same tracks (SO219A and SO251A cruises) (**Figure 2**). The 2012 and 2016 surveys were repeats of the 2010 and 2007 surveys, respectively. The bathymetric data in the March 2012 survey were collected using an EM120 with a frequency of 12 kHz and a beam width of 2° × 2°. The along-track sampling interval was rather short, ~70 m, in the deepest trench axial area at a slower speeds of 6 knots. In the October 2016 survey, the bathymetric data were collected with R/V 'New' *Sonne* equipped with a 12 kHz frequency EM122 which has a beam width of 0.5° along and 1° across the ship. The survey ship speed was 5 knots and the along-track sampling interval of ~35 m was achieved even in the deepest trench axial area. The R/V *Sonne* went the opposite directions of the previous surveys. The R/V *Mirai* cruised along the previous R/V *Mirai's* survey track in March 2017 (MR16-09 Leg 4 cruise). At the time of this cruise, the R/V *Mirai's* echo sounder had been replaced by a new SeaBeam 3012 with a 12 kHz frequency and a beam width of 1.6° along and 2° across the ship. The survey ship speed was 5 knots. The ship went the same direction of the previous survey (**Figure 2**). These survey tracks ran over each side of the Japan Trench and crossed the trench at 39.2°N, 39.3°N and 39.5°N. The SO251A survey track

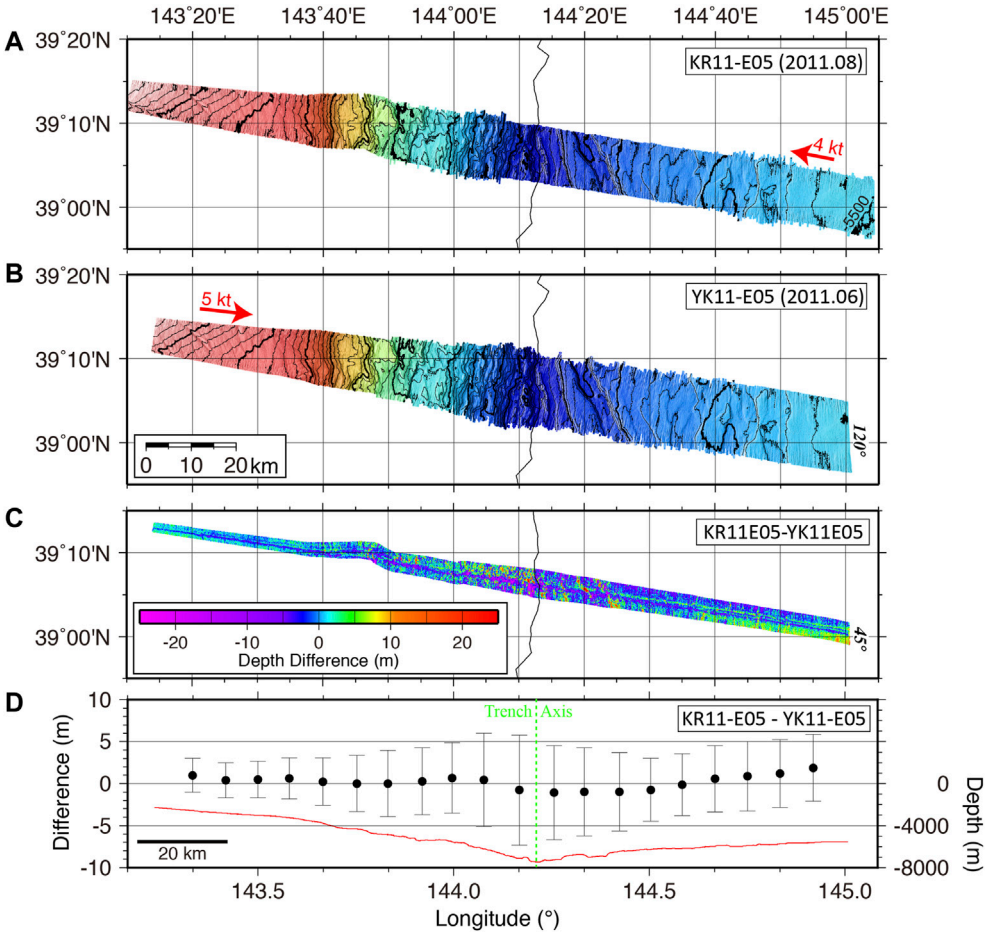

FIGURE 3 | Multibeam bathymetry collected both in 2011 **(A)** KR11-E05 (August 2011) and **(B)** YK11-E05 (June 2011). Red arrows point survey ship's traveling directions and speeds **(C)** Depth difference by subtracting the YK11-E05 bathymetric data from the KR11-E05 data (positive is shallower). **(D)** Along track profile of the depth difference. Black circles correspond to average values of the depth difference within ~15 km wide area. Locations of the black circles point the center of the area. Vertical bars show standard deviations. A red line shows the along track bathymetric profile using center-beam depths of YK11-E05.

intersects with the SO219A track around 143°16'E (water depth ~2200 m), and intersects with the MR1609 track around 143°53′E (~4600 m).

In the south of the study area, one survey was conducted in June 2011, after the March 11, 2011 earthquake, aboard the JAMSTEC R/V *Yokosuka* (YK11-E05 cruise) (**Figure 2**). The R/V *Yokosuka* was also equipped with a SeaBeam 2112 echo sounder. The ship went from landward to seaward at a speed of 5 knots. Two months later, bathymetric data along the same track were collected by the R/V *Kairei* (KR11-E05 cruise) in August 2011 (**Figure 3A**). The ship sailed in the opposite direction with a speed of 4 knots. The survey track crossed the Japan Trench at 39.1°N. These acquisition parameters of the repeated multibeam bathymetric surveys are summarized in **Table 1**.

The sound velocity profiles (SVP) in the water column were calculated using measurements from expandable bathothermographs (XBT) or conductivity temperature depth profilers (CTD) prior to the bathymetric surveys. However, no nearby XBT or CTD profiles were collected during the KR07–08 cruise. The SVP of water depth deeper than ~2000 m was derived from Levitus database (Levitus, 1982) because variation of the SVP in deep water is small in time and space. Surface sound velocities were measured in real-time. Therefore, the contribution of the surface sound velocity error is expected to be small enough.

Bathymetric Data Editing

MB-System seafloor mapping software (Caress et al., 2021) was used to remove erroneous bathymetric data. Firstly, the erroneous data were automatically flagged using a 'mbclean' tool. Then the data were manually edited. Sounding data near the nadir were rather noisy, however the erroneous data were difficult to be discriminated and completely removed.

All bathymetric data were ocean tide corrected using the NAO.99jb regional model around Japan (Matsumoto et al., 2000). The estimated sea surface height variation due to ocean tide was less than ±0.8 m.

To compare the different surveys with random sounding locations, post-earthquake bathymetric data were gridded by using the Generic Mapping Tools (GMT) software (Wessel and

Smith, 1991). Because the post-earthquake data are densely distributed and have lower noise levels since the data have been collected with lower ship speeds. And also, some data were collected using modern echo sounders. In the case of the surveys both post-earthquake bathymetric data between KR11-E05 (August 2011) and YK11-E05 (June 2011), the YK11-E05 data were gridded because the YK11-E05 data have a lower noise level (**Figures 3A,B**). The gridding algorithm 'surface' with a tension factor of 0.35 was operated after 'blockmedian' pre-processor filtering. The grid spacing was 0.025 arc-minutes. This is rather fine relative to the average spacing of the raw soundings, so that short-wavelength features of the bathymetry are retained. The short-wavelength features are useful to check the coherency between two bathymetric datasets.

Seafloor Morphology

The water depth ranges from 2000 m at the most landward side of the survey area to 7500 m at the trench axis (**Figure 2**). The seaward slope is characterized by horst and graben structure associated with oceanic plate bending in the strike of N-S to NNE-SSW. In the landward slope, the lower slope, ~20 km in width, inclines with a steep angle at an average of 6° or up to 10°. The mid-slope terrace between the steep middle slope and the lower slope is distinctive in the northern study area (**Figure 2B**). The mid-slope terrace at the depth of 4600–5000 m is ~20 km in width with a gentle angle of 0–1°.

Correction for Roll and Pitch Biases

The gridded (post-earthquake) data were sampled and depth differences were calculated at sounding locations of the other (pre-earthquake) data for the comparison, so that the gridding and interpolation errors can be reduced. A 'grdtrack' tool was used to sample the grid data at given sounding locations. Characteristic and artificial errors were more or less found in all bathymetric difference data. The depth difference in the across-track direction was positive on one side and negative on the other side, and the errors are greater in the outer beams, indicating a systematic tilt of one survey relative to the other, suggesting that there may be a roll bias error in one or both echo sounder systems.

The depth difference in the along-track direction was positive or negative over slopes, indicating systematic horizontal offset of sounding locations of one survey relative to the other, suggesting that there may be a pitch bias error in one or both echo sounder systems. Roll and pitch biases are due to a misalignment of the vertical reference supplied to the system. The measurement errors depend on water depth and increase with the water depth.

As these roll and pitch calibration values were not available, we needed to examine the roll and pitch bias effects. Although the repeated survey data are not a pair of datasets collecting while moving in opposite directions by the same ship and system and thus true calibration values of each ship are not determined, effective calibration values of the roll and pitch biases were searched in each survey tracks.

MB-System was used to manipulate the roll and pitch biases. The roll and pitch bias values were input using a 'mbset' tool, and the bathymetric data were reprocessed using a 'mbprocess' tool. We searched for a set of roll bias calibration values that suppress the systematic tilt of depth differences between ship's starboard and port sides. The set of roll bias calibration values are in a trade-off relationship, and thus an equal roll bias value was allocated to each cruise data in each survey tracks. The pitch bias value was examined to minimize the standard deviations of the areal depth differences. The horst and graben structure on the seaward slope was able to utilized. There are local east-facing and west-facing slopes and scarps regularly (**Figure 2**). The local seafloor slope variation can lead to coherent short-wavelength features of bathymetry.

Estimation of Seafloor Displacement

Only the bathymetric data collected within beam angle of 45° (+/−22.5°) among 120° swath were used for analysis because these inner beam soundings have higher measurement accuracy (**Figure 3C** in comparison with 3B). To avoid the apparent offsets of locations from different surveys, a set of the bathymetric data was horizontally shifted relative to the others in order to minimize the standard deviation of depth differences (maximize the cross-correlation of the bathymetry). Offsets were examined separately for the seaward and landward slopes, because the seaward slope is thought to have suffered little change from the 2011 earthquake. The offsets of locations and depths estimated on the seaward slope are considered to be systematic errors for the entire area. Consequently, after subtraction of these systematic errors, the average value of the depth difference on the seaward slope becomes zero (**Figures 3C,D**, **4A**). The average values of the depth differences on the landward slope should represent the average uplifts caused by the coseismic vertical displacement of the 2011 earthquake. The horizontal displacements on the landward slopes were estimated by dislocations of the amounts of horizontal shifts relative to those on the seaward slope (**Figure 4B**).

RESULTS

Comparison of Bathymetry After and After the Earthquake

Depth difference between the KR11-E05 (August 2011) data and the YK11-E05 (June 2011) data is shown in three different **Figures 3C,D**, **4A**. Because both data were collected after the March 11, 2011 earthquake, our method is verified and evaluated from the result.

In the map view, there is no apparent change in seafloor elevation for the entire area, although spiky noisy data associated with abrupt changes in bathymetry, for instance, steep scarps are conspicuous (**Figure 3C**). Also, the spiky noisy data along near the center of the track became visible in the map. The artificial differences between ship's port and starboard sides are still visible in some locations even after the roll bias correction. Because the applied constant of roll bias correction through the survey track did not match in some locations and the best fit roll bias values were slightly varied by location. In the cross sectional view, the profile of average values of the depth difference

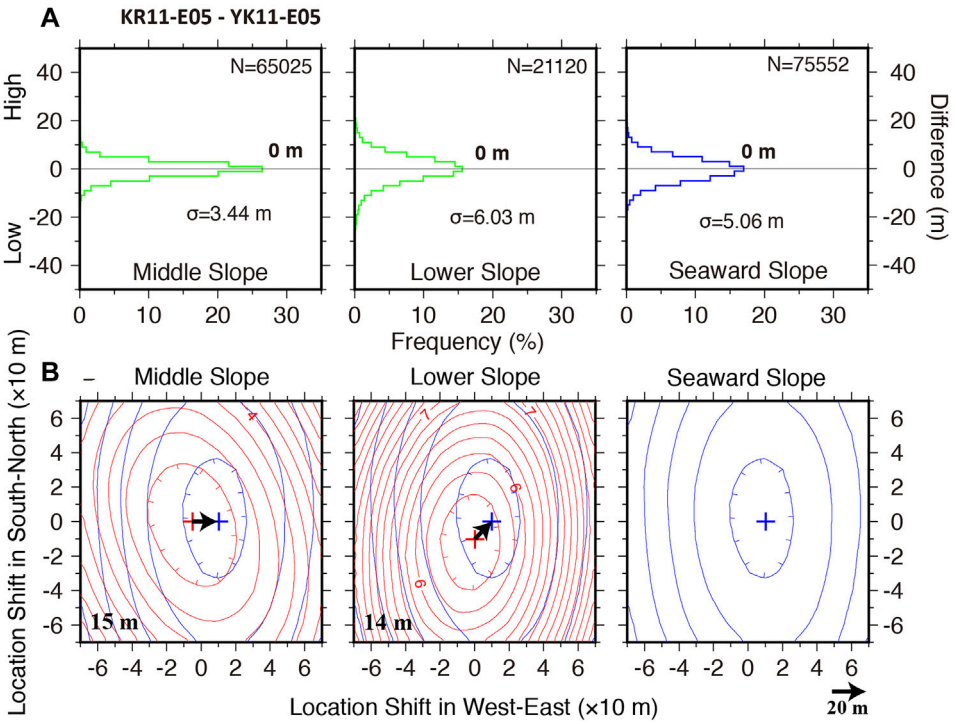

FIGURE 4 | (A) Histograms of depth differences after the optical offset adjustments between KR11-E05 and YK11-E05 data in the morphological areas. Values in the histograms indicate the averages and standard deviations **(B)** Contour maps showing standard deviations of the depth differences between KR11-E05 and YK11-E05 for given shifted locations. Crosses indicate the minimum peaks of the standard deviations. Arrows show vectors of horizontal shifts from landward to seaward. Values in the maps indicate lengths of the arrows.

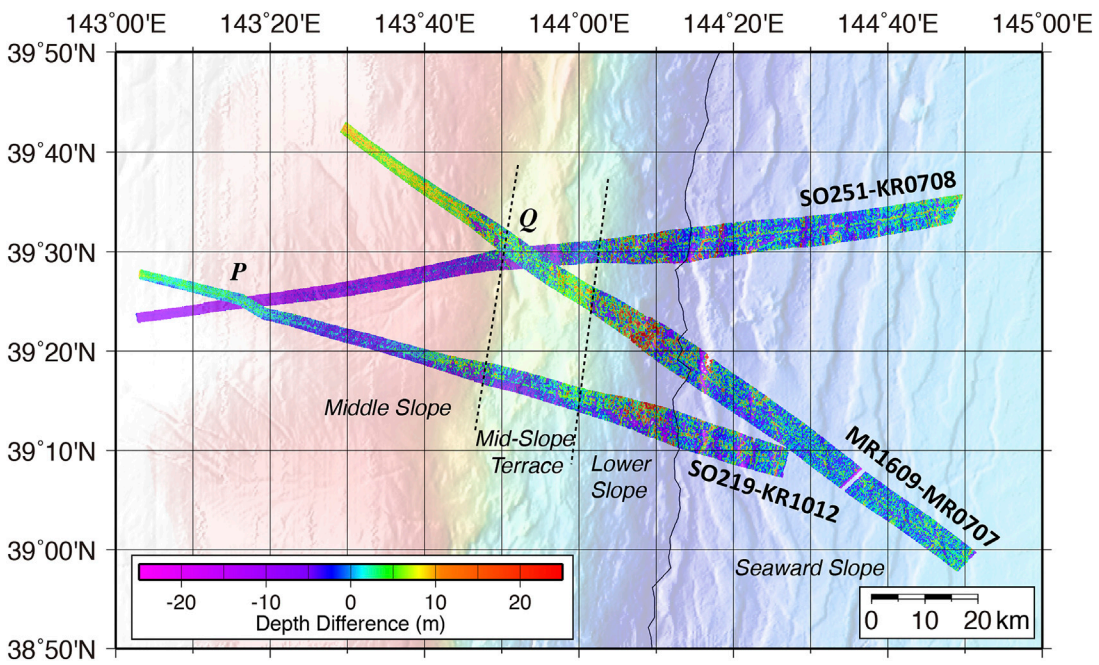

FIGURE 5 | Change in seafloor elevation by subtracting the KR07-08 (2007) bathymetric data from the SO251A (2016) data (positive is shallower), by subtracting the KR10-12 (2010) data from the SO219A (2012) data, and by MR07-07 Leg 3 (2008) data from the MR16-09 Leg 4 (2017) data, respectively.

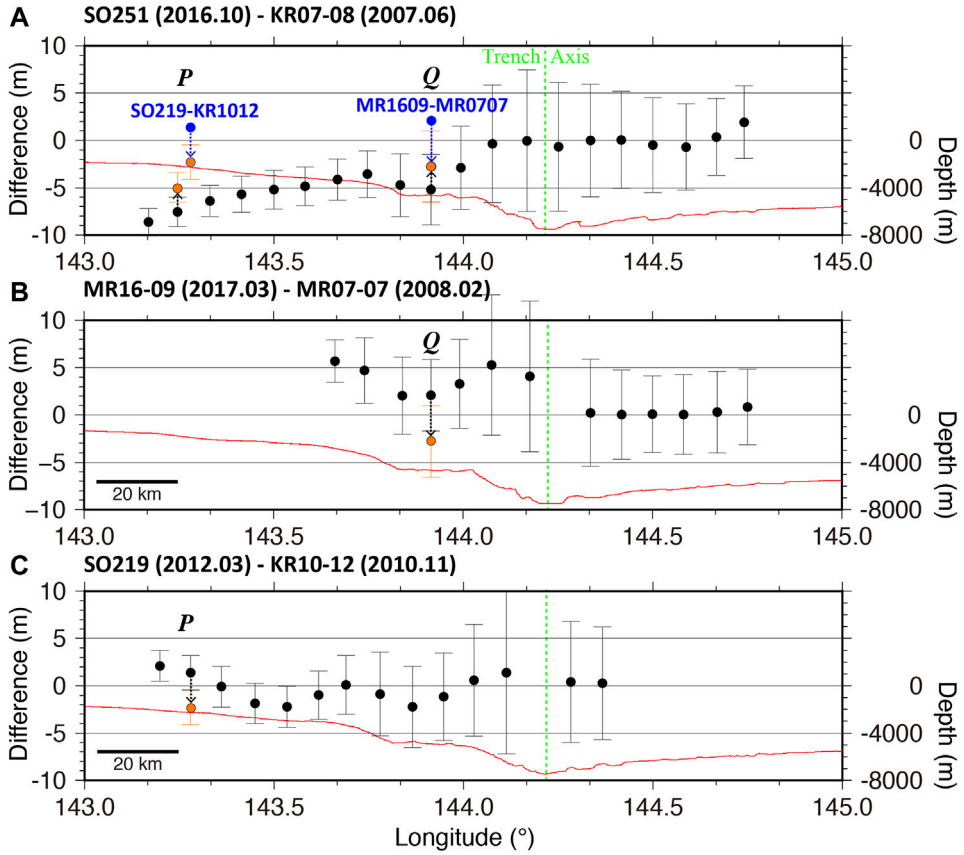

FIGURE 6 | Along track profiles of the depth differences. Black circles correspond to average values of the depth difference within ~15 km wide area. Locations of the black circles point the center of the area. Vertical bars show standard deviations. Orange circles show corrected average values after sound velocity corrections. A red line shows the along track bathymetric profile using center-beam depths. **(A)** Comparison between KR07-08 and SO251A,, **(B)** Comparison between MR07-07 Leg 3 and MR16-09 Leg 4, and **(C)** Comparison between KR10-12 and SO219A.

within 15 km wide area along the track show variation in amplitude of ±1 m, although the displacement is presumed to be quite small (**Figure 3D**).

For the areas divided by the morphological features, i.e., the seaward slope, the landward lower slope, and the middle slope, the ~20–50 km long-range averages converge to zero (**Figure 4A**). The standard deviations fall within the criterion of multibeam measurement (the depth accuracy (inner beams) 0.2% of water depth (~4–15 m in 2000–7600 m depth)). Note that there is less than 15 m dislocation between the two datasets, although displacement is presumed to be quite small (**Figure 4B**). The offset may suggest uncertainty in the estimation of the amount of shift. This result corroborated the uncertainty estimation previously described (Fujiwara et al., 2011; Fujiwara et al., 2015).

Comparison of Bathymetry Before and After the Earthquake

The calculation from KR10–12 (2010) to SO219A (2012), from MR07-07 (2008) to MR16-09 (2016), and also from KR07-08 (2007) to SO251A (2016) followed the same procedure. Comparisons of the bathymetry before and after the 2011 earthquake are shown in **Figures 5–8**. Relative change in the depth difference on the landward slope suggests seafloor vertical displacement due to the earthquake.

The depth differences with amplitudes of several meters were found (**Figures 5**, **6**). The amplitudes are larger than the comparison of after and after earthquake data as described in the previous section. About discrepancies in absolute values of the depth differences among the survey tracks will be discussed in the later *Repeated Bathymetric Survey Plan for Seafloor Geodesy*. The depth difference variation is correlated to areas divided by the morphological features. The lower slope is relatively uplifted, the mid-slope terrace is relatively subsided, and the middle slope is slightly uplifted within the same survey track profile (**Figures 6**, **7**). These profiles of depth difference show the same trend even though the depth change is somewhat different. The relative depth differences between the morphological areas are ~1–5 m (**Figure 7**). The standard deviations of depth differences are attributed to measurement accuracy of multibeam bathymetry, and these are also within 0.2% of water depth (**Figure 7**).

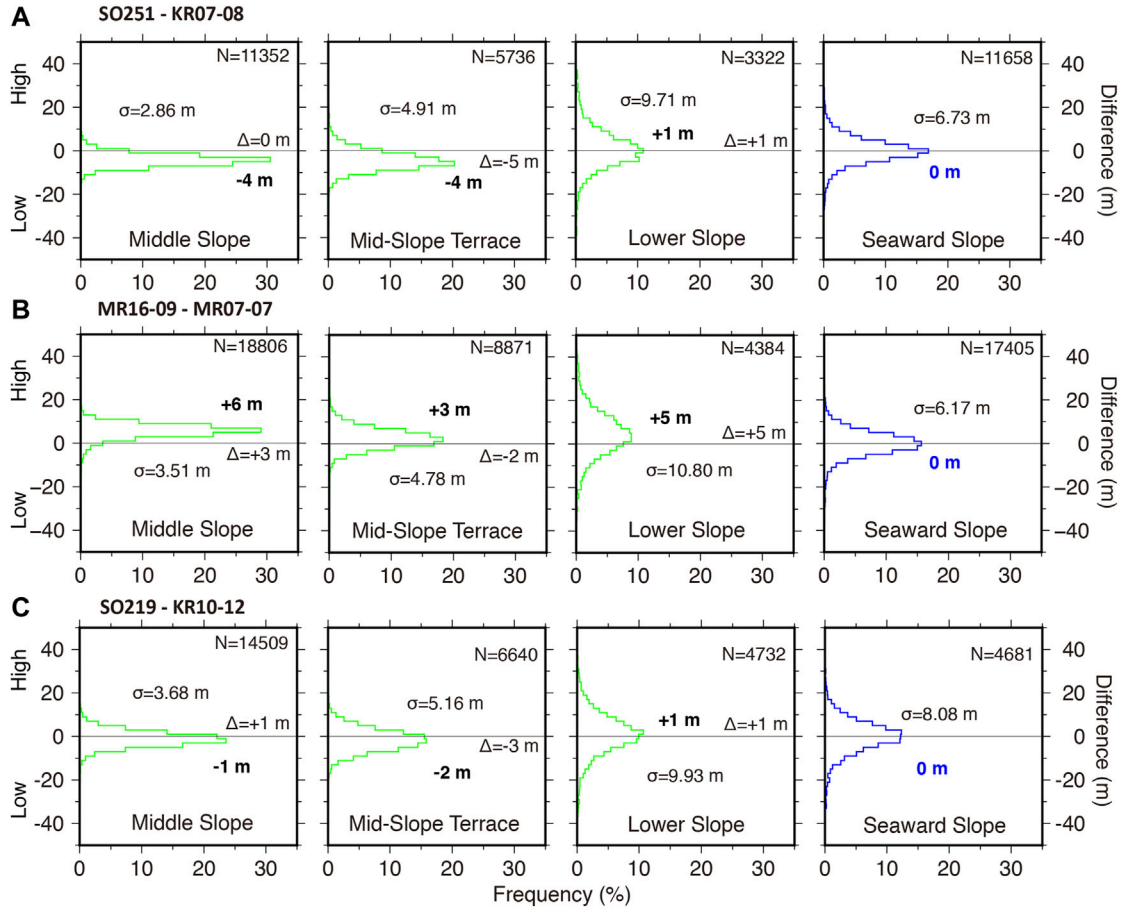

FIGURE 7 | Histograms of depth differences after the optical offset adjustments between different surveys in the morphological areas. **(A)** Comparison between KR07-08 and SO251A **(B)** Comparison between MR07-07 Leg 3 and MR16-09 Leg 4, and **(C)** Comparison between KR10-12 and SO219A. Values in the histograms indicate the averages, the standard deviations (σ), and relative differences of the averages from the right panel (Δ).

Fujiwara et al. (2017) argued that the observed small amplitude but coherent seafloor elevation change possibly reflect the coseismic seafloor displacement due to inelastic deformation or subsidiary fault movements, even though these values are comparable with potential errors. The result of newly added the MR1609-MR0707 survey track also demonstrates the similar trend of seafloor change, therefore may support the argument. Further consideration will be needed to discuss about the coseismic seafloor displacement in the tsunami source area.

However, as shown in the elongation of contours of **Figure 8**, the N-S direction is less constrained because the general trend of the bathymetry is subparallel to the N-S direction and the bathymetric variation in the direction is small (**Figure 2**). In consideration of the primary component of the coseismic displacements of the 2011 earthquake as suggested by seafloor geodetic measurements (Kido et al., 2011; Sato et al., 2011), horizontal displacements in the trench-normal direction seem plausible. Therefore, horizontal displacements in the trench-normal direction were also estimated. The horizontal displacements fall off less than 20 m (values in parentheses in **Figure 8**). Again, note that the uncertainty of 20 m may be involved in our estimation. Also due to the low spatial resolution of the pre-earthquake multibeam surveys, more than 20 m uncertainty in the distance may arise.

DISCUSSION

Estimation of Effects of Sound Velocity Correction

The SO251-KR0708 survey track intersects with the SO219-KR1012 track around 143°16′E (water depth ~2200 m), and also intersects with the MR1609-MR0707 track around 143°53′E (~4600 m) (marked P and Q in **Figure 5**). There are large discrepancies in depth difference values between two survey tracks at these intersections (**Figure 6A**). There are gaps of 8.9 m between the SO251-KR0708 data and the SO219-KR1012 data at the P intersection, and 7.3 m the SO251-KR0708 data and the MR1609-MR0707 data at the Q intersection.

Use of erroneous SVP is suggested as the cause of the discrepancy. Once input a SVP based on XBP or CTD

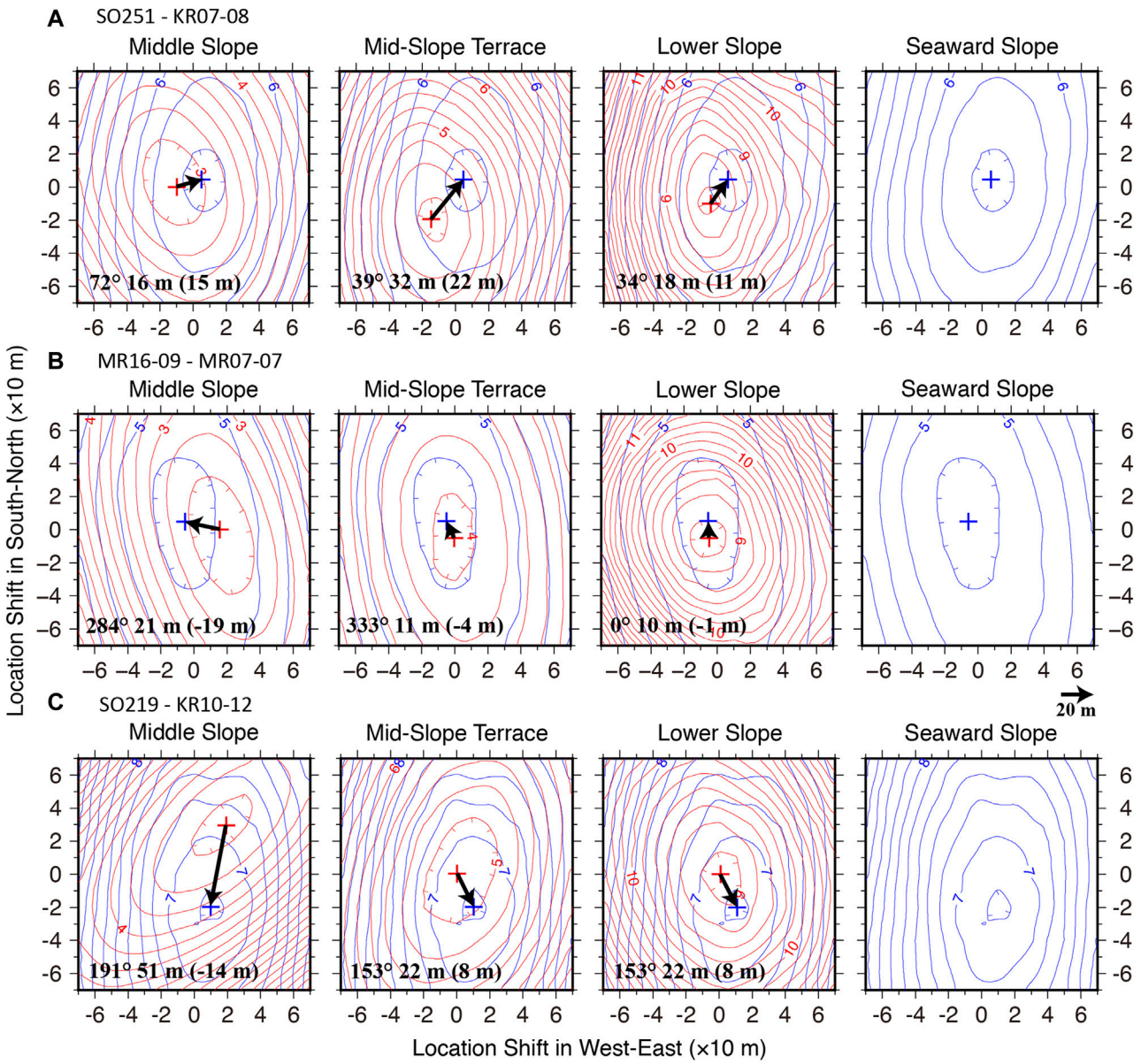

FIGURE 8 | Contour maps showing standard deviations of depth differences between different surveys for given shifted locations. **(A)** Comparison between KR07-08 and SO251A data, **(B)** comparison between MR07-07 Leg 3 and MR16-09 Leg 4 data, and **(C)** comparison between KR10-12 and SO219A data, respectively. The crosses indicate the minimum peaks of the standard deviations. The arrows show vectors of horizontal shifts from landward to seaward. Values in the maps indicate directions and lengths of the arrows, and values in parentheses are components in the trench-normal direction.

measurements into the echo sounder system gradually deviated from the actual SVP and probably became inaccurate because of the spatiotemporal change of the sound velocity structure. **Figure 9A** shows across track plots of depth differences of the post-earthquake SO251A sounding data from the post-earthquake SO219A depth grid of inner beams nadir parts at the P intersection. Water depths at inner beams are deeper, and the water depths at outer beams are shallower. Curvature of the measured profile is clearly visible. This phenomenon is nicknamed a 'smile' curve.

This is a typical feature that the used SVP is incorrect and the velocity through the water column from sea surface to seafloor is faster than the real one. The miscalculation results in the curvature bathymetry of over-estimate of water depth, which shallows with distance from center of the swath (**Figures 9C,G**, **10A,C,G**). In case the used SVP is slower than the real sound pathway velocity, the across track profile becomes a 'frown' curve (**Figures 9E**, **10E**). Usage of the correct SVP should make the shape of the depth difference profile flat across the track even though there is a static depth offset.

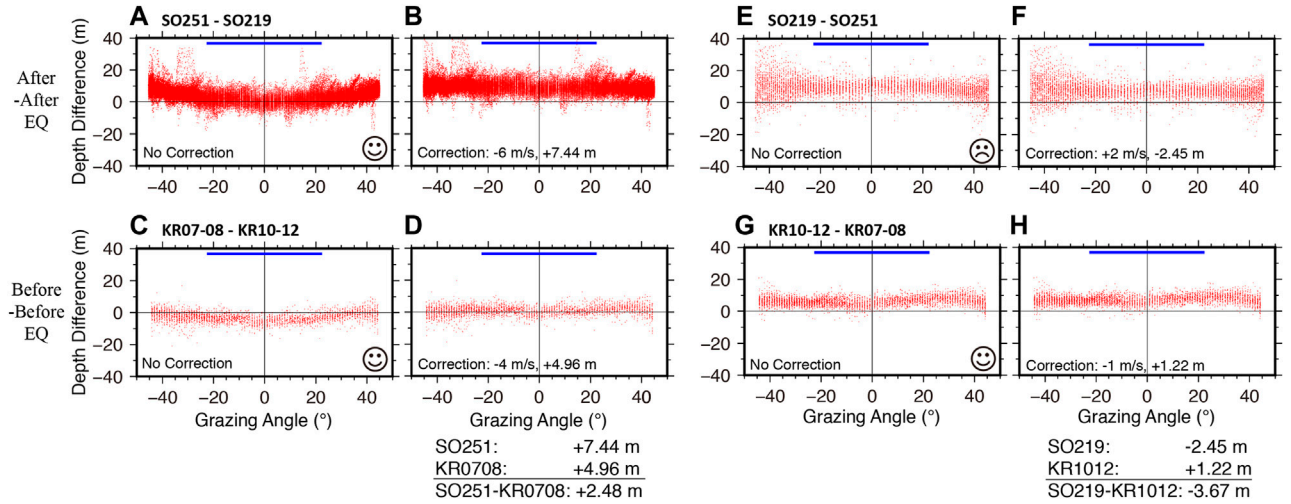

FIGURE 9 | Across track plots of depth differences at the P intersection. Red dots mark the depth differences at sounding locations. The location of grazing angle of 0° corresponds to the nadir of ship and the center of the swath. Upper panels show comparisons between data collected after the earthquake, and lower panels show comparisons between data collected before the earthquake. **(A)** Depth differences of the SO251A data from the SO219A data. **(B)** Sound velocity correction with decrease the average sound velocity of 0–2000 m by 6 m/s. **(C)** Depth differences of the KR07–08 data from the KR10–12 data. **(D)** Correction with decrease the average velocity by 4 m/s. **(E)** Depth differences of the SO219A data from the SO251A data. **(F)** Correction with increase the average sound velocity of 0–2000 m by 2 m/s. **(G)** Depth differences of the KR10-12 data from the KR07-08 data. **(H)** Correction with decrease the average velocity by 1 m/s. Blue bar scales indicate the swath range used for the seafloor displacement analysis (+/−22.5°).

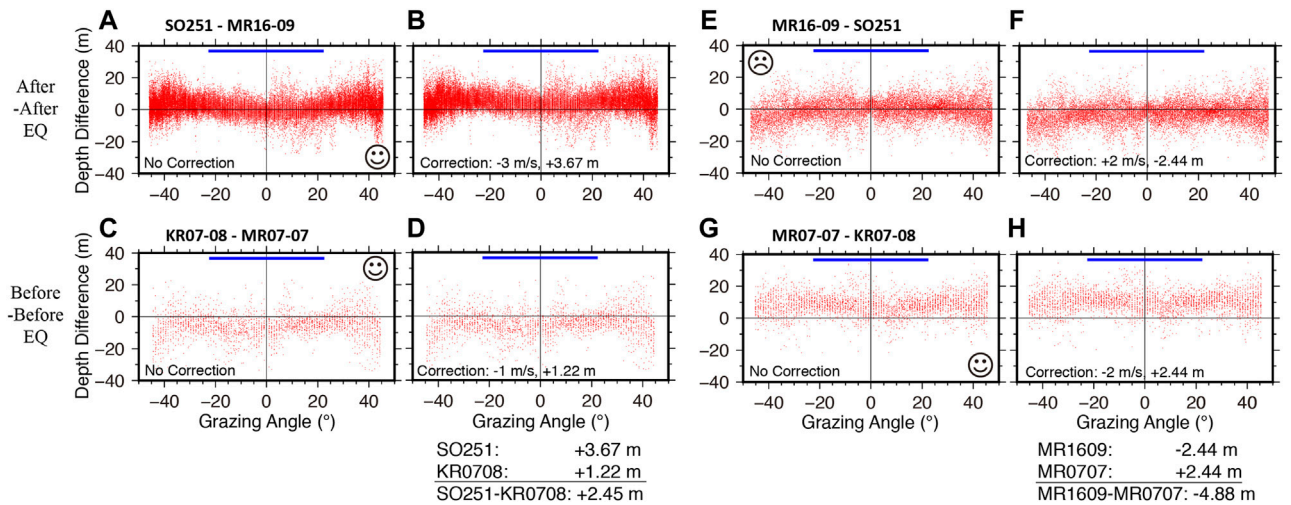

FIGURE 10 | Across track plots of depth differences at the Q intersection. Red dots mark the depth differences at sounding locations. The location of grazing angle of 0° corresponds to the nadir of ship and the center of the swath. Upper panels show comparisons between data collected after the earthquake, and lower panels show comparisons between data collected before the earthquake. **(A)** Depth differences of the SO251A data from the MR16-09 Leg 4 data. **(B)** Sound velocity correction with decrease the average sound velocity of 0–2000 m by 3 m/s **(C)** Depth differences of the KR07-08 data from the MR0707 Leg 3 data **(D)** Correction with decrease the average velocity by 1 m/s **(E)** Depth differences of the MR16-09 Leg 4 data from the SO251A data. **(F)** Correction with increase the average sound velocity of 0–2000 m by 2 m/s. **(G)** Depth differences of the MR07-07 Leg 3 data from the KR07-08 data.. **(H)** Correction with decrease the average velocity by 2 m/s. Blue bar scales indicate the swath range used for the seafloor displacement analysis (+/−22.5°).

We attempted sound velocity corrections for the multibeam bathymetric data by changing the average sound velocity from the water depth of 0 m down to 2000 m. The sound velocity deeper than 2000 m was not changed. In the situation that there is an error in the sound velocity, according to Snell's law, the following equation is established (**Figure 11**).

$$\frac{\sin\theta}{V_{ave}} = \frac{\sin(\theta + \Delta\theta)}{V_{ave} + \Delta V_{ave}} \quad (1)$$

where V_{ave} is average sound velocity from sea surface to seafloor, and ΔV_{ave} is error of the average sound velocity. θ is beam angle and the center of the swath is zero. $\Delta\theta$ is error of the beam angle.

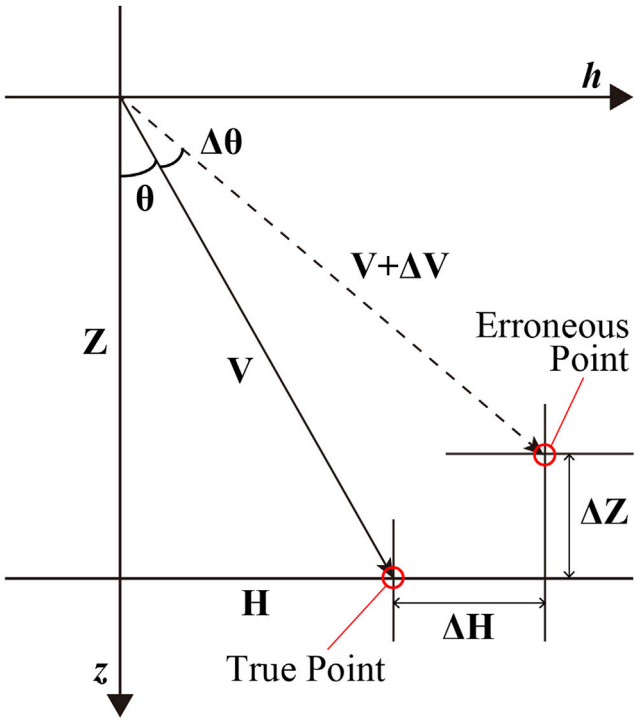

FIGURE 11 | Schematic figure of the bathymetric error derived from the sound velocity error.

In the case that $\Delta\theta$ is small, the relation of the error of beam angle and the error of average sound velocity is given as

$$\Delta\theta \approx \frac{\Delta V_{ave}}{V_{ave}} \tan\theta \tag{2}$$

The geometrical relations between the true sounding point and the erroneous sounding point are described by the following equations (**Figure 11**).

$$\frac{Z+\Delta Z}{Z} = \frac{V_{ave}+\Delta V_{ave}}{V_{ave}} \frac{\cos(\theta+\Delta\theta)}{\cos\theta} \tag{3}$$

$$\frac{H+\Delta H}{H} = \frac{V_{ave}+\Delta V_{ave}}{V_{ave}} \frac{\sin(\theta+\Delta\theta)}{sin\theta} \tag{4}$$

where Z is water depth, and ΔZ is error of the water depth. H is horizontal distance of sounding location, and ΔH is error of the horizontal distance of sounding location. H is denoted as

$$H = Z\tan\theta \tag{5}$$

Substituting **Eq. 2** into **Eq. 3** and **Eq. 4**, the following equations are derived.

$$\frac{\Delta Z}{Z} \approx \frac{\Delta V_{ave}}{V_{ave}}(1-\tan^2\theta) \tag{6}$$

$$\frac{\Delta H}{Z} \approx 2tan\,\theta \frac{\Delta V_{ave}}{V_{ave}} \tag{7}$$

The correction for the bathymetric data was performed using the approximation **Eqs 6**, **7**.

We searched the correction value by minimizing the standard deviation of the depth difference (**Figure 12**). As the result of the searching in the case of the SO251A data, sound velocity correction with decrease the average sound velocity of 0–2000 m by 6 m/s satisfies the condition. The average value of the water depth within the beam angle of 45° moved 7.44 m upward from the uncorrected data (**Figure 9B**). On the other hand, across track depth of the KR07-08 sounding data were compared with the pre-earthquake KR10-12 depth grid (**Figure 9C**). This profile also shows a 'smile'. Sound velocity correction with decrease the average sound velocity of 0–2000 m by 4 m/s satisfies the condition. The average value of the water depth within the beam angle of 45° moved 4.96 m upward from the uncorrected data (**Figure 9D**). Consequently, the depth difference value of the SO251-KR0708 survey is expected to be

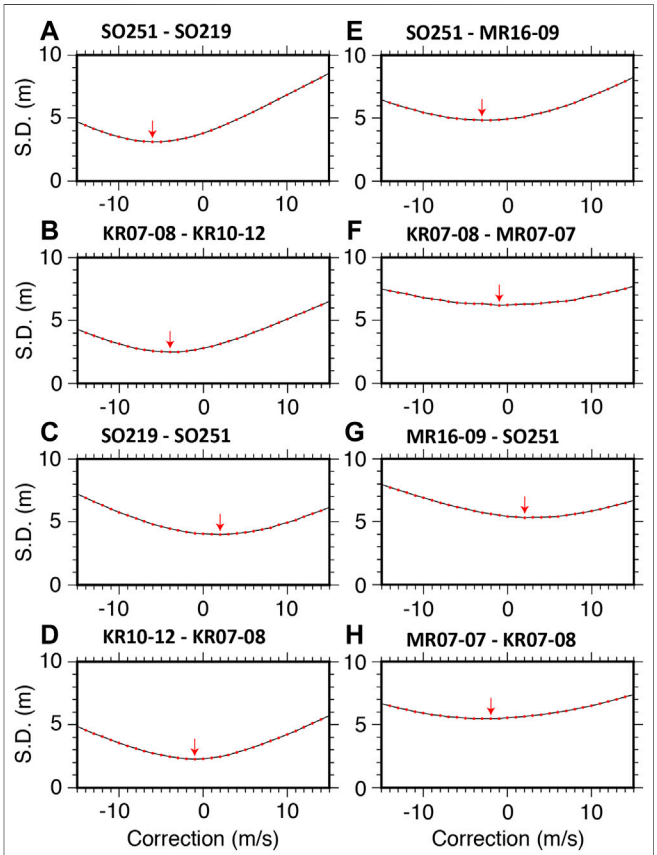

FIGURE 12 | Line graphs showing standard deviations of depth differences for given sound velocity corrections. At the P intersection, the standard deviations of depth differences of **(A)** the SO251A data from the SO219A data **(B)** the KR07-08 data from the KR10-12 data **(C)** the SO219A data from the SO251A data, and **(D)** the KR10-12 data from the KR07-08 data, respectively. At the Q intersection **(E)** the SO251A data from the MR16-09 Leg 4 data **(F)** the KR07-08 data from the MR07-07 Leg 3 data **(G)** the MR16-09 Leg 4 data from the SO251A data. **(H)** the MR07-07 Leg 3 data from the KR07-08 data, respectively. Red arrows point locations where the standard deviations are minimum, and indicate estimated values of the sound velocity corrections. S.D.: Standard deviation.

TABLE 1 | Acquisition parameters of the repeated multibeam bathymetric surveys.

Survey	Date	Echo-sounder	Survey speed (knot)	Course
Sonne SO251A	Oct. 2016	EM122	5	L*←S**
Kairei KR07-08	Jun. 2007	SeaBeam 2112	16	L→S
Mirai MR16-09	Mar. 2017	SeaBeam 3012	5	L←S
Mirai MR07-07	Feb. 2008	SeaBeam 2112	12	L←S
Sonne SO219A	Mar. 2012	EM120	6	L→S
Kairei KR10-12	Nov. 2010	SeaBeam 2112	16	L←S
Kairei KR11-E05	Aug. 2011	SeaBeam 2112	4	L←S
Yokosuka YK11-E05	Jun. 2011	SeaBeam 2112	5	L→S

*Landward.
**Seaward.

TABLE 2 | Sound velocity corrections on the SO251-KR0708 survey track.

After/Before EQ	Survey	Intersection			
		P		Q	
		Velocity correction (m/s)	Depth correction (m)	Velocity correction (m/s)	Depth correction (m)
A*	SO251	−6	+7.44	−3	+3.67
B**	KR0708	−4	+4.96	−1	+1.22
A-B	SO251-KR0708		+2.48		+2.45
A	MR1609			+2	−2.44
B	MR0707			−2	+2.44
A-B	MR1609-MR0707				−4.88
A	SO219	+2	−2.45		
B	KR1012	−1	+1.22		
A-B	SO219-KR1012		−3.67		

*After.
**Before.

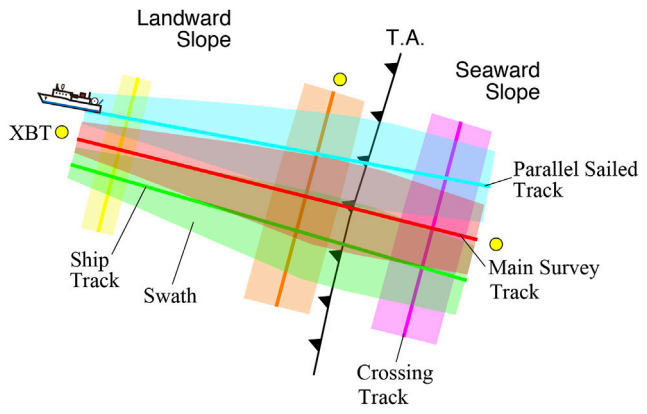

FIGURE 13 | Schematic figure of the repeated multibeam bathymetric survey.

2.48 m higher at the P intersection (Orange circles in **Figures 6A**, **9**). Other results of the sound velocity corrections following the same procedure are summarized in **Figures 9**, **10**; **Table 2**.

After the sound velocity corrections, the discrepancies of the depth differences between the survey tracks can be reduced successfully (**Figure 6A**). There will be gaps of 2.7 m between the SO251-KR0708 data and the SO219-KR1012 data at the P intersection, and 0 m the SO251-KR0708 data and the MR1609-MR0707 data at the Q intersection. The gap of 2.7 m still remains at the P intersection. The following are possible causes. The bathymetric data may be affected by ship's course changes in the *P* intersection area as shown in the bends of the SO219-KR1012 survey track (**Figure 5**). Since the adjustment of static depth differences and offsets of locations was estimated on the seaward slope, the error may be due to the inadequate and short length of the seaward slope area of the SO219-KR1012 survey track. The result of the attempt of sound velocity correction suggests that an appropriate sound velocity correction contributes improvement of estimation of the seafloor vertical displacement, although complete sound velocity corrections are not allowed in our surveys because of the limited number of cross tracks and no cross track on the seaward slope as the reference area.

Repeated Bathymetric Survey Plan for Seafloor Geodesy

During the bathymetric survey, multiple measurements of XBT or CTD along the survey track are necessary to know the spatiotemporal variation of SVPs. Designing of multi-track survey is of benefit to the sound velocity correction afterward. Several crossing tracks can observe a set of across-track curvature of the bathymetric profiles (**Figure 13**). Or parallel sailed tracks overlapping these multibeam swaths may be able to acquire data

for the sound velocity correction continuously. The frequency of XBT or CTD measurements and the number of auxiliary survey tracks probably depend on the oceanographic condition in the survey area. For example, the Japan Trench off Tohoku is a converging area of a warm current (Kuroshio) and a cold current (Oyashio). The oceanographic condition is complex and varies seasonally and spatially. Therefore, we should have conducted frequent SVP measurements and set several cross tracks. To constrain the sound velocity profile the whole length of the survey track, probably at least three control points are needed on the landward slope, at the trench axis, and on the seaward slope. Especially the reference point on the seaward slope is necessary because the adjustment of static depth differences was estimated on the seaward slope. An accomplished method for sound velocity correction in deep water and rough topography areas would be valuable. In the area, depth soundings vary widely and distort the shape of the curvature bathymetry. Gentle curves around the minimums as shown in **Figure 12** suggest the uncertainty of estimation and the less constraint condition.

The resolution and uncertainty of the results shown in our analyses largely depend on the quality of the pre-earthquake bathymetric data. These surveys were conducted with a speed of 12–16 knots in transit. Such high speed results in low spatial resolution (Fujiwara et al., 2015). An adequate survey speed keeping a good balance between a slow speed and a stable ship's attitude to obtain high spatial resolution and low noise data should be chosen.

In our surveys, precise roll and pitch biases calibration values were not given and thus were calibrated using the survey track data in the study area. However, the seaward slope is not always appropriate place for the roll and pitch bias calibrations. Especially, the pitch bias error seriously affects the estimation of the seafloor displacement. The pitch bias also could cause an error in estimation of depth difference on sloped seafloor areas. Obviously, calibration values of roll and pitch biases should be independently determined by a well-organized bias inspection survey. In the future, we will investigate these strategies and develop a more optimal design for the bathymetric survey.

CONCLUSION

The repeated bathymetric survey was carried out under the condition of the post-earthquake at an interval of two months using multibeam echo sounders one generation ago with slower speeds of 4-5 knots. XBT measurements to know *in-situ* sound velocity profiles (SVPs) might not be sufficient in time and space. The survey achieved the repeatability of less than ±1 m in the vertical direction and less than 20 m in the horizontal direction as shown in the results of the KR11E05-YK11E05 survey.

The repeated bathymetric surveys were conducted before and after the March 11, 2011 Tohoku-oki earthquake in the northern Japan Trench. We probably observed less than several meters in seafloor vertical displacements and less than 20 m in seafloor horizontal displacement on the outermost landward slope as shown in the results of the SO251-KR0708, the MR1609-MR0707, and the SO219-KR1012 surveys.

In light of the lessons learned from our surveys, the following strategies should be implemented to reduce uncertainties of measurements and to carry a potential to improve accuracy of the seafloor displacement observation when repeated bathymetric surveys for the purpose of seafloor geodesy are newly planed. The survey ship maintains a slower and stable speed so that high-density sampling and low noise data are obtained. The calibration values of roll and pitch biases independently determined should be given. During the bathymetric survey, multiple measurements of SVPs along the survey track are necessary to know the spatiotemporal variation of SVPs. A multi-track survey having crossing tracks or overlapping tracks may be of benefit to the sound velocity correction afterward.

Technology of multibeam echo sounders is constantly evolving. For the future, repeated acquisition of high resolution and accuracy bathymetric data using state-of-the-art technology is important to quantitative discussion of the seafloor displacement and the seafloor deformation caused by even smaller magnitude earthquakes and following tsunamis.

DATA AVAILABILITY STATEMENT

The original contributions presented in the study are included in the article, further inquiries can be directed to the corresponding author.

AUTHOR CONTRIBUTIONS

TF designed the research, contributed to the data acquisition, analyzed the data, prepared all figures, and wrote the manuscript.

FUNDING

The R/Vs Kairei, Yokosuka, and Mirai cruises' funding were from JAMSTEC, and the R/V Sonne cruises were supported by the Federal Ministry of Education and Research of Germany (BMBF) and German Research Foundation (DFG).

ACKNOWLEDGMENTS

I am grateful to A.K. Bachmann, C. dos Santos Ferreira, G. Fujie, Y. Kaiho, T. Kanamatsu, Y. Kaneda, T. Kasaya, S. Kodaira, A. Murata, T. No, T. Sato, M. Strasser, N. Takahashi, T. Takahashi, T. Sun, and G. Wefer for contribution to acquisitions of bathymetric data after the 2011 Tohoku-oki earthquake and in scientific discussions. I am also indebted to JAMSTEC Data Management Office for providing archived bathymetric data before the 2011 earthquake. I wish to thank two reviewers for their valuable comments in improving the manuscript. Bathymetric data used in this paper are available at JAMSTEC (http://www.godac.jamstec.go.jp/darwin/e) and at German Hydrographic Survey (BSH) databases (http://www.bsh.de/en/Marine_data/Hydrographic_surveys_and_wreck_search/Bathymetry/index.jsp). All the other datasets generated for this study are available on request to the corresponding author.

REFERENCES

Caress, D. W., Chayes, D. N., and dos Santos Ferreira, C. (2021). *MB-System: seafloor mapping software: Processing and display of swath sonar data*, CA, United States: Monterey Bay Aquarium Research Institute (MBARI). Available at: https://www.mbari.org/products/research-software/mb-system/

Dettmer, J., Hawkins, R., Cummins, P. R., Hossen, J., Sambridge, M., Hino, R., et al. (2016). Tsunami Source Uncertainty Estimation: The 2011 Japan Tsunami. *J. Geophys. Res. Solid Earth.* 121 (6), 4483–4505. doi:10.1002/2015JB012764

Fujiwara, T., dos Santos Ferreira, C., Bachmann, A. K., Strasser, M., Wefer, G., Sun, T., et al. (2017). Seafloor Displacement after the 2011 Tohoku-Oki Earthquake in the Northern Japan Trench Examined by Repeated Bathymetric Surveys. *Geophys. Res. Lett.* 44 (23), 833–911. doi:10.1002/2017GL075839

Fujiwara, T., Kodaira, S., No, T., Kaiho, Y., Takahashi, N., and Kaneda, Y. (2011). The 2011 Tohoku-Oki Earthquake: Displacement Reaching the Trench axis. *Science.* 334 (6060), 1240. doi:10.1126/science.1211554

Fujiwara, T., Masaki, Y., and Yamamoto, F. (2015). Evaluation of Spatial Resolution and Estimation Error of Seafloor Displacement Observation from Vessel-Based Bathymetric Survey by Use of AUV-Based Bathymetric Data. *Mar. Geophys. Res.* 36 (1), 45–60. doi:10.1007/s11001-014-9242-8

Hossen, M. J., Cummins, P. R., Dettmer, J., and Baba, T. (2015). Tsunami Waveform Inversion for Sea Surface Displacement Following the 2011 Tohoku Earthquake: Importance of Dispersion and Source Kinematics. *J. Geophys. Res. Solid Earth.* 120 (9), 6452–6473. doi:10.1002/2015JB011942

Hydrographic and Oceanographic Department, Japan Coast Guard and JAMSTEC (2011). Compilation of Tohoku-Oki Bathymetric Data before the 2011 Tohoku-Oki Earthquake (In Japanese). *Seismol Soc. Jpn. News Lett.* 23 (2), 35–36.

Kido, M., Osada, Y., Fujimoto, H., Hino, R., and Ito, Y. (2011). Trench-normal Variation in Observed Seafloor Displacements Associated with the 2011 Tohoku-Oki Earthquake. *Geophys. Res. Lett.* 38 (24), L24303. doi:10.1029/2011GL050057

Kodaira, S., Fujiwara, T., Fujie, G., Nakamura, Y., and Kanamatsu, T. (2020). Large Coseismic Slip to the Trench during the 2011 Tohoku-Oki Earthquake. *Annu. Rev. Earth Planet. Sci.* 48 (1), 321–343. doi:10.1146/annurev-earth-071719-055216

Kodaira, S., No, T., Nakamura, Y., Fujiwara, T., Kaiho, Y., Miura, S., et al. (2012). Coseismic Fault Rupture at the Trench axis during the 2011 Tohoku-Oki Earthquake. *Nat. Geosci.* 5 (9), 646–650. doi:10.1038/NGEO1547

Levitus, S. E. (1982). *Climatological Atlas of the World Ocean*. Washington DC: NOAA Professional Paper 13, US Government Printing Office, 173pp

Maksymowicz, A., Chadwell, C. D., Ruiz, J., Tréhu, A. M., Contreras-Reyes, E., Weinrebe, W., et al. (2017). Coseismic Seafloor Deformation in the Trench Region during the Mw8.8 Maule Megathrust Earthquake. *Sci. Rep.* 7, 45918. doi:10.1038/srep45918

Matsumoto, K., Takanezawa, T., and Ooe, M. (2000). Ocean Tide Models Developed by Assimilating TOPEX/POSEIDON Altimeter Data into Hydrodynamical Model: A Global Model and a Regional Model Around Japan. *J. Oceanography.* 56, 567–581. doi:10.1023/A:1011157212596

Nakamura, Y., Fujiwara, T., Kodaira, S., Miura, S., and Obana, K. (2020). Correlation of Frontal Prism Structures and Slope Failures Near the Trench axis with Shallow Megathrust Slip at the Japan Trench. *Sci. Rep.* 10, 11607. doi:10.1038/s41598-020-68449-6

Romano, F., Trasatti, E., Lorito, S., Piromallo, C., Piatanesi, A., Ito, Y., et al. (2014). Structural Control on the Tohoku Earthquake Rupture Process Investigated by 3D FEM, Tsunami and Geodetic Data. *Sci. Rep.* 4, 5631. doi:10.1038/srep05631

Satake, K., Fujii, Y., Harada, T., and Namegaya, Y. (2013). Time and Space Distribution of Coseismic Slip of the 2011 Tohoku Earthquake as Inferred from Tsunami Waveform Data. *Bull. Seismological Soc. America.* 103, 1473–1492. doi:10.1785/0120120122

Sato, M., Ishikawa, T., Ujihara, N., Yoshida, S., Fujita, M., Mochizuki, M., et al. (2011). Displacement above the Hypocenter of the 2011 Tohoku-Oki Earthquake. *Science.* 332, 1395. doi:10.1126/science.1207401

Sun, T., Wang, K., Fujiwara, T., Kodaira, S., and He, J. (2017). Large Fault Slip Peaking at Trench in the 2011 Tohoku-Oki Earthquake. *Nat. Commun.* 8, 14044. doi:10.1038/ncomms14044

Tappin, D. R., Grilli, S. T., Harris, J. C., Geller, R. J., Masterlark, T., Kirby, J. T., et al. (2014). Did a Submarine Landslide Contribute to the 2011 Tohoku Tsunami? *Mar. Geology.* 357, 344–361. doi:10.1016/j.margeo.2014.09.043

Tomita, F., Kido, M., Ohta, Y., Iinuma, T., and Hino, R. (2017). Along-trench Variation in Seafloor Displacements after the 2011 Tohoku Earthquake. *Sci. Adv.* 3, e1700113, doi:10.1126/sciadv.1700113

Watanabe, S.-i., Sato, M., Fujita, M., Ishikawa, T., Yokota, Y., Ujihara, N., et al. (2014). Evidence of Viscoelastic Deformation Following the 2011 Tohoku-Oki Earthquake Revealed from Seafloor Geodetic Observation. *Geophys. Res. Lett.* 41, 5789–5796. doi:10.1002/2014GL061134

Wessel, P., and Smith, W. H. F. (1991). Free Software Helps Map and Display Data. *EOS Trans. AGU.* 72, 441. doi:10.1029/90eo00319

Yamazaki, Y., Cheung, K. F., and Lay, T. (2018). A Self-Consistent Fault Slip Model for the 2011 Tohoku Earthquake and Tsunami. *J. Geophys. Res. Solid Earth.* 123, 1435–1458. doi:10.1002/2017JB014749

Conflict of Interest: The author declares that the research was conducted in the absence of any commercial or financial relationships that could be construed as a potential conflict of interest.

Advantages of publishing in Frontiers

OPEN ACCESS
Articles are free to read for greatest visibility and readership

FAST PUBLICATION
Around 90 days from submission to decision

HIGH QUALITY PEER-REVIEW
Rigorous, collaborative, and constructive peer-review

TRANSPARENT PEER-REVIEW
Editors and reviewers acknowledged by name on published articles

Frontiers
Avenue du Tribunal-Fédéral 34
1005 Lausanne | Switzerland

Visit us: www.frontiersin.org
Contact us: frontiersin.org/about/contact

REPRODUCIBILITY OF RESEARCH
Support open data and methods to enhance research reproducibility

DIGITAL PUBLISHING
Articles designed for optimal readership across devices

FOLLOW US
@frontiersin

IMPACT METRICS
Advanced article metrics track visibility across digital media

EXTENSIVE PROMOTION
Marketing and promotion of impactful research

LOOP RESEARCH NETWORK
Our network increases your article's readership